

# Guidelines for Determining Design Basis Ground Motions

## Volume 3: Appendices for Field Investigations



**WARNING:**  
Please read the Export Control  
Agreement on the back cover.

*Technical Report*

---

## **Guidelines for Determining Design Basis Ground Motions**

### **Volume 3: Appendices for Field Investigations**

Procedures currently used to assess the nature of earthquake ground motion in Eastern North America introduce considerable uncertainty to the design parameters of nuclear power plants and other critical facilities. This report examines that issue in-depth and provides an engineering model and guideline for selecting a site and assessing its seismic suitability.

#### **INTEREST CATEGORIES**

Nuclear seismic risk, design,  
and qualification  
Advanced light water  
reactors  
Risk analysis; management  
and assessment  
Nuclear plant life extension

#### **KEYWORDS**

Earthquakes  
Site characterization  
Hazard assessment  
Seismic engineering  
Seismology  
Geotechnical engineering

**BACKGROUND** Eastern North America has sparse earthquake activity with rare occurrences of large earthquakes; thus, little data exists to empirically quantify the characteristics of ground motions. Procedures currently used to estimate ground motion effects in this region introduce considerable uncertainty into the process of developing seismic designs, either due to the procedure's subjectivity or the lack of physical calibration.

**OBJECTIVES** To develop generic relations for estimating ground motion appropriate for site screening; to develop a guideline for conducting a thorough site investigation needed to define the seismic design basis.

**APPROACH** The project team specifically considered ground motions resulting from earthquakes with magnitudes from 5 to 8, fault distances from 0 to 500 km, and frequencies from 1 to 35 Hz. To develop generic ground motion relations for Eastern North America, they used theoretical models calibrated against data from earthquakes throughout North America and the world. In these models, the contributions to ground motion, including its variability, were evaluated using physical representations of earthquake processes. Earthquake processes involve the initial generation of seismic energy or waves at the earthquake fault ("source effects"), followed by the propagation of seismic waves through the earth's crust ("path effects"), and finally the modification of seismic waves as they travel through soils near the earth's surface ("site effects"). The team also collected and analyzed extensive geotechnical data at three reference sites. This information provided the basis for developing a guideline to help assess site suitability.

**RESULTS** This project resulted in an engineering model for estimating earthquake ground motions in Eastern North America. The model considers a wide range of earthquake sizes and site conditions and may be used directly for site screening purposes. The work also resulted in a guideline for conducting geotechnical and seismic engineering investigations needed to determine the design basis for a site. This guideline is appropriate for investigating a wide range of site conditions and soil depths within and outside Eastern North America.

**EPRI PERSPECTIVE** Cost-effective seismic regulation of nuclear power plants requires site-specific definition of seismic ground motions. The development of engineering procedures for estimating earthquake ground motion can thus benefit both operating and future plants. For licensing application, these procedures are needed

to define the safe shutdown earthquake (SSE). The regulatory guidance found in Section 2.5 of the Standard Review Plan (NUREG 0800) is quite limited in scope and does not reflect the current state of knowledge on earthquake phenomena. With no accepted generic procedures in place, utilities constantly face uncertainty associated with site-specific developments and applications. These factors result in seismic design bases that are excessively conservative and/or contribute to licensing delays, regulatory instability, and high utility costs in the licensing process.

In 1988, EPRI completed a seismic hazard model for the central and eastern United States (NP-4726), including a ground motion model (NP-6074). The present work directly complements NP-4726, while replacing and going significantly beyond the results of NP-6074. The engineering ground-motion model can be used for screening potential sites before conducting extensive site investigations. The guideline provides needed background information to conduct an appropriate geotechnical and seismic engineering investigation of a site for licensing purposes. Additional EPRI reports that provide a basis for the current report include: NP-5577, NP-5875, NP-6304, TR-100409, TR-100410, TR-102261, and TR-102262.

This report is presented in five volumes. Essential background, approach and results are given mainly in Volume 1. Volumes 2, 3, and 4 are appendices containing detailed analyses. Volume 5 (licensed material) contains *Quantification of Seismic Source Effects*, which is summarized in Volume 1, Section 4.

---

## **PROJECT**

RP3302

EPRI Project Manager: J. F. Schneider  
Nuclear Power Division

For further information on EPRI research programs, call  
EPRI Technical Information Specialists (415) 855-2411.

---

# **Guidelines for Determining Design Basis Ground Motions**

Volume 3:  
Appendices for Field Investigations

**TR-102293**  
**Research Project 3302**

Final Report, November 1993

Prepared by  
**ELECTRIC POWER RESEARCH INSTITUTE**  
in cooperation with the Joint Contractors  
(Southern Electric International, Commonwealth Research Corporation,  
and Public Service Corporation of New Jersey),  
the Nuclear Management and Resources Council,  
the U.S. Department of Energy and Sandia National Laboratories.

Prepared for  
**Electric Power Research Institute**  
3412 Hillview Avenue  
Palo Alto, California 94304

EPRI Project Manager  
J. F. Schneider

Advanced Reactors Development Administration  
Nuclear Power Division



## **DISCLAIMER OF WARRANTIES AND LIMITATION OF LIABILITIES**

THIS REPORT WAS PREPARED BY THE ORGANIZATION(S) NAMED BELOW AS AN ACCOUNT OF WORK SPONSORED OR COSPONSORED BY THE ELECTRIC POWER RESEARCH INSTITUTE INC. (EPRI). NEITHER EPRI, ANY MEMBER OF EPRI, ANY COSPONSOR, THE ORGANIZATION(S) NAMED BELOW, NOR ANY PERSON ACTING ON BEHALF OF ANY OF THEM:

(A) MAKES ANY WARRANTY OR REPRESENTATION WHATSOEVER, EXPRESS OR IMPLIED, (I) WITH RESPECT TO THE USE OF ANY INFORMATION, APPARATUS, METHOD, PROCESS, OR SIMILAR ITEM DISCLOSED IN THIS REPORT, INCLUDING MERCHANTABILITY AND FITNESS FOR A PARTICULAR PURPOSE, OR (II) THAT SUCH USE DOES NOT INFRINGE ON OR INTERFERE WITH PRIVATELY OWNED RIGHTS, INCLUDING ANY PARTY'S INTELLECTUAL PROPERTY, OR (III) THAT THIS REPORT IS SUITABLE TO ANY PARTICULAR USER'S CIRCUMSTANCE; OR

(B) ASSUMES RESPONSIBILITY FOR ANY DAMAGES OR OTHER LIABILITY WHATSOEVER (INCLUDING ANY CONSEQUENTIAL DAMAGES, EVEN IF EPRI OR ANY EPRI REPRESENTATIVE HAS BEEN ADVISED OF THE POSSIBILITY OF SUCH DAMAGES) RESULTING FROM YOUR SELECTION OR USE OF THIS REPORT OR ANY INFORMATION, APPARATUS, METHOD, PROCESS OR SIMILAR ITEM DISCLOSED IN THIS REPORT.

ORGANIZATION(S) THAT PREPARED THIS REPORT:

**ELECTRIC POWER RESEARCH INSTITUTE**

## **ORDERING INFORMATION**

Requests for copies of this report should be directed to the EPRI Distribution Center, 207 Coggins Drive, P.O. Box 23205, Pleasant Hill, CA 94523, (510) 934-4212. There is no charge for reports requested by EPRI member utilities.

Electric Power Research Institute and EPRI are registered service marks of Electric Power Research Institute, Inc.

Copyright © 1993 Electric Power Research Institute, Inc. All rights reserved.

# LIST OF COSPONSORS

---

## Early Site Permit Demonstration Program (ESPDP) Participants

Southern Electric International  
42 Inverness Center Parkway  
Birmingham, AL 25242

Commonwealth Research Corporation  
1400 Opus Place  
Downers Grove, IL 60515

Public Service Corporation of New Jersey  
80 Park Plaza, 11-A  
Newark, NJ 07101

Electric Power Research Institute  
3412 Hillview Ave.  
Palo Alto, CA 94303

Nuclear Management and Resources Council  
1776 Eye Street, Suite 300  
Washington, DC 2006

Department of Energy  
Office of Nuclear Energy  
19901 Germantown, MD 20874

Sandia National Laboratories  
1515 Eubank Boulevard Southeast  
Albuquerque, NM 87123



# PROGRAM PARTICIPANTS

---

## Participants

### Project Manager

Dr. John Schneider

## Affiliation

Electric Power Research Institute

### Principal Participants

Dr. Norman Abrahamson

Consultant

Dr. Donald Anderson

CH2M Hill, Inc.

Dr. Gail Atkinson

Consultant

Prof. Carl Costantino

City University of New York

Prof. I.M. Idriss

University of California at Davis

Dr. Robin K. McGuire

Risk Engineering, Inc.

Dr. Robert Nigbor

Agbabian Associates

Dr. Robert Pyke

Consultant

Dr. Walter Silva

Pacific Engineering & Analysis

Dr. Paul Somerville

Woodward-Clyde Consultants—Pasadena

Dr. J. Carl Stepp

Electric Power Research Institute

Prof. Kenneth Stokoe

University of Texas at Austin

Prof. M. Nafi Toksoz

Massachusetts Institute of Technology

Dr. Gabriel Toro

Risk Engineering, Inc.

Dr. Robert Youngs

Geomatrix Consultants

### Contributors

Prof. Keiiti Aki

Consultant

Dr. C. T. Chin

Moh & Associates, Taiwan

Dr. James Chin

University of Southern California

Dr. Shyh-Jeng Chiou

Geomatrix Consultants

Mr. Mark Fuhrman

University of Texas at Austin

Dr. Robert Graves

Woodward-Clyde Consultants

Prof. Robert Herrmann

St. Louis University

Mr. Seon-Keun Hwang

University of Texas at Austin

Mr. Athar Khwaja

University of Texas at Austin

Mr. Joseph Laird

University of Texas at Austin

Mr. David Lapp

Geomatrix Consultants

Mr. Ben T. Lin

Moh & Associates, Taiwan

Mr. Mihalios Madianos

Geomatrix Consultants

## Contributors

Dr. Batakrishna Mandal  
Mr. James McLaren  
Mr. Bruce Redpath  
Ms. Nancy Smith  
Ms. Cathy Stark  
Mr. Robert Steller  
Dr. Joseph Sun  
Dr. Y. T. Gu  
Mr. Ernest Heymsfield  
Dr. Xiao-ming Tang  
Mr. Chris Volksen  
Mr. Donald Wells  
Mr. Doug Wright  
Dr. Shen-Chyun Wu  
Ms. Joanne Yoshimura

Massachusetts Institute of Technology  
Woodward-Clyde Consultants  
Redpath Geophysics  
Woodward-Clyde Consultants  
Pacific Engineering & Analysis  
Agbabian Associates  
Woodward-Clyde Consultants  
City University of New York  
City University of New York  
Massachusetts Institute of Technology  
University of California at Davis  
Geomatrix Consultants  
Pacific Engineering & Analysis  
Risk Engineering, Inc.  
Consultant

# LIST OF CONTRACTORS

---

## Guidelines for Determining Design Basis Ground Motions

### TR-102293

Contract	Contractor
RP3302-02	Professor M. Nafi Toksoz Consultant 15 Walsingham St. Newton, MA 02162
RP3302-04	Professor Kenneth Stokoe Consultant 4602 Laurel Canyon Dr. Austin, TX 78731
RP3302-05	Professor I.M. Idriss Consultant P.O. Box 330 Davis, CA 95617-0330
RP3302-06	Dr. Gail Atkinson Consultant 125 Dunbar Road South Waterloo, Ontario N2L 2E8 CANADA
RP3302-07	Dr. Norman Abrahamson Consultant 5319 Camino Alta Mora Castro Valley, CA 94546
RP3302-08	Dr. Paul Somerville Woodward-Clyde Consultants 566 El Dorado St. Pasadena, CA 91101

**Contract**

RP3302-09

**Contractor**

Dr. Robin K. McGuire  
Risk Engineering, Inc.  
5255 Pine Ridge Road  
Golden, CO 80403

RP3302-10

Dr. Walter Silva  
Pacific Engineering and Analysis  
311 Pomona Avenue  
El Cerrito, CA 94530

RP3302-11

Dr. Robert Pyke  
Consultant  
1076 Carol Lane #136  
Lafayette, CA 94549

RP3302-12

Dr. Robert Youngs  
Geomatrix Consultants  
100 Pine Street—10th Floor  
San Francisco, CA 94111

RP3302-13

Dr. Donald Anderson  
CH2M Hill, Inc.  
P.O. Box 91500  
Bellevue, WA 98009-2050

RP3302-14

Professor Keiiti Aki  
Consultant  
622 Paseo de la Playa  
Redondo Beach, CA 90277

RP3302-15

Dr. Joseph Sun  
Woodward-Clyde Consultants  
500 12th Street, Suite 100  
Oakland, CA 94607-4014

RP3302-16

Dr. Robert Nigbor  
Agbabian Associates  
1111 South Arroyo Parkway  
Suite 405  
Pasadena, CA 91105

RP3302-18

Prof. Carl Costantino  
Consultant  
4 Rockingham Rd.  
Spring Valley, NY 10977

# ABSTRACT

---

This report develops and applies a method for estimating strong earthquake ground motion. The emphasis of this study is on ground motion estimation in Eastern North America (east of the Rocky Mountains), with particular emphasis on the Eastern United States and southeastern Canada. Specifically considered are ground motions resulting from earthquakes with magnitudes from 5 to 8, fault distances from 0 to 500 km, and frequencies from 1 to 35 Hz. The two main objectives were: (1) to develop generic relations for estimating ground motion appropriate for site screening; and (2) to develop a guideline for conducting a thorough site investigation needed to define the seismic design basis. For the first objective, an engineering model was developed to predict the expected ground motion on rock sites, with an additional set of amplification factors to account for the response of the soil column over rock at soil sites. The results incorporate best estimates of ground motion as well as the randomness and uncertainty associated with those estimates. For the second objective, guidelines were developed for gathering geotechnical information at a site and using this information in calculating site response. As a part of this development, an extensive set of geotechnical and seismic investigations was conducted at three reference sites. Together, the engineering model and guidelines provide the means to select and assess the seismic suitability of a site.





## ACKNOWLEDGMENTS

---

This project was made possible through extensive support from a great number of institutions and individuals.

For review of draft copies of the report, conducted under an extremely tight schedule, we much appreciate the thoughtful comments by the following individuals: Dr. Michael Bohn, Sandia National Laboratory; Prof. Ricardo Dobry, Rensselaer Polytechnic Institute; Mr. Jeff Kimball, Department of Energy; Dr. Takeji Kokusho, Central Research Institute of Electric Power Industry, Japan; and Dr. Scott Slezak, Sandia National Laboratory.

Field measurements at the reference sites at Treasure Island and Gilroy 2 in California and at Lotung, Taiwan, required considerable logistical coordination and cooperation between institutions and individuals. Major contributions to seismic and other geophysical measurements at Treasure Island and Gilroy 2 were made by Mr. Takashi Kanamori and Mr. Finn Michelson of Oyo Geospace, Mr. Kenji Tanaka of Oyo Corporation, and Mr. Ed Steller of Agbabian Associates. Extensive seismic measurements at Treasure Island and Gilroy 2 were also made by Dr. Ronald Andrus, Mr. Marwan Aouad, and Mr. James Bay of the University of Texas at Austin. Generous support from Mr. Thomas Fumal and Mr. James Gibbs of the U.S. Geological Survey is also acknowledged for their contribution to geologic and seismic logging, respectively, of boreholes at the Gilroy 2 and Treasure Island sites. The following companies assisted the project by providing special equipment used in the measurements: ANCO Engineers, Kinematics, Inc., Oyo Corporation, and Redpath Geophysics.

For making arrangements or generously providing access to the reference sites, we are grateful to numerous individuals. We thank Ms. Susan Chang and Dr. Lelio Mejia of Woodward-Clyde Associates for assistance in logistics of drilling at Gilroy 2. Special thanks to Mr. Richard Lake and Mr. Roger Kostenko of Pitcher Drilling Co. for their excellence in drilling and sampling at the Gilroy 2 and Treasure Island sites. Drilling at Lotung, Taiwan, was coordinated expertly by Moh & Associates. We thank Mr. Y. H. Cheng, Deputy Director of the Nuclear Engineering Department at Taiwan Power Co., for helping with access to drilling at the Lotung site owned by Taiwan Power Co. For access to Gilroy 2, we thank Mr. John Belleau, site owner, and Mr. Roger and Ms. Marie Ellissondo, site managers (National 9 Inn). For Treasure Island site access, we thank Mr. Thomas Cuckler and Mr. Donald Brown of the Civil Engineering Department of the Treasure Island Naval Air Station.

Additional data were also generously provided by many individuals and institutions from complementary field measurements at various field test sites. Prof. Pedro de Alba of the University of New Hampshire, Mr. John Egan of Geomatrix Consultants, Prof. Roman Hryciw of the University of Michigan, and Prof. Kyle Rollins of Brigham Young University all generously provided data for our use from other geotechnical studies at Treasure Island. Sponsors of studies that produced these data were the U.S. Naval Air Station and the National Science Foundation. Prof. Pedro de Alba also provided access to boreholes drilled for several of these studies, also sponsored by the National

Science Foundation. Mr. Jeff Kimball of the Department of Energy made it possible to use a collection of geotechnical data from a site at the Savannah River site, South Carolina.

All of the laboratory measurements of dynamic properties of soil samples from the reference sites were performed at the Geotechnical Engineering Center of the University of Texas at Austin (GEC-UT). The large-scale chamber tests used to study field damping measurements were also performed at the GEC-UT. We thank Mr. Ngarkok Lee and Mr. Mark Twede of that institution for their assistance in this work. Further, the assistance of Ms. Teresa Tice-Boggs of the Geotechnical Engineering Center contributed significantly to the success of this work.

Several people assisted in providing and assembling data for the earthquake database used in this project. We appreciate the help of Mr. Phillip Munro of the Geological Survey of Canada for information regarding characteristics of strong-motion instrument sites for data recorded during the 1988 Saguenay, Quebec, earthquake and aftershocks.

Dr. David Boore of the U. S. Geological Survey provided an analysis of the distribution of selected ground motion data recorded on Wood-Anderson seismographs in southern California. Dr. Gail Atkinson provided seismic data and site descriptions from the Eastern Canada Telemetered Seismic Network.

We would like to thank the following people for their participation in various workshops held during the course of the project: Dr. David Boore, Dr. Jon Fletcher, Mr. Thomas Fumal, Mr. James Gibbs, Dr. William Joyner, and Dr. John Vidale of the U.S. Geological Survey; Mr. Scott Ashford, University of California at Berkeley; Ms. Ornella Bonamassa, University of California at Santa Cruz; Dr. David Rodgers, Rogers Pacific Consultants; Mr. Takashi Kanamori and Mr. Finn Michelson of Oyo Geospace; Dr. Clifford Roblee, California Department of Transportation; and Dr. Richard Lee, Westinghouse Savannah River Co. These individuals participated in numerous stimulating discussions that greatly contributed to the final product.

Finally, it is with great appreciation for the financial and managerial support, and, equally important the trust and confidence provided us, that we thank various individuals within and associated with the Department of Energy and utility industry for making the project possible. Special thanks to Ms. Susan Gray, Mr. Murv Little, and Mr. Joseph Santucci of the EPRI Advanced Reactor Program for their generous support, and especially to Ms. Gray for her direction as project manager of the Early Site Permit Demonstration Program. Thanks to Mr. Walter Pasedag of the Department of Energy and Mr. Ajoy Moonka of Sandia National Laboratory; to the Industry Siting Group, especially Mr. Louis Long; to the Nuclear Management and Resources Council (NUMARC), especially Mr. John Ronafalvy; to the Joint Contractors comprised of Southern Electric International, Commonwealth Research Corporation, and Public Service Company of New Jersey, especially Dr. Ninu Kaushal (Commonwealth Edison Co.).

# CONTENTS

---

## Volume 3: APPENDICES FOR FIELD INVESTIGATION

Appendix	Page
<b>Executive Summary</b> .....	<b>ES-1</b>
<b>8.A.1 Crosshole Seismic Tests at the Gilroy 2 and Treasure Island Sites</b>	
1— Introduction .....	8.A.1-13
8.A.1.1.1 Background Information .....	8.A.1-13
8.A.1.1.2 Objectives .....	8.A.1-13
8.A.1.1.3 Organization .....	8.A.1-13
2— Crosshole Equipment, Procedures and Analyses .....	8.A.1-16
8.A.1.2.1 Introduction .....	8.A.1-16
8.A.1.2.2 Equipment .....	8.A.1-16
8.A.1.2.3 Field Procedures .....	8.A.1-25
8.A.1.2.4 Wave Velocity Analysis .....	8.A.1-27
8.A.1.2.5 Material Damping Analyses at Gilroy 2 .....	8.A.1-32
8.A.1.2.6 Summary .....	8.A.1-38
3— Wave Velocities from Crosshole Testing at Gilroy 2 .....	8.A.1-39
8.A.1.3.1 Introduction .....	8.A.1-39
8.A.1.3.2 Borehole Inclination Survey .....	8.A.1-47
8.A.1.3.3 Shear Wave Velocities .....	8.A.1-47
8.A.1.3.4 Anisotropy in SV- and SH-Wave Velocities .....	8.A.1-64
8.A.1.3.5 Compression Wave Velocities .....	8.A.1-72
8.A.1.3.6 Summary and Conclusions .....	8.A.1-83
4— Wave Velocities from Crosshole Testing at Treasure Island .....	8.A.1-84
8.A.1.4.1 Introduction .....	8.A.1-84
8.A.1.4.2 Borehole Inclination Survey .....	8.A.1-88
8.A.1.4.3 Shear Wave Velocities .....	8.A.1-94
8.A.1.4.4 Anisotropy in SV- and SH-Wave Velocities .....	8.A.1-114
8.A.1.4.5 Compression Wave Velocities .....	8.A.1-122
8.A.1.4.6 Summary and Conclusions .....	8.A.1-131

5—Material Damping Measurements at Gilroy 2 .....	8.A.1-132
8.A.1.5.1 Introduction .....	8.A.1-132
8.A.1.5.2 Time-Domain in Windowing of Waveforms .....	8.A.1-132
8.A.1.5.3 Material Damping Using the Short Time Window .....	8.A.1-134
8.A.1.5.4 Material Damping Using the Long Time Window .....	8.A.1-139
8.A.1.5.5 Results of All Material Damping Analyses at Gilroy 2 .....	8.A.1-145
8.A.1.5.6 Summary and Conclusions .....	8.A.1-167
6—Summary and Conclusions .....	8.A.1-168
8.A.1.6.1 Summary .....	8.A.1-168
8.A.1.6.2 Conclusions .....	8.A.1-168
Appendix 8.A.1.A—Tabulated Results of Crosshole Tests at Gilroy 2 .....	8.A.1-170
Appendix 8.A.1.B—Tabulated Results of Crosshole Tests at Treasure Island .....	8.A.1-193
References .....	8.A.1-220

## 8.A.2 Borehole Geophysical Measurements at the Gilroy 2 and Treasure Island Sites

1—Overview .....	8.A.2-5
2—Measurement Techniques and Procedures .....	8.A.2-8
8.A.2.2.1 Resistivity Logging .....	8.A.2-8
8.A.2.2.2 Natural Gamma Logging .....	8.A.2-8
8.A.2.2.3 Caliper Logging .....	8.A.2-9
8.A.2.2.4 Borehole Drift Logging .....	8.A.2-9
8.A.2.2.5 Suspension PS Velocity Logging .....	8.A.2-9
8.A.2.2.6 Cross-Hole Velocity Measurement .....	8.A.2-13
8.A.2.2.7 Attenuation Measurement .....	8.A.2-17
3—Results .....	8.A.2-20
8.A.2.3.1 Gilroy 2 .....	8.A.2-20
8.A.2.3.2 Treasure Island .....	8.A.2-34
4—Summary .....	8.A.2-45
References .....	8.A.2-46

## 8.A.3 Determination of In Situ Seismic Attenuation

1—Introduction .....	8.A.3-7
8.A.3.1.1 Definitions of the Attenuation Parameter .....	8.A.3-8
8.A.3.1.2 Determination of Site Attenuation .....	8.A.3-10
2—In-Situ Measurement of Attenuation .....	8.A.3-12
8.A.3.2.1 Field Measurements .....	8.A.3-12
8.A.3.2.2 Attenuation Determination .....	8.A.3-13

## Appendix

Page

3—Attenuation Results From Field Data .....	8.A.3-19
8.A.3.3.1 Treasure Island Cross-Hole Data .....	8.A.3-19
8.A.3.3.2 Gilroy 2 Cross-Hole Data .....	8.A.3-34
8.A.3.3.3 Attenuation From Downhole (VSP) Data .....	8.A.3-34
4—Conclusions .....	8.A.3-64
References .....	8.A.3-65
Appendix 8.A.3.A. Estimating Attenuation Through Waveform Inversion .....	8.A.3-67
Appendix 8.A.3.B. Q Measurements: The Effect of Layering .....	8.A.3-73

### 8.A.4 Downhole Seismic Tests at Gilroy 2 and Treasure Island

8.A.4.1 Introduction .....	8.A.4-1
8.A.4.2 Instrumentation and Procedures .....	8.A.4-1
8.A.4.2.1 Downhole Velocity Surveys .....	8.A.4-1
8.A.4.3 Results .....	8.A.4-2
8.A.4.3.1 Downhole Surveys .....	8.A.4-2
Appendix 8.A.4.A. Reproductions of Downhole Shear Wave Records .....	8.A.4-11

### 8.A.5 Geotechnical Boring and Sampling at Treasure Island and Gilroy 2 Strong Motion Accelerograph Sites

1—Introduction .....	8.A.5-1
2—Geotechnical Field Investigation Procedures .....	8.A.5-2
8.A.5.2.1 Soil Sites .....	8.A.5-2
3—Naval Station Treasure Island .....	8.A.5-4
8.A.5.3.1 Authorization and Permitting .....	8.A.5-4
8.A.5.3.2 Subsurface Site Conditions .....	8.A.5-4
8.A.5.3.3 Loma Prieta Earthquake .....	8.A.5-8
8.A.5.3.4 Site Contacts .....	8.A.5-8
4—Gilroy Array 2 (National 9 Inn) .....	8.A.5-9
8.A.5.4.1 Authorization and Permitting .....	8.A.5-9
8.A.5.4.2 Subsurface Site Conditions .....	8.A.5-9
8.A.5.4.3 Loma Prieta Earthquake .....	8.A.5-13
8.A.5.4.4 Site Contacts .....	8.A.5-13
5—Limitations .....	8.A.5-14
Appendix 8.A.5.A. Boring Logs for Treasure Island and Gilroy 2 .....	8.A.5-15
Appendix 8.A.5.B. Additional Boring Logs at Gilroy 2 by USGS .....	8.A.5-48

**8.A.6 Geotechnical Boring and Sampling of the Lotung, Taiwan Site**

Summary .....	8.A.6-1
1—Introduction .....	8.A.6-5
2—Scope of Work .....	8.A.6-6
3—Site Investigation .....	8.A.6-7
8.A.6.3.1 Background .....	8.A.6-7
8.A.6.3.2 Drilling and Sampling .....	8.A.6-7
8.A.6.3.3 SPT's .....	8.A.6-8
8.A.6.3.4 PVC Casing Installation .....	8.A.6-8
8.A.6.3.5 Laboratory Testing .....	8.A.6-8
8.A.6.3.6 Subsoil Conditions .....	8.A.6-8
8.A.6.3.7 Groundwater Condition .....	8.A.6-9
References .....	8.A.6-10
Appendix 8.A.6.A—Subsurface Exploration Logs .....	8.A.6-19
Appendix 8.A.6.B—Laboratory Testing .....	8.A.6-28

# EXECUTIVE SUMMARY

---

## Introduction

This report develops and applies a method for estimating strong earthquake ground motion. The motivation for this development was the need for a systematic, physically based, empirically calibrated method that can be used to estimate ground motions for input to the design of nuclear power plants and other critical facilities. These ground motions are a function of the earthquake's magnitude and the physical properties of the earth through which the seismic waves travel from the earthquake fault to the site of interest. Procedures currently used to account for these effects introduce considerable uncertainty into the ground motion determination, either due to subjectivity of the procedure or the lack of physical calibration.

The emphasis of this study is on ground motion estimation in Eastern North America (east of the Rocky Mountains), with particular emphasis on the Eastern United States and southeastern Canada. Eastern North America is a stable continental region, having sparse earthquake activity with rare occurrences of large earthquakes. In the absence of large earthquakes within the region of interest, little data exist to empirically quantify the characteristics of ground motions associated with these events. While methods developed in more seismically active areas such as Western North America can be applied to Eastern North America, fundamental differences in the regional geology can lead to variations in ground motion characteristics. Therefore, empirically based approaches that are applicable for other regions, such as Western North America, do not appear to be appropriate for Eastern North America.

Recent advances in science and technology have now made it possible to combine theoretical and empirical methods to develop new procedures and models for estimating ground motion within Eastern North America. Specifically considered are ground motions resulting from earthquakes with magnitudes from 5 to 8, fault distances from 0 to 500 km, and frequencies from 1 to 35 Hz. The results of this report can be used to determine seismic hazards, provided the magnitudes and distances of potential earthquakes are predetermined. In particular, this report is intended for use in site screening as well as detailed characterization of ground motion at a site, such as may be required for structural design.

This study was conducted by a team of experts in seismology, geotechnical engineering, and seismic engineering. The investigations were carried out over a period of approximately 18 months from September 1991 to March 1993. Work included a series of focused workshops with project participants to help achieve consensus recommendations. The project was sponsored by the U. S. Department of Energy (DOE), Sandia National Laboratories, Southern Electric International, Commonwealth Research Corporation, Public Service Company of New Jersey, and the Electric Power Research Institute as part of the DOE's Early Site Permit Demonstration Program. The project was managed by the Electric Power Research Institute.



## Objectives

There were two central objectives of the project: (1) to develop generic relations for estimating ground motion appropriate for site screening; and (2) to develop a guideline for conducting a thorough site investigation needed to define the seismic design basis. For the first objective, a set of relations was needed that could be used to predict the expected ground motion on rock or on soil for a future earthquake. The approach was to develop an engineering model consisting of relations appropriate for rock sites and an additional set of amplification factors to account for the response of the soil column over rock at soil sites. For the second objective, a guideline was developed for gathering geotechnical information at a site and using this information in calculating site response. Together, the engineering model and guideline provide the means to select and assess the seismic suitability of a site.

## Approach

The method that was used to develop generic ground motion relations in this effort is markedly different from the approach of previous studies. In this study, theoretical models, which have been calibrated against data from earthquakes throughout North America and the world, are used to characterize earthquake ground motion in Eastern North America. In these models, the contributions to ground motion, including its variability, are evaluated using physical representations of earthquake processes. These processes involve the initial generation of seismic energy or waves at the earthquake fault ("source effects"), followed by the propagation of seismic waves through the earth's crust ("path effects"), and finally the modification of seismic waves as they travel through soils near the earth's surface ("site effects"). For a given earthquake magnitude and distance, the source, path, and site each contribute to the observed ground motion, as follows:

- The source controls both the seismic energy generated by rupture of an earthquake fault as well as the accompanying dynamic characteristics.
- The seismic path contributes to ground motion through reflection, refraction, and damping of seismic waves within the earth's crust in response to the various physical properties along the wave path.
- The site contributes to the evolution of seismic waves in much the same way as the path, though on a smaller scale. Site effects are a function primarily of soil depth and type.

The characteristics of the seismic source, path, and site effects form the basis for the parameters in the theoretical models.

The ground motion relations for rock sites were developed using a physically based, empirically calibrated ground motion model. In the model, a wide range of values was assigned to the ground motion parameters. Using the combination of all model parameters and their ranges of values, computer simulations produced hundreds of records of earthquake ground motion for each magnitude and distance considered. While each earthquake simulation represents a possible future earthquake, each earthquake is not equally likely to occur. Therefore, based upon extensive analyses of past earthquakes and comparisons to model predictions, distributions were assigned to the values for all model parameters. The parameter value distributions were based on partitioning their variability into two types: uncertainty, which is due to the lack of knowledge of earthquake characteristics; and randomness, which is due to the inherent variability of those characteristics. Finally, individual parameter weights were combined for each earthquake simulation to produce the appropriate "distribution" of earthquake ground motion for every magnitude, distance, and frequency considered. Together, these distributions constitute a family of functional relations that define the final engineering ground motion model for rock sites. In turn, the engineering model defines ground motion for median levels and associated variability.

To accommodate sites with soil overlying rock (referred to as local site effects), site amplification factors were developed for a range of soil types and depths representative of soil conditions in Eastern North America. The factors were derived by first accumulating data that describe the behavior of various soils during seismic loading. These

data were then used to assess the variability in seismic properties, especially the wave velocity as it changes with depth. In addition, seismic velocity and material damping data were gathered from three reference sites using a variety of field and laboratory techniques. The reference site data were used (1) to improve physical understanding of the dynamic processes of soil response and (2) to assess procedures for measuring the physical properties needed to estimate site effects. The estimation problem is particularly difficult because the seismic properties of soils change depending upon the level of shaking. The resulting “nonlinear” effects generally cause the ratio of soil-to-rock motions (i.e., soil amplification) to decrease as the corresponding rock motion increases. The quantification of these effects through theoretical modeling and comparisons to empirical data resulted in factors that describe the amplification of soils relative to rock for several soil categories. The amplification factors were developed for a wide range of rock motions and are given as median values with variability.

Finally, based upon extensive geotechnical data that were collected at the three reference sites and analyzed as part of this program, a guideline was developed for assessing soil characteristics and site response. This guideline applies to planning and conducting a systematic and thorough geotechnical investigation of soil properties at a potential site. Guidance is also provided for performing dynamic analyses required to determine the response of the soil column to earthquake shaking at (and beyond) the levels of motion of interest to the seismic design.

## Conclusions

The engineering ground motion model developed in this study can be used for screening potential sites in Eastern North America before conducting extensive site investigations. However, the application of these procedures to site screening requires information regarding earthquake magnitudes and distances as well as certain site properties such as soil depth and site geology. Magnitudes and distances of potential earthquakes may be derived either probabilistically or deterministically.

The guideline—together with the results of investigations of the three reference sites—provides the means to conduct an appropriate geotechnical and seismic engineering site investigation. In all, this guideline is appropriate for use given a wide range of site conditions and soil depths. While there are certain soil types (e.g., those with liquefaction potential) for which this guideline may not be directly applicable, it may be used widely both within and outside Eastern North America.

The information compiled in this report represents a comprehensive assessment of the nature of earthquake ground motion in Eastern North America. The results incorporate best estimates of ground motion as well as the randomness and uncertainty associated with those estimates for a wide range of earthquake magnitudes, distances, and frequencies. Overall, the results of this study will be useful in performing seismic hazard evaluations and establishing seismic design standards for many years to come.

## Organization

The results of this study are presented in five volumes. *Volume I: Methodology and Guidelines for Estimating Earthquake Ground Motion in Eastern North America*, representing the main body of the report, presents the model development and summarizes the key results and conclusions of the study. *Volume II: Appendices for Ground Motion Estimation*, presents the appendices to Sections 2 to 7 of Volume I, and consists primarily of data and details of analyses used to develop the engineering ground motion model and geotechnical guidelines. *Volume III: Appendices for Field Investigations*, and *Volume IV: Appendices for Laboratory Investigations*, present the details of field and laboratory investigations of reference sites; Section 8 of Volume 1 constitutes a summary of these appendices. *Volume V: Seismic Source Effects*, presents separately (as a licensed report) the analyses of the seismic source performed for input to the engineering ground motion model; a summary of this volume is given as Section 4 of Volume 1.



# APPENDIX 8.A.1

## CROSSHOLE SEISMIC TESTS AT THE GILROY 2 AND TREASURE ISLAND SITES

---

### CONTENTS

Section	Page
<b>1—Introduction</b> .....	<b>8.A.1-13</b>
8.A.1.1.1 Background Information .....	8.A.1-13
8.A.1.1.2 Objectives .....	8.A.1-13
8.A.1.1.3 Organization .....	8.A.1-13
<b>2—Crosshole Equipment, Procedures and Analyses</b> .....	<b>8.A.1-16</b>
8.A.1.2.1 Introduction.....	8.A.1-16
8.A.1.2.2 Equipment .....	8.A.1-16
8.A.1.2.2.1 Seismic Sources .....	8.A.1-17
8.A.1.2.2.2 Seismic Receivers .....	8.A.1-23
8.A.1.2.2.3 Recording Equipment .....	8.A.1-24
8.A.1.2.3 Field Procedures .....	8.A.1-25
8.A.1.2.3.1 Test Set-Up .....	8.A.1-25
8.A.1.2.3.2 Data Collection .....	8.A.1-27
8.A.1.2.4 Wave Velocity Analysis .....	8.A.1-27
8.A.1.2.4.1 Travel Time Determination .....	8.A.1-27
8.A.1.2.4.2 Borehole Inclination Survey .....	8.A.1-31
8.A.1.2.5 Material Damping Analyses at Gilroy 2 .....	8.A.1-32
8.A.1.2.5.1 Spectral Ratio Method .....	8.A.1-34
8.A.1.2.5.2 Spectral Slope Method .....	8.A.1-37
8.A.1.2.6 Summary .....	8.A.1-38
<b>3—Wave Velocities from Crosshole Testing at Gilroy 2</b> .....	<b>8.A.1-39</b>
8.A.1.3.1 Introduction .....	8.A.1-39
8.A.1.3.2 Borehole Inclination Survey .....	8.A.1-47

Section	Page
8.A.1.3.3 Shear Wave Velocities .....	8.A.1-47
8.A.1.3.3.1 SV-Wave Velocities .....	8.A.1-52
8.A.1.3.3.2 Comparison of $V_S$ with Empirical Results .....	8.A.1-62
8.A.1.3.3.3 SH-Wave Velocities .....	8.A.1-64
8.A.1.3.4 Anisotropy in SV- and SH-Wave Velocities .....	8.A.1-64
8.A.1.3.5 Compression Wave Velocities .....	8.A.1-72
8.A.1.3.6 Summary and Conclusions .....	8.A.1-83
<b>4—Wave Velocities from Crosshole Testing at Treasure Island .....</b>	<b>8.A.1-84</b>
8.A.1.4.1 Introduction .....	8.A.1-84
8.A.1.4.2 Borehole Inclination Survey .....	8.A.1-88
8.A.1.4.3 Shear Wave Velocities .....	8.A.1-94
8.A.1.4.3.1 SV-Wave Velocities .....	8.A.1-94
8.A.1.4.3.2 Comparison of $V_S$ with Empirical Results .....	8.A.1-108
8.A.1.4.3.3 SH-Wave Velocities .....	8.A.1-110
8.A.1.4.4 Anisotropy in SV-Wave and SH-Wave Velocities .....	8.A.1-114
8.A.1.4.5 Compression Wave Velocities .....	8.A.1-122
8.A.1.4.6 Summary and Conclusions .....	8.A.1-131
<b>5—Material Damping Measurements at Gilroy 2 .....</b>	<b>8.A.1-132</b>
8.A.1.5.1 Introduction .....	8.A.1-132
8.A.1.5.2 Time-Domain Windowing of Waveforms .....	8.A.1-132
8.A.1.5.3 Material Damping Using the Short Time Window .....	8.A.1-134
8.A.1.5.3.1 Spectral Ratio Method .....	8.A.1-136
8.A.1.5.3.2 Spectral Slope Method .....	8.A.1-139
8.A.1.5.4 Material Damping Using the Long Time Window .....	8.A.1-139
8.A.1.5.4.1 Spectral Ratio Method .....	8.A.1-139
8.A.1.5.4.2 Spectral Slope Method .....	8.A.1-139
8.A.1.5.5 Results of All Material Damping Analyses at Gilroy 2 .....	8.A.1-145
8.A.1.5.6 Summary and Conclusions .....	8.A.1-167
<b>6—Summary and Conclusions .....</b>	<b>8.A.1-168</b>
8.A.1.6.1 Summary .....	8.A.1-168
8.A.1.6.2 Conclusions .....	8.A.1-168
8.A.1.6.2.1 Body Wave Velocities .....	8.A.1-168
8.A.1.6.2.2 In Situ Damping Measurements .....	8.A.1-169

Section	Page
Appendix 8.A.1.A—Tabulated Results of Crosshole Tests at Gilroy 2 ....	8.A.1-170
Appendix 8.A.1.B—Tabulated Results of Crosshole Tests at Treasure Island .....	8.A.1-193
References .....	8.A.1-220

## LIST OF TABLES

Table		Page
8.A.1-1	Specifications of Horizontal Solenoid Exciter .....	8.A.1-22
8.A.1-2	Physical Description of Horizontal Solenoid Exciter .....	8.A.1-22
8.A.1-3	Depths and Diameters of Cased Boreholes Used in Seismic Crosshole Testing at Gilroy 2 .....	8.A.1-42
8.A.1-4	Center-to-Center Distances Between Boreholes Measured at the Surface at Gilroy 2 .....	8.A.1-42
8.A.1-5	Crosshole Measurement Depth Intervals at Gilroy 2 with the Mechanical Wedge Source (P- and SV-Waves) .....	8.A.1-44
8.A.1-6	Crosshole Measurement Depth Intervals at Gilroy 2; Forward Profile with the Solenoid Source (P- and SH-Waves) .....	8.A.1-44
8.A.1-7	Crosshole Testing Schedule at Gilroy 2 .....	8.A.1-46
8.A.1-8	Comparison of Shear (SV) Wave Velocities Measured at Gilroy 2 by the Crosshole Method and by the Resonant Column Method; Path 1 .....	8.A.1-60
8.A.1-9	Shear Wave Velocity Ratio (SV/SH) Measured Along All Crosshole Paths at Gilroy 2 .....	8.A.1-70
8.A.1-10	Comparison of P-Wave Velocities Measured at Gilroy 2 Using the Mechanical Wedge and Solenoid Sources; Depths 5–120 ft for the Forward Direction Only .....	8.A.1-79
8.A.1-11	Comparison of P-Wave Velocities Measured Along Forward and Reverse Testing Profiles at Gilroy 2 Using the Mechanical Wedge Source; Depths of 5–195 ft .....	8.A.1-81
8.A.1-12	Depths and Cased Inner Diameters of Boreholes Used in Seismic Crosshole Testing at Treasure Island .....	8.A.1-86
8.A.1-13	Center-to-Center Distances Between Boreholes Measured at the Surface at Treasure Island .....	8.A.1-86
8.A.1-14	Crosshole Depth Intervals Used at Treasure Island .....	8.A.1-88
8.A.1-15	Maximum Differences in Center-to-Center Distances Between Boreholes as Reported by The University of Texas and the Earth Technology Corporation .....	8.A.1-91
8.A.1-16	Comparison of Shear (SV) Wave Velocities Measured at Treasure Island by the Crosshole Method and by the Resonant Column Method; Path 1 .....	8.A.1-106
8.A.1-17	Shear Wave Velocity Ratio (SV/SH) Measured Along Three Crosshole Paths at Treasure Island .....	8.A.1-120

<b>Table</b>	<b>Page</b>
8.A.1-18      Summary of Material Damping Results from Gilroy 2 Calculated from Time-Domain Analyses of Crosshole Waveforms .....	<b>8.A.1-166</b>
Appendix 8.A.1.A:	
Tabulated Results of Crosshole Tests at Gilroy 2 .....	<b>8.A.1-170</b>
Appendix 8.A.1.B:	
Tabulated Results of Crosshole Tests at Treasure Island .....	<b>8.A.1-193</b>



## LIST OF FIGURES

Figure		Page
8.A.1-1	Map of the San Francisco Bay Area Showing Locations of the Gilroy 2 and Treasure Island Sites (after Wagner, 1991) .....	8.A.1-15
8.A.1-2	Schematic Diagram of Crosshole Seismic Test .....	8.A.1-16
8.A.1-3	Schematic Diagram of In-Hole Mechanical Wedge Source ....	8.A.1-18
8.A.1-4	Solenoid Operation in Horizontal Solenoid Source .....	8.A.1-20
8.A.1-5	Schematic Diagram of Horizontal Solenoid Source .....	8.A.1-21
8.A.1-6	Three-Component Velocity Transducer Used in Crosshole Testing .....	8.A.1-24
8.A.1-7	Plan View of a Typical Borehole Layout for Crosshole Tests with Definitions of Forward and Reverse Testing Profiles with Direct and Interval Travel Paths .....	8.A.1-26
8.A.1-8	Examples of Determination of SV-Wave Travel Times for Direct and Interval Travel Path Measurements for Type I Data .....	8.A.1-29
8.A.1-9	Example of Type II Data from Direct Crosshole Tests at Treasure Island; SV-Wave, Forward Profile; Depth = 110 ft (33.53 m) .....	8.A.1-30
8.A.1-10	Example of Type III Data from Direct Crosshole Tests at Treasure Island; SV-Wave, Forward Profile; Depth = 96 ft (29.3 m) .....	8.A.1-30
8.A.1-11	Illustration of Travel Path Determination .....	8.A.1-31
8.A.1-12	Schematic of Borehole Layout for In Situ Damping Measurements at Gilroy 2 .....	8.A.1-33
8.A.1-13	Location of Gilroy 2 Site (after Gibbs et al., 1992) .....	8.A.1-40
8.A.1-14	Geologic Log at Gilroy 2 (after Gibbs et al., 1992) .....	8.A.1-41
8.A.1-15	General Borehole Locations at Gilroy 2 .....	8.A.1-43
8.A.1-16	North-South Borehole Drift Measurements at Gilroy 2 Performed by Agbabian Associates of Pasadena, California .	8.A.1-48
8.A.1-17	East-West Borehole Drift Measurements at Gilroy 2 Performed by Agbabian Associates of Pasadena, California .	8.A.1-49

<b>Figure</b>		<b>Page</b>
8.A.1-18	Examples of SV-Wave Travel Time Records Collected at Gilroy 2 Using the Mechanical Wedge Source in B1 and a Three-Component Velocity Transducer in B2 (S-R1, Forward Profile); Depths 5–35 ft .....	8.A.1-50
8.A.1-19	Examples of SH-Wave Travel Time Records Collected at Gilroy 2 Using the Solenoid Source in B1 and a Three-Component Velocity Transducer in B2 (S-R1, Forward Profile); Depths 5–40 ft .....	8.A.1-51
8.A.1-20	Summary of All Shear (SV) Wave Velocities Measured at Gilroy 2 .....	8.A.1-53
8.A.1-21	Comparison of All Shear (SV) Wave Velocities Measured at Gilroy 2 Compared with the Shear Wave Velocity Profile Measured by SASW .....	8.A.1-54
8.A.1-22	Comparison of Shear (SV) Wave Velocities Measured in the Forward and Reverse Directions Along Path 1 at Gilroy 2; Depths 5–200 ft .....	8.A.1-56
8.A.1-23	Comparison of Shear (SV) Wave Velocities Measured in the Forward and Reverse Directions Along Path 2 at Gilroy 2 .....	8.A.1-57
8.A.1-24	Comparison of Shear (SV) Wave Velocities Measured in the Forward and Reverse Directions Along Path 3 at Gilroy 2 .....	8.A.1-58
8.A.1-25	Histogram of Percent Difference Between SV-Wave Velocities from Forward and Reverse Crosshole Tests at Gilroy 2 .....	8.A.1-59
8.A.1-26	Comparison of Shear Wave Velocities at Gilroy 2 Obtained from Crosshole and Torsional Resonant Column Tests .....	8.A.1-61
8.A.1-27	Comparison of Shear (SV) Wave Velocities Measured Along Path 1 at Gilroy 2 with Theoretical Velocities Predicted Using the Equation Proposed by Hardin and Drnevich (1972) for a Normally-Consolidated Soil with Void Ratios (e) of 0.5 and 1.0 .....	8.A.1-63
8.A.1-28	Summary of All Shear (SH) Wave Velocities Measured at Gilroy 2 .....	8.A.1-65
8.A.1-29	Comparison of SV- and SH-Wave Velocities Along Path 1 at Gilroy 2 (Forward Direction Only) .....	8.A.1-66
8.A.1-30	Comparison of SV- and SH-Wave Velocities Along Path 2 at Gilroy 2 (Forward Direction Only) .....	8.A.1-67
8.A.1-31	Comparison of SV- and SH-Wave Velocities Along Path 3 at Gilroy 2 (Forward Direction Only) .....	8.A.1-68

<b>Figure</b>		<b>Page</b>
8.A.1-32	Average Shear Wave Velocity Ratio (SV/SH) Along Paths 1, 2 and 3 at Gilroy 2 .....	8.A.1-71
8.A.1-33	Examples of P-Wave Travel Time Records Collected at Gilroy 2 Using the Mechanical Wedge Source in B1 and a Three-Component Velocity Transducer in B2 (S-R1, Forward Profile); Depths 200–235 ft .....	8.A.1-73
8.A.1-34	Summary of All Compression Wave Velocities Measured at Gilroy 2 Using the Mechanical Wedge Source .....	8.A.1-74
8.A.1-35	Comparison of Compression Wave Velocities Measured in the Forward and Reverse Directions Along Path 1 at Gilroy 2 .....	8.A.1-76
8.A.1-36	Comparison of Compression Wave Velocities Measured in the Forward and Reverse Directions Along Path 2 at Gilroy 2 .....	8.A.1-77
8.A.1-37	Comparison of Compression Wave Velocities Measured in the Forward and Reverse Directions Along Path 3 at Gilroy 2 .....	8.A.1-78
8.A.1-38	General Location of Fire Station on Treasure Island on Treasure Island (after Hryciw et al., 1991) .....	8.A.1-85
8.A.1-39	Borehole Arrangement and Wave Travel Paths for Crosshole Seismic Testing at Treasure Island .....	8.A.1-87
8.A.1-40	North-South Borehole Drift Measurements at Treasure Island Performed by Agbabian Associates of Pasadena, California .	8.A.1-89
8.A.1-41	East-West Borehole Drift Measurements at Treasure Island Performed by Agbabian Associates of Pasadena, California .	8.A.1-90
8.A.1-42	Comparison of Center-to-Center Spacings Between Boreholes B3 and B2 as Computed by the Earth Technology Corporation and The University of Texas at Austin .....	8.A.1-92
8.A.1-43	Comparison of Center-to-Center Spacings Between Boreholes B2 and B1 as Computed by the Earth Technology Corporation and The University of Texas at Austin .....	8.A.1-93
8.A.1-44	Examples of SV-Wave Travel Time Records Collected at Treasure Island Using the Solenoid Source in B1 and a Three-Component Velocity Transducer in B2 (S-R1, Forward Profile); Depths 27–50 ft .....	8.A.1-95

<b>Figure</b>		<b>Page</b>
8.A.1-45	Examples of SH-Wave Travel Time Records Collected at Treasure Island Using the Solenoid Source in B1 and a Three-Component Velocity Transducer in B2 (S-R1, Forward Profile); Depths 3–24 ft .....	8.A.1-96
8.A.1-46	Summary of All Shear (SV) Wave Velocities Measured at Treasure Island .....	8.A.1-97
8.A.1-47	Comparison of All Shear (SV) Wave Velocities Measured at Treasure Island Compared with the Shear Wave Velocity Profile Measured by SASW Testing .....	8.A.1-98
8.A.1-48	Comparison of SV-Wave Velocity Profile with CPT No. 9 Data at Treasure Island .....	8.A.1-99
8.A.1-49	Tip Resistance Measured in the University of New Hampshire CPT No. 1 Test at Treasure Island .....	8.A.1-100
8.A.1-50	Comparison of Shear (SV) Wave Velocities Measured in the Forward and Reverse Directions Along Path 1 at Treasure Island .....	8.A.1-102
8.A.1-51	Comparison of Shear (SV) Wave Velocities Measured in the Forward and Reverse Directions Along Path 2 at Treasure Island .....	8.A.1-103
8.A.1-52	Comparison of Shear (SV) Wave Velocities Measured by The University of Texas and Earth Technology Along Path 1 at Treasure Island .....	8.A.1-104
8.A.1-53	Comparison of Shear (SV) Wave Velocities Measured by The University of Texas and Earth Technology Along Path 2 at Treasure Island .....	8.A.1-105
8.A.1-54	Comparison of Shear Wave Velocities at Gilroy 2 Obtained from Crosshole and Torsional Resonant Column Tests .....	8.A.1-107
8.A.1-55	Comparison of Shear (SV) Wave Velocities Measured Along Path 1 at Treasure Island with Theoretical S-Wave Velocities Predicted by Hardin and Drnevich (1972) for a Normally-Consolidated Soil with Void Ratios ( $e$ ) of 0.5 and 1.0 .....	8.A.1-109
8.A.1-56	Summary of All Shear (SH) Wave Velocities Measured at Treasure Island .....	8.A.1-111
8.A.1-57	Comparison of Shear (SH) Wave Velocities Measured in the Forward and Reverse Directions Along Path 1 at Treasure Island .....	8.A.1-112

<b>Figure</b>		<b>Page</b>
8.A.1-58	Comparison of Shear (SH) Wave Velocities Measured in the Forward and Reverse Directions Along Path 2 at Treasure Island .....	8.A.1-113
8.A.1-59	Comparison of SV- and SH-Wave Velocities Along Path 1 at Treasure Island (Forward Direction Only) .....	8.A.1-115
8.A.1-60	Comparison of SV- and SH-Wave Velocities Along Path 2 at Treasure Island (Forward Direction Only) .....	8.A.1-116
8.A.1-61	Comparison of SV- and SH-Wave Velocities Along Path 3 at Treasure Island .....	8.A.1-117
8.A.1-62	Comparison of SV- and SH-Wave Velocities Along Path 4 at Treasure Island .....	8.A.1-118
8.A.1-63	Comparison of SV- and SH-Wave Velocities Along Path 5 at Treasure Island .....	8.A.1-119
8.A.1-64	Average Shear Wave Velocity Ratio (SV/SH) Along Paths 1, 2 and 3 at Treasure Island .....	8.A.1-121
8.A.1-65	Examples of P-Wave Travel Time Records Collected at Treasure Island Using the Mechanical Wedge Source in B1 and a Three-Component Velocity Transducer in B2 (S-R1, Forward Profile); Depths 27–50 ft .....	8.A.1-123
8.A.1-66	Summary of All Compression Wave Velocities Measured at Treasure Island Using the Mechanical Wedge Source .....	8.A.1-124
8.A.1-67	Comparison of Compression Wave Velocities Measured in the Forward and Reverse Directions Along Path 1 at Treasure Island .....	8.A.1-126
8.A.1-68	Comparison of Compression Wave Velocities Measured in the Forward and Reverse Directions Along Path 2 at Treasure Island .....	8.A.1-127
8.A.1-69	Comparison of Compression Wave Velocities Measured by The University of Texas and the Earth Technology Corporation Along Path 1 at Treasure Island .....	8.A.1-129
8.A.1-70	Comparison of Compression Wave Velocities Measured by The University of Texas and the Earth Technology Corporation Along Path 2 at Treasure Island .....	8.A.1-130
8.A.1-71	Use of an Extended Cosine Bell Window to Gate Original Signal; SV-Wave Measured at 15-ft Depth, Receiver 2 (after Mok, 1987) .....	8.A.1-133

<b>Figure</b>		<b>Page</b>
8.A.1-72	Windowed SV-Wave Time Records for Material Damping Analyses at Gilroy 2 at 15-ft Depth; Short Time Window .....	<b>8.A.1-135</b>
8.A.1-73	Material Damping, Wave Velocity and Linear Spectra Versus Frequency for 15-ft Depth at Gilroy 2; Short Time Window; Spectral Ratio Method .....	<b>8.A.1-137</b>
8.A.1-74	Material Damping, Wave Velocity and Linear Spectra Versus Wavelength for 15-ft Depth at Gilroy 2; Short Time Window; Spectral Ratio Method .....	<b>8.A.1-138</b>
8.A.1-75	Material Damping at 15-ft Depth at Gilroy 2 by Spectral Slope Method; Short Time Window .....	<b>8.A.1-140</b>
8.A.1-76	Windowed SV-Wave Time Records for Material Damping Analyses at Gilroy 2 at 15-ft Depth; Long Time Window .....	<b>8.A.1-141</b>
8.A.1-77	Material Damping, Wave Velocity and Linear Spectra Versus Frequency for 15-ft Depth at Gilroy 2; Long Time Window; Spectral Ratio Method .....	<b>8.A.1-142</b>
8.A.1-78	Material Damping, Wave Velocity and Linear Spectra Versus Wavelength for 15-ft Depth at Gilroy 2; Long Time Window; Spectral Ratio Method .....	<b>8.A.1-143</b>
8.A.1-79	Material Damping at 15-ft Depth at Gilroy 2 by Spectral Slope Method; Long Time Window .....	<b>8.A.1-144</b>
8.A.1-80	Windowed SV-Wave Time Records for Material Damping Analyses at Gilroy 2 at 25-ft Depth; Long Time Window .....	<b>8.A.1-146</b>
8.A.1-81	Material Damping, Wave Velocity and Linear Spectra Versus Frequency for 25-ft Depth at Gilroy 2; Long Time Window; Spectral Ratio Method .....	<b>8.A.1-147</b>
8.A.1-82	Material Damping, Wave Velocity and Linear Spectra Versus Wavelength for 25-ft Depth at Gilroy 2; Long Time Window; Spectral Ratio Method .....	<b>8.A.1-148</b>
8.A.1-83	Material Damping at 25-ft Depth at Gilroy 2 by Spectral Slope Method; Long Time Window .....	<b>8.A.1-149</b>
8.A.1-84	Windowed SV-Wave Time Records for Material Damping Analyses at Gilroy 2 at 115-ft Depth; Short Time Window .....	<b>8.A.1-150</b>
8.A.1-85	Material Damping, Wave Velocity and Linear Spectra Versus Frequency for 115-ft Depth at Gilroy 2; Short Time Window; Spectral Ratio Method .....	<b>8.A.1-151</b>

<b>Figure</b>		<b>Page</b>
8.A.1-86	Material Damping, Wave Velocity and Linear Spectra Versus Wavelength for 115-ft Depth at Gilroy 2; Short Time Window; Spectral Ratio Method .....	8.A.1-152
8.A.1-87	Material Damping at 115-ft Depth at Gilroy 2 by Spectral Slope Method; Short Time Window .....	8.A.1-153
8.A.1-88	Windowed SV-Wave Time Records for Material Damping Analyses at Gilroy 2 at 115-ft Depth; Long Time Window .....	8.A.1-154
8.A.1-89	Material Damping, Wave Velocity and Linear Spectra Versus Frequency for 115-ft Depth at Gilroy 2; Long Time Window; Spectral Ratio Method .....	8.A.1-155
8.A.1-90	Material Damping, Wave Velocity and Linear Spectra Versus Wavelength for 115-ft Depth at Gilroy 2; Long Time Window; Spectral Ratio Method .....	8.A.1-156
8.A.1-91	Material Damping at 115-ft Depth at Gilroy 2 by Spectral Slope Method; Long Time Window .....	8.A.1-157
8.A.1-92	Windowed SV-Wave Time Records for Material Damping Analyses at Gilroy 2 at 125-ft Depth; Short Time Window .....	8.A.1-158
8.A.1-93	Material Damping, Wave Velocity and Linear Spectra Versus Frequency for 125-ft Depth at Gilroy 2; Short Time Window; Spectral Ratio Method .....	8.A.1-159
8.A.1-94	Material Damping, Wave Velocity and Linear Spectra Versus Wavelength for 125-ft Depth at Gilroy 2; Short Time Window; Spectral Ratio Method .....	8.A.1-160
8.A.1-95	Material Damping at 125-ft Depth at Gilroy 2 by Spectral Slope Method; Short Time Window .....	8.A.1-161
8.A.1-96	Windowed SV-Wave Time Records for Material Damping Analyses at Gilroy 2 at 125-ft Depth; Long Time Window .....	8.A.1-162
8.A.1-97	Material Damping, Wave Velocity and Linear Spectra Versus Frequency for 125-ft Depth at Gilroy 2; Long Time Window; Spectral Ratio Method .....	8.A.1-163
8.A.1-98	Material Damping, Wave Velocity and Linear Spectra Versus Wavelength for 125-ft Depth at Gilroy 2; Long Time Window; Spectral Ratio Method .....	8.A.1-164
8.A.1-99	Material Damping at 125-ft Depth at Gilroy 2 by Spectral Slope Method; Long Time Window .....	8.A.1-165

# **APPENDIX 8.A.1**

## **CROSSHOLE SEISMIC TESTS AT THE GILROY 2 AND TREASURE ISLAND SITES**

---

### **1—INTRODUCTION**

#### **8.A.1.1.1 Background Information**

The Electric Power Research Institute (EPRI) is conducting a comprehensive study of strong ground motions measured during earthquakes to evaluate dynamic soil properties used in the design of nuclear power plants. As part of the EPRI project, this study was conducted to measure in situ the small-strain dynamic properties of soils at two Northern California sites affected by the 1989 Loma Prieta earthquake.

The locations of the two sites, called Gilroy 2 and Treasure Island, are shown in Figure 8.A.1-1. Crosshole seismic tests were conducted at both sites to determine in situ soil stiffnesses at small strains in terms of compression and shear wave velocities. At the Gilroy 2 site, a four-borehole array was installed so that measurements of material damping in shear could also be performed.

#### **8.A.1.1.2 Objectives**

The objectives of this study include:

1. measurement of in situ body wave velocities by the crosshole seismic method at the Gilroy 2 and Treasure Island sites. The body waves measured were compression (P), vertically-polarized shear (SV) waves and horizontally-polarized shear (SH) waves;
2. investigation of anisotropy in soil stiffness at both sites by comparing SV- and SH-wave velocities; and
3. application of the crosshole method to evaluate material damping in the field at the Gilroy 2 site.

#### **8.A.1.1.3 Organization**

A brief discussion of the crosshole method, including descriptions of the equipment for performing the measurements and data acquisition, is presented in Section 2. Descriptions of the analytical procedures for time-domain analyses of the data for determining seismic wave velocities and the equations used to evaluate material damping are also included in Section 2. Equipment calibration procedures and sample calculations of borehole spacings and body wave velocities are presented by Fuhriman (1993).

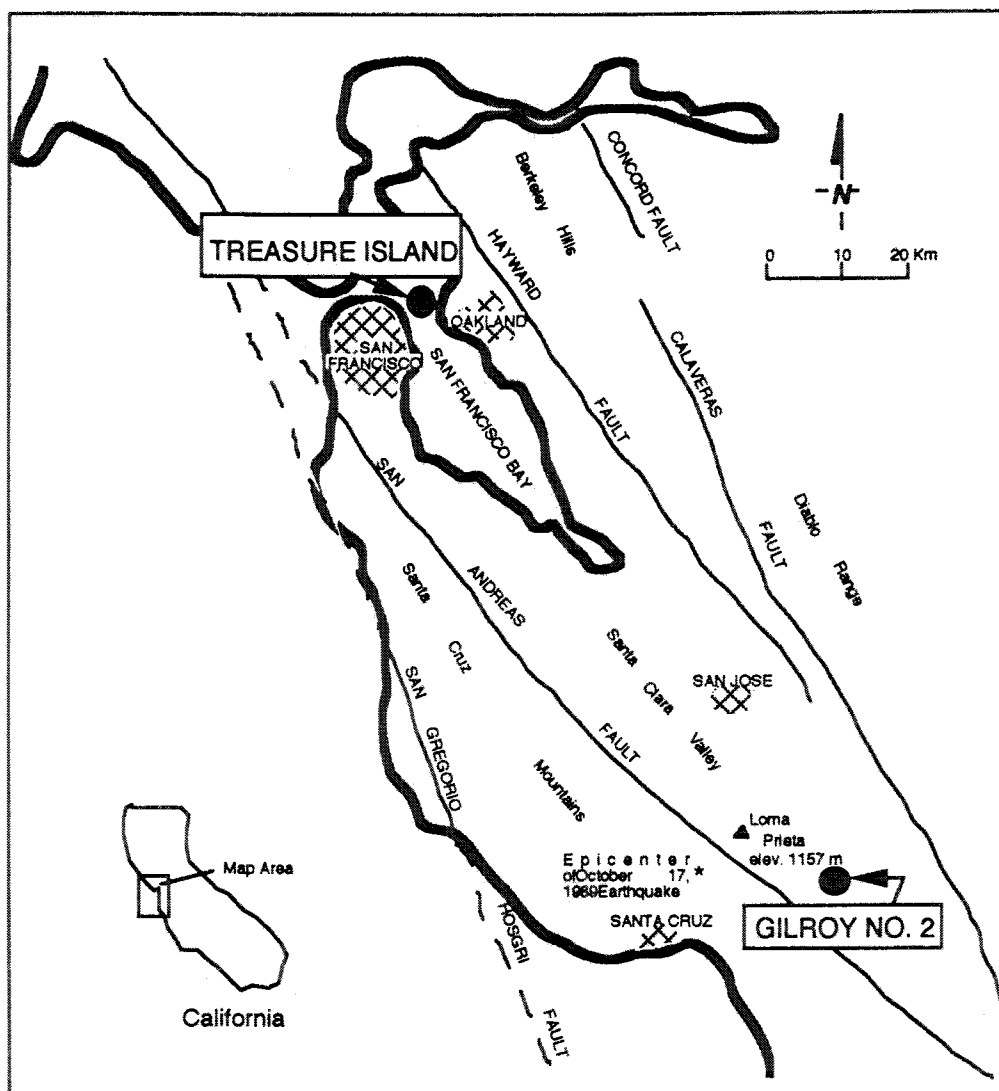
The crosshole P- and S-wave velocities at the Gilroy 2 site are presented in Section 3. Results of shear wave velocities measured in the field are also compared with shear wave velocities measured in the laboratory. Fuhriman (1993) presents all waveforms collected during the crosshole tests at Gilroy 2. Typical waveforms from SV-, SH- and P-wave measurements at Gilroy 2 are presented in Section 3. Appendix 8.A.1.A contains the crosshole results in tabular form.



The crosshole P- and S-wave velocities measured at the Treasure Island site are presented in Section 4. The results for shear wave velocity are compared with shear wave velocities measured in the laboratory. All waveforms collected during the crosshole testing at Treasure Island are presented by Fuhrman (1993). Typical waveforms from SV-, SH- and P-wave measurements at Treasure Island are presented in Section 4. Appendix 8.A.1.B of this work contains the crosshole results for Treasure Island in tabular form.

Results of the material damping analyses at Gilroy 2 are presented in Section 5. These results are compared with laboratory measurements of material damping of undisturbed soil samples from the site.

Finally, the major findings from this study and conclusions are presented in Section 6.



**Figure 8.A.1-1**

Map of the San Francisco Bay Area showing locations of the Gilroy 2 and Treasure Island sites (after Wagner, 1991).

## 2—CROSSHOLE EQUIPMENT, PROCEDURES AND ANALYSES

### 8.A.1.2.1 Introduction

The crosshole seismic method, as applied traditionally, involves generating and sensing body waves which propagate horizontally within a soil-rock mass. The seismic source is positioned at one point in the ground, and the times for body waves to travel to receivers at the same depth but at various distances away from the source are measured. This approach to crosshole testing was employed in this study. Testing was conducted in general accordance with ASTM D 4428/D 4428M. Measurements of body wave velocities and material damping were performed. The body waves measured were compression (P) waves, vertically-polarized shear (SV) waves and horizontally-polarized shear (SH) waves.

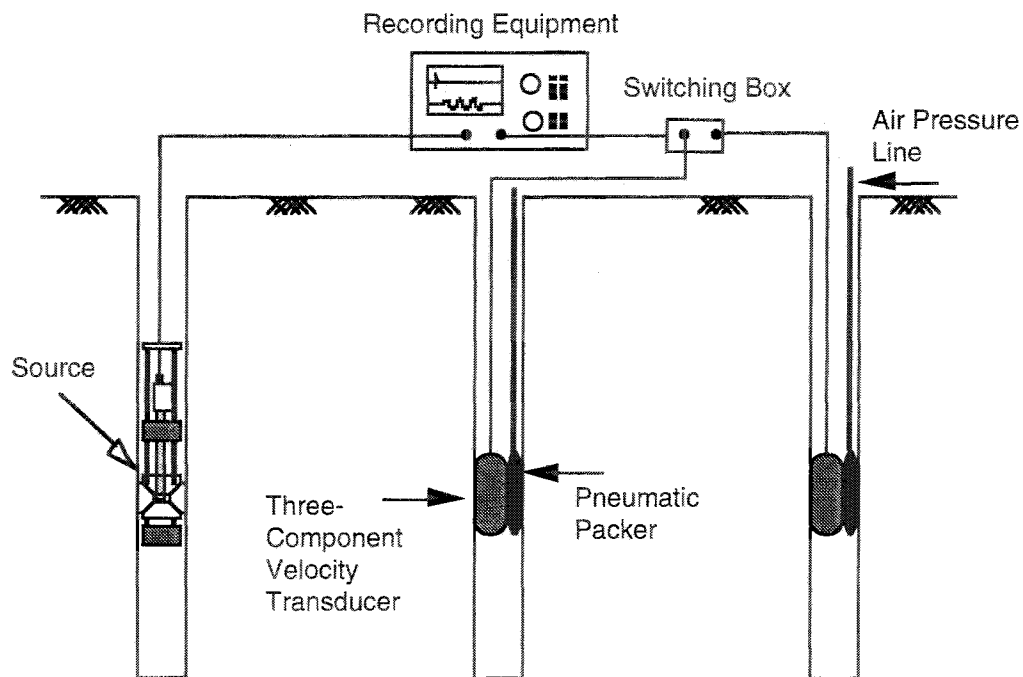
An overview of the crosshole seismic method is presented in this section. The following parts of the testing program are discussed: 1) equipment, 2) field procedures, 3) wave velocity analysis, and 4) material damping analyses.

### 8.A.1.2.2 Equipment

The field equipment used in the crosshole tests includes:

1. sources,
2. three-directional (3-D) velocity transducers (also called 3-D geophones or 3-D receivers herein), and
3. waveform recording equipment.

A schematic arrangement of this equipment is shown in Figure 8.A.1-2. Each piece of equipment is described below.



**Figure 8.A.1-2**  
Schematic diagram of crosshole seismic test.

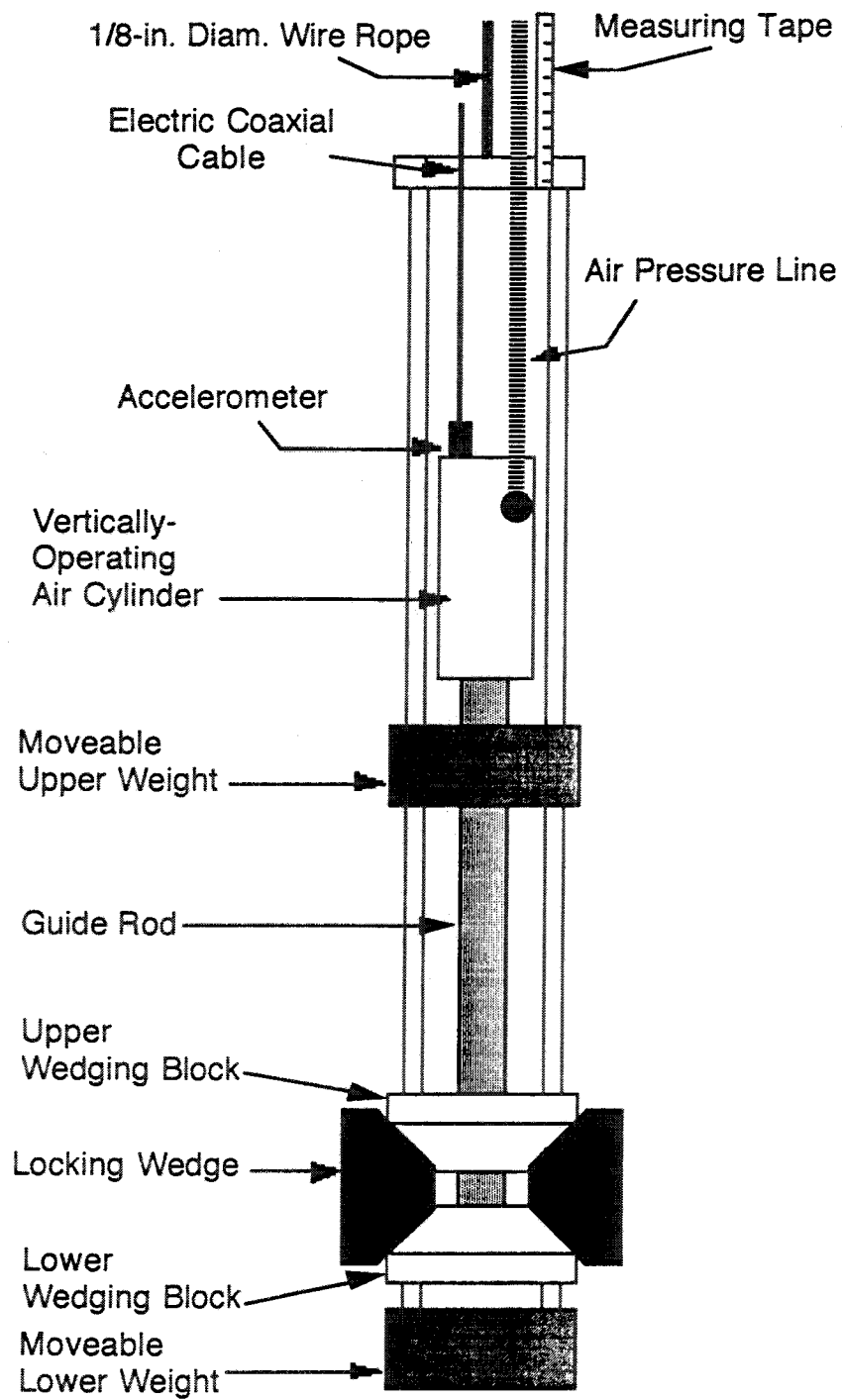
#### **8.A.1.2.2.1 Seismic Sources**

Two in-hole seismic sources were used: 1) a pneumatically-operated wedge with a manually-operated vertical hammer and 2) a horizontal exciter driven by an electrically-actuated solenoid. The wedge-and-hammer, or mechanical wedge, source generates energy rich in SV-waves while simultaneously generating some P-wave energy. This source was developed in previous work by Y. J. Mok and K. Stokoe (Stokoe, 1992) and is briefly discussed below. The solenoid source, developed just prior to this project (Fuhrman, 1993) in conjunction of a U. S. Bureau of Mines project, was designed to generate SH- and P-wave energy.

**Mechanical Wedge Source.** The mechanical wedge source is shown in Figure 8.A.1-3. The main components of the mechanical wedge and hammer source are: 1) pneumatically-operated upper and lower wedging blocks, 2) four locking wedges, 3) a guide rod, 4) a 7-lb (3.2 kg) sliding hammer composed of upper and lower weights and connecting rods and 5) an air cylinder that delivers air pressure to move the wedging mechanism. This source is coupled to the borehole wall by the four locking wedges, which are controlled by the air cylinder. The total weight of the source is 13.5 lb (6.1 kg). An accelerometer (PCB model 305-A04 manufactured by Piezotronics, Inc. of Depew, New York) mounted on the source establishes a zero-time reference and triggers the recording equipment.

The mechanical wedge source is operated as follows. Using the air cylinder, the wedging mechanism is contracted to its smallest diameter (about 2.7 in. (6.9 cm) without extension feet). The wire rope is then used to lower the source to the desired depth, and the wedging mechanism is expanded (by air pressure) to lock the source in the borehole. The wire rope (cable) is attached to the moveable weight, or hammer. With this cable, the source is operated from the surface by pulling up on the hammer or allowing the hammer to drop. In either case, the hammer strikes the wedging block. When the hammer strikes the wedging block, frictional forces holding the source in place increase momentarily, causing the soil around the casing to strain and induce wave motion in the vertical direction, which produces an SV-wave. The same impact also briefly compresses the locking wedges, producing a simultaneous radial component of the impact. This radial force, combined with the finite length of the source, produces a P-wave.

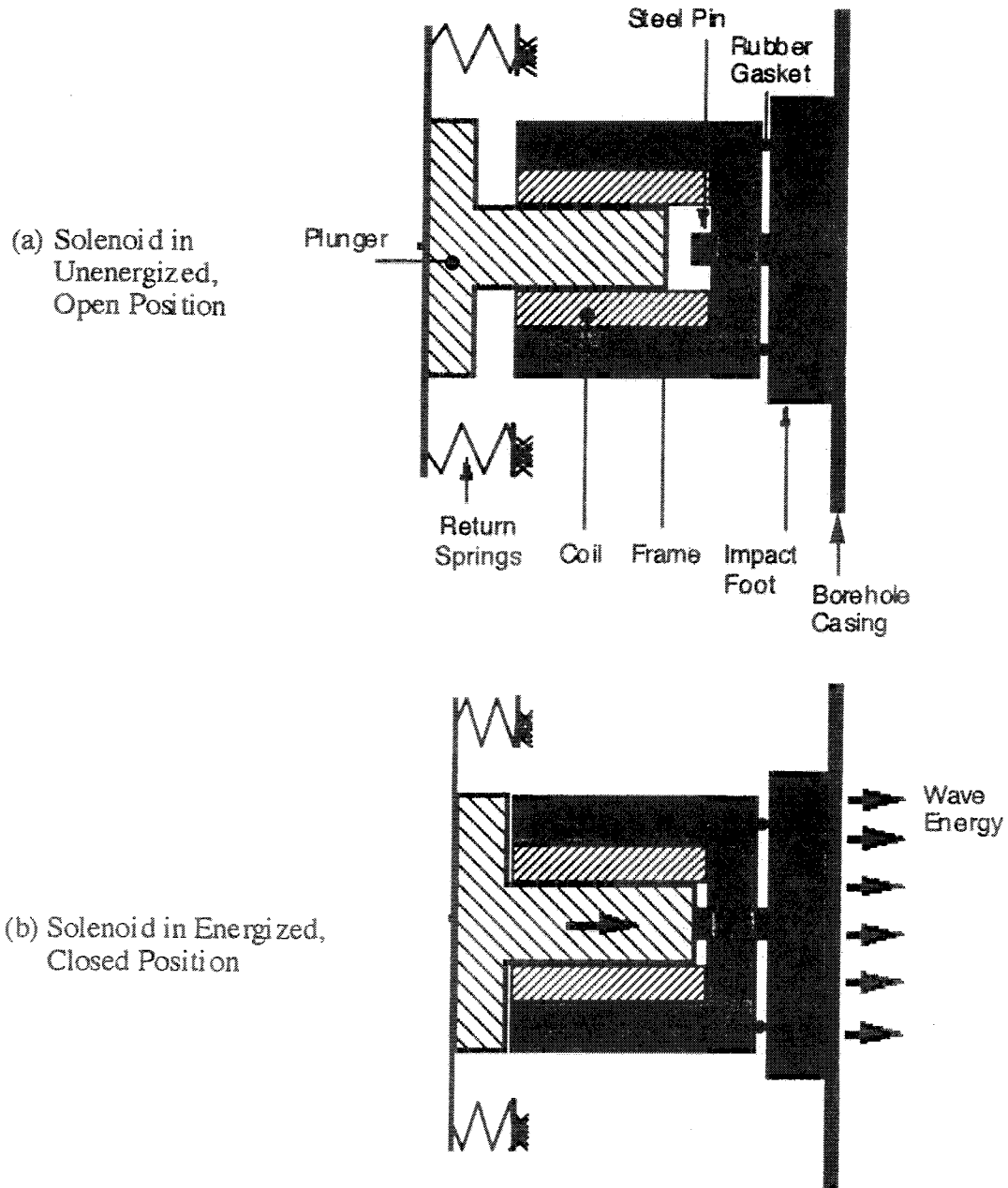
The mechanical wedge source is reversible; that is, it produces SV-waves with either downward or upward impacts. When allowed to drop from a certain height, the upper weight strikes the upper wedging block, creating an SV-wave whose initial polarity is downward. Similarly, when the sliding hammer is pulled upward by the cable, the lower weight strikes the lower wedging block, creating an SV-wave whose initial polarity is upward. This reversal in wave motion often makes initial arrivals of the shear waves easier to identify (see Section 8.A.1.2.4).



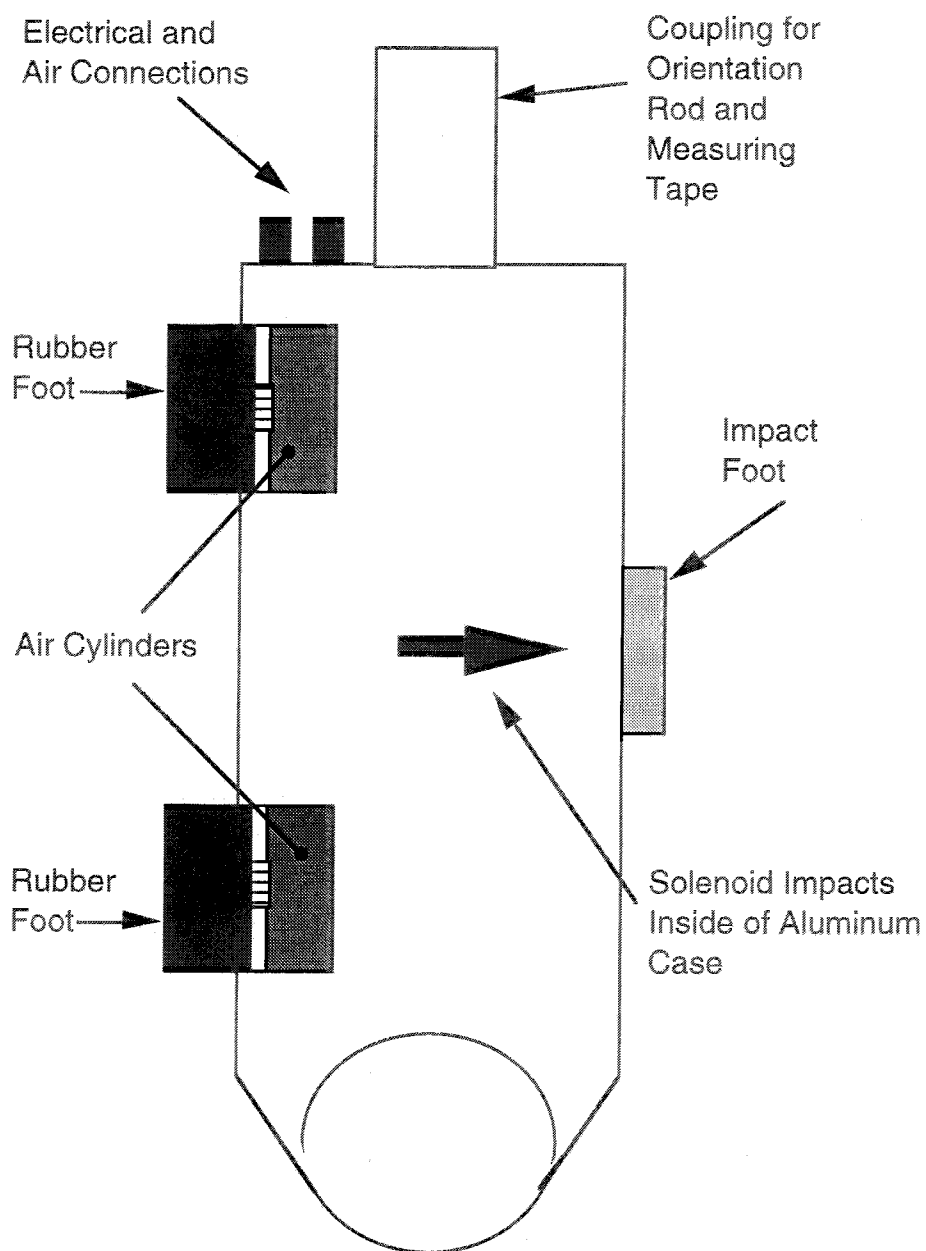
**Figure 8.A.1-3**  
Schematic diagram of in-hole mechanical wedge source.

**Horizontal Solenoid Source.** The horizontal solenoid incorporates a linear-acting solenoid that produces horizontal impacts for P- and SH- wave measurements. Operation of the solenoid is illustrated in Figure 8.A.1-4. Upon application of an electrical current, an electro-magnetic field is induced through the coil of the solenoid, which draws the plunger toward a hardened steel pin (see Figure 8.A.1-4). Upon impact the solenoid plunger imparts energy to the borehole casing through the steel pin and a steel impact foot. The impact foot is isolated from the solenoid and the aluminum case (source case) by a rubber O-ring and a silicon gasket so that the impact foot can move independently of the case. To ensure good coupling and transfer of energy, the curvature of the impact foot is matched to the inside curvature of the borehole casing. (The source is designed to fit in either a 4-in. (10.16-cm) or 5-in. (12.7-cm) diameter borehole.) Two springs return the plunger to the open, unenergized position when the current is stopped.

The solenoid assembly is housed in an aluminum case. Figure 8.A.1-5 shows a schematic illustration of the complete solenoid source. Two moveable rubber feet (or pads) are used to couple the source to the borehole wall. Each rubber pad is on the end of a piston in a small air cylinder. Air pressure applied to the cylinders is used to move the rubber pads either out from the aluminum case or back into the case. The rubber feet exert a high force on the borehole wall which in turn presses the impact foot of the solenoid against the borehole wall. The rubber feet are intended also to isolate seismically the borehole wall opposite from the impact foot, thereby allowing the source to impart energy that is highly uni-directional. The air cylinders, manufactured by Airmite of Chicago, Illinois, are 2 in. (5.1 cm) in diameter and have a maximum stroke of 1 in. (2.5 cm). The solenoid source incorporates a PCB Model 303A accelerometer as a trigger. This accelerometer is potted into the impact foot with epoxy. Table 8.A.1-1 summarizes the specifications of the solenoid source. Table 8.A.1-2 summarizes the physical characteristics of the complete source.



**Figure 8.A.1-4**  
Solenoid operation in horizontal solenoid source.



**Figure 8.A.1-5**  
Schematic diagram of horizontal solenoid source.



**Table 8.A.1-1**  
Specifications of Horizontal Solenoid Exciter

Solenoid Motion	Linear Horizontal
Seismic Waves Produced	P- and SH-Waves, depending on the orientation of the source
Frequency Content	< 5 kHz (see Figures 8.A.1-16 through 8.A.1-19)
Pulse Duration	Variable: 40 msec to 440 msec
Repetition Interval	Variable: 0.5 sec to 5.5 sec
Stroke	~0.25 in. (6.35 mm)
Trigger Accelerometer: PCB 303A, Sensitivity	10 mV/g

**Table 8.A.1-2**  
Physical Description of Horizontal Solenoid Exciter

Diameter	3.5 in. (89 mm) max.
Height	22 in. (559 mm)
Weight	5.5 lb (2.45 kg)
Clamping Force	< 250 lb (113 kg)
External Support	115-VAC, 60-Hz Power; Compressed Air
Miscellaneous	Uni-directional; Non-submergible

The top of the source couples directly to a square aluminum guide rod. The guide rod (assembled in sections) is used to lower the source into the borehole and to orient the source in the direction of intended wave propagation. With the source and receivers at the intended depth, the source operates automatically from a control box that controls the impulse repetition rate and pulse duration (how long the solenoid remains closed). This control box was designed and built by Mr. Frank Wise of the Aerospace Engineering Department at the University of Texas at Austin. The ranges for pulse duration and repetition rate are listed in Table 8.A.1-1.

The repetition rate of the solenoid source can be adjusted to have the source produce seismic waves at the maximum rate that the HP 3562A dynamic signal analyzer (described in Section 8.A.1.2.2.3) can gather the data. Automatic control of the repetition rate expedites the data gathering process and reduces the manual labor involved in performing crosshole tests.

### 8.A.1.2.2.2 Seismic Receivers

Receiver units consisting of velocity transducers, or geophones, were used in all crosshole tests to monitor the waveforms. The geophones were manufactured by Mark Products, Inc. of Houston, Texas. A geophone is a coil-spring-magnet system housed in an aluminum case. In a geophone, a coil is attached to a spring with a support to the geophone case. A magnet is attached to the geophone case. When the geophone moves, the magnet and support also move. The coil tends to remain stationary while the magnet and geophone case move. The relative motion between the coil and the magnetic field induces a voltage proportional to velocity of the motion for movements with frequencies above the natural frequency ( $f_n$ ) of the spring-coil system ( $f_n = 4.5$  Hz in these receivers). Geophone output yields essentially non-distorted signals over a frequency range of 20 to about 800 Hz (see Appendix 8.A.1.A).

Each receiver unit contains three orthogonally-oriented geophones mounted in an aluminum case. The three-directional (3-D) geophone unit senses wave motions in the vertical, radial horizontal, and transverse horizontal directions. Figure 8.A.1-6 shows a schematic representation of a 3-D geophone. The vertical component is used to monitor SV-waves; the radial horizontal component, oriented toward the source along the direction of the arrows, is used to monitor P-waves; the transverse horizontal component, oriented transverse to a line connecting the source and receiver, is used to monitor SH-waves. The 3-D geophone is oriented manually from the surface using inter-connecting lengths of aluminum or PVC rod which extend to the ground surface.

The components of the 3-D receivers are summarized below.

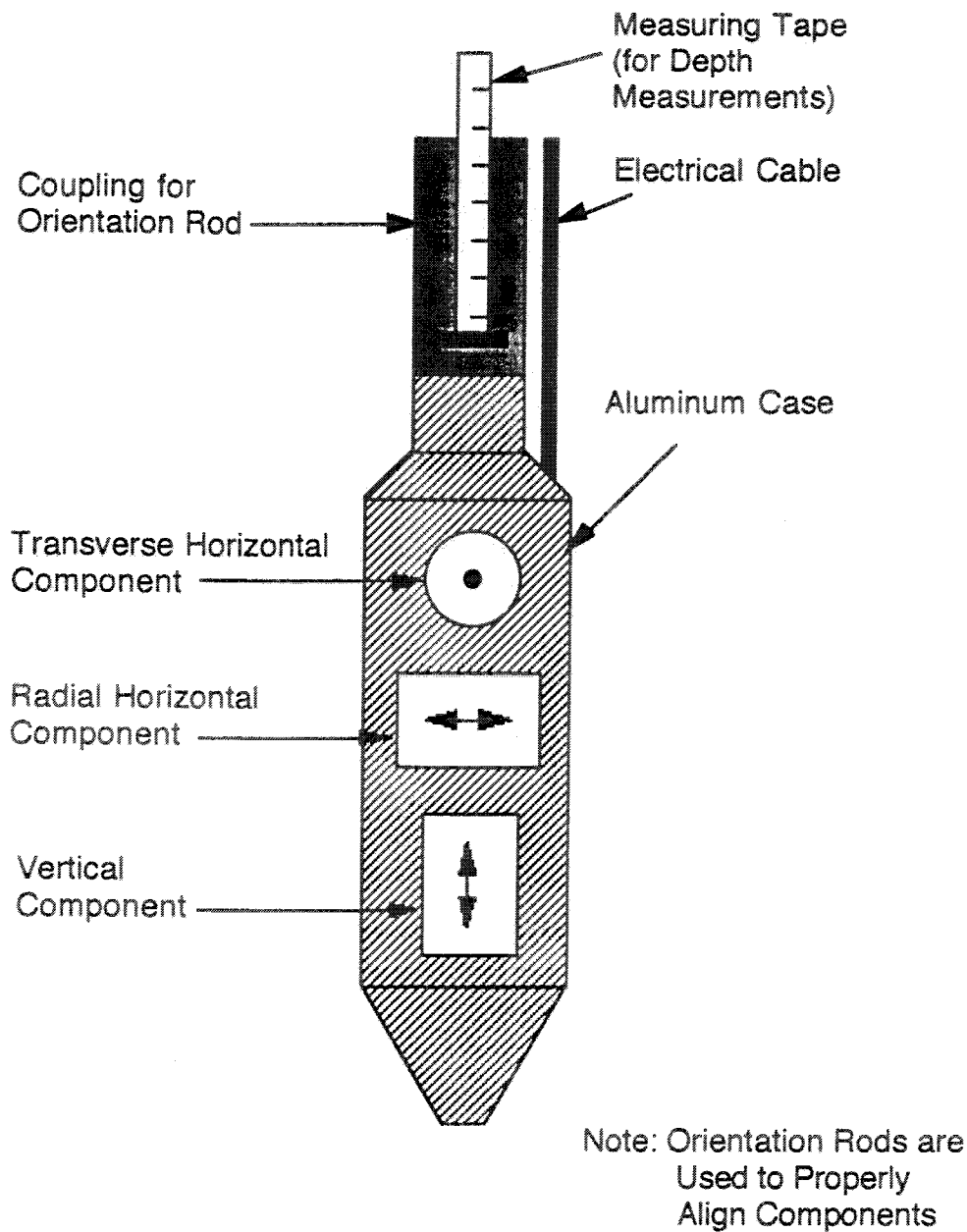
#### Geophone

Type .....Mark Products Model L-15B  
Natural Frequency.....4.5 Hz  
Coil Resistance .....380  $\Omega$   
Damping ..... 50% of critical  
Height..... 1.4 in. (3.6 cm)  
Diameter .....1.25 in (3.2 cm)  
Weight .....5 oz (142 g)

#### Aluminum Case (With Three Geophones)

Height..... 8 in. (20.3 cm)  
Diameter .....2.5 in (6.3 cm)  
Weight .....5 lb (2.3 kg)

All receivers used in the crosshole test are connected to a switching box at the surface. The switching box allows easy monitoring of a particular waveform with the proper geophone without any disconnecting/reconnecting operations.



**Figure 8.A.1-6**  
Three-component velocity transducer used in crosshole testing.

#### **8.A.1.2.2.3 Recording Equipment**

The recording equipment used in this work consisted of a two-channel dynamic signal analyzer (Model 3562A) and a disk drive unit (Model 9122D), both manufactured by Hewlett-Packard, Inc. of Palo Alto, California. The waveforms were collected with the two-channel analyzer and then stored (for future analysis in the office) on 3.5-in. (89-mm) micro floppy disks.

The HP 3562A analyzer has a frequency-domain measurement range of 64 mHz to 100 kHz, with an accuracy of 0.004% of full scale. The timing resolution of the analyzer is 10  $\mu$ s, with a minimum full-range sensitivity of 4 mV and an 80-dB dynamic range. The recording buffer collects 2048 data points per channel.

### 8.A.1.2.3 Field Procedures

Before crosshole testing, three or more boreholes were drilled in a linear array and lined with PVC well casing (schedule 40). This casing was grouted in place to couple the casing to the soil. The shear wave velocity,  $V_s$ , and unconstrained compression wave velocity,  $V_c$ , of a typical sample of the grout were measured in the laboratory. The values were found to be:  $V_s \approx 4525$  fps (1380 m/sec) and  $V_c = 7350$  fps (2240 m/sec).

The cased boreholes had inner diameters of either 4 in. or 5 in. (7.6 cm or 12.7 cm) and were spaced between 9 ft and 15 ft (~3 m and ~5 m) apart. Actual borehole diameters and spacings used at the Gilroy 2 and Treasure Island sites are discussed in Sections 3 and 4, respectively. Any water in the boreholes that were used as source boreholes was bailed to prevent electrical shorts and to maximize energy generated by the source.

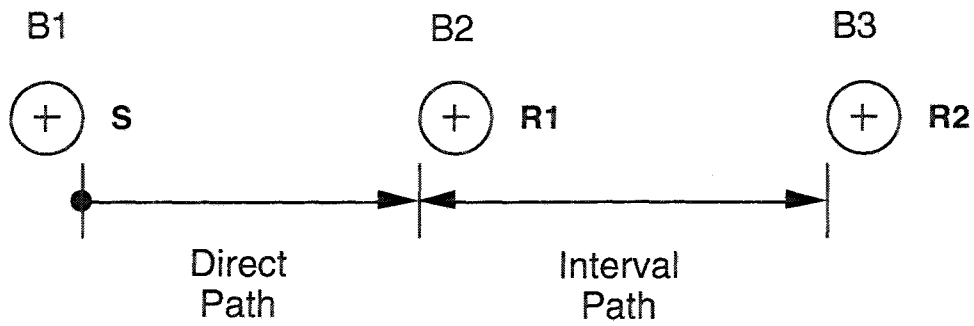
#### 8.A.1.2.3.1 Test Set-Up

To begin a crosshole test, a seismic source is lowered either by cable or guide rods to the desired depth in the source borehole. Receivers are lowered into the other boreholes and oriented such that the axis of the radial geophone in the receiver package is aligned along a line connecting the source and receiver borehole. Orientation of receivers is necessary for accurate measurements of P and SH-waves; orientation is not critical for SV-wave measurements since the vertical geophone is always oriented nearly vertically (in the direction of maximum wave motion). For SH-wave measurements, the SH-wave generator must also be properly oriented—transverse to a line connecting the source and receiver boreholes. Orientation is accomplished by means of aluminum or PVC guide rods, also called orientation rods.

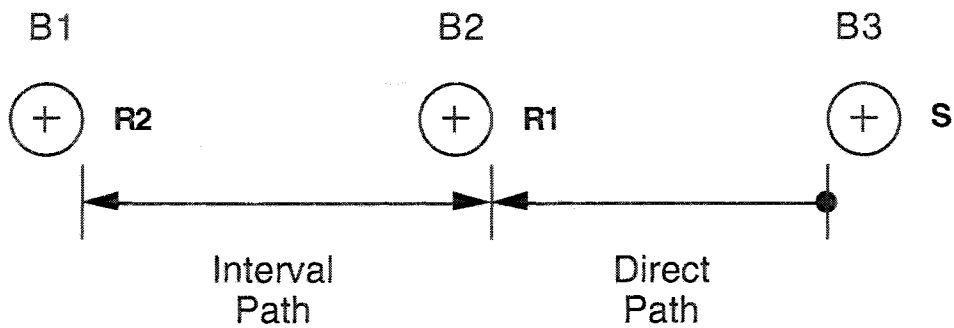
Accurate crosshole measurements require that the source and receivers be firmly coupled against the borehole casing. The sources were locked into place by pneumatically controlled mechanisms. Coupling for the receivers was accomplished with pneumatic bladders attached to the aluminum receiver cases. These bladders were inflated with a hand pump at the surface with a net air pressure of about 10 to 20 psi (69 to 138 kPa).

Figure 8.A.1-7 shows a hypothetical borehole arrangement for crosshole testing. The three boreholes are labeled B1, B2 and B3. Crosshole measurements can be made along direct (source-to-receiver) and interval (receiver-to-receiver) travel paths. Interval measurements minimize undesirable factors such as trigger calibration, borehole casing, soil-grout compatibility and soil disturbance. Such factors can adversely affect travel times (Hoar, 1982). Travel times measured from direct paths must be corrected by a calibration factor (Fuhrman, 1993); no time correction factor is applied to interval travel times. With the source (S) in Borehole B1 and receivers (R1 and R2) in Boreholes B2 and B3, respectively, crosshole measurements are performed for the forward testing profile (Figure 8.A.1-7a). Following this forward series of tests, reverse profile tests (Figure 8.A.1-7b) are performed by removing the source from B1 and placing it into B3; the receiver in B3 (R2) is removed and placed into B1.

When crosshole tests are performed in both forward and reverse profiles, direct and interval seismic wave velocities may be compared across the same path. Such comparisons are useful in identifying a possible trigger calibration error, since interval travel times are independent of the source trigger; interval travel times depend only on the time between arrivals of the wave at the two receivers.



a. Forward Profile



b. Reverse Profile

Notes: S = Source Location  
 R1 = Location of 3-D Receiver Closest to the Source  
 R2 = Location of 3-D Receiver Farthest from the Source

**Figure 8.A.1-7**

Plan view of a typical borehole layout for crosshole tests with definitions of forward and reverse testing profiles with direct and interval travel paths.

#### **8.A.1.2.3.2 Data Collection**

For direct path measurements, the electrical cable on the source accelerometer is connected to channel one of the HP 3562A analyzer, and the geophone switching box is connected to channel two (Figure 8.A.1-2). The electrical signal from the source accelerometer triggers the recording equipment from channel one, and the appropriate receiver output enters the recorder through channel two. Compression (P) waves and shear (SV or SH) waves are usually measured and recorded at each depth. For interval path measurements, two geophones are connected to channels one and two of the recording equipment. The recording equipment is triggered by the source accelerometer, which is connected to an external trigger jack on the analyzer.

At each measurement depth, the procedure of operating the source and recording the wave arrivals was done several times, typically 3 to 9 times (up to 300 times in some cases), with the equipment in the initial position to ensure the reproducibility of the test and to measure an averaged waveform. Digitized records of the waveforms were then stored on magnetic disks for future analysis.

#### **8.A.1.2.4 Wave Velocity Analysis**

Determination of body wave velocity requires wave travel time and the distance traveled by the wave. Determination of these two parameters is discussed below.

##### **8.A.1.2.4.1 Travel Time Determination**

After the field tests were completed, all waveforms were analyzed in the office on the HP 3562A signal analyzer to identify initial wave arrivals and to determine travel times. The HP 3562A analyzer can expand the waveforms vertically and horizontally for more precise identification of initial wave arrivals. At the time initial wave arrivals were identified, a subjective rating of relative quality of the raw data was assigned to each measurement. Data are indexed as either Type I, Type II or Type III data as follows:

- Type I data: initial wave arrival clearly identified (within 5% of total travel time),
- Type II data: initial wave arrival less distinct than Type I but identifiable (within about 10% of total travel time) and
- Type III data: some interpretation required to identify initial wave arrival.

If the wave arrival could not be interpreted, then no data was reported for the wave at that measurement depth and spacing.

Figure 8.A.1-8 shows typical time records for direct (Figure 8.A.1-8a) and interval (Figure 8.A.1-8b) shear (SV) wave measurements. These measurements are classified as Type I data. The waveforms in Figure 8.A.1-8a were measured at Treasure Island at a depth of 15 ft (4.6 m), and the waveforms in Figure 8.A.1-8b were measured at Gilroy 2 at a depth of 115 ft (35.1 m). For comparison, examples of Type II data and Type III data are shown in Figures 8.A.1-9 and 8.A.1-10, respectively. These records are also SV-waves measured in direct (source-receiver) tests at Treasure Island at depths of 110 ft (33.5 m) and 96 ft (29.3 m), respectively. The SV-waves were generated by the mechanical wedge source.

In Figures 8.A.1-8a, 8.A.1-9 and 8.A.1-10, the top waveform, called the trigger, is the output from the accelerometer mounted on the wedge and hammer source. The first abrupt departure in the trigger waveform indicates the time of hammer impact at the source (see Figure 8.A.1-3). The lower waveform pair contains output from the vertical geophone in the near receiver borehole. The solid waveform is the averaged waveform generated by downward impacts at the source, and the dashed waveform is the averaged waveform from upward impacts. Similar waveforms are obtained from direct tests for SH- and P-waves; however, only one waveform (no reversals) is recorded from P-wave measurements.

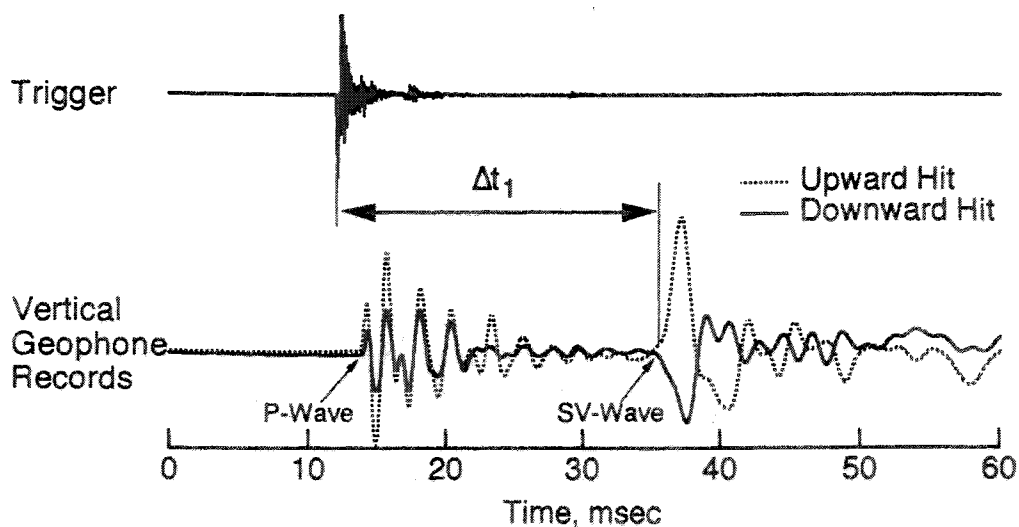
Figure 8.A.1-8b contains two pairs of waveforms recorded from interval SV-wave measurements. The upper pair is the vertical geophone output from the receiver nearer to the source (R1), and the lower waveforms are from the receiver farther from the source (R2). Again, similar waveforms are recorded for interval measurements of P- and SH-waves.

Time domain analysis of the direct path data (Figure 8.A.1-8a) requires identification of the trigger time and initial arrival of the compression or shear wave on the respective waveform records. (The solid dots, "•", in Figures 8.A.1-9 and 8.A.1-10 indicate the arrival times selected for the direct SV-waves.) The difference between these times,  $\Delta t_1$ , is the total travel time. The source calibration factor must be subtracted from this time for wave velocity determination. Interval path travel times (Figure 8.A.1-8b) are determined by identifying the initial arrival of the compression or shear wave on each waveform and determining the difference between these times ( $\Delta t_2$ ).

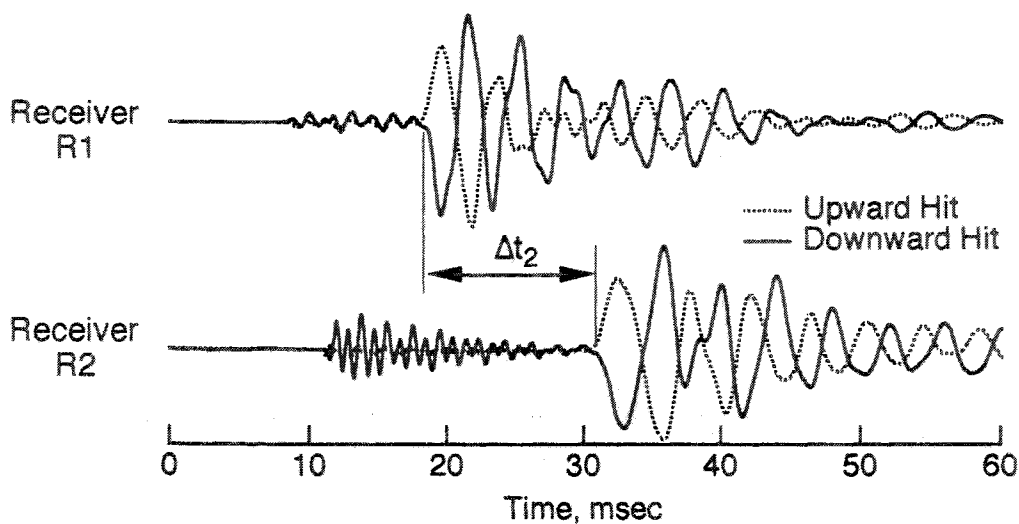
To determine the wave velocity, it is necessary to compute the correct center-to-center spacing of the boreholes with depth and the travel path distances. This procedure is described below in Section 8.A.1.2.4.2. The wave velocity,  $v$ , is the travel path distance,  $d$ , divided by the travel time,  $t$ :

$$v = \frac{d}{t} \quad (2.1)$$

Computation of the center-to-center borehole spacings and the travel path distances is discussed in Section 8.A.1.2.4.2.



a) Example of Direct Travel Time Determination. Shear Wave Travel Time Records from Seismic Crosshole Testing Using the Mechanical Wedge Source at Treasure Island; Forward Profile, Depth= 15 ft; Type I Data

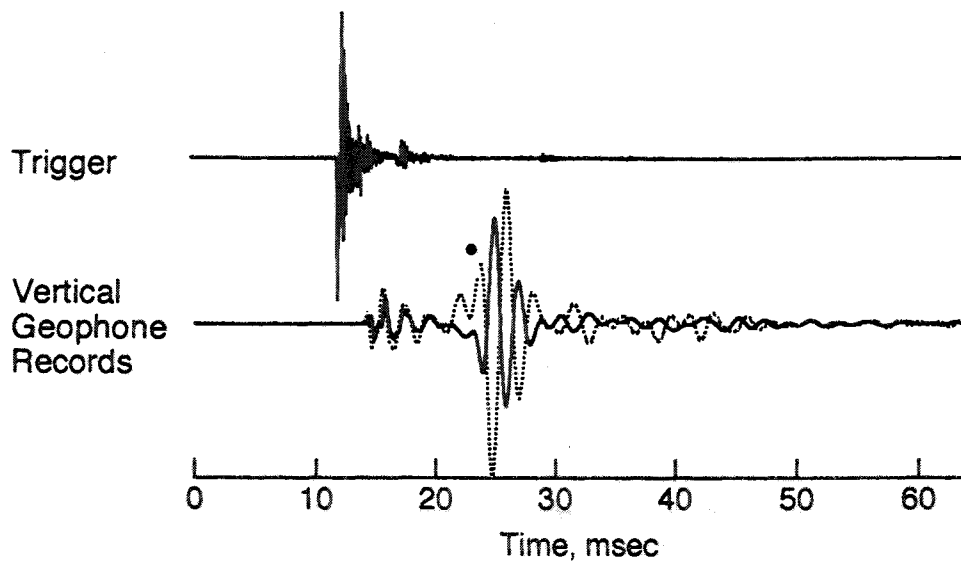


b) Example of Interval Travel Time Determination. Shear Wave Travel Time Records from Seismic Crosshole Testing Using the Mechanical Wedge Source at Gilroy No. 2; Reverse Profile, Depth= 115 ft; Type I Data

Figure 8.A.1-8

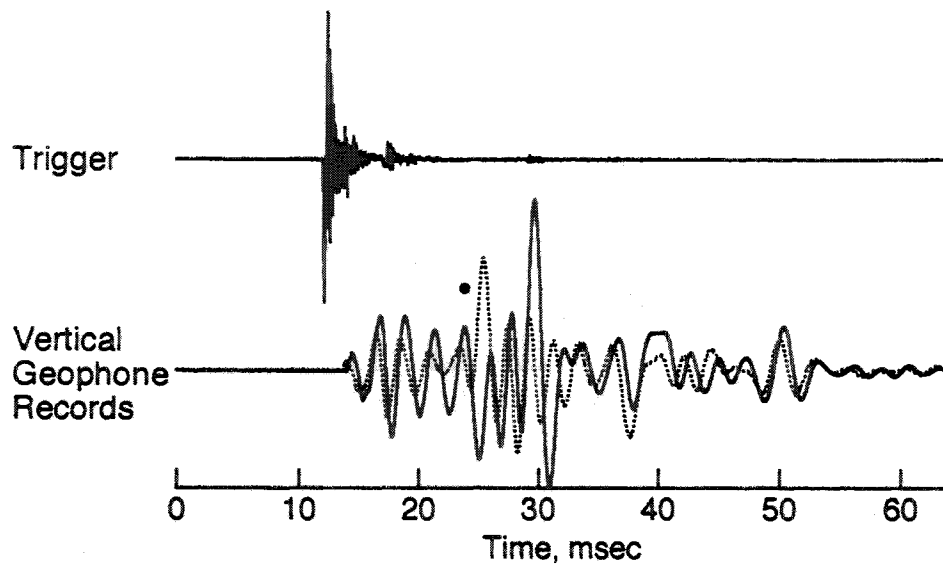
Examples of determination of SV-wave travel times for direct and interval travel path measurements for Type I data.





**Figures 8.A.1-9**

Example of Type II data from direct crosshole tests at Treasure Island; SV-wave, forward profile; depth = 110 ft (33.53 m).



**Figure 8.A.1-10**

Example of Type III data from direct crosshole tests at Treasure Island; SV-wave, forward profile; depth = 96 ft (29.3 m).

#### 8.A.1.2.4.2 Borehole Inclination Survey

Due to limitations of drilling equipment and inhomogeneities in the subsurface materials, installation of perfectly straight boreholes is not possible. Therefore, the center-to-center distance between boreholes at depth does not equal the center-to-center distance measured between the same boreholes at the surface. The proper center-to-center distance as a function of depth is determined using the results of a borehole inclination survey. Such a survey produces borehole deviations, or drift, from vertical in two orthogonal directions. Agbabian Associates of Pasadena, California measured borehole drift in the True North and True West directions at approximately 1-meter (3.3 ft) increments down each borehole at Gilroy 2 and Treasure Island. Their results were used to calculate borehole spacings at depth.

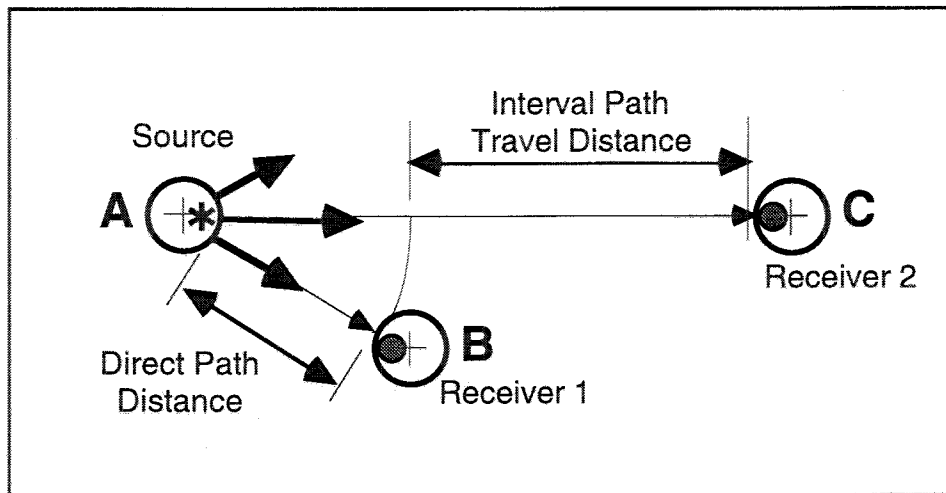
The simplest way to determine the correct center-to-center borehole spacings as a function of depth employs a coordinate system to locate the position of each borehole as a function of depth relative to a common origin. The method for establishing this coordinate system is described by Fuhrman (1993). The distance between two hypothetical boreholes, B1 and B2, is determined using the borehole offsets in global coordinates in the distance formula:

$$\text{center - to - center} = \sqrt{(x_1 - x_2)^2 + (y_1 - y_2)^2} \quad (2.2)$$

where  $x_1$  and  $x_2$  = X-direction offsets of B1 and B2, respectively, and

$y_1$  and  $y_2$  = Y-direction offsets of B1 and B2, respectively.

After the center-to-center distances between boreholes as a function of depth are determined using Eq. 2.2, the travel path distances are calculated. Figure 8.A.1-11 shows the relative locations of three hypothetical boreholes, A, B and C, at some depth below the ground surface.



**Figure 8.A.1-11**  
Illustration of travel path determination.

Ray theory suggests that the energy generated at the source will propagate radially from the source borehole. Therefore, the direct travel path distance will be the center-to-center distance between the source and receiver boreholes minus one borehole diameter (due to the positions of the source and receiver in the boreholes). The distance used in interval path computations must be based upon the path traveled by a hypothetical single ray of seismic wave energy, whose interval travel time is equivalent to the measured time between initial wave arrivals at Boreholes B and C. This distance is the difference between the center-to-center distances between Boreholes A and C and between Boreholes A and B; that is:

$$\overline{BC} = \overline{AC} - \overline{AB} \quad (2.3)$$

where  $\overline{BC}$  is the interval travel path distance.

It should be noted that because the computation procedures for direct and interval path distance calculations are different, the direct path distance for forward profile measurements,

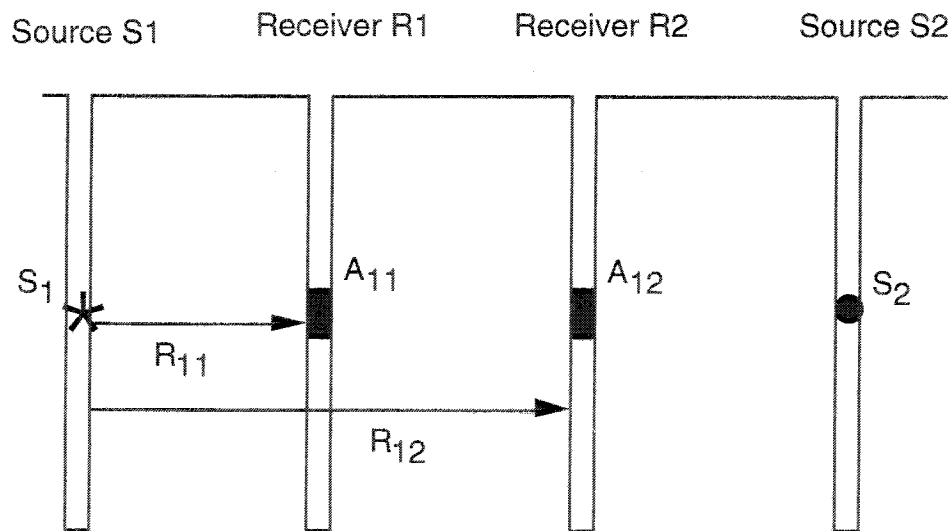
$\overline{AB}$ , usually will not equal the interval path distance,

$\overline{BA}$  for reverse profile measurements.

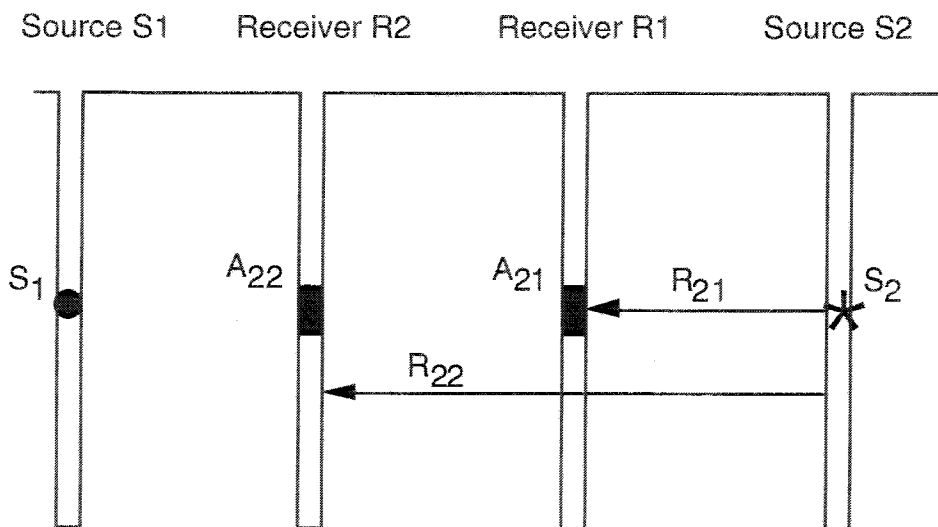
It should also be noted that the procedures described above were generally followed except at the Gilroy 2 site, where P-waves generated with the mechanical wedge source were measured without orienting the radial geophones in the direction of maximum wave motion. At Gilroy 2, the receivers were lowered by wire rope, as discussed in Section 3, due to the limited quantity of orientation rod lengths. Because the orientation of the 3-D receiver in the borehole was unknown, both the radial and the transverse geophones were monitored, and the record showing the earliest P-wave arrival was recorded. Also, because the receivers were lowered by wire rope with no means to ensure their orientation, the average position of the receivers was assumed to be in the center of the borehole for travel path computations. Again, these exceptions to the usual practice described above apply only to measurements made using the mechanical wedge source at Gilroy 2.

#### 8.A.1.2.5 Material Damping Analyses At Gilroy 2

Figure 8.A.1-12 is a schematic representation of the Gilroy 2 crosshole array that was used to make in-situ damping measurements. Tests were conducted in both the forward and reverse directions. This study applies two similar methods to evaluate material damping,  $D$ , using the travel time records of SV-waves collected in these tests. Both methods of analysis are based on measuring the attenuation of the various frequency components of a particular seismic wave. The first method, hereafter called the spectral ratio method, is a variation of a method proposed by Mok (1987). This method assumes that material damping is variable over the frequency span excited in the test and that the geometric component of attenuation is known and equal to  $1/R$ , where  $R$  is the distance traveled by the wave from the source to a receiver. The second method, outlined by Redpath et al. (1982) and Redpath and Lee (1986), assumes that damping is constant over the frequency span excited in the test and that no geometric spreading law needs to be assumed because it can be excluded from the computation. This second method is hereafter called the spectral slope method.



(a) Forward Direction



(b) Reverse Direction

**Figure 8.A.1-12**

Schematic of borehole layout for in-situ damping measurements at Gilroy 2.

#### 8.A.1.2.5.1 Spectral Ratio Method

Based on the assumptions that different frequency components can propagate and attenuate at different rates and attenuation can be related to changes in the spectral ratios with distance, a spectral ratio is defined as the ratio of two body wave amplitudes at different distances from a seismic source. The body wave amplitudes at Receivers R1 and R2 are defined as:

$$A_{11} = S_1 \frac{1}{R_{11}} I_1 e^{-\alpha R_{11}} \quad (2.4)$$

and

$$A_{12} = S_1 \frac{1}{R_{12}} I_2 e^{-\alpha R_{12}} \quad (2.5)$$

where  $A_{11}$  = body wave amplitude at Receiver R1 at a distance  $R_{11}$  from Source S1,

$A_{12}$  = body wave amplitude at Receiver R2 at a distance  $R_{12}$  from Source S1,

$S_1$  = amplitude of impulse from Source S1

$I_1$  = interaction function at Receiver R1 that contains effects of coupling and verticality of Receiver R1 and frequency characteristics of the receiver-borehole system,

$I_2$  = interaction function at Receiver R2,

$\alpha$  = attenuation coefficient,

$R_{11}$  = near edge-to-near edge distance between Source S1 and Receiver R1, and

$R_{12}$  = near edge-to-near edge distance between Source S1 and Receiver R2.

The term  $1/R$  accounts for geometric spreading. With the body wave amplitudes at receivers R1 and R2, the spectral ratio from the forward direction,  $SR_f$ , becomes:

$$SR_f = \frac{A_{12}}{A_{11}} = \frac{R_{11}}{R_{12}} \frac{I_2}{I_1} e^{-\alpha(R_{12}-R_{11})} \quad (2.6)$$

The spectral ratio method for material damping assumes that the phase of the spectral ratio varies with frequency spectrum of the body wave; therefore, the wave velocity can also vary with frequency. The phase of the spectral ratio is described by:

$$\phi_f = 2\pi f \frac{R_{12} - R_{11}}{v} \quad (2.7)$$

where  $\phi_f$  = phase of wave velocity in the forward direction,

$f$  = frequency, and

$v$  = wave propagation velocity.

If one assumes  $I_1 \approx I_2$ , then the attenuation coefficient,  $\alpha$ , may be expressed as:

$$\alpha = \frac{-\ln\left(SR_f \cdot \frac{R_{12}}{R_{11}}\right)}{R_{12} - R_{11}} \quad (2.8)$$

The quality factor  $Q$ , a common measure of attenuation, may be defined as (Toksoz and Johnston, 1981):

$$\frac{1}{Q} = \frac{\delta}{\pi} = \frac{\alpha v}{\pi f} \quad (2.9)$$

where  $Q$  = quality factor,

$\delta$  = logarithmic decrement, and

$\alpha$  = attenuation coefficient.

For engineering applications, material damping,  $D$ , is usually used to describe attenuation. For low values of attenuation, the relationship between  $Q$  and  $D$  is:

$$D = \frac{1}{2Q} \quad (2.10)$$

By combining Eqs. (2.6) through (2.10), one obtains an equation for material damping from crosshole tests performed in the forward direction:

$$D_f = \frac{\ln\left(SR_f \cdot \frac{R_{11}}{R_{12}}\right)}{\phi_f} \quad (2.11)$$

A similar equation may be developed for  $D$  in the reverse direction (denoted as  $D_r$  in this case).

When the forward test is complete, the source is removed from Borehole S1 and placed into Borehole S2. The receivers R1 and R2 remain in their respective boreholes but are renamed R2 and R1, respectively. This arrangement is called the reverse direction and is shown in Figure 8.A.1-12b. After travel time records are recorded in the reverse array, the spectral ratio from the reverse array,  $SR_r$ , is calculated:

$$SR_r = \frac{A_{22}}{A_{21}} = \frac{R_{21}}{R_{22}} \frac{I_1}{I_2} e^{-\alpha(R_{22}-R_{21})} \quad (2.12)$$

where  $A_{21}$  = body wave amplitude at Receiver R1 at a distance  $R_{21}$  from Source S2,

$A_{22}$  = body wave amplitude at Receiver R2 at a distance  $R_{22}$  from Source S2,

$R_{21}$  = near edge-to-near edge distance between Source S2 and Receiver R1, and

$R_{22}$  = near edge-to-near edge distance between Source S1 and Receiver R2.

The undesirable effects of  $I_1$  and  $I_2$  mathematically cancel when Eq. (2.6) is multiplied by Eq. (2.12):

$$SR_f \cdot SR_r = \frac{R_{11}}{R_{12}} \frac{R_{21}}{R_{22}} \frac{I_1}{I_2} \frac{I_2}{I_1} e^{-\alpha[(R_{12}-R_{11})+(R_{22}-R_{21})]} \quad (2.13)$$

The attenuation coefficient,  $\alpha$ , for a damping analysis for the forward and reverse directions follows as:

$$\alpha = \frac{\ln\left(\frac{SR_f SR_r R_{12} R_{22}}{R_{11} R_{21}}\right)}{(R_{12} - R_{11}) + (R_{22} - R_{21})} \quad (2.14)$$

When Eqs. (2.9), (2.10) and (2.14) are combined, the expression for material damping, which is based on travel time records from the forward and reverse directions, is:

$$D_{fr} = \frac{-\ln\left(SR_f SR_r \frac{R_{12} R_{22}}{R_{11} R_{21}}\right)}{(\phi_f + \phi_r)} \quad (2.15)$$

Again, Eq. (2.15) is based on the assumption that different frequencies of a wave attenuate at different rates and that wave velocity can vary with frequency. The term  $(R_{12}R_{22}/R_{11}R_{21})$  accounts for geometrical spreading. Equation (2.15) is valid also for frequency-independent damping. In fact, (Eq. 2.15) may be modified to produce an expression for material damping that assumes a constant wave velocity:

$$D_{fr} \text{ (constant velocity)} = \frac{-\ln\left(SR_f SR_r \frac{R_{12} R_{22}}{R_{11} R_{21}}\right)}{2\pi f(\Delta t_f + \Delta t_r)} \quad (2.16)$$

where  $\Delta t_f$  is the wave travel time between Receivers 1 and 2 in the forward direction, and  $\Delta t_r$  is the wave travel time between receivers in the reverse direction.

#### 8.A.1.2.5.2 Spectral Slope Method

Redpath (1982) and Redpath and Lee (1986) describe a second method to evaluate material damping. Although this method is presented in terms of downhole travel time records, the method may be used for time records from crosshole tests as well. This second method, hereafter called the spectral slope method, is similar to the variable-damping method described above but assumes that material damping is constant throughout the frequency spectrum of the body wave and that a geometric damping law does not need to be assumed in determining D.

The expression for spectral ratio presented by Redpath et al. is similar to Eqs. (2.6) and (2.12):

$$SR_f = \frac{A_{12}}{A_{11}} = \frac{R_{11}}{R_{12}} \frac{I_2}{I_1} e^{-kf(R_{12} - R_{11})} \quad (2.17)$$

where  $k$  = attenuation constant ( $k = \alpha/f$ ). Equation (2.16) represents the spectral ratio from a forward direction test. Taking the natural logarithm of both sides of Eq. (2.17) yields:

$$\ln SR_f = \ln \left( \frac{R_{11}}{R_{12}} \frac{I_2}{I_1} \right) - kf(R_{12} - R_{11}) \quad (2.18)$$

A spectral slope is then defined as:

$$\frac{\Delta \ln SR_f}{\Delta f} = -k(R_{12} - R_{11}) \quad (2.19)$$

Note that at this point the geometric damping term and the geophone interaction terms,

$$\left( \frac{R_{11}}{R_{12}} \frac{I_2}{I_1} \right),$$

mathematically drop out of the formulation because they are constants. An equation for attenuation follows as:

$$k = \frac{-\Delta \ln SR_f}{\Delta f(R_{12} - R_{11})} \quad (2.20)$$

and

$$k = \frac{\pi}{Qv} \quad (2.21)$$



By combining Eqs. (2.10), (2.20) and (2.21), an equation for material damping in the forward test direction, assuming constant material damping throughout the frequency spectrum and negligible geometrical scattering, results:

$$D_f = \frac{-\Delta \ln SR_f}{\Delta f} \frac{1}{2\pi\Delta t_f} \quad (2.22)$$

An expression for D similar to Eq. (2.21) can also be obtained for the reverse test direction. If one combines equations for the spectral ratio in both the forward and reverse directions, an equation for material damping,  $D_{fr}$ , that eliminates (or at least minimizes) undesirable effects of the boreholes and receivers is:

$$D_{fr} = \frac{-\ln(SR_f SR_r)}{\Delta f} \cdot \frac{1}{2\pi(\Delta t_f + \Delta t_r)} \quad (2.23)$$

#### 8.A.1.2.6 Summary

Crosshole seismic tests were performed to evaluate body wave velocities at the Gilroy 2 and Treasure Island sites. Material damping measurements were also performed at the Gilroy 2 site. At each testing depth, three types of seismic waves were monitored: P-, SV- and SH-waves. Shear waves of opposite polarities were usually measured at each testing depth. Wave velocities were computed by dividing travel distances by the travel times. Performance of these tests and computation of the resulting parameters are discussed in this section.

Measurements of SV-waves at the Gilroy 2 site were also analyzed for evaluation of material damping. Two methods were employed: the spectral ratio method and the spectral slope method. The spectral ratio method assumes variable material damping and variable wave velocity across the frequency spectrum of the body wave. The spectral slope method assumes constant material damping at all frequencies. The other major difference between the two methods is that the spectral ratio method explicitly assumes that geometrical spreading of the body wave is equal to  $(1/R)$ , where R is the travel distance from the source to the receiver. In the spectral slope method, no geometrical spreading law is assumed in the solution for material damping.

### **3—WAVE VELOCITIES FROM CROSSHOLE TESTING AT GILROY 2**

#### **8.A.1.3.1 Introduction**

The Gilroy 2 site is located approximately 30 miles (48 km) south of San Jose, California within the city limits of Gilroy, Santa Clara County. As shown in Figure 8.A.1-1, the site lies approximately 20 miles (32 km) east of the epicenter of the 1989 Loma Prieta earthquake. The California Department of Conservation, Division of Mines and Geology, maintains a strong-motion seismograph that recorded strong ground motions at the site during the 1989 earthquake (Shakal et al., 1990). The actual testing area is located behind the National 9 Inn in the vicinity shown in Figure 8.A.1-13. Testing was conducted from 9 to 21 December 1991.

A USGS boring log from Gilroy 2 (Gibbs et al., 1992) is shown in Figure 8.A.1-14. The boring log shows approximately 40 ft (12 m) of Holocene alluvium consisting of sandy loam and silty clay loam underlain by about 33 ft (10 m) of Late Pleistocene alluvium consisting of approximately 10 ft (3 m) of clay and 23 ft (7 m) of sandy fine gravel. Pleistocene lake deposits exist between depths of about 72 ft (22 m) and 131 ft (40 m); these deposits consist of about 33 ft (10 m) of clay underlain by 26 ft (8 m) of sandy loam and silty clay. Pleistocene alluvium, consisting of gravelly sand, sandy clay and gravel, extends from a depth of about 130 ft (40 m) to approximately 550 ft (168 m), where Monterey shale is encountered.

Four borings were drilled prior to the crosshole testing. Each boring was cased with PVC, schedule 40 well casing. The depth and ID of each cased borehole is given in Table 8.A.1-3. The thickness of all well casing was 0.25 in. (0.64 cm).

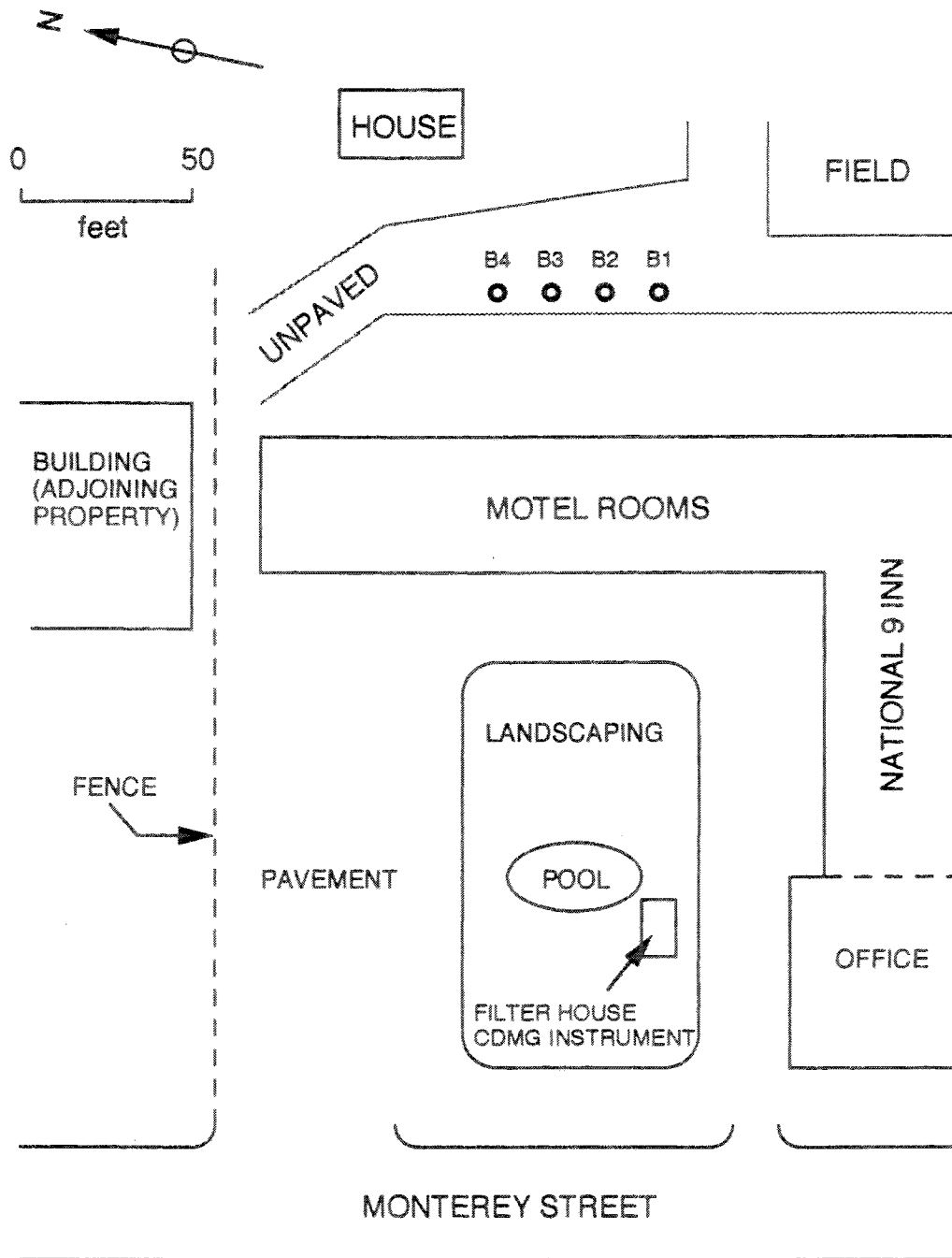
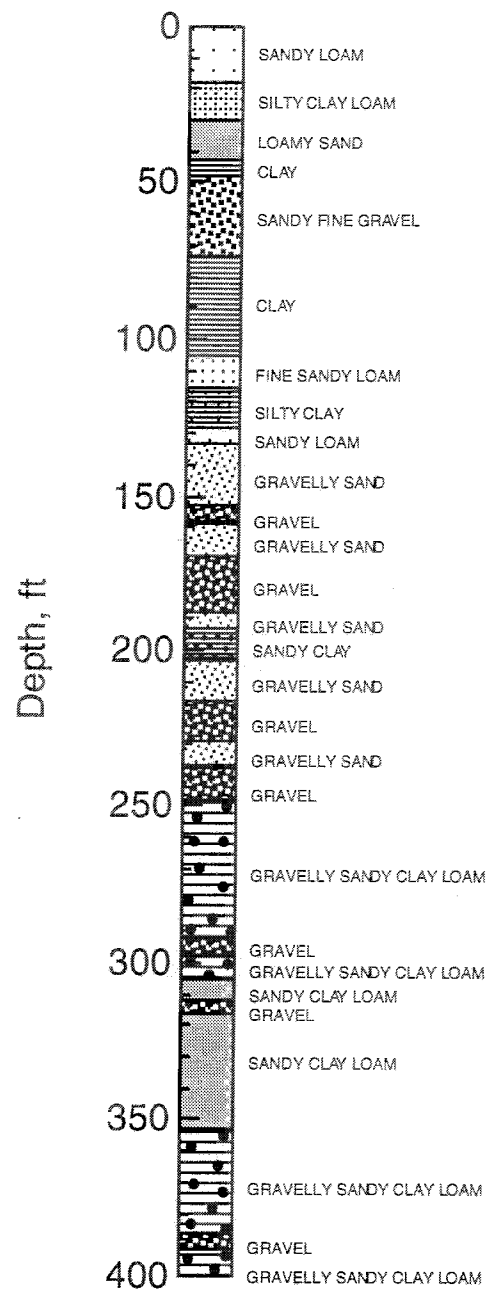


Figure 8.A.1-13  
Location of Gilroy 2 site (after Gibbs et al., 1992).



**Figure 8.A.1-14**  
Geologic log at Gilroy 2 (after Gibbs et al., 1992).

**Table 8.A.1-3**

Depths and Diameters of Cased Boreholes Used in Seismic Crosshole Testing at Gilroy 2

Borehole	Depth, ft (m)	ID, in. (cm)
B1	600 (183)	5 (12.7)
B2	800 (244)	4 (10.2)
B3	200 (61)	4 (10.2)
B4	200 (61)	4 (10.2)

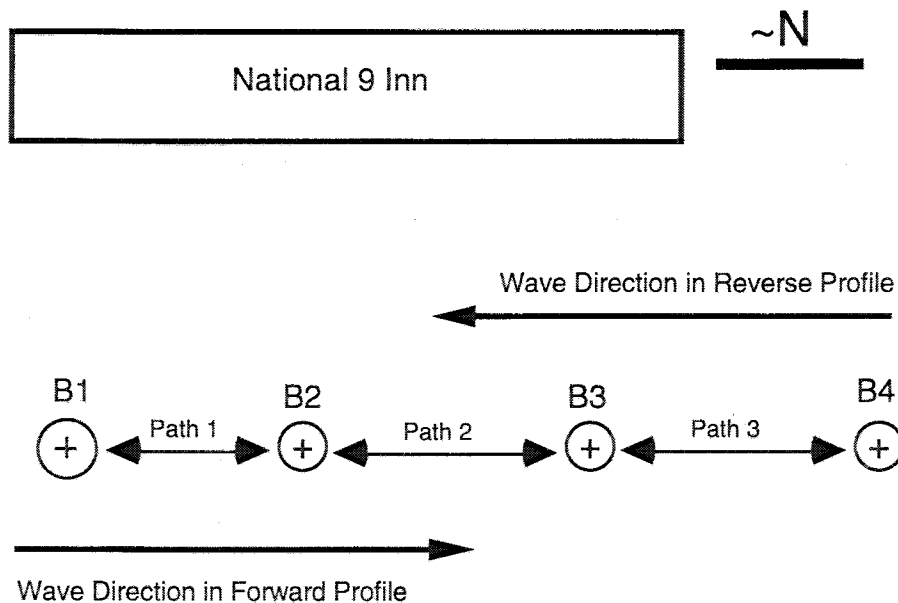
The center-to-center distances between boreholes measured at the surface are summarized in Table 8.A.1-4. These measurements were made with a fiberglass hand-held measuring tape. Unfortunately, borehole offsets transverse to the borehole array were not measured. Based on a visual inspection made during seismic testing, these offsets are assumed to be very small compared to the center-to-center distances and are therefore neglected in path length computations.

**Table 8.A.1-4**

Center-to-Center Distances Between Boreholes Measured at the Surface at Gilroy 2

Path	Distance, ft (m)
B1-B2	14.02 (4.27)
B1-B3	27.63 (8.42)
B2-B3	13.58 (4.14)
B3-B4	14.23 (4.34)
B4-B2	27.85 (8.49)
B4-B1	41.88 (12.77)

The four boreholes are arranged in a linear array as shown in Figure 8.A.1-15. The array runs in an approximate north-south direction. With the source in borehole B1, boreholes B2, B3 and B4 were used as first, second and third receiver boreholes, respectively. This arrangement of source and receivers is called the forward testing profile. A reverse testing profile was created by switching the locations of the source and the third receiver (R3); that is, the source was removed from B1 and placed in B4, and R3 was placed in B1. Three wave paths were used in these tests as illustrated in Figure 8.A.1-15: Path 1 (between B1 and B2), Path 2 (between B2 and B3) and Path 3 (between B3 and B4). Measurements were performed across these three paths with waves traveling in both forward and reverse directions.



**Figure 8.A.1-15**  
General borehole locations at Gilroy 2. Note: drawing not to scale.

Crosshole measurements at Gilroy 2 were performed at various depth intervals as outlined in Tables 8.A.1-5 and 8.A.1-6. The shallowest depth at which measurements were recorded is 5 ft (1.5 m). The mechanical wedge source (Table 8.A.1-5) was used to a maximum depth of 390 ft (119 m) in direct tests between boreholes B1 and B2. The maximum depths (200 ft or 61 m) of boreholes B3 and B4 limited interval and reverse profile tests with the mechanical wedge source to 195 ft (59.4 m). The wedge source was used to generate both P- and SV-waves in the forward and reverse test directions. Wire rope was used to lower the source and receivers for all measurements made using the mechanical wedge source.

**Table 8.A.1-5**

Crosshole Measurement Depth Intervals at Gilroy 2 with the Mechanical Wedge Source  
(P- and SV-Waves)

Forward Profile				Reverse Profile			
Direct Measurements <sup>a</sup>		Interval Measurements <sup>b</sup>		Direct Measurements <sup>c</sup>		Interval Measurements <sup>d</sup>	
Depths (ft)	Test Interval (ft)	Depths (ft)	Test Interval (ft)	Depths (ft)	Test Interval (ft)	Depths (ft)	Test Interval (ft)
5-10	2.5	5-195	5	5-195	10	5-195	10
10-390	5						

- <sup>a</sup> in the forward profile, direct measurements were performed between boreholes B1 and B2
- <sup>b</sup> in the forward profile, interval measurements were performed between boreholes B2 and B3 and between B3 and B4
- <sup>c</sup> in the reverse profile, direct measurements were performed between boreholes B4 and B3
- <sup>d</sup> in the reverse profile, interval measurements were performed between boreholes B3 and B2 and between B2 and B1

**Table 8.A.1-6**

Crosshole Measurement Depth Intervals at Gilroy 2; Forward Profile with the Solenoid Source  
(P- and SH-Waves)

Forward Profile			
Direct Measurements <sup>a</sup>		Interval Measurements <sup>b</sup>	
Depths (ft)	Test Interval (ft)	Depths (ft)	Test Interval (ft)
5-40	5	5-40	5
40-80	10	40-80	10
80-120	5	80-120	5

- <sup>a</sup> direct measurements were performed between boreholes B1 and B2
- <sup>b</sup> interval measurements were performed between boreholes B2 and B3 and between boreholes B3 and B4

The solenoid source (Table 8.A.1-6) was used to a depth of only 120 ft (36.5 m) in the forward direction only. Because of time constraints, reverse profile measurements were not conducted using the solenoid source. Tests performed with the solenoid source were limited to 120 ft (36.5 m) because there was not enough orientation rod (see Section 8.A.1.2.3) to lower the source and three receivers beyond this depth. Both P- and SH-waves were measured using the solenoid source.

Crosshole testing was performed at Gilroy 2 over seven days as outlined in Table 8.A.1-7. Crosshole testing was performed first between boreholes B1 and B2 in the forward profile over the 200 to 390 ft (61 to 119 m) depth range with the mechanical wedge source. The forward and reverse profiles were then completed with the mechanical wedge source. All interval and reverse profile tests performed with the wedge source were performed to a maximum depth of 195 ft (59.4 m). Next, testing with the solenoid source was completed over two days in the forward direction to a depth of 120 ft (36.6 m).

In the course of crosshole tests using the mechanical wedge source, the trigger accelerometer on the source was changed twice due to failure of electrical connectors at the accelerometer and its cable. These instances are noted chronologically in Table 8.A.1-7. For each trigger configuration, the source was re-calibrated according to the methods described by Fuhrman (1993).



Table 8.A.1-7

Crosshole Testing Schedule at Gilroy 2

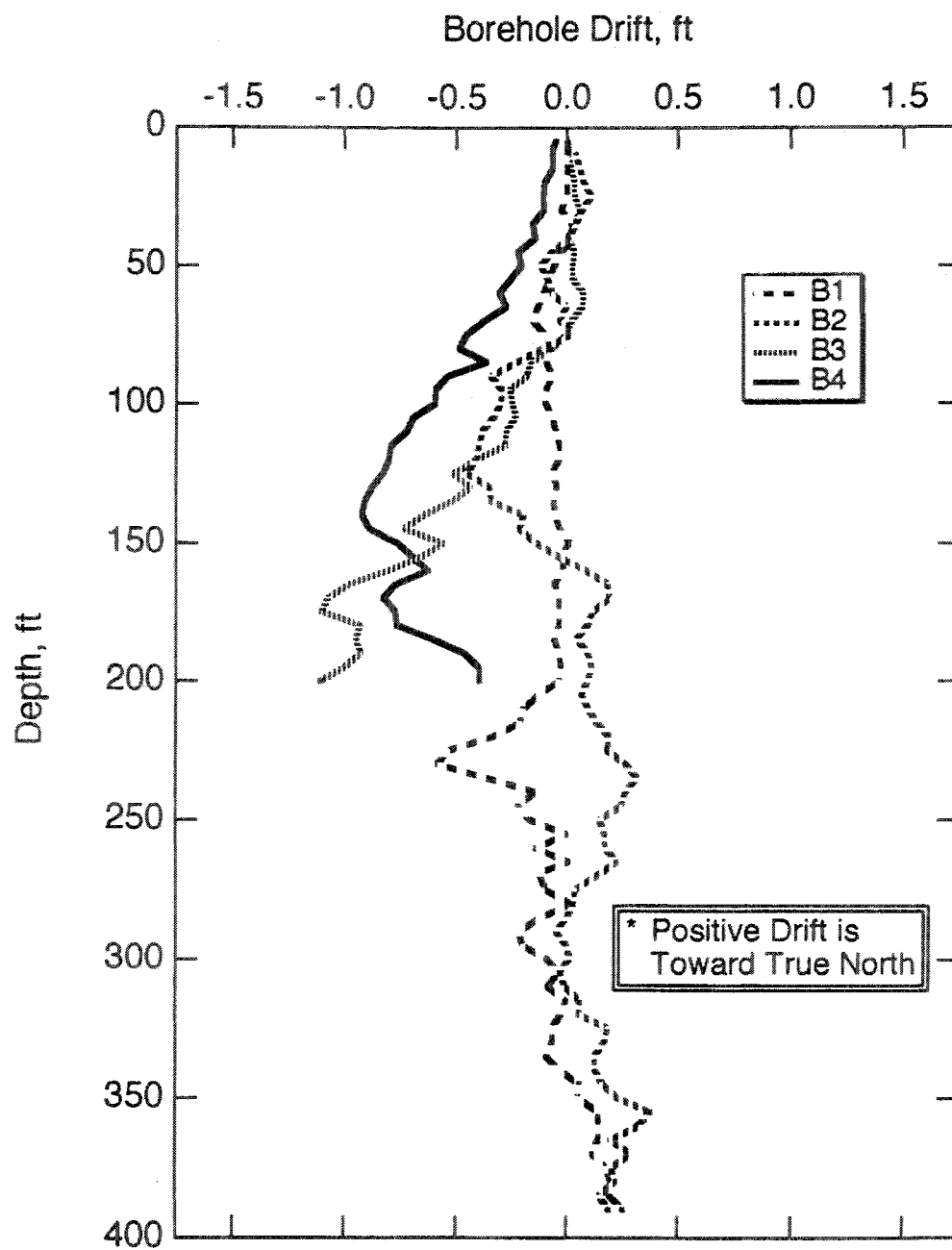
Date	Source	Testing Direction	Boreholes	Depths Tested	Comments
12/12/91	Mechanical Wedge	Forward	B1-B2	200 ft - 300 ft	-----
12/13/91	Mechanical Wedge	Forward	B1-B2	305 ft - 390 ft	-----
12/14/91	Mechanical Wedge	Forward	B1-B2, B2-B3, B3-B4	5 ft - 95 ft	•Changed trigger accelerometer at 60 ft
12/16/91	Mechanical Wedge	Forward	B1-B2, B2-B3, B3-B4	100 ft - 195 ft	-----
12/17/91	Mechanical Wedge	Reverse	B4-B3, B3-B2, B2-B1	195 ft - 5 ft	•Changed trigger accelerometer at 125 ft •Tested from bottom to top
12/18/91	Solenoid	Forward	B1-B2, B2-B3, B3-B4	10 ft - 50 ft	•Tested at 10-ft intervals
12/19/91	Solenoid	Forward	B1-B2, B2-B3, B3-B4	60 ft - 120 ft and 85 ft, 35 ft, 25 ft, 15 ft, 5 ft	•Tested at 10-ft intervals between 60 ft and 120 ft

#### **8.A.1.3.2 Borehole Inclination Survey**

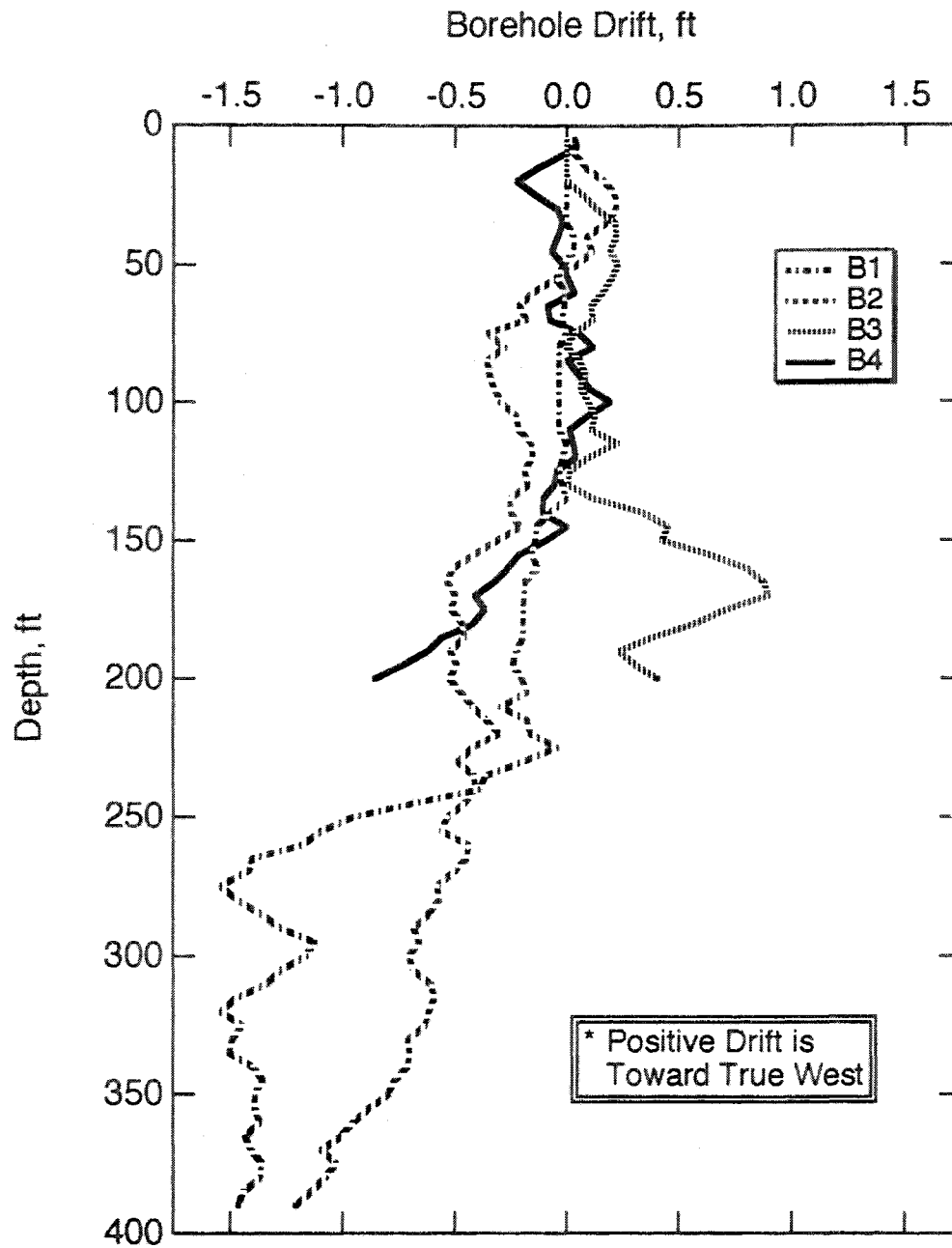
After crosshole testing, personnel from Agbabian Associates of Pasadena, California, surveyed the cased borings for verticality, and their results were used in this study. Figure 8.A.1-16 presents the results of the borehole inclination (or drift) survey in terms of drift toward True North, and Figure 8.A.1-17 shows borehole drifts in terms of drift toward True West. The borehole drift measurements were used to compute wave travel path lengths according to the method described in Section 8.A.1.2.4.1.

#### **8.A.1.3.3 Shear Wave Velocities**

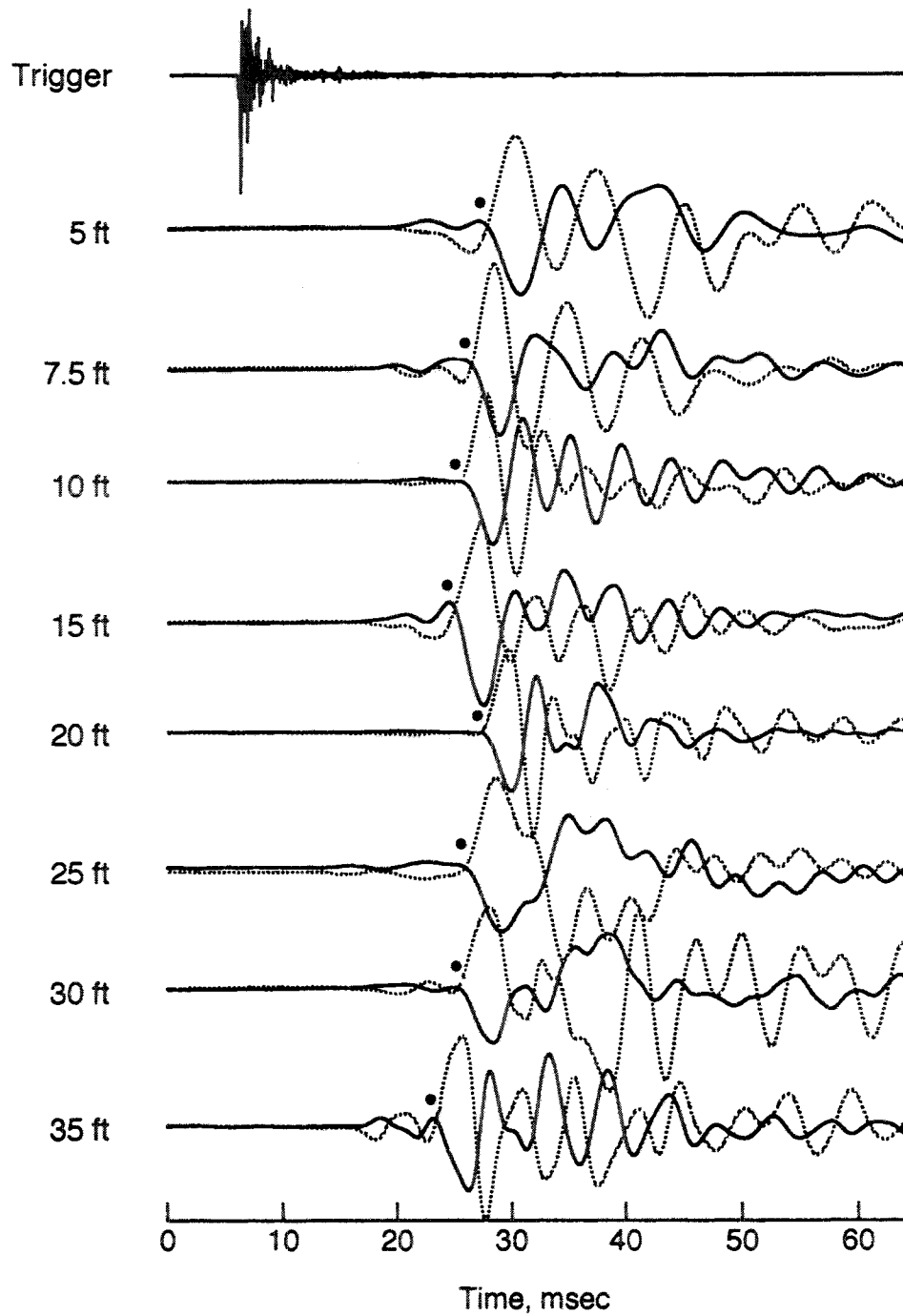
Both vertically-polarized shear (SV) waves and horizontally-polarized shear (SH) waves were measured at Gilroy 2. Approximately one hundred direct and one hundred and twenty interval SV-wave measurements were performed, and approximately twenty direct and forty interval SH-wave measurements were performed. Averaged time records, or waveforms, from all SV-wave and SH-wave measurements are presented by Fuhrman (1993). Typical waveforms of SV- and SH-waves collected at Gilroy 2 are shown in Figures 8.A.1-18 and 8.A.1-19, respectively. In all waveforms, labeled by measurement depth, solid waveforms indicate downward-arriving waves, and dashed waveforms indicate upward-arriving waves. A solid dot, "•", is positioned above the selected shear wave arrival on each record. Results of the SV-wave velocities are discussed in Section 8.A.1.3.3.1, and SH-wave velocities are discussed in Section 8.A.1.3.3.3.



**Figure 8.A.1-16**  
North-south borehole drift measurements at Gilroy 2 performed by Agbabian Associates of Pasadena, California.

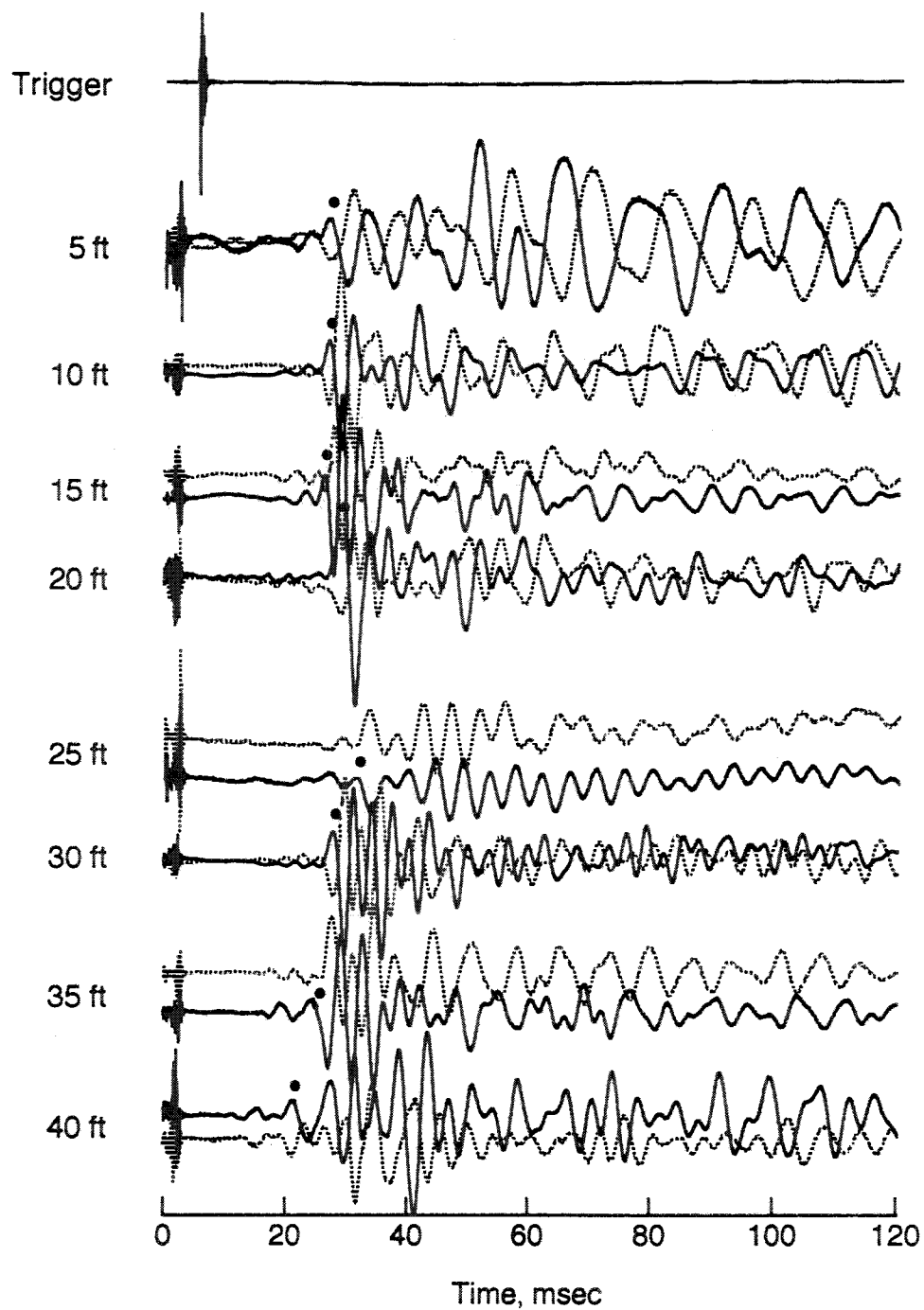


**Figure 8.A.1-17**  
East-west borehole drift measurements at Gilroy 2 performed by Agbabian Associates of Pasadena, California.



**Figure 8.A.1-18**

Examples of SV-wave travel time records collected at Gilroy 2 using the mechanical wedge source in B1 and a three-component velocity transducer in B2 (S-R1, forward profile); depths 5–35 ft.



**Figure 8.A.1-19**

Examples of SH-wave travel time records collected at Gilroy 2 using the solenoid source in B1 and a three-component velocity transducer in B2 (S-R1, forward profile); depths 5–40 ft.

#### **8.A.1.3.3.1 SV-Wave Velocities**

A summary of all SV-waves measured at Gilroy 2 is plotted in Figure 8.A.1-20. Solid circular symbols represent data measured along Path 1; solid diamonds represent Path 2 data; and open squares represent Path 3 data. Figure 8.A.1-20 shows that the data from each of the three paths follow a similar pattern to a depth of about 150 ft (45.7 m). Between 150 ft and 200 ft (45.7 m and 61.0 m), the data along one of the three paths (Path 3) vary considerably from the other data. Below 200 ft (61.0 m), the data along Path 1 is quite variable. Possible reasons for this variability are discussed below.

In addition to the variability of shear wave velocities vertically, Figure 3.8 indicates lateral variability in stiffness, especially below about 140 ft (42.7 m). Between about 75 ft (22.9 m) and 190 ft (57.9 m), the SV-wave velocities along Path 3 are consistently higher than the velocities measured along Paths 1 and 2.

For comparison with the crosshole shear wave data, the Spectral-Analysis-of-Surface-Waves (SASW) method (Stokoe et al., 1988) was employed to evaluate the shear wave velocity profile at this site, and the resulting shear wave velocity profile is shown in Figure 8.A.1-21, along with the crosshole shear (SV) wave velocities. Figure 8.A.1-21 shows good agreement between the crosshole and SASW methods to a depth of about 50 ft (15.2 m). At about 60 ft (18.3 m), the SASW shear wave velocities are nearly 500 fps (152 m/sec) lower than the crosshole SV-wave velocities. From about 75 to 100 ft (22.9 to 30.5 m) the SASW shear wave velocities are about 500 fps (152 m/sec) higher than the crosshole SV-wave velocities. The difference between the SASW and the crosshole results in this depth range is probably attributable the difference between local stiffnesses reflected by the crosshole measurements and the global stiffness reflected by the SASW measurements.

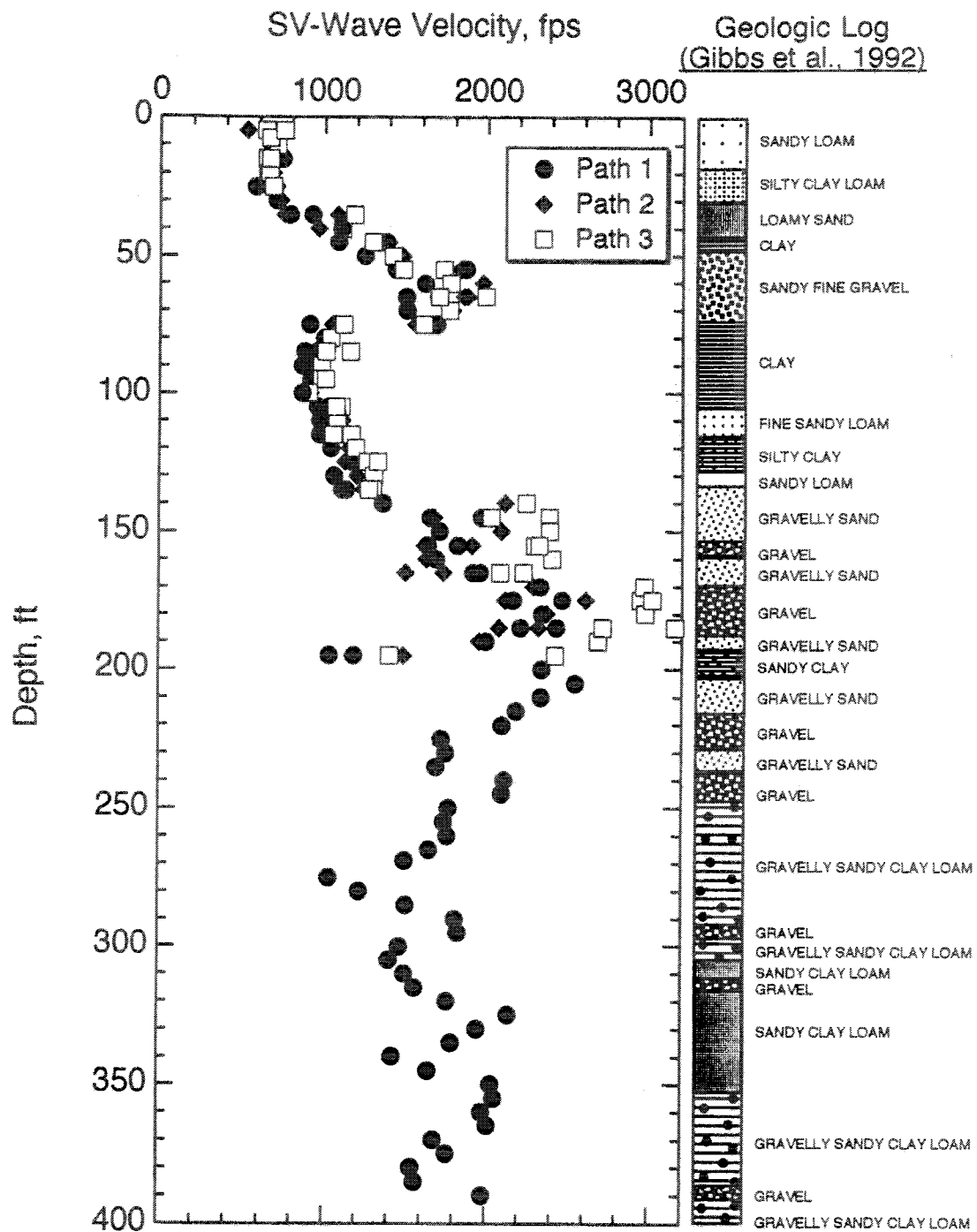
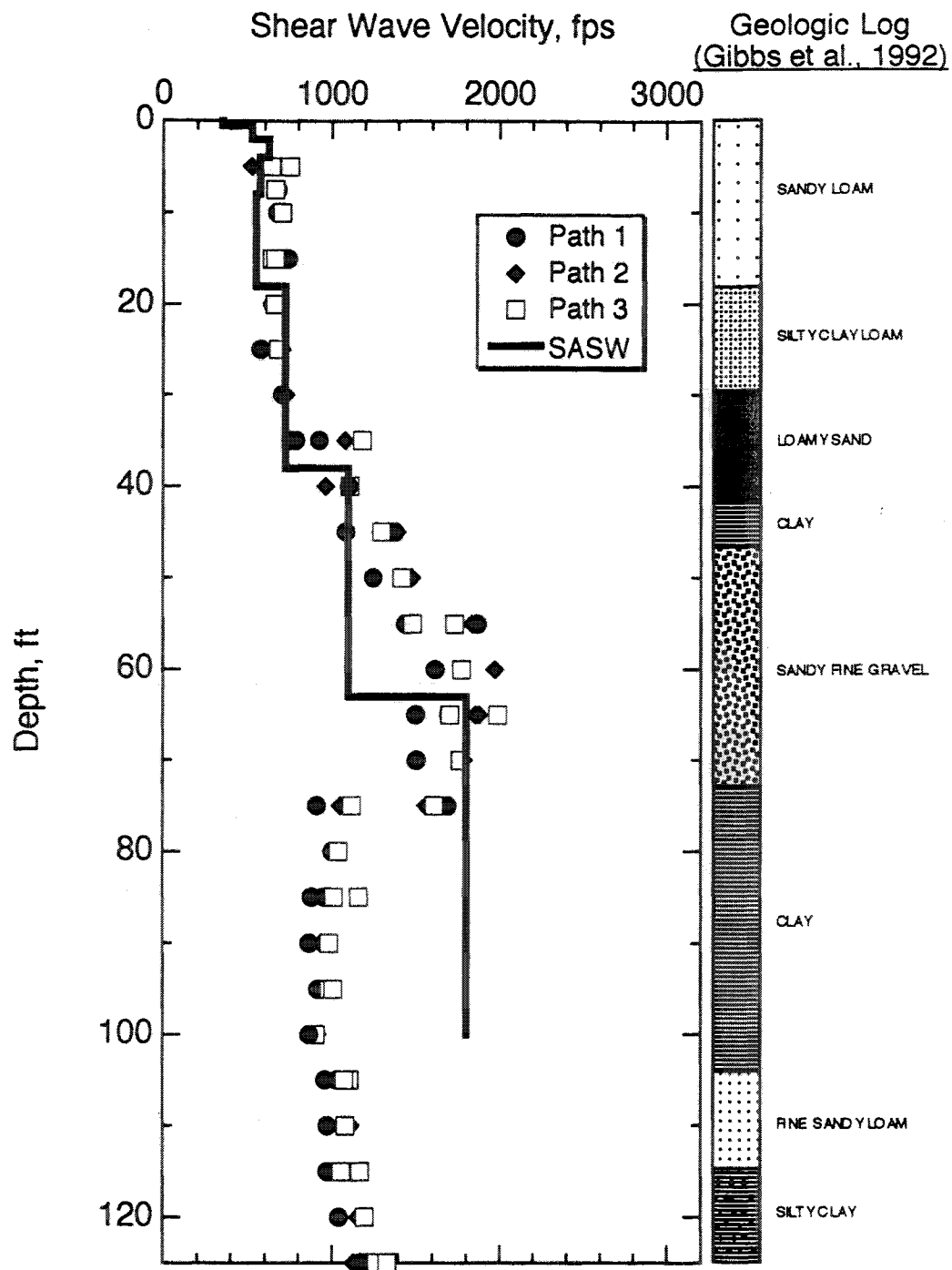


Figure 8.A.1-20  
Summary of all shear (SV) wave velocity profiles measured at Gilroy 2.





**Figure 8.A.1-21**

Comparison of all shear (SV) wave velocities measured at Gilroy 2 with the shear wave velocity profile measured by SASW testing.

**Forward Profile Measurements.** Values of path length, travel time and direct SV-wave velocity for forward profile measurements along Path 1 are presented in Table 8.A.1-19 (Appendix 8.A.1.A). Subjective ratings of relative data quality (see Section 8.A.1.2.4.1) are associated with the travel times. Tables 8.A.1-20 and 8.A.1-21 contain similar information for interval measurements across Paths 2 and 3, respectively.

**Reverse Profile Measurements.** Values of path length, travel time and direct SV-wave velocity for reverse profile measurements along Path 3 are presented in Table 8.A.1-22. Subjective ratings of relative data quality (see Section 8.A.1.2.4.1) are associated with the travel times. Tables 8.A.1-23 and 8.A.1-24 contain similar information for interval measurements across Paths 2 and 1, respectively.

**Direct and Interval Measurements Along Paths 1, 2 and 3.** All forward profile SV-wave velocities measured along Path 1 are shown in Figure 8.A.1-22 with solid symbols. Reverse profile SV-wave velocities measured along the same path are also plotted in Figure 8.A.1-22, but with open symbols. Similar plots for data measured along Paths 2 and 3 are presented in Figures 8.A.1-23 and 8.A.1-24. It should be noted that along Path 2 (Figure 8.A.1-23), both the forward and reverse profile seismic wave velocity measurements were interval measurements. Along Path 1 (Figure 8.A.1-22), the forward profile measurements were direct measurements, and the reverse profile measurements were interval measurements. Along Path 3 (Figure 8.A.1-24), the reverse profile measurements were direct measurements, while the forward profile measurements were interval measurements.

Figures 8.A.1-22 through 8.A.1-24 generally show very good agreement between forward and reverse profile measurements. Figures 8.A.1-22 through 8.A.1-24 show that the largest scatter between the forward and reverse tests occurred at a depth of 75 ft (22.9 m), where the soil profile changes from a gravelly material to a clay. In this case, the scatter actually appears to result from refraction. Further examination of Figures 8.A.1-22 through 8.A.1-24 shows that much of the scatter between forward and reverse profile tests occurs at layer boundaries or in regions where the geology is complex.

Figure 8.A.1-25 shows a statistical representation of the SV-wave velocity data from forward and reverse tests, excluding data from regions of apparent stiffness contrast (depths of 75, 145 and 195 ft (22.9, 44.2 and 59.4 m)). The average percent difference between SV-wave velocities from forward and reverse tests is only about 6%, with a standard deviation of 8.3%. The generally very good agreement between direct and interval SV-wave measurements shows that there were probably no serious equipment calibration or timing errors in the crosshole testing system.

**Comparisons with Laboratory Results.** The shear wave velocities of soil samples taken from various depths were measured in the laboratory using the torsional resonant column apparatus at the University of Texas at Austin (Hwang and Stokoe, 1993). These laboratory results are presented in Table 8.A.1-9 with the field values measured at the same depths along Path 1 in the forward direction.

The laboratory values were determined at the estimated in-situ mean effective stress after being confined for one day at that stress level. Table 8.A.1-8 and Figure 8.A.1-26 show that the laboratory measurements of shear wave velocity are, on average, about 30% lower than the shear wave velocity measured in the field using the crosshole method. However, the laboratory and the field values follow the same general trend throughout the soil profile.

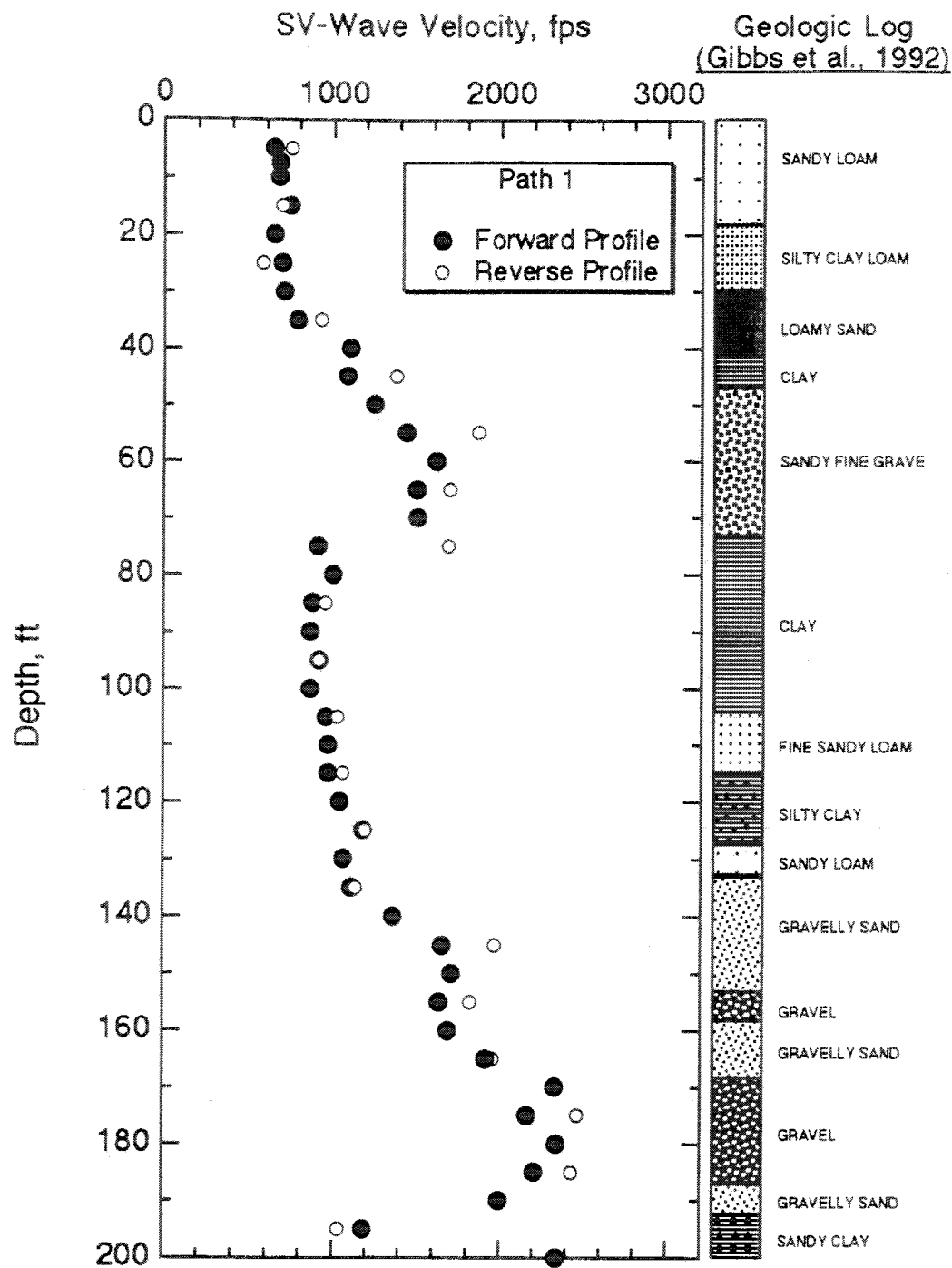
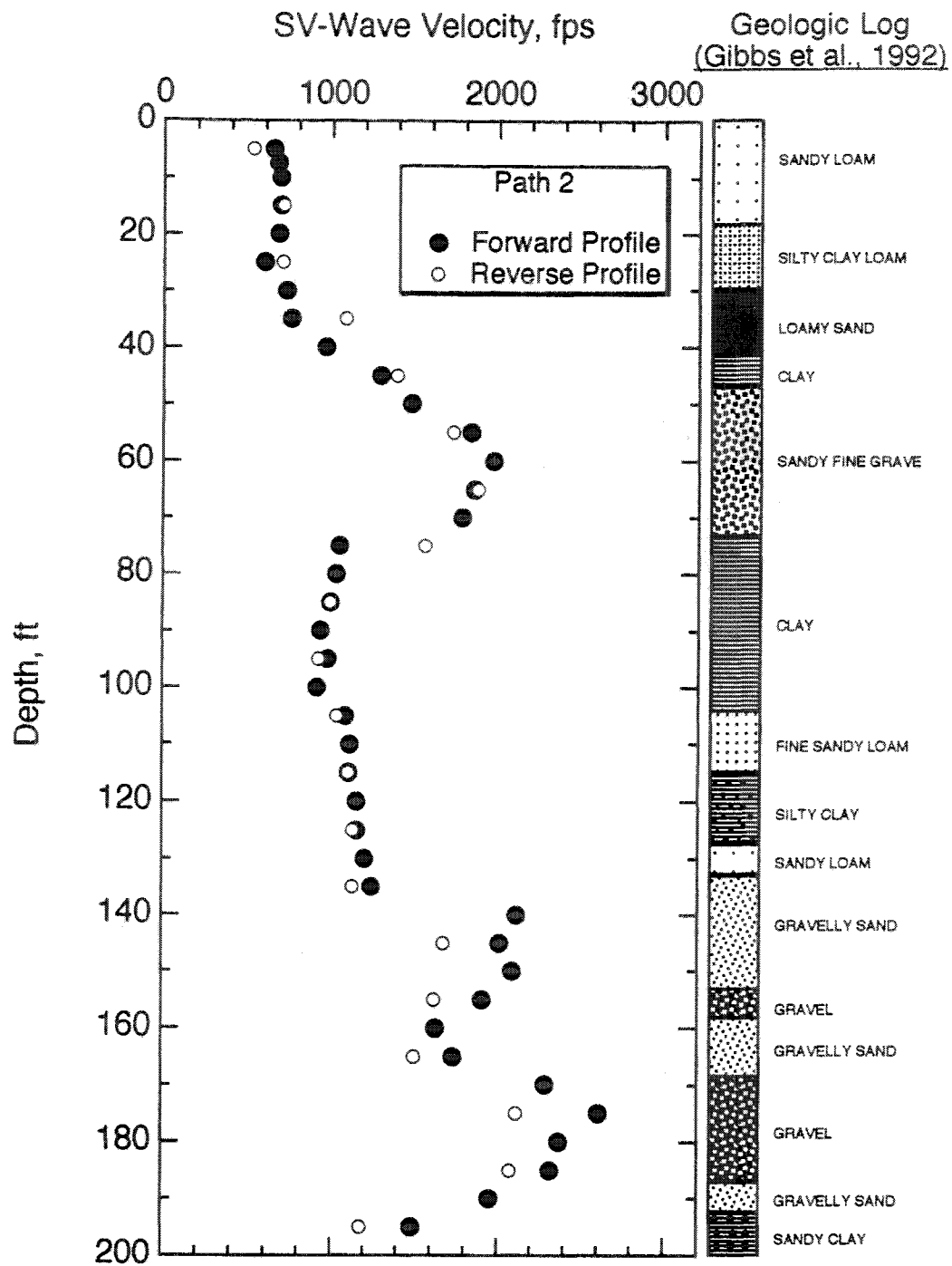


Figure 8.A.1-22

Comparison of shear (SV) wave velocities measured in the forward and reverse directions along Path 1 at Gilroy 2; depths 5-200 ft.



**Figure 8.A.1-23**

Comparison of shear (SV) wave velocities measured in the forward and reverse directions along Path 2 at Gilroy 2.

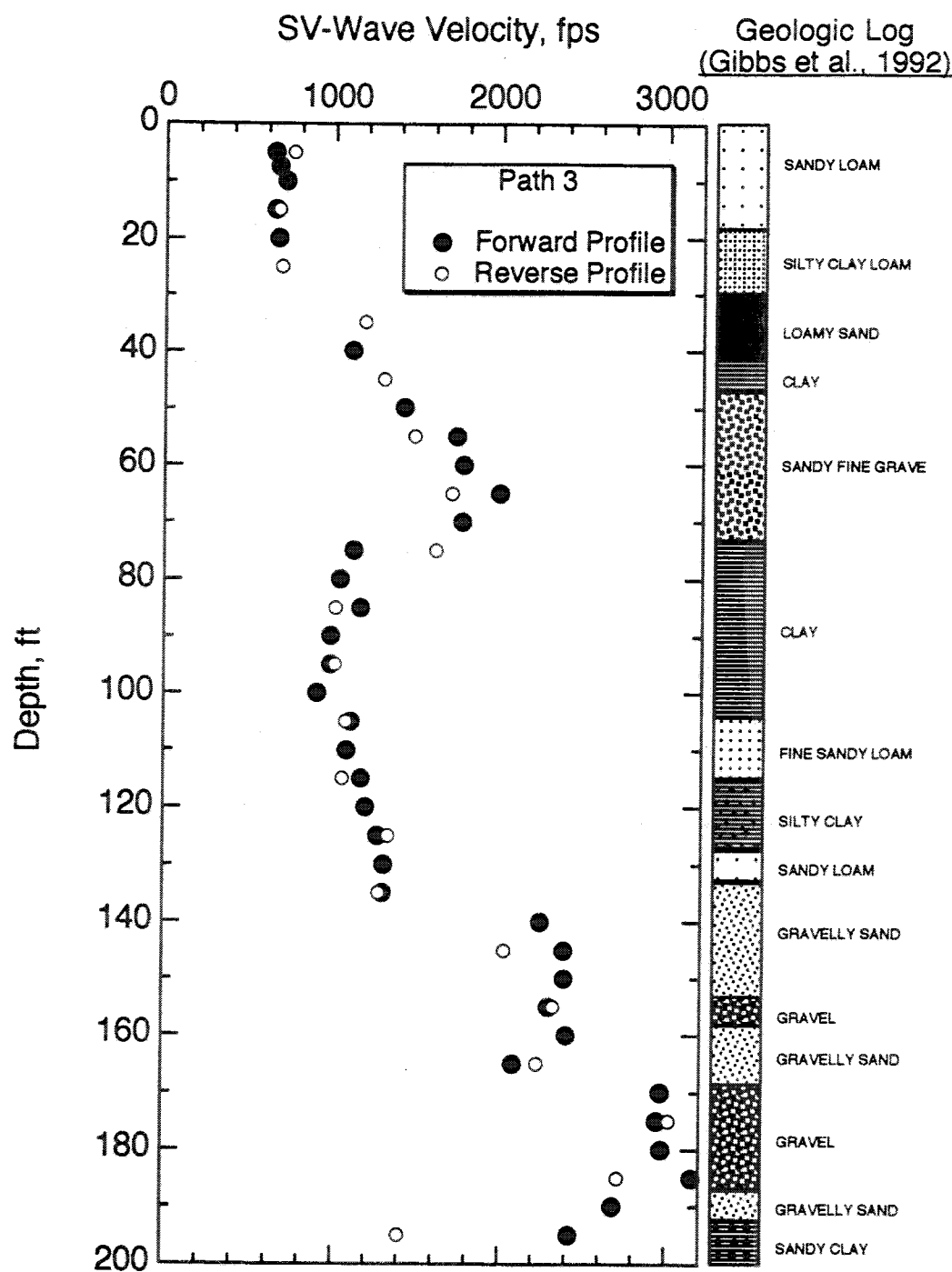


Figure 8.A.1-24

Comparison of shear (SV) wave velocities measured in the forward and reverse directions along Path 3 at Gilroy 2.

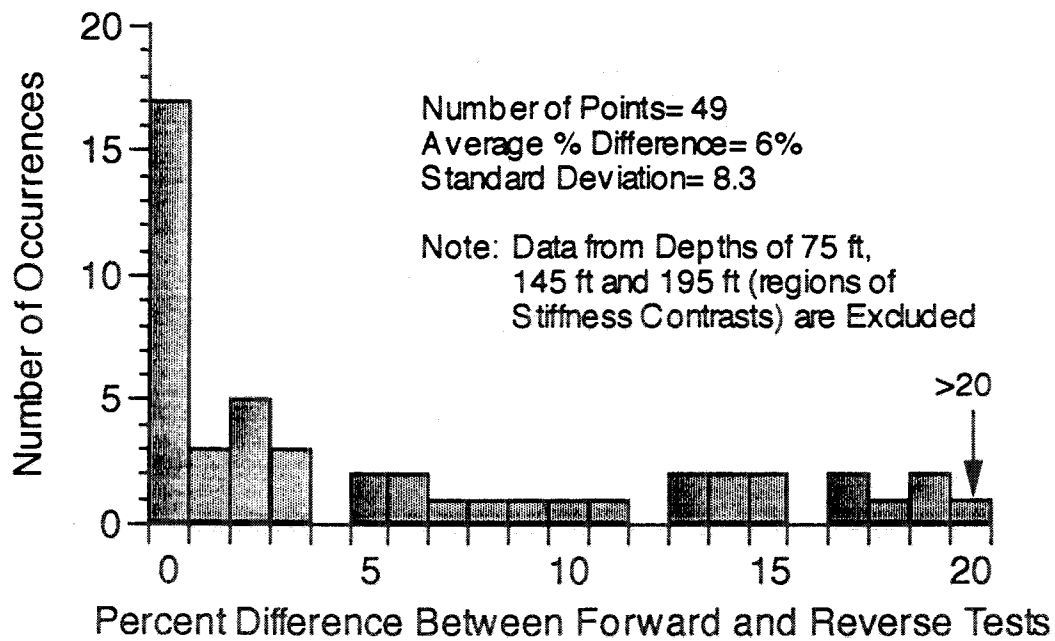


Figure 8.A.1-25

Histogram of percent difference between SV-wave velocities from forward and reverse crosshole tests at Gilroy 2.

**Table 8.A.1-8**

Comparison of Shear (SV) Wave Velocities Measured at Gilroy 2 by the Crosshole Method and by the Resonant Column Method; Path 1

Depth (ft)	Crosshole V <sub>SV</sub> (fps)**	Laboratory V <sub>S</sub> (fps)	Percent Difference*
10	675	449	33.5
20	647	387 and 436 <sup>a</sup>	36.4
50	1250	808	35.4
85	879	682 and 723 <sup>a</sup>	20.1
120	1042	879 and 975 <sup>a</sup>	11.0
170	2332	1688	27.6
348	2036 <sup>b</sup>	953	53.2
420	— <sup>c</sup>	1746	—

Notes:

\* percent difference between field- and average laboratory-measured shear wave velocities

\*\* measured along Path 1 from B1 to B2

<sup>a</sup> 1.5-in. diameter sample

<sup>b</sup> measured performed at 350-ft depth

<sup>c</sup> crosshole measurement not performed

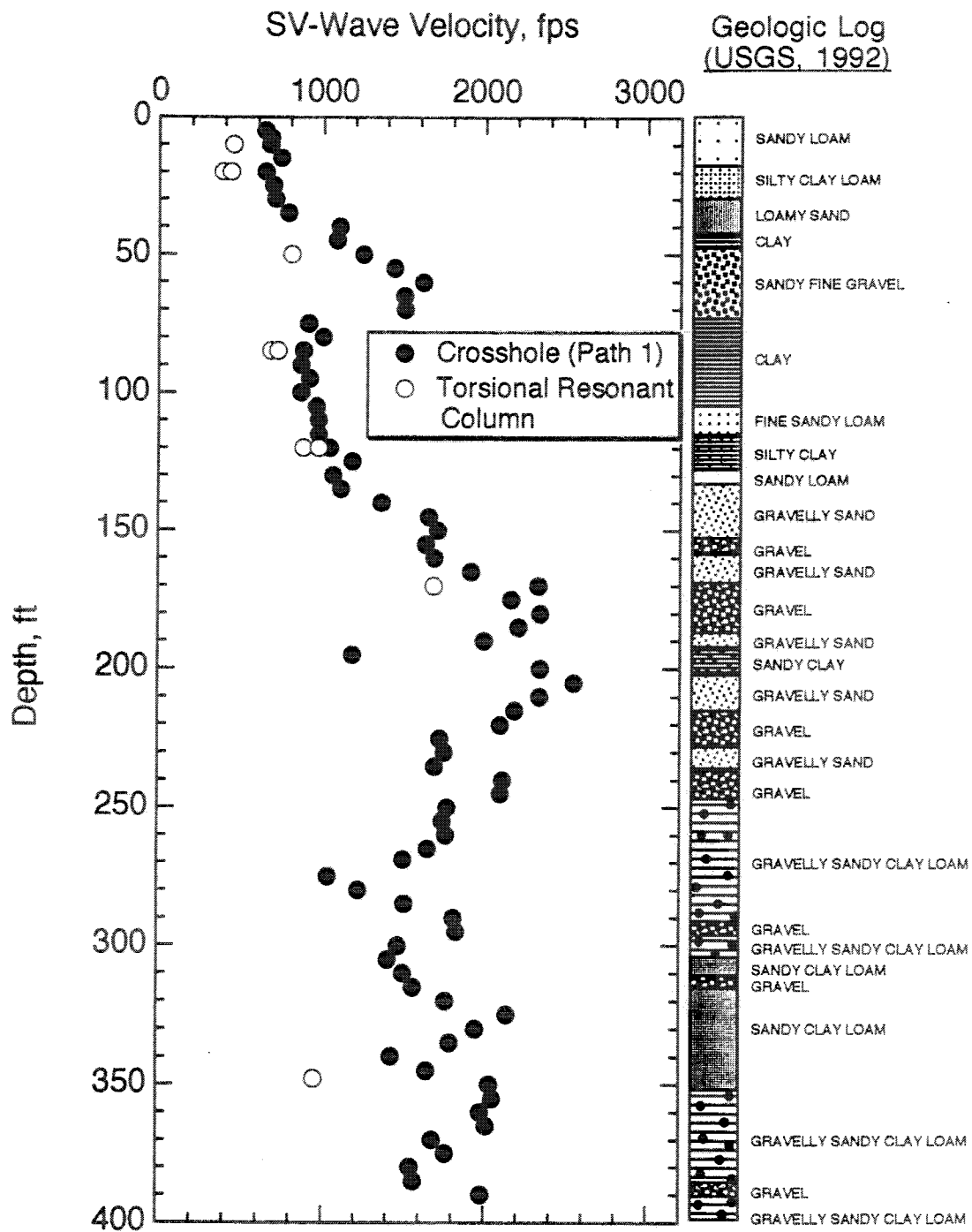


Figure 8.A.1-26

Comparison of shear wave velocities at Gilroy 2 obtained from crosshole and torsional resonant column tests.



### 8.A.1.3.3.2 Comparison of $V_s$ With Empirical Results

It is worthwhile to examine the stiffness of the soil profile at Gilroy 2 in terms of the shear wave velocities. According to Hardin and Drnevich (1972), the small-strain shear modulus of uncemented normally consolidated soils may be derived from:

$$G_{\max} = 1230 \frac{(2.973 - e)^2}{1 + e} (\bar{\sigma}_0)^{0.5} \quad (3.1)$$

where  $G_{\max}$  = small-strain shear modulus of the soil (in psi),

$e$  = void ratio, and

$\bar{\sigma}_0$  = mean effective stress (in psi).

Additionally,

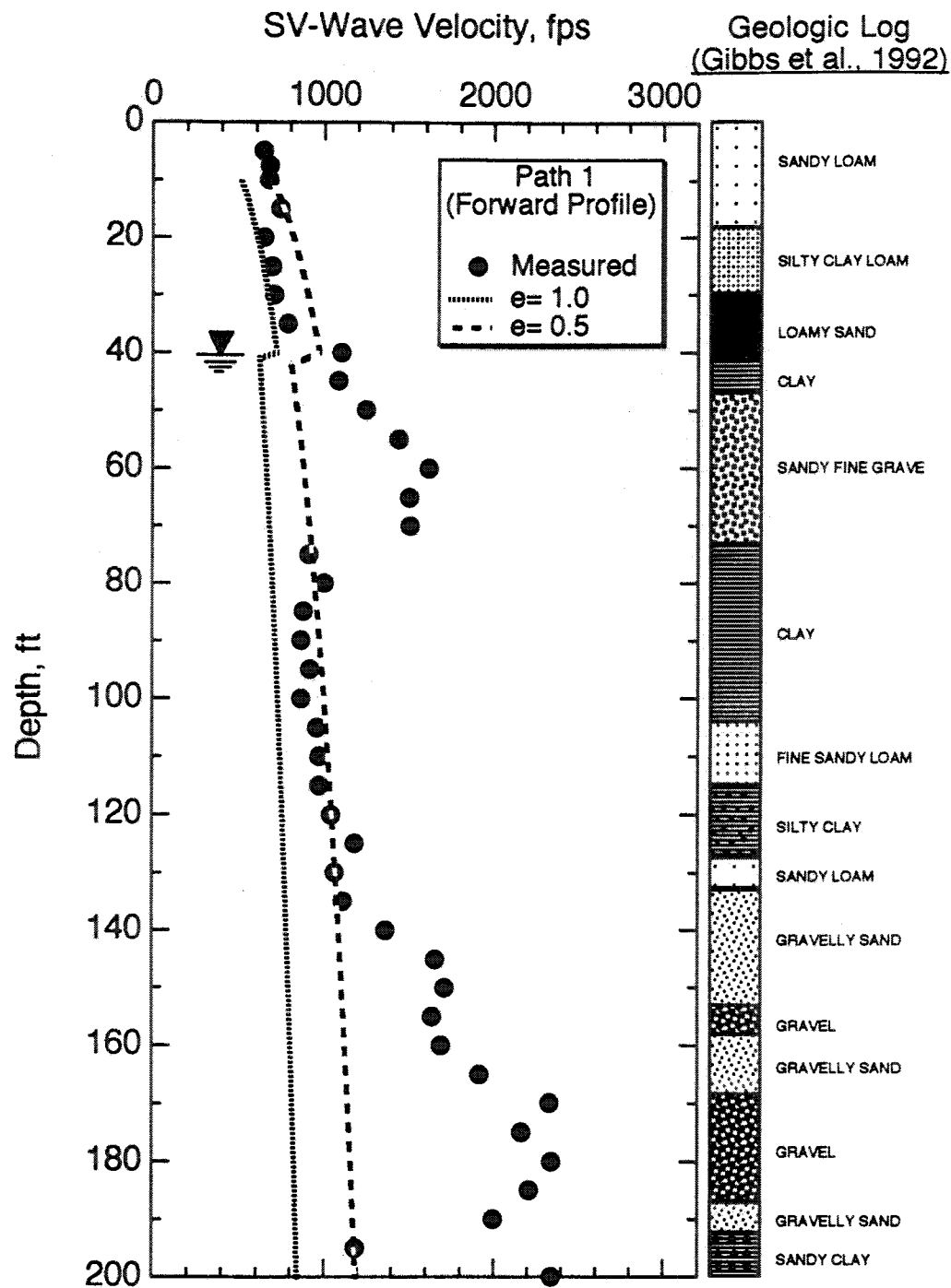
$$G = \rho V_s \quad (3.2)$$

where  $\rho$  = mass density of the soil, and

$V_s$  = shear wave velocity.

By combining Eqs. (3.1) and (3.2), one obtains an equation for shear wave velocity as a function of depth and void ratio. Figure 8.A.1-27 shows the shear (SV) wave velocity profile measured along Path 1 in the forward direction. Measured SV-wave velocities are compared with empirically-predicted shear wave velocities for normally consolidated soil predicted by Eqs. (3.1) and (3.2), assuming void ratios of 1.0, typical for a clay, and 0.5, which is typical for a sand. The stiffness coefficient "1230" in Eq. 3.1 can vary with soil type and the characteristics of the soil skeleton, and 1230 was simply used as a first approximation.

If the empirical shear wave velocity profile is reasonably representative of the shear wave velocities of normally consolidated soil, then most of the soil profile as represented by shear wave velocities is dense, possibly slightly cemented, and of mean effective stresses above those for normally consolidated soils. The Hardin and Drnevich equation suggests that the region between depths of 75 and 135 ft (22.9 and 41.1 m), the soil may be around the normal consolidation stress, or the stiffness coefficient may be somewhat less than the value of 1230.



**Figure 8.A.1-27**

Comparison of shear (SV) wave velocities along Path 1 at Gilroy 2 with theoretical velocities predicted using the equation proposed by Hardin and Drnevich (1972) for a normally-consolidated soil with void ratios ( $e$ ) of 0.5 and 1.0.

#### **8.A.1.3.3.3 SH-Wave Velocities**

Values of path length, travel time and direct SH-wave velocity for measurements along Path 1 are presented in Table 8.A.1-25 (Appendix 8.A.1.A). Subjective ratings of relative data quality are associated with the travel times. Tables 8.A.1-26 and 8.A.1-27 contain the same information for interval measurements along Paths 2 and 3, respectively. Data quality for the SH-wave measurements was generally highest for the direct (Path 1) measurements, while data quality was generally lower for the interval measurements in the upper 80 ft (24.4 m) of the soil profile. Below 80 ft, (24.4 m) data quality was high for all measurements.

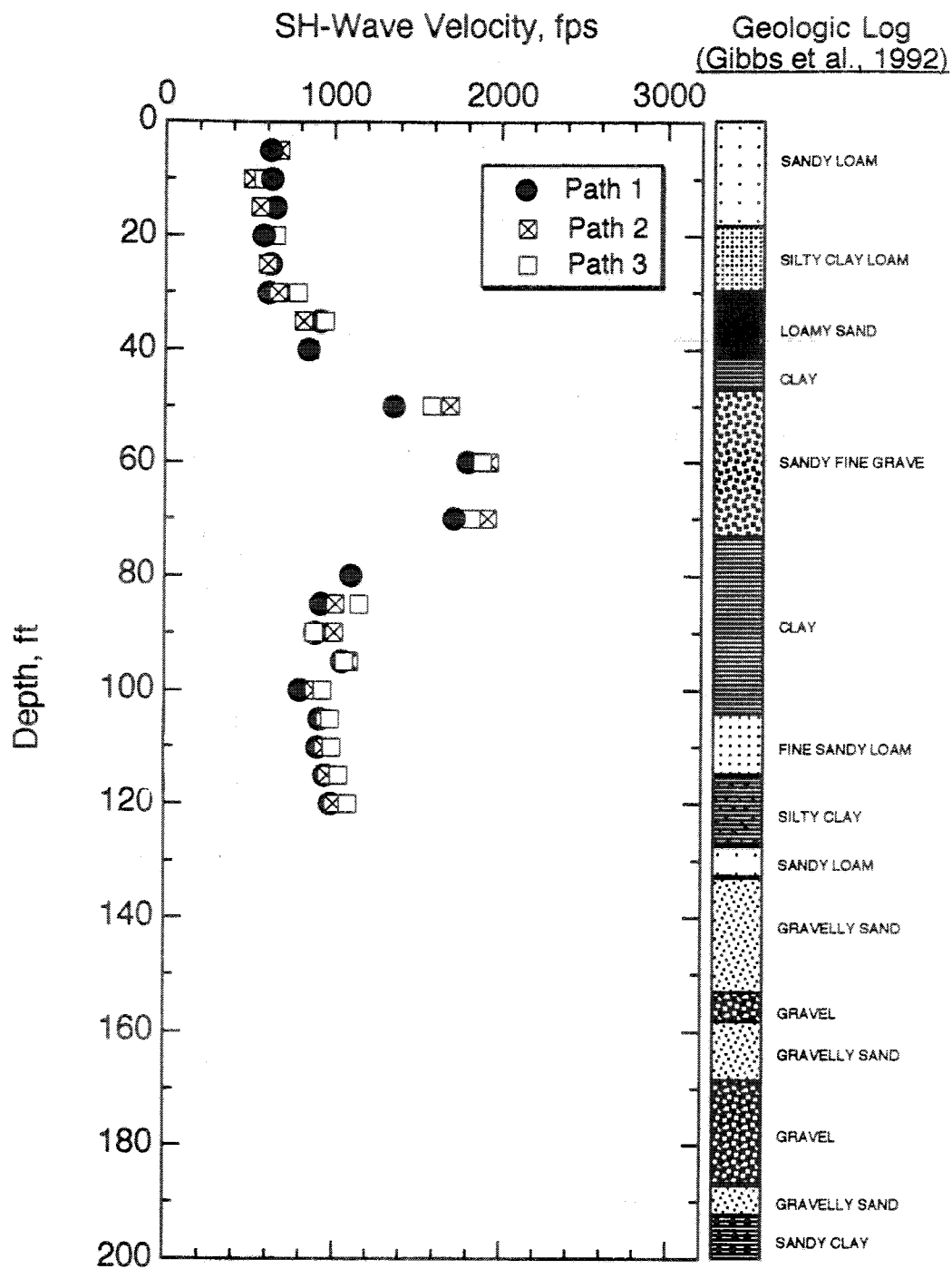
A summary of all SH-wave velocity profiles measured along each of the three paths at Gilroy 2 is presented in Figure 8.A.1-28. Although SH-wave velocity measurements were conducted to a depth of only 120 ft (36.6 m), the depth scale in Figure 8.A.1-28 extends to 200 ft (61.0 m). This allows convenient comparison of the SH- and SV-wave velocity profiles.

As with the SV-wave velocities, the SH-wave velocities exhibit a slight lateral variability in soil stiffness. Below a depth of 40 ft (12.2 m), the SH-wave velocities along Paths 2 and 3 were almost always higher than along Path 1. Below a depth of 95 ft (29 m) the SH-wave velocities were consistently higher than the SH-wave velocities along either Path 1 or Path 2.

A comparison of SH- and SV-wave velocities follows in Section 8.A.1.3.4. Since SH-wave velocity measurements were conducted in the forward profile only, it is not possible to compare forward and reverse profiles.

#### **8.A.1.3.4 Anisotropy In SV- And SH-Wave Velocities**

Figures 8.A.1-29, 8.A.1-30 and 8.A.1-31 compare the SV- and SH-wave velocity profiles from forward tests across Paths 1, 2 and 3, respectively. These figures show that SV- and SH-waves exhibit similar variation in velocity with depth. At depths shallower than 45 ft (13.7 m) and at depths greater than 95 ft (29.0 m), SV-wave velocities are generally the faster of the two shear waves. At depths between 45 and 95 ft (13.7 and 29.0 m), SH-wave velocities are higher than SV-wave velocities.



**Figure 8.A.1-28**  
Summary of all shear (SH) wave velocities measured at Gilroy 2.

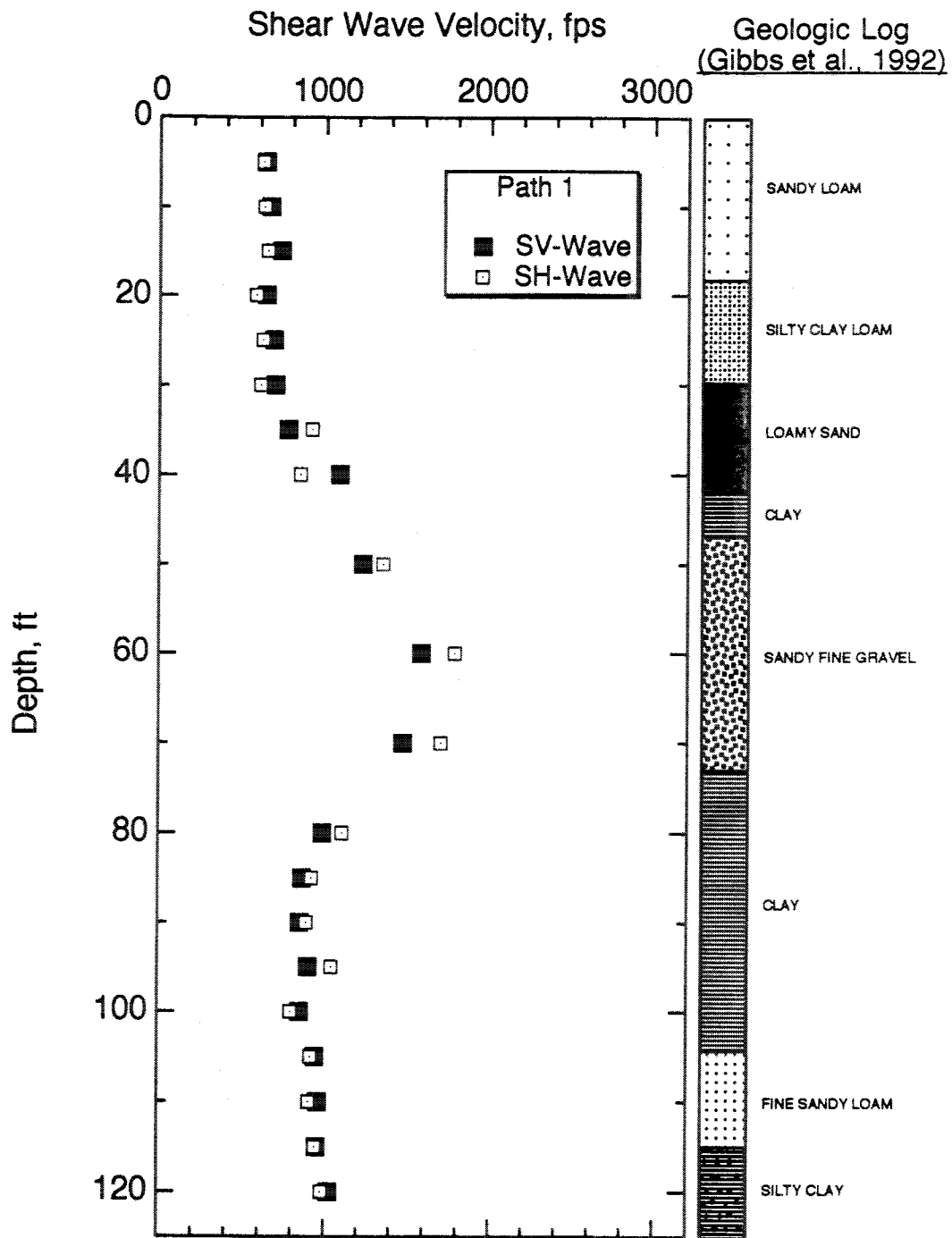
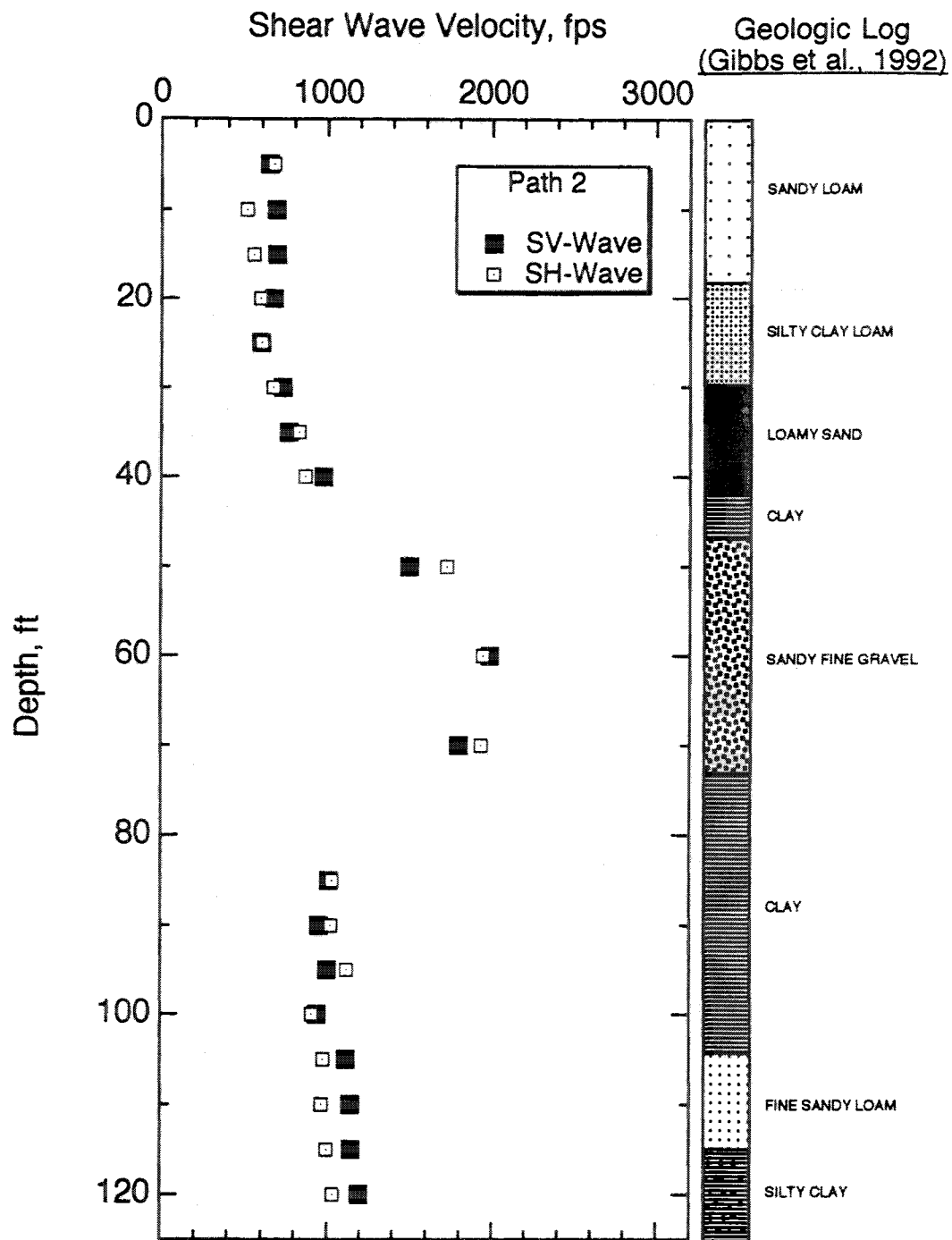


Figure 8.A.1-29  
Comparison of SV- and SH-wave velocities along Path 1 at Gilroy 2 (forward direction only).



**Figure 8.A.1-30**  
Comparison of SV- and SH-wave velocities along Path 2 at Gilroy 2 (forward direction only).

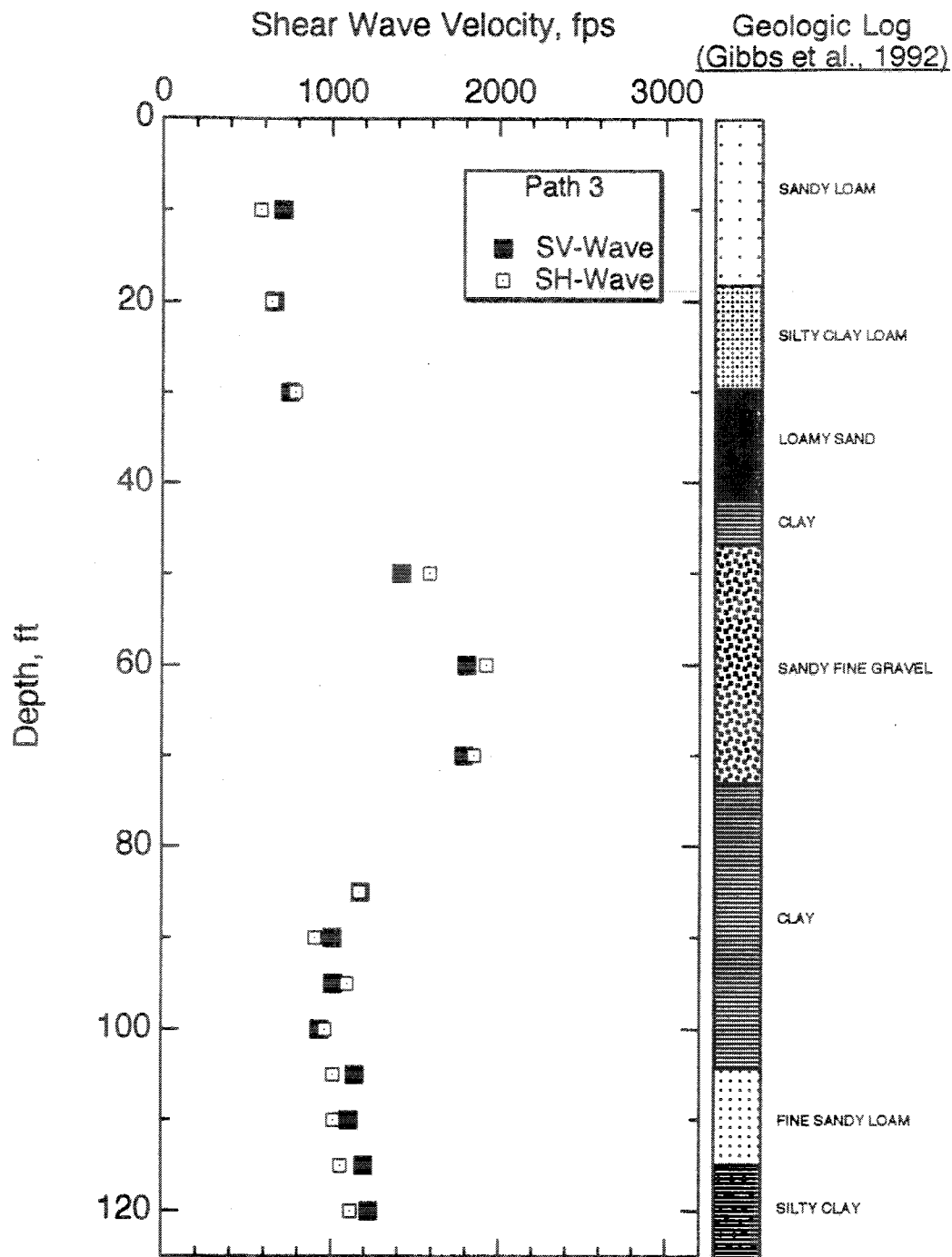


Figure 8.A.1-31  
Comparison of SV- and SH-wave velocities along Path 3 at Gilroy 2 (forward direction only).

The ratio of SV- and SH-wave velocities,  $(SV/SH)$ , is one measure of soil anisotropy. This shear wave velocity ratio is shown in Table 8.A.1-9 for all three crosshole paths at each depth where both SV- and SH-waves were measured. The average value from the three paths is also included in the table. Figure 8.A.1-32 shows the average shear wave velocity ratio plotted versus depth. A shear wave velocity ratio of less than unity implies a stiffer soil in the horizontal direction than in the vertical direction. Conversely, when  $(SV/SH) > 1$ , the soil is stiffer in the vertical direction.

At depths less than 35 ft (10.7 m), the average shear wave velocity ratio is greater than unity which indicates that the soil is stiffer in the vertical direction than in the horizontal direction. At depths between 50 ft and about 100 ft (15.2 m and 30.5 m), a region of sandy fine gravel and clay layers in the soil profile, the average ratio  $(SV/SH)$  is slightly less than unity, which indicates that the soil is stiffer in the horizontal direction than in the vertical direction. Below 100 ft (30.5 m), the average ratio  $(SV/SH)$  again becomes greater than unity. Interpretation of this profile beyond the general relationship between relative stiffnesses requires more laboratory testing than was performed in this study.



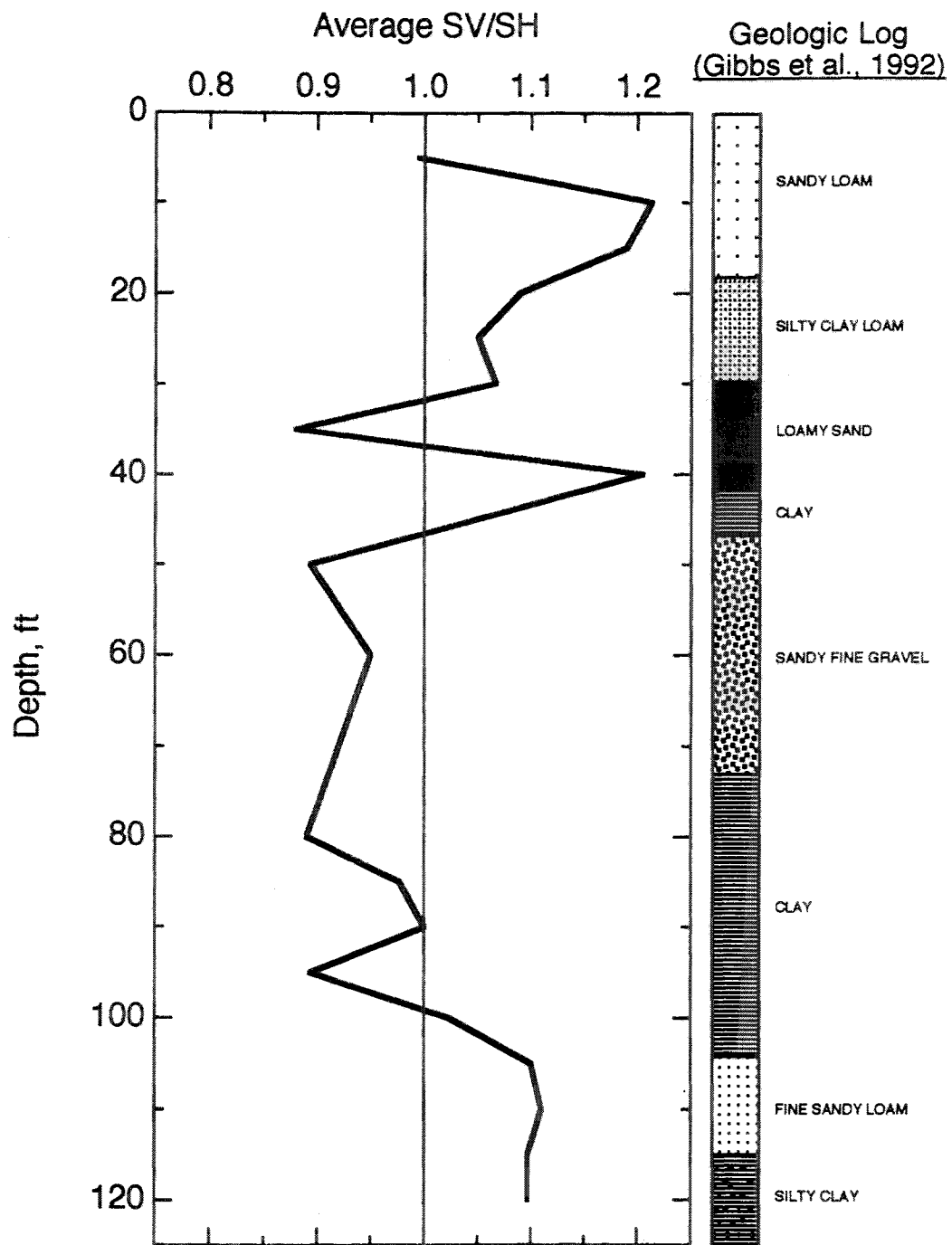
**Table 8.A.1-9**

Shear Wave Velocity Ratio (SV/SH) Measured Along All Crosshole Paths at Gilroy 2

Depth (ft)	SV/SH Path 1 <sup>a</sup>	SV/SH Path 2 <sup>b</sup>	SV/SH Path 3 <sup>c</sup>	SV/SH Average
5	1.03	0.96	— <sup>d</sup>	1.00
10	1.06	1.35	1.23	1.21
15	1.13	1.25	— <sup>d</sup>	1.19
20	1.11	1.14	1.02	1.09
25	1.11	0.99	— <sup>d</sup>	1.10
30	1.15	1.09	0.96	1.07
35	0.84	0.92	— <sup>d</sup>	0.88
40	1.28	1.13	— <sup>d</sup>	1.21
50	0.91	0.87	0.90	0.89
60	0.89	1.02	0.94	0.95
70	0.86	0.93	0.97	0.92
80	0.89	— <sup>d</sup>	— <sup>d</sup>	0.89
85	0.94	0.98	1.01	0.98
90	0.96	0.93	1.11	1.00
95	0.86	0.89	0.93	0.89
100	1.07	1.03	0.97	1.02
105	1.03	1.14	1.13	1.10
110	1.06	1.18	1.09	1.11
115	1.01	1.15	1.13	1.10
120	1.04	1.15	1.10	1.10

Notes on Table 8.A.1-9

<sup>a</sup> Path 1 is between boreholes B1 and B2<sup>b</sup> Path 2 is between boreholes B2 and B3<sup>c</sup> Path 3 is between boreholes B3 and B4<sup>d</sup> one or both velocities not measured for the (SV/SH) computation



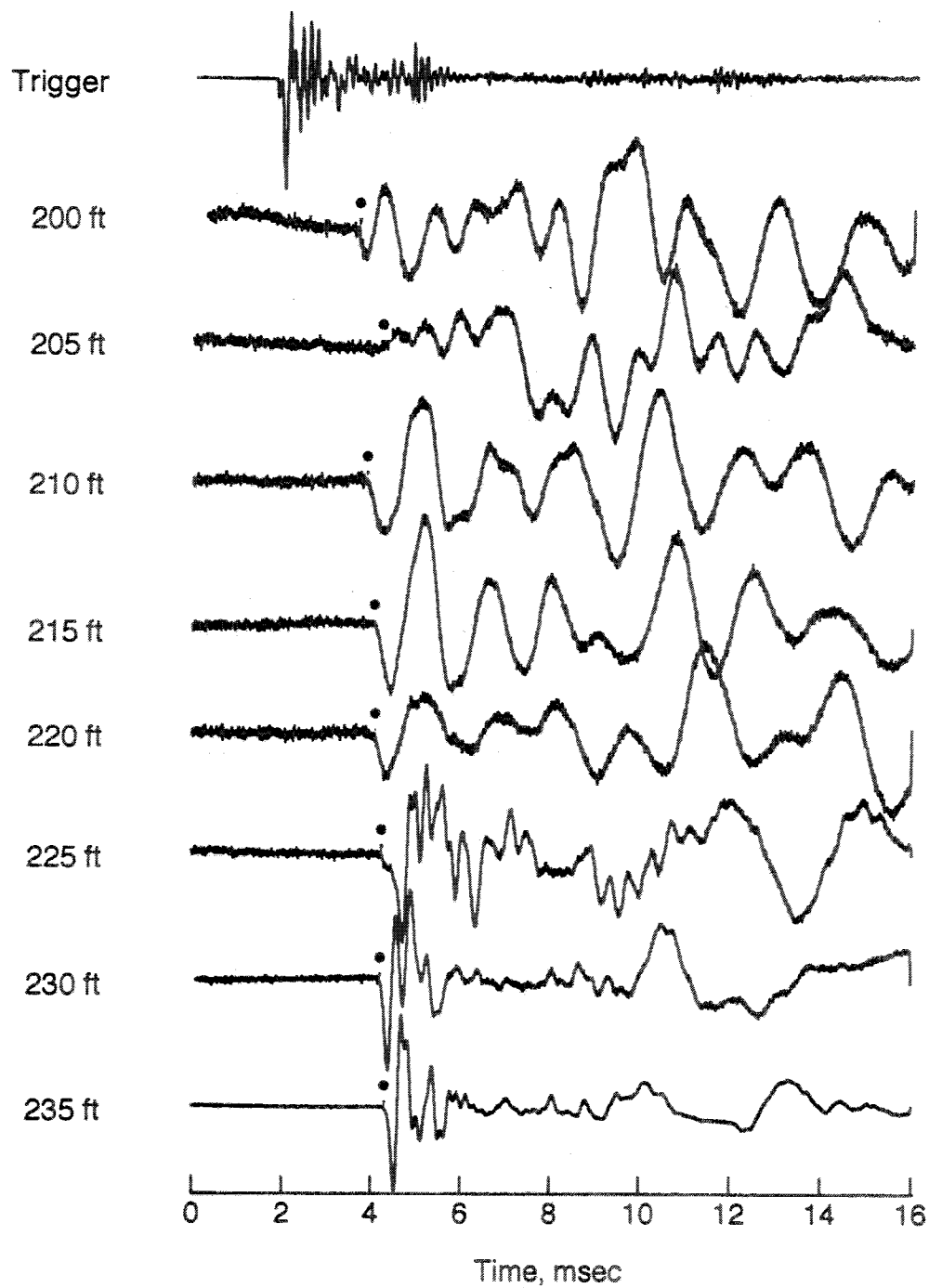
**Figure 8.A.1-32**  
Average shear wave velocity ratio (SV/SH) along Paths 1, 2 and 3 at Gilroy 2.

### 8.A.1.3.5 Compression Wave Velocities

Approximately one hundred direct and eighty interval P-wave velocity measurements were made using the mechanical wedge source; twenty-five direct and approximately forty interval P-wave velocity measurements were performed using the solenoid source at the Gilroy 2 crosshole array. All waveforms collected using both the mechanical wedge source and the solenoid source are presented by Fuhrman (1993). Typical waveforms of P-waves collected using the mechanical wedge source are shown in Figure 8.A.1-33. Because the P-wave has the fastest velocity of all elastic waves, P-wave arrivals are the first departure in the waveforms. Solid dots, "•", identify the compression wave arrivals on the waveforms.

All P-wave velocity profiles measured using the mechanical wedge source are presented in Figure 8.A.1-34. The P-wave velocities measured using the solenoid source are excluded from Figure 8.A.1-34 for simplicity, since the two sources yielded similar P-wave velocity profiles (as discussed below). Below a depth of 200 ft (61.0 m), P-wave velocities range from 4000 fps (1219 m/s) to 7000 fps (2134 m/s). P-wave velocity measurements below 200 ft (61.0 m) were performed only in the forward profile along Path 1 because only boreholes B1 and B2 were deeper than 200 ft (61.0 m).

There appears to be considerable scatter in the P-wave velocities shown in Figure 8.A.1-34. Therefore, the P-wave velocities measured along each path are discussed separately below.



**Figure 8.A.1-33**

Examples of P-wave travel time records collected at Gilroy 2 using the mechanical wedge source in B1 and a three-component velocity transducer in B2 (S-R1, forward profile); depths 200–235 ft.

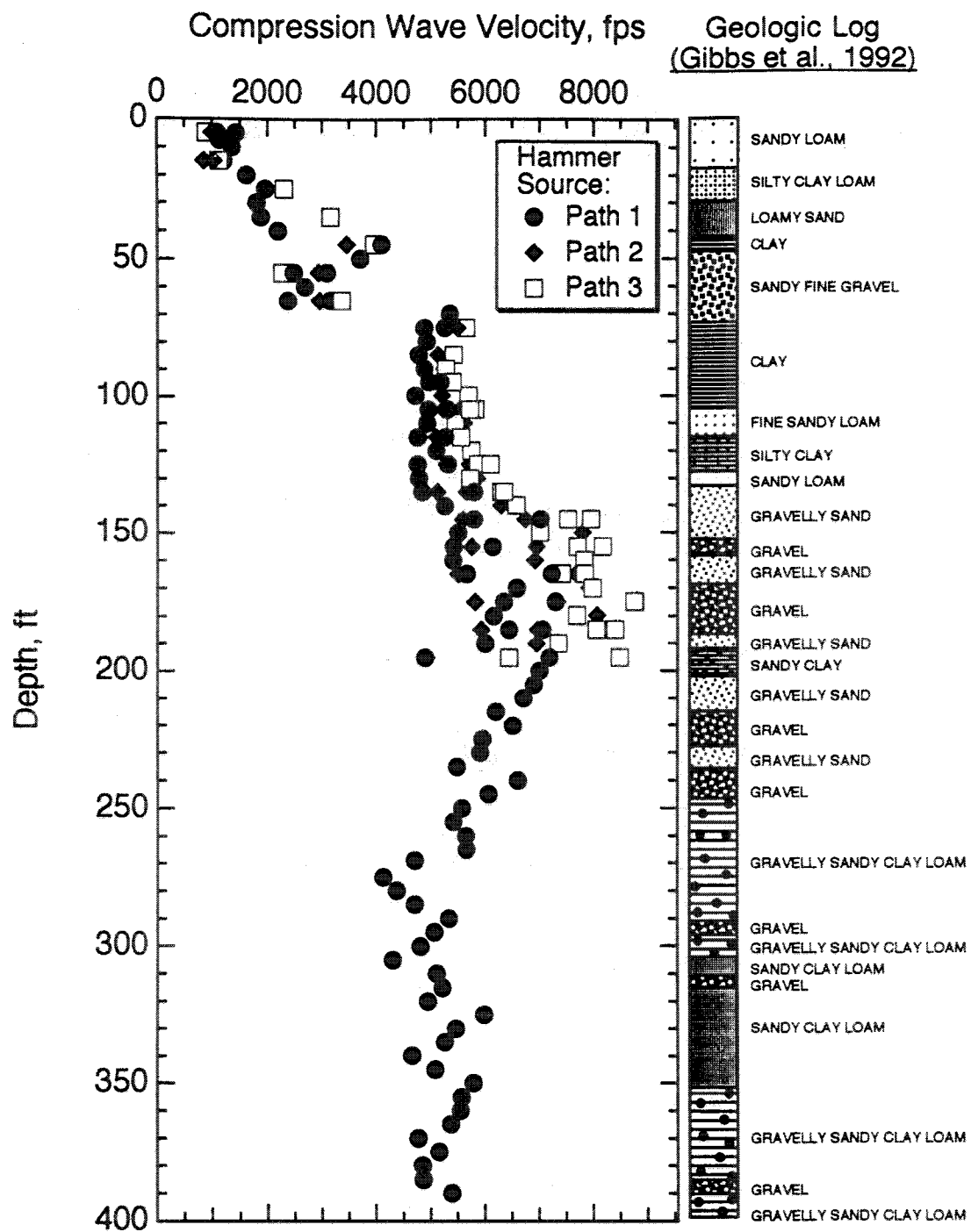


Figure 8.A.1-34

Summary of all compression wave velocities measured at Gilroy 2 using the mechanical wedge source.

**Forward Profile Measurements.** Values of path length, travel time and direct (S-R1) P-wave velocity for forward profile measurements along Path 1 are presented in Table 8.A.1-28 (Appendix 8.A.1.A). The results are tabulated for measurements made using both the mechanical wedge and solenoid sources, and subjective ratings of relative data quality (see Section 8.A.1.2.4.1) are associated with the travel times. Tables 8.A.1-29 and 8.A.1-30 contain the same information for interval (R1–R2 and R2–R3) measurements along Paths 2 and 3, respectively.

**Reverse Profile Measurements.** Values of path length, travel time and direct (S-R1) P-wave velocity for reverse profile measurements along Path 3 are presented in Table 8.A.1-31. The results are tabulated from measurements made using the mechanical wedge source; the solenoid source was not used in reverse profile tests due to time constraints. Subjective ratings of relative data quality (see Section 8.A.1.2.4.1) are associated with the travel times. Tables 8.A.1-32 and 8.A.1-33 contain the same information for interval (R1–R2 and R2–R3) measurements along Paths 2 and 1, respectively.

**Forward and Reverse Profile Comparisons.** Figures 8.A.1-35, 8.A.1-36 and 8.A.1-37 compare the P-wave velocity profiles obtained from forward and reverse tests along Paths 1, 2 and 3, respectively, using both sources. Circular symbols in Figures 8.A.1-35 through 8.A.1-37 denote data collected using the mechanical wedge source, and triangular symbols denote data collected using the solenoid source. Solid symbols represent forward profile tests, and open symbols represent reverse profile tests. Again, the solenoid source was used to a depth of 120 ft (36.6 m) in the forward profile only.

Figures 8.A.1-35 through 8.A.1-37 show excellent agreement between the two sources for P-wave velocities measured below a depth of about 70 ft (21.3 m). Table 8.A.1-10 shows that below 70 ft (21.3 m), P-wave velocities measured with both the mechanical wedge and solenoid sources fall within 5 percent of each other; above 70 ft (21.3 m) the velocities vary by as much as 67 percent (see Path 1 at 60 ft (18.3 m), Table 8.A.1-10). The higher variability in P-wave velocities above 70 ft (21.3 m) may be caused by partially saturated soil conditions above this depth. In dry or partially saturated soils, P-waves are more difficult to excite than in saturated soils, and the waves are more highly damped. These conditions can also lead to variability in the P-wave velocity profile as variability in the degree of saturation occurs.

Figures 8.A.1-35, 8.A.1-36 and 8.A.1-37 show that below a depth of about 135 ft (31.2 m), P-wave velocities varied considerably along Paths 1 and 2 between the forward and reverse directions. Table 8.A.1-11 shows the percent difference in P-wave velocities measured along the three paths in the forward and reverse directions. P-wave velocities in both the forward and reverse direction were measured to a depth of 195 ft (59.4 m). Velocities measured using the solenoid source are omitted from Table 8.A.1-11 because the solenoid source was not used in the reverse testing profile. The largest difference in forward and reverse P-wave velocities occurs along Path 1 at a depth of 195 ft (59.4 m), where the difference is about 47 percent.

Possible reasons for the variations in measured P-wave velocity include refracted wave arrivals (which are faster than direct wave arrivals), lateral variability in the soil profile, lateral variability in soil saturation, complex geology (shown in the geologic log in Figures 8.A.1-33 through 8.A.1-37), and perhaps imprecise borehole drift measurements for computing the travel path distances. Another possible reason for the inconsistencies in P-wave velocities is inconsistent or incorrect calibration factors applied to the source trigger. It should be noted that much of the scatter and variability associated with the P-wave velocity profiles are observed the same depths in the SV- and SH-wave velocity profiles.

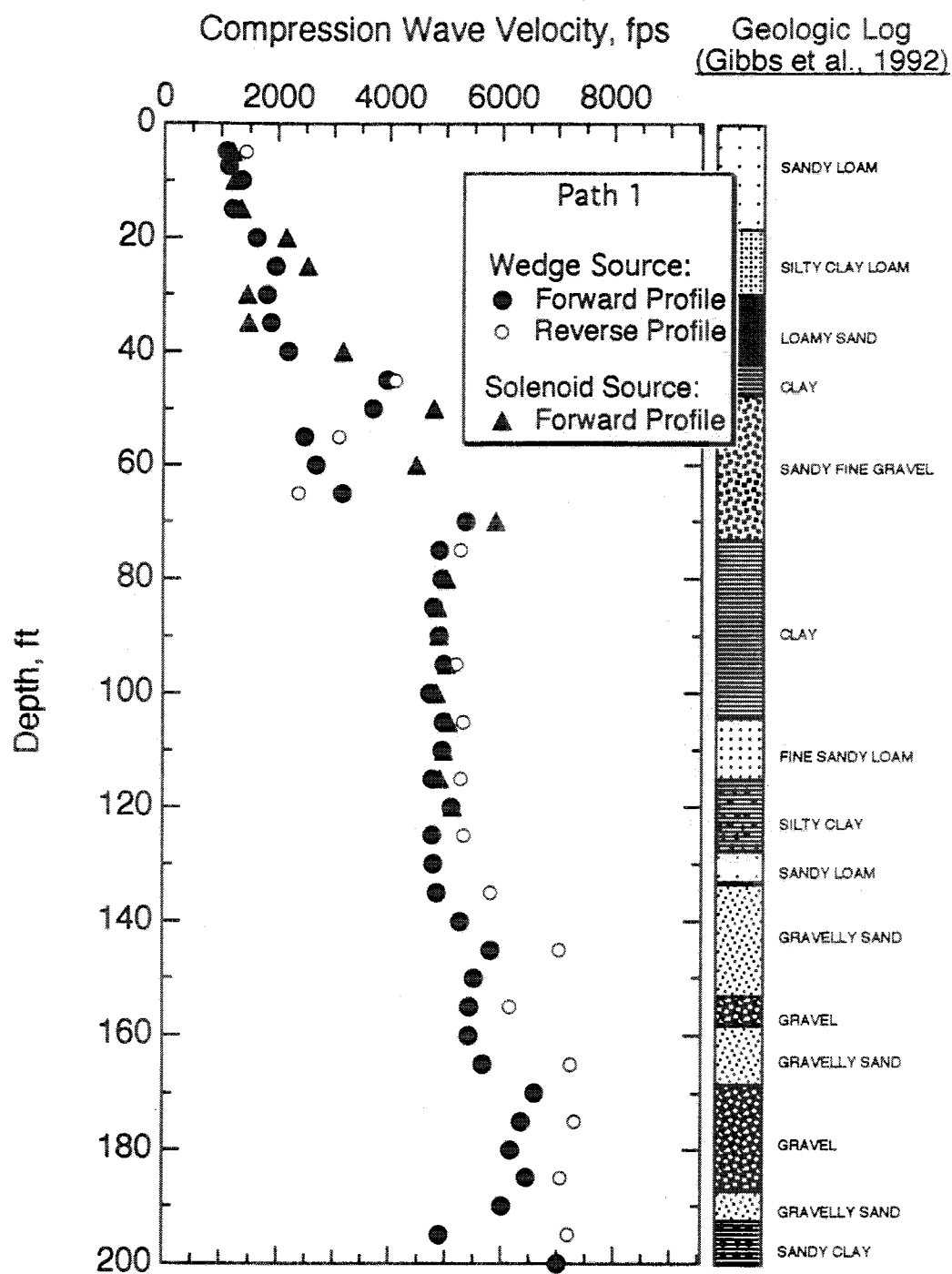


Figure 8.A.1-35

Comparison of compression wave velocities measured in the forward and reverse directions along Path 1 at Gilroy 2.

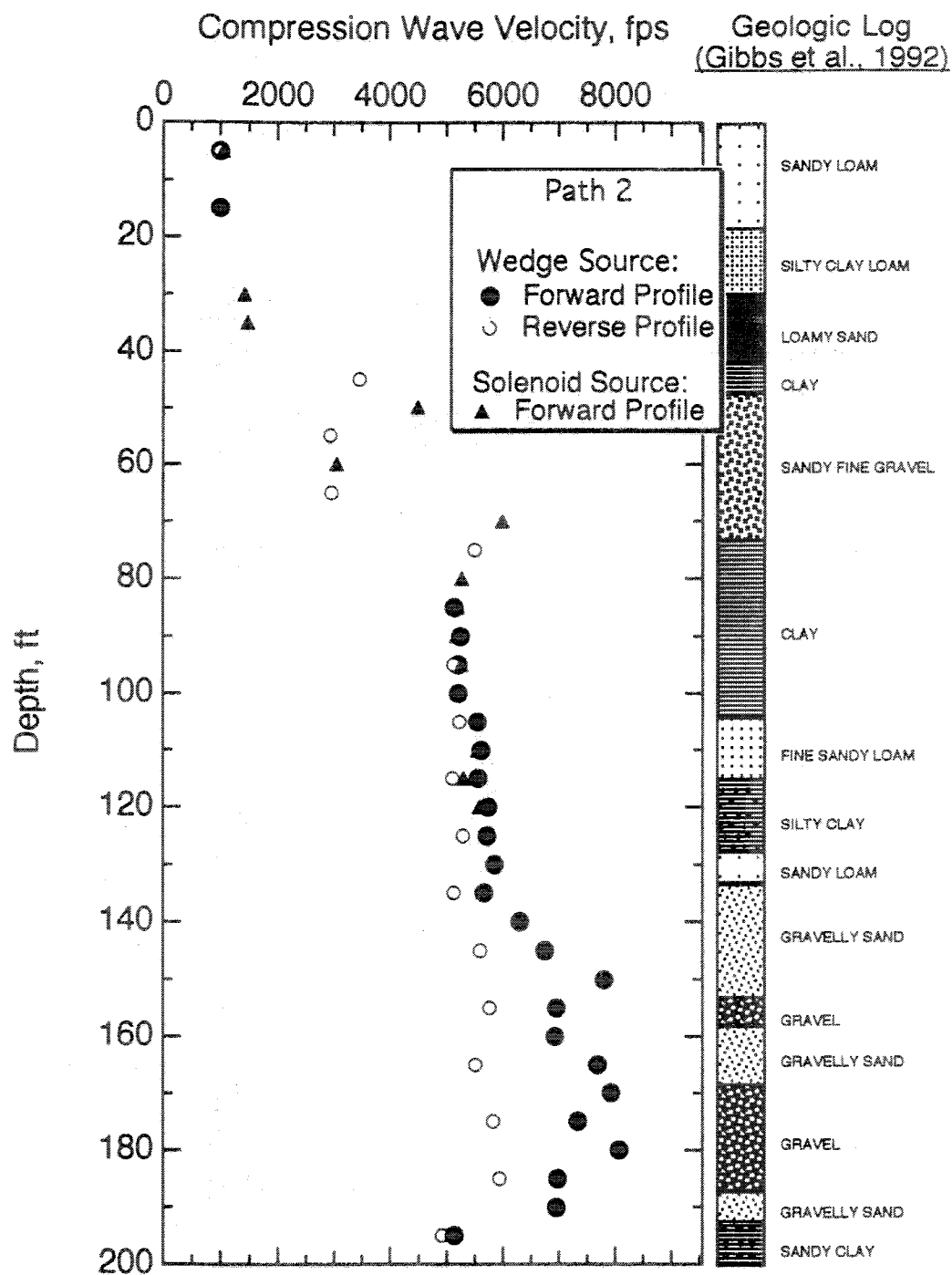


Figure 8.A.1-36

Comparison of compression wave velocities measured in the forward and reverse directions along Path 2 at Gilroy 2.



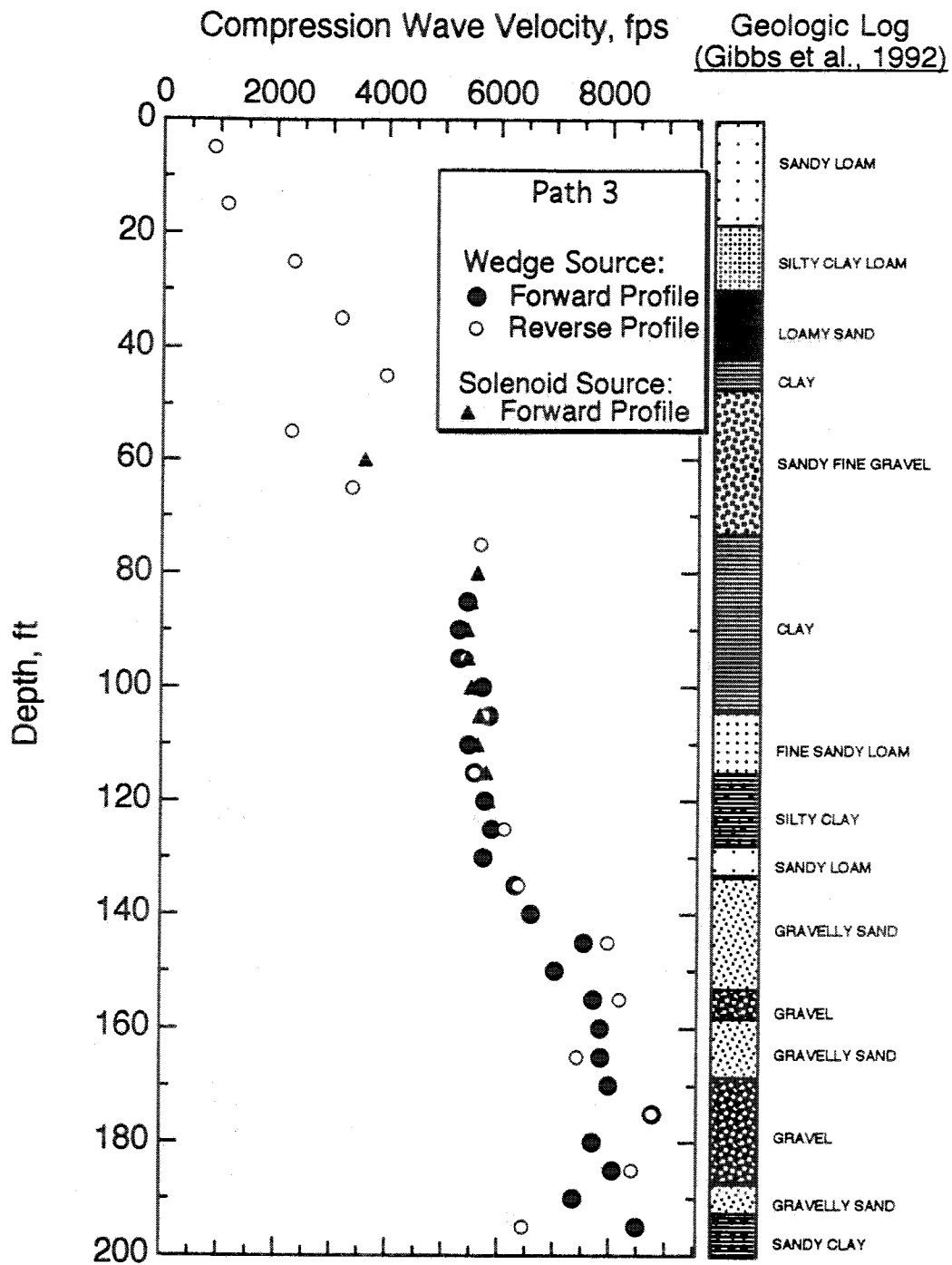


Figure 8.A.1-37

Comparison of compression wave velocities measured in the forward and reverse directions along Path 3 at Gilroy 2.

**Table 8.A.1-10**  
Comparison of P-Wave Velocities Measured at Gilroy 2 Using the Mechanical Wedge and Solenoid Sources; Depths 5–120 ft for the Forward Direction Only

Depth (ft)	PATH 1 <sup>1</sup>			PATH 2 <sup>2</sup>			PATH 3 <sup>3</sup>		
	Wedge Source P-Wave Velocity (fps)	Solenoid Source P-Wave Velocity (fps)	Percent Difference	Wedge Source P-Wave Velocity (fps)	Solenoid Source P-Wave Velocity (fps)	Percent Difference	Wedge Source P-Wave Velocity (fps)	Solenoid Source P-Wave Velocity (fps)	Percent Difference
5	1099a	1197b	8.9	994a	1052b	5.8	---e	---	---
7.5	1142a	---d	---	---e	---	---	---e	---	---
10	1379a	1224b	11.2	---	---	---	---	---	---
15	1219a	1354b	11.1	850b	---	---	---	---	---
20	1638a	2144a	30.9	---	---	---	---	---	---
25	1961b	2533b	29.2	---	---	---	---	---	---
30	1811c	1462c	19.3	---	1427c	---	---	---	---
35	1882c	1479b	21.4	---	1470c	---	---	---	---
40	2193b	3161c	44.1	---	---	---	---	---	---
45	3956a	---	---	---	---	---	---	---	---
50	3707b	4783c	29.0	---	4495c	---	---	---	---
55	2479b	---	---	---	---	---	---	---	---
60	2684b	4472a	66.6	---	3056c	---	---	3590	---
65	3155a	---	---	---	---	---	---	---	---
70	5359a	5883a	9.8	---	5993a	---	---	---	---
75	4894a	---	---	---	---	---	---	---	---
80	4935a	5019a	1.7	---	5269a	---	---	5602a	---

Table 8.A.1-10 (continued)

Comparison of P-Wave Velocities Measured at Gilroy 2 Using the Mechanical Wedge and Solenoid Sources; Depths 5–120 ft for the Forward Direction Only

Depth (ft)	PATH 1 <sup>1</sup>			PATH 2 <sup>2</sup>			PATH 3 <sup>3</sup>		
	Wedge Source P-Wave Velocity (fps)	Solenoid Source P-Wave Velocity (fps)	Percent Difference	Wedge Source P-Wave Velocity (fps)	Solenoid Source P-Wave Velocity (fps)	Percent Difference	Wedge Source P-Wave Velocity (fps)	Solenoid Source P-Wave Velocity (fps)	Percent Difference
85	4784a	4862a	1.6	5140a	5198a	1.1	5424a	5488a	1.2
90	4887a	4880a	0.2	5255a	5176a	1.5	5283a	5429a	2.7
95	4969a	5018a	1.0	5207a	5267a	1.2	5293a	5439a	2.7
100	4728a	4838a	2.3	5213a	5213a	0.0	5699a	5497a	3.6
105	4963a	5050a	1.7	5550a	5550a	0.0	5818a	5650a	2.9
110	4939a	4969a	0.6	5620a	5552a	1.2	5458a	5612a	2.8
115	4769a	4901a	2.8	5559a	5301a	4.6	5561a	5768a	3.7
120	5110a	5125a	0.3	5745a	5580a	2.9	5747a	5816a	1.2

Notes on Table

- <sup>1</sup> Path 1 is between boreholes B1 and B2
- <sup>2</sup> Path 2 is between boreholes B2 and B3
- <sup>3</sup> Path 3 is between boreholes B3 and B4
- <sup>a</sup> Type I data (initial wave arrival clearly identifiable within 5% of total travtime))
- <sup>b</sup> Type II data (initial wave arrival less distinct than a) but identifiable (with about 10 % of total travel time))
- <sup>c</sup> Type III data (some interpretation required to identify initial wave arrival)
- <sup>d</sup> initial wave arrival not identifiable
- <sup>e</sup> measurement not performed

**Table 8.A.1-11**  
Comparison of P-Wave Velocities Measured Along Forward and Reverse Testing Profiles at Gilroy 2 Using the Mechanical Wedge Source;  
Depths 5–195 ft

PATH 1 <sup>1</sup>				PATH 2 <sup>2</sup>				PATH 3 <sup>3</sup>			
Depth (ft)	Forward Test Velocity (fps)	Reverse Test Velocity (fps)	Percent Difference	Forward Test Velocity (fps)	Reverse Test Velocity (fps)	Percent Difference		Forward Test Velocity (fps)	Reverse Test Velocity (fps)	Percent Difference	
5	1099a	1431b	30.2	994a	999b	0.5		-----e	897b	-----	
15	1219a	-----e	----	850b	1029c	21.1		-----e	1126b	-----	
25	1961b	-----e	----	-----e	-----d	----		-----e	2304b	-----	
35	1882c	-----d	----	-----e	-----d	----		-----e	3157b	-----	
45	3956a	4099c	3.6	-----e	3453b	----		-----e	3961a	-----	
55	2479b	3094b	24.8	-----e	2938c	----		-----e	2269b	-----	
65	3155a	2382c	24.5	-----e	2961b	----		-----e	3359b	-----	
75	4894a	5260b	7.5	-----e	5500a	----		-----e	5657a	-----	
85	4784a	-----e	----	5140a	-----e	----		5424a	-----e	----	
95	4969a	5195a	4.5	5207a	5131a	1.5		5293a	5413a	2.3	
105	4963a	5310a	7.0	5550a	5234a	5.7		5818a	5726a	1.6	
115	4769a	5272a	10.5	5559a	5104a	8.2		5561a	5562a	0.0	
125	4762a	5326a	11.8	5717a	5293a	7.4		5880a	6099a	3.7	
135	4851a	5798a	19.5	5666a	5126a	9.5		6298a	6349a	0.8	
145	5800a	7025a	21.1	6752a	5592a	17.2		7534a	7958a	5.6	
155	5432a	6142a	13.1	6953a	6764a	2.7		7717a	8178a	6.0	

**Table 8.A.1-11 (continued)**  
Comparison of P-Wave Velocities Measured Along Forward and Reverse Testing Profiles at Gilroy 2 Using the Mechanical Wedge Source;  
Depths 5-195 ft

PATH 1 <sup>1</sup>				PATH 2 <sup>2</sup>				PATH 3 <sup>3</sup>			
Depth (ft)	Forward Test Velocity (fps)	Reverse Test Velocity (fps)	Percent Difference	Forward Test Velocity (fps)	Reverse Test Velocity (fps)	Percent Difference		Forward Test Velocity (fps)	Reverse Test Velocity (fps)	Percent Difference	
165	5668a	7239a	27.7	7697a	5512a	28.4		7846a	7421a	5.4	
175	6348a	7305a	15.1	7340a	5827a	20.6		8773a	8763a	0.1	
185	6442a	7061a	9.6	6973a	5937a	14.9		8063a	8410a	4.3	
195	4896a	7189b	46.8	6443b	4925a	23.6		8488b	6442a	24.1	

**Notes on Table**

- 1 Path 1 is between boreholes B1 and B2
- 2 Path 2 is between boreholes B2 and B3
- 3 Path 3 is between boreholes B3 and B4
- a Type I data (initial wave arrival clearly identifiable (within 5% of total travel time))
- b Type II data (initial wave arrival less distinct than (a) but identifiable (within about 10 % of total travel time))
- c Type III data (some interpretation required to identify initial wave arrival)
- d initial wave arrival not identifiable

#### **8.A.1.3.6 Summary and Conclusions**

Crosshole seismic tests were performed at the Gilroy 2 site to measure compression and shear (SV and SH) wave velocities. The mechanical wedge source was used to generate SV-waves, and the solenoid source was used to generate SH-waves. Both sources were used to generate P-waves, and their results are compared herein. The P-wave velocities measured using the two sources match well. Below the water table, P-wave velocities varied between 4000 fps and about 8000 fps (1200 m/sec and 2400 m/sec).

The soil at Gilroy appears to be generally stiff in terms of shear wave velocity. Shear wave measurements indicate higher stiffness in the horizontal direction than in the vertical direction at most depths between 35 ft and 100 ft (10.7 m and 30.5 m). The SASW method produced a velocity profile similar to that from the crosshole tests. Changes in the S- and P-wave velocity profiles often occurred at changes in the soil profile. Some lateral variability in soil stiffness was also observed in both S- and P-wave velocity profiles measured along all travel paths at the site. Values of shear wave velocity measured in the laboratory using the torsional resonant column device at the University of Texas were on average about 30% lower than the shear waves measured in the field.

## **4—WAVE VELOCITIES FROM CROSSHOLE TESTING AT TREASURE ISLAND**

### **8.A.1.4.1 Introduction**

Treasure Island is a manmade island built of hydraulic fill north of Yerba Buena Island in the San Francisco Bay (see Figure 8.A.1-38). Strong ground motions were recorded at this site during the 1989 Loma Prieta earthquake, whose epicenter was approximately 60 miles (97 km) to the south of Treasure Island (Reichle et al., 1990). During the earthquake, liquefaction occurred at numerous locations around the island.

As part of a geotechnical study to determine the dynamic characteristics of the subsurface materials, crosshole seismic tests were performed at a site just behind the fire station on the island. Crosshole testing was conducted to measure in situ body wave velocities of the subsurface materials. Testing was conducted from 3 through 11 January 1992.

Although numerous manifestations of liquefaction appeared on the island, it should be noted that there were no sand boils or other surface manifestations of soil liquefaction at the location of the crosshole tests at the fire station site (personal communication with Mike White, the chief at the fire station). The site was selected as a protected location where a deep vertical array of accelerometers (involving several boreholes) could be installed for future earthquake monitoring.

Five borings were made prior to the crosshole testing. Each boring was cased with PVC, schedule 40 well casing with an inner diameter (ID) of 5.0 in. (12.7 cm). The thickness of the casing is 0.25 in. (0.64 cm). Table 8.A.1-12 lists the depth and ID of each cased borehole. Center-to-center distances measured between boreholes at the surface are summarized in Table 8.A.1-13. These measurements were made using a fiberglass hand-held measuring tape.

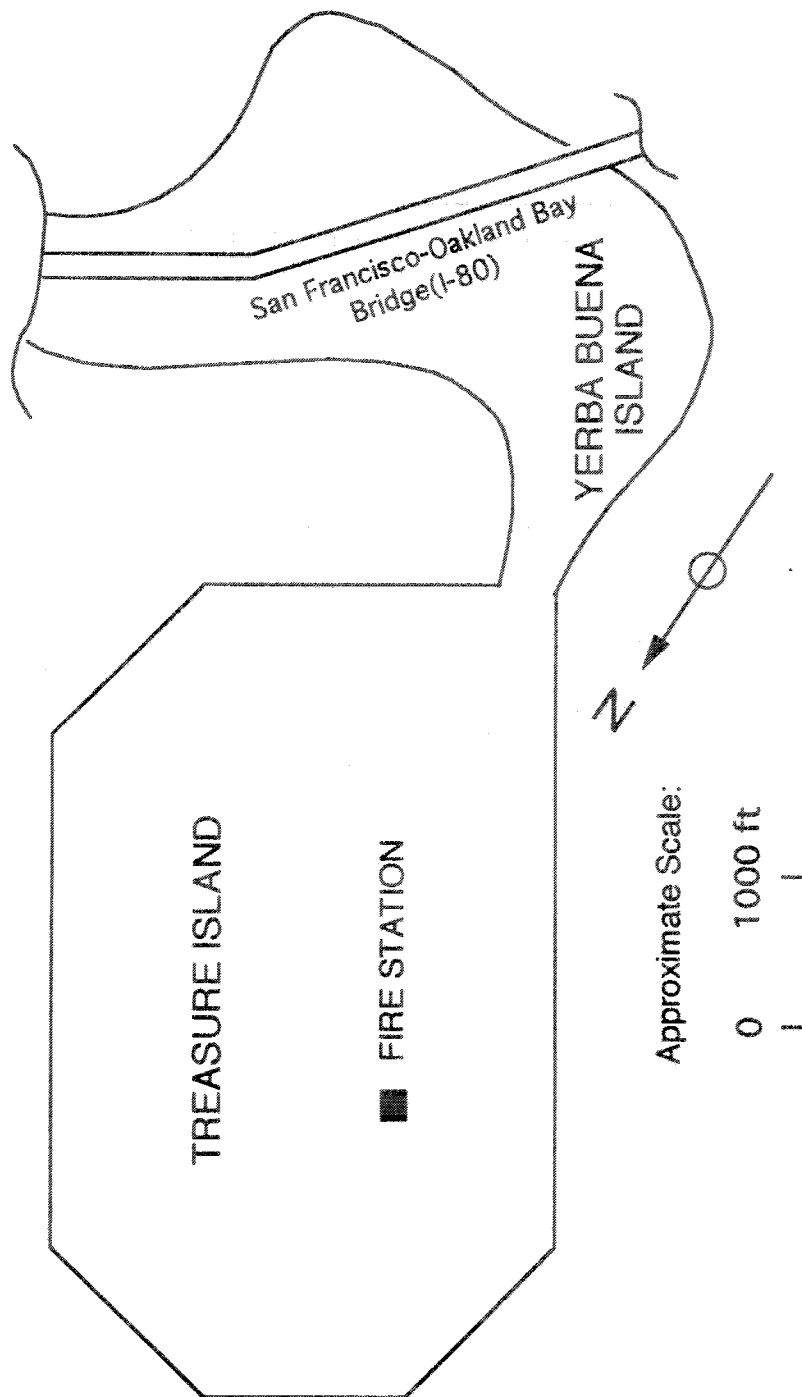


Figure 8.A.1-38  
General location of the Fire Station on Treasure Island (after Hryciw et al., 1991).



**Table 8.A.1-12**

Depths and Cased Inner Diameters of Boreholes Used in Seismic Crosshole Testing at Treasure Island

Borehole	Depth, ft (m)	ID, in. (cm)
B1	102 (31.1)	5 (12.7)
B2	145 (44.2)	5 (12.7)
B3	340 (103.6)	5 (12.7)
B4	51 (15.5)	5 (12.7)
B5	24 (7.3)	5 (12.7)

**Table 8.A.1-13**

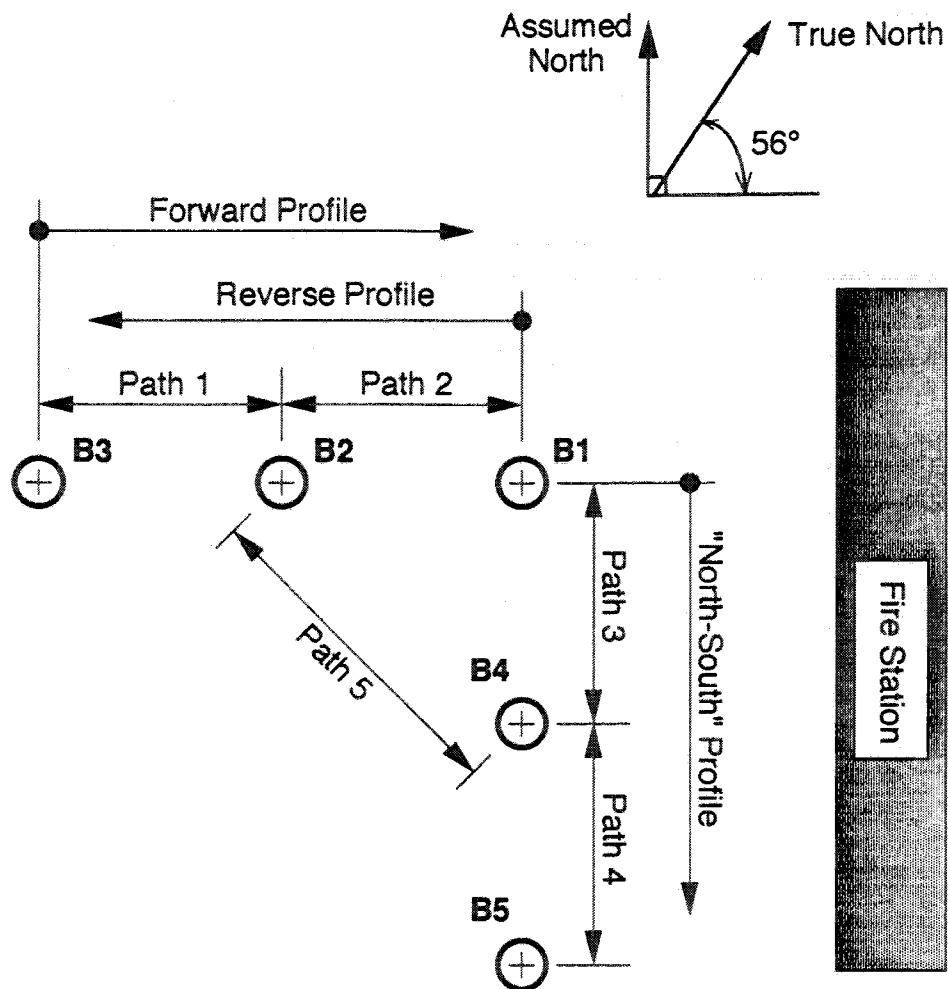
Center-to-Center Distances Between Boreholes Measured at the Surface at Treasure Island

Path	Distance, ft (m)
B1-B2	9.7 (3.0)
B1-B3	19.7 (6.0)
B2-B3	10.0 (3.0)
B1-B4	10.0 (3.0)
B1-B5	20.7 (6.3)
B2-B4	13.5 (4.1)

The boreholes are arranged in two linear arrays that are approximately orthogonal, as shown in Figure 8.A.1-39. The first array consists of boreholes B1, B2 and B3, and the second array consists of boreholes B1, B4 and B5. With the source in borehole B3, boreholes B2 and B1 were used as the first and second receiver boreholes, respectively. This arrangement of source and receivers is called the forward testing array. A reverse testing array was created by reversing the locations of the source and the second receiver; that is, the source was placed in borehole B1, and the first and second receivers were placed in boreholes B2 and B3, respectively. For these tests, Path 1 is defined between B3 and B2, and Path 2 is between B2 and B1. Both forward and reverse measurements were performed along Paths 1 and 2. Also, the majority of the crosshole tests conducted at Treasure Island were performed along these paths.

Measurements along the second array were made using the source in borehole B1, with first and second receivers in boreholes B4 and B5, respectively. This arrangement of source and receivers is called the "North-South" profile because the centerline of the array runs in the North and South directions assumed in the field. Path 3 is defined between boreholes B1 and B4, and Path 4 is between boreholes B4 and B5. Measurements along Paths 4 and 5 were made in one direction only.

A few measurements (five of each wave type) were also performed with the source in B2 and a receiver in B4. This source-receiver arrangement is called Path 5, as noted in Figure 8.A.1-39.



\*Notes: Drawing For Layout Only  
(Not to Scale)

Elevation Datum for Crosshole  
Tests is the Ground Surface  
at Borehole B3

Figure 8.A.1-39

Borehole arrangement and wave travel paths for crosshole seismic testing at Treasure Island.

The depth intervals used in crosshole testing along each of the five paths at Treasure Island are listed in Table 8.A.1-14. Most measurements were performed at depth intervals between 2 ft and 5 ft (0.6 m and 1.5 m).

Personnel from the Earth Technology Corporation of San Bernardino, California also performed crosshole seismic tests along the forward testing profile (B3-B2 and B2-B1) in September, 1991. Their results for the compression wave and shear (SV) wave velocity profiles are also compared with the results of this study.

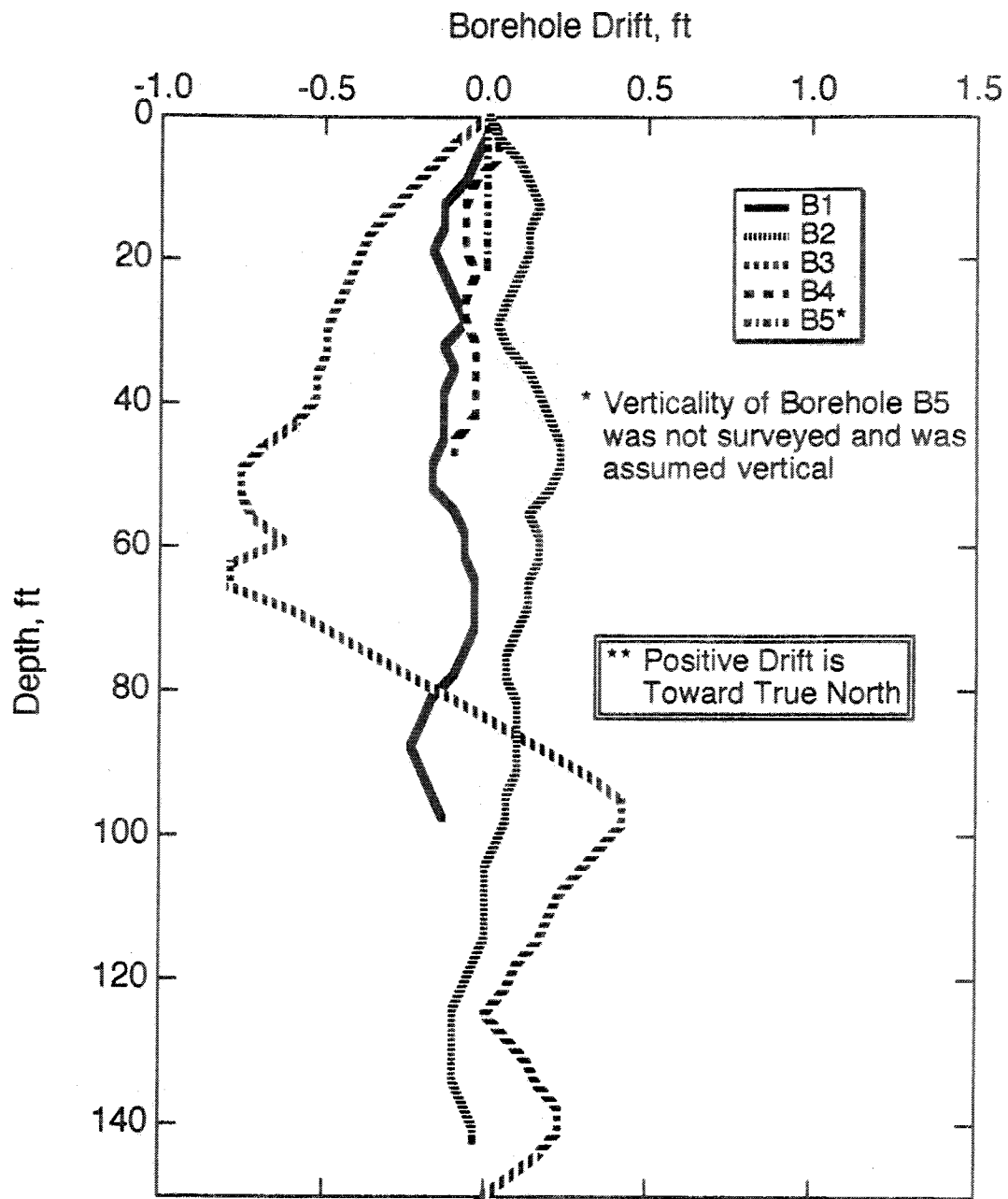
#### 8.A.1.4.2 Borehole Inclination Survey

Following the crosshole testing, personnel from Agabian Associates of Pasadena, California, surveyed the inclinations the cased borings, and their results were used in this study. Borehole B5 was not surveyed and was assumed to be vertical because the maximum depth for crosshole measurements using borehole B5 was 21 ft (6.4 m); any borehole drift to this depth was assumed small (from a visual inspection of the borehole in the field) and, therefore, neglected. Figure 8.A.1-40 presents the results of the borehole drift survey in terms of drift toward True North, and Figure 8.A.1-41 shows borehole drifts toward True West as measured by Agabian Associates. These drift measurements were then used to compute path lengths according to the method described in Section 8.A.1.2.4 and Appendix 8.A.1.B.

**Table 8.A.1-14**  
Crosshole Depth Intervals Used at Treasure Island

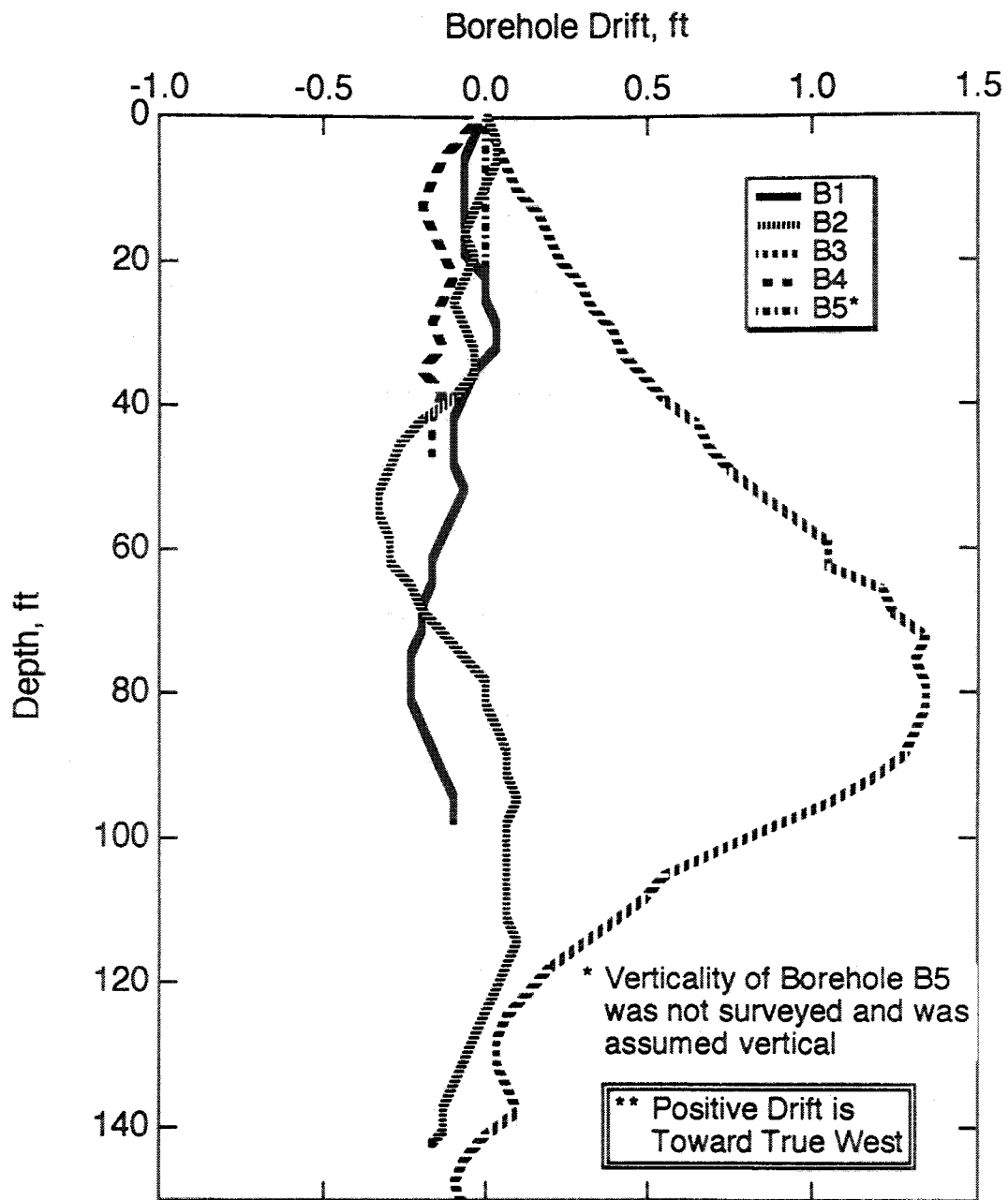
Path	Forward Profile		Reverse Profile	
	Depths	Test Interval	Depths	Test Interval
Path 1	3-30	3	6-30	6
	30-35	5	30-35	5
	38-42	2		
	45-90	5		
	94-100	2		
	100-140*	5		
Path 2	3-30	3	6-30	6
	30-35	5	30-35	5
	38-42	2		
	45-90	5		
	94-100	2		
Path 3	3-30	3		
	30-35	5		
	38-42	2		
	45-49	4		
Path 4	3-21	3		
Path 5	15-27	3		

\*The solenoid source was not used below 100 ft.



**Figure 8.A.1-40**

North-south borehole drift measurements at Treasure Island performed by Agbabian Associates of Pasadena, California.



**Figure 8.A.1-41**

East-west borehole drift measurements at Treasure Island performed by Agbabian Associates of Pasadena, California.

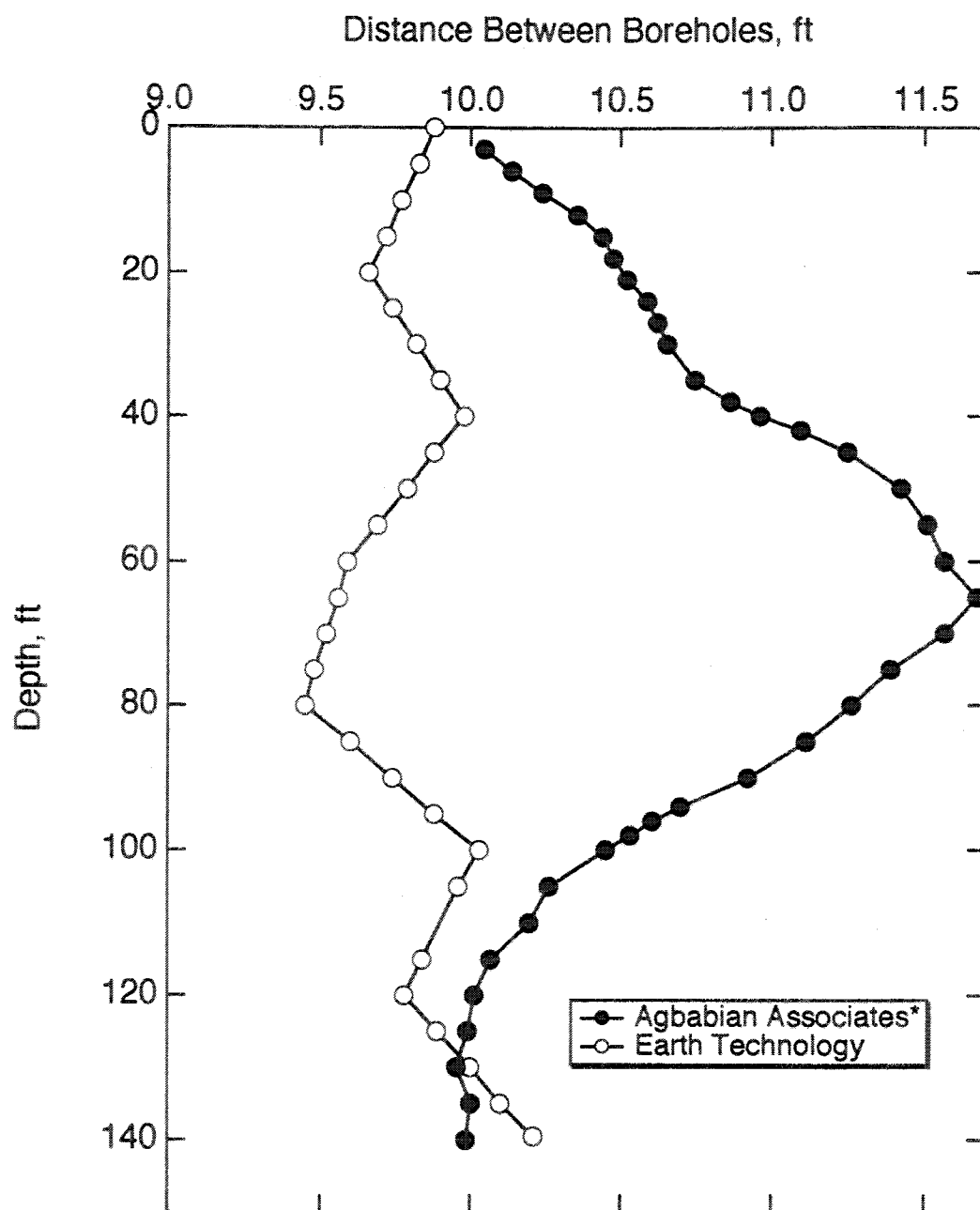
As part of their crosshole seismic measurements at the site, Earth Technology Corp. performed a borehole drift survey and computed center-to-center distances between boreholes. Figure 8.A.1-42 compares the center-to-center distances as a function of depth for the path from boreholes B3 to B2 (Path 1, forward profile) computed using borehole drift data from Agbabian Associates with the distances reported by Earth Technology Corp. A similar comparison for the path from B2 to B1 (Path 2, forward profile) is presented in Figure 8.A.1-43. The maximum differences in center-to-center distances as reported by the writer and Earth Technology Corp. are compared in Table 8.A.1-15.

**Table 8.A.1-15**

Maximum Differences in Center-to-Center Distances Between Boreholes as Reported by The University of Texas and the Earth Technology Corporation

Path	Distance (ft)		Percent Difference
	University of Texas	Earth Technology Corporation	
B3-B2 (@ 65 ft)	11.67	9.56	18.1%
B2-B1 (@ 95 ft)	9.71	10.31	6.2%

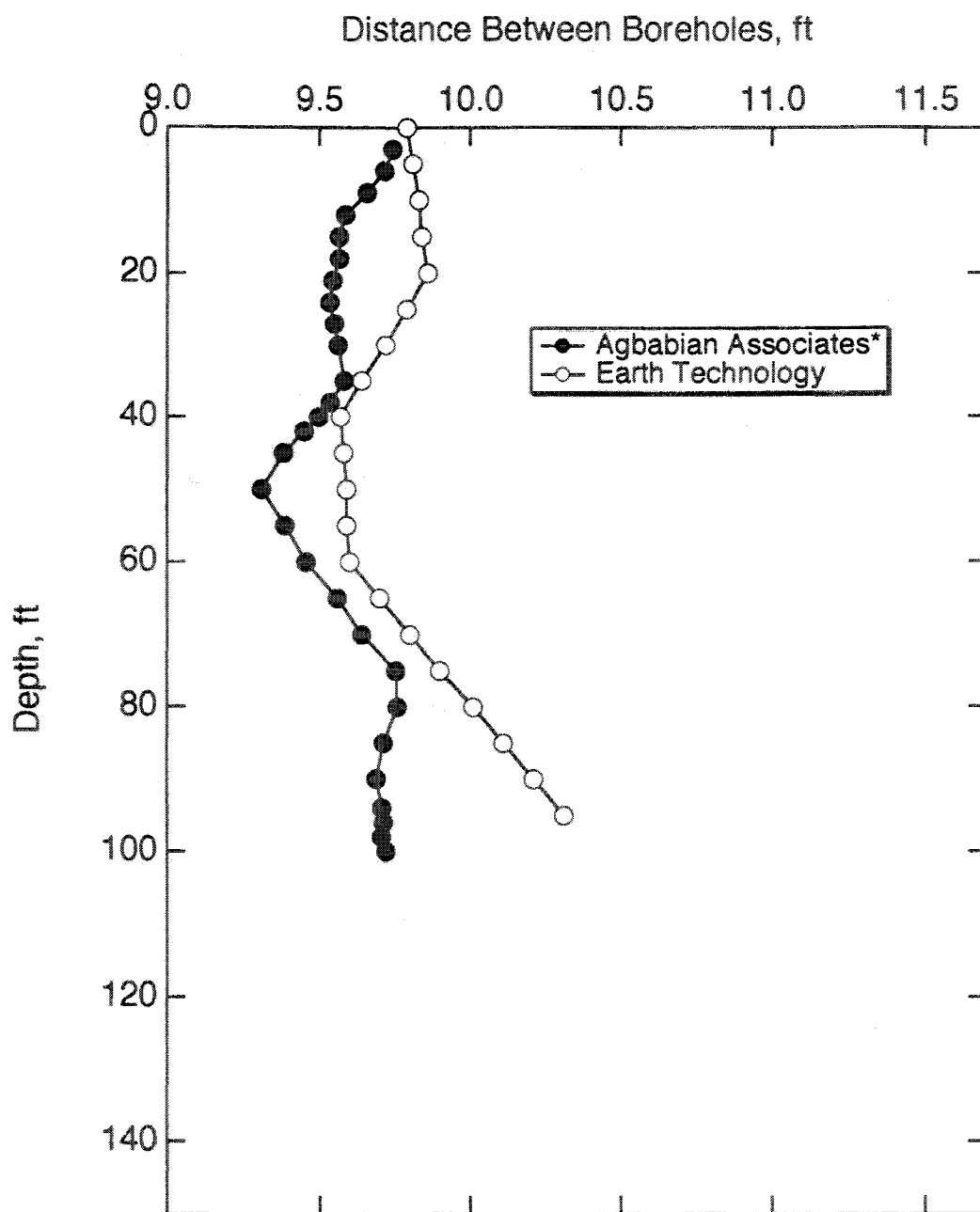
Figure 8.A.1-42 shows wide variability in the reported distance and underscores the need for careful borehole drift measurements for accurate travel path length calculations in crosshole testing. Initially, the borehole drift measurements performed by Agbabian Associates were to be used for all wave travel path distance calculations in this study because the Agbabian group was part of the EPRI project. However, upon comparison of wave velocities computed using the two sets (Agbabian and Earth Technology) of borehole spacings, it was determined that the borehole inclination survey of borehole B3 performed by Agbabian Associates was probably inaccurate. Therefore, in this study, the borehole spacings reported by the Earth Technology Corp. were used in computing all wave velocities along Paths 1 and 2 in the forward direction and along Path 1 in the reverse direction. (The distance for Path 2 in the reverse direction does not depend on the inclination of B3.)



\*Distances Computed Using Borehole Survey Data  
 Provided by Agbabian Associates, Pasadena, California

Figure 8.A.1-42

Comparison of center-to-center spacings between boreholes B3 and B2 as computed by the Earth Technology Corporation and The University of Texas at Austin.



\*Distances Computed Using Borehole Survey Data  
 Provided by Agbabian Associates, Pasadena, California

Figure 8.A.1-43

Comparison of center-to-center spacings between boreholes B2 and B1 as computed by the Earth Technology Corporation and The University of Texas at Austin.



#### **8.A.1.4.3 Shear Wave Velocities**

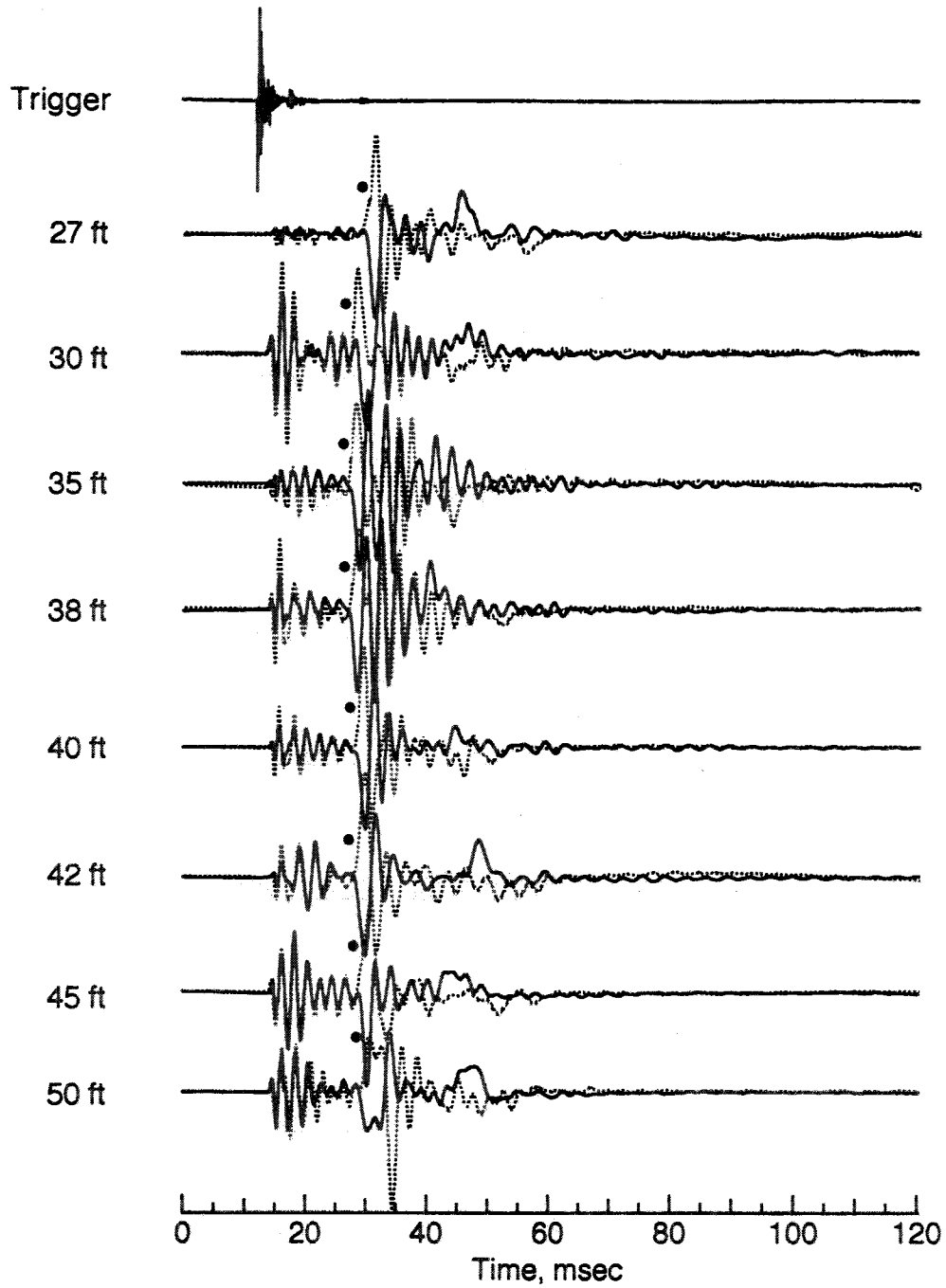
Vertically-polarized shear (SV) waves and horizontally-polarized shear (SH) waves were both measured at Treasure Island. Approximately sixty direct and forty interval SV-wave measurements were performed, and approximately fifty direct and forty interval SH-wave measurements were performed. Time records from all SV-wave and SH-wave measurements are presented by Fuhriman (1993). Typical waveforms from direct tests of SV- and SH-waves at Treasure Island are shown in Figures 8.A.1-44 and 8.A.1-45, respectively. The first abrupt departure in the trigger waveform indicates the time of impact at the source. In the other waveforms, labeled by depth, the solid waveforms are the averaged waveforms that show downward initial wave arrivals, and the dashed waveforms are the averaged waveforms that show upward initial wave arrivals. A solid dot, "•", is positioned at the chosen shear wave arrival on each waveform.

##### **8.A.1.4.3.1 SV-Wave Velocities**

A summary of all SV-wave velocities measured along the five travel paths at Treasure Island is plotted in Figure 8.A.1-46. The shear wave velocity measurements were generally quite uniform (within about 30%) along all paths at a given depth. The highest SV-wave velocities measured at the site are in a layer of sand and shells just below the Young Bay Mud, at a depth of about 98 ft (30 m). In this region, SV-wave velocity was measured to be as high as 1254 fps (382 m/sec), suggesting that the soil at this depth is dense or slightly cemented.

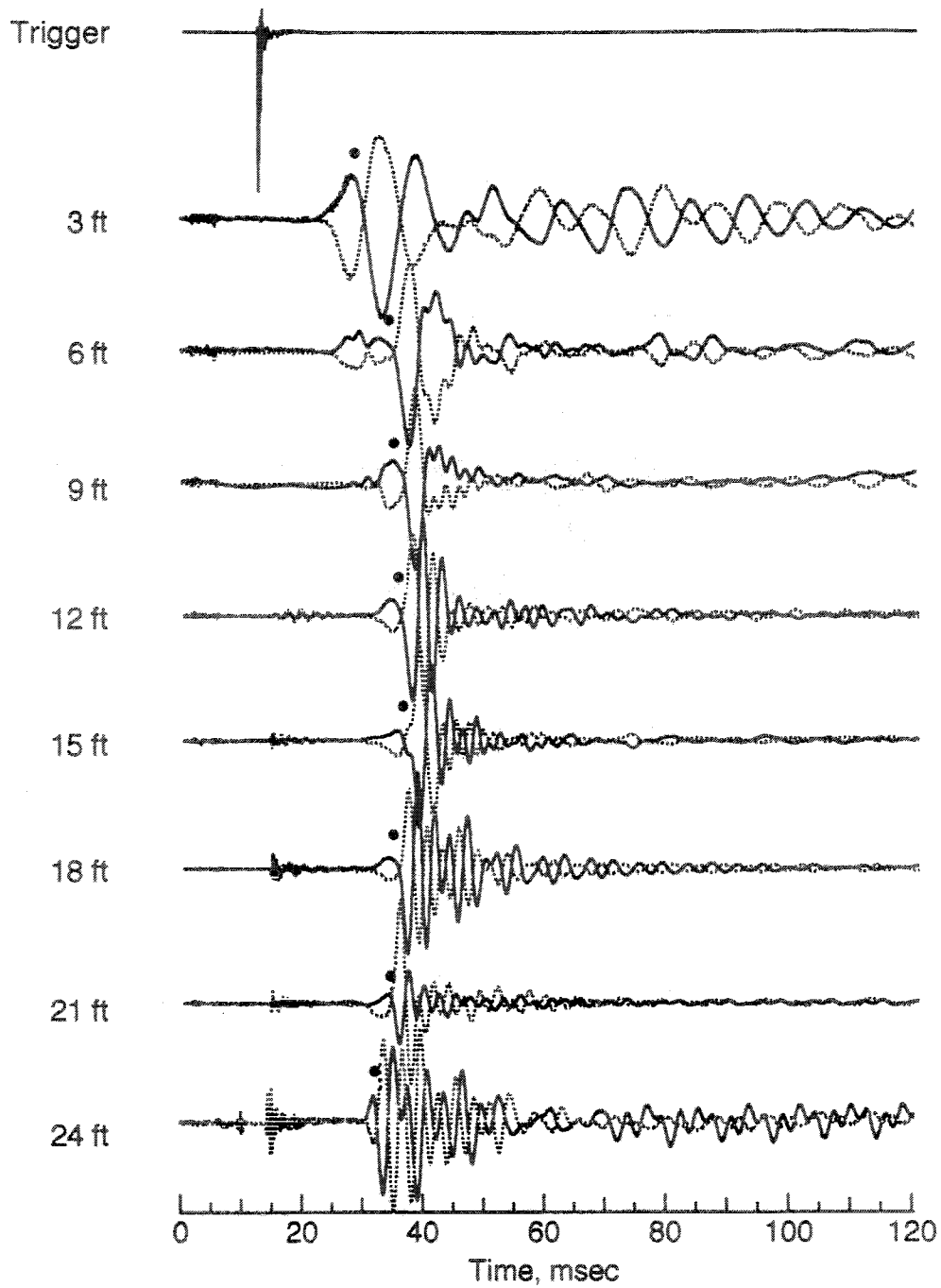
The Spectral-Analysis-of-Surface-Waves (SASW) method was also employed to measure the shear wave velocity profile at the site near the crosshole test location. A comparison of the shear wave velocity profile from the SASW tests with the SV-waves measured by crosshole tests is shown in Figure 8.A.1-47. The SASW and the crosshole measurements agree closely at this site, which exhibits a simple soil profile. The SASW test could be used to evaluate shear wave velocity only to 50 ft because only small drop weights (140 lb (63.5 kg)), dropped from a height of about 5 ft (1.5 m), were available for use as sources.

The University of New Hampshire conducted a cone penetration test near Borehole B3 (de Alba et al., 1992). Results of this particular cone sounding, called Cone 9, are shown in Figure 8.A.1-48 along with the SV-wave profile summary. Changes in the soil stiffness as represented in the CPT tip resistance are reflected in changes in the shear wave velocity profile, particularly at about 5 ft (1.5 m) and 35 ft (10.7 m). Figure 8.A.1-49 shows that another University of New Hampshire CPT sounding, called Cone 1, which was approximately 100 ft (30.5 m) away from the crosshole testing location. This sounding is similar to Cone 9 except that it shows a stiff layer at about 70 ft (~21 m), which coincides with an increase in SV-wave velocity observed near the same depth in the crosshole tests. These CPT results seem to indicate the lack of continuity in the stiff layer in the Young Bay Mud.



**Figure 8.A.1-44**

Examples of SV-wave travel time records collected at Treasure Island using the mechanical wedge source in B3 and a three-component velocity transducer in B2 (S-R1, forward profile); depths 27–50 ft.



**Figure 8.A.1-45**

Examples of SHI-wave travel time records collected at Treasure Island using the solenoid source in B3 and a three-component velocity transducer in B2 (S-R1, forward profile); depths 3–24 ft.

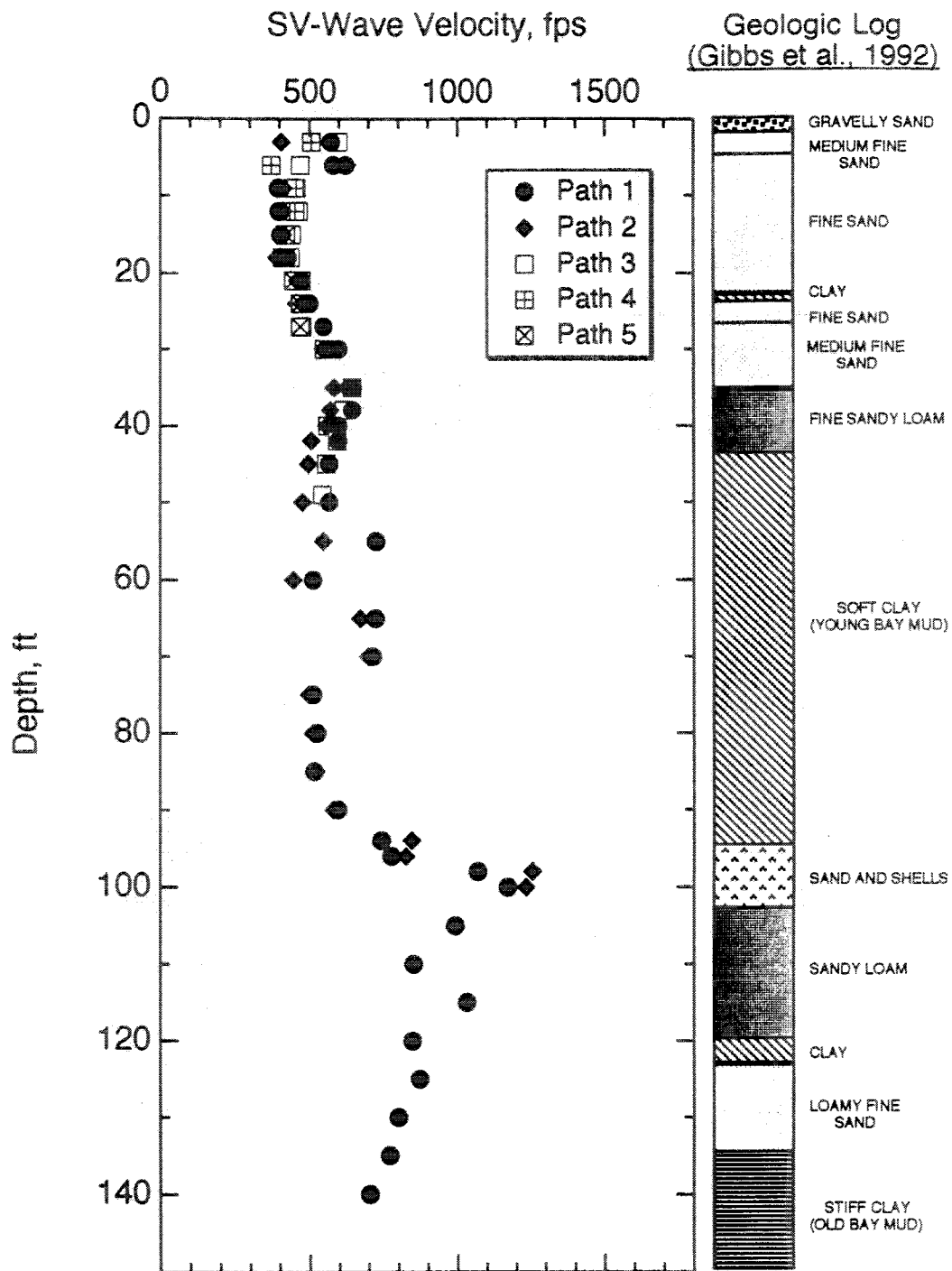
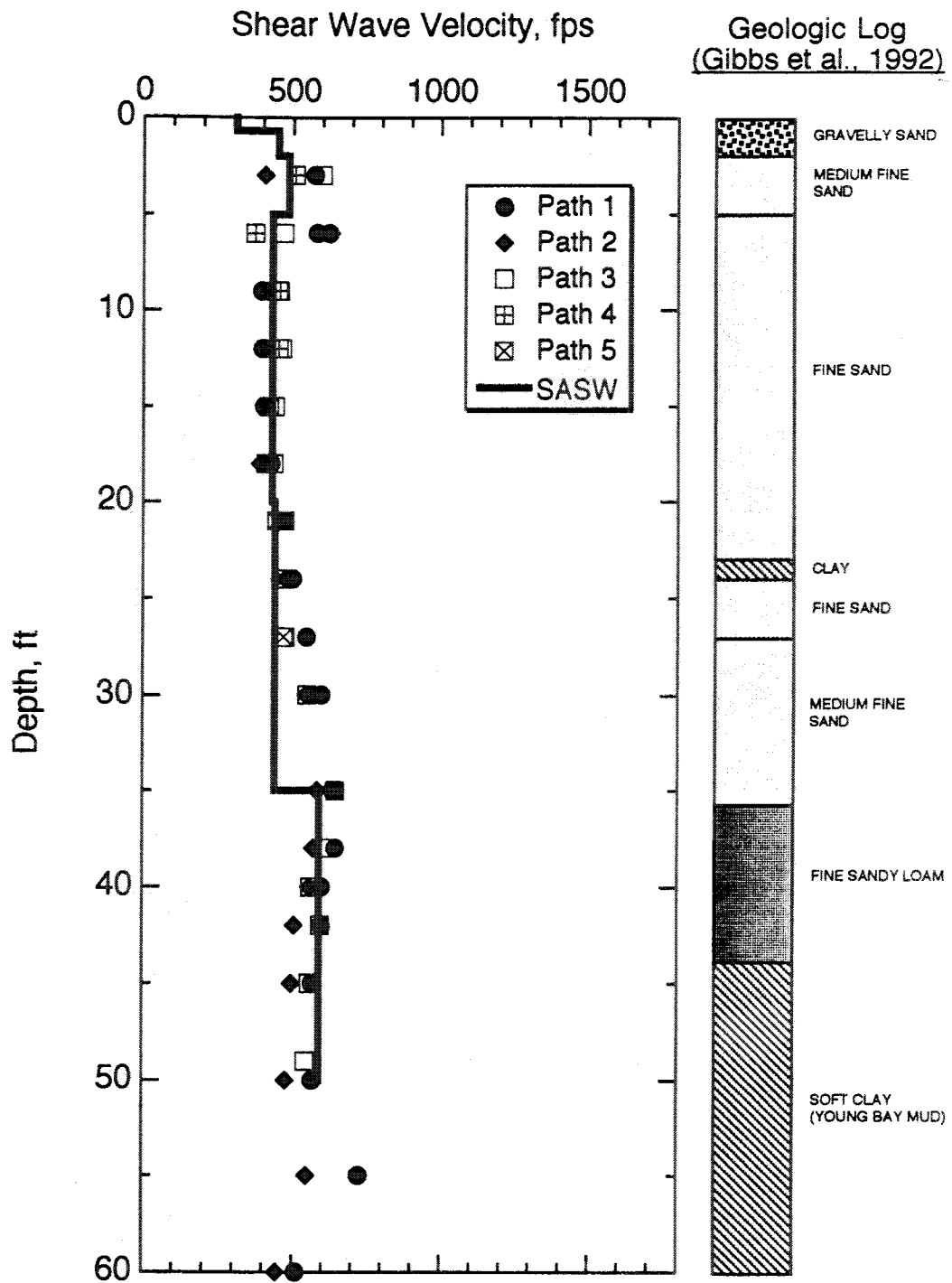
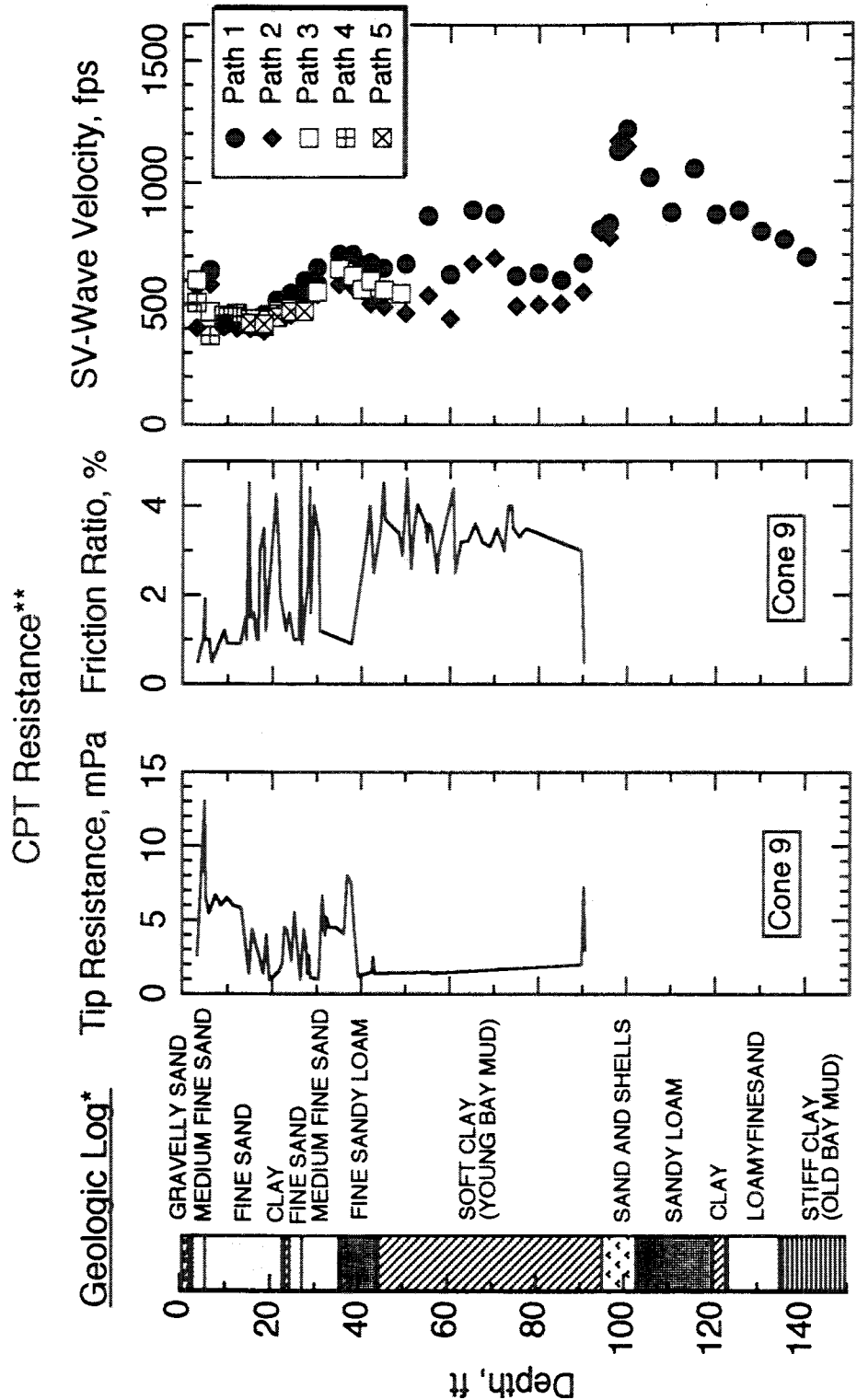


Figure 8.A.1-46  
Summary of all shear (SV) wave velocities measured at Treasure Island.



**Figure 8.A.1-47**

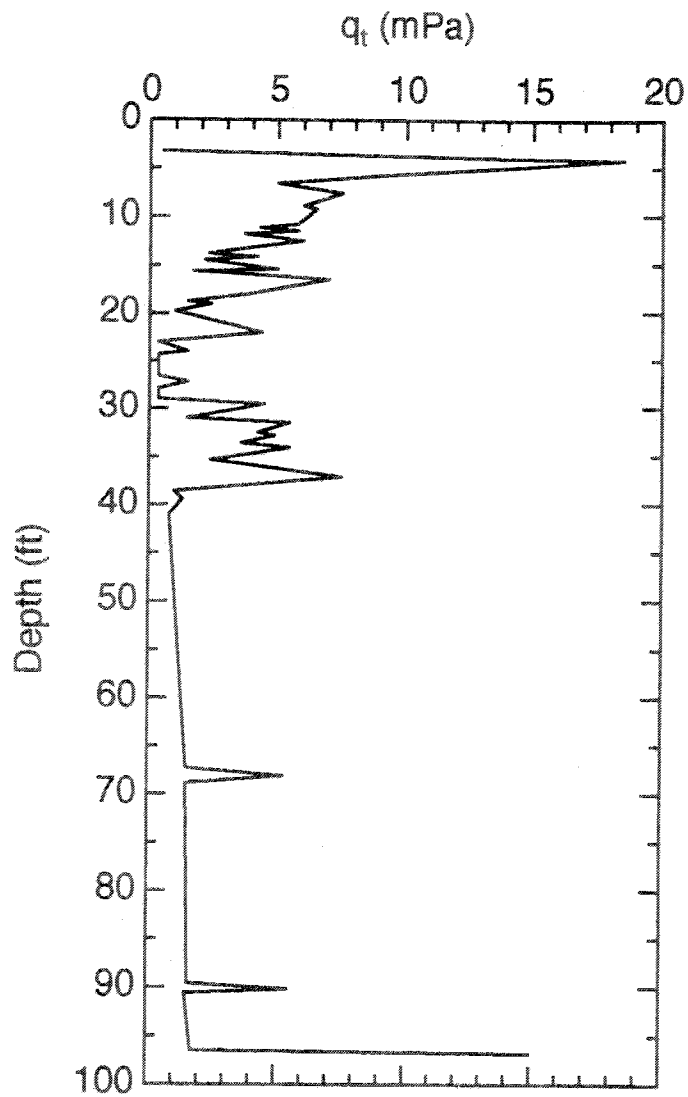
Comparison of all shear (SV) wave velocities measured at Treasure Island compared with the shear wave velocity profile measured by SASW testing.



\*From Gibbs et al., 1992

\*\*Data From de Alba et al., 1992

Figure 8.A.1-48  
Comparison of SV-wave velocity profile with CPT No. 9 data at Treasure Island.



**Figure 8.A.1-49**

Tip resistance measured in the University of New Hampshire CPT No. 1 test at Treasure Island (from de Alba et al., 1992).

**Forward Profile Measurements (Paths 1 and 2).** Values of path length, travel time and direct (S-R1) SV-wave velocity for forward profile measurements along Path 1 are presented in Table 8.A.1-34 (Appendix B). Subjective ratings of relative data quality are associated with the travel times. Table 8.A.1-35 contains the same information for interval (R1-R2) measurements along Path 2.

**Reverse Profile Measurements (Paths 1 and 2).** Values of path length, travel time and direct (S-R1) SV-wave velocity for reverse profile measurements along Path 2 are presented in Table 8.A.1-36; the same information for interval (R1-R2) measurements along Path 1 is tabulated in Table 8.A.1-37.

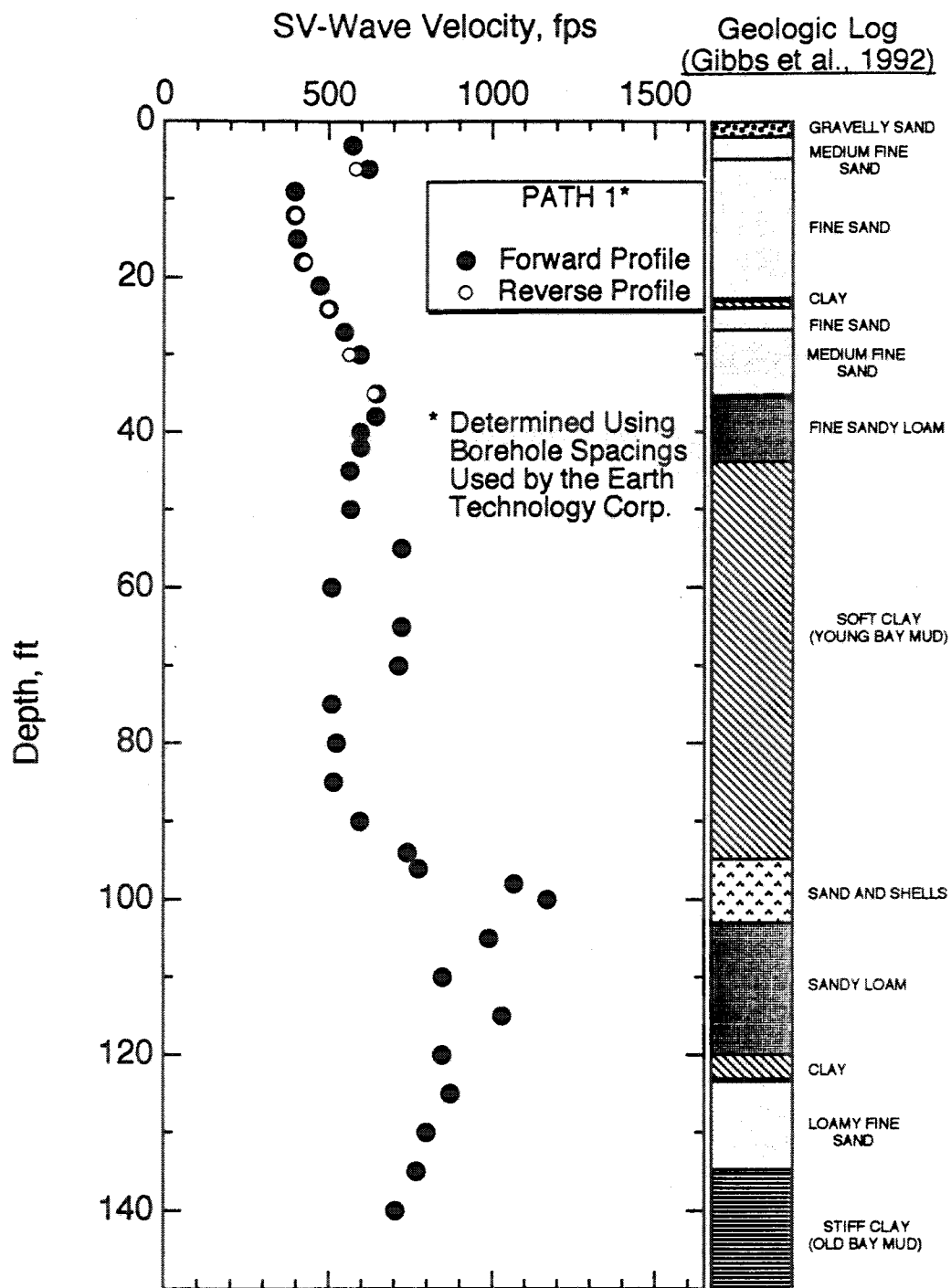
**Direct and Interval Measurements Along Paths 1 and 2.** All forward profile (direct) SV-wave velocities from Path 1 are plotted in Figure 8.A.1-50 with solid symbols. Reverse (interval) SV-wave velocities from the same path are also plotted, but with open symbols. A similar plot for Path 2 appears in Figure 8.A.1-51. In both cases, the reverse profile data, although limited, are in excellent agreement with the forward profile data. Because the direct and interval measurements result in the same velocities, these tests establish that correct field procedures were followed and that the equipment had no timing or calibration problems during the testing. However, it should be noted that agreement between forward and reverse-profile velocities does not prove that the travel distances were calculated correctly; they are a separate and independent matter.

**"North-South" Profile Measurements.** Values of path length, travel time and direct (S-R1) SV-wave velocity for measurements along Path 3 (from borehole B1 to borehole B4) are presented in Table 8.A.1-38. Subjective ratings of relative data quality are associated with the travel times. Measurements along Path 3 were conducted to a final depth of 49 ft (~15 m). Table 8.A.1-39 lists all pertinent information for interval (R1-R2) SV-wave computations along Path 4 (between boreholes B4 and B5). SV-waves were measured along Path 4 to a depth of 21 ft (6.4 m). The SV-wave velocities from tests along Paths 3 and 4 are shown in Figure 8.A.1-46.

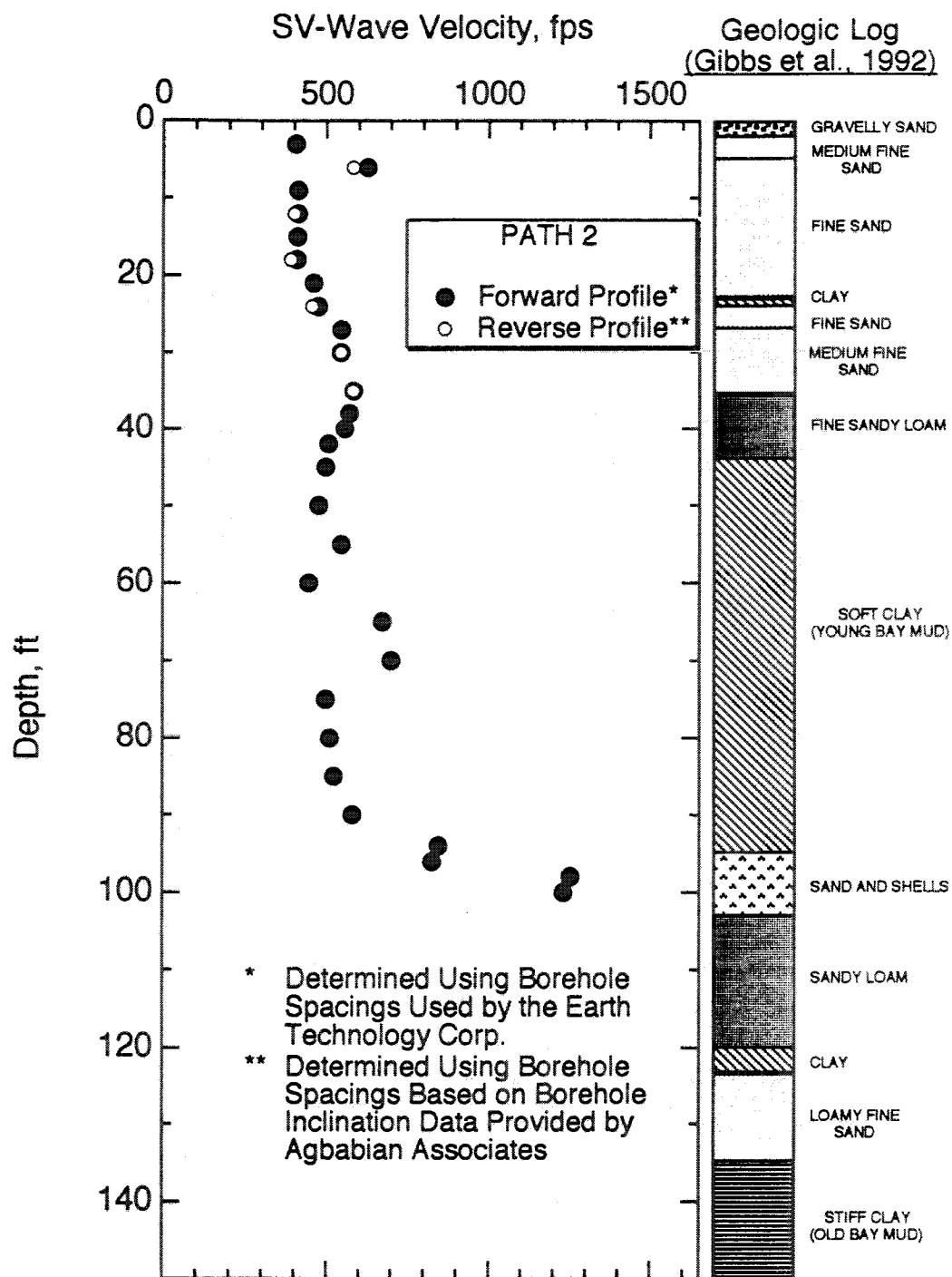
**Path 5 Measurements.** Values of path length, travel time and direct (S-R1) SV-wave velocity for measurements along Path 5 (from borehole B2 to borehole B4) are presented in Table 8.A.1-40. A data quality rating is associated with the travel times. SV-wave velocities were measured between the depths 15 ft and 27 ft (4.6 m and 8.2 m). The SV-wave velocities measured along this path match the velocity profiles established along the other four crosshole paths at the site (see Figure 8.A.1-46).

**Comparisons With Earth Technology Measurements.** It is useful to compare the SV-wave velocities measured in this work with those measured by personnel from the Earth Technology Corporation. Figure 8.A.1-52 compares the SV-wave velocity profiles obtained by both groups along Path 1 (boreholes B3-B2), and Figure 8.A.1-53 shows the results along Path 2 (boreholes B2-B1).





**Figure 8.A.1-50**  
Comparison of shear (SV) wave velocities measured in the forward and reverse directions along Path 1 at Treasure Island.



**Figure 8.A.1-51**

Comparison of shear (SV) wave velocities measured in the forward and reverse directions along Path 2 at Treasure Island.

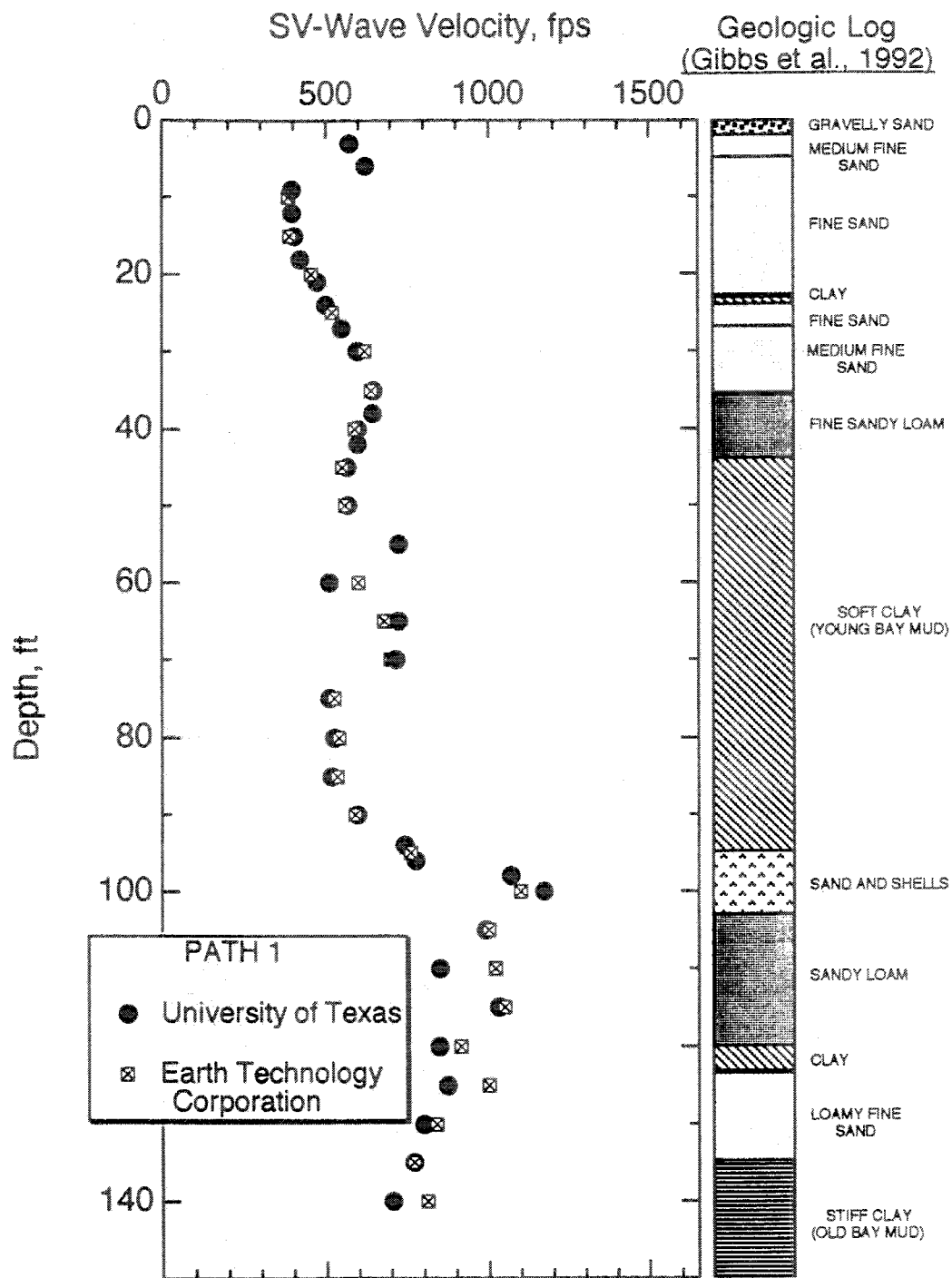
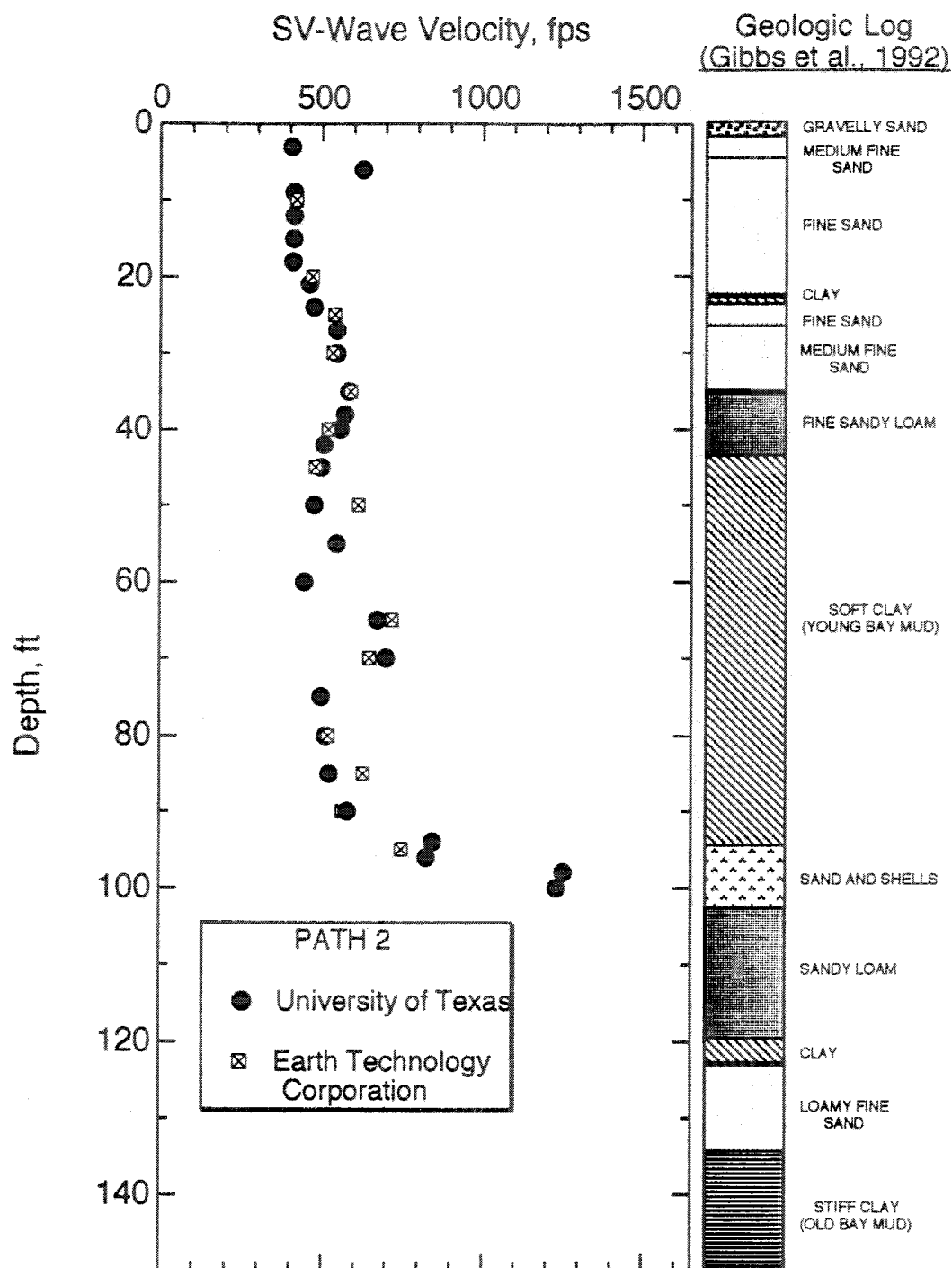


Figure 8.A.1-52

Comparison of shear (SV) wave velocities measured by The University of Texas and Earth Technology along Path 1 at Treasure Island.



**Figure 8.A.1-53**  
Comparison of shear (SV) wave velocities measured by The University of Texas and Earth Technology along Path 2 at Treasure Island.

The two data sets for Path 1 and Path 2 compare very well, with velocities varying by not more than about 30% (Path 2 at 50 ft (15.2 m), Figure 8.A.1-53) but usually by much less. This close comparison for shear waves is not surprising since the University of Texas data and the Earth Technology data are based on the same center-to-center borehole spacings.

**Comparisons with Laboratory Results.** The shear wave velocities of soil samples taken from various depths were measured in the laboratory using the torsional resonant column apparatus at the University of Texas at Austin (Hwang and Stokoe, 1993). These laboratory results are presented in Table 8.A.1-16 with the field values measured at the same depths along Path 1 in the forward direction. The laboratory values were determined at the estimated in-situ mean effective stress after being confined for one day at that stress level. Table 8.A.1-16 and Figure 8.A.1-54 show that the laboratory measurements of shear wave velocity are, on average, about 9% lower than the shear wave velocity measured in the field using the crosshole method. The laboratory and the field values follow the same general trend throughout the soil profile.

**Table 8.A.1-16**

Comparison of Shear (SV) Wave Velocities Measured at Treasure Island by the Crosshole Method and by the Resonant Column Method; Path 1

Depth (ft)	Crosshole	Laboratory	Percent Difference*
	V <sub>SV</sub> (fps)**	V <sub>S</sub> (fps)	
17.5	421 <sup>a</sup>	491 <sup>b</sup>	16.6
30	598	594	0.7
60	512	474	7.4
90	597	608	1.8
130	800	656	18.0
170	— <sup>c</sup>	934	—
232	— <sup>c</sup>	727	—

Notes on Table 8.A.1-16

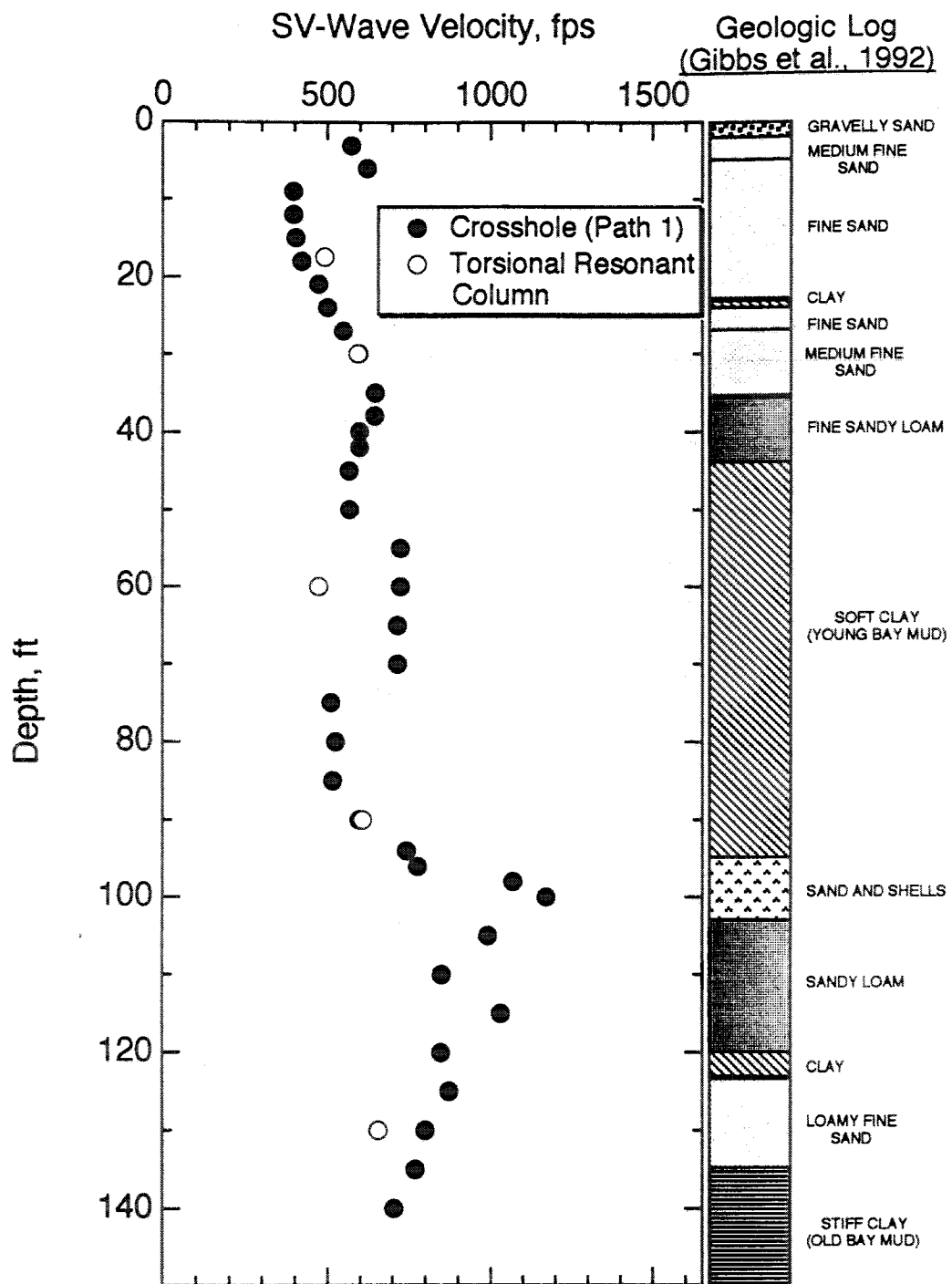
\* percent difference between field- and laboratory-measured shear wave velocities

\*\* measured along Path 1 from B3 to B2

a measured performed at 18-ft depth

b 1.5-in. diameter sample

c crosshole measurement not performed



**Figure 8.A.1-54**

Comparison of shear wave velocities at Gilroy 2 obtained from crosshole and torsional resonant column tests.

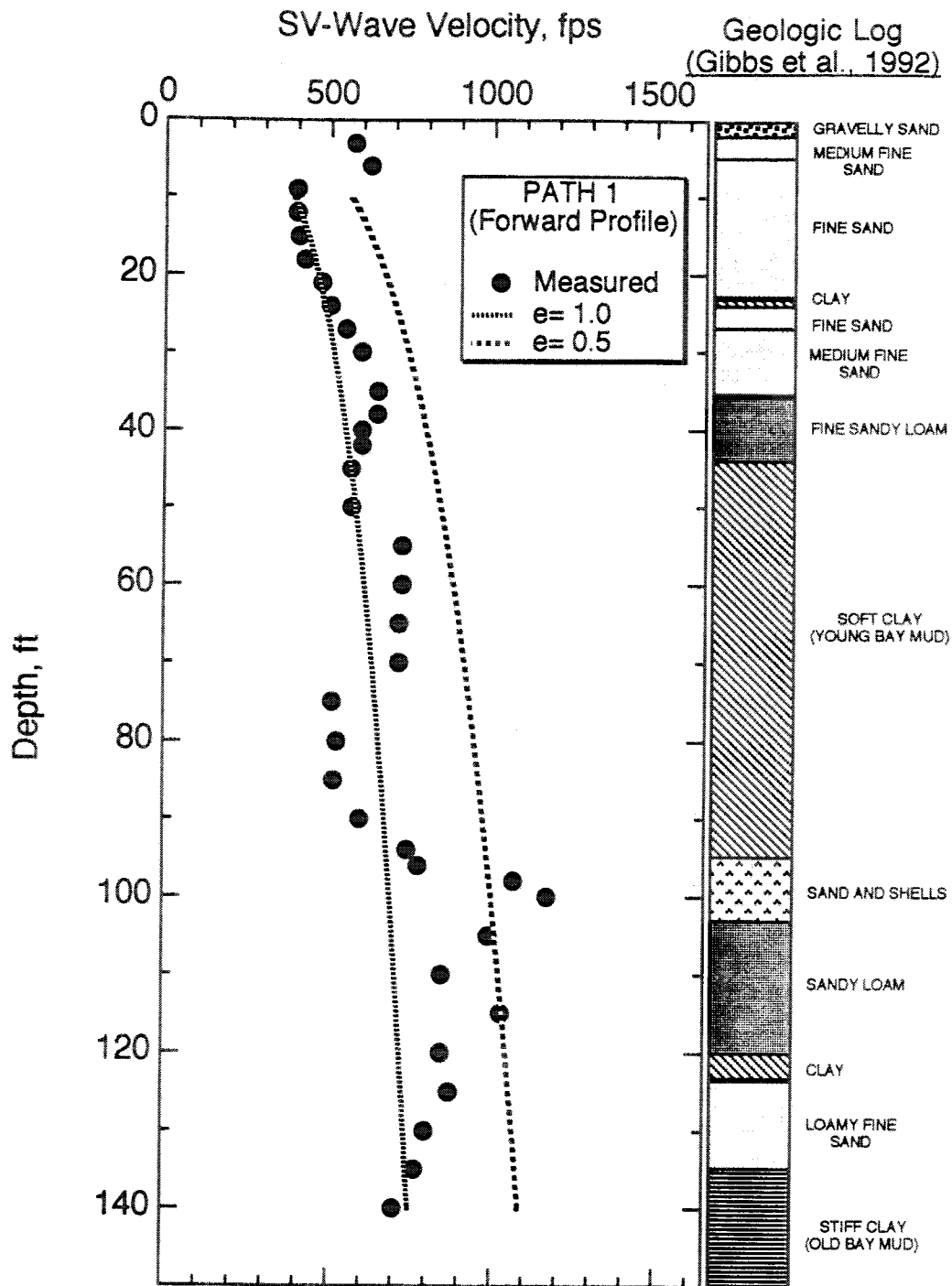
#### **8.A.1.4.3.2 Comparison of $V_s$ With Empirical Results**

As with the data from Gilroy 2, it is interesting to examine the stiffness of the soil profile at Treasure Island in terms of the shear wave velocities. The values of SV-wave velocity are compared with empirical values of shear wave velocity. According to Hardin and Drnevich (1972), the small-strain shear modulus of an uncemented normally consolidated soil may be determined using Eq. (3.1).

By combining Eqs. (3.1) and (3.2), one obtains an equation for shear wave velocity as a function of depth and void ratio. Figure 8.A.1-55 shows the shear (SV) wave velocity profile measured along Path 1 in the forward direction. Measured SV-wave velocities are compared with empirically-predicted shear wave velocities for normally consolidated soils predicted by Eqs. (3.1) and (3.2), assuming void ratios of 1.0, typical for a clay, and 0.5, which is typical for a sand.

If the empirical curves in Figure 8.A.1-55 represent the shear wave velocities of a normally-consolidated soil, then it can be concluded that all sand layers in the soil profile (mostly in the upper 45 ft (13.7 m)) are rather loose, since the measured shear waves fall below those predicted for a normally-consolidated soil. A notable exception is in the sand and shell layer in the vicinity of 100 ft (30.5 m), where the measured SV-wave velocities are higher than the velocity predicted for a normally-consolidated soil at that depth. This material, therefore, is dense or perhaps slightly cemented, which can cause the shear wave velocity to be higher than for a normally-consolidated soil.

On the other hand, most of the clay layers in Figure 8.A.1-55 seem at or above the mean effective stress for a normally-consolidated soil. At least two regions in the Young Bay Mud (between 55 and 70 ft (16.8 and 22.9 m)) exhibit higher shear wave velocities than those predicted for normally consolidated soil at their respective depths. Most of the soil profile below a depth of about 90 ft (27.4 m) appears to be dense or over-consolidated, at least in terms of shear wave velocity.



**Figure 8.A.1-55**

Comparison of shear (SV) wave velocities measured along Path 1 at Treasure Island with theoretical S-wave velocities predicted by Hardin and Drnevich (1972) for a normally-consolidated soil with void ratios ( $e$ ) of 0.5 and 1.0.



#### **8.A.1.4.3.3 SH-Wave Velocities**

A summary of all SH-wave velocities measured along the five paths at Treasure Island is plotted in Figure 8.A.1-56. As for the SV-waves, the SH-wave measurements were generally quite uniform (within about 20%, but often less) throughout the soil profile. Also like the SV-waves, the highest SH-wave velocities measured at the site are in a layer of sand and shells just below the Young Bay Mud, at a depth around 100 ft (30.5 m). In this region SH-wave velocities exceed 1700 fps (520 m/sec). A more detailed discussion of SV- and SH-wave comparisons follows in Section 8.A.1.4.4.

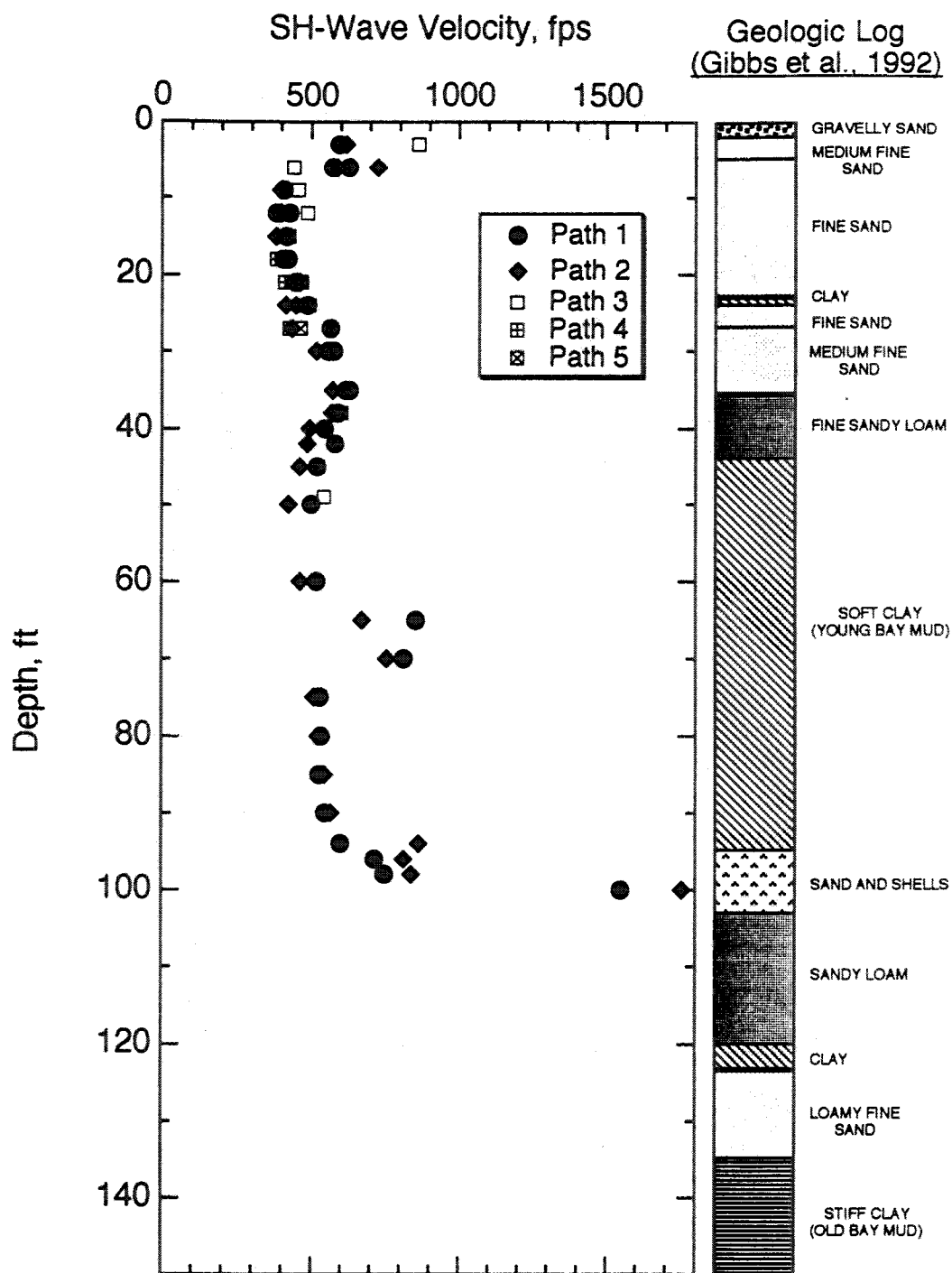
**Forward Profile Measurements (Paths 1 and 2).** Values of path length, travel time and direct (S-R1) SH-wave velocity for forward profile measurements along Path 1 are presented in Table 8.A.1-41. Subjective ratings of relative data quality are associated with the travel times. Table 8.A.1-42 contains the same information for interval (R1-R2) measurements along Path 2. Data quality for the forward SH-wave measurements was usually high.

**Reverse Profile Measurements (Paths 1 and 2).** Values of path length, travel time and direct (S-R1) SH-wave velocity for reverse profile measurements along Path 2 are presented in Table 8.A.1-43; the same information for interval (R1-R2) measurements along Path 1 is tabulated in Table 8.A.1-44. Reverse profile measurements were performed in the upper 35 ft (10.7 m) at six depths.

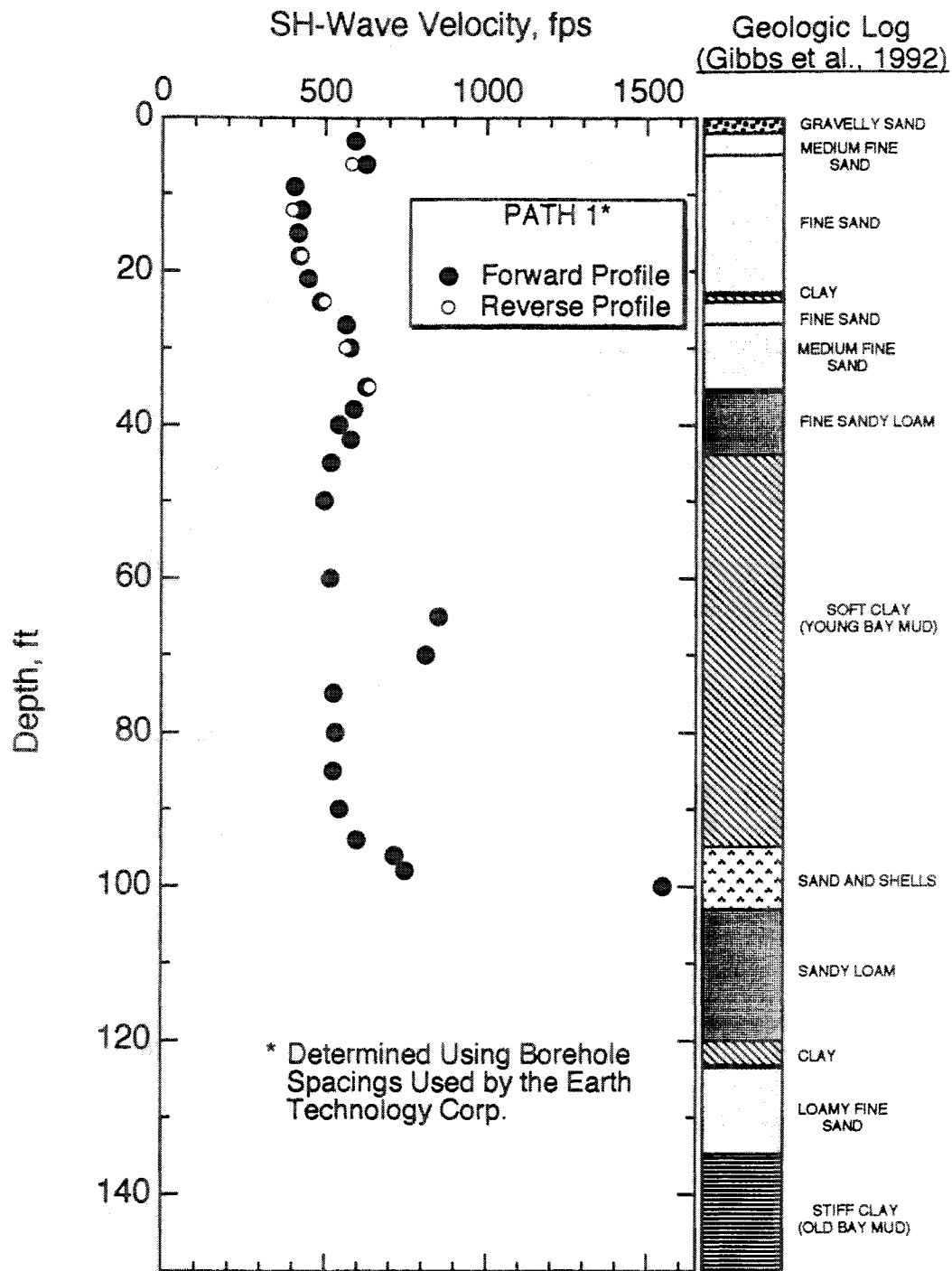
**Direct and Interval Measurements Along Paths 1 and 2.** All forward profile (direct) SH-wave velocities from Path 1 are plotted in Figure 8.A.1-57 with solid symbols. Reverse (interval) SH-wave velocities from the same path are also plotted, but with open symbols. A similar plot for Path 2 appears in Figure 8.A.1-58. In both cases, the reverse profile data, although limited, are in excellent agreement with the forward profile data. Because the direct and interval measurements give the same velocities, one can conclude that correct field procedures were followed and that the equipment had no timing or calibration problems during the testing.

**"North-South" Profile Measurements.** Values of path length, travel time and direct (S-R1) SH-wave velocity for measurements along Path 3 (from borehole B1 to borehole B4) are presented in Table 8.A.1-45. Subjective ratings of relative data quality are associated with the travel times. As in the case of the SV-waves, SH-wave measurements along Path 3 were conducted to a final depth of 49 ft (~15 m). Table 8.A.1-46 lists all pertinent information for interval (R1-R2) SH-wave computations along Path 4 (between boreholes B4 and B5). SH-waves were measured along Path 4 to a depth of 21 ft (6.4 m). The SH-wave velocities measured along Paths 3 and 4 are shown in Figure 8.A.1-56. The SH-wave velocities measured in the "North-South" profile are in general agreement with the SH-wave velocities measured along all other testing paths.

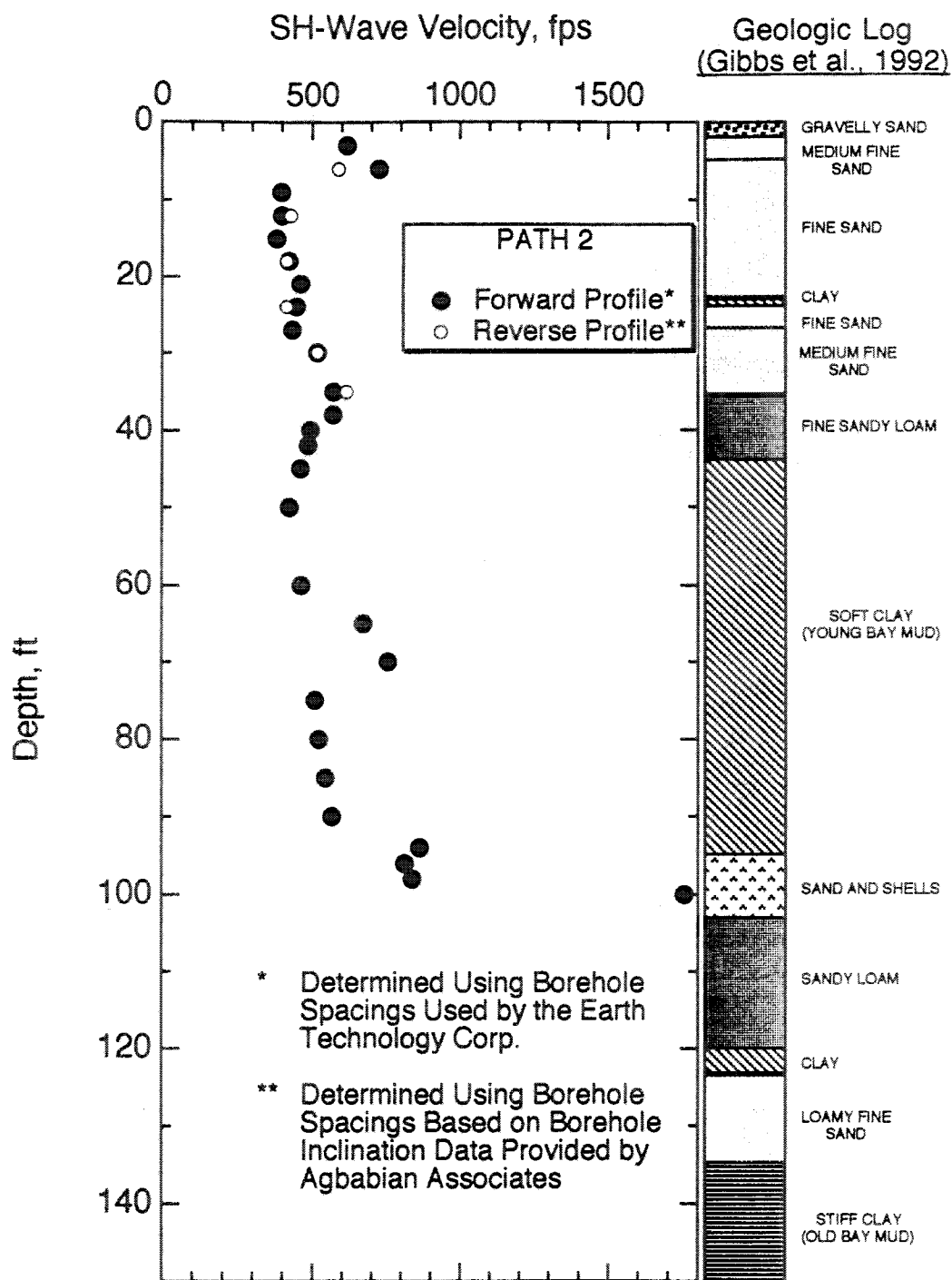
**Path 5 Measurements.** Values of path length, travel time and direct (S-R1) SH-wave velocity for measurements along Path 5 (from borehole B2 to borehole B4) are presented in Table 8.A.1-47. The data quality associated with each travel time along Path 5 is high. SH-waves were measured between the depths 15 ft and 27 ft (4.6 m and 8.2 m) and are plotted in Figure 8.A.1-56. The SH-wave velocities measured along this path match the velocity profiles established along the other four crosshole paths at the site.



**Figure 8.A.1-56**  
Summary of all shear (SH) wave velocities measured at Treasure Island.



**Figure 8.A.1-57**  
Comparison of shear (SH) wave velocities measured in the forward and reverse directions along Path 1 at Treasure Island.

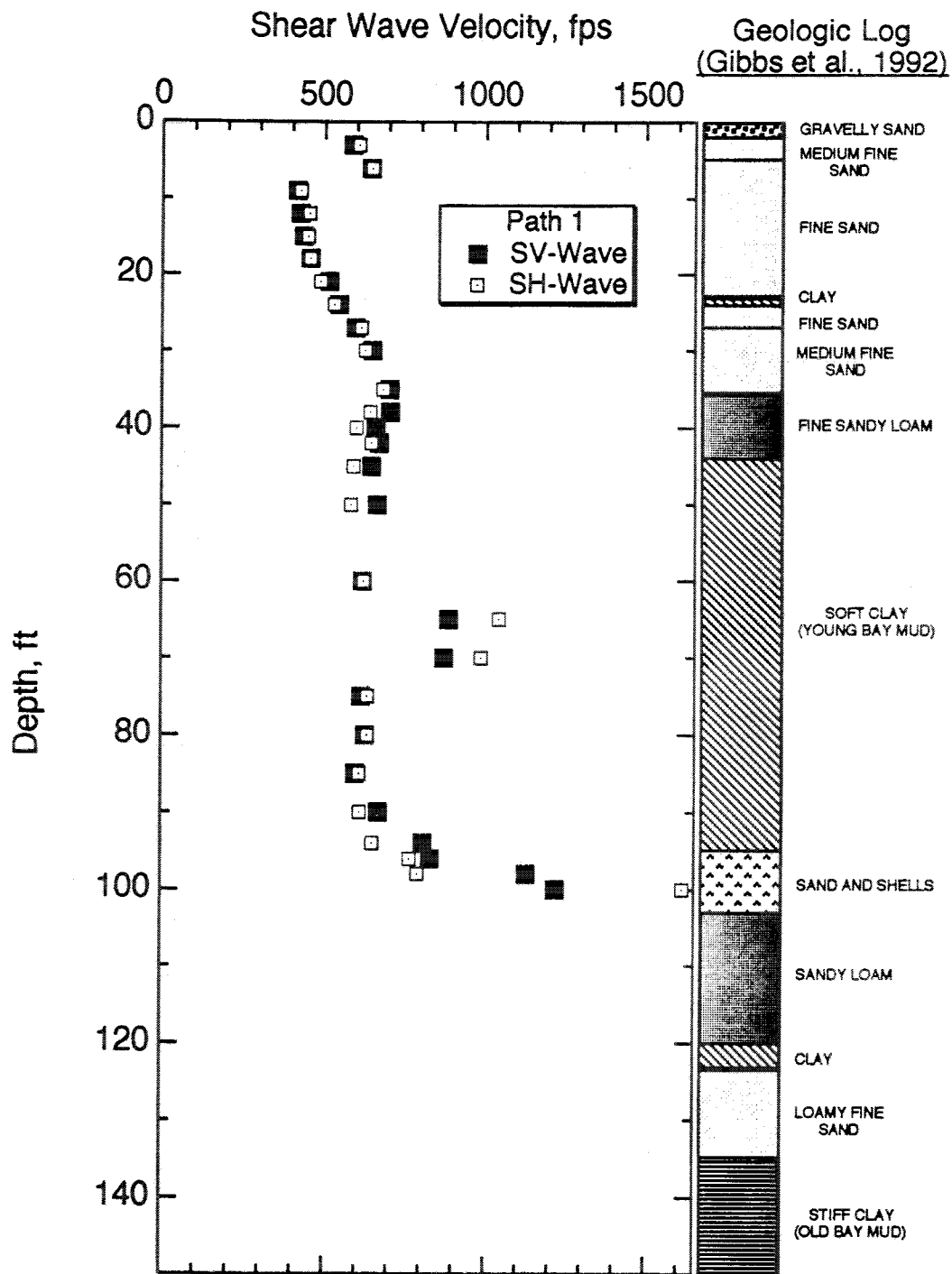


**Figure 8.A.1-58**  
Comparison of shear (SH) wave velocities measured in the forward and reverse directions along Path 2 at Treasure Island.

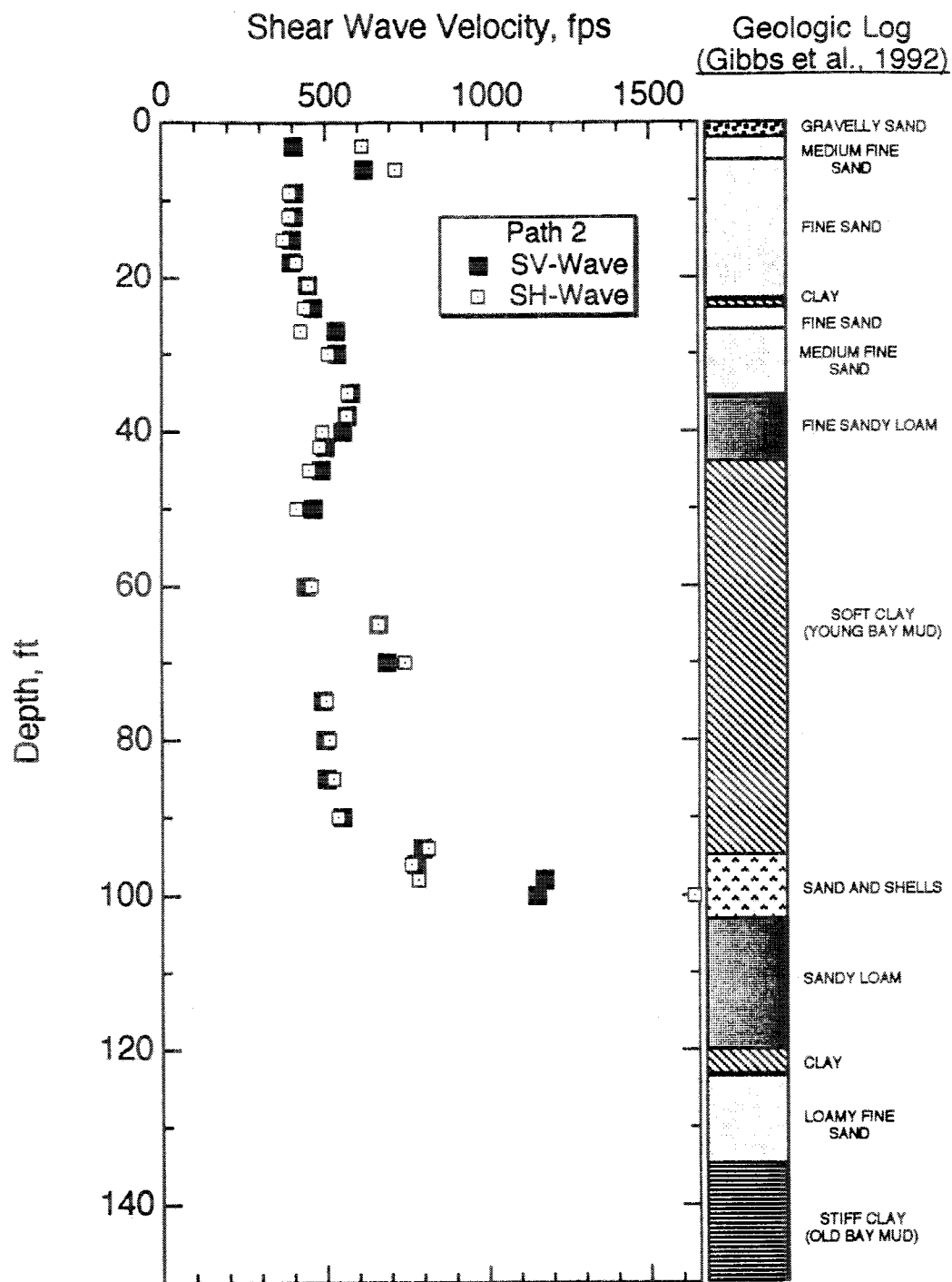
#### 8.A.1.4.4 Anisotropy in SV-Wave and SH-Wave Velocities

It is useful to compare vertically-polarized (SV) and horizontally-polarized (SH) shear wave velocities to study soil anisotropy. SV- and SH-waves from the forward tests along Path 1 are plotted together in Figure 8.A.1-59. Similar plots for Paths 2, 3, 4 and 5 are presented in Figures 8.A.1-60, 8.A.1-61, 8.A.1-62 and 8.A.1-63, respectively. There is too little data in Figures 8.A.1-62 and 8.A.1-63 to draw any firm conclusions, so these data are excluded from the following discussion of anisotropy.

The shear wave velocity ratio, (SV/SH), is listed in Table 8.A.1-17 for S-wave velocities measured along Paths 1, 2 and 3. A shear wave velocity ratio of less than unity implies a stiffer soil in the horizontal direction than in the vertical direction. Conversely, when (SV/SH) >1, the soil is stiffer in the vertical direction. The average ratio (SV/SH) is plotted versus depth in Figure 8.A.1-64. Table 8.A.1-17 and Figure 8.A.1-64 indicate at least two regions where the ratio (SV/SH) is clearly less than unity. One of these regions, between 70 ft and 75 ft (21.3 m and 23 m), appears in the middle of the Young Bay Mud, where the shear wave velocity profiles (Figures 8.A.1-46 and 8.A.1-56) and the CPT soundings (Figures 8.A.1-48 and 8.A.1-49) indicate that the geology is more complex than what is shown in the boring log. Unfortunately, 100 ft (30.5 m) is the maximum measurement depth for SH-waves, which makes comparisons of (SV/SH) beyond this depth impossible. Table 8.A.1-17 and Figure 8.A.1-64 show that in the first 60 ft (18.3 m) of the soil profile the ratio (SV/SH) is generally greater than or roughly equal to unity, except near the surface. Generally, the vertical stresses are higher than the horizontal stresses, which cause higher SV-wave velocities than SH-wave velocities.



**Figure 8.A.1-59**  
Comparison of SV- and SH-wave velocities measured along Path 1 at Treasure Island (forward direction only).



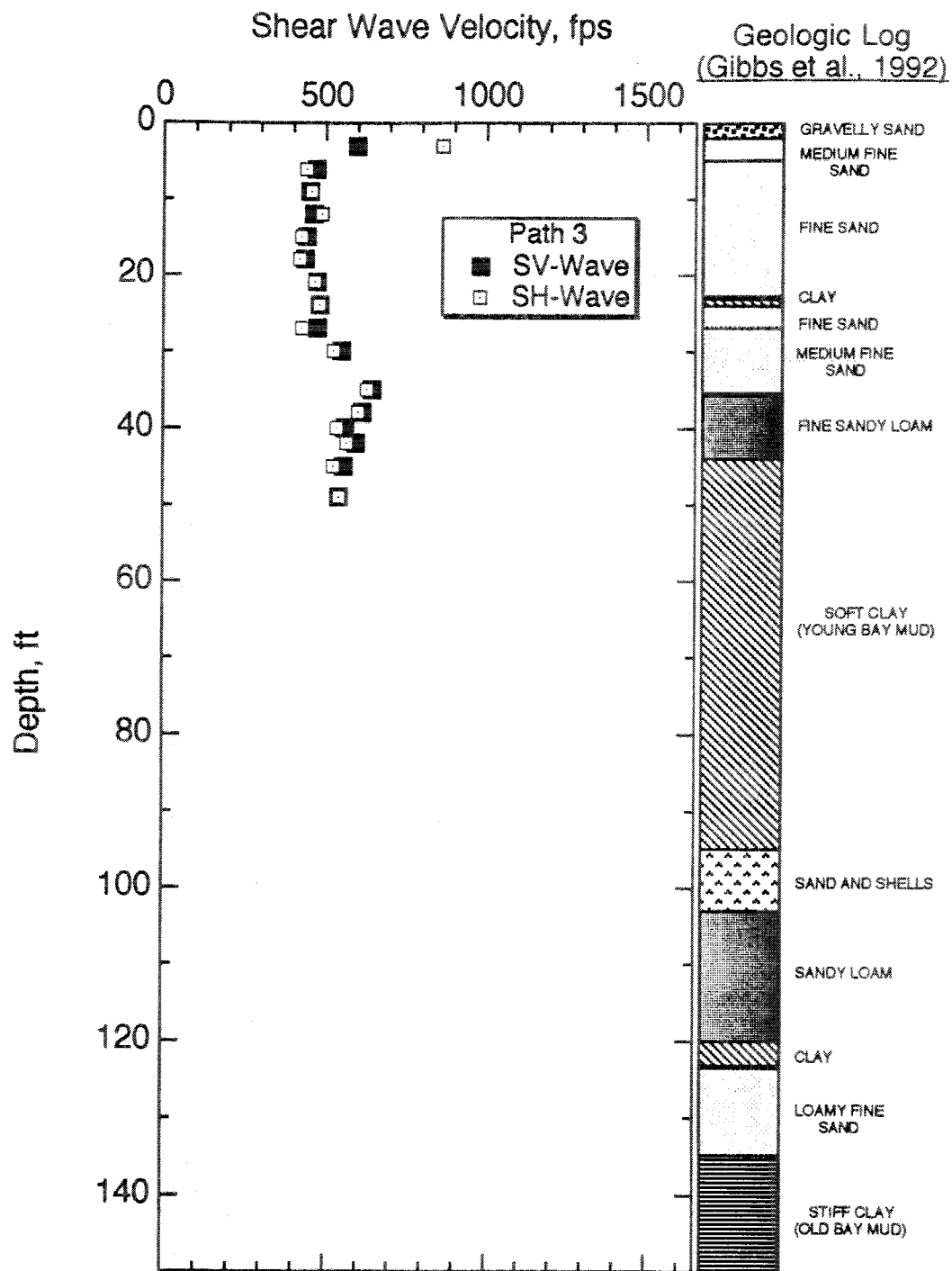
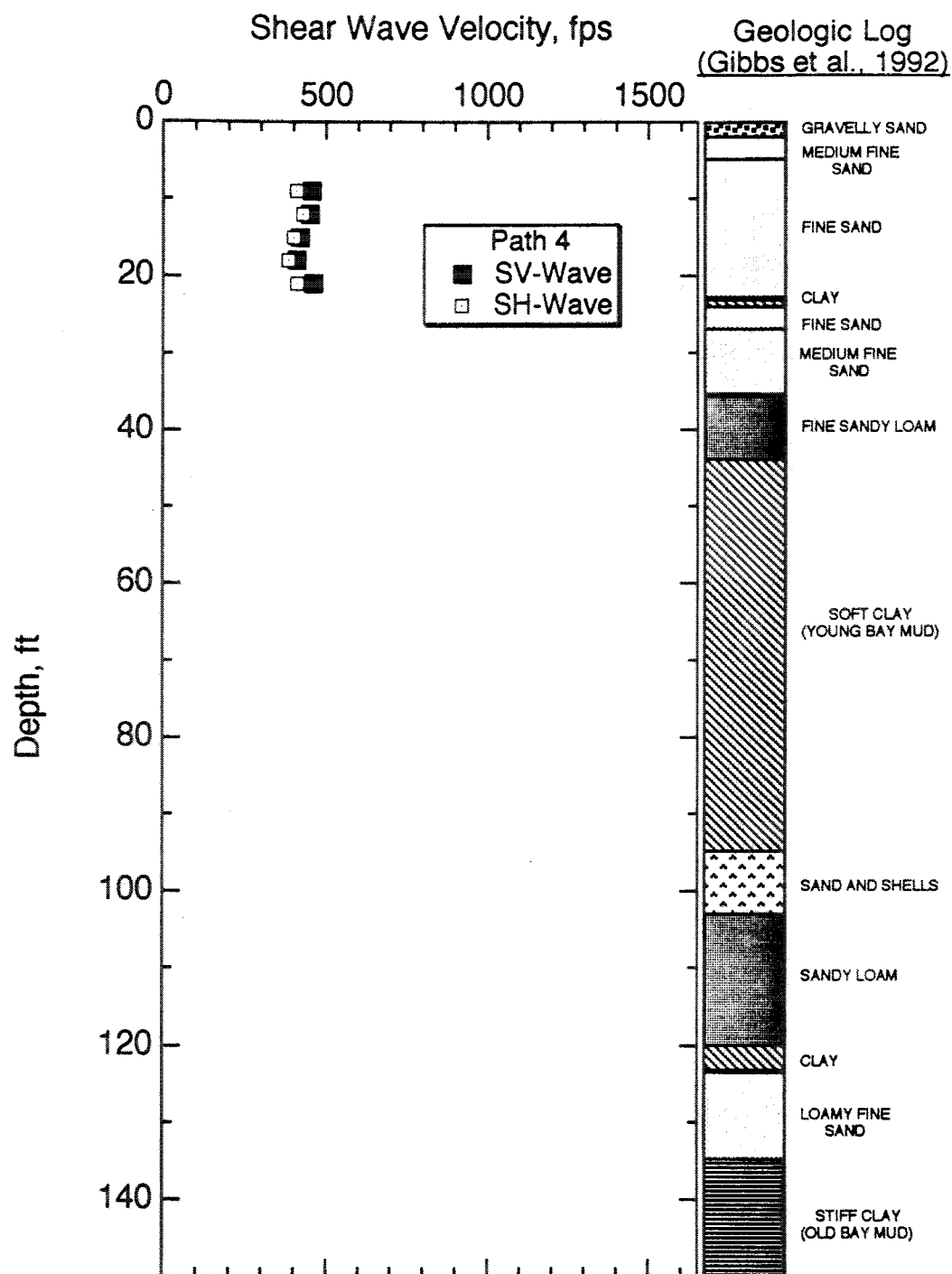


Figure 8.A.1-61  
Comparison of SV- and SH-wave velocities measured along Path 3 at Treasure Island.





**Figure 8.A.1-62**  
Comparison of SV- and SH-wave velocities measured along Path 4 at Treasure Island.

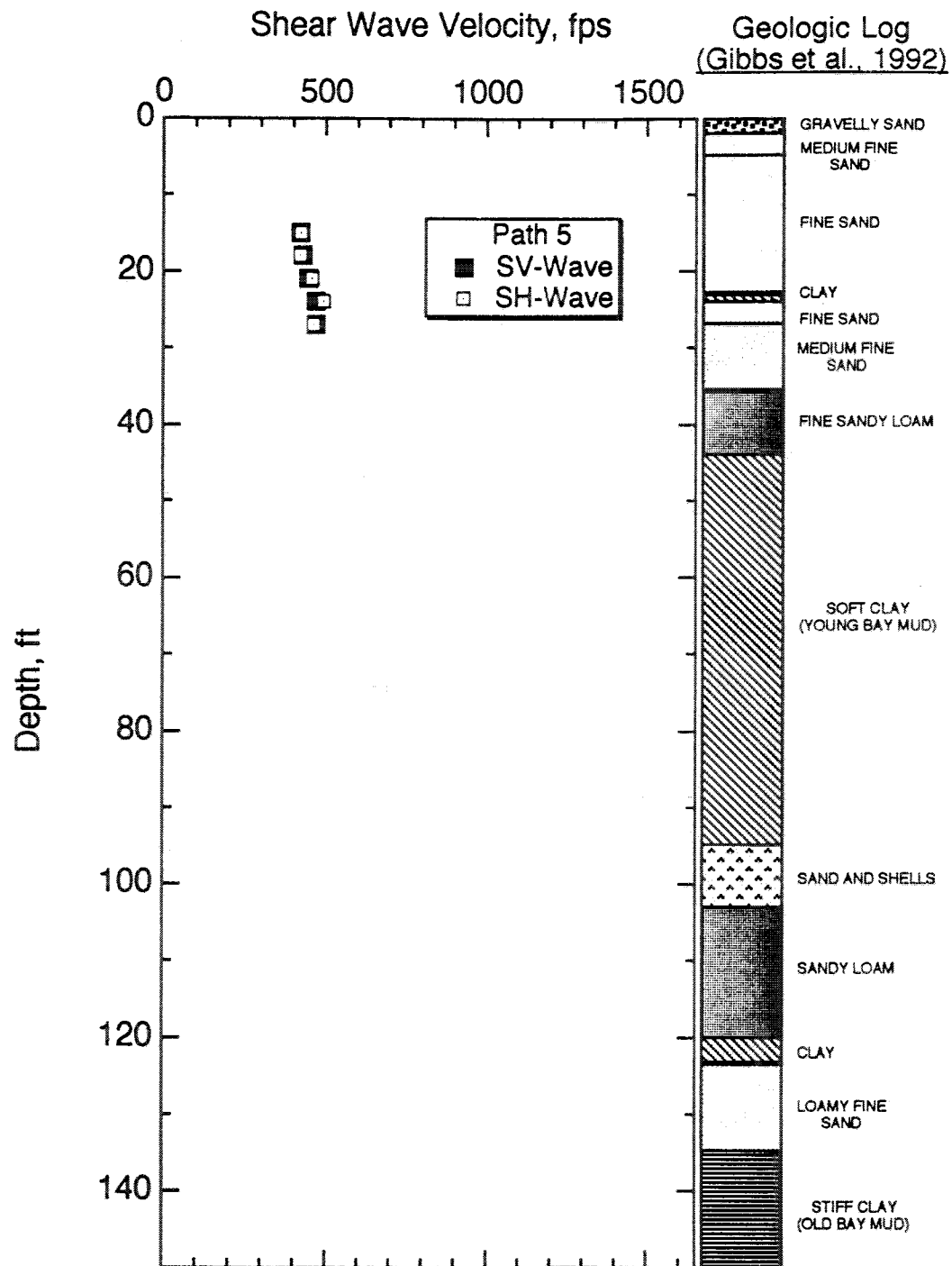


Figure 8.A.1-63  
Comparison of SV- and SH-wave velocities measured along Path 5 at Treasure Island.

**Table 8.A.1-17**

Shear Wave Velocity Ratio (SV/SH) Measured Along Three Crosshole Paths at Treasure Island

Depth (ft)	SV/SH Path 1 <sup>a</sup>	SV/SH Path 2 <sup>b</sup>	SV/SH Path 3 <sup>c</sup>
3	0.97	0.65	0.69
6	0.99	0.87	1.07
9	0.98	1.04	0.99
12	0.94	1.03	0.95
15	0.97	1.08	1.04
18	1.00	0.97	1.04
21	1.06	1.00	1.02
24	1.03	1.06	1.00
27	0.97	1.26	1.11
30	1.04	1.05	1.04
35	1.03	1.02	1.03
38	1.09	1.00	1.02
40	1.10	1.12	1.04
42	1.03	1.04	1.05
45	1.09	1.08	1.06
50	1.14	1.12	1.00*
55	1.08	1.11	—
60	0.99	0.97	—
65	0.85	1.00	—
70	0.88	0.92	—
75	0.96	0.98	—
80	0.99	0.98	—
85	0.98	0.96	—
90	1.09	1.02	—
94	1.24	0.98	—
96	1.08	1.02	—
98	1.42	1.49	—
100	0.75	0.70	—

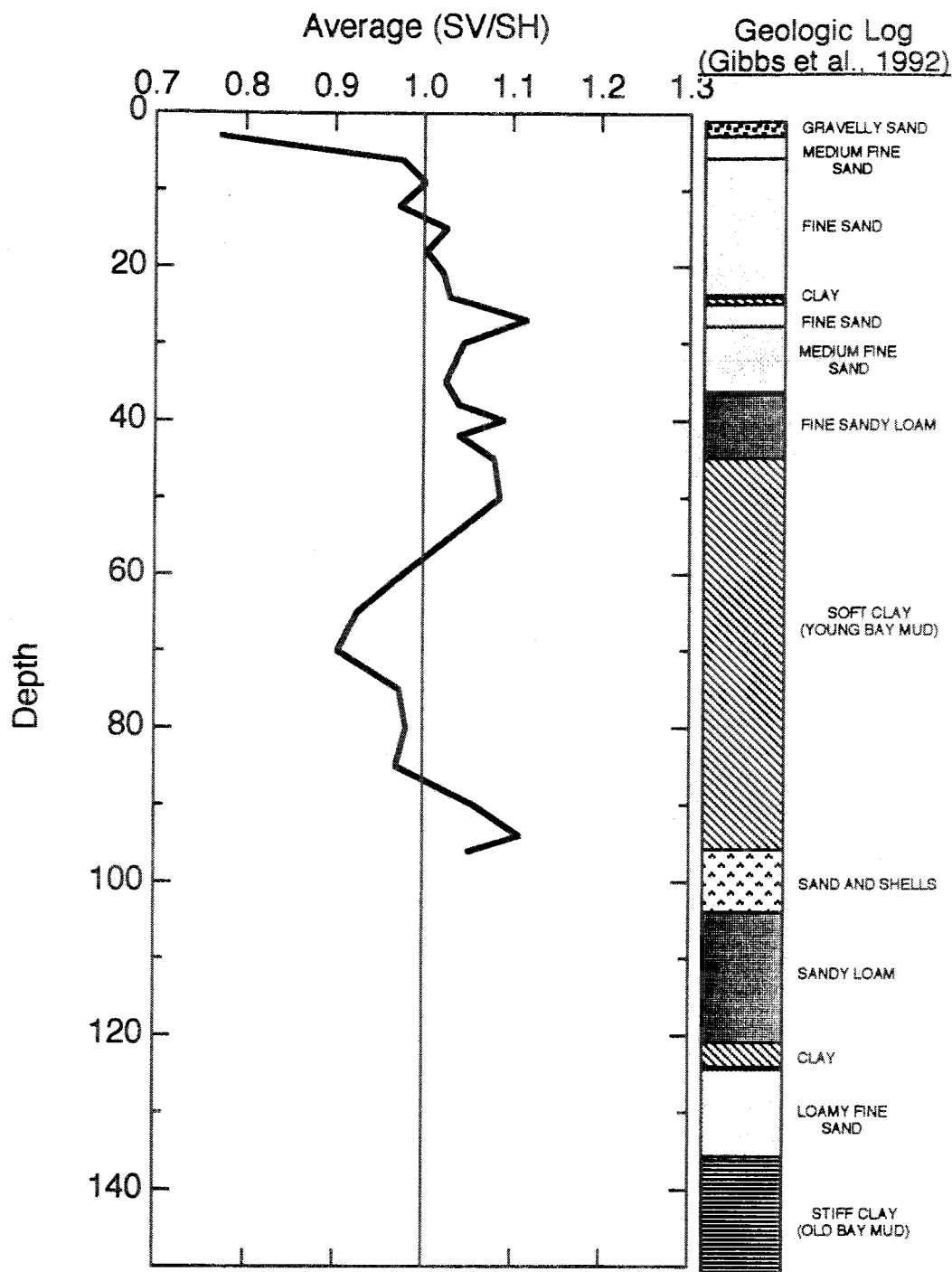
Notes on Table 8.A.1-17

a Path 1 is between B1 and B2 (see Figure 8.A.1-39)

b Path 2 is between B2 and B3 (see Figure 8.A.1-39)

c Path 3 is between B3 and B4 (see Figure 8.A.1-39)

\* Measurement performed at 49 ft



**Figure 8.A.1-64**

Average shear wave velocity ratio (SV/SH) along Paths 1, 2 and 3 at Treasure Island.

#### 8.A.1.4.5 Compression Wave Velocities

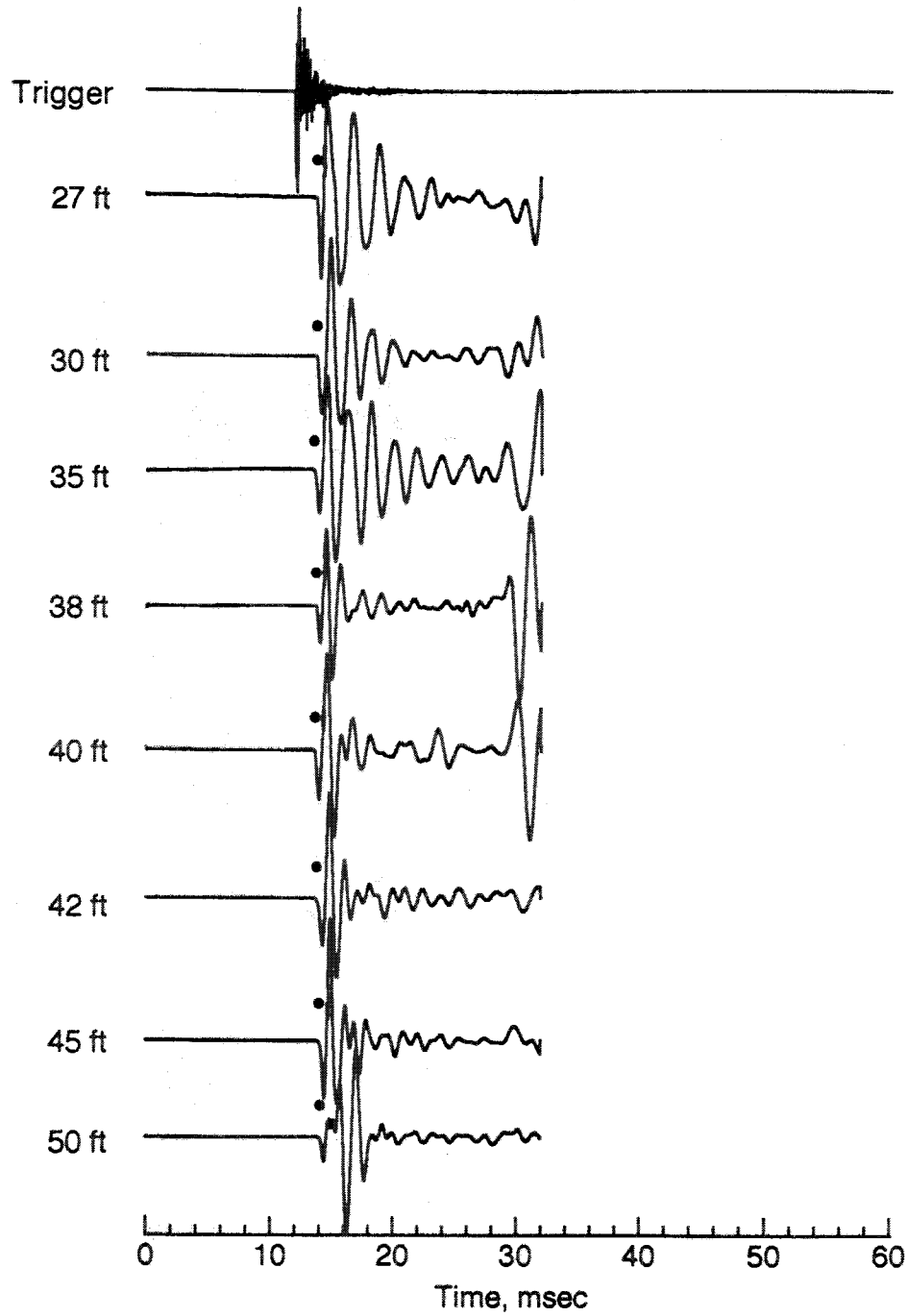
Approximately sixty direct and forty interval P-wave measurements were conducted using both the mechanical wedge and the solenoid sources at Treasure Island. Fuhrman (1993) presents all waveforms of P-waves measured using the mechanical wedge and the solenoid sources. Figure 8.A.1-65 shows typical P-wave waveforms collected at Treasure Island during direct (source-receiver) measurements using the mechanical wedge source. The top waveform in Figure 8.A.1-65, designated as the trigger, is the output from the accelerometer mounted on the source. The first abrupt departure in the trigger waveform indicates the time of impact at the source. The other waveforms, labeled by depth, are the averaged P-wave waveforms. Because the P-wave has the fastest velocity of all elastic waves, P-wave arrivals are the first departure in the waveforms. The solid dots, "•", identify the compression wave arrivals in the figures.

All direct and interval P-wave velocities measured at Treasure Island using the mechanical wedge source are plotted versus depth in Figure 8.A.1-66. The P-wave velocities measured using the solenoid source are excluded from Figure 8.A.1-66 for simplicity since the two sources yielded similar P-wave velocity measurements, as discussed below. At most depths, P-wave velocities along Path 2 (between B1 and B2) are lower than P-wave velocities measured along the other paths. P-wave velocities at a single depth vary by a maximum of about 23% (35 ft (10.7 m)). The fastest P-wave velocity exceeds 6000 fps (1830 m/sec) and was measured at a depth of 35 ft (10.7 m). Velocities measured along Paths 3, 4 and 5 generally follow the trends set by the data from Paths 1 and 2.

The lower P-wave velocities observed along Path 2 may be due to varying degrees of saturation, although the water table was reported at 4 ft (1.2 m) (oral communication with Pedro de Alba, University of New Hampshire). Another possible reason is inaccurate wave travel path distances used in the velocity calculations.

Some changes in the P-wave velocity profile coincide with changes in the soil profile, such as where the sandy loam interfaces with the Young Bay Mud. At 70 ft (21.3 m) the P-wave velocity falls below 3000 fps (914 m/sec). Below 70 ft (21.3 m) the measured P-wave velocities are less variable, with values just above 4000 fps, which suggests that the Young Bay Mud must be slightly (perhaps 0.1%) unsaturated.

**Forward Profile Measurements (Paths 1 and 2).** Values of path length, travel time and direct (S-R1) P-wave velocity for forward profile measurements along Path 1 are presented in Table 8.A.1-48 (Appendix 8.A.1.B). The results are tabulated for measurements made using both the mechanical wedge and solenoid sources, and subjective ratings of relative data quality associated with the travel times are given in the table. Table 8.A.1-49 contains the same information for interval (R1-R2) measurements along Path 2.



**Figure 8.A.1-65**

Examples of P-wave travel time records collected at Treasure Island using the mechanical wedge source in B3 and a three-component velocity transducer in B2 (S-R1, forward profile); depths 27–50 ft.

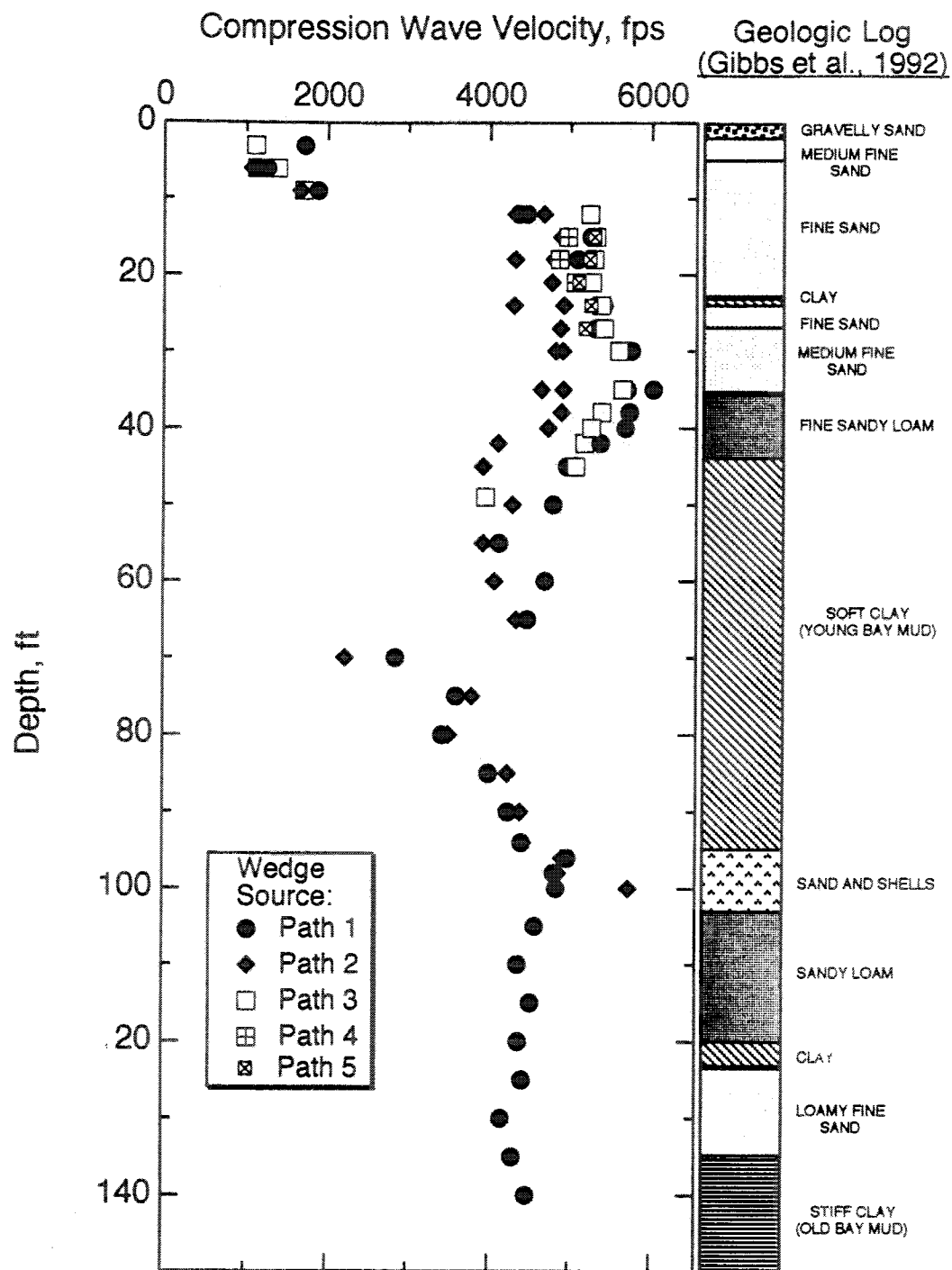


Figure 8.A.1-66

Summary of all compression wave velocities measured at Treasure Island using the mechanical wedge source.

**Reverse Profile Measurements (Paths 1 and 2).** Values of path length, travel time and direct (S-R1) P-wave velocity for reverse profile measurements along Path 2 are presented in Table 8.A.1-50; the same information for interval (R1-R2) measurements along Path 1 is tabulated in Table 8.A.1-51. Reverse profile measurements were performed in the upper 35 ft (10.7 m) at six depths.

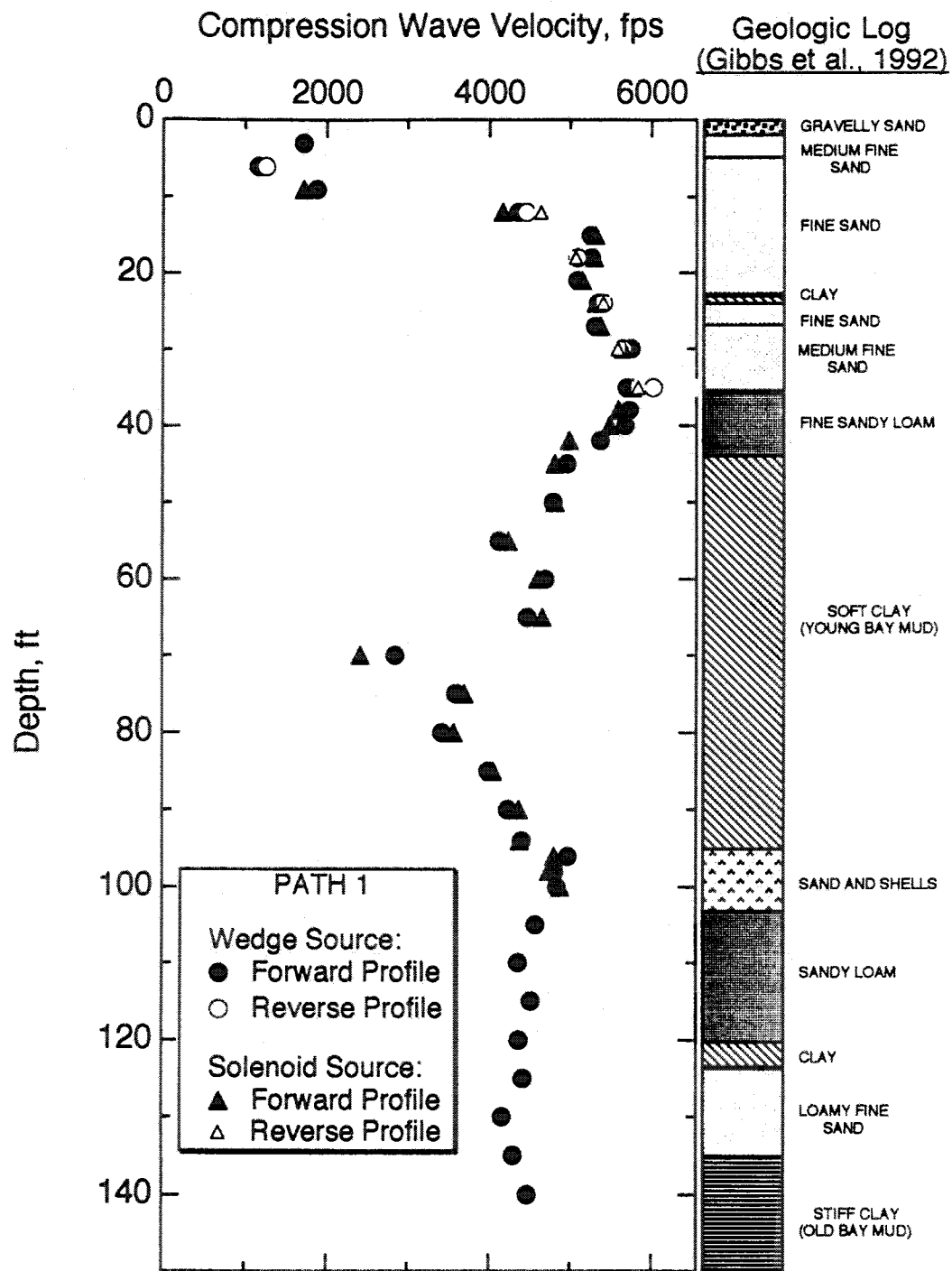
**Direct and Interval Measurements Along Paths 1 and 2.** Comparison of the direct and interval measurements along Paths 1 and 2 is useful in identifying possible equipment timing or calibration errors made during crosshole testing. Figure 8.A.1-67 compares the P-wave velocity profiles obtained from forward (direct) and reverse (interval) tests along Path 1 using both sources. Figure 8.A.1-67 shows excellent agreement between the forward and reverse tests. In addition, the mechanical wedge source and the solenoid source produced nearly identical P-wave velocities at the same depths. Because the direct and the interval tests produced nearly identical P-wave velocities, equipment triggering must have been consistent and correct for the direct tests along Path 1.

P-wave velocities measured along Path 2, shown in Figure 8.A.1-68, exhibit more variability between the forward and reverse directions. Refracted wave arrivals due to lateral variability in the interval (forward) tests may contribute to the differences in wave velocity from the forward and reverse tests. Slightly faster P-wave were determined with the solenoid source than with the mechanical wedge source. The greatest differences in P-wave velocities between the two sources occurs for measurements above about 40 ft (12.2 m). Below this depth, the P-waves measured using the solenoid source average about 5% higher than the P-waves measured using the mechanical wedge source. This difference may be due to an unaccountable trigger error of about 0.1 msec.

**"North-South" Profile Measurements.** Values of path length, travel time and direct (S-R1) P-wave velocity measurements along Path 3 (between boreholes B1 and B4) are presented in Table 8.A.1-52. The results are tabulated from measurements made using both sources, and subjective ratings of relative data quality are associated with the travel times. Measurements along Path 3 were conducted to a final depth of 49 ft (14.9 m). Table 8.A.1-53 lists all pertinent information for interval (R1-R2) P-wave computations along Path 4 (between boreholes B4 and B5). P-waves were measured along Path 4 to a depth of 21 ft (6.4 m). The P-wave velocities from tests along Paths 3 and 4 are shown in Figure 8.A.1-66.

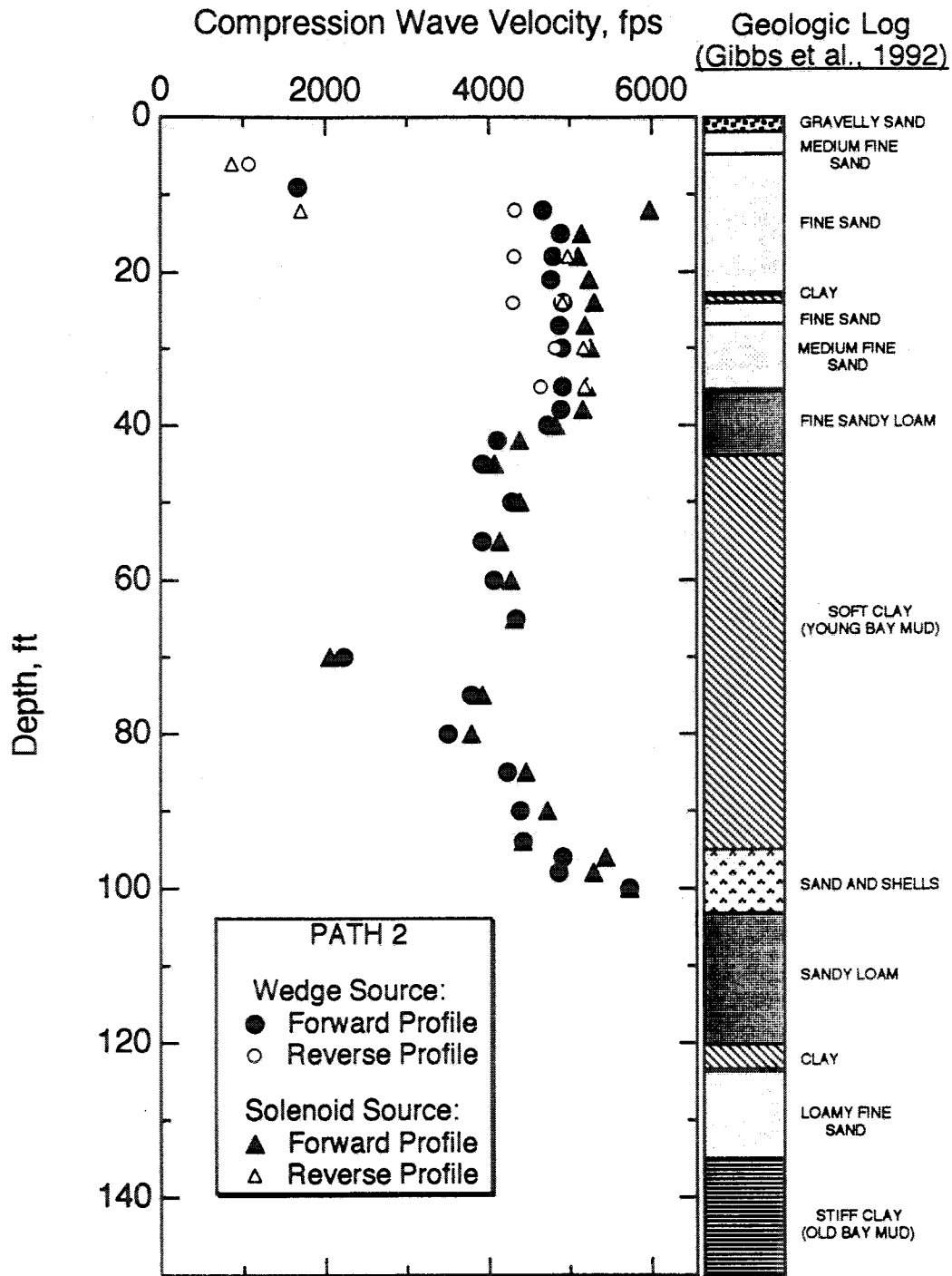
Figure 8.A.1-66 shows P-wave velocities along Paths 3 and 4 at around 5000 fps (1500 m/sec) between the depths 10 ft and 42 ft (3.0 m and 12.8 m), which is typical for P-waves traveling through a saturated soil. In the Young Bay Mud (below 42 ft, or 12.8 m), the P-wave velocity decreases to about 4000 fps (1200 m/sec), suggesting a region that is partially saturated. P-wave velocity profiles along Paths 1 and 2 (Figures 8.A.1-67 and 8.A.1-68) exhibit this same decrease in P-wave velocity at the boundary between the sand and the Young Bay Mud. The data along Path 4, while limited, show P-wave velocities similar to those measured along Path 3 to a depth of 21 ft (6.4 m), and essentially identical velocities were measured with both sources at a given depth.





**Figure 8.A.1-67**

Comparison of compression wave velocities measured in the forward and reverse directions along Path 1 at Treasure Island.



**Figure 8.A.1-68**

Comparison of compression wave velocities measured in the forward and reverse directions along Path 2 at Treasure Island.

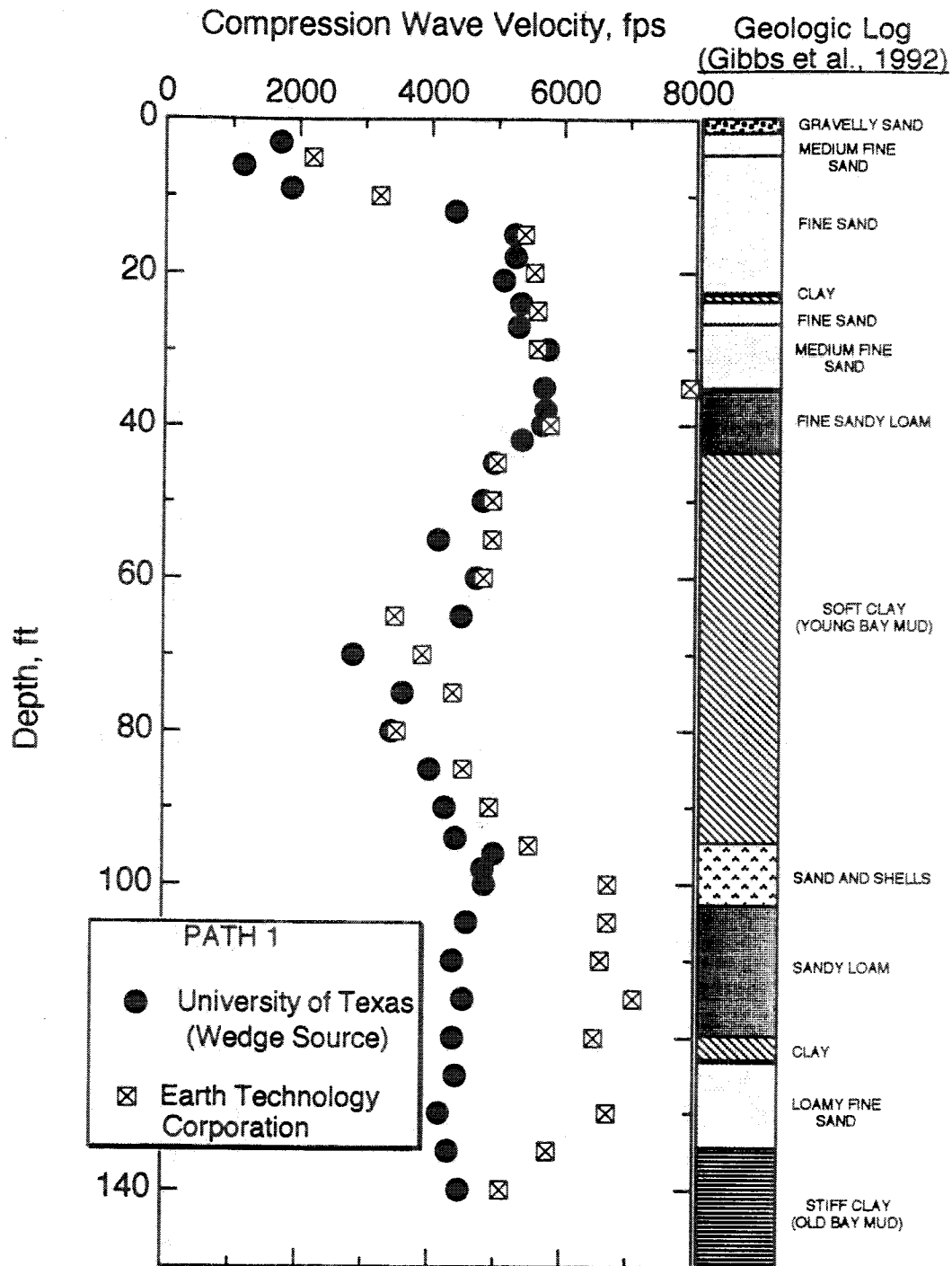
**Path 5 Measurements.** Values of path length, travel time and direct (S-R1) P-wave velocity for measurements along Path 5 (between boreholes B2 and B4) are presented in Table 8.A.1-54. The results are tabulated from measurements made using only the mechanical wedge source. The relative data quality at each measurement depth was high. The P-wave velocity profile along Path 5 is plotted in Figure 8.A.1-66. The data along Path 5 is very limited, but it also confirms that the P-wave velocity between the depths 15 ft and 27 ft (4.6 m and 8.2 m) is about 5000 fps (1500 m/sec), indicating that the soil is saturated.

**Comparisons With Earth Technology Measurements.** It is useful to compare the P-wave velocity profile measured from this work with that measured by personnel from the Earth Technology Corporation. Figure 8.A.1-69 compares the P-wave velocity profiles obtained by both groups along Path 1 (boreholes B3-B2), and Figure 8.A.1-70 compares the results along Path 2 (boreholes B2-B1).

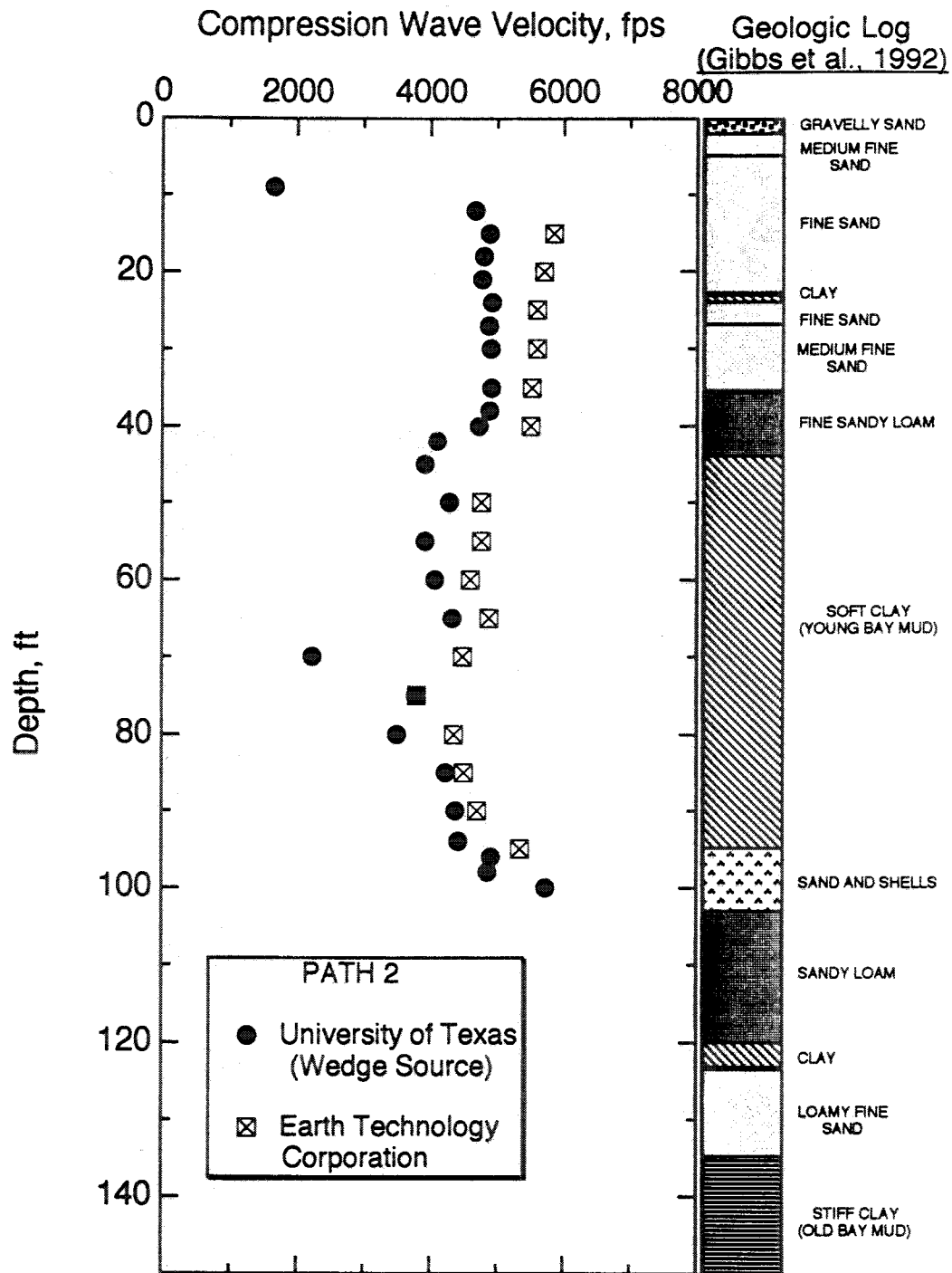
Along Path 1 (see Figure 8.A.1-69), the two data sets match quite well (except at 35 ft or 10.7 m) to a depth of about 100 ft (30.5 m). Below 80 ft (24.3 m), the University of Texas data show a fairly uniform profile of between 4000 fps and 5000 fps (1200 m/sec and 1500 m/sec), while the Earth Technology data show velocities steadily increasing to above 7000 fps (>2100 m/sec) at 115 ft (35 m) and then steadily decreasing to around 5000 fps (1500 m/sec) at 140 ft (42.7 m). At 35 ft (10.7 m) the Earth Technology P-wave velocity is about 30% higher than that measured by the University of Texas; between depths of 100 ft and 140 ft (30.5 m and 42.7 m) the Earth Technology P-wave velocity is as much as 62% higher than the University of Texas P-wave velocity (at 130 ft (39.6 m)). It should be noted that the SV-wave velocities measured by the two groups are in close agreement over this depth range.

Similar comparisons along Path 2 (Figure 8.A.1-70) also show different P-wave velocity profiles. Although the two data sets show tendencies to vary similarly at certain depths, the velocity profiles are rather different; the Earth Technology profile is generally higher (in terms of P-wave velocity) than the profile measured by the University of Texas group.

Since compression wave velocity is rather fast (for soils) in this predominately saturated material, travel times were short, and the resulting compression wave velocities are sensitive to errors in path length, equipment calibration, time-zero measurements and different methods of identifying the initial wave arrival. The P-wave velocity profiles from the two investigative groups (University of Texas and Earth Technology) match at some places but differ significantly at other depths.



**Figure 8.A.1-69**  
Comparison of compression wave velocities measured by The University of Texas and the Earth Technology Corporation along Path 1 at Treasure Island.



**Figure 8.A.1-70**  
Comparison of compression wave velocities measured by The University of Texas and the Earth Technology Corporation along Path 2 at Treasure Island.

#### 8.A.1.4.6 Summary and Conclusions

Crosshole seismic tests were performed at the Treasure Island Fire Station site to measure compression and shear (SV and SH) wave velocities. The mechanical wedge source was used to generate SV-waves, and the solenoid source was used to generate SH-waves. Both sources were used to generate P-waves, and their results are compared herein. The P-wave velocities measured using the two sources matched well. Below the water table the P-wave velocities ranged from about 2000 fps to over 6000 fps (600 m/sec to 1800 m/sec), indicating that at some depths the soil was not completely saturated.

The sandy soil at Treasure Island is generally soft in terms of shear wave velocity. The Young Bay Mud, however, seems to be normally- to over-consolidated in terms of shear wave velocity. Shear wave measurements indicate higher stiffness in the horizontal direction than in the vertical direction at depths between 70 ft and 75 ft (21.3 m and 23 m) and at about 100 ft (30.5 m). Both SV- and SH-waves exhibited some variation in velocity with depth, and these variations are reflected in the results of two cone penetration soundings. The SASW method produced a velocity profile similar to that from the crosshole testing. Changes in the S-wave velocity profile often occurred at changes in the soil profile. Shear wave velocities were measured in the laboratory using the torsional resonant column device at the University of Texas, and the laboratory values of  $V_s$  were about 18% lower than the SV-wave velocities measured in the field. The shear wave velocities from forward and reverse-profile tests agreed well. P-wave velocities were more variable, particularly along Path 2.

The results of crosshole testing performed by the University of Texas group were compared with results reported by the Earth Technology Corporation. The calculated travel path lengths measured by the two organizations varied by as much as 18 percent. When the distances reported by the Earth Technology Corp. were combined with the wave travel times measured in this study by the University of Texas, the shear wave velocity measurements of the two groups were generally in fair agreement (usually within about 10%), but at some depths variations in compression wave velocity measurements were significant (up to 62%). These differences in crosshole measurements underscore the importance of careful and consistent field procedures in crosshole measurements. More careful attention to detail by one or both investigative groups would have produced closer agreement in seismic wave velocity between the two groups.

## 5—MATERIAL DAMPING MEASUREMENTS AT GILROY 2

### 8.A.1.5.1 Introduction

The spectral ratio and the spectral slope methods discussed in Section 8.A.1.2.5 were applied to evaluate material damping in shear at depths of 15, 25, 115 and 125 ft (4.6, 7.6, 35.1 and 38.1 m) at Gilroy 2 using SV-wave records collected during the crosshole tests. The borehole arrangements for the crosshole tests at Gilroy 2 are shown in Figure 8.A.1-10. Attenuation in shear is typically of most interest in geotechnical engineering practice; therefore, SV-wave records were used in the damping analyses in this study. The analyses that follow, however, are also applicable to attenuation studies using SH- and P-waves.

A discussion of the material damping analyses at the 15-ft (4.6-m) depth follows to illustrate the procedures. The results discussed in this section are presented in terms of a combination of tests in the forward and reverse directions as represented by Eqs. (2.15), (2.16) and (2.23). Finally, the results of all material damping analyses from the in situ measurements are compared with laboratory results of material damping determined using intact samples and torsional testing.

### 8.A.1.5.2 Time-Domain Windowing of Waveforms

All waveforms recorded in the crosshole tests included various complications in the actual amplitude spectra of the SV-waves. These complications include reflected and refracted waves and borehole and receiver effects (see Section 8.A.1.2.5). To reduce the effects of wave interference, the measured SV-wave was gated, or windowed, from the waveform with an extended cosine bell window,  $W(t)$  (Ramirez, 1985). This window is illustrated in Figure 8.A.1-71 and is defined as a function of time below:

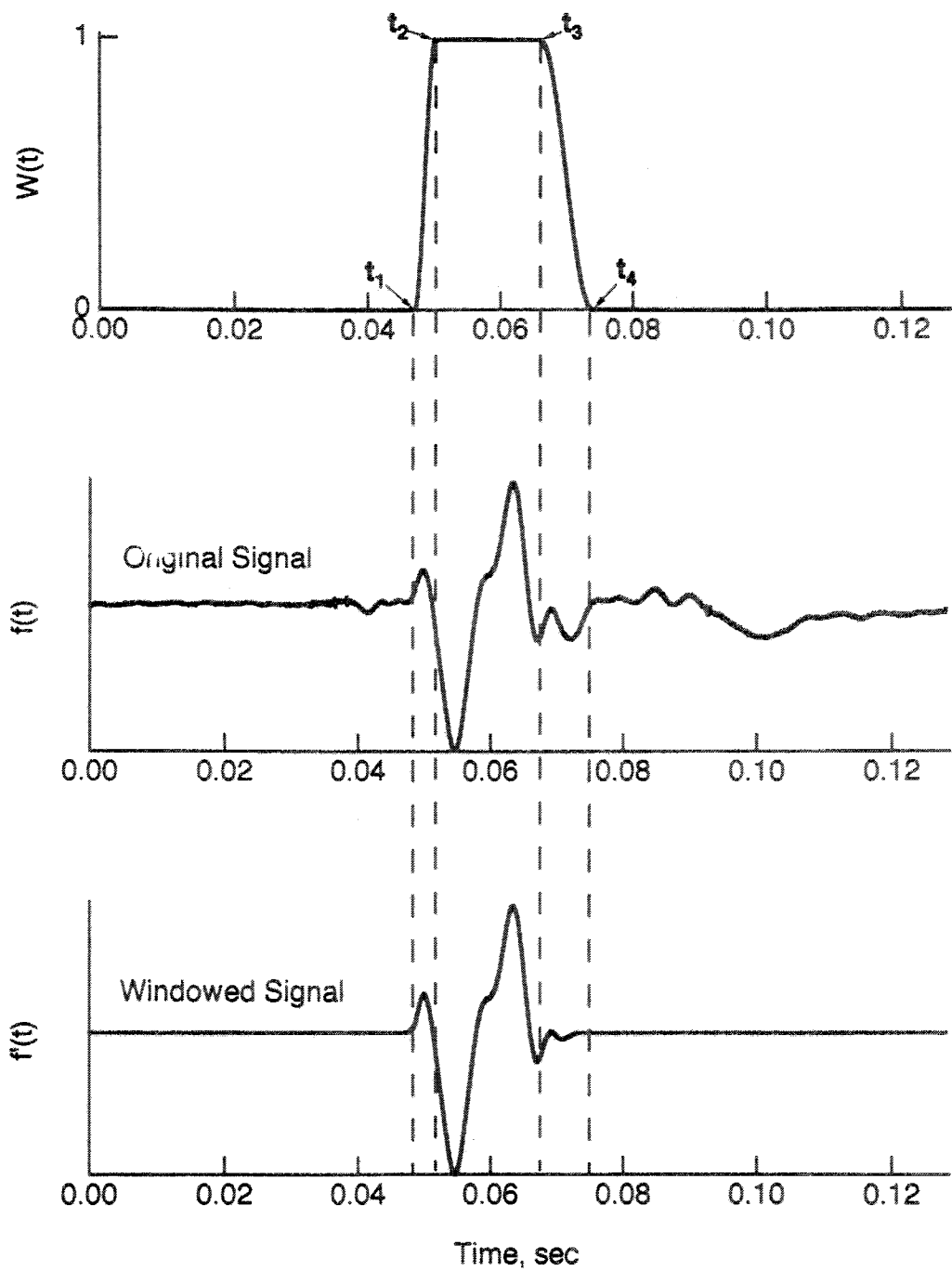
$$W(t) = \begin{cases} 0, & \text{for } 0 \leq t < t_1 \\ \frac{1}{2} \left[ 1 - \cos \frac{\pi(t - t_1)}{t_2 - t_1} \right], & \text{for } t_1 \leq t < t_2 \\ 1, & \text{for } t_2 \leq t < t_3 \\ \frac{1}{2} \left[ 1 - \cos \frac{\pi(t - t_3)}{t_4 - t_3} \right], & \text{for } t_3 \leq t < t_4 \\ 0, & \text{for } t \geq t_4 \end{cases} \quad (5.1)$$

where  $t_2$  is at the arrival point (time) of the SV-wave recorded with Receiver 2,

$t_3$  is at the end of the first cycle of the SV-wave recorded with Receiver 2,

$t_1$  is at a point on the waveform whose distance from  $t_2$  is 20% of the distance between  $t_2$  and  $t_3$ ,  
and

$t_4$  is at a point on the waveform whose distance from  $t_3$  is 50% of the distance between  $t_2$  and  $t_3$ .



**Figure 8.A.1-71**  
 Use of an extended cosine bell window to gate original signal; SV-wave measured at 15 ft depth, Receiver 2 (after Mok, 1987).



If the original waveform is represented by  $f(t)$ , the windowing operation is described by

$$f'(t) = W(t) \cdot f(t) \quad (5.2)$$

with  $f'(t)$  containing the windowed, or gated, waveform.

The purpose of a window function such as Eq. (5.1) is to terminate the waveform smoothly at zero, thereby minimizing the appearance of artificial frequency components in the analyses. The window size applied to the Receiver 2 waveform is also applied to the Receiver 1 waveform for consistency. The only difference is that, for Receiver 1,  $t_2$  is at the arrival time at the SV-wave recorded at Receiver 1. The Receiver 2 waveform will be more damped than the Receiver 1 waveform because the wave travels through more soil to reach Receiver 2; therefore, for all analyses, the window size is based on the Receiver 2 waveform so that at least one full cycle of waveform is used and that the gated waveforms of Receivers 1 and 2 are of equal length. Additionally, the same window size is applied to waveform sets from both the forward and reverse test directions.

**Short Time Window.** An extended cosine bell window applied to a waveform using the parameters  $t_1$ ,  $t_2$ ,  $t_3$  and  $t_4$  as defined above (using one cycle of the second receiver waveform) is hereafter called a short time window. Although a waveform gated with the short time window will contain less reflected and refracted energy than an un-gated waveform, the amplitude spectrum of a gated waveform will probably still contain some waveform interference.

**Long Time Window.** To study the sensitivity of the material damping analyses to window size, a longer time window was also applied to the waveforms. This long time window is created by lengthening the distance between  $t_2$  and  $t_3$  as follows:

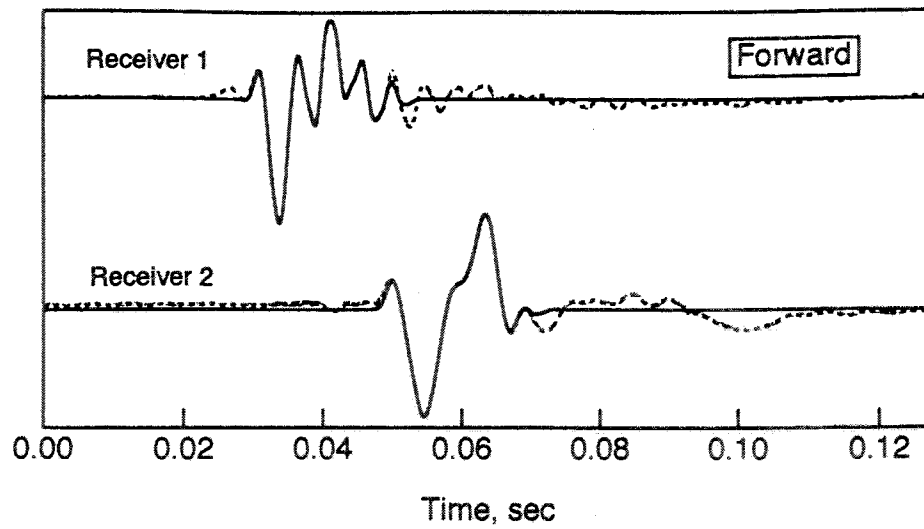
$t_2$  is at the arrival point of the SV-wave recorded with Receiver 2, and

$t_3$  is toward the end of the SV-waveform recorded with Receiver 2; this point is chosen arbitrarily.

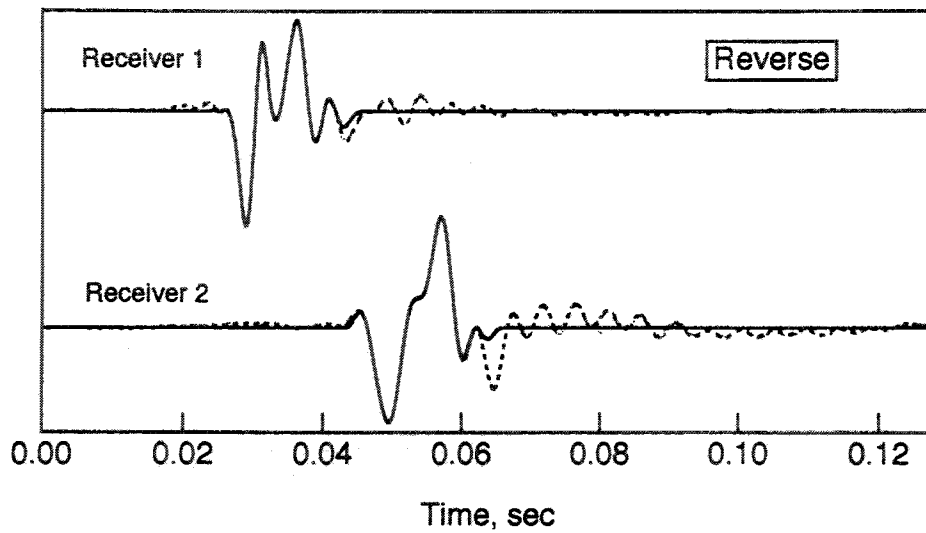
The points  $t_1$  and  $t_4$  remain defined as for the short time window. It should be noted that the long time window described above could negate much of the benefit gained by applying a window such as Eq. (5.1) since little reflected and refracted energy might be gated out of the damping analyses.

### 8.A.1.5.3 Material Damping Using the Short Time Window

Figure 8.A.1-72a shows two SV-wave time records collected at Gilroy 2 at a depth of 15 ft (4.6 m) using the forward direction shown in Figure 8.A.1-10a. The dashed lines are the original, un-windowed waveforms, and the solid lines represent the short-windowed waveforms. Figure 8.A.1-72b shows the original and the short-windowed waveforms collected from reverse-direction tests at the same depth. In this case, the time length  $t_3 - t_2 = 16$  msec. Both the spectral ratio and the spectral slope methods for material damping analyses are applied to the windowed waveforms, and a comparison of the results follows.



a) Windowed Time Records from Forward Direction



b) Windowed Time Records from Reverse Direction

**Figure 8.A.1-72**

Windowed SV-wave time records for material damping analysis at Gilroy 2 at 15 ft depth; short time window.

### 8.A.1.5.3.1 Spectral Ratio Method

Figures 8.A.1-73 and 8.A.1-74 contain the results of the damping analysis performed on the forward and reverse waveforms shown in Figure 8.A.1-72 using the spectral ratio method (Section 8.A.1.2.5.1). Figure 8.A.1-73 shows material damping, wave velocity and magnitudes of the linear spectra of the two receivers plotted versus frequency. Figure 8.A.1-74 shows the same information plotted versus wavelength. The results for material damping in Figures 8.A.1-73 and 8.A.1-74 are based on Eqs. (2.15) and (2.16), which are based on measurements from both the forward and reverse (two-direction) measurements. Four criteria influenced the selection of ranges for frequency and wavelength shown in Figures 8.A.1-73 and 8.A.1-74 as follows.

1. In crosshole tests, it is desirable to have a distance on the order of 1.5 to 2.0 wavelengths between the source and first receiver to avoid near-field effects.
2. The wavelength should not be less than about one-third of the borehole diameter.
3. The frequency range must be chosen such that the frequency response of the receiver is not exceeded.
4. The amplitudes of wave motion at both receivers (particularly at the second receiver) should have magnitudes of linear spectra above the noise floor of the equipment, which is considered to be -140 dB in these tests.

At the Gilroy 2 site, the spacing between all borings was approximately 15 ft (4.6 m); therefore, a 10-ft (3 m) wavelength was chosen to represent an upper limit for valid damping data. A lower limit for wavelength was chosen to be 2 ft (0.6 m) so as not to have a wavelength shorter than about three times the borehole diameter. The other two criteria (numbers three and four above) were automatically satisfied in this case. Therefore, the wavelength range shown in Figure 8.A.1-74 was 2 to 10 ft (0.6 and 3.0 m).

Frequency may be related to wavelength by:

$$f = \frac{v}{\lambda} \quad (5.3)$$

where  $f$  is frequency,  $v$  is wave velocity and  $\lambda$  is wavelength. The average SV-wave velocity at the 15-ft (4.6-m) depth was 706 fps (215 m/sec). By substituting values of  $v = 706$  fps (215 m/sec) and  $\lambda = 10$  and 2 ft (3.0 and 0.6 m) into Eq. (5.3), a frequency range of about 70 to 350 Hz was found. This is the frequency range shown in Figure 8.A.1-73.

Both Eq. (2.15), for a variable wave velocity analysis, and Eq. (2.16), for a constant velocity analysis, were applied to the windowed waveforms in Figure 8.A.1-72 to arrive at the two data sets for material damping shown in Figures 8.A.1-73 and 8.A.1-74. The solid circular symbols represent the values for material damping using the variable-velocity analysis (Eq. (2.15)), and the open symbols represent the damping values obtained by the constant-velocity analysis (Eq. (2.16)). Figures 8.A.1-73 and 8.A.1-74 show that the damping results are not sensitive to the analysis type (i. e., variable velocity or constant velocity). However, the wave velocities calculated from the variable-velocity analysis are somewhat lower in this analysis than the constant velocity determined by the "picks" of the initial arrivals. Figure I.1 shows the results for material damping in Figures 8.A.1-73 and 8.A.1-74 compared with the one-direction solutions. For the analyses using the waveforms shown in Figure 8.A.1-72, the average values of  $D$  obtained using one-direction solutions (using Eq. (2.11)) are close to the average values of  $D$  using the two-direction (forward and reverse) solutions (using Eq. (2.15)). The values of material damping shown in Figures 8.A.1-73 and 8.A.1-74 are highly variable and range from about 1% to about 7%, with an average of about 4%.

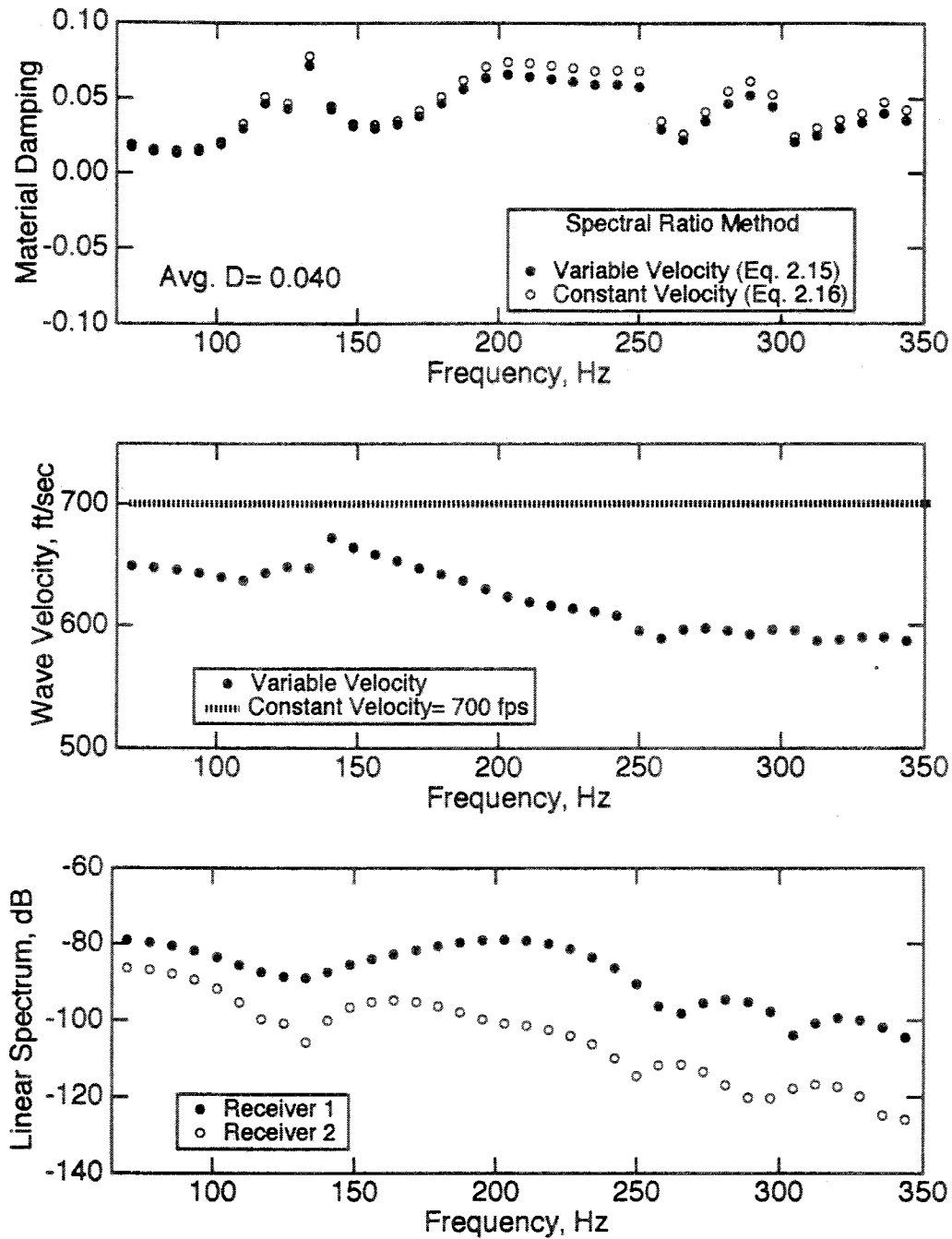


Figure 8.A.1-73

Material damping, wave velocity and linear spectra versus frequency for 15-ft depth at Gilroy 2; short time window; spectral ratio method.

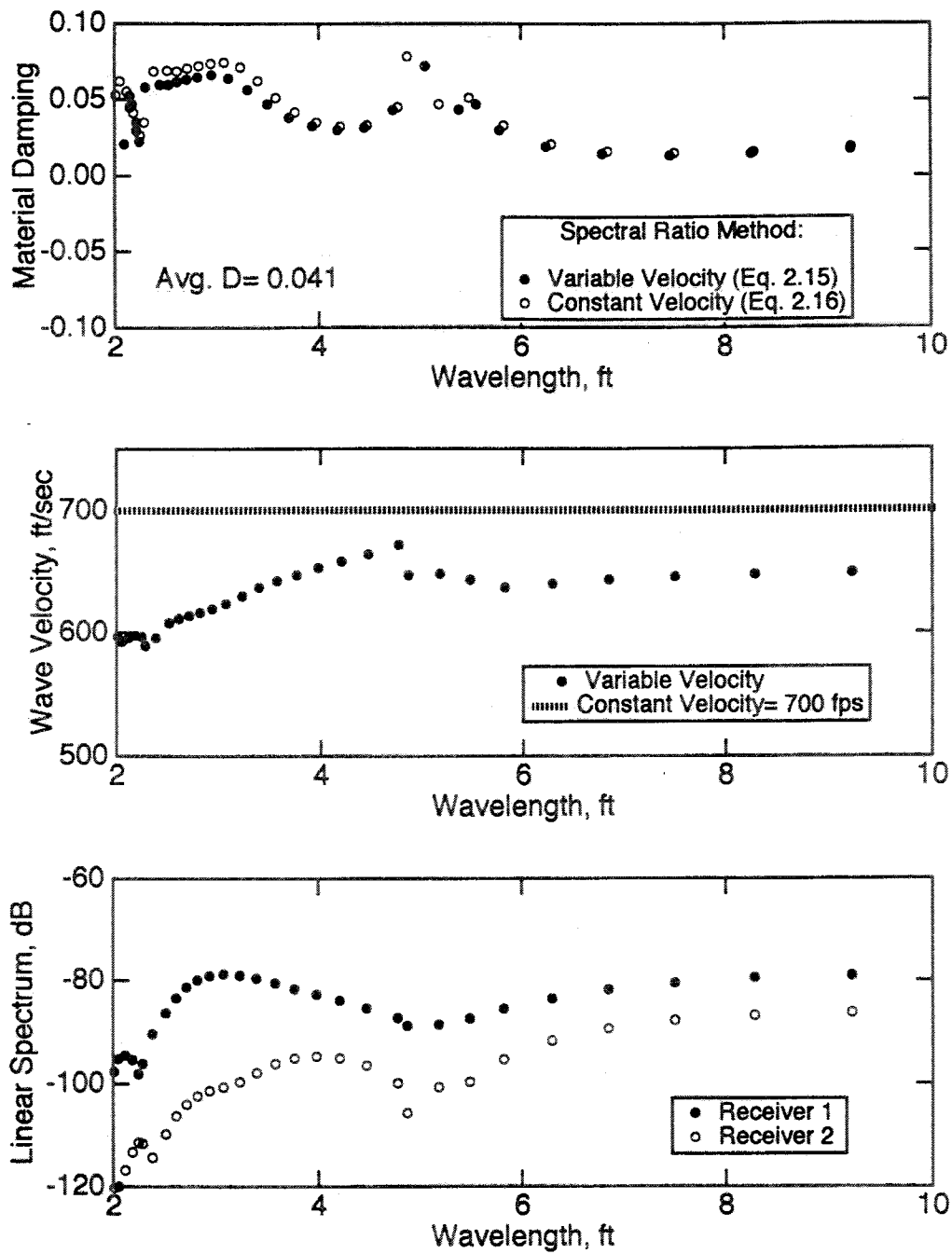


Figure 8.A.1-74

Material damping, wave velocity and linear spectra versus wavelength for 15-ft depth at Gilroy 2; short time window; spectral ratio method.

#### **8.A.1.5.3.2 Spectral Slope Method**

Figure 8.A.1-75 shows the results for material damping at the 15-ft depth using the spectral slope method (Section 8.A.1.2.5.2) using the short-windowed waveforms shown in Figure 8.A.1-72. The natural logarithm of the spectral ratio is plotted versus frequency. The frequency range shown in Figure 8.A.1-75 is the same as the frequency range shown in Figure 8.A.1-73. The results are shown in terms of analysis for the forward and reverse directions (solid circular symbols). Figure I.1 shows the results of this two-direction analysis (using Eq. 2.23) compared with the one-direction solutions for the forward and the reverse directions (using Eq. 2.22), each analyzed separately.

A linear regression analysis was performed on the data in Figure 8.A.1-75 to obtain the best-fit line through the data over the given frequency range in Figure 8.A.1-75. The slope of this line is the spectral slope used in Eq. (2.23). The combined forward and reverse data (the solid black line) yielded  $D_{fr} = 0.048$ , or 4.8% (Eq. (2.23)). Using similar procedures, Eq. (2.22) was applied to the "forward" and "reverse" data in Figure I.1, and the one-direction solutions yielded  $D = 1.7\%$  and  $7.9\%$  for the forward and reverse directions, respectively. The two-direction solution (Eq. 2.23) yielded a value of  $D$  of 4.8%, which falls between the values arrived at using the one-direction solutions (Eq. 2.22). This averaged value of material damping is slightly above the average material damping obtained using the spectral ratio method, which is  $D = 0.040$ . However, it can be seen that both methods result in about the same values of material damping.

#### **8.A.1.5.4 Material Damping Using the Long Time Window**

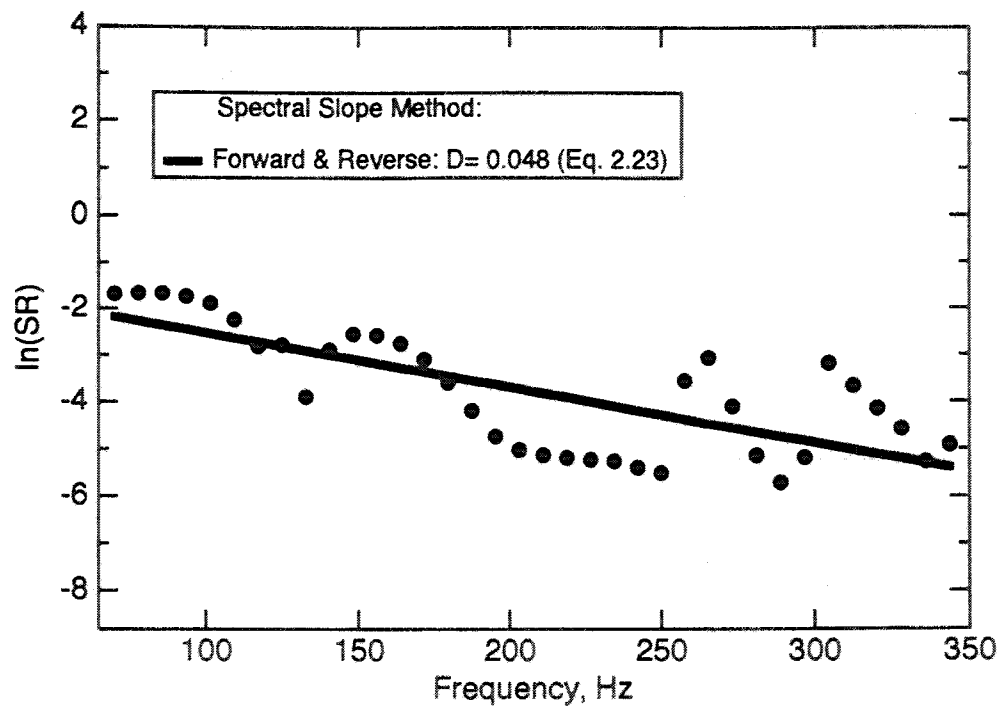
Figure 8.A.1-76 shows the long time window applied to the waveforms collected at the 15-ft (4.6-m) depth at Gilroy 2. The time windows applied to the waveforms are of equal length. In this case, the length of the time window,  $t_3 - t_2$ , is 42.3 msec. Both the spectral ratio and the spectral slope methods for material damping analysis are applied to the windowed waveforms, and a comparison of the results follows.

##### **8.A.1.5.4.1 Spectral Ratio Method**

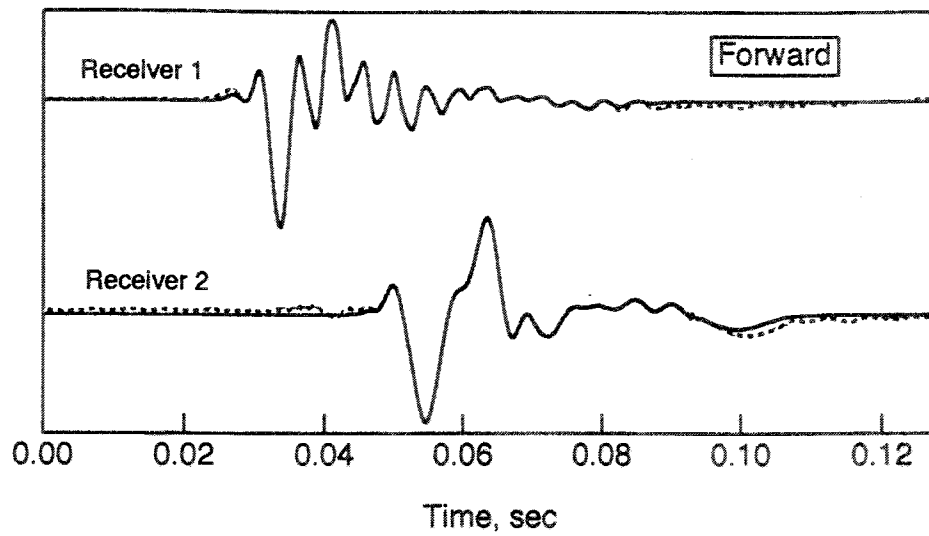
Figures 8.A.1-77 and 8.A.1-78 show the values of material damping, wave velocity and the linear spectra of the receivers plotted versus frequency and wavelength, respectively, for the spectral ratio method. The mean value for material damping by this method turns out to be  $D \approx 0.045$ , or 4.5% for both the variable-velocity and constant-velocity analyses. As in the case with the short time window at the 15-ft (4.6-m) depth, the wave velocity calculated by the variable-velocity analysis is lower than the velocity measured by time-domain analysis of the waveforms. In addition, the average values for material damping calculated using the short time window and the long time window are close ( $D_{\text{(short window)}} \approx 4.0\%$ , while  $D_{\text{(long window)}} \approx 4.5\%$ ).

##### **8.A.1.5.4.2 Spectral Slope Method**

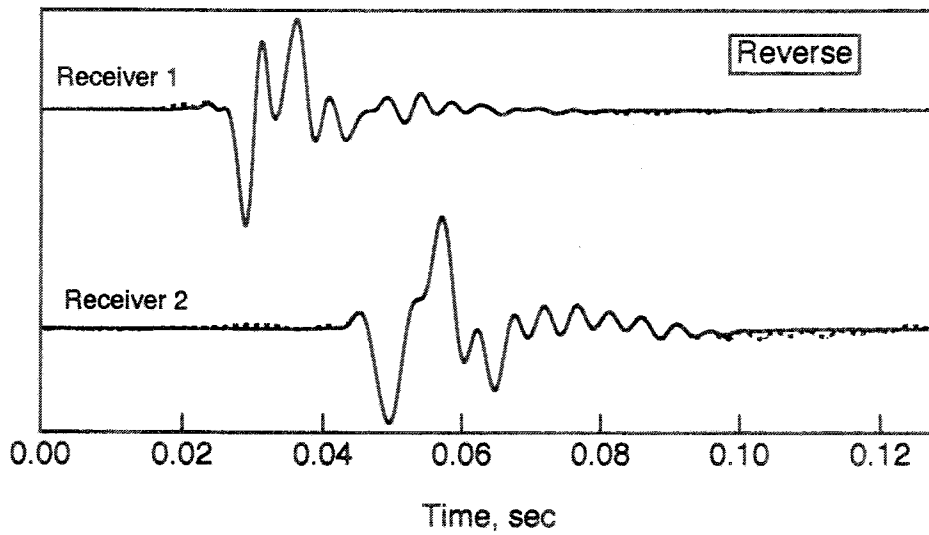
Figure 8.A.1-79 shows the results for the spectral slope method at the 15-ft depth using the long time window. The combined forward and reverse spectral slope yields a value of  $D \approx 7.3\%$ . This value is higher than the value obtained using the short time window (about 4.8%). The value for  $D$  calculated by the spectral ratio method using the long time window increased by only about 0.5% over the short-windowed results, but  $D$  by the spectral slope method increased from about 4.8% to about 7.3% with the long time window at the 15-ft (4.6-m) depth.



**Figure 8.A.1-75**  
Material damping at 15 ft depth at Gilroy 2 by spectral slope method; short time window.



a) Windowed Time Records from Forward Direction

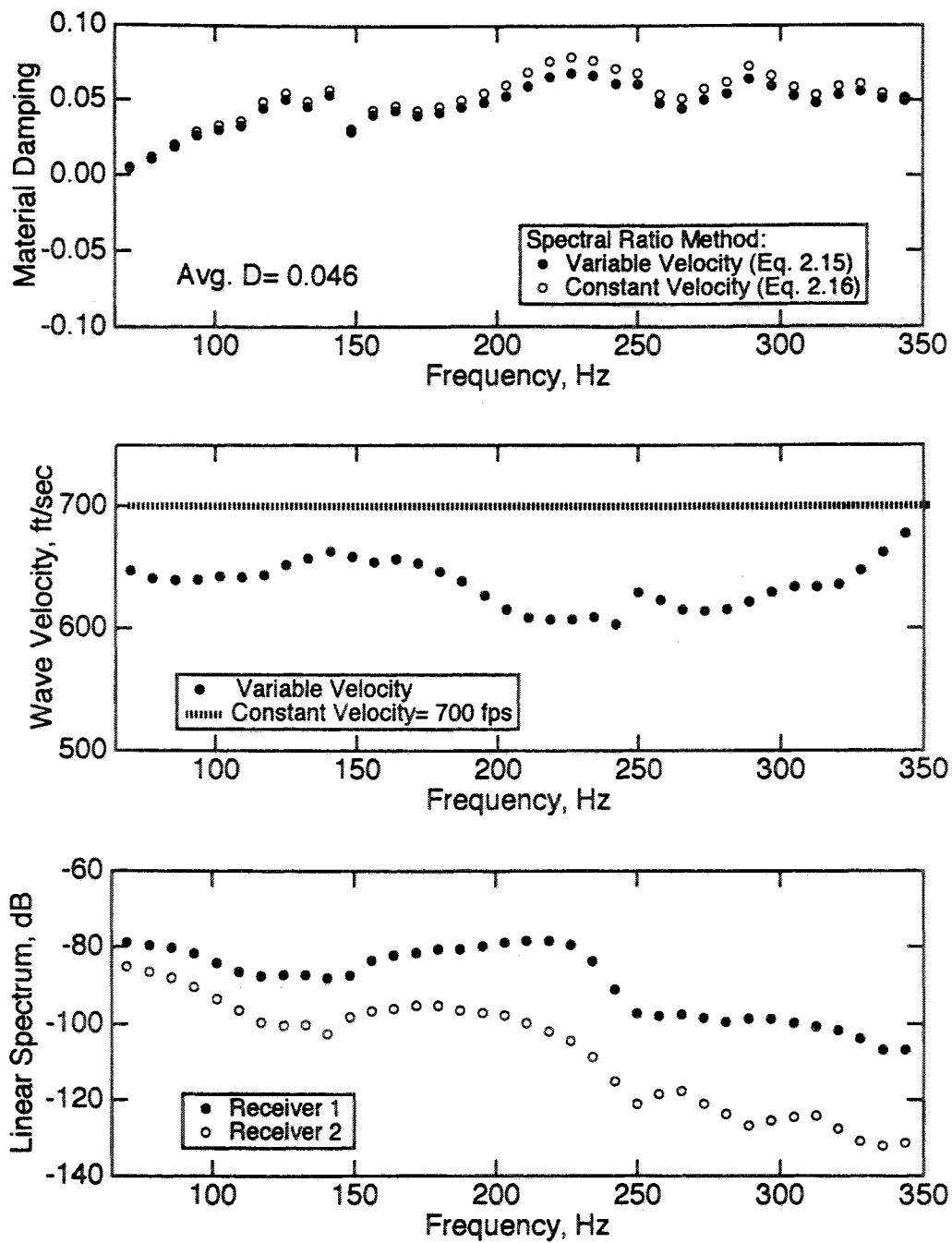


b) Windowed Time Records from Reverse Direction

**Figure 8.A.1-76**

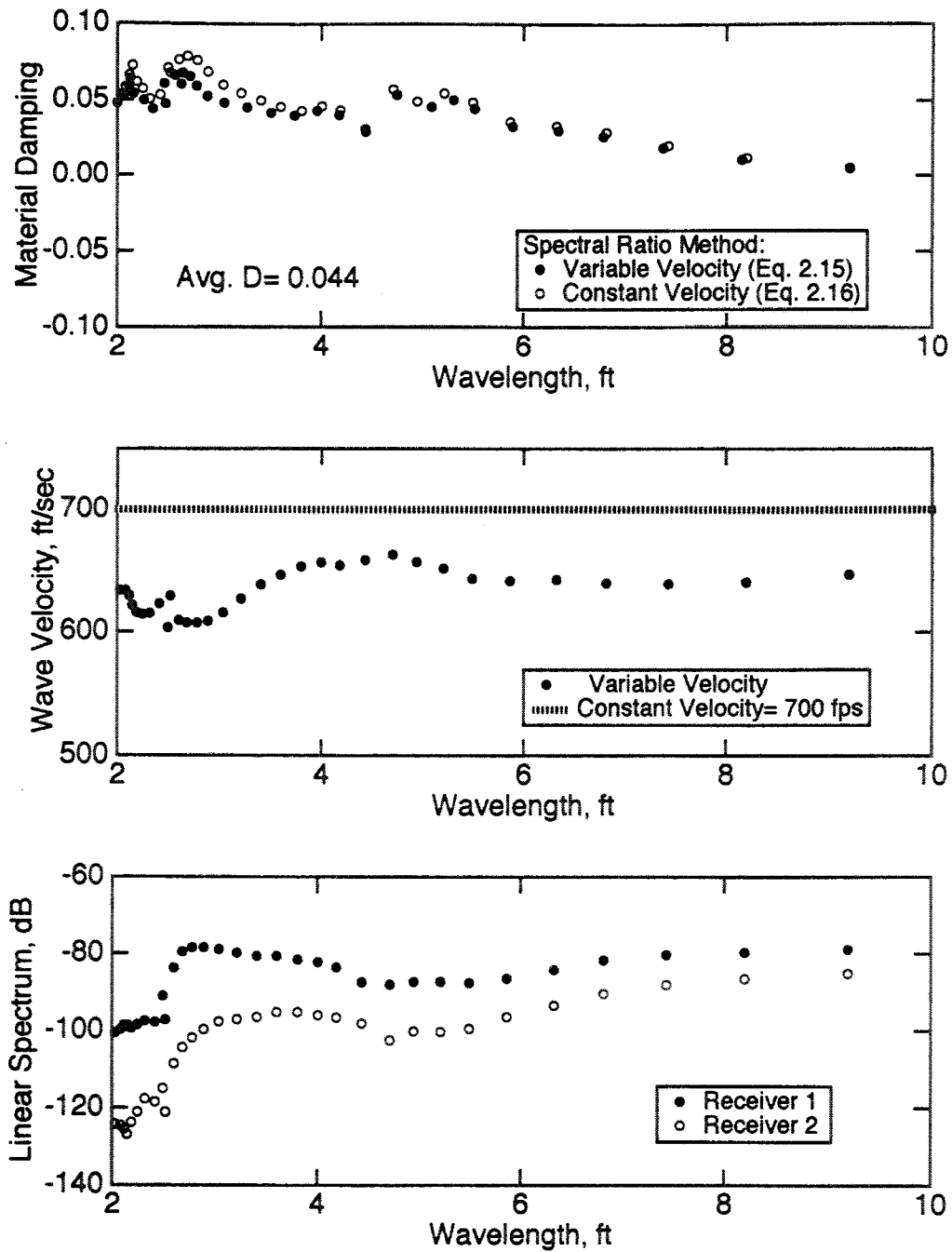
Windowed SV-wave time records for material damping analyses at Gilroy 2 at 15-ft depth; long time window.





**Figure 8.A.1-77**

Material damping, wave velocity and linear spectra versus frequency for 15-ft depth at Gilroy 2; long time window; spectral ratio method.



**Figure 8.A.1-78**

Material damping, wave velocity and linear spectra versus wavelength for 15-ft depth at Gilroy 2; long time window; spectral ratio method.

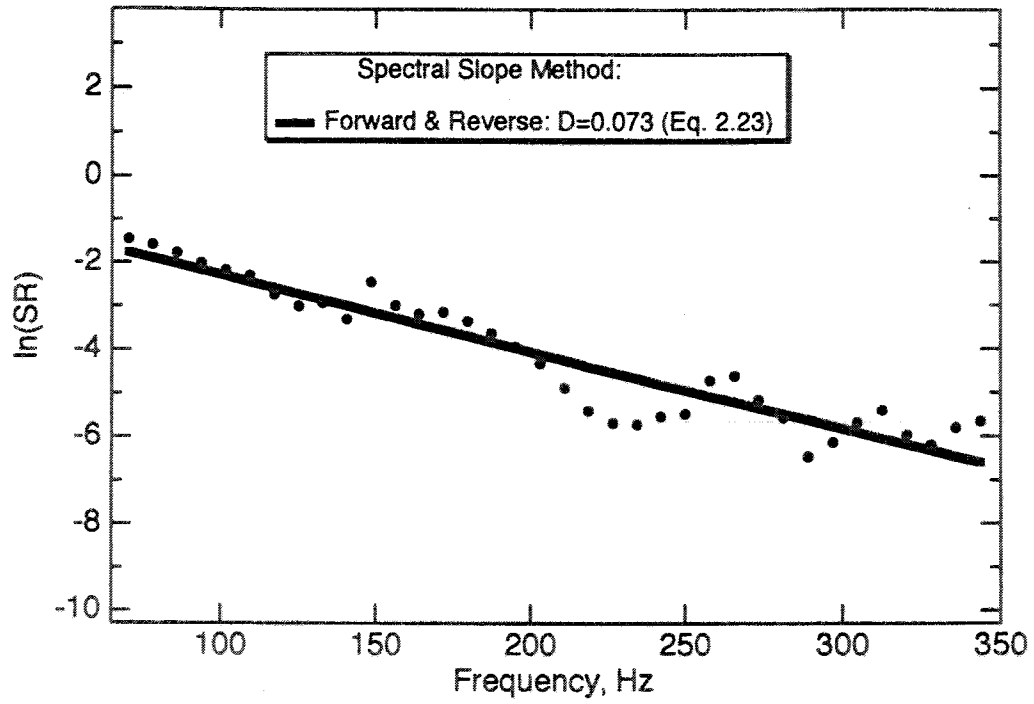
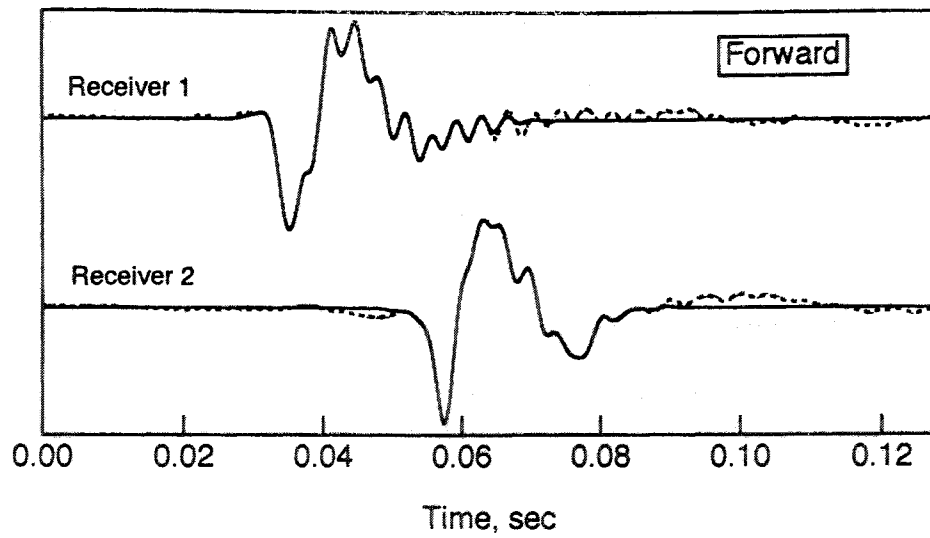


Figure 8.A.1-79  
Material damping at 15-ft depth at Gilroy 2 by spectral slope method; long time window.

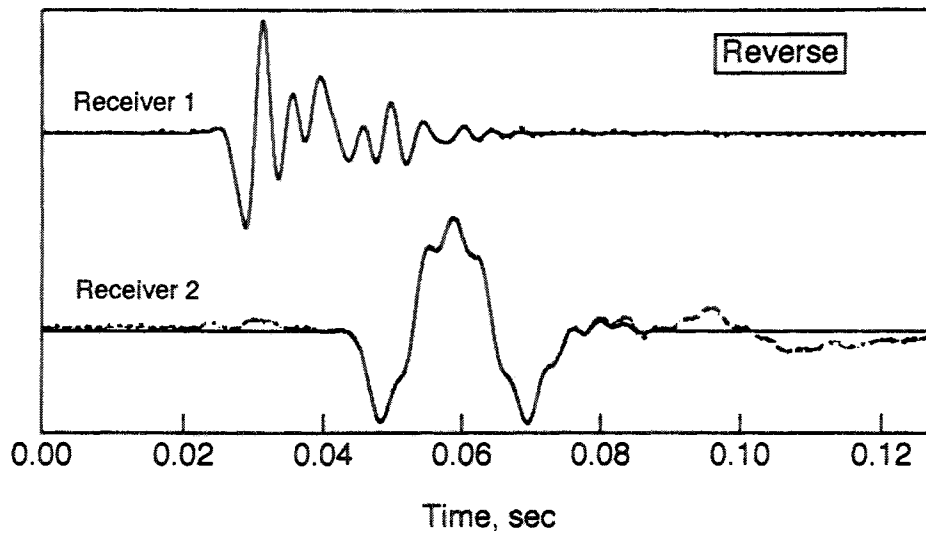
#### **8.A.1.5.5 Results of All Material Damping Analyses at Gilroy 2**

Figures 8.A.1-80 through 8.A.1-83 present the results of the material damping analyses at the 25-ft (7.6-m) depth according to the procedures and presentations described above. Due to the nature of the waveform of Receiver 2 for the 25-ft (7.6-m) depth (see Figure 8.A.1-76), short-window analyses for  $D$  were not possible. Figures 8.A.1-84 through 8.A.1-87 and Figures 8.A.1-88 through 8.A.1-91 contain the short-windowed and long-windowed results, respectively, for damping measurements at 115 ft (35.1 m). Similarly, Figures 8.A.1-92 through 8.A.1-95 and 8.A.1-96 through 8.A.1-99 present the short-windowed and long-windowed results, respectively, for measurements of  $D$  at the 125-ft (38.1-m) depth.

Average values of  $D$  from all material damping analyses are presented in Table 8.A.1-18. The method of analysis (spectral ratio or spectral slope) and the window type (short or long) used in determining each value of  $D$  is also shown, as are the lengths of each time window used in terms of  $t_3-t_2$ . Values of material damping of soil samples taken from 20-ft and 120-ft (6.1-m and 36.6-m) depths were measured in the laboratory using the torsional resonant column apparatus at the University of Texas at Austin (Hwang and Stokoe, 1992). These laboratory results are included in Table 8.A.1-18 for comparison with the field values. The laboratory values were determined at the estimated in-situ mean effective stress after being confined for one day at that stress level. The measured frequencies were 39 Hz and 92 Hz for the samples from 20 ft and 120-ft (6.1-m and 36.6-m), respectively.



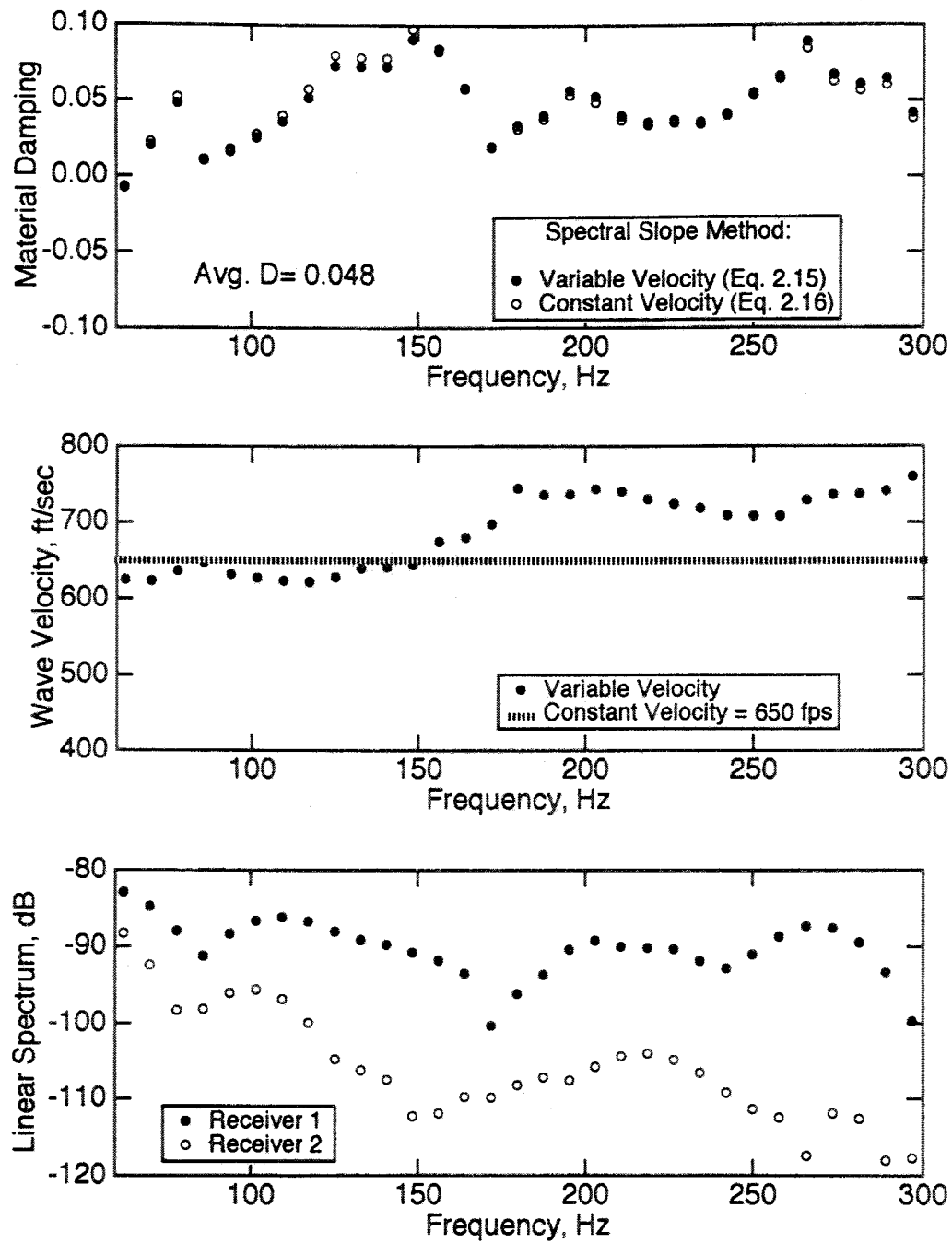
a) Windowed Time Records from Forward Direction



b) Windowed Time Records from Reverse Direction

**Figure 8.A.1-80**

Windowed SV-wave time records for material damping analyses at Gilroy 2 at 25-ft depth; long time window.



**Figure 8.A.1-81**

Material damping, wave velocity and linear spectra versus frequency for 25-ft depth at Gilroy 2; long time window; spectral ratio method.

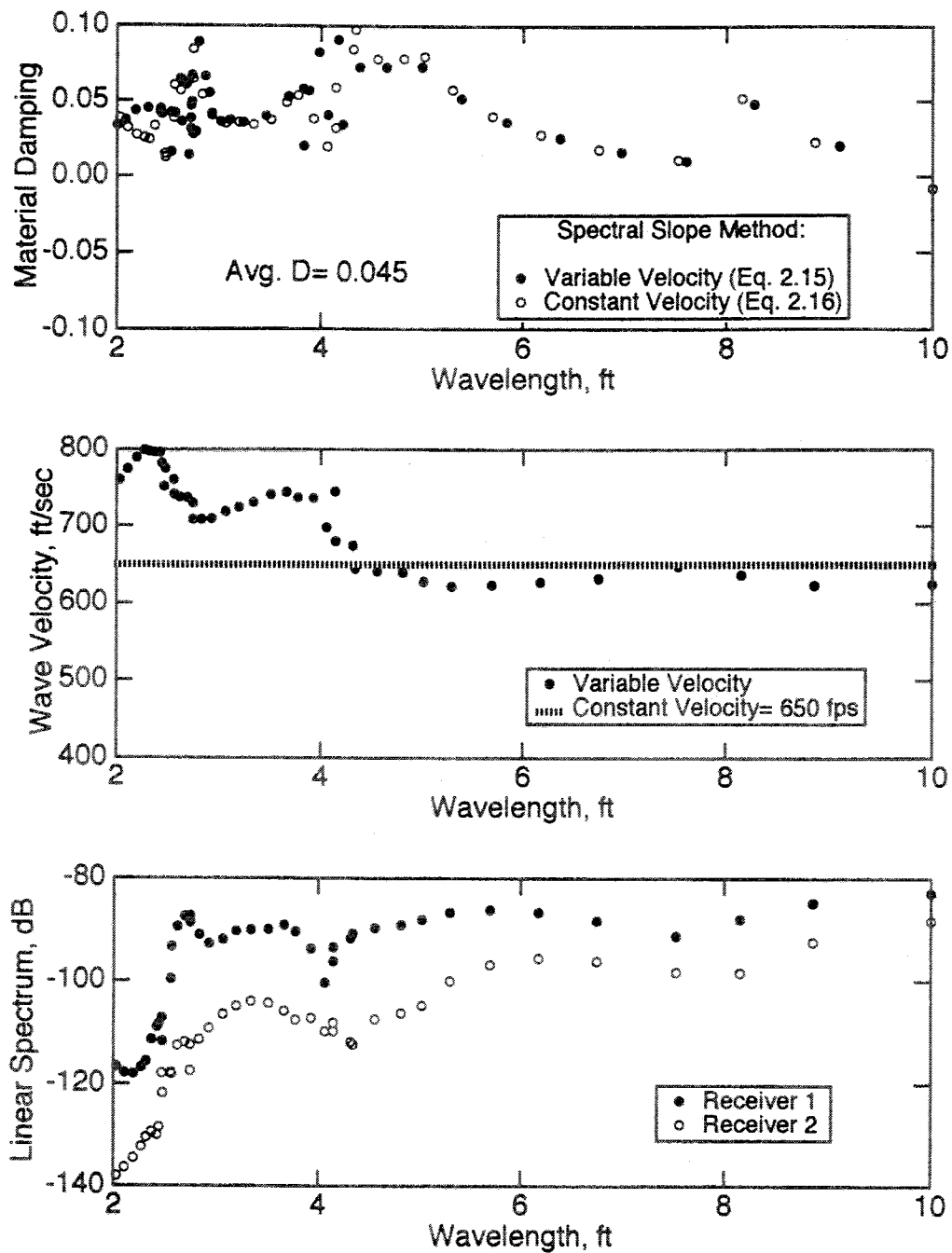
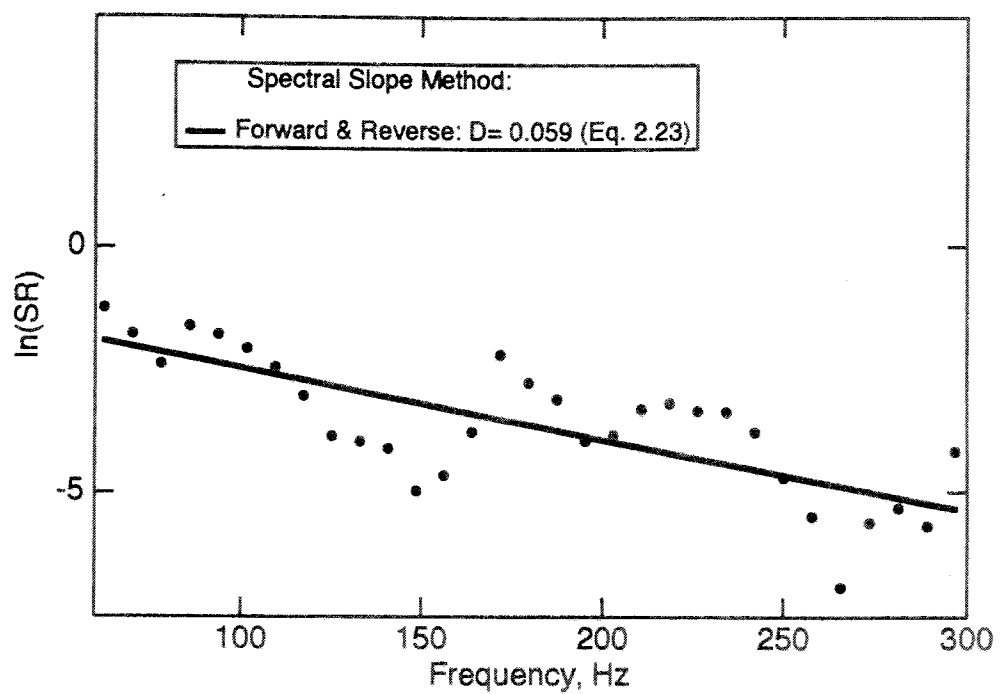
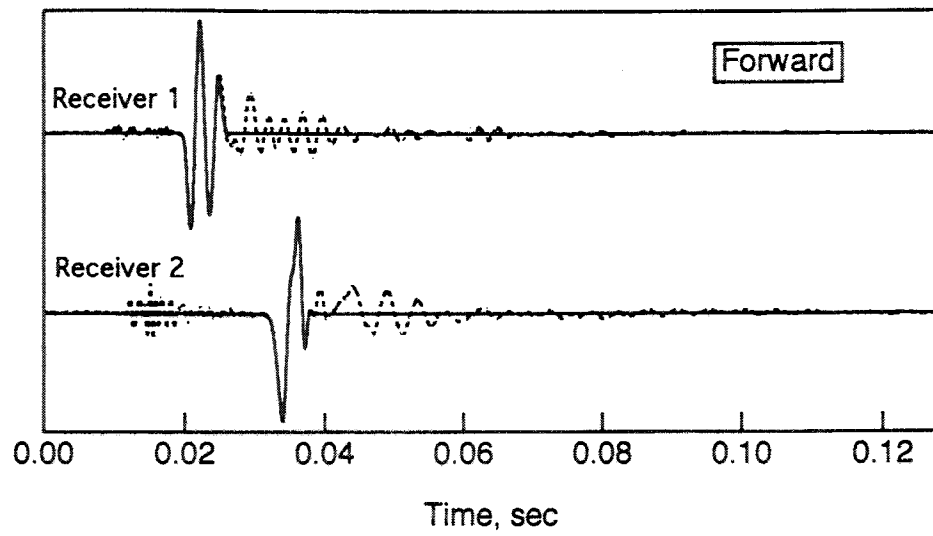


Figure 8.A.1-82  
 Material damping, wave velocity and linear spectra versus wavelength for 25-ft depth at Gilroy 2; long time window; spectral ratio method.

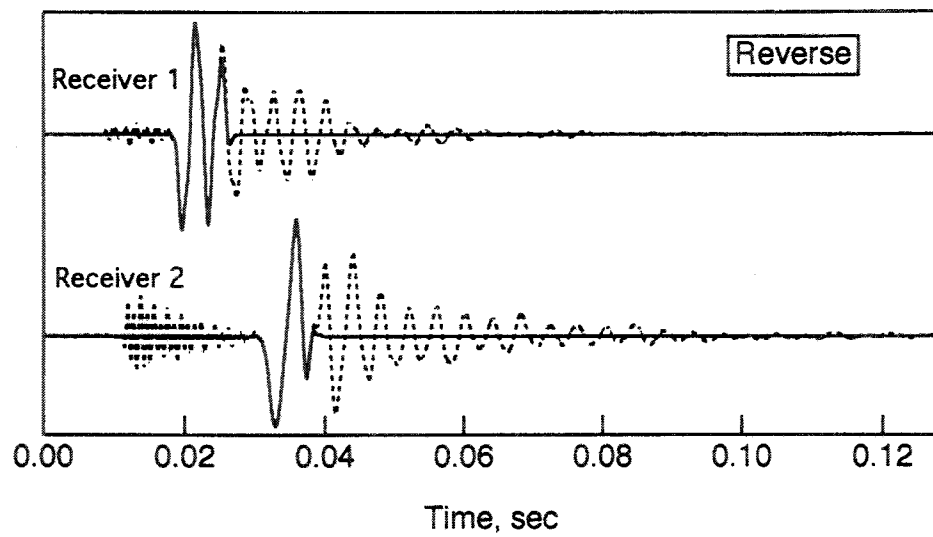


**Figure 8.A.1-83**  
Material damping at 25-ft depth at Gilroy 2 by spectral slope method; long time window.





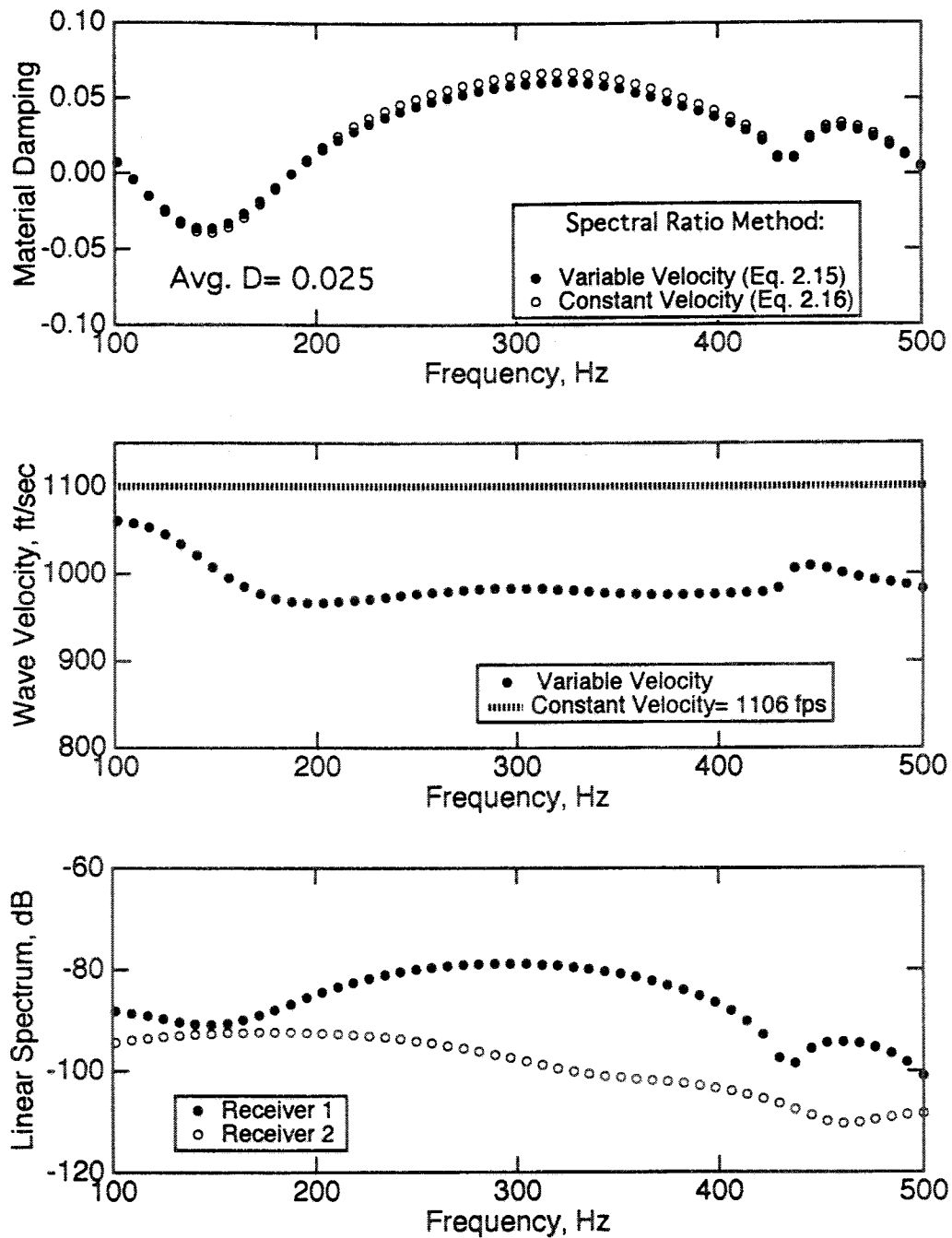
a) Windowed Time Records from Forward Direction



b) Windowed Time Records from Reverse Direction

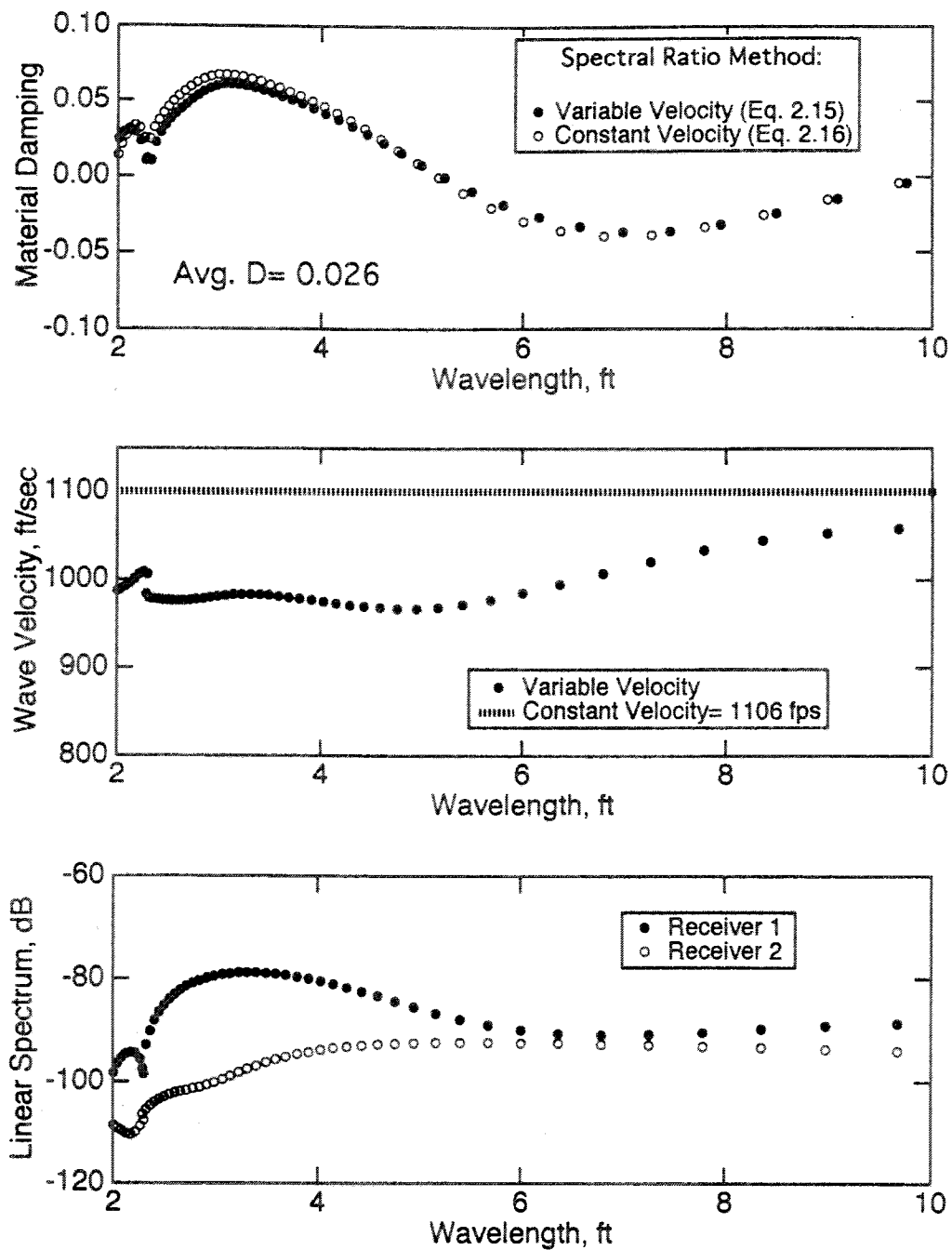
**Figure 8.A.1-84**

Windowed SV-wave time records for material damping analyses at Gilroy 2 at 115-ft depth; short time window.



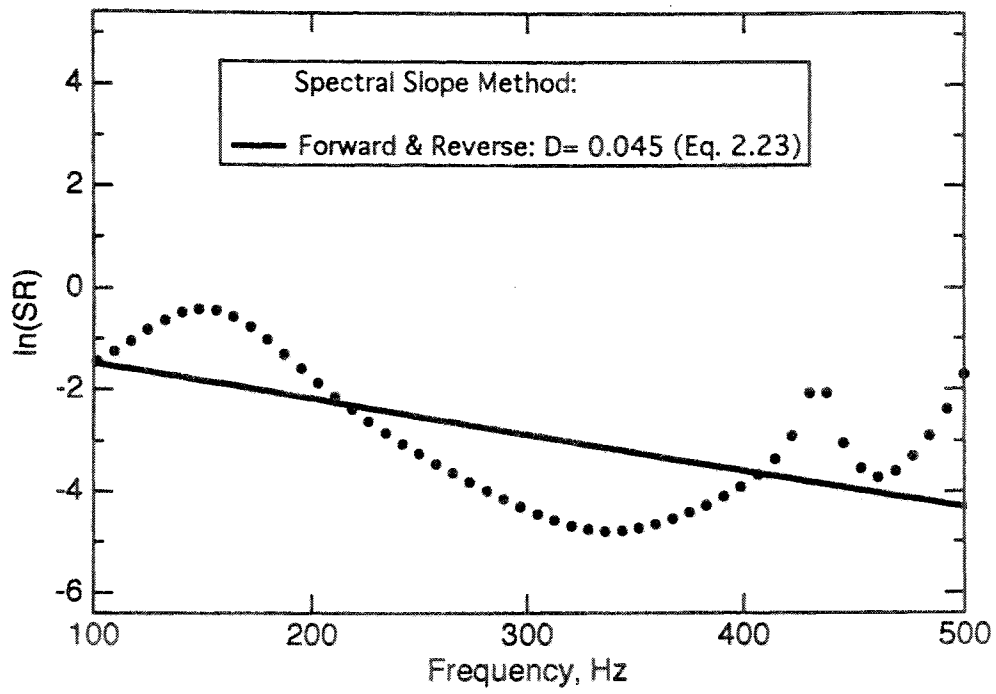
**Figure 8.A.1-85**

Material damping, wave velocity and linear spectra versus frequency for 115-ft depth at Gilroy 2; short time window; spectral ratio method.

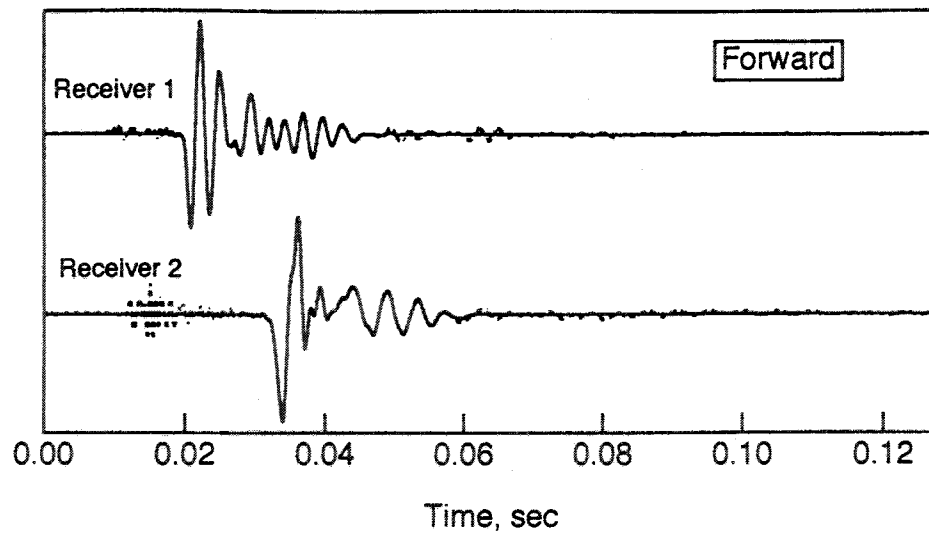


**Figure 8.A.1-86**

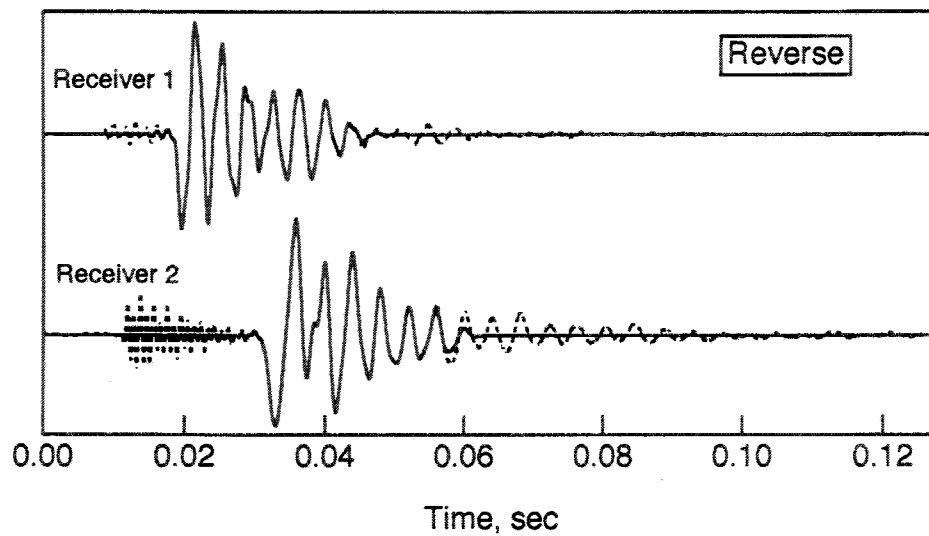
Material damping, wave velocity and linear spectra versus wavelength for 115-ft depth at Gilroy 2; short time window; spectral ratio method.



**Figure 8.A.1-87**  
Material damping at 115-ft depth at Gilroy 2 by spectral slope method; short time window.



a) Windowed Time Records from Forward Direction



b) Windowed Time Records from Reverse Direction

**Figure 8.A.1-88**

Windowed SV-wave time records for material damping analyses at Gilroy 2 at 115-ft depth; long time window.

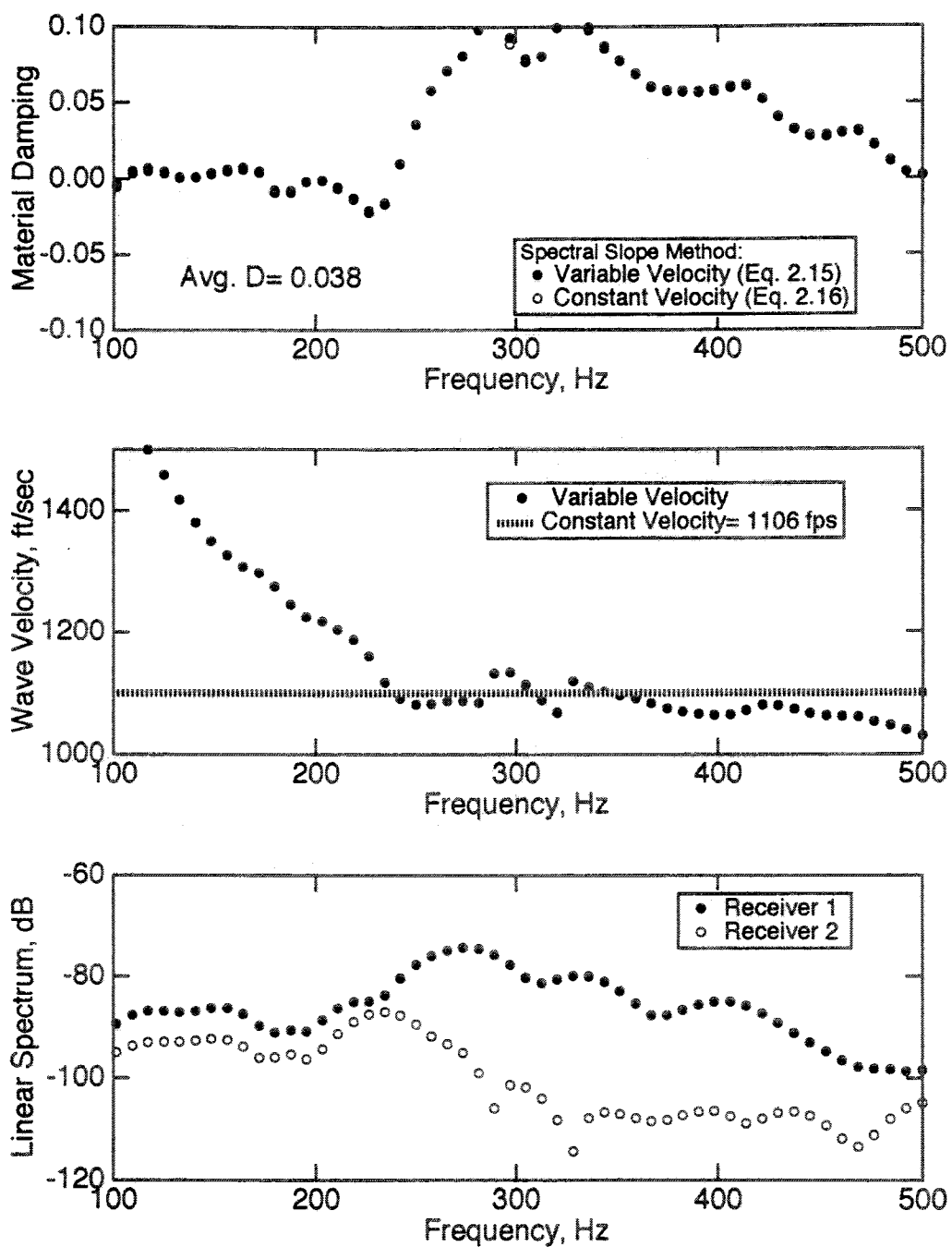
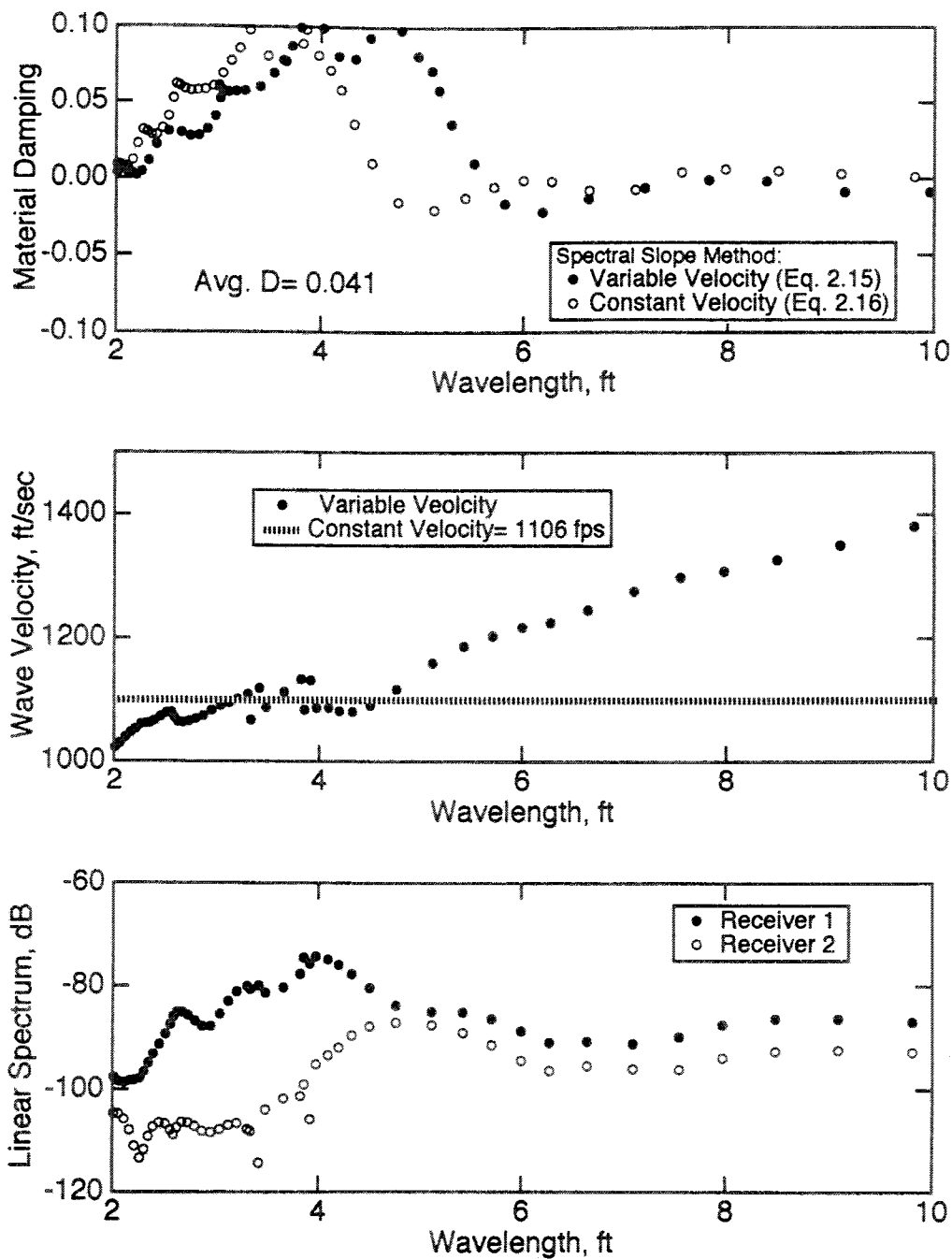


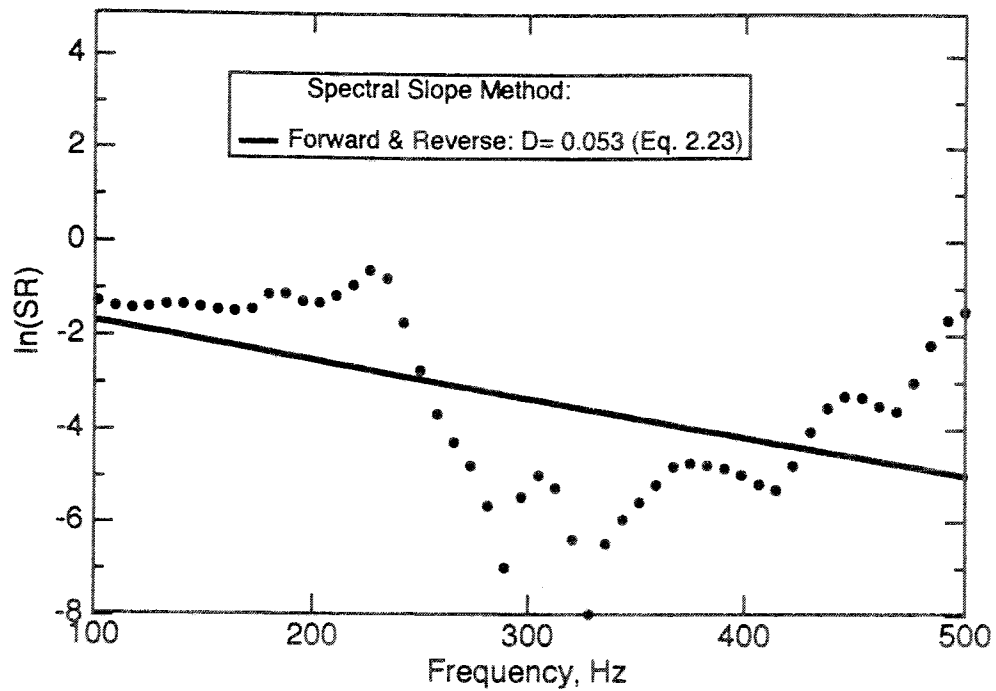
Figure 8.A.1-89

Material damping, wave velocity and linear spectra versus frequency for 115-ft depth at Gilroy 2; long time window; spectral ratio method.



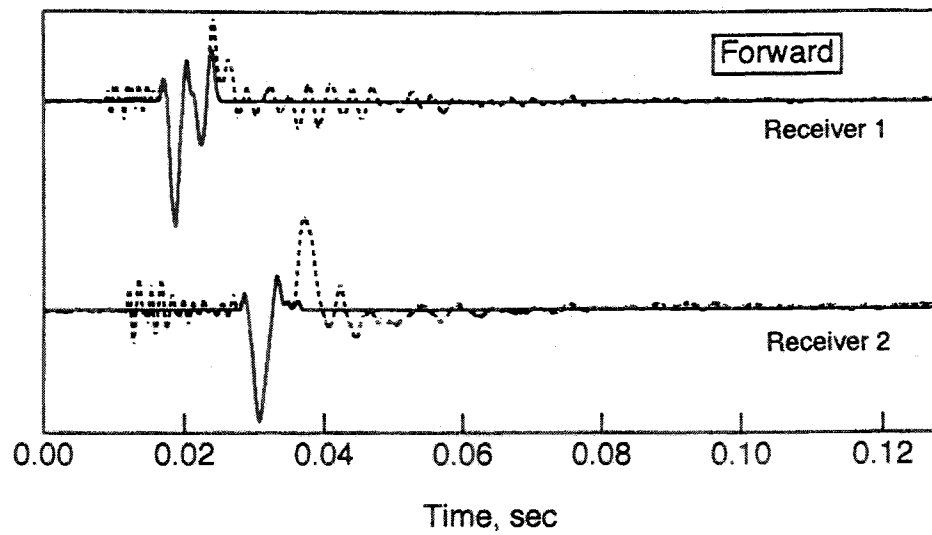
**Figure 8.A.1-90**

Material damping, wave velocity and linear spectra versus wavelength for 115-ft depth at Gilroy 2; long time window; spectral ratio method.

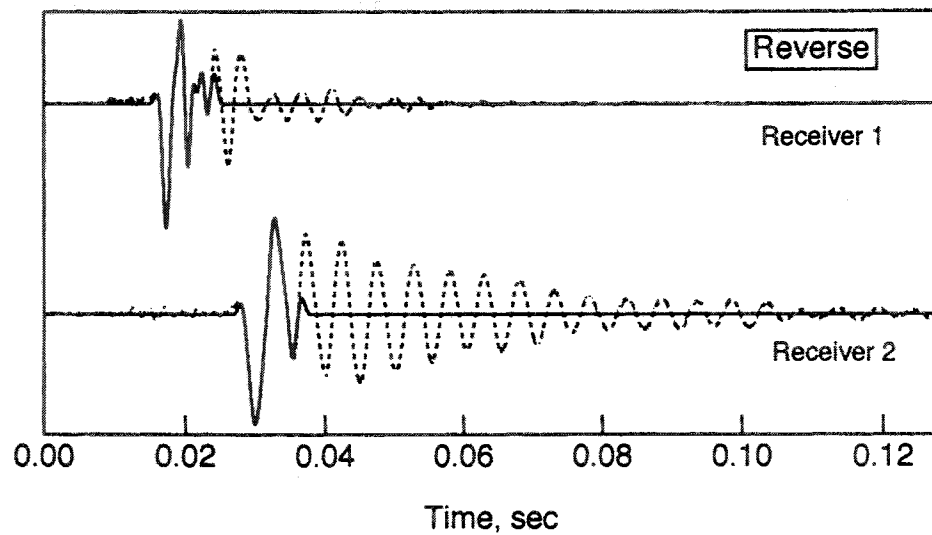


**Figure 8.A.1-91**  
Material damping at 115-ft depth at Gilroy 2 by spectral slope method; long time window.





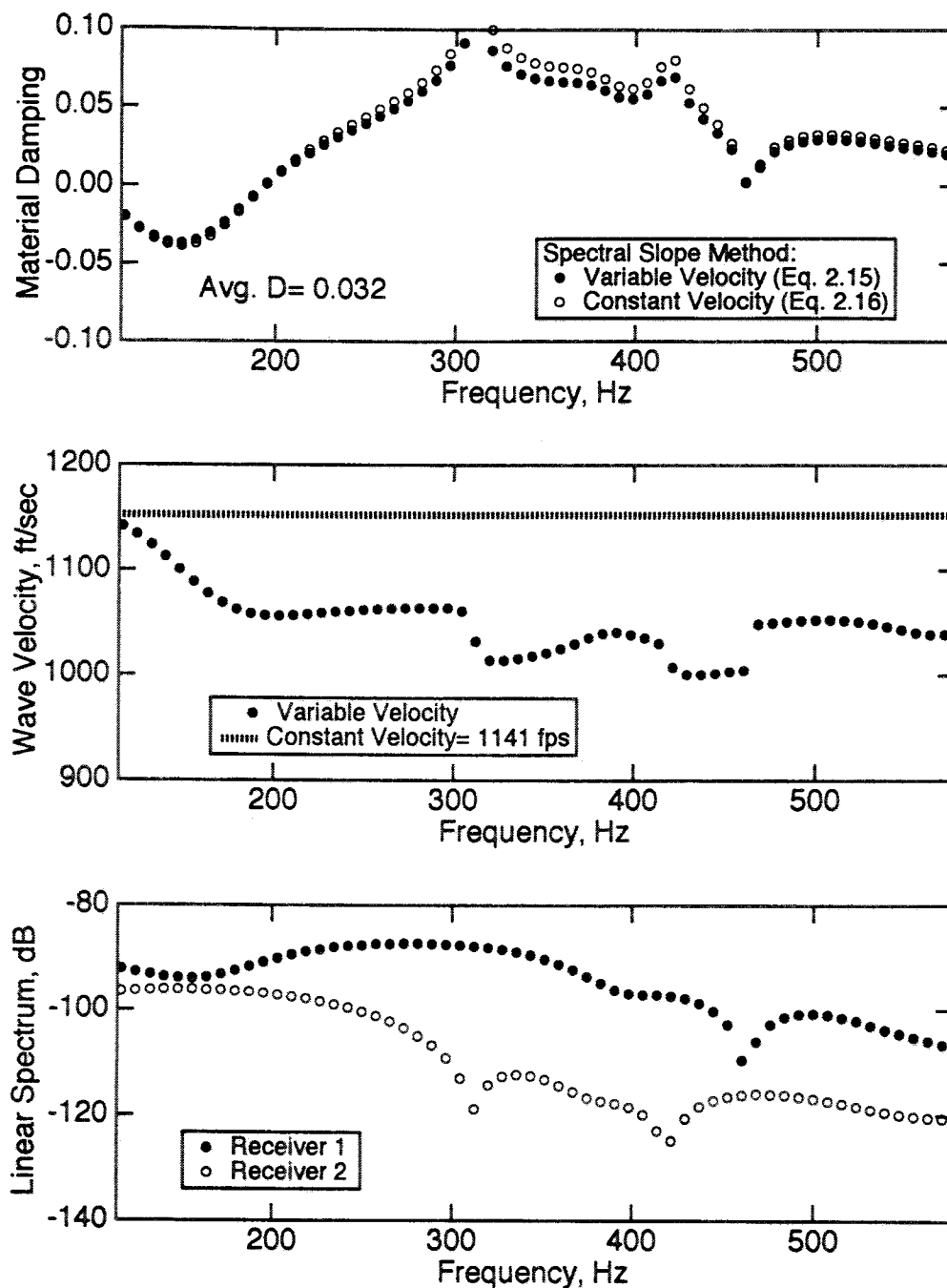
a) Windowed Time Records from Forward Direction



b) Windowed Time Records from Reverse Direction

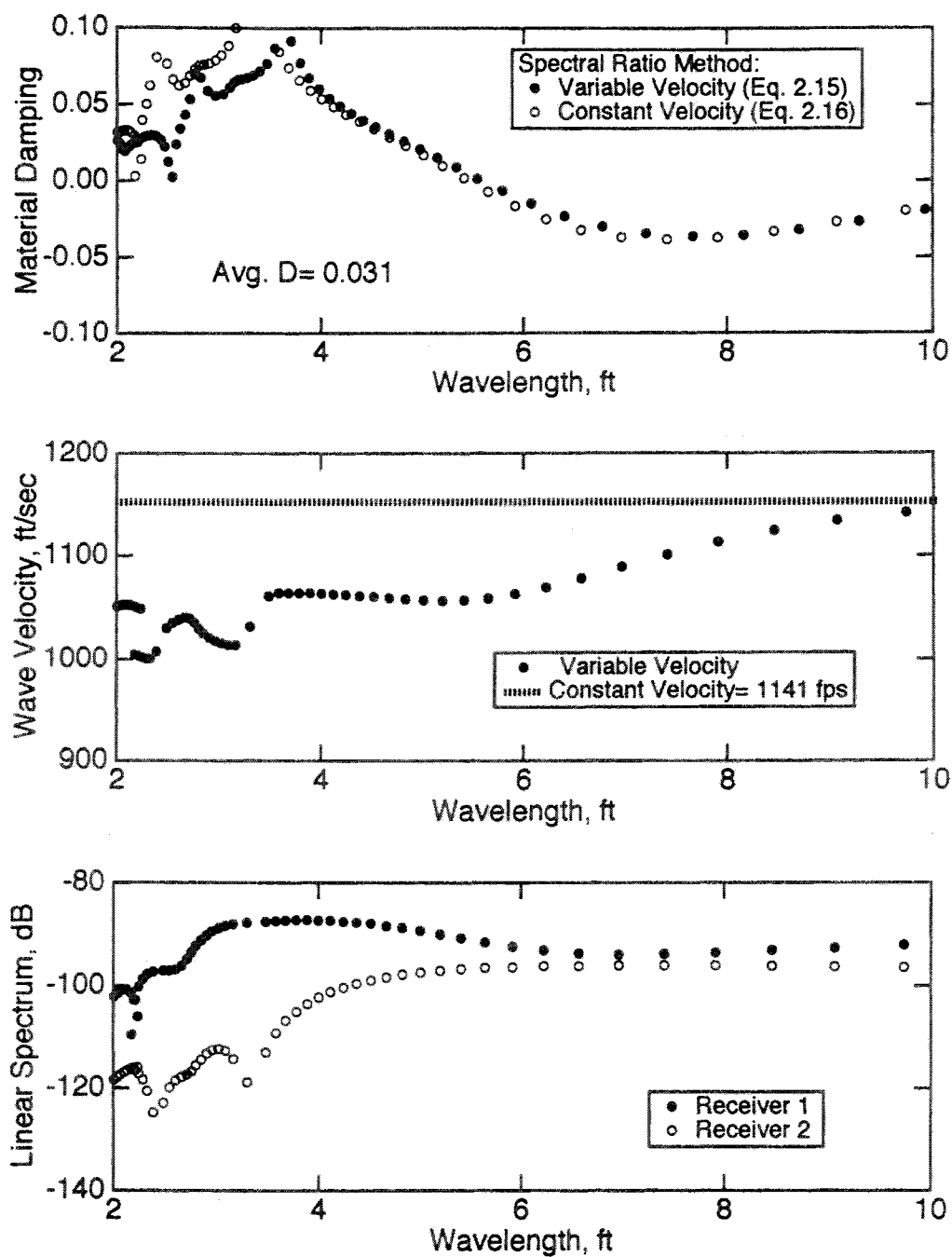
**Figure 8.A.1-92**

Windowed SV-wave time records for material damping analyses at Gilroy 2 at 125-ft depth; short time window.



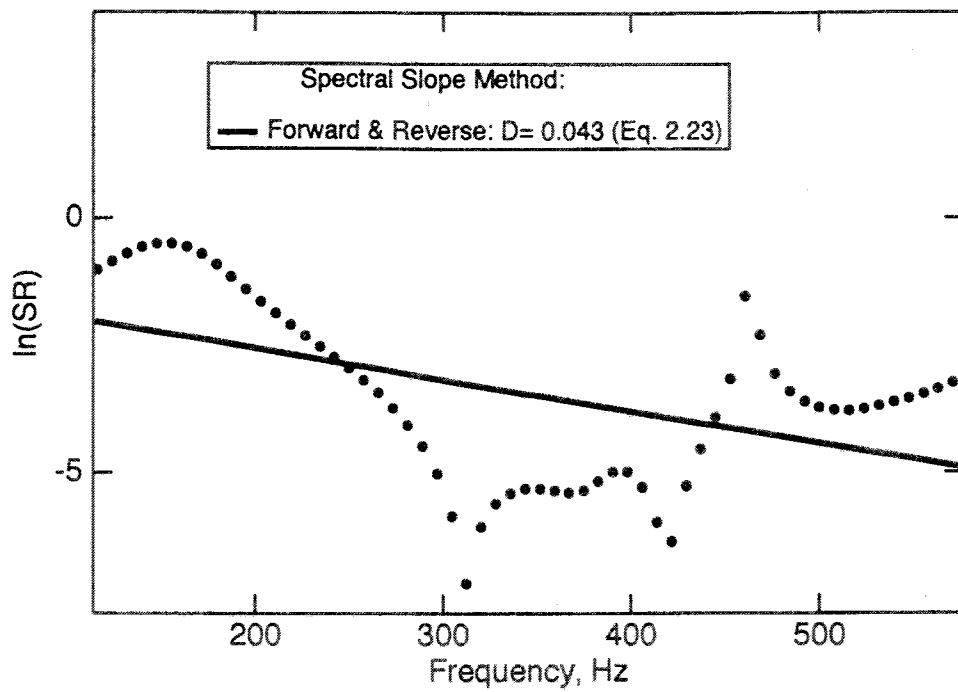
**Figure 8.A.1-93**

Material damping, wave velocity and linear spectra versus frequency for 125-ft depth at Gilroy 2; short time window; spectral ratio method.

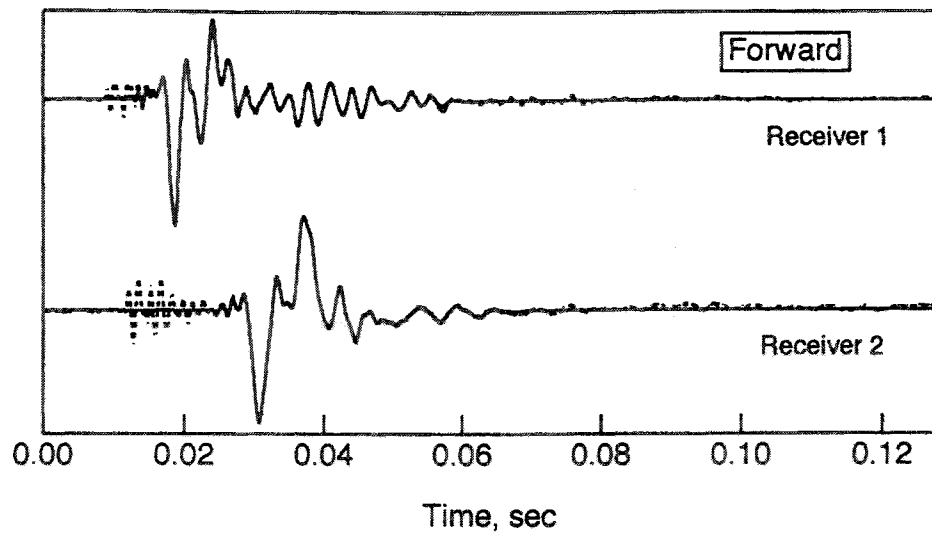


**Figure 8.A.1-94**

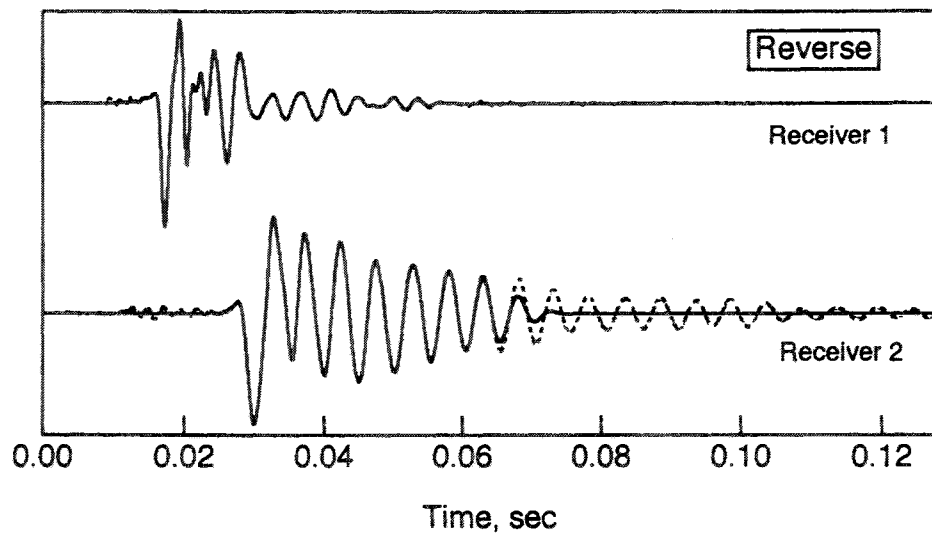
Material damping, wave velocity and linear spectra versus wavelength for 125-ft depth at Gilroy 2; short time window; spectral ratio method.



**Figure 8.A.1-95**  
Material damping at 125-ft depth at Gilroy 2 by spectral slope method; short time window.



a) Windowed Time Records from Forward Direction



b) Windowed Time Records from Reverse Direction

**Figure 8.A.1-96**

Windowed SV-wave time records for material damping analyses at Gilroy 2 at 125-ft depth; long time window.

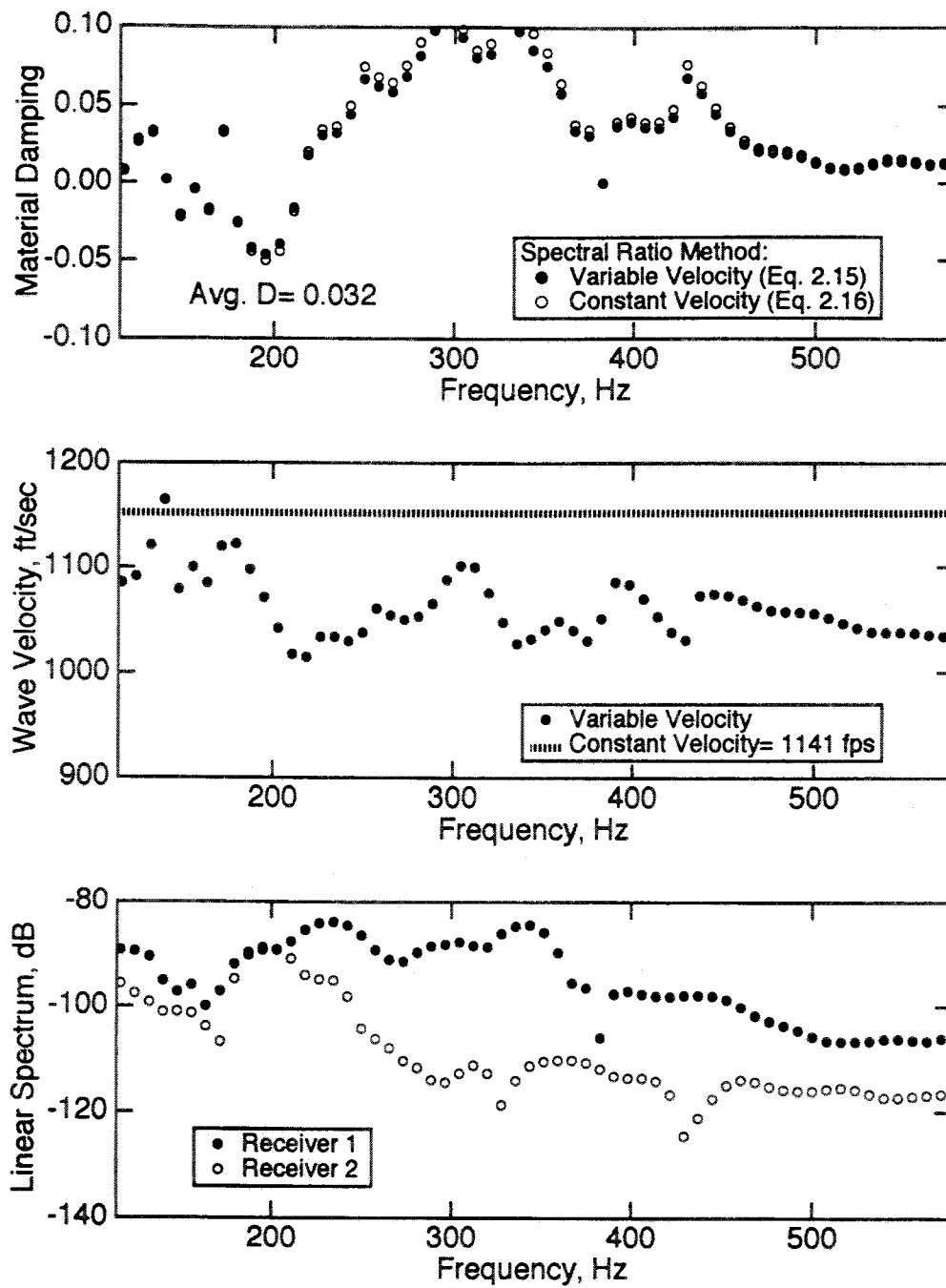


Figure 8.A.1-97

Material damping, wave velocity and linear spectra versus frequency for 125-ft depth at Gilroy 2; long time window; spectral ratio method.

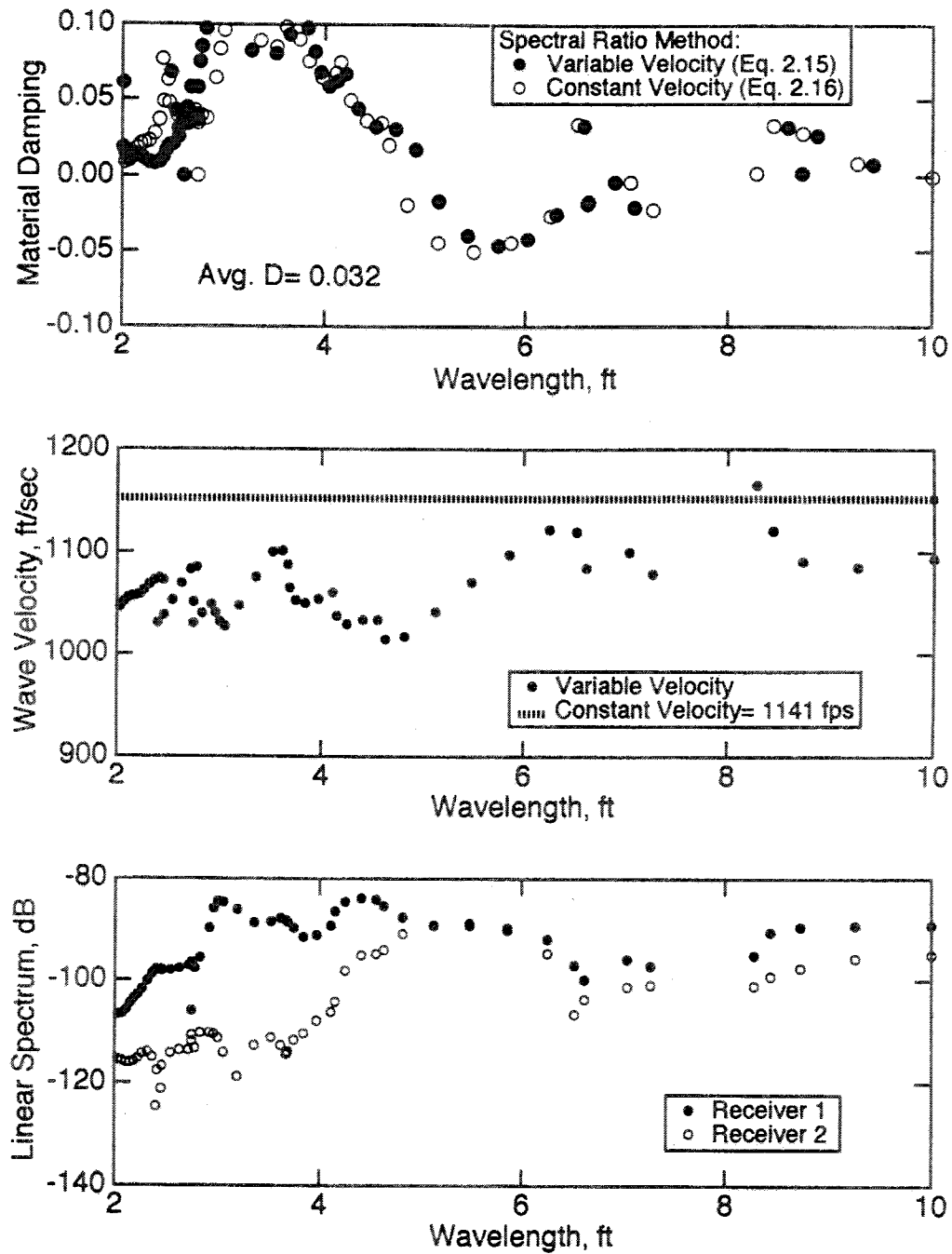


Figure 8.A.1-98  
Material damping, wave velocity and linear spectra versus wavelength for 125-ft depth at Gilroy 2; long time window; spectral ratio method.

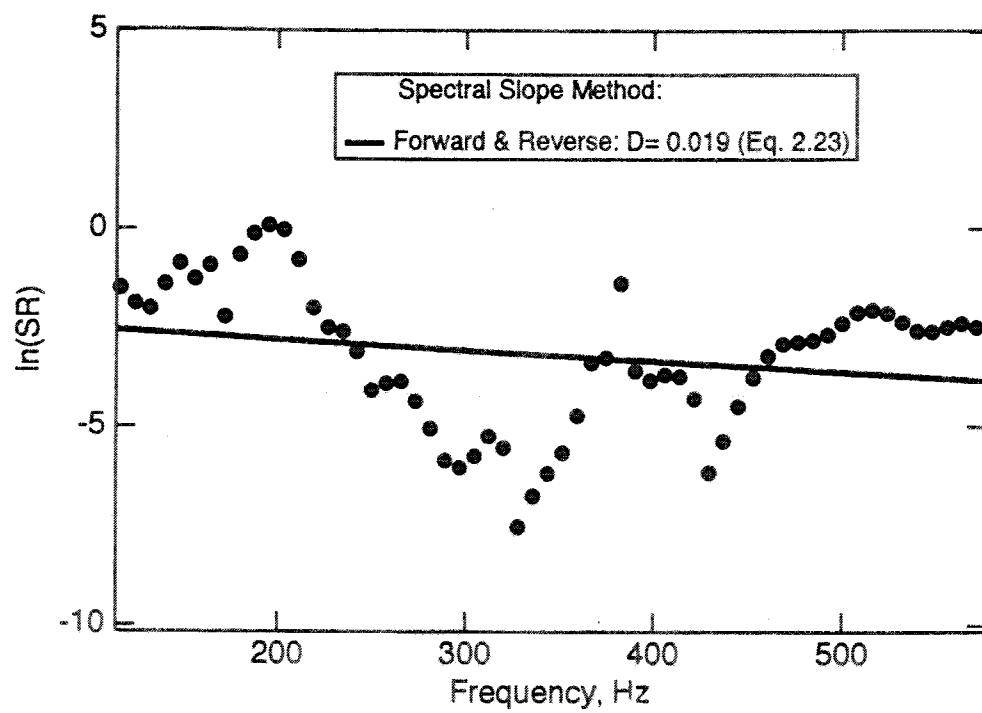


Figure 8.A.1-99

Material damping at 125-ft depth at Gilroy 2 by spectral slope method; long time window.



**Table 8.A.1-18**

Summary of Material Damping Results from Gilroy 2 Calculated from Time-Domain Analyses of Crosshole Waveforms

Depth (ft)	Method of Analysis*	Time Window	Window $t_3-t_2$ (msec)	Crosshole D <sup>†</sup> (%) [Q]	Laboratory D <sup>††</sup> (%) [Q]
15	Spectral Ratio	Short	16.0	4.0 [12.3]	3.9 [12.8] (at 20-ft depth)  f= 39 Hz, $\overline{\sigma}_0$ = 6 psi
15	Spectral Ratio	Long	42.3	4.5 [11.1]	
15	Spectral Slope	Short	16.0	4.8 [10.4]	
15	Spectral Slope	Long	42.3	7.3 [6.8]	
25	Spectral Ratio	Short	—	— <sup>1</sup>	3.9 [12.8] (at 20-ft depth)  f= 39 Hz, $\overline{\sigma}_0$ = 6 psi
25	Spectral Ratio	Long	2.71	4.7 [10.6]	
25	Spectral Slope	Short	—	— <sup>1</sup>	
25	Spectral Slope	Long	2.71	5.9 [10.6]	
115	Spectral Ratio	Short	5.81	2.6 [19.2]	1.3 [38.5] (at 120-ft depth)  f= 92 Hz, $\overline{\sigma}_0$ = 48 psi
115	Spectral Ratio	Long	22.1	4.0 [12.5]	
115	Spectral Slope	Short	5.81	4.5 [11.1]	
115	Spectral Slope	Long	22.1	5.3 [9.4]	
125	Spectral Ratio	Short	5.56	3.2 [15.6]	1.3 [38.5] (at 120-ft depth)  f= 92 Hz, $\overline{\sigma}_0$ = 48 psi
125	Spectral Ratio	Long	32.0	3.2 [15.6]	
125	Spectral Slope	Short	5.56	4.3 [11.6]	
125	Spectral Slope	Long	32.0	1.9 [26.3]	

Notes on Table 8.A.1-18:

- \* Spectral Ratio Method is based on Eq. 2.14  
Spectral Slope Method is based on Eq. 2.20
- \*\* Short time window is based on one full cycle of the waveform collected using Receiver 2 (see discussion in Section 8.A.1.5.2)  
Long time window is based on almost all of the waveform collected using Receiver 2 (see discussion in Section 8.A.1.5.2)
- † Average material damping over a wavelength range of 2 to 10 ft (0.6 to 3.0 m)
- †† Measured using resonant column test apparatus at the University of Texas at Austin (2-in. diameter specimens; D is corrected for equipment damping)
- 1 Short Window was not applied due to the nature of the data (see Figure 8.A.1-80)

In every case, field measurements of  $D$  are higher than the laboratory values. In general, the values of  $D$  calculated using the short time window for both the spectral ratio and spectral slope methods were lower than the values of  $D$  determined using a long time window. Due to the limited data, it is difficult to quantify how sensitive each analysis method is to window length, but the data show that window length does generally affect the results. The one notable exception is at the 125-ft (38.1-m) depth using the spectral ratio method, where the average values of  $D$  determined using the short and long windows are identical.

The values of  $D$  shown in Figures 8.A.1-73 through 8.A.1-75; 8.A.1-77 through 8.A.1-79; 8.A.1-81 through 8.A.1-83; 8.A.1-85 through 8.A.1-87; 8.A.1-89 through 8.A.1-91; 8.A.1-93 through 8.A.1-95; and 8.A.1-97 through 8.A.1-99 are highly variable over the given respective frequency and wavelength ranges. Apparently, the windowed waveforms used in the analyses contained enough wave interference from receiver-borehole effects and from reflected and refracted energy that the amplitude spectra were too complex to yield uniform results. However, the limited data seem to indicate that the spectral ratio and spectral slope methods generally yield similar results. Since the two methods are similar in theory, they should be expected to yield the same results if the data were perfect and free from all types of wave interference. Further, the field values may exhibit higher values of  $D$  due to geological inhomogeneities that cause wave scattering. Such inhomogeneities are not present in the laboratory specimens.

### 8.A.1.5.6 Summary and Conclusions

Material damping was evaluated at four depths at the Gilroy 2 site using time-domain crosshole records. Both the spectral ratio and spectral slope methods discussed in Section 8.A.1.2.5 were used to analyze the data. The results were then compared with laboratory measurements of material damping performed on intact samples.

Based on the results of this study, the following conclusions can be drawn:

- 1) As applied in this study, material damping measurements by the crosshole method are not very robust, and the data exhibit much scatter.
- 2) The spectral ratio and spectral slope methods yield similar results for material damping. Both methods have potential for use in material damping analysis using data measured by the crosshole method.
- 3) In these tests, windowing of time-domain waveforms was useful in reducing, but not eliminating, waveform interference.
- 4) Attention should be paid to possible interference from interaction between the receiver-borehole system. Methods to quantify the interaction functions,  $I_1$  and  $I_2$  (see Section 8.A.1.2.5.1), need to be developed. Reduction of wave interference, or at least the ability to quantify it, will improve the quality of amplitude spectra used in material damping analyses.
- 5) The limited data available from this study suggest that the values of  $D$  evaluated from data collected from crosshole tests are higher than the values of  $D$  measured in the laboratory using the torsional resonant column apparatus. While the values are not identical, there is a consistent trend in the results. It appears that the difference between field and laboratory measurements increases as the value of  $D$  decreases.

## **6—SUMMARY AND CONCLUSIONS**

### **8.A.1.6.1 Summary**

As part of a comprehensive study of dynamic soil behavior sponsored by the Electric Power Research Institute (EPRI), this study was conducted to measure in situ small-strain dynamic properties of soils at two Northern California sites affected by the 1989 Loma Prieta Earthquake. The sites studied are called Gilroy 2 and Treasure Island. The field testing involved the crosshole seismic method.

The field procedures and equipment used in performing crosshole tests at the study sites are discussed, along with data reduction procedures to determine body wave velocities. Additionally, two methods for evaluating material damping using time-domain crosshole records are presented. The two methods used to evaluate material damping, called the spectral ratio and the spectral slope methods, have a similar theoretical basis. Two notable differences in the methods are that the spectral ratio method explicitly assumes: 1) that geometrical spreading is equal to  $(1/R)$  and 2) that the receiver-borehole systems at each measurement point have the same response functions.

At both the Gilroy 2 and Treasure Island sites, body wave velocities were measured in situ by the crosshole seismic method. The body waves measured were compression (P), vertically-polarized shear (SV) waves and horizontally-polarized shear (SH) waves. At the Gilroy 2 site, material damping was also evaluated at four depths using time-domain crosshole records. Additional crosshole records were sent to Professor Toksoz at the Massachusetts Institute of Technology for further damping analyses.

### **8.A.1.6.2 Conclusions**

Principal conclusions from this work pertain to a discussion of velocities, comparisons of SV- and SH-wave velocities, comparisons of P-wave velocities using the two different sources, and the results of material damping.

#### **8.A.1.6.2.1 Body Wave Velocities**

Using a mechanical wedge source, SV-waves were successfully measured at both the Gilroy 2 and Treasure Island sites. The Gilroy 2 site was generally stiff in terms of shear wave velocity, with SV-wave velocities ranging from about 700 fps (213 m/sec) to about 2500 fps (762 m/sec) in the top 200 ft (61 m). Lateral variability in soil stiffness was observed in both the P- and S-wave velocity profiles at the Gilroy 2 site.

The Treasure Island site was generally rather soft, with most SV-wave velocities ranging from about 400 fps (12 m/sec) to about 800 fps (244 m/sec) in the top 90 ft (27 m). The shear wave velocities from forward- and reverse-profile tests agreed well, but P-wave velocities were more variable. This variability in P-wave velocity may be due to inaccurate travel path distances used in the velocity computations. Also at Treasure Island, the shear wave velocities measured by the University of Texas and the Earth Technology Corporation were generally in fair agreement (within 10%), but at some depths the P-wave velocities reported by the two groups varied significantly (by as much as 62%).

The horizontally-impacting solenoid source allowed comparisons of SV- and SH-wave velocities at Gilroy 2 and Treasure Island. Such comparisons provide a general evaluation of soil anisotropy. At both sites, there were regions in the soil profile that had lower SH-wave velocities than SV-wave velocities. Between depths of 35 ft and 100 ft (10.7 m and 30.5 m) at Gilroy 2, the SH-wave velocities were usually higher than the SV-wave velocities, indicating higher soil stiffness in the horizontal direction than in the vertical direction. At Treasure Island, the SH-wave velocities are higher than the SV-wave velocities in the Young Bay Mud at depths between 70 ft and 75 ft (21.3 m and 23 m) and in a layer of sand and shells at about 100 ft (30.5 m).

At both sites, the shear wave velocities measured in the field by the crosshole method were slightly higher than the shear wave velocities measured in the laboratory by the resonant column method. At Gilroy 2, the field values of  $V_S$  were, on average, about 30% higher than the laboratory values; at Treasure Island, the field values of  $V_S$  averaged about 18% higher.

Both the mechanical wedge source and the solenoid sources were used to generate P-waves at both study sites, and the P-wave velocities measured using the two sources matched well. Below the water table at Gilroy 2, the P-waves varied from about 4000 fps to over 8000 fps (1200 m/sec to 2400 m/sec). At Treasure Island the P-wave velocities generally ranged from 4000 fps to 6000 fps (1200 m/sec to 1800 fps), but at a depth of about 70 ft (21.3 m) in the Young Bay Mud, the P-wave velocity drops to about 2000 fps (610 m/sec), indicating that the soil is not completely saturated at that depth.

#### **8.A.1.6.2.2 In Situ Damping Measurements**

In situ damping measurements in shear were performed with SV-waves at the Gilroy 2 site. Measurements were evaluated in both the forward and reverse directions separately and also by combining data from both directions. Using both the spectral ratio and the spectral slope methods, much scatter occurred in the results for material damping. This scatter was reduced when data from the forward and reverse directions were combined. At the depths studied, the values of material damping in shear,  $D$ , ranged from about 1.9% to 7.3% ( $Q = 26.3$  to 6.8). Values of  $D$  measured in the laboratory using the torsional resonant column method were lower than the values evaluated using the crosshole data.

The spectral ratio and the spectral slope methods yielded similar results for material damping. At this point, neither method is very robust, which causes much of the scatter in the results for  $D$ . However, both methods have the potential to evaluate material damping using data collected in crosshole tests. Further study is required to quantify the possible interference from interaction between the receiver-borehole system. The ability to reduce, or at least quantify, wave interference will improve the quality of the amplitude spectra used in material damping analyses. In this study, windowing of time-domain waveforms was useful in reducing, but not eliminating, waveform interference.

## APPENDIX 8.A.1.A—TABULATED RESULTS OF CROSSHOLE TESTS AT GILROY 2

Table 8.A.1-19

Direct SV-Wave Velocities Measured at Gilroy 2 Between B1 and B2 (S-R1, Forward Profile), Path 1

Depth (ft)	Center- to- Center Dist. <sup>1</sup> (ft)	Travel Path Dist. <sup>2</sup> (ft)	SV-Up Travel Time (ms)	Adjusted Up Travel Time <sup>3</sup> (ms)	SV- Down Travel Time (ms)	Adjusted Down Travel Time <sup>4</sup> (ms)	Avg. SV Travel Time (ms)	SV-Wave Velocity (fps)
(1)	(2)	(3)	(4)	(5)	(6)	(7)	(8)	(9)
5	14.02	13.81	21.16 <sup>a</sup>	21.19	21.81 <sup>a</sup>	21.81	21.50	642
7.5	14.03	13.82	20.41 <sup>a</sup>	20.44	20.25 <sup>a</sup>	20.25	20.35	679
10	14.06	13.85	20.44 <sup>a</sup>	20.47	20.59 <sup>a</sup>	20.59	20.53	675
15	14.08	13.87	18.41 <sup>a</sup>	18.44	19.00 <sup>a</sup>	19.00	18.72	741
20	14.10	13.89	21.44 <sup>a</sup>	21.47	21.47 <sup>a</sup>	21.47	21.47	647
25	14.13	13.92	20.25 <sup>a</sup>	20.28	19.91 <sup>a</sup>	19.91	20.10	693
30	14.12	13.91	19.81 <sup>a</sup>	19.84	19.56 <sup>a</sup>	19.56	19.70	706
35	14.04	13.83	17.62 <sup>a</sup>	17.65	17.56 <sup>a</sup>	17.56	17.61	786
40	14.00	13.79	12.66 <sup>b</sup>	12.69	12.37 <sup>b</sup>	12.37	12.53	1101
45	13.98	13.77	12.72 <sup>a</sup>	12.75	12.66 <sup>a</sup>	12.66	12.71	1084
50	13.96	13.75	11.00 <sup>a</sup>	11.03	10.97 <sup>a</sup>	10.97	11.00	1250
55	14.01	13.81	9.53 <sup>a</sup>	9.56	9.63 <sup>a</sup>	9.63	9.60	1439
60	14.06	13.85	8.44 <sup>a</sup>	8.54	8.59 <sup>a</sup>	8.59	8.57	1617
65	14.15	13.94	9.41 <sup>a</sup>	9.51	9.00 <sup>a</sup>	9.06	9.29	1502
70	14.14	13.93	9.25 <sup>a</sup>	9.35	9.09 <sup>a</sup>	9.15	9.25	1506
75	14.16	13.95	15.19 <sup>c</sup>	15.29	15.22 <sup>c</sup>	15.28	15.29	912
80	13.98	13.77	13.87 <sup>a</sup>	13.97	13.44 <sup>a</sup>	13.50	13.74	1002
85	13.89	13.68	15.62 <sup>a</sup>	15.72	15.34 <sup>a</sup>	15.40	15.56	879
90	13.75	13.54	15.62 <sup>a</sup>	15.72	15.47 <sup>a</sup>	15.53	15.63	866
95	13.82	13.62	14.81 <sup>a</sup>	14.91	14.69 <sup>a</sup>	14.75	14.83	918
100	13.82	13.62	15.62 <sup>b</sup>	15.72	15.62 <sup>b</sup>	15.68	15.70	867
105	13.76	13.55	14.06 <sup>a</sup>	14.16	14.00 <sup>a</sup>	14.06	14.11	960
110	13.69	13.48	13.69 <sup>a</sup>	13.79	13.81 <sup>a</sup>	13.87	13.83	975
115	13.66	13.45	13.75 <sup>a</sup>	13.85	13.75 <sup>a</sup>	13.81	13.83	972
120	13.65	13.44	12.69 <sup>a</sup>	12.79	12.94 <sup>a</sup>	13.00	12.90	1042
125	13.64	13.43	11.25 <sup>a</sup>	11.35	11.31 <sup>a</sup>	11.37	11.36	1182
130	13.72	13.51	12.69 <sup>a</sup>	12.79	12.56 <sup>a</sup>	12.62	12.71	1063

Table 8.A.1-19 (continued)

Direct SV-Wave Velocities Measured at Gilroy 2 Between B1 and B2 (S-R1, Forward Profile), Path 1

Depth (ft)	Center- to- Center Dist. <sup>1</sup> (ft)	Travel Path Dist. <sup>2</sup> (ft)	SV-Up Travel Time (ms)	Adjusted Up Travel Time <sup>3</sup> (ms)	SV- Down Travel Time (ms)	Adjusted Down Travel Time <sup>4</sup> (ms)	Avg. SV Travel Time (ms)	SV-Wave Velocity (fps)
(1)	(2)	(3)	(4)	(5)	(6)	(7)	(8)	(9)
135	13.74	13.54	12.19 <sup>a</sup>	12.29	12.00 <sup>a</sup>	12.06	12.18	1112
140	13.88	13.67	9.97 <sup>b</sup>	10.07	9.94 <sup>b</sup>	10.00	10.04	1362
145	13.84	13.63	8.13 <sup>a</sup>	8.23	8.19 <sup>a</sup>	8.25	8.24	1654
150	13.87	13.66	7.88 <sup>a</sup>	7.98	7.94 <sup>a</sup>	8.00	7.99	1710
155	14.01	13.80	8.38 <sup>a</sup>	8.48	8.31 <sup>a</sup>	8.37	8.43	1638
160	14.12	13.92	8.31 <sup>c</sup>	8.41	8.00 <sup>c</sup>	8.06	8.24	1690
165	14.27	14.06	7.12 <sup>b</sup>	7.22	7.38 <sup>b</sup>	7.44	7.33	1918
170	14.25	14.04	6.00 <sup>a</sup>	6.10	5.88 <sup>a</sup>	5.94	6.02	2332
175	14.17	13.97	6.37 <sup>a</sup>	6.47	6.38 <sup>a</sup>	6.44	6.46	2164
180	14.15	13.95	5.87 <sup>a</sup>	5.97	5.89 <sup>a</sup>	5.95	5.96	2340
185	14.12	13.91	6.19 <sup>a</sup>	6.29	6.25 <sup>a</sup>	6.31	6.30	2209
190	14.15	13.95	7.00 <sup>b</sup>	7.10	6.81 <sup>b</sup>	6.87	6.99	1997
195	14.16	13.95	11.81 <sup>a</sup>	11.91	11.56 <sup>a</sup>	11.62	11.77	1186
200	14.16	13.95	5.80 <sup>a</sup>	5.90	5.96 <sup>a</sup>	6.02	5.96	2340
205	14.22	14.01	5.47 <sup>a</sup>	5.57	5.36 <sup>a</sup>	5.42	5.50	2549
210	14.32	14.11	5.89 <sup>a</sup>	5.99	6.03 <sup>a</sup>	6.09	6.04	2336
215	14.37	14.16	6.37 <sup>a</sup>	6.47	6.44 <sup>a</sup>	6.50	6.49	2183
220	14.54	14.34	6.98 <sup>b</sup>	7.08	6.54 <sup>b</sup>	6.60	6.84	2096
225	14.74	14.53	8.33 <sup>b</sup>	8.43	8.34 <sup>b</sup>	8.40	8.42	1727
230	14.87	14.66	8.22 <sup>a</sup>	8.32	8.34 <sup>a</sup>	8.40	8.36	1754
235	14.69	14.48	8.28 <sup>b</sup>	8.38	8.68 <sup>b</sup>	8.74	8.56	1692
240	14.43	14.22	6.50 <sup>b</sup>	6.60	6.80 <sup>b</sup>	6.86	6.73	2113
245	14.49	14.28	6.89 <sup>a</sup>	6.99	6.56 <sup>a</sup>	6.62	6.81	2098
250	14.34	14.13	7.92 <sup>b</sup>	8.02	7.89 <sup>b</sup>	7.95	7.99	1769
255	14.21	14.00	8.00 <sup>b</sup>	8.10	7.92 <sup>b</sup>	7.98	8.04	1741
260	14.35	14.15	8.06 <sup>b</sup>	8.16	7.81 <sup>b</sup>	7.87	8.02	1765
265	14.27	14.06	8.45 <sup>b</sup>	8.55	8.41 <sup>b</sup>	8.47	8.51	1652
269	14.33	14.13	9.53 <sup>b</sup>	9.63	9.09 <sup>b</sup>	9.15	9.39	1504
275	14.18	13.97	13.66 <sup>a</sup>	13.76	13.19 <sup>a</sup>	13.25	13.51	1035
280	14.05	13.84	11.25 <sup>a</sup>	11.35	11.22 <sup>a</sup>	11.28	11.32	1223
285	14.16	13.95	8.47 <sup>c</sup>	8.57	9.84 <sup>c</sup>	9.90	9.24	1511

Table 8.A.1-19 (Continued)

Direct SV-Wave Velocities Measured at Gilroy 2 Between B1 and B2 (S-R1, Forward Profile), Path 1

Depth (ft)	Center- to- Center Dist. <sup>1</sup> (ft)	Travel Path Dist. <sup>2</sup> (ft)	SV-Up Travel Time (ms)	Adjusted Up Travel Time <sup>3</sup> (ms)	SV- Down Travel Time (ms)	Adjusted Down Travel Time <sup>4</sup> (ms)	Avg. SV Travel Time (ms)	SV-Wave Velocity (fps)
(1)	(2)	(3)	(4)	(5)	(6)	(7)	(8)	(9)
290	14.20	13.99	7.66 <sup>a</sup>	7.76	7.63 <sup>a</sup>	7.69	7.73	1811
295	14.22	14.02	7.63 <sup>a</sup>	7.73	7.52 <sup>a</sup>	7.58	7.66	1831
300	14.13	13.92	9.45 <sup>a</sup>	9.55	9.32 <sup>a</sup>	9.38	9.47	1471
305	14.04	13.83	9.70 <sup>a</sup>	9.80	9.77 <sup>a</sup>	9.83	9.82	1409
310	14.12	13.91	9.06 <sup>b</sup>	9.16	9.30 <sup>b</sup>	9.36	9.26	1502
315	14.11	13.90	9.00 <sup>b</sup>	9.10	8.61 <sup>b</sup>	8.67	8.89	1565
320	14.13	13.92	— <sup>d</sup>	—	7.83 <sup>b</sup>	7.89	7.89	1765
325	14.30	14.09	6.61 <sup>a</sup>	6.71	6.40 <sup>a</sup>	6.46	6.59	2140
330	14.28	14.07	7.17 <sup>a</sup>	7.27	7.12 <sup>a</sup>	7.18	7.23	1947
335	14.27	14.06	7.73 <sup>a</sup>	7.83	7.81 <sup>a</sup>	7.87	7.85	1791
340	14.20	13.99	9.98 <sup>a</sup>	10.08	9.44 <sup>a</sup>	9.50	9.79	1429
345	14.14	13.93	8.02 <sup>b</sup>	8.12	8.72 <sup>b</sup>	8.78	8.45	1648
350	14.21	14.01	6.77 <sup>a</sup>	6.87	6.83 <sup>a</sup>	6.89	6.88	2036
355	14.26	14.05	6.88 <sup>a</sup>	6.98	6.66 <sup>a</sup>	6.72	6.85	2052
360	14.20	14.00	7.02 <sup>a</sup>	7.12	6.97 <sup>a</sup>	7.03	7.08	1978
365	14.08	13.87	6.78 <sup>a</sup>	6.88	6.84 <sup>a</sup>	6.90	6.89	2013
370	14.20	13.99	7.98 <sup>b</sup>	8.08	8.47 <sup>b</sup>	8.53	8.31	1685
375	14.05	13.84	7.70 <sup>a</sup>	7.80	7.84 <sup>a</sup>	7.90	7.85	1763
380	14.04	13.83	9.00 <sup>b</sup>	9.10	8.70 <sup>b</sup>	8.76	8.93	1549
385	13.98	13.77	8.77 <sup>b</sup>	8.87	8.62 <sup>b</sup>	8.68	8.78	1569
390	13.96	13.75	6.92 <sup>a</sup>	7.02	6.78 <sup>a</sup>	6.84	6.93	1984

Notes on Table 8.A.1-19:

- <sup>1</sup> center-to-center spacings determined using borehole survey data from Agbabian Associates, Pasadena, California
- <sup>2</sup> one-half borehole diameter of only the source borehole (2.5 in.) is subtracted from the center-to-center spacing due to the assumed average position of the receiver in the center of the borehole
- <sup>3</sup> calibration factor (trigger delay) = -0.03 ms, 0-55 ft; calibration factor = -0.10 ms, 60-390 ft
- <sup>4</sup> calibration factor (trigger delay) = -0.00 ms, 0-60 ft; calibration factor = -0.06 ms, 65-390 ft
- <sup>a</sup> initial wave arrival clearly identified (within 5% of total travel time)—Type I data
- <sup>b</sup> initial wave arrival less distinct than (a) but identifiable (within 10% of total travel time)—Type II data
- <sup>c</sup> some interpretation required to identify initial wave arrival—Type III data
- <sup>d</sup> measurement not performed

Table 8.A.1-20

Interval SV-Wave Velocities Measured at Gilroy 2 Between B2 and B3 (R1-R2, Forward Profile), Path 2

Depth (ft)	Travel Path Distance <sup>1</sup> (ft)	SV-Up Travel Time (ms)	SV-Down Travel Time (ms)	Average SV Travel Time (ms)	SV-Wave Velocity (fps)
(1)	(2)	(3)	(4)	(5)	(6)
5	13.61	21.19a	20.94a	21.07	646
7.5	13.60	20.12a	20.12a	20.12	676
10	13.57	19.69a	19.69a	19.69	689
15	13.57	19.75a	19.44a	19.60	693
20	13.57	20.12a	19.94a	20.03	677
25	13.53	22.31b	23.06b	22.69	596
30	13.60	18.75a	18.75a	18.75	726
35	13.60	17.81a	18.25a	18.03	754
40	13.61	13.75c	14.50c	14.13	963
45	13.71	10.12b	11.06b	10.59	1294
50	13.76	9.31a	9.31a	9.31	1477
55	13.72	7.47a	7.47a	7.47	1837
60	13.75	6.97a	6.97a	6.97	1973
65	13.68	7.37a	7.37a	7.37	1856
70	13.66	7.81a	7.50a	7.66	1785
75	13.58	12.84c	13.06c	12.95	1049
80	13.65	13.31a	13.25a	13.28	1028
85	13.67	13.56a	13.94a	13.75	994
90	13.77	14.72a	14.72a	14.72	935
95	13.64	14.09a	13.81a	13.95	978
100	13.66	14.94c	14.87c	14.91	916
105	13.71	12.62a	12.62a	12.62	1086
110	13.71	12.25a	12.37a	12.31	1114
115	13.73	12.37a	12.44a	12.41	1107
120	13.61	11.81a	11.81a	11.81	1153
125	13.55	11.75a	11.75a	11.75	1153
130	13.52	11.25a	11.25a	11.25	1202
135	13.43	10.56c	11.00c	10.78	1246
140	13.16	6.19b	6.25b	6.22	2116
145	13.10	6.50a	6.50a	6.50	2015
150	13.20	6.62a	6.00a	6.31	2091
155	13.00	6.81a	6.81a	6.81	1909



Table 8.A.1-20 (continued)

Interval SV-Wave Velocities Measured at Gilroy 2 Between B2 and B3 (R1-R2, Forward Profile), Path 2

Depth (ft)	Travel Path Distance <sup>1</sup> (ft)	SV-Up Travel Time (ms)	SV-Down Travel Time (ms)	Average SV Travel Time (ms)	SV-Wave Velocity (fps)
(1)	(2)	(3)	(4)	(5)	(6)
160	12.73	7.81 <sup>c</sup>	7.81 <sup>c</sup>	7.81	1630
165	12.47	7.19 <sup>b</sup>	7.19 <sup>b</sup>	7.19	1734
170	12.37	5.37 <sup>a</sup>	5.44 <sup>a</sup>	5.41	2288
175	12.40	4.81 <sup>a</sup>	4.69 <sup>a</sup>	4.75	2611
180	12.59	5.31 <sup>a</sup>	5.31 <sup>a</sup>	5.31	2372
185	12.62	5.44 <sup>a</sup>	5.44 <sup>a</sup>	5.44	2320
190	12.59	6.25 <sup>b</sup>	6.62 <sup>b</sup>	6.44	1956
195	12.50	8.31 <sup>c</sup>	8.50 <sup>c</sup>	8.41	1487

Notes on Table 8.A.1-20:

- <sup>1</sup> center-to-center spacings determined using borehole survey data from Agbabian Associates, Pasadena, California
- <sup>a</sup> initial wave arrival clearly identified (within 5% of total travel time)—Type I data
- <sup>b</sup> initial wave arrival less distinct than (a) but identifiable (within 10% of total travel time)—Type II data
- <sup>c</sup> some interpretation required to identify initial wave arrival—Type III data

Table 8.A.1-21

Interval SV-Wave Velocities Measured at Gilroy 2 Between B3 and B4 (R2-R3, Forward Profile), Path 3

Depth (ft)	Travel Path Distance <sup>1</sup> (ft)	SV-Up Travel Time (ms)	SV-Down Travel Time (ms)	Average SV Travel Time (ms)	SV-Wave Velocity (fps)
(1)	(2)	(3)	(4)	(5)	(6)
5	14.20	22.19 <sup>b</sup>	22.12 <sup>b</sup>	22.16	641
7.5	14.18	21.05 <sup>c</sup>	21.62 <sup>c</sup>	21.34	665
10	14.18	20.37 <sup>b</sup>	19.75 <sup>b</sup>	20.06	707
15	14.17	22.00 <sup>a</sup>	22.00 <sup>a</sup>	22.00	644
20	14.12	21.31 <sup>b</sup>	21.31 <sup>b</sup>	21.31	662
25	14.11	20.19 <sup>b</sup>	20.19 <sup>b</sup>	20.19	699
30	14.08	— <sup>e</sup>	18.75 <sup>c</sup>	18.75	751
35	14.06	— <sup>e</sup>	— <sup>e</sup>	—	—
40	14.10	12.87 <sup>c</sup>	12.56 <sup>c</sup>	12.72	1109
45	14.00	— <sup>e</sup>	— <sup>e</sup>	—	—
50	14.02	9.87 <sup>a</sup>	9.87 <sup>a</sup>	9.87	1420
55	13.97	8.06 <sup>a</sup>	8.06 <sup>a</sup>	8.06	1733
60	13.87	7.66 <sup>a</sup>	7.97 <sup>a</sup>	7.82	1775
65	13.90	7.06 <sup>a</sup>	6.91 <sup>a</sup>	6.99	1990
70	13.86	7.97 <sup>a</sup>	7.72 <sup>a</sup>	7.85	1766
75	13.80	12.31 <sup>c</sup>	12.31 <sup>c</sup>	12.31	1121
80	13.84	13.37 <sup>a</sup>	13.25 <sup>a</sup>	13.31	1040
85	14.05	12.09 <sup>a</sup>	12.06 <sup>a</sup>	12.08	1163
90	13.89	14.00 <sup>a</sup>	14.25 <sup>a</sup>	14.13	984
95	13.92	14.12 <sup>a</sup>	14.12 <sup>a</sup>	14.12	986
100	13.90	15.31 <sup>c</sup>	15.50 <sup>c</sup>	15.41	903
105	13.79	12.44 <sup>a</sup>	12.44 <sup>a</sup>	12.44	1108
110	13.81	12.75 <sup>a</sup>	12.75 <sup>a</sup>	12.75	1083
115	13.74	11.87 <sup>a</sup>	11.62 <sup>a</sup>	11.75	1169
120	13.85	11.75 <sup>a</sup>	11.37 <sup>a</sup>	11.56	1198
125	13.94	10.87 <sup>a</sup>	11.06 <sup>a</sup>	10.97	1271
130	13.81	10.50 <sup>a</sup>	10.62 <sup>a</sup>	10.56	1308
135	13.86	10.69 <sup>c</sup>	10.62 <sup>c</sup>	10.66	1300
140	13.96	6.25 <sup>b</sup>	6.19 <sup>b</sup>	6.22	2245
145	14.09	5.81 <sup>a</sup>	6.00 <sup>a</sup>	5.91	2386
150	14.04	5.75 <sup>b</sup>	6.00 <sup>b</sup>	5.88	2389
155	14.20	6.19 <sup>a</sup>	6.19 <sup>a</sup>	6.19	2294

Table 8.A.1-21 (continued)

Interval SV-Wave Velocities Measured at Gilroy 2 Between B3 and B4 (R2-R3, Forward Profile), Path 3

Depth (ft)	Travel Path Distance <sup>1</sup> (ft)	SV-Up Travel Time (ms)	SV-Down Travel Time (ms)	Average SV Travel Time (ms)	SV-Wave Velocity (fps)
(1)	(2)	(3)	(4)	(5)	(6)
160	14.41	5.94 <sup>b</sup>	6.06 <sup>b</sup>	6.00	2402
165	14.44	6.87 <sup>c</sup>	7.00 <sup>c</sup>	6.94	2082
170	14.47	4.87 <sup>b</sup>	4.87 <sup>b</sup>	4.87	2972
175	14.56	4.94 <sup>a</sup>	4.94 <sup>a</sup>	4.94	2948
180	14.40	4.87 <sup>a</sup>	4.81 <sup>a</sup>	4.84	2976
185	14.59	4.62 <sup>a</sup>	4.62 <sup>a</sup>	4.62	3159
190	14.71	5.56 <sup>b</sup>	5.38 <sup>b</sup>	5.47	2689
195	14.85	6.13 <sup>c</sup>	— <sup>d</sup>	6.13	2425

Notes on Table 8.A.1-21:

- <sup>1</sup> center-to-center spacings determined using borehole survey data from Agbabian Associates, Pasadena, California
- <sup>a</sup> initial wave arrival clearly identified (within 5% of total travel time)—Type I data
- <sup>b</sup> initial wave arrival less distinct than (a) but identifiable (within 10% of total travel time)—Type II data
- <sup>c</sup> some interpretation required to identify initial wave arrival—Type III data
- <sup>d</sup> initial wave arrival not identifiable
- <sup>e</sup> measurement not performed

Table 8.A.1-22

Direct SV-Wave Velocities Measured at Gilroy 2 Between B4 and B3 (S-R1, Reverse Profile), Path 3

Depth (ft)	Center- to- Center Dist <sup>1</sup> (ft)	Travel Path Dist. <sup>2</sup> (ft)	SV-Up Travel Time (ms)	Adjusted Up Travel Time <sup>3</sup> (ms)	SV- Down Travel Time (ms)	Adjusted Down Travel Time <sup>4</sup> (ms)	Average SV-Wave Travel Time (ms)	SV-Wave Velocity (fps)
(1)	(2)	(3)	(4)	(5)	(6)	(7)	(8)	(9)

5	14.20	13.87	— <sup>d</sup>	—	18.37 <sup>b</sup>	18.43	18.43	752
15	14.17	13.83	20.87 <sup>a</sup>	20.97 <sup>a</sup>	20.50 <sup>a</sup>	20.56	20.77	666
25	14.11	13.78	20.31 <sup>a</sup>	20.41 <sup>a</sup>	20.00 <sup>a</sup>	20.06	20.24	681
35	14.06	13.73	11.50 <sup>a</sup>	11.60 <sup>a</sup>	11.56 <sup>a</sup>	11.62	11.61	1183
45	14.00	13.67	10.44 <sup>c</sup>	10.54 <sup>c</sup>	10.44 <sup>c</sup>	10.50	10.52	1299
55	13.97	13.64	9.19 <sup>b</sup>	9.29	9.06 <sup>a</sup>	9.12	9.21	1481
65	13.90	13.57	7.94 <sup>b</sup>	8.04	7.81 <sup>a</sup>	7.87	7.96	1706
75	13.80	13.46	8.25 <sup>b</sup>	8.35	8.31 <sup>a</sup>	8.37	8.36	1611
85	14.05	13.71	13.75 <sup>a</sup>	13.85	13.19 <sup>a</sup>	13.25	13.55	1012
95	13.92	13.59	13.44 <sup>a</sup>	13.54	13.31 <sup>a</sup>	13.37	13.46	1010
105	13.79	13.46	12.37 <sup>a</sup>	12.47	12.56 <sup>a</sup>	12.62	12.55	1073
115	13.74	13.40	12.50 <sup>a</sup>	12.60	12.69 <sup>a</sup>	12.75	12.68	1058
125	13.94	13.60	10.00 <sup>a</sup>	10.10	10.31 <sup>a</sup>	10.31	10.21	1333
135	13.86	13.52	10.69 <sup>b</sup>	10.72	10.50 <sup>b</sup>	10.50	10.61	1275
145	14.10	13.77	7.94 <sup>a</sup>	7.97	5.62 <sup>a</sup>	5.62	6.80	2026
155	14.24	13.90	5.81 <sup>a</sup>	5.84	6.12 <sup>a</sup>	6.12	5.98	2325
165	14.51	14.17	— <sup>d</sup>	—	6.37 <sup>a</sup>	6.37	6.37	2225
175	14.62	14.28	4.56 <sup>a</sup>	4.59	4.87 <sup>a</sup>	4.87	4.73	3020
185	14.63	14.30	5.19 <sup>a</sup>	5.22	5.31 <sup>a</sup>	5.31	5.27	2715
195	14.89	14.56	10.62 <sup>b</sup>	10.65	10.06 <sup>b</sup>	10.06	10.36	1406

Notes on Table 8.A.1-22:

- <sup>1</sup> center-to-center spacings determined using borehole survey data from Agbabian Associates, Pasadena, California
- <sup>2</sup> one-half borehole diameter of only the source borehole (2 in.) is subtracted from the center-to-center spacing due to the assumed average position of the receiver in the center of the borehole
- <sup>3</sup> calibration factor (trigger delay) = -0.03 ms, 0-125 ft; calibration factor = -0.10 ms, 135-390 ft
- <sup>4</sup> calibration factor (trigger delay) = 0.00 ms, 0-115 ft; calibration factor = -0.06 ms, 125-390 ft
- <sup>a</sup> initial wave arrival clearly identified (within 5% of total travel time)—Type I data
- <sup>b</sup> initial wave arrival less distinct than (a) but identifiable (within 10% of total travel time)—Type II data
- <sup>c</sup> some interpretation required to identify initial wave arrival—Type III data
- <sup>d</sup> measurement not performed

Table 8.A.1-23

Interval SV-Wave Velocities Measured at Gilroy 2 Between B3 and B2 (R1-R2, Reverse Profile), Path 2

Depth (ft)	Travel Path Distance <sup>1</sup> (ft)	SV-Up Travel Time (ms)	SV-Down Travel Time (ms)	Average SV Travel Time (ms)	SV-Wave Velocity (fps)
(1)	(2)	(3)	(4)	(5)	(6)
5	13.61	25.87 <sup>b</sup>	26.00 <sup>b</sup>	25.94	525
15	13.57	19.12 <sup>a</sup>	19.31 <sup>a</sup>	19.22	706
25	13.53	19.12 <sup>a</sup>	19.37 <sup>a</sup>	19.25	703
35	13.60	12.50 <sup>b</sup>	12.69 <sup>b</sup>	12.60	1080
45	13.71	9.56 <sup>c</sup>	10.12 <sup>c</sup>	9.84	1393
55	13.72	7.50 <sup>b</sup>	8.37 <sup>b</sup>	7.94	1729
65	13.68	7.25 <sup>b</sup>	7.31 <sup>b</sup>	7.28	1879
75	13.59	8.19 <sup>c</sup>	9.19 <sup>c</sup>	8.69	1563
85	13.68	13.87 <sup>b</sup>	13.69 <sup>b</sup>	13.78	993
95	13.65	14.81 <sup>a</sup>	14.75 <sup>a</sup>	14.78	923
105	13.71	13.25 <sup>a</sup>	13.31 <sup>a</sup>	13.28	1033
115	13.73	12.44 <sup>a</sup>	12.44 <sup>a</sup>	12.44	1104
125	13.55	12.06 <sup>b</sup>	11.94 <sup>b</sup>	12.00	1129
135	13.43	12.00 <sup>b</sup>	11.75 <sup>b</sup>	11.88	1131
145	13.09	7.69 <sup>a</sup>	7.94 <sup>a</sup>	7.82	1675
155	12.97	7.94 <sup>a</sup>	8.06 <sup>a</sup>	8.00	1621
165	12.40	8.62 <sup>b</sup>	7.87 <sup>b</sup>	8.25	1504
175	12.35	5.81 <sup>a</sup>	5.87 <sup>a</sup>	5.84	2115
185	12.59	6.19 <sup>b</sup>	5.94 <sup>b</sup>	6.07	2075
195	12.46	10.87 <sup>b</sup>	10.25 <sup>b</sup>	10.56	1180

Notes on Table 8.A.1-23:

- <sup>1</sup> center-to-center spacings determined using borehole survey data from Agbabian Associates, Pasadena, California
- <sup>a</sup> initial wave arrival clearly identified (within 5% of total travel time)—Type I data
- <sup>b</sup> initial wave arrival less distinct than (a) but identifiable (within 10% of total travel time)—Type II data
- <sup>c</sup> some interpretation required to identify initial wave arrival—Type III data
- <sup>d</sup> measurement not performed

Table 8.A.1-24

Interval SV-Wave Velocities Measured at Gilroy 2 Between B2 and B1 (R2-R3, Reverse Profile), Path 1

Depth (ft)	Travel Path Distance <sup>1</sup> (ft)	SV-Up Travel Time (ms)	SV-Down Travel Time (ms)	Average SV Travel Time (ms)	SV-Wave Velocity (fps)
(1)	(2)	(3)	(4)	(5)	(6)
5	14.02	19.06 <sup>b</sup>	18.50 <sup>b</sup>	18.78	747
15	14.08	20.31 <sup>a</sup>	20.31 <sup>a</sup>	20.31	693
25	14.13	24.62 <sup>a</sup>	24.19 <sup>a</sup>	24.41	579
35	14.04	15.00 <sup>b</sup>	15.31 <sup>b</sup>	15.16	927
45	13.98	10.50 <sup>c</sup>	9.81 <sup>c</sup>	10.16	1376
55	14.01	7.50 <sup>b</sup>	7.50 <sup>b</sup>	7.50	1869
65	14.15	8.44 <sup>b</sup>	8.25 <sup>b</sup>	8.35	1696
75	14.15	8.37 <sup>c</sup>	8.37 <sup>c</sup>	8.37	1690
85	13.89	14.50 <sup>b</sup>	14.50 <sup>b</sup>	14.50	958
95	13.82	15.06 <sup>b</sup>	15.06 <sup>b</sup>	15.06	918
105	13.75	13.37 <sup>a</sup>	13.37 <sup>a</sup>	13.37	1029
115	13.65	12.94 <sup>a</sup>	12.81 <sup>a</sup>	12.88	1061
125	13.64	11.44 <sup>a</sup>	11.44 <sup>a</sup>	11.44	1192
135	13.74	12.06 <sup>c</sup>	— <sup>d</sup>	12.06	1139
145	13.84	7.12 <sup>b</sup>	6.94 <sup>b</sup>	7.03	1968
155	14.00	7.75 <sup>b</sup>	7.62 <sup>b</sup>	7.69	1822
165	14.26	7.25 <sup>c</sup>	7.31 <sup>c</sup>	7.28	1959
175	14.17	5.75 <sup>b</sup>	5.75 <sup>b</sup>	5.75	2465
185	14.12	5.81 <sup>b</sup>	5.81 <sup>b</sup>	5.81	2431
195	14.16	13.75 <sup>b</sup>	13.56 <sup>b</sup>	13.66	1037

Notes on Table 8.A.1-24:

- <sup>1</sup> center-to-center spacings determined using borehole survey data from Agbabian Associates, Pasadena, California
- <sup>a</sup> initial wave arrival clearly identified (within 5% of total travel time)—Type I data
- <sup>b</sup> initial wave arrival less distinct than (a) but identifiable (within 10% of total travel time)—Type II data
- <sup>c</sup> some interpretation required to identify initial wave arrival—Type III data
- <sup>d</sup> initial wave arrival not identifiable

Table 8.A.1-25

Direct SH-Wave Velocities Measured at Gilroy 2 Between B1 and B2 (S-R1, Forward Profile), Path 1

Depth (ft)	Center -to- Center Dist. <sup>1</sup> (ft)	Travel Path Dist. <sup>2</sup> (ft)	SH-East Travel Time (ms)	Adjusted East Travel Time <sup>3</sup> (ms)	SH-West Travel Time (ms)	Adjusted West Travel Time <sup>3</sup> (ms)	Average SH Travel Time (ms)	SH-Wave Velocity (fps)
(1)	(2)	(3)	(4)	(5)	(6)	(7)	(8)	(9)
5	14.02	13.85	22.12 <sup>b</sup>	22.02	22.87 <sup>b</sup>	22.77	22.40	619
7.5	14.03	13.86	— <sup>d</sup>	—	— <sup>d</sup>	—	—	—
10	14.06	13.89	22.25 <sup>b</sup>	22.15	22.25 <sup>b</sup>	22.15	22.15	627
15	14.08	13.91	21.62 <sup>a</sup>	21.52	21.56 <sup>a</sup>	21.46	21.49	647
20	14.10	13.93	24.25 <sup>b</sup>	24.15	24.12 <sup>b</sup>	24.02	24.09	578
25	14.13	13.96	22.69 <sup>c</sup>	22.59	22.62 <sup>c</sup>	22.52	22.56	619
30	14.12	13.95	23.12 <sup>a</sup>	23.02	23.00 <sup>a</sup>	22.90	22.96	608
35	14.04	13.88	15.22 <sup>c</sup>	15.12	15.19 <sup>c</sup>	15.09	15.11	919
40	14.00	13.83	16.31 <sup>b</sup>	16.21	16.50 <sup>b</sup>	16.40	16.31	848
45	13.98	13.81	— <sup>d</sup>	—	— <sup>d</sup>	—	—	—
50	13.96	13.79	10.25 <sup>a</sup>	10.15	10.25 <sup>a</sup>	10.15	10.15	1359
55	14.01	13.85	— <sup>d</sup>	—	— <sup>d</sup>	—	—	—
60	14.06	13.89	7.75 <sup>a</sup>	7.65	7.87 <sup>a</sup>	7.77	7.71	1802
65	14.15	13.99	— <sup>d</sup>	—	— <sup>d</sup>	—	—	—
70	14.14	13.98	8.19 <sup>b</sup>	8.09	8.25 <sup>b</sup>	8.15	8.12	1721
75	14.16	13.99	— <sup>d</sup>	—	— <sup>d</sup>	—	—	—
80	13.98	13.81	12.44 <sup>c</sup>	12.34	12.69 <sup>c</sup>	12.59	12.47	1108
85	13.89	13.73	14.81 <sup>a</sup>	14.71	15.00 <sup>a</sup>	14.90	14.81	927
90	13.75	13.58	15.25 <sup>a</sup>	15.15	15.44 <sup>a</sup>	15.34	15.25	891
95	13.82	13.66	13.12 <sup>a</sup>	13.02	13.12 <sup>a</sup>	13.02	13.02	1049
100	13.82	13.66	17.19 <sup>a</sup>	17.09	17.12 <sup>a</sup>	17.02	17.06	801
105	13.76	13.59	14.87 <sup>a</sup>	14.77	14.87 <sup>a</sup>	14.77	14.77	920
110	13.69	13.52	15.00 <sup>a</sup>	14.90	15.00 <sup>a</sup>	14.90	14.90	908
115	13.66	13.49	14.37 <sup>a</sup>	14.27	14.25 <sup>a</sup>	14.15	14.21	949
120	13.65	13.48	13.81 <sup>a</sup>	13.71	13.75 <sup>a</sup>	13.65	13.68	985

Notes on Table 8.A.1-25:

- <sup>1</sup> center-to-center spacings determined using borehole survey data from Agbabian Associates, Pasadena, California
- <sup>2</sup> a one-half borehole diameter of the receiver borehole (total 2 in.) is subtracted from the center-to-center spacings due to the positioning of the receiver in B2
- <sup>3</sup> calibration factor (trigger delay)= 0.1 ms
- <sup>a</sup> initial wave arrival clearly identified (within 5% of total travel time)—Type I data
- <sup>b</sup> initial wave arrival less distinct than (a) but identifiable (within 10% of total travel time)—Type II data
- <sup>c</sup> some interpretation required to identify initial wave arrival—Type III data
- <sup>d</sup> measurement not performed

Table 8.A.1-26

Interval SH-Wave Velocities Measured at Gilroy 2 Between B2 and B3 (R1–R2, Forward Profile), Path 2

Depth (ft)	Travel Path Distance <sup>1</sup> (ft)	SH-East Travel Time (ms)	SH-West Travel Time (ms)	Average SH Travel Time (ms)	SH-Wave Velocity (fps)
(1)	(2)	(3)	(4)	(5)	(6)
5	13.61	20.31 <sup>c</sup>	20.00 <sup>c</sup>	20.16	675
7.5	13.60	— <sup>e</sup>	— <sup>e</sup>	—	—
10	13.57	26.25 <sup>b</sup>	26.81 <sup>b</sup>	26.53	512
15	13.57	24.44 <sup>c</sup>	24.44 <sup>c</sup>	24.44	555
20	13.57	22.19 <sup>b</sup>	23.31 <sup>b</sup>	22.75	596
25	13.53	22.31 <sup>c</sup>	22.75 <sup>c</sup>	22.53	601
30	13.60	20.37 <sup>a</sup>	20.50 <sup>a</sup>	20.44	666
35	13.60	16.62 <sup>a</sup>	16.69 <sup>a</sup>	16.66	817
40	13.61	15.94 <sup>c</sup>	15.94 <sup>c</sup>	15.94	854
45	13.71	— <sup>e</sup>	— <sup>e</sup>	—	—
50	13.76	7.94 <sup>a</sup>	8.25 <sup>a</sup>	8.10	1699
55	13.72	— <sup>e</sup>	— <sup>e</sup>	—	—
60	13.75	7.12 <sup>c</sup>	— <sup>d</sup>	7.12	1931
65	13.68	— <sup>e</sup>	— <sup>e</sup>	—	—
70	13.66	7.12 <sup>b</sup>	7.12 <sup>b</sup>	7.12	1919
75	13.58	— <sup>e</sup>	— <sup>e</sup>	—	—
80	13.65	— <sup>d</sup>	— <sup>d</sup>	—	—
85	13.67	13.50 <sup>a</sup>	13.50 <sup>a</sup>	13.50	1013
90	13.77	13.81 <sup>a</sup>	13.62 <sup>a</sup>	13.72	1004
95	13.64	12.56 <sup>a</sup>	12.37 <sup>a</sup>	12.47	1094
100	13.66	15.44 <sup>a</sup>	15.37 <sup>a</sup>	15.41	887
105	13.71	14.50 <sup>a</sup>	14.31 <sup>a</sup>	14.41	952
110	13.71	14.56 <sup>a</sup>	14.56 <sup>a</sup>	14.56	942
115	13.73	14.25 <sup>a</sup>	14.25 <sup>a</sup>	14.25	964
120	13.61	13.62 <sup>a</sup>	13.62 <sup>a</sup>	13.62	1000

Notes on Table 8.A.1-26:

<sup>1</sup> center-to-center spacings determined using borehole survey data from Agbabian Associates, Pasadena, California<sup>a</sup> initial wave arrival clearly identified (within 5% of total travel time)—Type I data<sup>b</sup> initial wave arrival less distinct than (a) but identifiable (within 10% of total travel time)—Type II data<sup>c</sup> some interpretation required to identify initial wave arrival—Type III data<sup>d</sup> initial wave arrival not identifiable<sup>e</sup> measurement not performed



Table 8.A.1-27

Interval SH-Wave Velocities Measured at Gilroy 2 Between B3 and B4 (R2-R3, Forward Profile), Path 3

Depth (ft)	Center-to-Center Distance <sup>1</sup> (ft)	Travel Path Distance <sup>2</sup> (ft)	SH-East Travel Time (ms)	SH-West Travel Time (ms)	Average SH Travel Time (ms)	SH-Wave Velocity (fps)
(1)	(2)	(3)	(4)	(5)	(6)	(7)
5	14.20	14.37	— <sup>e</sup>	— <sup>e</sup>	—	—
7.5	14.18	14.35	— <sup>e</sup>	— <sup>e</sup>	—	—
10	14.18	14.35	25.50 <sup>c</sup>	24.56 <sup>c</sup>	25.03	573
15	14.17	14.33	— <sup>e</sup>	— <sup>e</sup>	—	—
20	14.12	14.28	22.50 <sup>c</sup>	21.00 <sup>c</sup>	21.75	649
25	14.11	14.27	— <sup>e</sup>	— <sup>e</sup>	—	—
30	14.08	14.25	18.19 <sup>c</sup>	18.19 <sup>c</sup>	18.19	783
35	14.06	14.23	15.06 <sup>c</sup>	— <sup>d</sup>	15.06	945
40	14.10	14.27	— <sup>d</sup>	— <sup>d</sup>	—	—
45	14.00	14.16	— <sup>e</sup>	— <sup>e</sup>	—	—
50	14.02	14.18	8.94 <sup>b</sup>	8.94 <sup>b</sup>	8.94	1587
55	13.97	14.13	— <sup>e</sup>	— <sup>e</sup>	—	—
60	13.87	14.04	7.37 <sup>c</sup>	7.50 <sup>c</sup>	7.44	1888
65	13.90	14.07	— <sup>e</sup>	— <sup>e</sup>	—	—
70	13.86	14.02	7.69 <sup>c</sup>	— <sup>e</sup>	7.69	1823
75	13.80	13.96	— <sup>e</sup>	— <sup>e</sup>	—	—
80	13.84	14.00	— <sup>d</sup>	— <sup>d</sup>	—	—
85	14.05	14.21	12.31 <sup>a</sup>	12.31 <sup>a</sup>	12.31	1155
90	13.89	14.06	15.87 <sup>a</sup>	15.87 <sup>a</sup>	15.87	886
95	13.92	14.09	13.25 <sup>c</sup>	13.19 <sup>c</sup>	13.22	1066
100	13.90	14.07	15.06 <sup>a</sup>	15.06 <sup>a</sup>	15.06	934
105	13.79	13.96	14.12 <sup>a</sup>	14.31 <sup>a</sup>	14.22	982
110	13.81	13.97	14.12 <sup>a</sup>	14.12 <sup>a</sup>	14.12	990
115	13.74	13.90	13.37 <sup>a</sup>	13.56 <sup>a</sup>	13.47	1032
120	13.85	14.02	12.87 <sup>a</sup>	12.87 <sup>a</sup>	12.87	1089

Notes on Table 8.A.1-27:

- <sup>1</sup> center-to-center spacings determined using borehole survey data from Agbabian Associates, Pasadena, California
- <sup>2</sup> a one-half diameter of B4 (total 2 in.) is added to the center-to-center spacings because of the position of the receiver in B4
- <sup>a</sup> initial wave arrival clearly identified (within 5% of total travel time)—Type I data
- <sup>b</sup> initial wave arrival less distinct than (a) but identifiable (within 10% of total travel time)—Type II data
- <sup>c</sup> some interpretation required to identify initial wave arrival—Type III data
- <sup>d</sup> initial wave arrival not identifiable
- <sup>e</sup> measurement not performed

Table 8.A.1-28

Direct P-Wave Velocities Measured at Gilroy 2 Between B1 and B2 (S-R1, Forward Profile), Path 1

Depth (ft)	Center -to- Center Dist. <sup>1</sup> (ft)	Travel Path Dist. <sup>2</sup> (ft)	Wedge and Hammer Source <sup>3</sup>			Solenoid Source <sup>4</sup>		
			Travel Time (ms)	Adjusted Travel Time <sup>5</sup> (ms)	P-Wave Velocity (fps)	Travel Time (ms)	Adjusted Travel Time <sup>6</sup> (ms)	P-Wave Velocity (fps)
(1)	(2)	(3)	(4)	(5)	(6)	(7)	(8)	(9)
5	14.02	13.81	12.53a	12.57	1099	11.50b	11.40	1197
7.5	14.03	13.82	12.06a	12.10	1142	—d	—	—
10	14.06	13.85	10.00a	10.04	1379	11.28b	11.18	1224
15	14.08	13.87	11.34a	11.38	1219	10.22b	10.12	1354
20	14.10	13.89	8.44a	8.48	1638	6.50a	6.40	2144
25	14.13	13.92	7.06b	7.10	1961	5.53b	5.43	2533
30	14.12	13.91	7.64c	7.68	1811	9.50c	9.40	1462
35	14.04	13.83	7.31c	7.35	1882	9.34b	9.24	1479
40	14.00	13.79	6.25b	6.29	2193	4.41c	4.31	3161
45	13.98	13.77	3.44a	3.48	3956	—d	—	—
50	13.96	13.75	3.67b	3.71	3707	2.94c	2.84	4783
55	14.01	13.81	5.53b	5.57	2479	—d	—	—
60	14.06	13.85	5.12b	5.16	2684	3.16a	3.06	4472
65	14.15	13.94	4.38a	4.42	3155	—d	—	—
70	14.14	13.93	2.56a	2.60	5359	2.44a	2.34	5883
75	14.16	13.95	2.81a	2.85	4894	—d	—	—
80	13.98	13.77	2.75a	2.79	4935	2.81a	2.71	5019
85	13.89	13.68	2.82a	2.86	4784	2.88a	2.78	4862
90	13.75	13.54	2.73a	2.77	4887	2.84a	2.74	4880
95	13.82	13.62	2.70a	2.74	4969	2.78a	2.68	5018
100	13.82	13.62	2.84a	2.88	4728	2.88a	2.78	4838
105	13.76	13.55	2.69a	2.73	4963	2.75a	2.65	5050
110	13.69	13.48	2.69a	2.73	4939	2.78a	2.68	4969
115	13.66	13.45	2.78a	2.82	4769	2.81a	2.71	4901
120	13.65	13.44	2.59a	2.63	5110	2.69a	2.59	5125
125	13.64	13.43	2.78a	2.82	4762	—d	—	—
130	13.72	13.51	2.78a	2.82	4790	—d	—	—
135	13.74	13.54	2.75a	2.79	4851	—d	—	—
140	13.88	13.67	2.56a	2.60	5259	—d	—	—

Table 8.A.1-28 (continued)

Direct P-Wave Velocities Measured at Gilroy 2 Between B1 and B2 (S-R1, Forward Profile), Path 1

Depth (ft)	Center -to- Center Dist. <sup>1</sup> (ft)	Travel Path Dist. <sup>2</sup> (ft)	Wedge and Hammer Source <sup>3</sup>			Solenoid Source <sup>4</sup>		
			Travel Time (ms)	Adjusted Travel Time <sup>5</sup> (ms)	P-Wave Velocity (fps)	Travel Time (ms)	Adjusted Travel Time <sup>6</sup> (ms)	P-Wave Velocity (fps)
(1)	(2)	(3)	(4)	(5)	(6)	(7)	(8)	(9)
145	13.84	13.63	2.31 <sup>a</sup>	2.35	5800	— <sup>d</sup>	—	—
150	13.87	13.66	2.44 <sup>a</sup>	2.48	5509	— <sup>d</sup>	—	—
155	14.01	13.80	2.50 <sup>a</sup>	2.54	5432	— <sup>d</sup>	—	—
160	14.12	13.92	2.53 <sup>a</sup>	2.57	5415	— <sup>d</sup>	—	—
165	14.27	14.06	2.44 <sup>a</sup>	2.48	5668	— <sup>d</sup>	—	—
170	14.25	14.04	2.09 <sup>a</sup>	2.13	6592	— <sup>d</sup>	—	—
175	14.17	13.97	2.16 <sup>a</sup>	2.20	6348	— <sup>d</sup>	—	—
180	14.15	13.95	2.22 <sup>a</sup>	2.26	6171	— <sup>d</sup>	—	—
185	14.12	13.91	2.12 <sup>a</sup>	2.16	6442	— <sup>d</sup>	—	—
190	14.15	13.95	2.28 <sup>a</sup>	2.32	6011	— <sup>d</sup>	—	—
195	14.16	13.95	2.81 <sup>a</sup>	2.85	4896	— <sup>d</sup>	—	—
200	14.16	13.95	1.95 <sup>a</sup>	1.99	7010	— <sup>d</sup>	—	—
205	14.22	14.01	1.99 <sup>a</sup>	2.03	6900	— <sup>d</sup>	—	—
210	14.32	14.11	2.06 <sup>a</sup>	2.10	6718	— <sup>d</sup>	—	—
215	14.37	14.16	2.24 <sup>a</sup>	2.28	6210	— <sup>d</sup>	—	—
220	14.54	14.34	2.16 <sup>a</sup>	2.20	6516	— <sup>d</sup>	—	—
225	14.74	14.53	2.40 <sup>a</sup>	2.44	5956	— <sup>d</sup>	—	—
230	14.87	14.66	2.44 <sup>a</sup>	2.48	5912	— <sup>d</sup>	—	—
235	14.69	14.48	2.60 <sup>a</sup>	2.64	5486	— <sup>d</sup>	—	—
240	14.43	14.22	2.11 <sup>a</sup>	2.15	6615	— <sup>d</sup>	—	—
245	14.49	14.28	2.31 <sup>a</sup>	2.35	6076	— <sup>d</sup>	—	—
250	14.34	14.13	2.49 <sup>a</sup>	2.53	5585	— <sup>d</sup>	—	—
255	14.21	14.00	2.54 <sup>b</sup>	2.58	5426	— <sup>d</sup>	—	—
260	14.35	14.15	2.46 <sup>a</sup>	2.50	5658	— <sup>d</sup>	—	—
265	14.27	14.06	2.44 <sup>a</sup>	2.48	5669	— <sup>d</sup>	—	—
269	14.33	14.13	2.96 <sup>b</sup>	3.00	4708	— <sup>d</sup>	—	—
275	14.18	13.97	3.34 <sup>b</sup>	3.38	4134	— <sup>d</sup>	—	—
280	14.05	13.84	3.12 <sup>b</sup>	3.16	4379	— <sup>d</sup>	—	—
285	14.16	13.95	2.92 <sup>a</sup>	2.96	4713	— <sup>d</sup>	—	—
290	14.20	13.99	2.58 <sup>a</sup>	2.62	5341	— <sup>d</sup>	—	—

Table 8.A.1-28 (continued)

Direct P-Wave Velocities Measured at Gilroy 2 Between B1 and B2 (S-R1, Forward Profile), Path 1

Depth (ft)	Center -to- Center Dist. <sup>1</sup> (ft)	Travel Path Dist. <sup>2</sup> (ft)	Wedge and Hammer Source <sup>3</sup>			Solenoid Source <sup>4</sup>		
			Travel Time (ms)	Adjusted Travel Time <sup>5</sup> (ms)	P-Wave Velocity (fps)	Travel Time (ms)	Adjusted Travel Time <sup>6</sup> (ms)	P-Wave Velocity (fps)
(1)	(2)	(3)	(4)	(5)	(6)	(7)	(8)	(9)
295	14.22	14.02	2.72 <sup>b</sup>	2.76	5078	— <sup>d</sup>	—	—
300	14.13	13.92	2.85 <sup>a</sup>	2.89	4817	— <sup>d</sup>	—	—
305	14.04	13.83	3.17 <sup>a</sup>	3.21	4308	— <sup>d</sup>	—	—
310	14.12	13.91	2.68 <sup>a</sup>	2.72	5113	— <sup>d</sup>	—	—
315	14.11	13.90	2.62 <sup>a</sup>	2.66	5226	— <sup>d</sup>	—	—
320	14.13	13.92	2.77 <sup>a</sup>	2.81	4954	— <sup>d</sup>	—	—
325	14.30	14.09	2.31 <sup>a</sup>	2.35	5995	— <sup>d</sup>	—	—
330	14.28	14.07	2.53 <sup>a</sup>	2.57	5474	— <sup>d</sup>	—	—
335	14.27	14.06	2.63 <sup>a</sup>	2.67	5265	— <sup>d</sup>	—	—
340	14.20	13.99	2.96 <sup>a</sup>	3.00	4664	— <sup>d</sup>	—	—
345	14.14	13.93	2.70 <sup>a</sup>	2.74	5083	— <sup>d</sup>	—	—
350	14.21	14.01	2.38 <sup>a</sup>	2.42	5788	— <sup>d</sup>	—	—
355	14.26	14.05	2.48 <sup>a</sup>	2.52	5577	— <sup>d</sup>	—	—
360	14.20	14.00	2.48 <sup>a</sup>	2.52	5554	— <sup>d</sup>	—	—
365	14.08	13.87	2.54 <sup>a</sup>	2.58	5377	— <sup>d</sup>	—	—
370	14.20	13.99	2.89 <sup>a</sup>	2.93	4775	— <sup>d</sup>	—	—
375	14.05	13.84	2.64 <sup>b</sup>	2.68	5163	— <sup>d</sup>	—	—
380	14.04	13.83	2.81 <sup>a</sup>	2.85	4854	— <sup>d</sup>	—	—
385	13.98	13.77	2.79 <sup>b</sup>	2.83	4865	— <sup>d</sup>	—	—
390	13.96	13.75	2.51 <sup>a</sup>	2.55	5393	— <sup>d</sup>	—	—

Notes on Table 8.A.1-28:

- <sup>1</sup> center-to-center spacings determined using borehole survey data from Agbabian Associates, Pasadena, California
- <sup>2</sup> — for the wedge hammer source, one-half borehole diameter of only the source borehole (2.5 in.) is subtracted from the center-to-center spacing due to the assumed average position of the receiver in the center of the receiver borehole  
— for the solenoid source, one-half borehole diameter of both the source and receiver boreholes (4.5 in.) is subtracted from the center-to-center spacing due to the position of the receiver in the borehole
- <sup>3</sup> wedge and hammer source consists of a hammer impacting a pneumatically-locking wedge in the borehole
- <sup>4</sup> solenoid source produces a horizontal impact from the plunger of the solenoid
- <sup>5</sup> calibration factor (trigger delay) = -0.04 ms
- <sup>6</sup> calibration factor (trigger delay) = -0.04 ms
- <sup>a</sup> initial wave arrival clearly identified (within 5% of total travel time)—Type I data
- <sup>b</sup> initial wave arrival less distinct than (a) but identifiable (within 10% of total travel time)—Type II data
- <sup>c</sup> some interpretation required to identify initial wave arrival—Type III data
- <sup>d</sup> measurement not performed

Table 8.A.1-29

Interval P-Wave Velocities Measured at Gilroy 2 Between B2 and B3 (R1-R2, Forward Profile), Path 2

Depth (ft)	Travel Path Distance <sup>1</sup> (ft)	Wedge and Hammer Source <sup>2</sup>		Solenoid Source <sup>3</sup>	
		Travel Time (ms)	P-Wave Velocity (fps)	Travel Time (ms)	P-Wave Velocity (fps)
(1)	(2)	(3)	(4)	(5)	(6)
5	13.61	13.69 <sup>a</sup>	994	12.94 <sup>b</sup>	1052
7.5	13.60	— <sup>e</sup>	—	— <sup>e</sup>	—
10	13.57	— <sup>e</sup>	—	— <sup>d</sup>	—
15	13.57	15.97 <sup>b</sup>	850	— <sup>d</sup>	—
20	13.57	— <sup>e</sup>	—	— <sup>d</sup>	—
25	13.53	— <sup>e</sup>	—	— <sup>d</sup>	—
30	13.60	— <sup>e</sup>	—	9.53 <sup>c</sup>	1427
35	13.60	— <sup>e</sup>	—	9.25 <sup>c</sup>	1470
40	13.61	— <sup>e</sup>	—	— <sup>d</sup>	—
45	13.71	— <sup>e</sup>	—	— <sup>e</sup>	—
50	13.76	— <sup>e</sup>	—	3.06 <sup>c</sup>	4495
55	13.72	— <sup>e</sup>	—	— <sup>e</sup>	—
60	13.75	— <sup>e</sup>	—	4.50 <sup>c</sup>	3056
65	13.68	— <sup>e</sup>	—	— <sup>e</sup>	—
70	13.66	— <sup>e</sup>	—	2.28 <sup>a</sup>	5993
75	13.58	— <sup>e</sup>	—	— <sup>e</sup>	—
80	13.65	— <sup>e</sup>	—	2.59 <sup>a</sup>	5269
85	13.67	2.66 <sup>a</sup>	5140	2.63 <sup>a</sup>	5198
90	13.77	2.62 <sup>a</sup>	5255	2.66 <sup>a</sup>	5176
95	13.64	2.62 <sup>a</sup>	5207	2.59 <sup>a</sup>	5267
100	13.66	2.62 <sup>a</sup>	5213	2.62 <sup>a</sup>	5213
105	13.71	2.47 <sup>a</sup>	5550	2.47 <sup>a</sup>	5550
110	13.71	2.44 <sup>a</sup>	5620	2.47 <sup>a</sup>	5552
115	13.73	2.47 <sup>a</sup>	5559	2.59 <sup>a</sup>	5301
120	13.61	2.37 <sup>a</sup>	5745	2.44 <sup>a</sup>	5580
125	13.55	2.37 <sup>a</sup>	5717	— <sup>e</sup>	—
130	13.52	2.31 <sup>a</sup>	5855	— <sup>e</sup>	—
135	13.43	2.37 <sup>a</sup>	5666	— <sup>e</sup>	—
140	13.16	2.09 <sup>a</sup>	6297	— <sup>e</sup>	—
145	13.10	1.94 <sup>a</sup>	6752	— <sup>e</sup>	—

Table 8.A.1-29 (continued)

Interval P-Wave Velocities Measured at Gilroy 2 Between B2 and B3 (R1-R2, Forward Profile), Path 2

Depth (ft)	Travel Path Distance <sup>1</sup> (ft)	Wedge and Hammer Source <sup>2</sup>		Solenoid Source <sup>3</sup>	
		Travel Time (ms)	P-Wave Velocity (fps)	Travel Time (ms)	P-Wave Velocity (fps)
(1)	(2)	(3)	(4)	(5)	(6)
150	13.20	1.69 <sup>a</sup>	7809	— <sup>e</sup>	—
155	13.00	1.87 <sup>a</sup>	6953	— <sup>e</sup>	—
160	12.73	1.84 <sup>a</sup>	6921	— <sup>e</sup>	—
165	12.47	1.62 <sup>a</sup>	7697	— <sup>e</sup>	—
170	12.37	1.56 <sup>a</sup>	7926	— <sup>e</sup>	—
175	12.40	1.69 <sup>a</sup>	7340	— <sup>e</sup>	—
180	12.59	1.56 <sup>a</sup>	8073	— <sup>e</sup>	—
185	12.62	1.81 <sup>a</sup>	6973	— <sup>e</sup>	—
190	12.59	1.81 <sup>a</sup>	6955	— <sup>e</sup>	—
195	12.50	1.94 <sup>b</sup>	6443	— <sup>e</sup>	—

Notes on Table 8.A.1-29:

- <sup>1</sup> center-to-center spacings determined using borehole survey data from Agbabian Associates, Pasadena, California
- <sup>2</sup> wedge and hammer source consists of a hammer impacting a pneumatically-locking wedge in the borehole
- <sup>3</sup> solenoid source produces a horizontal impact from the plunger of the solenoid
- <sup>a</sup> initial wave arrival clearly identified (within 5% of total travel time)—Type I data
- <sup>b</sup> initial wave arrival less distinct than (a) but identifiable (within 10% of total travel time)—Type II data
- <sup>c</sup> some interpretation required to identify initial wave arrival—Type III data
- <sup>d</sup> initial wave arrival not identifiable
- <sup>e</sup> measurement not performed

Table 8.A.1-30

Interval P-Wave Velocities Measured at Gilroy 2 Between B3 and B4 (R2-R3, Forward Profile), Path 3

Depth (ft)	Travel Path Distance <sup>1</sup> (ft)	Wedge and Hammer Source <sup>2</sup>		Solenoid Source <sup>3</sup>	
		Travel Time (ms)	P-Wave Velocities (fps)	Travel Time (ms)	P-Wave Velocities <sup>4</sup> (fps)
(1)	(2)	(3)	(4)	(5)	(6)
5	14.20	—e	—	—e	—
7.5	14.18	—e	—	—e	—
10	14.18	—e	—	—d	—
15	14.17	—e	—	—e	—
20	14.12	—e	—	—d	—
25	14.11	—e	—	—e	—
30	14.08	—e	—	—d	—
35	14.06	—e	—	—d	—
40	14.10	—e	—	—d	—
45	14.00	—e	—	—d	—
50	14.02	—e	—	—d	—
55	13.97	—e	—	—e	—
60	13.87	—e	—	3.91 <sup>c</sup>	3590
65	13.90	—e	—	—e	—
70	13.86	—e	—	—d	—
75	13.80	—e	—	—e	—
80	13.84	—e	—	2.50 <sup>a</sup>	5602
85	14.05	2.59 <sup>a</sup>	5424	2.59 <sup>a</sup>	5488
90	13.89	2.63 <sup>a</sup>	5283	2.59 <sup>a</sup>	5429
95	13.92	2.63 <sup>a</sup>	5293	2.59 <sup>a</sup>	5439
100	13.90	2.44 <sup>a</sup>	5699	2.56 <sup>a</sup>	5497
105	13.79	2.37 <sup>a</sup>	5818	2.47 <sup>a</sup>	5650
110	13.81	2.53 <sup>a</sup>	5458	2.49 <sup>a</sup>	5612
115	13.74	2.47 <sup>a</sup>	5561	2.41 <sup>a</sup>	5768
120	13.85	2.41 <sup>a</sup>	5747	2.41 <sup>a</sup>	5816
125	13.94	2.37 <sup>a</sup>	5880	—e	
130	13.81	2.41 <sup>a</sup>	5730	—e	
135	13.86	2.20 <sup>a</sup>	6298	—e	
140	13.96	2.12 <sup>a</sup>	6586	—e	
145	14.09	1.87 <sup>a</sup>	7534	—e	

Table 8.A.1-30 (continued)

Interval P-Wave Velocities Measured at Gilroy 2 Between B3 and B4 (R2-R3, Forward Profile), Path 3

Depth (ft)	Travel Path Distance <sup>1</sup> (ft)	Wedge and Hammer Source <sup>2</sup>		Solenoid Source <sup>3</sup>	
		Travel Time (ms)	P-Wave Velocities (fps)	Travel Time (ms)	P-Wave Velocities <sup>4</sup> (fps)
(1)	(2)	(3)	(4)	(5)	(6)
150	14.04	2.00 <sup>a</sup>	7019	— <sup>e</sup>	
155	14.20	1.84 <sup>a</sup>	7717	— <sup>e</sup>	
160	14.41	1.84 <sup>a</sup>	7833	— <sup>e</sup>	
165	14.44	1.84 <sup>a</sup>	7846	— <sup>e</sup>	
170	14.47	1.81 <sup>a</sup>	7996	— <sup>e</sup>	
175	14.56	1.66 <sup>a</sup>	8773	— <sup>e</sup>	
180	14.40	1.87 <sup>a</sup>	7703	— <sup>e</sup>	
185	14.59	1.81 <sup>a</sup>	8063	— <sup>e</sup>	
190	14.71	2.00 <sup>b</sup>	7356	— <sup>e</sup>	
195	14.85	1.75 <sup>b</sup>	8488	— <sup>e</sup>	

Notes on Table 8.A.1-30:

- <sup>1</sup> center-to-center spacings determined using borehole survey data from Agbabian Associates, Pasadena, California
- <sup>2</sup> wedge and hammer source consists of a hammer impacting a pneumatically-locking wedge in the borehole
- <sup>3</sup> solenoid source produces a horizontal impact from the plunger of the solenoid
- <sup>4</sup> a one-half borehole diameter was subtracted from the center-to-center travel path distance for solenoid measurements due to receiver positioning in BH #4
- <sup>a</sup> initial wave arrival clearly identified (within 5% of total travel time)—Type I data
- <sup>b</sup> initial wave arrival less distinct than (a) but identifiable (within 10% of total travel time)—Type II data
- <sup>c</sup> some interpretation required to identify initial wave arrival—Type III data
- <sup>d</sup> initial wave arrival not identifiable
- <sup>e</sup> measurement not performed



Table 8.A.1-31

Direct P-Wave Velocities Measured at Gilroy 2 Between B4 and B3 (S-R1, Reverse Profile), Path 3

Depth (ft)	Center-to-Center Distance <sup>1</sup> (ft)	Travel Path Distance <sup>2</sup> (ft)	Wedge and Hammer Source <sup>3</sup>		
			Travel Time (ms)	Adjusted Travel Time <sup>4</sup> (ms)	P-Wave Velocity (fps)
(1)	(2)	(3)	(4)	(5)	(6)
5	14.20	13.87	15.41 <sup>b</sup>	15.45	897
15	14.17	13.83	12.25 <sup>b</sup>	12.29	1126
25	14.11	13.78	5.94 <sup>b</sup>	5.98	2304
35	14.06	13.73	4.31 <sup>b</sup>	4.35	3157
45	14.00	13.67	3.41 <sup>a</sup>	3.45	3961
55	13.97	13.64	5.97 <sup>b</sup>	6.01	2269
65	13.90	13.57	4.00 <sup>b</sup>	4.04	3359
75	13.80	13.46	2.34 <sup>a</sup>	2.38	5657
85	14.05	13.71	— <sup>c</sup>	—	—
95	13.92	13.59	2.47 <sup>a</sup>	2.51	5413
105	13.79	13.46	2.31 <sup>a</sup>	2.35	5726
115	13.74	13.40	2.37 <sup>a</sup>	2.41	5562
125	13.94	13.60	2.19 <sup>a</sup>	2.23	6099
135	13.86	13.52	2.09 <sup>a</sup>	2.13	6349
145	14.10	13.77	1.69 <sup>a</sup>	1.73	7958
155	14.24	13.90	1.66 <sup>a</sup>	1.70	8178
165	14.51	14.17	1.87 <sup>a</sup>	1.91	7421
175	14.62	14.28	1.59 <sup>a</sup>	1.63	8763
185	14.63	14.30	1.66 <sup>a</sup>	1.70	8410
195	14.89	14.56	2.22 <sup>a</sup>	2.26	6442

Notes on Table 8.A.1-31:

- <sup>1</sup> center-to-center spacings determined using borehole survey data from Agbabian Associates, Pasadena, California
- <sup>2</sup> one-half borehole diameter of only the source borehole (2 in.) is subtracted from the center-to-center spacing due to the assumed average position of the receiver in the center of the receiver borehole
- <sup>3</sup> wedge and hammer source consists of a hammer impacting a pneumatically-locking wedge in the borehole
- <sup>4</sup> calibration factor (trigger delay) = -0.04 ms
- <sup>a</sup> initial wave arrival clearly identified (within 5% of total travel time)—Type I data
- <sup>b</sup> initial wave arrival less distinct than (a) but identifiable (within 10% of total travel time)—Type II data
- <sup>c</sup> measurement not performed

**Table 8.A.1-32**

Interval P-Wave Velocities Measured at Gilroy 2 Between B3 and B2 (R1-R2, Reverse Profile), Path 2

Depth (ft)	Travel Path Distance <sup>1</sup> (ft)	Wedge and Hammer Source <sup>2</sup>	
		Travel Time (ms)	P-Wave Velocity (fps)
(1)	(2)	(3)	(4)
5	13.61	13.62 <sup>b</sup>	999
15	13.57	13.19 <sup>c</sup>	1029
25	13.53	— <sup>d</sup>	—
35	13.60	— <sup>d</sup>	—
45	13.71	3.97 <sup>b</sup>	3453
55	13.72	4.67 <sup>c</sup>	2938
65	13.68	4.62 <sup>b</sup>	2961
75	13.59	2.47 <sup>a</sup>	5500
85	13.68	— <sup>e</sup>	—
95	13.65	2.66 <sup>a</sup>	5131
105	13.71	2.62 <sup>a</sup>	5234
115	13.73	2.69 <sup>a</sup>	5104
125	13.55	2.56 <sup>a</sup>	5293
135	13.43	2.62 <sup>a</sup>	5126
145	13.09	2.34 <sup>a</sup>	5592
155	12.97	2.25 <sup>a</sup>	5764
165	12.40	2.25 <sup>a</sup>	5512
175	12.35	2.12 <sup>a</sup>	5827
185	12.59	2.12 <sup>a</sup>	5937
195	12.46	2.53 <sup>a</sup>	4925

Notes on Table 8.A.1-32:

- <sup>1</sup> center-to-center spacings determined using borehole survey data from Agbabian Associates, Pasadena, California
- <sup>2</sup> drop hammer source consists of a hammer impacting a pneumatically-locking wedge in the borehole
- <sup>a</sup> initial wave arrival clearly identified (within 5% of total travel time)—Type I data
- <sup>b</sup> initial wave arrival less distinct than (a) but identifiable (within 10% of total travel time)—Type II data
- <sup>c</sup> some interpretation required to identify initial wave arrival—Type III data
- <sup>d</sup> initial wave arrival not identifiable
- <sup>e</sup> measurement not performed

Table 8.A.1-33

Interval P-Wave Velocities Measured at Gilroy 2 Between B2 and B1 (R2-R3, Reverse Profile), Path 1

Depth (ft)	Travel Path Distance <sup>1</sup> (ft)	Wedge and Hammer Source <sup>2</sup>	
		Travel Time (ms)	P-Wave Velocity (fps)
(1)	(2)	(3)	(4)
5	14.02	9.80 <sup>b</sup>	1431
15	14.08	— <sup>e</sup>	—
25	14.13	— <sup>e</sup>	—
35	14.04	— <sup>d</sup>	—
45	13.98	3.41 <sup>c</sup>	4099
55	14.01	4.53 <sup>b</sup>	3094
65	14.15	5.94 <sup>c</sup>	2382
75	14.15	2.69 <sup>b</sup>	5260
85	13.89	— <sup>e</sup>	—
95	13.82	2.66 <sup>a</sup>	5195
105	13.75	2.59 <sup>a</sup>	5310
115	13.65	2.59 <sup>a</sup>	5272
125	13.64	2.56 <sup>a</sup>	5326
135	13.74	2.37 <sup>a</sup>	5798
145	13.84	1.97 <sup>a</sup>	7025
155	14.00	2.28 <sup>a</sup>	6142
165	14.26	1.97 <sup>a</sup>	7239
175	14.17	1.94 <sup>a</sup>	7305
185	14.12	2.00 <sup>a</sup>	7061
195	14.16	1.97 <sup>b</sup>	7189

Notes on Table 8.A.1-33:

- <sup>1</sup> center-to-center spacings determined using borehole survey data from Agbabian Associates, Pasadena, California
- <sup>2</sup> wedge and hammer source consists of a hammer impacting a pneumatically-locking wedge in the borehole
- <sup>a</sup> initial wave arrival clearly identified (within 5% of total travel time)—Type I data
- <sup>b</sup> initial wave arrival less distinct than (a) but identifiable (within 10% of total travel time)—Type II data
- <sup>c</sup> some interpretation required to identify initial wave arrival—Type III data
- <sup>d</sup> initial wave arrival not identifiable
- <sup>e</sup> measurement not performed

## APPENDIX 8.A.1.B—TABULATED RESULTS OF CROSSHOLE TESTS AT TREASURE ISLAND

Table 8.A.1-34

Direct SV-Wave Velocities Measured at Treasure Island Between B3 and B2 (S-R1, Forward Profile), Path 1

Depth (ft)	Center- to- Center Dist. <sup>1</sup> (ft)	Travel Path Dist. <sup>2</sup> (ft)	SV-Up Travel Time (ms)	Adjusted Up Travel Time <sup>3</sup> (ms)	SV- Down Travel Time (ms)	Adjusted Down Travel Time <sup>4</sup> (ms)	Avg. SV Travel Time (ms)	SV-Wave Velocity (fps)
(1)	(2)	(3)	(4)	(5)	(6)	(7)	(8)	(9)
3	9.85	9.64	16.75a	16.70	16.94a	16.90	16.80	574
6	9.82	9.61	15.50a	15.45	15.44a	15.40	15.43	623
9	9.78	9.57	—d	—	24.19b	24.15	24.15	396
12	9.75	9.54	24.12a	24.07	24.00a	23.96	24.02	397
15	9.72	9.51	23.81a	23.76	23.44a	23.40	23.58	403
18	9.68	9.48	—d	—	22.56a	22.52	22.52	421
21	9.68	9.47	19.94a	19.89	20.19a	20.15	20.02	473
24	9.72	9.52	18.81a	18.76	19.37a	19.33	19.05	500
27	9.77	9.56	17.37a	17.32	17.62a	17.58	17.45	548
30	9.82	9.61	15.75a	15.70	16.50a	16.46	16.08	598
35	9.90	9.69	14.81a	14.76	15.25a	15.21	14.99	647
38	9.95	9.74	15.19a	15.14	15.12a	15.08	15.11	645
40	9.98	9.77	16.44a	16.39	16.25a	16.21	16.30	599
42	9.94	9.73	16.50a	16.45	16.06a	16.02	16.24	599
45	9.88	9.67	17.25a	17.20	16.94a	16.90	17.05	567
50	9.79	9.58	17.25a	17.20	16.56a	16.52	16.86	568
55	9.69	9.48	12.81c	12.76	13.44c	13.40	13.08	725
60	9.59	9.38	18.37b	18.32	—d	—	18.32	512
65	9.56	9.35	13.00c	12.95	12.94c	12.90	12.93	724
70	9.52	9.31	13.31b	13.26	12.81b	12.77	13.02	715
75	9.48	9.27	18.06a	18.01	18.25a	18.21	18.11	512
80	9.45	9.24	17.66a	17.61	17.58a	17.54	17.58	526
85	9.60	9.39	18.55a	18.50	17.93a	17.89	18.20	516
90	9.74	9.53	16.25a	16.20	15.78a	15.74	15.97	597
94	9.85	9.64	12.89a	12.84	13.16a	13.12	12.98	743
96	9.91	9.70	12.84a	12.79	12.22a	12.18	12.49	777

**Table 8.A.1-34 (continued)**

Direct SV-Wave Velocities Measured at Treasure Island Between B3 and B2 (S-R1, Forward Profile),  
Path 1

Depth (ft)	Center- to- Center Dist. <sup>1</sup> (ft)	Travel Path Dist. <sup>2</sup> (ft)	SV-Up Travel Time (ms)	Adjusted Up Travel Time <sup>3</sup> (ms)	SV- Down Travel Time (ms)	Adjusted Down Travel Time <sup>4</sup> (ms)	Avg. SV Travel Time (ms)	SV-Wave Velocity (fps)
(1)	(2)	(3)	(4)	(5)	(6)	(7)	(8)	(9)
98	9.97	9.76	9.53 <sup>a</sup>	9.48	8.83 <sup>a</sup>	8.79	9.14	1069
100	10.03	9.82	8.24 <sup>a</sup>	8.19	8.63 <sup>a</sup>	8.59	8.39	1171
105	9.96	9.75	9.94 <sup>a</sup>	9.89	9.81 <sup>a</sup>	9.77	9.83	992
110	9.90	9.69	11.37 <sup>a</sup>	11.32	11.50 <sup>a</sup>	11.46	11.39	851
115	9.84	9.63	9.62 <sup>a</sup>	9.57	9.16 <sup>a</sup>	9.12	9.35	1031
120	9.78	9.57	11.41 <sup>a</sup>	11.36	11.25 <sup>a</sup>	11.21	11.29	848
125	9.89	9.68	11.09 <sup>a</sup>	11.04	11.17 <sup>a</sup>	11.13	11.09	873
130	10.00	9.79	12.50 <sup>a</sup>	12.45	12.07 <sup>a</sup>	12.03	12.24	800
135	10.10	9.89	13.01 <sup>a</sup>	12.96	12.77 <sup>a</sup>	12.73	12.85	770
140	10.22	10.01	14.61 <sup>a</sup>	14.56	13.87 <sup>a</sup>	13.83	14.20	705

Notes on Table 8.A.1-34:

- 1 center-to-center spacings interpolated from data reported by the Earth Technology Corporation of San Bernardino, California
- 2 one-half borehole diameter is subtracted from the center-to-center spacing due to receiver positioning in B2
- 3 calibration factor (trigger delay)=0.05 ms
- 4 calibration factor (trigger delay)= 0.04 ms
- a initial wave arrival clearly identified (within 5% of total travel time)—Type I data
- b initial wave arrival less distinct than (a) but identifiable (within 10% of total travel time)—Type II data
- c some interpretation required to identify initial wave arrival—Type III data
- d measurement not performed

**Table 8.A.1-35**

Interval SV-Wave Velocities Measured at Treasure Island Between B2 and B1 (R1-R2, Forward Profile), Path 2

Depth (ft)	Center-to-Center Distance <sup>1</sup> (ft)	Travel Path Distance <sup>2</sup> (ft)	SV-Up Travel Time (ms)	SV-Down Travel Time (ms)	Average SV Travel Time (ms)	SV-Wave Velocity (fps)
(1)	(2)	(3)	(4)	(5)	(6)	(7)
3	9.80	9.59	23.37 <sup>a</sup>	24.00 <sup>a</sup>	23.69	405
6	9.81	9.61	15.19 <sup>c</sup>	15.44 <sup>c</sup>	15.32	627
9	9.83	9.62	23.56 <sup>c</sup>	23.12 <sup>c</sup>	23.34	412
12	9.83	9.63	23.06 <sup>a</sup>	23.50 <sup>a</sup>	23.28	413
15	9.84	9.63	23.31 <sup>a</sup>	23.56 <sup>a</sup>	23.44	411
18	9.85	9.64	— <sup>d</sup>	23.56 <sup>a</sup>	23.56	409
21	9.85	9.64	20.87 <sup>a</sup>	21.00 <sup>a</sup>	20.94	460
24	9.80	9.60	20.00 <sup>a</sup>	20.37 <sup>a</sup>	20.19	475
27	9.76	9.55	17.50 <sup>b</sup>	17.44 <sup>b</sup>	17.47	547
30	9.72	9.51	17.12 <sup>a</sup>	17.69 <sup>a</sup>	17.41	546
35	9.64	9.43	16.25 <sup>a</sup>	16.06 <sup>a</sup>	16.16	584
38	9.60	9.39	16.75 <sup>a</sup>	16.06 <sup>a</sup>	16.41	572
40	9.57	9.36	17.19 <sup>a</sup>	16.37 <sup>a</sup>	16.78	558
42	9.57	9.37	18.62 <sup>a</sup>	18.31 <sup>a</sup>	18.47	507
45	9.58	9.37	19.56 <sup>a</sup>	18.06 <sup>a</sup>	18.81	498
50	9.59	9.38	19.62 <sup>b</sup>	19.75 <sup>b</sup>	19.69	477
55	9.59	9.38	16.94 <sup>c</sup>	17.37 <sup>c</sup>	17.16	547
60	9.60	9.39	21.00 <sup>b</sup>	21.00 <sup>b</sup>	21.00	447
65	9.70	9.49	14.12 <sup>b</sup>	14.06 <sup>b</sup>	14.09	674
70	9.80	9.59	13.94 <sup>b</sup>	13.44 <sup>b</sup>	13.69	701
75	9.90	9.69	19.31 <sup>b</sup>	19.50 <sup>b</sup>	19.41	499
80	10.01	9.80	18.98 <sup>a</sup>	19.34 <sup>a</sup>	19.16	512
85	10.11	9.90	18.91 <sup>b</sup>	18.98 <sup>b</sup>	18.95	523

Table 8.A.1-35 (continued)

Interval SV-Wave Velocities Measured at Treasure Island Between B2 and B1 (R1-R2, Forward Profile), Path 2

Depth (ft)	Center-to-Center Distance <sup>1</sup> (ft)	Travel Path Distance <sup>2</sup> (ft)	SV-Up Travel Time (ms)	SV-Down Travel Time (ms)	Average SV Travel Time (ms)	SV-Wave Velocity (fps)
(1)	(2)	(3)	(4)	(5)	(6)	(7)
90	10.21	10.00	16.91 <sup>b</sup>	17.54 <sup>b</sup>	17.23	581
94	10.29	10.08	12.07 <sup>c</sup>	11.76 <sup>c</sup>	11.92	846
96	10.33	10.12	11.81 <sup>c</sup>	12.69 <sup>c</sup>	12.25	826
98	10.37	10.16	7.62 <sup>b</sup>	8.59 <sup>b</sup>	8.11	1254
100	10.41	10.20	8.16 <sup>a</sup>	8.40 <sup>a</sup>	8.28	1232

Notes on Table 8.A.1-35:

- <sup>1</sup> center-to-center spacings interpolated from data reported by the Earth Technology Corporation of San Bernardino, California
- <sup>2</sup> a half borehole diameter is subtracted from the center-to-center distance due to receiver positioning in B2
- <sup>a</sup> initial wave arrival clearly identified (within 5% of total travel time)—Type I data
- <sup>b</sup> initial wave arrival less distinct than (a) but identifiable (within 10% of total travel time)—Type II data
- <sup>c</sup> some interpretation required to identify initial wave arrival—Type III data
- <sup>d</sup> measurement not performed

**Table 8.A.1-36**

Direct SV-Wave Velocities Measured at Treasure Island Between B1 and B2 (S-R1, Reverse Profile), Path 2

Depth (ft)	Center- to- Center Dist. <sup>1</sup> (ft)	Travel Path Dist. <sup>2</sup> (ft)	SV-Up Travel Time (ms)	Adjusted Up Travel Time <sup>3</sup> (ms)	SV-Down Travel Time (ms)	Adjusted Down Travel Time <sup>4</sup> (ms)	Average SV Travel Time (ms)	SV- Wave Velocity (fps)
(1)	(2)	(3)	(4)	(5)	(6)	(7)	(8)	(9)

6	9.72	9.51	— <sup>c</sup>	—	16.37 <sup>a</sup>	16.33	16.13	582
12	9.59	9.38	23.25 <sup>a</sup>	23.20	23.69 <sup>a</sup>	23.65	23.23	400
18	9.57	9.36	— <sup>c</sup>	—	24.12 <sup>b</sup>	24.08	23.88	389
24	9.54	9.33	20.56 <sup>b</sup>	20.51	20.56 <sup>b</sup>	20.52	20.32	455
30	9.57	9.36	17.44 <sup>b</sup>	17.39	16.94 <sup>b</sup>	16.90	16.95	546
35	9.58	9.38	15.94 <sup>b</sup>	15.89	16.31 <sup>b</sup>	16.27	15.88	583

Notes on Table 8.A.1-36:

- 1 center-to-center spacings determined using borehole survey data from Agbabian Associates, Pasadena, California
- 2 one-half borehole diameter is subtracted from the center-to-center spacing due to receiver positioning in B2
- 3 calibration factor (trigger delay) = 0.05 ms
- 4 calibration factor (trigger delay) = 0.04 ms
- a initial wave arrival clearly identified (within 5% of total travel time)—Type I data
- b initial wave arrival less distinct than (a) but identifiable (within 10% of total travel time)—Type II data
- c measurement not performed



**Table 8.A.1-37**

Interval SV-Wave Velocities Measured at Treasure Island Between B2 and B3 (R1-R2, Reverse Profile),  
Path 1

Depth (ft)	Center-to-Center Distance <sup>1</sup> (ft)	Travel Path Distance <sup>2</sup> (ft)	SV-Up Travel Time (ms)	SV-Down Travel Time (ms)	Average SV Travel Time (ms)	SV-Wave Velocity (fps)
(1)	(2)	(3)	(4)	(5)	(6)	(7)

6	9.82	9.61	— <sup>c</sup>	16.50 <sup>b</sup>	16.50	582
12	9.75	9.54	24.37 <sup>a</sup>	23.56 <sup>a</sup>	23.97	398
18	9.68	9.48	21.12 <sup>b</sup>	23.31 <sup>b</sup>	22.22	427
24	9.68	9.47	18.69 <sup>b</sup>	19.25 <sup>b</sup>	18.97	499
30	9.82	9.61	17.12 <sup>b</sup>	17.00 <sup>b</sup>	17.06	563
35	9.90	9.69	15.19 <sup>b</sup>	15.19 <sup>b</sup>	15.19	638

Notes on Table 8.A.1-37:

- <sup>1</sup> center-to-center spacings interpolated from forward-profile distances reported by the Earth Technology Corporation of San Bernardino, California (assuming forward and reverse-profile distances are equal)
- <sup>2</sup> a half borehole diameter is subtracted from the center-to-center distance due to receiver positioning in B2
- <sup>a</sup> initial wave arrival clearly identified (within 5% of total travel time)—Type I data
- <sup>b</sup> initial wave arrival less distinct than (a) but identifiable (within 10% of total travel time)—Type II data
- <sup>c</sup> measurement not performed

**Table 8.A.1-38**

Direct SV-Wave Velocities Measured at Treasure Island Between B1 and B4 (S-R1, "North-South" Profile), Path 3

Depth (ft)	Center -to- Center Dist. <sup>1</sup> (ft)	Travel Path Dist. <sup>2</sup> (ft)	SV-Up Travel Time (ms)	Adjusted Up Travel Time <sup>3</sup> (ms)	SV-Down Travel Time (ms)	Adjusted Down Travel Time <sup>4</sup> (ms)	Average SV Travel Time (ms)	SV-Wave Velocity (fps)
(1)	(2)	(3)	(4)	(5)	(6)	(7)	(8)	(9)
3	9.98	9.56	16.44 <sup>b</sup>	16.39	15.62 <sup>b</sup>	15.58	15.99	598
6	9.97	9.56	— <sup>d</sup>	—	20.37 <sup>b</sup>	20.33	20.33	470
9	10.02	9.60	21.37 <sup>a</sup>	21.32	21.37 <sup>a</sup>	21.33	21.33	450
12	10.00	9.59	20.75 <sup>a</sup>	20.70	20.75 <sup>a</sup>	20.71	20.71	463
15	9.99	9.57	— <sup>d</sup>	—	21.75 <sup>b</sup>	21.71	21.71	441
18	9.95	9.53	21.62 <sup>a</sup>	21.57	22.19 <sup>a</sup>	22.15	21.86	436
21	9.95	9.53	19.94 <sup>b</sup>	19.89	20.44 <sup>b</sup>	20.40	20.15	473
24	10.00	9.58	19.75 <sup>b</sup>	19.70	20.12 <sup>b</sup>	20.08	19.89	482
27	10.06	9.64	20.00 <sup>c</sup>	19.95	20.62 <sup>c</sup>	20.58	20.27	476
30	10.05	9.63	17.25 <sup>b</sup>	17.20	17.87 <sup>b</sup>	17.83	17.52	550
35	10.02	9.60	15.19 <sup>a</sup>	15.14	14.62 <sup>a</sup>	14.58	14.86	646
38	9.95	9.53	15.87 <sup>a</sup>	15.82	15.19 <sup>a</sup>	15.15	15.49	616
40	9.94	9.52	17.19 <sup>a</sup>	17.14	16.87 <sup>a</sup>	16.83	16.99	561
42	9.94	9.53	16.00 <sup>a</sup>	15.95	16.12 <sup>a</sup>	16.08	16.02	595
45	9.99	9.58	17.25 <sup>a</sup>	17.20	17.19 <sup>a</sup>	17.15	17.18	558
49	9.97	9.56	17.62 <sup>a</sup>	17.57	17.69 <sup>a</sup>	17.65	17.61	543

Notes on Table 8.A.1-38:

- <sup>1</sup> center-to-center spacings determined using borehole survey data from Agbabian Associates, Pasadena, California
- <sup>2</sup> one borehole diameter is subtracted from the center-to-center spacing due to receiver positioning in B4
- <sup>3</sup> calibration factor (trigger delay) = 0.05 ms
- <sup>4</sup> calibration factor (trigger delay) = 0.04 ms
- <sup>a</sup> initial wave arrival clearly identified (within 5% of total travel time)—Type I data
- <sup>b</sup> initial wave arrival less distinct than (a) but identifiable (within 10% of total travel time)—Type II data
- <sup>c</sup> some interpretation required to identify initial wave arrival—Type III data
- <sup>d</sup> measurement not performed

**Table 8.A.1-39**

Interval SV-Wave Velocities Measured at Treasure Island Between B4 and B5 (R1-R2, "North-South" Profile), Path 4

Depth (ft)	Center-to- Center Dist. <sup>1</sup> (ft)	Travel Path Dist. <sup>2</sup> (ft)	SV-Up Travel Time (ms)	SV-Down Travel Time (ms)	Average SV Travel Time (ms)	SV-Wave Velocity (fps)
(1)	(2)	(3)	(4)	(5)	(6)	(7)
3	10.70	10.91	20.75 <sup>b</sup>	22.31 <sup>b</sup>	21.53	507
6	10.67	10.88	28.81 <sup>b</sup>	29.69 <sup>b</sup>	29.25	372
9	10.60	10.81	23.75 <sup>a</sup>	23.75 <sup>a</sup>	23.75	455
12	10.56	10.77	24.00 <sup>a</sup>	23.75 <sup>a</sup>	23.88	451
15	10.57	10.78	26.31 <sup>b</sup>	25.12 <sup>b</sup>	25.72	419
18	10.59	10.80	26.44 <sup>b</sup>	26.37 <sup>b</sup>	26.41	409
21	10.62	10.83	23.50 <sup>b</sup>	23.56 <sup>b</sup>	23.53	460

Notes on Table 8.A.1-39:

- <sup>1</sup> center-to-center spacings determined using borehole survey data from Agbabian Associates, Pasadena, California
- <sup>2</sup> a half borehole diameter is subtracted from the center-to-center distance due to receiver positioning in B5
- <sup>a</sup> initial wave arrival clearly identified (within 5% of total travel time)—Type I data
- <sup>b</sup> initial wave arrival less distinct than (a) but identifiable (within 10% of total travel time)—Type II data

Table 8.A.1-40

Direct SV-Wave Velocities Measured at Treasure Island Between B2 and B4 (S-R1), Path 5

Depth (ft)	Center- to- Center Dist. <sup>1</sup> (ft)	Travel Path Dist. <sup>2</sup> (ft)	SV-Up Travel Time (ms)	Adjusted Up Travel Time <sup>3</sup> (ms)	SV-Down Travel Time (ms)	Adjusted Down Travel Time <sup>4</sup> (ms)	Average SV Travel Time (ms)	SV- Wave Velocity (fps)
(1)	(2)	(3)	(4)	(5)	(6)	(7)	(8)	(9)
15	13.39	12.97	30.82 <sup>a</sup>	30.77	30.86 <sup>a</sup>	30.82	30.80	421
18	13.37	12.95	30.51 <sup>b</sup>	30.46	30.08 <sup>b</sup>	30.04	30.25	428
21	13.32	12.91	28.52 <sup>a</sup>	28.47	29.26 <sup>a</sup>	29.22	28.85	447
24	13.30	12.88	27.66 <sup>a</sup>	27.61	27.23 <sup>a</sup>	27.19	27.40	470
27	13.32	12.90	27.54 <sup>a</sup>	27.49	27.50 <sup>a</sup>	27.46	27.48	470

Notes on Table 8.A.1-40:

- <sup>1</sup> center-to-center spacings determined using borehole survey data from Agbabian Associates, Pasadena, California
- <sup>2</sup> one borehole diameter is subtracted from the center-to-center spacing due to receiver positioning in B4
- <sup>3</sup> calibration factor (trigger delay) = 0.05 ms
- <sup>4</sup> calibration factor (trigger delay) = 0.04 ms
- <sup>a</sup> initial wave arrival clearly identified (within 5% of total travel time)—Type I data
- <sup>b</sup> initial wave arrival less distinct than (a) but identifiable (within 10% of total travel time)—Type II data

Table 8.A.1-41

Direct SH-Wave Velocities Measured at Treasure Island Between B3 and B2 (S-R1, Forward Profile),  
Path 1

Depth (ft)	Center- to- Center Dist. <sup>1</sup> (ft)	Travel Path Dist. <sup>2</sup> (ft)	SH- North Travel Time (ms)	Adjusted SH North Travel Time <sup>3</sup> (ms)	SH-South Travel Time (ms)	Adjusted SH South Travel Time <sup>3</sup> (ms)	Average SH Travel Time (ms)	SH-Wave Velocity (fps)
(1)	(2)	(3)	(4)	(5)	(6)	(7)	(8)	(9)

3	9.85	9.64	16.50 <sup>a</sup>	16.40	16.87 <sup>a</sup>	16.77	16.59	16.77
6	9.82	9.61	— <sup>d</sup>	—	15.75 <sup>c</sup>	15.65	15.65	15.65
9	9.78	9.57	24.19 <sup>b</sup>	24.09	24.19 <sup>b</sup>	24.09	24.09	24.09
12	9.75	9.54	23.00 <sup>a</sup>	22.90	23.00 <sup>a</sup>	22.90	22.90	22.90
15	9.72	9.51	23.31 <sup>a</sup>	23.21	23.50 <sup>a</sup>	23.40	23.31	23.40
18	9.68	9.48	23.25 <sup>a</sup>	23.15	23.00 <sup>a</sup>	22.90	23.03	22.90
21	9.68	9.47	21.69 <sup>a</sup>	21.59	21.75 <sup>a</sup>	21.65	21.62	21.65
24	9.72	9.52	20.12 <sup>a</sup>	20.02	20.00 <sup>a</sup>	19.90	19.96	19.90
27	9.77	9.56	17.37 <sup>b</sup>	17.27	17.37 <sup>b</sup>	17.27	17.27	17.27
30	9.82	9.61	17.25 <sup>a</sup>	17.15	16.94 <sup>a</sup>	16.84	17.00	16.84
35	9.90	9.69	16.00 <sup>a</sup>	15.90	15.69 <sup>a</sup>	15.59	15.75	15.59
38	9.95	9.74	17.00 <sup>a</sup>	16.90	16.94 <sup>a</sup>	16.84	16.87	16.84
40	9.98	9.77	18.44 <sup>a</sup>	18.34	18.31 <sup>a</sup>	18.21	18.28	18.21
42	9.94	9.73	17.25 <sup>a</sup>	17.15	17.19 <sup>a</sup>	17.09	17.12	17.09
45	9.88	9.67	19.12 <sup>a</sup>	19.02	19.06 <sup>a</sup>	18.96	18.99	18.96
50	9.79	9.58	20.00 <sup>a</sup>	19.90	19.26 <sup>a</sup>	19.16	19.53	19.16
55	9.69	9.48	— <sup>d</sup>	—	— <sup>d</sup>	— <sup>d</sup>	—	—
60	9.59	9.38	18.59 <sup>a</sup>	18.49	18.59 <sup>a</sup>	18.49	18.49	18.49
65	9.56	9.35	11.33 <sup>a</sup>	11.23	11.25 <sup>a</sup>	11.15	11.19	11.15
70	9.52	9.31	11.80 <sup>a</sup>	11.70	11.80 <sup>a</sup>	11.70	11.70	11.70
75	9.48	9.27	18.05 <sup>a</sup>	17.95	17.89 <sup>a</sup>	17.79	17.87	17.79
80	9.45	9.24	17.85 <sup>a</sup>	17.75	17.77 <sup>a</sup>	17.67	17.71	17.67
85	9.60	9.39	18.32 <sup>a</sup>	18.22	18.24 <sup>a</sup>	18.14	18.18	18.14

**Table 8.A.1-41 (continued)**

Direct SH-Wave Velocities Measured at Treasure Island Between B3 and B2 (S-R1, Forward Profile),  
Path 1

Depth (ft)	Center- to- Center Dist. <sup>1</sup> (ft)	Travel Path Dist. <sup>2</sup> (ft)	SH- North Travel Time (ms)	Adjusted SH North Travel Time <sup>3</sup> (ms)	SH-South Travel Time (ms)	Adjusted SH South Travel Time <sup>3</sup> (ms)	Average SH Travel Time (ms)	SH-Wave Velocity (fps)
(1)	(2)	(3)	(4)	(5)	(6)	(7)	(8)	(9)
90	9.74	9.53	17.91a	17.81	17.87a	17.77	17.79	17.77
94	9.85	9.64	16.53a	16.43	16.50a	16.40	16.42	16.40
96	9.91	9.70	13.94a	13.84	13.91a	13.81	13.83	13.81
98	9.97	9.76	13.25a	13.15	13.53a	13.43	13.29	13.43
100	10.03	9.82	6.53a	6.43	6.62a	6.52	6.48	6.52

Notes on Table 8.A.1-41:

- 1 center-to-center spacings interpolated from data reported by the Earth Technology Corporation of San Bernardino, California
- 2 one-half borehole diameter is subtracted from the center-to-center spacing due to receiver positioning in B2
- 3 calibration factor (trigger delay) = 0.10 ms
- a initial wave arrival clearly identified (within 5% of total travel time)—Type I data
- b initial wave arrival less distinct than (a) but identifiable (within 10% of total travel time)—Type II data
- c some interpretation required to identify initial wave arrival—Type III data
- d initial wave arrival not identifiable

**Table 8.A.1-42**

Interval SH-Wave Velocities Measured at Treasure Island Between B2 and B1 (R1-R2, Forward Profile),  
Path 2

Depth (ft)	Center-to- Center Distance <sup>1</sup> (ft)	Travel Path Distance <sup>2</sup> (ft)	SH-North Travel Time (ms)	SH-South Travel Time (ms)	Average SH Travel Time (ms)	SH-Wave Velocity (fps)
(1)	(2)	(3)	(4)	(5)	(6)	(7)
3	9.80	9.59	15.50 <sup>a</sup>	15.50 <sup>a</sup>	15.50	619
6	9.81	9.61	— <sup>d</sup>	13.25 <sup>c</sup>	13.25	725
9	9.83	9.62	24.06 <sup>b</sup>	24.31 <sup>b</sup>	24.19	398
12	9.83	9.63	24.00 <sup>a</sup>	24.12 <sup>a</sup>	24.06	400
15	9.84	9.63	25.25 <sup>a</sup>	25.12 <sup>a</sup>	25.19	382
18	9.85	9.64	22.87 <sup>a</sup>	22.81 <sup>a</sup>	22.84	422
21	9.85	9.64	21.00 <sup>a</sup>	20.69 <sup>a</sup>	20.85	462
24	9.80	9.60	21.62 <sup>a</sup>	21.12 <sup>a</sup>	21.37	449
27	9.76	9.55	21.75 <sup>b</sup>	22.19 <sup>b</sup>	21.97	435
30	9.72	9.51	18.37 <sup>b</sup>	18.37 <sup>b</sup>	18.37	518
35	9.64	9.43	16.37 <sup>b</sup>	16.50 <sup>b</sup>	16.44	574
38	9.60	9.39	16.44 <sup>a</sup>	16.44 <sup>a</sup>	16.44	571
40	9.57	9.36	18.94 <sup>a</sup>	18.81 <sup>a</sup>	18.88	496
42	9.57	9.37	19.06 <sup>a</sup>	19.31 <sup>a</sup>	19.19	488
45	9.58	9.37	20.44 <sup>b</sup>	20.25 <sup>b</sup>	20.35	461
50	9.59	9.38	21.84 <sup>a</sup>	22.46 <sup>a</sup>	22.15	424
55	9.59	9.38	— <sup>d</sup>	— <sup>d</sup>	—	—
60	9.60	9.39	20.31 <sup>a</sup>	20.20 <sup>a</sup>	20.26	464
65	9.70	9.49	14.14 <sup>a</sup>	14.06 <sup>a</sup>	14.10	673
70	9.80	9.59	12.58 <sup>a</sup>	12.73 <sup>a</sup>	12.66	758
75	9.90	9.69	19.02 <sup>a</sup>	18.91 <sup>a</sup>	18.97	511
80	10.01	9.80	18.71 <sup>a</sup>	18.63 <sup>a</sup>	18.67	525
85	10.11	9.90	18.16 <sup>a</sup>	18.16 <sup>a</sup>	18.16	545

**Table 8.A.1-42 (continued)**

Interval SH-Wave Velocities Measured at Treasure Island Between B2 and B1 (R1-R2, Forward Profile), Path 2

Depth (ft)	Center-to-Center Distance <sup>1</sup> (ft)	Travel Path Distance <sup>2</sup> (ft)	SH-North Travel Time (ms)	SH-South Travel Time (ms)	Average SH Travel Time (ms)	SH-Wave Velocity (fps)
(1)	(2)	(3)	(4)	(5)	(6)	(7)
90	10.21	10.00	17.53 <sup>a</sup>	17.72 <sup>a</sup>	17.63	567
94	10.29	10.08	11.62 <sup>a</sup>	11.72 <sup>a</sup>	11.67	864
96	10.33	10.12	12.53 <sup>a</sup>	12.37 <sup>a</sup>	12.45	813
98	10.37	10.16	11.69 <sup>c</sup>	12.53 <sup>c</sup>	12.11	839
100	10.41	10.20	5.91 <sup>c</sup>	5.72 <sup>c</sup>	5.82	1754

Notes on Table 8.A.1-42:

- <sup>1</sup> center-to-center spacings interpolated from data reported by the Earth Technology Corporation of San Bernardino, California
- <sup>2</sup> a half borehole diameter is subtracted from the center-to-center distance due to receiver positioning in B2
- <sup>a</sup> initial wave arrival clearly identified (within 5% of total travel time)—Type I data
- <sup>b</sup> initial wave arrival less distinct than (a) but identifiable (within 10% of total travel time)—Type II data
- <sup>c</sup> some interpretation required to identify initial wave arrival—Type III data
- <sup>d</sup> initial wave arrival not identifiable



**Table 8.A.1-43**

Direct SH-Wave Velocities Measured at Treasure Island Between B1 and B2 (S-R1, Reverse Profile), Path 2

Depth (ft)	Center- to- Center Dist. <sup>1</sup> (ft)	Travel Path Dist. <sup>2</sup> (ft)	SH- North Travel Time (ms)	Adjusted North Travel Time <sup>3</sup> (ms)	SH- South Travel Time (ms)	Adjusted South Travel Time <sup>3</sup> (ms)	Average SH Travel Time (ms)	SH-Wave Velocity (fps)
(1)	(2)	(3)	(4)	(5)	(6)	(7)	(8)	(9)

6	9.72	9.51	16.31 <sup>c</sup>	16.21	16.94 <sup>c</sup>	16.84	16.53	588
12	9.59	9.38	22.56 <sup>b</sup>	22.46	22.37 <sup>b</sup>	22.27	22.37	429
18	9.57	9.36	23.25 <sup>b</sup>	23.15	23.19 <sup>b</sup>	23.09	23.12	414
24	9.54	9.33	23.19 <sup>a</sup>	23.09	22.94 <sup>a</sup>	22.84	22.97	415
30	9.57	9.36	18.44 <sup>a</sup>	18.34	18.62 <sup>a</sup>	18.52	18.43	519
35	9.58	9.38	15.81 <sup>b</sup>	15.71	15.50 <sup>b</sup>	15.40	15.56	616

Notes on Table 8.A.1-43:

- <sup>1</sup> center-to-center spacings determined using borehole survey data from Agbabian Associates, Pasadena, California
- <sup>2</sup> one-half borehole diameter is subtracted from the center-to-center spacing due to receiver positioning in B2
- <sup>3</sup> calibration factor (trigger delay)= 0.10 ms
- a initial wave arrival clearly identified (within 5% of total travel time)—Type I data
- b initial wave arrival less distinct than (a) but identifiable (within 10% of total travel time)—Type II data
- c some interpretation required to identify initial wave arrival—Type III data

**Table 8.A.1-44**

Interval SH-Wave Velocities Measured at Treasure Island Between B2 and B3 (R1-R2, Reverse Profile), Path 1

Depth (ft)	Center-to-Center Distance <sup>1</sup> (ft)	Travel Path Distance <sup>2</sup> (ft)	SH-North Travel Time (ms)	SH-South Travel Time (ms)	Average SH Travel Time (ms)	SH-Wave Velocity (fps)
(1)	(2)	(3)	(4)	(5)	(6)	(7)
6	9.82	9.61	16.69 <sup>b</sup>	16.81 <sup>b</sup>	16.75	574
12	9.75	9.54	24.87 <sup>a</sup>	24.81 <sup>a</sup>	24.84	384
18	9.68	9.48	23.44 <sup>a</sup>	23.31 <sup>a</sup>	23.38	405
24	9.68	9.47	19.25 <sup>a</sup>	19.56 <sup>a</sup>	19.41	488
30	9.82	9.61	17.56 <sup>a</sup>	16.87 <sup>a</sup>	17.22	558
35	9.90	9.69	15.81 <sup>a</sup>	15.50 <sup>a</sup>	15.66	619

Notes on Table 8.A.1-44:

- <sup>1</sup> center-to-center spacings interpolated from forward-profile distances reported by the Earth Technology Corporation of San Bernardino, California (assuming forward and reverse-profile distances are equal)
- <sup>2</sup> a half borehole diameter is subtracted from the center-to-center distance due to receiver positioning in B2
- <sup>a</sup> initial wave arrival less distinct than Type I data but identifiable (within 10% of total travel time)—Type II data
- <sup>b</sup> some interpretation required to identify initial wave arrival—Type III data

**Table 8.A.1-45**

Direct SH-Wave Velocities Measured at Treasure Island Between B1 and B4 (S-R1, "North-South" Profile), Path 3

Depth (ft)	Center- to- Center Dist. <sup>1</sup> (ft)	Travel Path Dist. <sup>2</sup> (ft)	SH-East Travel Time (ms)	Adjusted East Travel Time <sup>3</sup> (ms)	SH-West Travel Time (ms)	Adjusted West Travel Time <sup>3</sup> (ms)	Average SH Travel Time (ms)	SH-Wave Velocity (fps)
(1)	(2)	(3)	(4)	(5)	(6)	(7)	(8)	(9)
3	9.98	9.56	11.19 <sup>b</sup>	11.09	— <sup>c</sup>	—	11.09	862
6	9.97	9.56	21.81 <sup>b</sup>	21.71	— <sup>c</sup>	—	21.71	440
9	10.02	9.60	21.19 <sup>b</sup>	21.09	— <sup>c</sup>	—	21.09	455
12	10.00	9.59	19.75 <sup>b</sup>	19.65	— <sup>c</sup>	—	19.65	488
15	9.99	9.57	22.62 <sup>b</sup>	22.52	— <sup>c</sup>	—	22.52	425
18	9.95	9.53	22.81 <sup>b</sup>	22.71	— <sup>c</sup>	—	22.71	420
21	9.95	9.53	20.62 <sup>b</sup>	20.52	20.43	20.33	20.43	467
24	10.00	9.58	20.04 <sup>b</sup>	19.94	— <sup>c</sup>	—	19.94	481
27	10.06	9.64	22.89 <sup>b</sup>	22.79	22.54 <sup>b</sup>	22.44	22.62	426
30	10.05	9.63	— <sup>c</sup>	—	18.40 <sup>b</sup>	18.30	18.30	526
35	10.02	9.60	15.12 <sup>a</sup>	15.02	15.62 <sup>a</sup>	15.52	15.27	629
38	9.95	9.53	15.90 <sup>a</sup>	15.80	15.90 <sup>a</sup>	15.80	15.80	603
40	9.94	9.52	— <sup>c</sup>	—	17.85 <sup>a</sup>	17.75	17.75	537
42	9.94	9.53	— <sup>c</sup>	—	16.91 <sup>a</sup>	16.81	16.81	567
45	9.99	9.58	18.28 <sup>a</sup>	18.18	18.44 <sup>a</sup>	18.34	18.26	525
49	9.97	9.56	17.81 <sup>a</sup>	17.71	17.50 <sup>a</sup>	17.40	17.56	544

Notes on Table 8.A.1-45:

- <sup>1</sup> center-to-center spacings determined using borehole survey data from Agbabian Associates, Pasadena, California
- <sup>2</sup> one borehole diameter is subtracted from the center-to-center spacing due to receiver positioning in B2
- <sup>3</sup> calibration factor (trigger delay) = 0.10 ms
- <sup>a</sup> initial wave arrival clearly identified (within 5% of total travel time)—Type I data
- <sup>b</sup> initial wave arrival less distinct than (a) but identifiable (within 10% of total travel time)—Type II data
- <sup>c</sup> measurement not performed

**Table 8.A.1-46**

Interval SH-Wave Velocities Measured at Treasure Island Between B4 and B5 (R1-R2, "North-South" Profile), Path 4

Depth (ft)	Center-to-Center Distance <sup>1</sup> (ft)	Travel Path Distance <sup>2</sup> (ft)	SH-East Travel Time (ms)	SH-West Travel Time (ms)	Average SH Travel Time (ms)	SH-Wave Velocity (fps)
(1)	(2)	(3)	(4)	(5)	(6)	(7)
3	10.70	10.91	— <sup>b</sup>	— <sup>b</sup>	—	—
6	10.67	10.88	— <sup>b</sup>	— <sup>b</sup>	—	—
9	10.60	10.81	26.52 <sup>a</sup>	— <sup>b</sup>	26.52	408
12	10.56	10.77	25.19 <sup>a</sup>	— <sup>b</sup>	25.19	428
15	10.57	10.78	26.94 <sup>a</sup>	— <sup>b</sup>	26.94	400
18	10.59	10.80	28.19 <sup>a</sup>	— <sup>b</sup>	28.19	383
21	10.62	10.83	26.00 <sup>a</sup>	26.87 <sup>a</sup>	26.44	410

Notes on Table 8.A.1-46:

- <sup>1</sup> center-to-center spacings determined using borehole survey data from Agbabian Associates, Pasadena, California
- <sup>2</sup> a half borehole diameter is subtracted from the center-to-center distance due to receiver positioning in B5
- <sup>a</sup> initial wave arrival less distinct than Type I data but identifiable (within 10% of total travel time)—Type II data
- <sup>b</sup> measurement not performed

**Table 8.A.1-47**

Direct SH-Wave Velocities Measured at Treasure Island Between B2 and B4 (S-R1), Path 5

Depth (ft)	Center- to- Center Dist. <sup>1</sup> (ft)	Travel Path Dist. <sup>2</sup> (ft)	SH-NE Travel Time (ms)	Adjusted NE Travel Time <sup>3</sup> (ms)	SH-SW Travel Time (ms)	Adjusted SW Travel Time <sup>3</sup> (ms)	Average SH Travel Time (ms)	SH-Wave Velocity (fps)
(1)	(2)	(3)	(4)	(5)	(6)	(7)	(8)	(9)

15	13.39	13.18	31.29 <sup>a</sup>	31.19	— <sup>b</sup>	—	31.19	423
18	13.37	13.16	31.37 <sup>a</sup>	31.27	— <sup>b</sup>	—	31.27	421
21	13.32	13.11	28.71 <sup>a</sup>	28.61	— <sup>b</sup>	—	28.61	458
24	13.30	13.09	26.60 <sup>a</sup>	26.50	— <sup>b</sup>	—	26.50	494
27	13.32	13.11	28.40 <sup>a</sup>	28.30	— <sup>b</sup>	—	28.30	463

Notes on Table 8.A.1-47:

- <sup>1</sup> center-to-center spacings determined using borehole survey data from Agbabian Associates, Pasadena, California
- <sup>2</sup> one-half borehole diameter is subtracted from the center-to-center spacing due to receiver positioning in B4
- <sup>3</sup> calibration factor (trigger delay) = 0.10 ms
- <sup>a</sup> initial wave arrival clearly identified (within 5% of total travel time)—Type I data
- <sup>b</sup> measurement not performed

Table 8.A.1-48

Direct P-Wave Velocities Measured at Treasure Island Between B3 and B2 (S-R1, Forward Profile), Path 1

Depth (ft)	Center -to- Center Dist. <sup>1</sup> (ft)	Travel Path Dist. <sup>2</sup> (ft)	Wedge and Hammer Source <sup>3</sup>			Solenoid Source <sup>4</sup>		
			Travel Time (ms)	Adjusted Travel Time <sup>5</sup> (ms)	P-Wave Velocity (fps)	Travel Time (ms)	Adjusted Travel Time <sup>6</sup> (ms)	P-Wave Velocity (fps)
(1)	(2)	(3)	(4)	(5)	(6)	(7)	(8)	(9)

3	9.85	9.64	5.66 <sup>a</sup>	5.63	1713	— <sup>d</sup>	—	—
6	9.82	9.61	8.32 <sup>b</sup>	8.29	1159	— <sup>d</sup>	—	—
9	9.78	9.57	5.12 <sup>a</sup>	5.09	1881	5.68 <sup>c</sup>	5.58	1716
12	9.75	9.54	2.22 <sup>a</sup>	2.19	4357	2.39 <sup>a</sup>	2.29	4167
15	9.72	9.51	1.84 <sup>a</sup>	1.81	5255	1.89 <sup>a</sup>	1.79	5314
18	9.68	9.48	1.83 <sup>a</sup>	1.80	5264	1.89 <sup>a</sup>	1.79	5294
21	9.68	9.47	1.89 <sup>a</sup>	1.86	5090	1.94 <sup>a</sup>	1.84	5145
24	9.72	9.52	1.81 <sup>a</sup>	1.78	5346	1.89 <sup>a</sup>	1.79	5316
27	9.77	9.56	1.83 <sup>a</sup>	1.80	5313	1.88 <sup>a</sup>	1.78	5373
30	9.82	9.61	1.70 <sup>a</sup>	1.67	5755	1.80 <sup>a</sup>	1.70	5654
35	9.90	9.69	1.73 <sup>a</sup>	1.70	5701	1.78 <sup>a</sup>	1.68	5769
38	9.95	9.74	1.73 <sup>a</sup>	1.70	5729	1.84 <sup>a</sup>	1.74	5598
40	9.98	9.77	1.75 <sup>a</sup>	1.72	5681	1.88 <sup>a</sup>	1.78	5490
42	9.94	9.73	1.84 <sup>a</sup>	1.81	5377	2.05 <sup>a</sup>	1.95	4991
45	9.88	9.67	1.98 <sup>a</sup>	1.95	4960	2.11 <sup>a</sup>	2.01	4812
50	9.79	9.58	2.03 <sup>a</sup>	2.00	4791	2.09 <sup>a</sup>	1.99	4815
55	9.69	9.48	2.33 <sup>a</sup>	2.30	4122	2.34 <sup>b</sup>	2.24	4233
60	9.59	9.38	2.03 <sup>a</sup>	2.00	4691	2.14 <sup>a</sup>	2.04	4599
65	9.56	9.35	2.12 <sup>a</sup>	2.09	4474	2.11 <sup>b</sup>	2.01	4653
70	9.52	9.31	3.30 <sup>a</sup>	3.27	2848	3.95 <sup>b</sup>	3.85	2419
75	9.48	9.27	2.61 <sup>a</sup>	2.58	3594	2.61 <sup>a</sup>	2.51	3694
80	9.45	9.24	2.73 <sup>a</sup>	2.70	3423	2.69 <sup>a</sup>	2.59	3568
85	9.60	9.39	2.38 <sup>a</sup>	2.35	3996	2.42 <sup>a</sup>	2.32	4048
90	9.74	9.53	2.28 <sup>a</sup>	2.25	4236	2.28 <sup>a</sup>	2.18	4372
94	9.85	9.64	2.22 <sup>a</sup>	2.19	4404	2.30 <sup>a</sup>	2.20	4383
96	9.91	9.70	1.98 <sup>a</sup>	1.95	4975	2.12 <sup>a</sup>	2.02	4803
98	9.97	9.76	2.06 <sup>a</sup>	2.03	4809	2.16 <sup>a</sup>	2.06	4739
100	10.03	9.82	2.06 <sup>a</sup>	2.03	4838	2.11 <sup>a</sup>	2.01	4886

Table 8.A.1-48 (continued)

Direct P-Wave Velocities Measured at Treasure Island Between B3 and B2 (S-R1, Forward Profile), Path 1

Depth (ft)	Center -to- Center Dist. <sup>1</sup> (ft)	Travel Path Dist. <sup>2</sup> (ft)	Wedge and Hammer Source <sup>3</sup>			Solenoid Source <sup>4</sup>		
			Travel Time (ms)	Adjusted Travel Time <sup>5</sup> (ms)	P-Wave Velocity (fps)	Travel Time (ms)	Adjusted Travel Time <sup>6</sup> (ms)	P-Wave Velocity (fps)
(1)	(2)	(3)	(4)	(5)	(6)	(7)	(8)	(9)
105	9.96	9.75	2.16 <sup>a</sup>	2.13	4578	— <sup>e</sup>	—	—
110	9.90	9.69	2.25 <sup>a</sup>	2.22	4366	— <sup>e</sup>	—	—
115	9.84	9.63	2.16 <sup>a</sup>	2.13	4522	— <sup>e</sup>	—	—
120	9.78	9.57	2.22 <sup>a</sup>	2.19	4371	— <sup>e</sup>	—	—
125	9.89	9.68	2.22 <sup>a</sup>	2.19	4421	— <sup>e</sup>	—	—
130	10.00	9.79	2.38 <sup>a</sup>	2.35	4167	— <sup>e</sup>	—	—
135	10.10	9.89	2.33 <sup>a</sup>	2.30	4301	— <sup>e</sup>	—	—
140	10.22	10.01	2.27 <sup>a</sup>	2.24	4470	— <sup>e</sup>	—	—

Notes on Table 8.A.1-48:

- <sup>1</sup> center-to-center spacings interpolated from data reported by the Earth Technology Corporation of San Bernardino, California
- <sup>2</sup> one-half borehole diameter is subtracted from the center-to-center spacing due to receiver positioning in B2
- <sup>3</sup> wedge and hammer source consists of a hammer impacting a pneumatically-locking wedge in the borehole
- <sup>4</sup> solenoid source produces a horizontal impact from the plunger of the solenoid
- <sup>5</sup> calibration factor (trigger delay) = 0.03 ms
- <sup>6</sup> calibration factor (trigger delay) = 0.10 ms
- <sup>a</sup> initial wave arrival clearly identified (within 5% of total travel time)—Type I data
- <sup>b</sup> initial wave arrival less distinct than (a) but identifiable (within 10% of total travel time)—Type II data
- <sup>c</sup> some interpretation required to identify initial wave arrival—Type III data
- <sup>d</sup> initial wave arrival not identifiable
- <sup>e</sup> measurement not performed

Table 8.A.1-49

Interval P-Wave Velocities Measured at Treasure Island Between B2 and B1 (R1-R2, Forward Profile),  
Path 2

Depth (ft)	Center Center Distance <sup>1</sup> (ft)	Travel Path Distance <sup>2</sup> (ft)	Wedge and Hammer Source <sup>3</sup>		Solenoid Source <sup>4</sup>	
			Travel Time (ms)	P-Wave Velocity (fps)	Travel Time (ms)	P-Wave Velocity (fps)
(1)	(2)	(3)	(4)	(5)	(6)	(7)
3	9.80	9.59	— <sup>d</sup>	—	— <sup>d</sup>	—
6	9.81	9.61	— <sup>d</sup>	—	— <sup>d</sup>	—
9	9.83	9.62	5.78 <sup>c</sup>	1664	— <sup>d</sup>	—
12	9.83	9.63	2.06 <sup>c</sup>	4673	1.61 <sup>a</sup>	5979
15	9.84	9.63	1.97 <sup>a</sup>	4889	1.87 <sup>a</sup>	5151
18	9.85	9.64	2.01 <sup>a</sup>	4798	1.89 <sup>a</sup>	5102
21	9.85	9.64	2.02 <sup>a</sup>	4771	1.84 <sup>a</sup>	5238
24	9.80	9.60	1.95 <sup>a</sup>	4921	1.81 <sup>a</sup>	5301
27	9.76	9.55	1.96 <sup>a</sup>	4874	1.84 <sup>a</sup>	5192
30	9.72	9.51	1.94 <sup>a</sup>	4903	1.81 <sup>a</sup>	5255
35	9.64	9.43	1.92 <sup>a</sup>	4912	1.81 <sup>a</sup>	5211
38	9.60	9.39	1.92 <sup>a</sup>	4890	1.82 <sup>a</sup>	5159
40	9.57	9.36	1.98 <sup>a</sup>	4728	1.94 <sup>a</sup>	4826
42	9.57	9.37	2.28 <sup>a</sup>	4108	2.14 <sup>a</sup>	4376
45	9.58	9.37	2.39 <sup>a</sup>	3921	2.30 <sup>a</sup>	4075
50	9.59	9.38	2.19 <sup>a</sup>	4284	2.14 <sup>a</sup>	4384
55	9.59	9.38	2.39 <sup>a</sup>	3925	2.27 <sup>b</sup>	4133
60	9.60	9.39	2.31 <sup>a</sup>	4066	2.20 <sup>a</sup>	4269
65	9.70	9.49	2.19 <sup>b</sup>	4334	2.20 <sup>c</sup>	4314
70	9.80	9.59	4.30 <sup>c</sup>	2231	4.67 <sup>b</sup>	2054
75	9.90	9.69	2.56 <sup>a</sup>	3786	2.47 <sup>a</sup>	3924
80	10.01	9.80	2.80 <sup>a</sup>	3501	2.59 <sup>a</sup>	3784
85	10.11	9.90	2.34 <sup>a</sup>	4231	2.22 <sup>a</sup>	4460



**Table 8.A.1-49 (continued)**

Interval P-Wave Velocities Measured at Treasure Island Between B2 and B1 (R1-R2, Forward Profile), Path 2

Depth (ft)	Center Center Distance <sup>1</sup> (ft)	Travel Path Distance <sup>2</sup> (ft)	Wedge and Hammer Source <sup>3</sup>		Solenoid Source <sup>4</sup>	
			Travel Time (ms)	P-Wave Velocity (fps)	Travel Time (ms)	P-Wave Velocity (fps)
(1)	(2)	(3)	(4)	(5)	(6)	(7)
90	10.21	10.00	2.28 <sup>a</sup>	4387	2.12 <sup>a</sup>	4718
94	10.29	10.08	2.28 <sup>a</sup>	4422	2.28 <sup>a</sup>	4422
96	10.33	10.12	2.06 <sup>a</sup>	4913	1.86 <sup>a</sup>	5442
98	10.37	10.16	2.09 <sup>a</sup>	4862	1.92 <sup>a</sup>	5293
100	10.41	10.20	1.78 <sup>a</sup>	5731	1.78 <sup>a</sup>	5731

Notes on Table 8.A.1-49:

- <sup>1</sup> center-to-center spacings interpolated from data reported by the Earth Technology Corporation of San Bernardino, California
- <sup>2</sup> a half borehole diameter is subtracted from the center-to-center distance due to receiver positioning in B2
- <sup>3</sup> wedge and hammer source consists of a hammer impacting a pneumatically-locking wedge in the borehole
- <sup>4</sup> solenoid source produces a horizontal impact from the plunger of the solenoid
- <sup>a</sup> initial wave arrival clearly identified (within 5% of total travel time)—Type I data
- <sup>b</sup> initial wave arrival less distinct than (a) but identifiable (within 10% of total travel time)—Type II data
- <sup>c</sup> some interpretation required to identify initial wave arrival—Type III data
- <sup>d</sup> initial wave arrival not identifiable

**Table 8.A.1-50**

Direct P-Wave Velocities Measured at Treasure Island Between B1 and B2 (S-R1, Reverse Profile), Path 2

Depth (ft)	Center -to- Center Dist. <sup>1</sup> (ft)	Travel Path Dist. <sup>2</sup> (ft)	Wedge and Hammer Source <sup>3</sup>			Solenoid Source <sup>4</sup>		
			Travel Time (ms)	Adjusted Travel Time <sup>5</sup> (ms)	P-Wave Velocity (fps)	Travel Time (ms)	Adjusted Travel Time <sup>6</sup> (ms)	P-Wave Velocity (fps)
(1)	(2)	(3)	(4)	(5)	(6)	(7)	(8)	(9)

6	9.75	9.54	8.91 <sup>c</sup>	8.88	1074	11.19 <sup>b</sup>	11.09	860
12	9.59	9.38	2.20 <sup>a</sup>	2.17	4321	5.62 <sup>b</sup>	5.52	1699
18	9.57	9.36	2.20 <sup>a</sup>	2.17	4312	1.98 <sup>a</sup>	1.88	4978
24	9.54	9.33	2.20 <sup>a</sup>	2.17	4298	2.00 <sup>a</sup>	1.90	4909
30	9.57	9.36	1.97 <sup>a</sup>	1.94	4823	1.91 <sup>a</sup>	1.81	5169
35	9.58	9.38	2.05 <sup>a</sup>	2.02	4641	1.91 <sup>a</sup>	1.81	5180

Notes on Table 8.A.1-50:

- <sup>1</sup> center-to-center spacings determined using borehole survey data from Agbabian Associates, Pasadena, California
- <sup>2</sup> one-half borehole diameter is subtracted from the center-to-center spacing due to receiver positioning in B2
- <sup>3</sup> wedge and hammer source consists of a hammer impacting a pneumatically-locking wedge in the borehole
- <sup>4</sup> solenoid source produces a horizontal impact from the plunger of the solenoid
- <sup>5</sup> calibration factor (trigger delay) = 0.03 ms
- <sup>6</sup> calibration factor (trigger delay) = 0.10 ms
- <sup>a</sup> initial wave arrival clearly identified (within 5% of total travel time)—Type I data
- <sup>b</sup> initial wave arrival less distinct than (a) but identifiable (within 10% of total travel time)—Type II data
- <sup>c</sup> some interpretation required to identify initial wave arrival—Type III data

**Table 8.A.1-51**

Interval P-Wave Velocities Measured at Treasure Island Between B2 and B3 (R1-R2, Reverse Profile),  
Path 1

Depth (ft)	Center -to- Center Distance <sup>1</sup> (ft)	Travel Path Distance <sup>2</sup> (ft)	Wedge and Hammer Source <sup>3</sup>		Solenoid Source <sup>4</sup>	
			Travel Time (ms)	P-Wave Velocity (fps)	Travel Time (ms)	P-Wave Velocity (fps)
(1)	(2)	(3)	(4)	(5)	(6)	(7)
6	9.82	9.61	7.66 <sup>c</sup>	1255	— <sup>d</sup>	—
12	9.75	9.54	2.14 <sup>b</sup>	4459	2.06 <sup>b</sup>	4632
18	9.68	9.48	1.86 <sup>a</sup>	5094	1.87 <sup>a</sup>	5067
24	9.68	9.47	1.75 <sup>a</sup>	5410	1.75 <sup>a</sup>	5410
30	9.82	9.61	1.70 <sup>a</sup>	5654	1.72 <sup>a</sup>	5588
35	9.90	9.69	1.61 <sup>a</sup>	6020	1.66 <sup>a</sup>	5838

Notes on Table 8.A.1-51:

- <sup>1</sup> center-to-center spacings interpolated from forward-profile distances reported by the Earth Technology Corporation of San Bernardino, California (assuming forward and reverse-profile distances are equal)
- <sup>2</sup> a half borehole diameter is subtracted from the center-to-center distance due to receiver positioning in B2
- <sup>3</sup> wedge and hammer source consists of a hammer impacting a pneumatically-locking wedge in the borehole
- <sup>4</sup> solenoid source produces a horizontal impact from the plunger of the solenoid
- <sup>a</sup> initial wave arrival clearly identified (within 5% of total travel time)—Type I data
- <sup>b</sup> initial wave arrival less distinct than (a) but identifiable (within 10% of total travel time)—Type II data
- <sup>c</sup> some interpretation required to identify initial wave arrival—Type III data
- <sup>d</sup> initial wave arrival not identifiable

**Table 8.A.1-52**

Direct P-Wave Velocities Measured at Treasure Island Between B1 and B4 (S-R1, "North-South" Profile), Path 3

Depth (ft)	Center -to- Center Dist. <sup>1</sup> (ft)	Travel Path Dist. <sup>2</sup> (ft)	Wedge and Hammer Source <sup>3</sup>			Solenoid Source <sup>4</sup>		
			Travel Time (ms)	Adjusted Travel Time <sup>5</sup> (ms)	P-Wave Velocity (fps)	Travel Time (ms)	Adjusted Travel Time <sup>6</sup> (ms)	P-Wave Velocity (fps)
(1)	(2)	(3)	(4)	(5)	(6)	(7)	(8)	(9)
3	9.98	9.56	8.62 <sup>b</sup>	8.59	1113	6.34 <sup>b</sup>	6.24	1532
6	9.97	9.56	6.94 <sup>b</sup>	6.91	1383	5.25 <sup>b</sup>	5.15	1856
9	10.02	9.60	5.66 <sup>b</sup>	5.63	1705	7.23 <sup>b</sup>	7.13	1346
12	10.00	9.59	1.86 <sup>a</sup>	1.83	5239	1.84 <sup>a</sup>	1.74	5510
15	9.99	9.57	1.83 <sup>a</sup>	1.80	5317	1.91 <sup>a</sup>	1.81	5288
18	9.95	9.53	1.83 <sup>a</sup>	1.80	5297	1.87 <sup>a</sup>	1.77	5386
21	9.95	9.53	1.84 <sup>a</sup>	1.81	5268	1.87 <sup>a</sup>	1.77	5387
24	10.00	9.58	1.81 <sup>a</sup>	1.78	5384	1.87 <sup>a</sup>	1.77	5415
27	10.06	9.64	1.81 <sup>a</sup>	1.78	5418	1.88 <sup>a</sup>	1.78	5418
30	10.05	9.63	1.75 <sup>a</sup>	1.72	5601	1.80 <sup>a</sup>	1.70	5667
35	10.02	9.60	1.73 <sup>a</sup>	1.70	5648	1.75 <sup>a</sup>	1.65	5819
38	9.95	9.53	1.80 <sup>a</sup>	1.77	5387	1.81 <sup>a</sup>	1.71	5576
40	9.94	9.52	1.84 <sup>a</sup>	1.81	5262	1.86 <sup>a</sup>	1.76	5411
42	9.94	9.53	1.87 <sup>b</sup>	1.84	5178	1.86 <sup>a</sup>	1.76	5414
45	9.99	9.58	1.92 <sup>a</sup>	1.89	5067	2.00 <sup>a</sup>	1.90	5041
49	9.97	9.56	2.45 <sup>a</sup>	2.42	3948	2.36 <sup>b</sup>	2.26	4228

Notes on Table 8.A.1-52:

- <sup>1</sup> center-to-center spacings determined using borehole survey data from Agabian Associates, Pasadena, California
- <sup>2</sup> one borehole diameter is subtracted from the center-to-center spacing due to receiver positioning in B4
- <sup>3</sup> wedge and hammer source consists of a hammer impacting a pneumatically-locking wedge in the borehole
- <sup>4</sup> solenoid source produces a horizontal impact from the plunger of the solenoid
- <sup>5</sup> calibration factor (trigger delay) = 0.03 ms
- <sup>6</sup> calibration factor (trigger delay) = 0.10 ms
- <sup>a</sup> initial wave arrival clearly identified (within 5% of total travel time)—Type I data
- <sup>b</sup> initial wave arrival less distinct than (a) but identifiable (within 10% of total travel time)—Type II data

**Table 8.A.1-53**

Interval P-Wave Velocities Measured at Treasure Island Between B4 and B5 (R1-R2, "North-South" Profile), Path 4

Depth (ft)	Center -to- Center Distance <sup>1</sup> (ft)	Travel Path Distance <sup>2</sup> (ft)	Wedge and Hammer Source <sup>3</sup>		Solenoid Source <sup>4</sup>	
			Travel Time (ms)	P-Wave Velocity (fps)	Travel Time (ms)	P-Wave Velocity (fps)
(1)	(2)	(3)	(4)	(5)	(6)	(7)
3	10.70	10.91	— <sup>c</sup>	—	— <sup>c</sup>	—
6	10.67	10.88	9.64 <sup>b</sup>	1128	— <sup>c</sup>	—
9	10.60	10.81	— <sup>c</sup>	—	— <sup>c</sup>	—
12	10.56	10.77	— <sup>c</sup>	—	2.55 <sup>b</sup>	4223
15	10.57	10.78	2.17 <sup>a</sup>	4968	2.16 <sup>a</sup>	4991
18	10.59	10.80	2.22 <sup>a</sup>	4863	2.17 <sup>a</sup>	4975
21	10.62	10.83	2.14 <sup>a</sup>	5060	2.14 <sup>a</sup>	5060

Notes on Table 8.A.1-53:

- <sup>1</sup> center-to-center spacings determined using borehole survey data from Agbabian Associates, Pasadena, California
- <sup>2</sup> a half borehole diameter is added to the center-to-center distance due to receiver positioning in B5
- <sup>3</sup> wedge and hammer source consists of a hammer impacting a pneumatically-locking wedge in the borehole
- <sup>4</sup> solenoid source produces a horizontal impact from the plunger of the solenoid
- <sup>a</sup> initial wave arrival clearly identified (within 5% of total travel time)—Type I data
- <sup>b</sup> some interpretation required to identify initial wave arrival—Type III data
- <sup>c</sup> measurement not performed

**Table 8.A.1-54**

Direct P-Wave Velocities Measured at Treasure Island Between B2 and B4 (S-R1), Path 5

Depth (ft)	Center -to- Center Dist. <sup>1</sup> (ft)	Travel Path Dist. <sup>2</sup> (ft)	Wedge and Hammer Source <sup>3</sup>			Solenoid Source <sup>4</sup>		
			Travel Time (ms)	Adjusted Travel Time <sup>5</sup> (ms)	P-Wave Velocity (fps)	Travel Time (ms)	Adjusted Travel Time <sup>6</sup> (ms)	P-Wave Velocity (fps)
(1)	(2)	(3)	(4)	(5)	(6)	(7)	(8)	(9)
15	13.39	12.97	2.48 <sup>a</sup>	2.45	5294	— <sup>b</sup>	—	—
18	13.37	12.95	2.50 <sup>a</sup>	2.47	5242	— <sup>b</sup>	—	—
21	13.32	12.91	2.56 <sup>a</sup>	2.53	5101	— <sup>b</sup>	—	—
24	13.30	12.88	2.48 <sup>a</sup>	2.45	5257	— <sup>b</sup>	—	—
27	13.32	12.90	2.52 <sup>a</sup>	2.49	5181	— <sup>b</sup>	—	—

Notes on Table 8.A.1-54:

- <sup>1</sup> center-to-center spacings determined using borehole survey data from Agbabian Associates, Pasadena, California
- <sup>2</sup> one borehole diameter is subtracted from the center-to-center spacing due to receiver positioning in B4
- <sup>3</sup> wedge and hammer source consists of a hammer impacting a pneumatically-locking wedge in the borehole
- <sup>4</sup> solenoid source produces a horizontal impact from the plunger of the solenoid
- <sup>5</sup> calibration factor (trigger delay) = 0.03 ms
- <sup>6</sup> calibration factor (trigger delay) = 0.10 ms
- <sup>a</sup> initial wave arrival clearly identified (within 5% of total travel time)—Type I data
- <sup>b</sup> measurement not performed

## REFERENCES

- American Society for Testing and Materials (1987). Standard D 4428/ D 4428 M. Annual Book of ASTM Standards, Section 4, Vol. 04.08, pp. 881-894.
- de Alba, P., J. Benoit, T. L. Youd, A. F. Shakal, D. G. Pass and J. J. Carter (1992). "Deep Instrumentation Array at Treasure Island Naval Station," NEHRP Report to Congress, the October 17, 1989 Loma Prieta, California, Earthquake, United States Geological Survey, in press.
- Gibbs, J. F., T. E. Fumal, D. M. Boore and W. B. Joyner (1992). "Seismic Velocities and Geologic Logs from Borehole Measurements at Seven Strong-Motion Stations That Recorded the Loma Prieta Earthquake," U. S. Geological Survey Open-File Report 92-287, Menlo Park, California.
- Fuhriman, M. D. (1993). "Crosshole Seismic Tests at Two Northern California Sites Affected by the 1989 Loma Prieta Earthquake," Master's Thesis, The University of Texas at Austin, Department of Civil Engineering, Austin, Texas.
- Hardin, B. O. and V. P. Drnevich (1972). "Shear Modulus and Damping in Soils: Design Equations and Curves." Journal of the Soil Mechanics and Foundation Engineering Division, American Society of Civil Engineers, Vol. 98, No. 7, pp. 667-692.
- Hoar, R. J. (1982). "Field Measurement of Seismic Wave Velocity and Attenuation for Dynamic Analyses," Doctoral Dissertation, The University of Texas at Austin, Department of Civil Engineering, Austin, Texas.
- Hryciw, R. D., K. M. Rollins, M. Homolka, S. E. Shewbridge, and M. McHood (1991). "Soil Amplification at Treasure Island During the Loma Prieta Earthquake." Proceedings Second International Conference on Recent Advances in Geotechnical Earthquake Engineering and Soil Dynamics, St. Louis, Missouri, pp. 1679-1685.
- Hwang, S. K. and K. H. Stokoe (1993). "Laboratory Measurement of G and D of Gilroy 2 Samples." Report to the Electric Power Research Institute, in progress.
- Mok, Y. J. (1987). "Analytical and Experimental Studies of Borehole Seismic Methods," Doctoral Dissertation, The University of Texas at Austin, Austin, Texas.
- Nigbor, Bob (1992); Telephone conversation.
- Ramirez, R. W. (1985). *The FFT, Fundamentals and Concepts*, Prentice-Hall, Inc., Englewood Cliffs, New Jersey.
- Redpath, B. B. and R. C. Lee (1986). "In Situ Measurements of Shear-Wave Attenuation at a Strong-Motion Recording Site," Unpublished Report Prepared by URS/ John A. Blume & Associates, USGS Contract No. 14-08-001-21823.
- Redpath, B. B., et al. (1982). "Development of Field Techniques to Measure Damping Values for Near-Surface Rocks and Soils," Unpublished Report Prepared by URS/ John A. Blume & Associates, NSF Grant No. PFR-7900192.
- Reichle, M. S., R. B. Darragh, M. J. Huang, T. Cao, U. R. Vetter, and A. F. Shakal (1990). "Preliminary Analysis of Processed Strong Motion Data from the Loma Prieta Earthquake," *The Loma Prieta (Santa Cruz Mountains), California, Earthquake of 17 October 1989*, S. R. McNutt and R. H. Sydnor, eds., California Department of Conservation, Division of Mines and Geology Special Publication 104, pp. 47-58.
- Richart, F. E., J. R. Hall and R. D. Woods (1970). *Vibrations of Soils and Foundations*, Prentice-Hall, Inc., Englewood Cliffs, New Jersey.
- Shakal, A. F., M. J. DeLisle, M. S. Reichle and R. B. Darragh (1990). "Strong Ground Shaking from the Loma Prieta Earthquake of 17 October 1989, and its Relation to Near Surface Geology in the Oakland Area," *The Loma Prieta (Santa Cruz Mountains), California, Earthquake of 17 October 1989*, S. R. McNutt and R. H. Sydnor, eds., California Department of Conservation, Division of Mines and Geology Special Publication 104, pp. 29-46.

- Stokoe, K. H., II, S. Nazarian, G. J. Rix, I. Sanchez-Salinero, J. C. Sheu, and Y. J. Mok (1988). "In Situ Seismic Testing of Hard-to-Sample Soils by Surface Wave Method," *Earthquake Engineering and Soil Dynamics II—Recent Advances in Ground Motion Evaluation*, Geotechnical Special Publication No. 20, ASCE, New York, New York, pp. 264–278.
- Stokoe, K. H., II (1992). Personal Communication. The University of Texas at Austin.
- Toksoz, M. N. and D. H. Johnston (1981). "Definitions and Terminology," *Seismic Wave Attenuation*, *Society of Exploration Geophysics Reprint Series No. 2*, M. N. Toksoz and D. H. Johnston, eds., pp. 1–5.
- Wagner, D. L. (1990). "Geologic and Tectonic Setting of the Epicentral Area of the Loma Prieta Earthquake, Santa Cruz Mountains, Central California," *The Loma Prieta (Santa Cruz Mountains), California, Earthquake of 17 October 1989*, S. R. McNutt and R. H. Sydnor, eds., California Department of Conservation, Division of Mines and Geology Special Publication 104, pp. 1–10.





## **APPENDIX 8.A.2 BOREHOLE GEOPHYSICAL MEASUREMENTS AT THE GILROY 2 AND TREASURE ISLAND SITES**

---

### **ABSTRACT**

As part of a detailed study of the sites, borehole geophysical measurements were performed at both the Gilroy 2 and Treasure Island sites. Measurements included resistivity, natural gamma, borehole drift, P- and S-wave velocities (suspension method), P- and S-wave velocities (crosshole method), and downhole attenuation.

These data will become part of the database for these sites, and will be used for further study of site response estimation methodologies.

## **ACKNOWLEDGEMENTS**

The measurements described in this report were made by a team of researchers led by the principal investigators Robert Nigbor and Robert Steller of Agbabian Associates. Major contributions were made by Bruce Redpath of Redpath Geophysics, Takashi Kanemori of OYO Geospace, Finn Michelson of OYO Geospace, Kenji Tanaka of OYO Corporation, and Ed Steller.

The following companies assisted the project by providing special equipment used in the measurements: ANCO Engineers, Kinematics, Inc., OYO Corporation, and Redpath Geophysics.

# CONTENTS

---

Section	Page
<b>1—Overview</b> .....	<b>8.A.2-5</b>
<b>2—Measurement Techniques and Procedures</b> .....	<b>8.A.2-8</b>
8.A.2.2.1 Resistivity Logging .....	<b>8.A.2-8</b>
8.A.2.2.2 Natural Gamma Logging .....	<b>8.A.2-8</b>
8.A.2.2.3 Caliper Logging .....	<b>8.A.2-9</b>
8.A.2.2.4 Borehole Drift Logging .....	<b>8.A.2-9</b>
8.A.2.2.5 Suspension PS Velocity Logging .....	<b>8.A.2-9</b>
8.A.2.2.6 Cross-Hole Velocity Measurement .....	<b>8.A.2-13</b>
8.A.2.2.7 Attenuation Measurement .....	<b>8.A.2-17</b>
<b>3—Results</b> .....	<b>8.A.2-20</b>
8.A.2.3.1 Gilroy 2 .....	<b>8.A.2-20</b>
<i>8.A.2.3.1.1 Resistivity, Natural Gamma, and Caliper Logs</i> .....	<b>8.A.2-20</b>
<i>8.A.2.3.1.2 Borehole Drift</i> .....	<b>8.A.2-20</b>
<i>8.A.2.3.1.3 Suspension Velocities</i> .....	<b>8.A.2-20</b>
<i>8.A.2.3.1.4 Cross-Hole Velocities</i> .....	<b>8.A.2-29</b>
<i>8.A.2.3.1.5 Attenuation</i> .....	<b>8.A.2-32</b>
8.A.2.3.2 Treasure Island .....	<b>8.A.2-34</b>
<i>8.A.2.3.2.1 Borehole Drift</i> .....	<b>8.A.2-34</b>
<i>8.A.2.3.2.2 Suspension Velocities</i> .....	<b>8.A.2-34</b>
<i>8.A.2.3.2.3 Cross-Hole Velocities</i> .....	<b>8.A.2-39</b>
<i>8.A.2.3.2.4 Attenuation</i> .....	<b>8.A.2-42</b>
<b>4—Summary</b> .....	<b>8.A.2-45</b>
<b>References</b> .....	<b>8.A.2-46</b>



# APPENDIX 8.A.2

## BOREHOLE GEOPHYSICAL MEASUREMENTS AT THE GILROY 2 AND TREASURE ISLAND SITES

---

### 1—OVERVIEW

The Gilroy Array Station 2 and Treasure Island accelerograph sites have been the source of anomalous strong-motion records from several earthquakes. These records and the desire to understand the soil characteristics that influence ground motion have prompted the detailed study of these two sites.

Part of these studies is a suite of geophysical measurements performed by Agabian Associates in cooperation with Redpath Geophysics and OYO Geospace. These measurements and the analysis of data are detailed in this report.

At the Gilroy Array Station 2 (hereafter called "Gilroy 2") site, three new boreholes were drilled to augment the existing 600' deep, 5" diameter cased hole. Figure 8.A.2-1 shows the borehole configuration at Gilroy 2. The existing borehole is denoted Borehole 4 in this report. The new holes were drilled along a north line from the existing hole at 14' spacing and cased with 4" PVC. Depths are 790, 200, and 200 feet for Boreholes 3, 2, and 1, respectively (Borehole 1 is the north-most).

Prior to casing Borehole 3, the following measurements were made:

- Long and Short Resistivity Log
- Caliper Log (borehole diameter)
- Natural Gamma Log
- Suspension PS Velocity Log

After all of the new holes were cased, the following measurements were made:

- Borehole Drift (horizontal deviation)
- Crosshole PS Velocity Measurements
- Downhole Attenuation (damping)

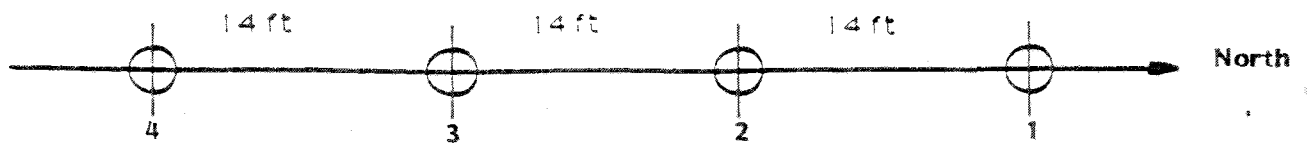
There are six existing, cased boreholes at the Treasure Island site as shown in Figure 8.A.2-2. Depths are 340, 145, 102, 60, 51, and 24 feet. The 340' hole is cased with 5" PVC; all others are cased with 4" PVC.

Because the boreholes were already cased, it was not possible to perform the resistivity, natural gamma, and caliper logs at this site. In addition, an attempt at suspension PS logging was unsuccessful because of the casing. The following measurements were successfully performed at the Treasure Island site:

- Borehole Drift
- Crosshole PS Velocity Measurements
- Downhole Attenuation (damping)

This report describes the various geophysical measurements at the two sites and presents the results of the measurements in graphical form. Data have also been provided to the EPRI Project Manager (as available throughout the past year) in digital form for use in the larger site response analysis project.

a.) Plan View



b.) Cross-Sectional View

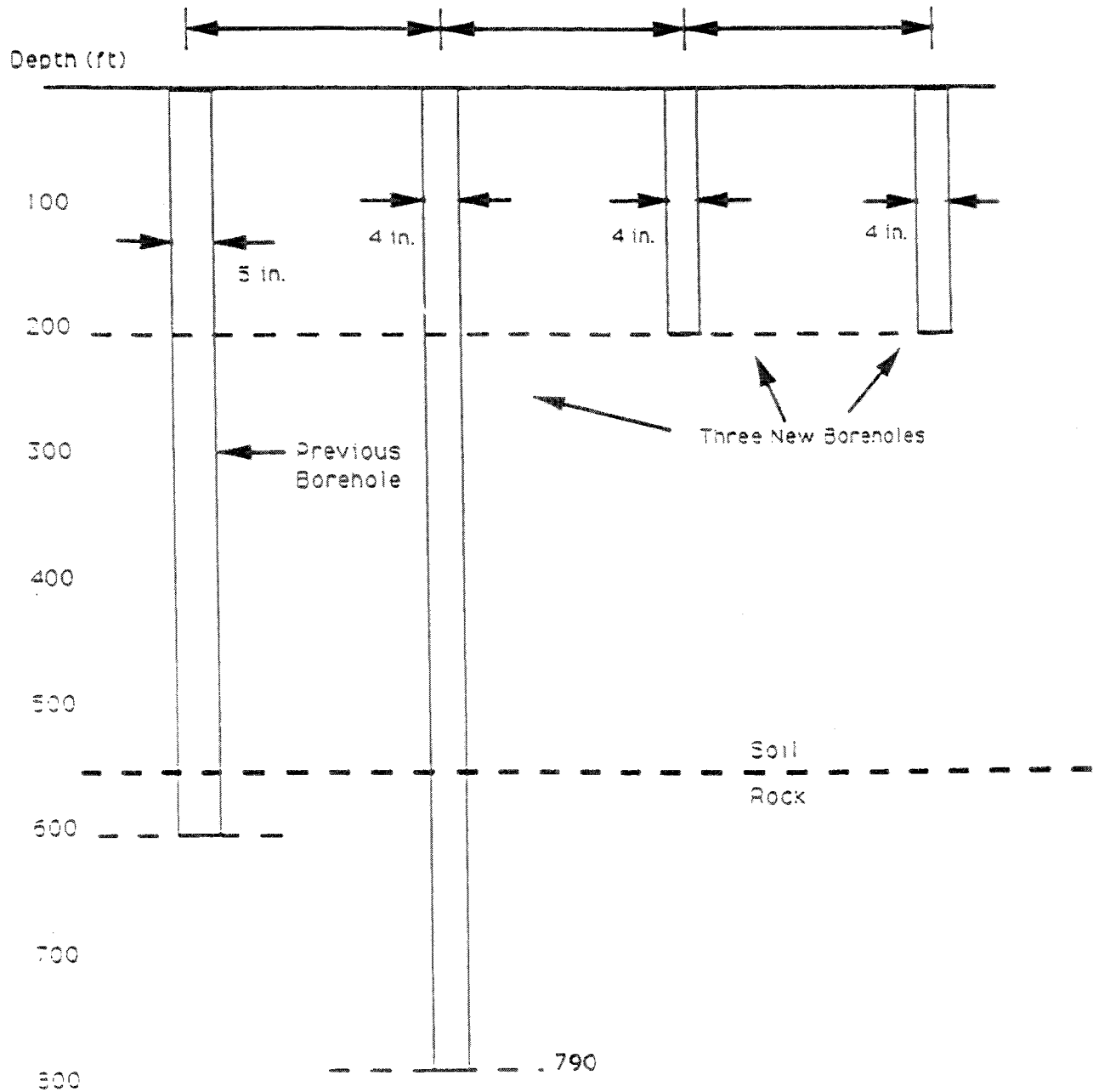


Figure 8.A.2-1  
Gilroy 2 site borehole layout.

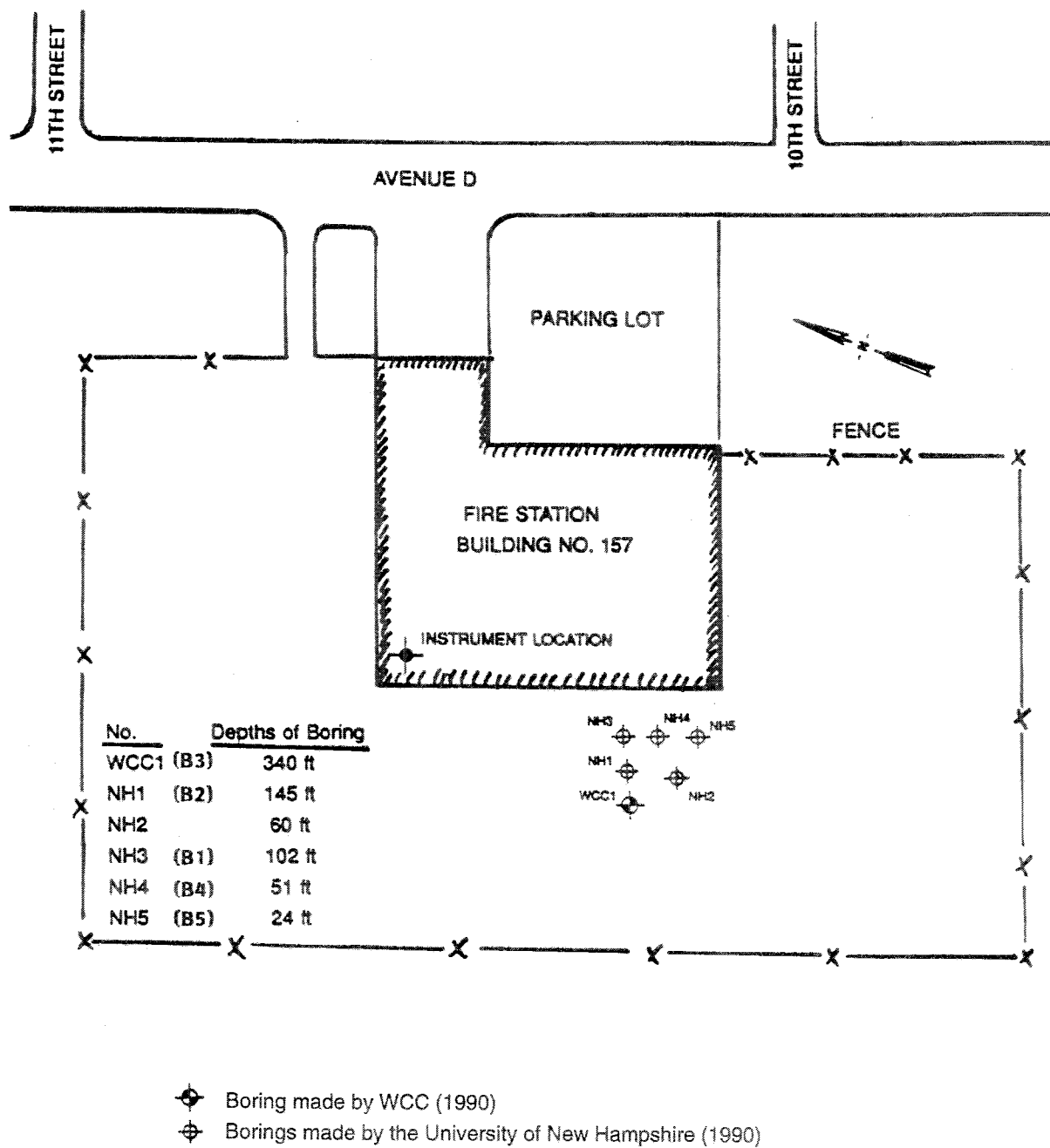


Figure 8.A.2-2  
Treasure Island site borehole layout.



## 2—MEASUREMENT TECHNIQUES AND PROCEDURES

This section details the following types of measurements made at one or both of the two sites:

- Resistivity Logging
- Natural Gamma Logging
- Caliper Logging
- Borehole Drift Logging
- Suspension PS Velocity Logging
- Crosshole PS Velocity Logging
- Attenuation Measurement

This report section describes the specific measurements at the Gilroy 2 and Treasure Island sites.

With the exception of the newer suspension PS logging and attenuation measurement techniques, excellent background regarding the geophysical measurements performed in this project can be found in a book by Spangler and Handy (1) and two reports by Shannon & Wilson/

Agbabian Associates

(2) and (3). Detailed descriptions of these common measurement techniques are therefore not included in this report.

Because the suspension PS logging and attenuation measurements are relatively new techniques, detailed descriptions of the techniques are included below.

### 8.A.2.2.1 Resistivity Logging

Soil resistivity is influenced by mineral content and porosity. It is often used as an indicator of sand and clay content, and as such it can assist in site stratigraphy interpretation. Spangler and Handy (1) describes the applications of this type of logging.

Resistivity is measured in an uncased borehole. "Short" normal resistivity is measured between two electrodes 16" apart. "Long" normal resistivity is measured with a 64 inch electrode separation. The long measurement will penetrate further from the borehole wall, and will therefore be less sensitive to the drilling mud and to borehole wall disturbances.

We measured resistivity in Borehole 3 at the Gilroy 2 site using the Combination Logging probe manufactured by OYO Corporation. This probe consists of a fiberglass cylinder containing a scintillation detector, and carrying three electrode rings on its surface to measure normal resistivity. One electrode is used as a common for the long and short resistivity determination; it is separated from the second electrode for short normal resistivity by 16 inches, and from the second electrode for long normal resistivity by 64 inches.

### 8.A.2.2.2 Natural Gamma Logging

A natural gamma log measures the rate of natural radiation emissions in the soil. In general, clay will have a higher gamma rate than sand. Natural gamma rates increase in igneous rock or recent sediments of igneous origin. As with the resistivity log, this log is used as an aid in determination of site stratigraphy.

We measured the natural gamma rate in Borehole 3 at the Gilroy 2 site using the OYO Combination Probe described in the previous section.

#### **8.A.2.2.3 Caliper Logging**

A caliper log of an uncased borehole is simply a measurement of the borehole diameter versus depth. This measurement can assist in stratigraphy determination, as softer soils will generally have a larger diameter due to erosion of the material during drilling. This log is also useful in the interpretation of the suspension PS velocity log.

We used the Caliper Logging probe, manufactured by OYO Corporation, in Borehole 3 at the Gilroy 2 site. This probe consists of a stainless steel cylinder supporting two spring loaded fingers designed to slide along the walls of the borehole. The position of each finger is monitored by a position sensor. The range of measurement for the probe is 2 inches to 11 inches. The fingers are held in the minimum diameter position by a locking mechanism that is released when the probe contacts the bottom of the borehole. The probe sends the resultant signals to an OYO Geologger 3030 Mk. II recorder on the surface via an armored 4 conductor cable. The cable is wound onto the drum of a winch and is used to support the probe. Cable travel is measured to provide depth data.

In operation, the probe is lowered to the bottom of the borehole, where contact with the bottom releases the caliper fingers, allowing them to spring outward and contact the wall of the borehole. The probe is then raised to the surface, with the fingers tracking the borehole walls. During the sampling run, the Geologger samples each signal at 10 cm. intervals, stores the values in memory, and plots them on a paper tape. Upon completion of the measurement run, the data can be stored on 3.5 inch floppy diskette for further processing.

#### **8.A.2.2.4 Borehole Drift Logging**

A borehole will never be exactly vertical. With proper care during drilling, however, horizontal deviation (called "Drift") can be small, less than 1% of the hole depth.

This small amount of borehole drift is usually not significant for single borehole measurements such as suspension PS velocity logging or downhole attenuation measurement. However, drift can be significant for crosshole velocity logging. Here, the distance between the two boreholes has a first order effect upon measured velocities.

At both the Gilroy 2 and Treasure Island sites, we measured the drift versus depth for each cased borehole. The Drift Probe made by OYO Corporation was used for these measurements.

The Drift Probe consists of an approximately 6 foot long housing containing a biaxial tilt sensor and a fluxgate compass to measure the rotational orientation. The probe sends the resultant signals to the OYO Geologger 3030 Mk. II recorder on the surface via an armored 4 conductor cable. The cable is wound onto the drum of a winch and is used to support the probe. Cable travel is measured to provide depth data.

In operation, the probe is lowered from the top to the bottom. During the sampling run, the Geologger samples each signal at 1 meter intervals and stores the values in memory. Upon completion of the measurement run, the tilt and orientation data are used to calculate the north (X) and west (Y) deviations of the borehole versus depth (Z). The raw and reduced data are then stored on 3.5 inch floppy diskette for further processing.

#### **8.A.2.2.5 Suspension PS Velocity Logging**

The purpose of this type of measurement is to acquire shear and compressional wave velocities as a function of depth which, in turn, will be used to characterize ground response to earthquake motion. The suspension method, developed by OYO Corporation, is unique because both the energy source and the receivers are in a single probe. The system measures P- and S-wave velocities over a 1 meter interval. It is intended to be used in an uncased borehole; results in cased boreholes are generally poor.

We used the OYO Suspension P-S Logging system to obtain in-situ horizontal shear and compressional wave velocity measurements in Borehole 3 at the Gilroy 2 site. Measurements were made in the uncased borehole at the same time as the resistivity and natural gamma logging described above. Suspension P-S velocity logging was unsuccessfully attempted in the deep, cased borehole at Treasure Island.

The acquired data was analyzed and a profile of velocity versus depth was produced for both compressional and horizontally polarized shear waves.

We performed the suspension velocity measurements using the Model 170 Suspension P-S Logging system, manufactured by OYO Corporation. Figure 8.A.2-3 shows a sketch of this system. The Model 170 directly determines the average velocity of a one meter high segment of the soil column surrounding the borehole of interest by measuring the elapsed time between arrivals of a wave propagating upward through the soil column. The geophones that detect the wave, and the source that generates the wave, are moved as a unit in the borehole, producing relatively constant amplitude signals at all depths.

The suspension system probe consists of a combined reversible polarity solenoid horizontal shear-wave generator ( $S_H$ ) and compressional-wave generator (P), joined to two biaxial geophones by a flexible isolation cylinder, as shown in Figure 8.A.2-3. The separation of the two geophones is one meter, allowing average wave velocity in the region between the geophones to be determined by inversion of the wave travel time between the two geophones. The total length of the probe is approximately 21 feet; the center point of the geophones is approximately 15 feet above the bottom end of the probe. The probe receives control signals from, and sends the amplified geophone signals to, instrumentation on the surface via an armored 7 conductor cable. The cable is wound onto the drum of a winch and is used to support the probe. Cable travel is measured to provide probe depth data.

The entire probe is suspended by the cable and centered in the borehole by nylon "whiskers," therefore, source motion is not coupled directly to the borehole walls; rather, the source motion creates a horizontally propagating pressure wave in the fluid filling the borehole and surrounding the source. This pressure wave produces a horizontal displacement of the soil forming the wall of the borehole. This displacement propagates up and down the borehole wall, in turn causing a pressure wave to be generated in the fluid surrounding the geophones as the soil displacement wave passes their location.

In operation, the P-S Logger activates the  $S_H$ -wave source in one direction and records the output of the two horizontally oriented geophone axes which are situated parallel to the axis of motion of the source. The source is then activated in the opposite direction, and the horizontal output signals are again recorded, producing a  $S_H$ -wave record of polarity opposite to the previous record. The source is finally actuated in the first direction again, and the responses of the vertical geophone axes to the resultant P-wave are recorded during this sampling.

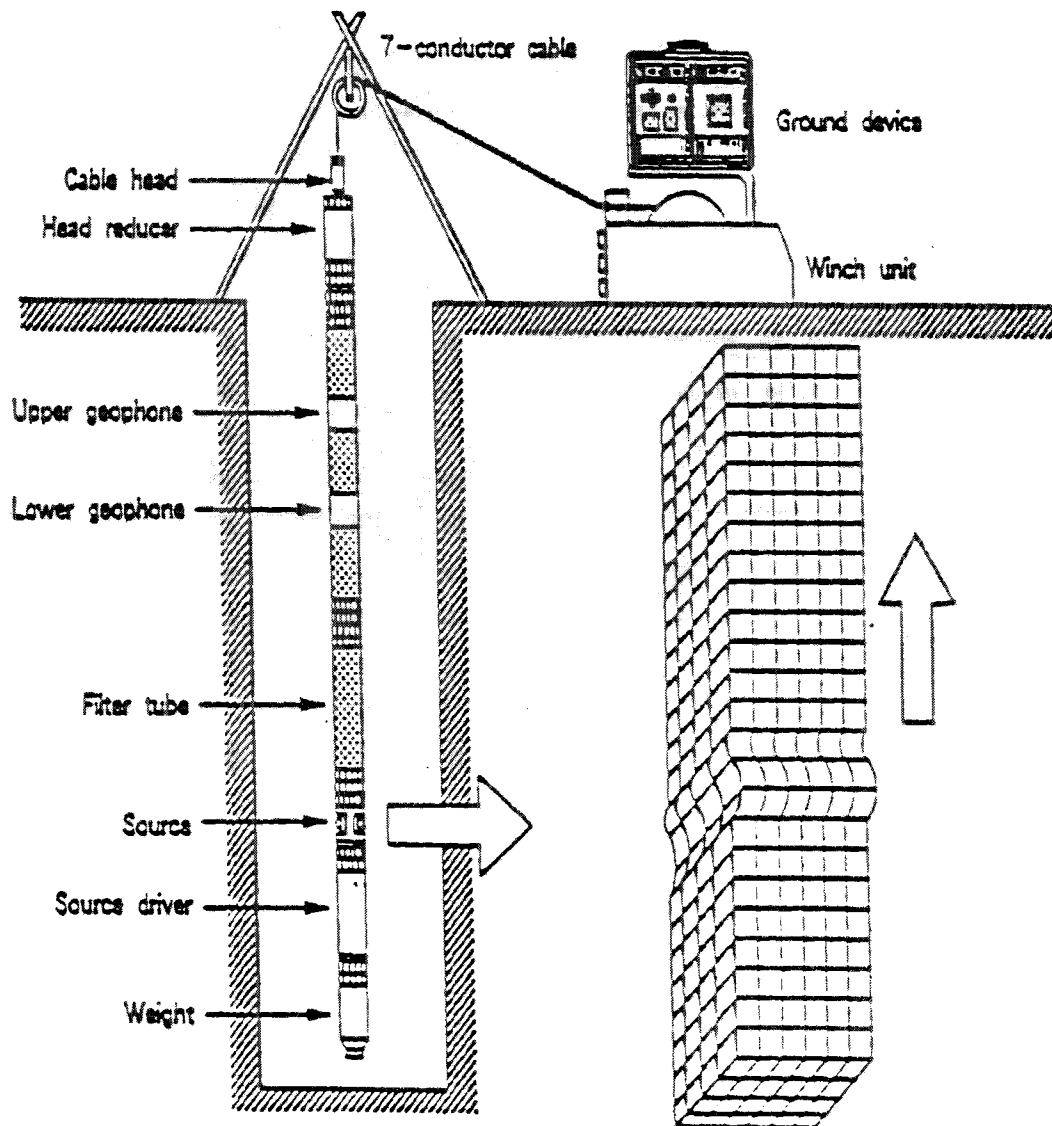
The data from each geophone during each source activation is recorded as a different channel on the recording system. The Model 170 has six channels (two simultaneous recording channels), each with a 12 bit 1024 sample record. The recorded data is displayed on a CRT display and on paper tape output as six channels with a common time scale. Data is stored on 3.5 inch floppy diskettes for further processing. Up to 8 sampling sequences can be "stacked" to improve the signal to noise ratio of the signals.

Review of the displayed data on the CRT or paper tape allows the operator to set the gains, filters, delay time, pulse length (energy), sample rate, and "stacking" number in order to optimize the quality of the data before recording. Figure 8.A.2-4 shows a sample of the paper record.

The suspension probe is lowered to the bottom of the borehole, with occasional stops to check system function. The probe was then raised according to preplanned sample intervals. At each sampling depth the measurement sequence of two opposite horizontal records and one vertical record was performed, and the gains were adjusted as required. The data from each depth is printed on paper tape, checked, and recorded on diskette before moving to the next depth.

The digital records are analyzed to locate the first minima on the vertical axis records, indicating the arrival of P-wave energy. The difference in travel time between these arrivals is used to calculate the P-wave velocity for that 1 meter interval. When observable, P-wave arrivals on the horizontal axis records is used to verify the velocities determined from the vertical axis data. In addition, the soil velocity calculated from the travel time from source to first receiver is compared to the velocity derived from the travel time between receivers.

The digital records are studied to establish the presence of clear  $S_H$ -wave pulses, as indicated by the presence of opposite polarity pulses on each pair of horizontal records. Ideally, the  $S_H$ -wave signals from the 'normal' and 'reverse' source pulses are very nearly inverted images of each other. Digital FFT-IFFT lowpass filtering are used to remove the higher frequency P-wave signal from the  $S_H$ -wave signal.



**Figure 8.A.2-3**  
Suspension P-S logging system diagram.

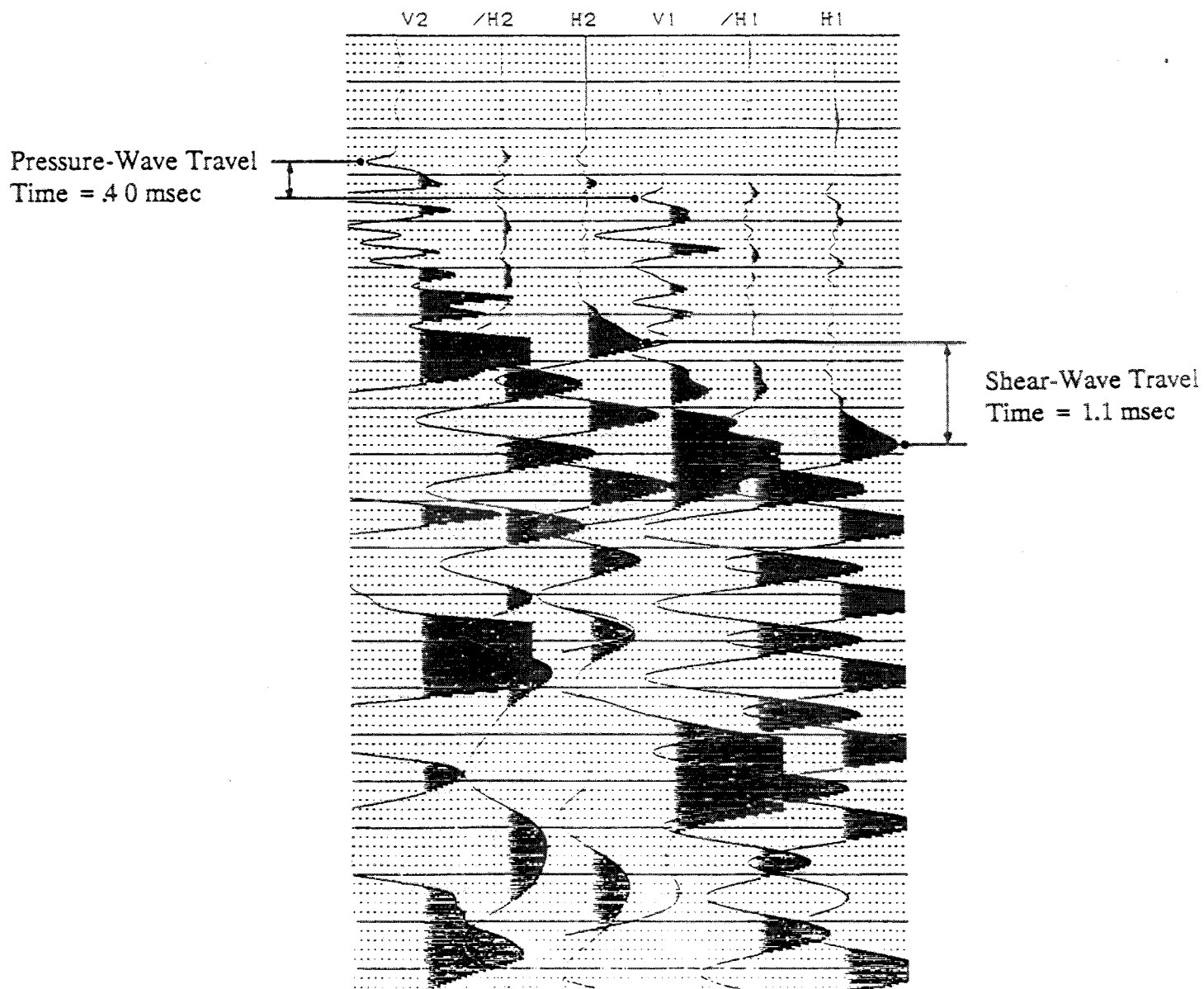


Figure 8.A.2-4  
Sample paper data record.

The first maxima is picked for the 'normal' signals and the first minima was picked for the 'reverse' signals. The absolute arrival time of the 'normal' and 'reverse' signals may vary by  $\pm 0.2$  milliseconds, due to differences in the actuation time of the solenoid source caused by constant mechanical bias in the source or by borehole inclination. This variation does not affect the velocity determinations, as the differential time is measured between arrivals of waves created by the same source actuation. The final velocity value is the average of the values obtained from the 'normal' and 'reverse' source actuations.

It should be noted that the suspension logging system measures velocities at frequencies between 500 and 2000 Hz. Also, because of differences in coupling between the two sources, it is not possible to accurately use the recorded time signals to measure attenuation.

#### **8.A.2.2.6 Cross-Hole Velocity Measurement**

The Suspension Method measures P- and S-wave velocities over 1 meter intervals in a single borehole. If two or more boreholes are available, average velocities between the boreholes at a given depth can be directly measured using the Crosshole Method. Shannon & Wilson/Agbabian Associates (3) details this method of velocity measurement.

We used this method to measure velocities at both the Gilroy 2 and Treasure Island sites. At each site, three collinear boreholes were used for the measurements. An impulsive source was inserted in an end hole, and receivers were inserted at the same depth in the other two holes. Both the source and the receivers were orientable, allowing their axes to be aligned for maximum signal strength. Actuation of the source triggered the digital recording of signals from the two receivers.

Figure 8.A.2-5 is a block diagram of the custom measurement system used for these crosshole velocity measurements. The source, shown in Figure 8.A.2-6, is a bidirectional horizontal solenoid suspended from a locking and orientation device. The source is the same as in the suspension system, so coupling with the soil is through the borehole fluid. The frequency range of the source is 500–2000 Hz.

The receivers are custom variable azimuth biaxial (horizontal and vertical) 10-Hz geophones designed and built by Bruce Redpath of Redpath Geophysics. They physically lock to the borehole wall using a gas bladder system.

The control and recording modules from the OYO Model 170 Suspension System were used to control the source and to digitally measure the horizontal and vertical signals from both of the biaxial receivers.

Specific details of the crosshole measurements at each site will be provided in Section 8.A.2.3. However, operation of the system was identical at each site as follows. The source and receivers were lowered to a given depth in each of three boreholes, oriented in the same direction perpendicular to a line connecting the holes, and locked in place. The source was actuated and data recorded. If necessary, data from several actuations were stacked to improve the signal to noise ratio.

Figure 8.A.2-7 is a sample of the recorded crosshole waveforms. Differential travel times are calculated from these waveforms as calculated for the suspension data. Velocity is then calculated by dividing the path length (distance between the two receivers) by the measured travel time.

For the suspension data the travel distance is 1 meter exactly. For the crosshole data, the travel path length must be calculated from the surface borehole spacing and the drift log data.

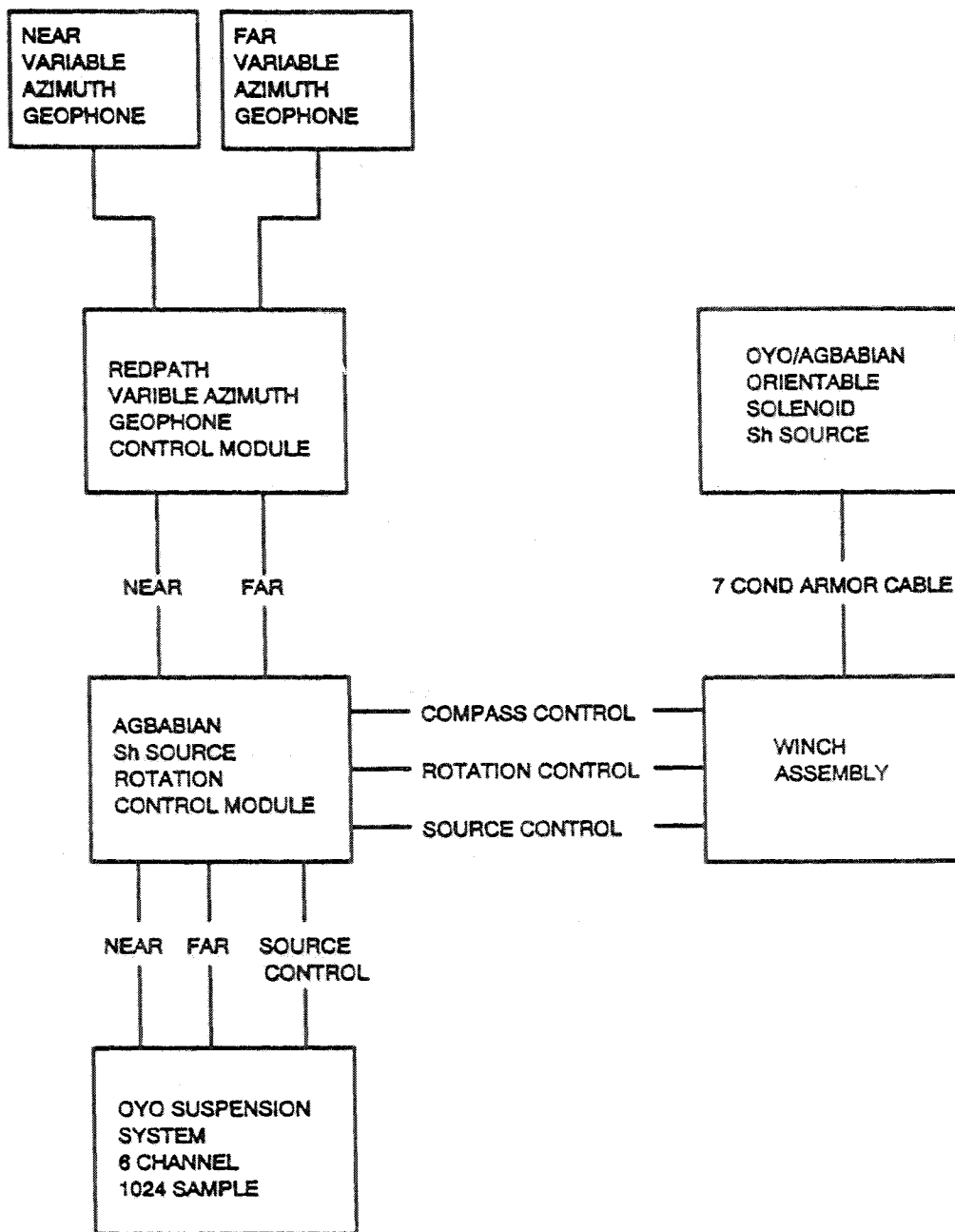
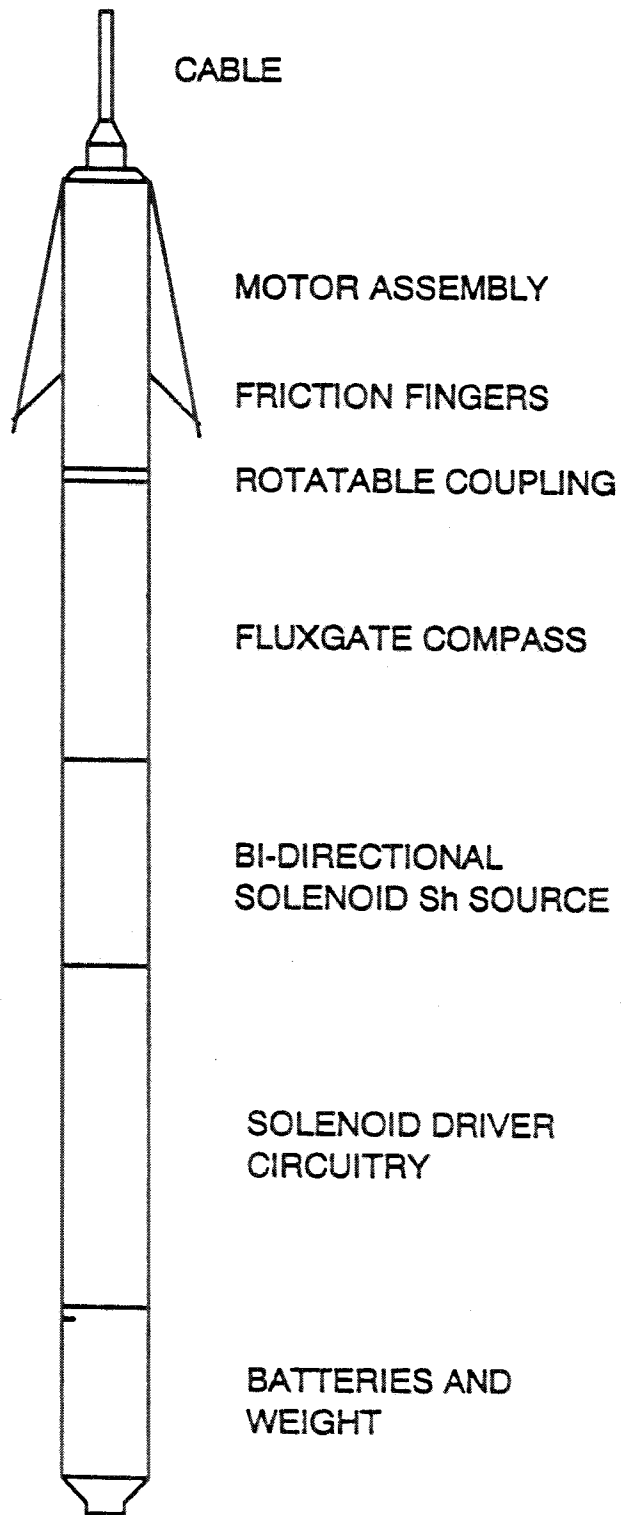


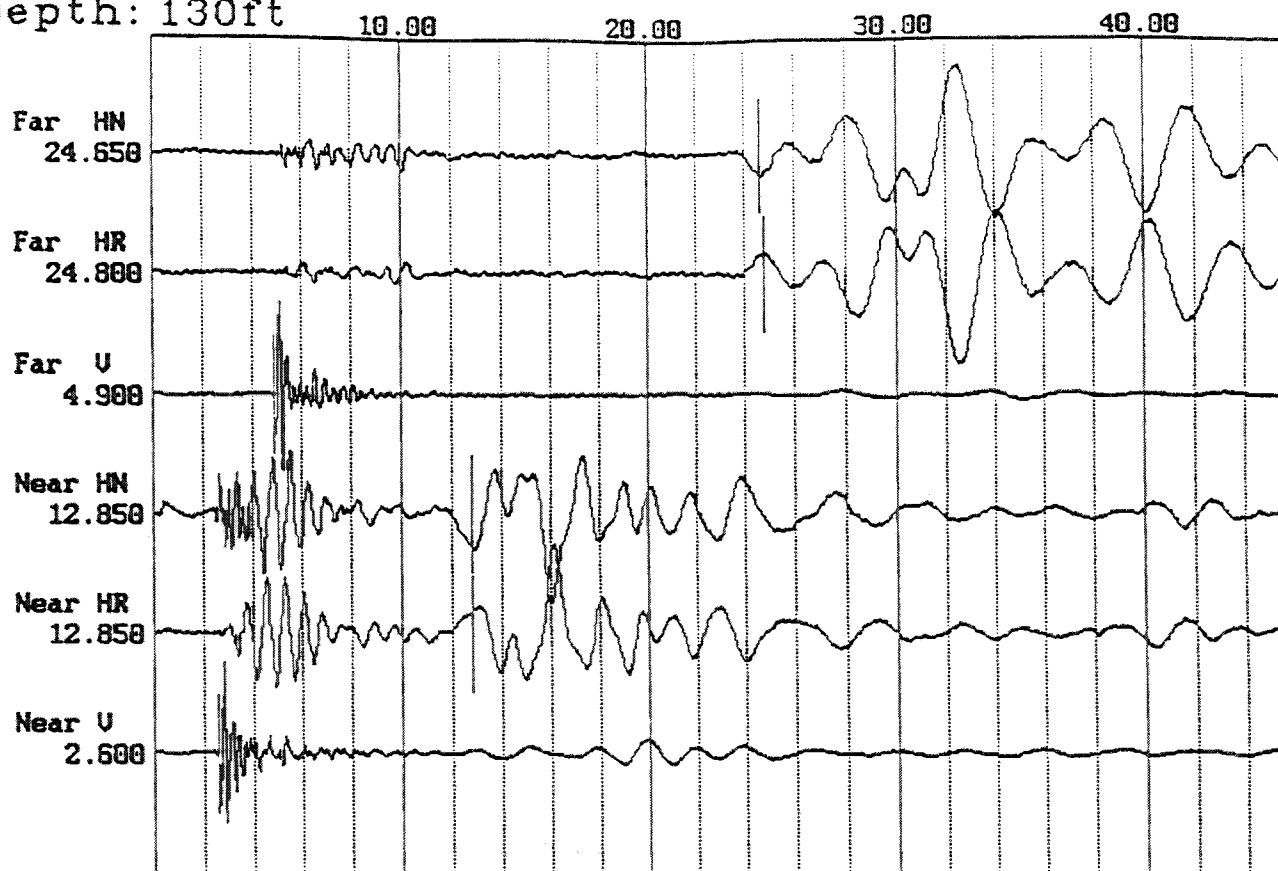
Figure 8.A.2-5  
Crosshole velocity system block diagram.



**Figure 8.A.2-6**  
Orientable suspension solenoid Sh source.



Depth: 130ft



**Gilroy, Sample Crosshole  $S_H$  Record**  
**Receiver 1 (near) to Receiver 2 (far)**

Figure 8.A.2-7  
Sample crosshole waveform data.

#### 8.A.2.2.7 Attenuation Measurement

An important property of soil for earthquake response analysis is its attenuation (denoted  $Q$ ) or damping (denoted  $D$ ,  $D=1/2Q$ ). These quantities describe the amount of energy absorbed by dynamic hysteretic or viscous action of the soil.

Attenuation varies with strain level. The only way to measure attenuation at earthquake strain levels is in the laboratory. However, small-strain attenuation can be measured in-situ. These in-situ values can then be used to anchor laboratory measurement results.

Attenuation characteristics of a vertical soil column can be estimated for low strains by measuring the waveforms from a surface source at various depths in a single borehole. This is called "downhole attenuation." This method is detailed in References (4), (5), and (6). "Crosshole attenuation" can also be estimated from the waveforms recorded during crosshole velocity measurements.

We attempted to measure crosshole attenuation from our crosshole velocity measurements described in the previous section. However, results were poor due to small signal amplitudes, nonuniform source coupling, and the high frequencies from our suspension source. Another source type should be used if crosshole attenuation is desired (we have developed such a source in the last six months, after these measurements were made).

We successfully performed downhole attenuation measurements in the deep boreholes at both the Gilroy 2 and Treasure Island sites. Several types of surface sources were used: a hammer on a horizontal plank, a large sinusoidal shaker (peak force above 2000 lbs), a small shaker (30 lb peak force) with random motion, and the small shaker with sinusoidal motion. Figure 8.A.2-8 shows the force-frequency curve for the large shaker.

## PEAK SINE SHAKER FORCE OUTPUT ATTENUATION STUDY, LARGE SHAKER

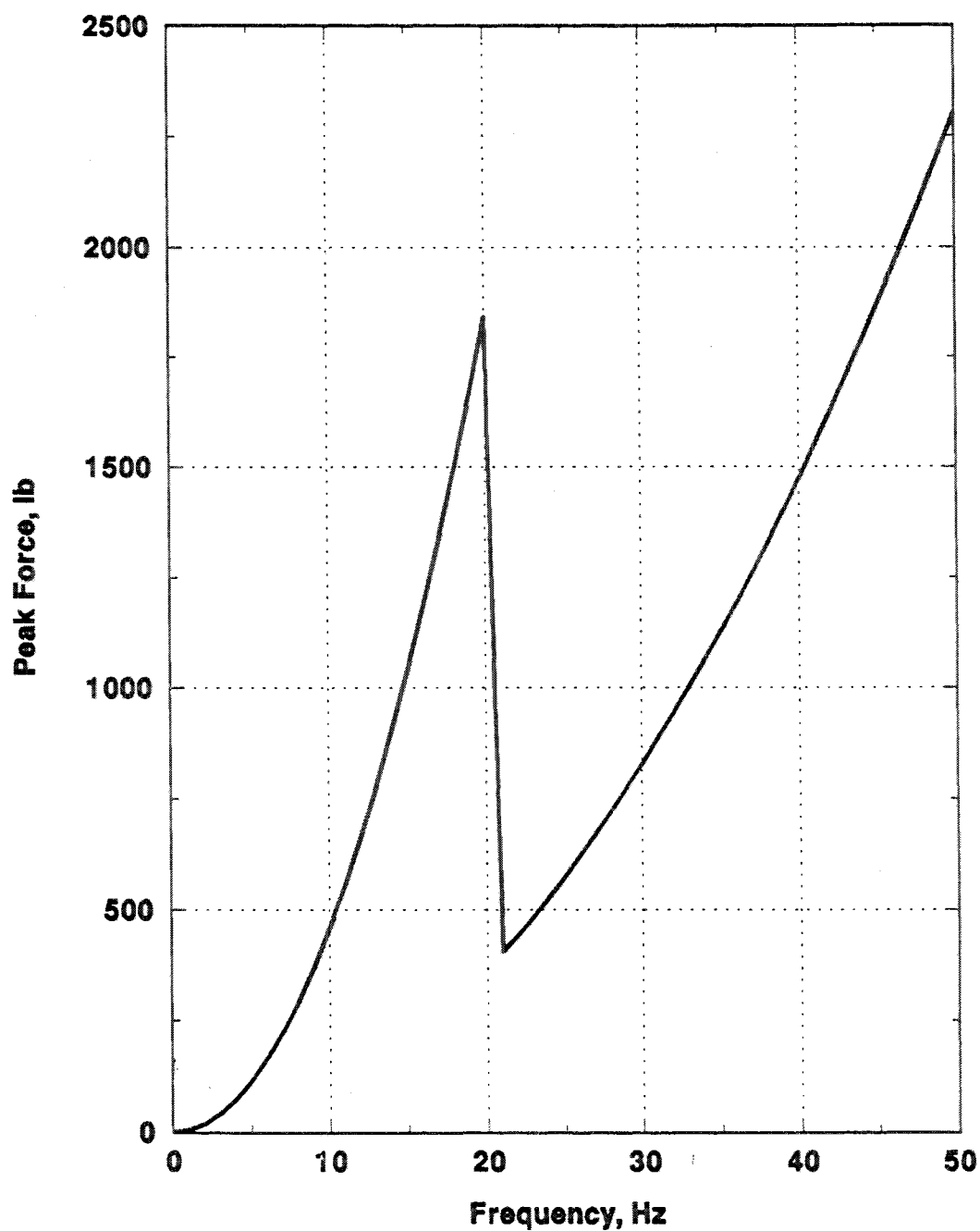


Figure 8.A.2-8  
Force output of the large shaker.

The various sources were coupled to the soil using the weight of a 5 ton truck. However, for the large shaker this was not completely adequate for the higher forces above about 30 Hz, as some relative motion between shaker and ground was observed. This likely affected both the transmission of the energy into the soil and the purity of the horizontal excitation.

The Redpath Geophysics orientable biaxial borehole geophone packages used for the crosshole testing were used for this test as well. At each site, one geophone package was locked at a depth of 50 feet and used as a reference. The other geophone package was locked at various lower depths. Both sensor packages were oriented in line with the surface excitation.

Data from the two depths were simultaneously recorded using a Kinometrics Model SSR-1 digital recorder for later computer analysis. Signals from the two horizontal receivers were sampled at 500 samples per second with a 250 Hz anti-aliasing filter. A Hewlett-Packard spectrum analyzer was used for on-site data analysis.

At each depth setting of the moving receiver, data were recorded for several hammer blows, 20 second sine dwells (frequencies between 10 and 50 Hz) from the large shaker, and 10 second sine dwells (between 10 and 80 Hz) from the small shaker. Random excitation from the small shaker was not large enough for accurate measurement, and was not used after the first attempt.

For each type of excitation, the recorded data were analyzed using the "Spectral Slope Method" described in Reference (4). This frequency domain analysis method makes the following assumptions:

- Attenuation is frequency independent
- Scattering effects are frequency independent
- Geometric spreading effects are frequency independent
- Near-source effects are not present in the shallower reference sensor
- Signal-to-noise ratios are acceptable over a wide frequency band

Proper measurement techniques can minimize effects of the last two assumptions. However, there is currently some question whether the first three assumptions are completely valid.

Nevertheless, we proceeded with spectral slope analysis of the recorded attenuation data for both sites. Results are given in Section 3.

### **3—RESULTS**

This section describes specific details of the field work, analysis, and results from the various geophysical measurements at Gilroy 2 and Treasure Island.

#### **8.A.2.3.1 Gilroy 2**

The resistivity, natural gamma, caliper, and suspension PS velocity measurements were performed in late October, 1991. A previous report to EPRI (Reference (7)) details these measurements. In January, 1992, borehole drift and crosshole velocity measurements were done. Attenuation studies were done in early March, 1992.

Results from each of the various measurements are presented below.

##### **8.A.2.3.1.1 Resistivity, Natural Gamma, and Caliper Logs**

Figure 8.A.2-9 plots the short and long resistivity measured in Borehole 3. Figure 8.A.2-10 plots the natural gamma log, and Figure 8.A.2-11 plots the caliper data.

Both the resistivity and natural gamma logs show several clear stratigraphic transitions in the region above 200 foot depth. These logs are then relatively constant below 200 feet until bedrock is reached at about 550 feet. There are significant variations in both logs in the rock to the bottom of the borehole.

The caliper logging probe failed to operate below 410 feet. Results in the upper 410 feet indicate significant washouts of the borehole walls, perhaps denoting softer sediments.

##### **8.A.2.3.1.2 Borehole Drift**

Figures 8.A.2-12 through 8.A.2-15 are 3-D plots of measured borehole drift for Boreholes 1-4, respectively. Refer to Figure 8.A.2-1 for the borehole layout.

Digital drift data have previously been provided to the EPRI project manager and are included in the project database.

##### **8.A.2.3.1.3 Suspension Velocities**

Figure 8.A.2-16 plots the P- and S-wave velocities measured using the OYO Suspension Logging system in Borehole 3 at the Gilroy 2 site. Digital data were previously provided to the EPRI project manager and are included in the project database.

These plots exhibit considerable variation when compared with traditional downhole velocity data. The suspension logging system measures velocities over a 1 meter interval. It is therefore reasonable to expect such variations, as the soil properties are not constant over small intervals.

The variation in the P-wave velocities sometimes appears to occur in discrete steps. This is due to the resolution limit determined by the digital data sampling rate.

Data Collected Oct. 31-Nov. 1, 1991

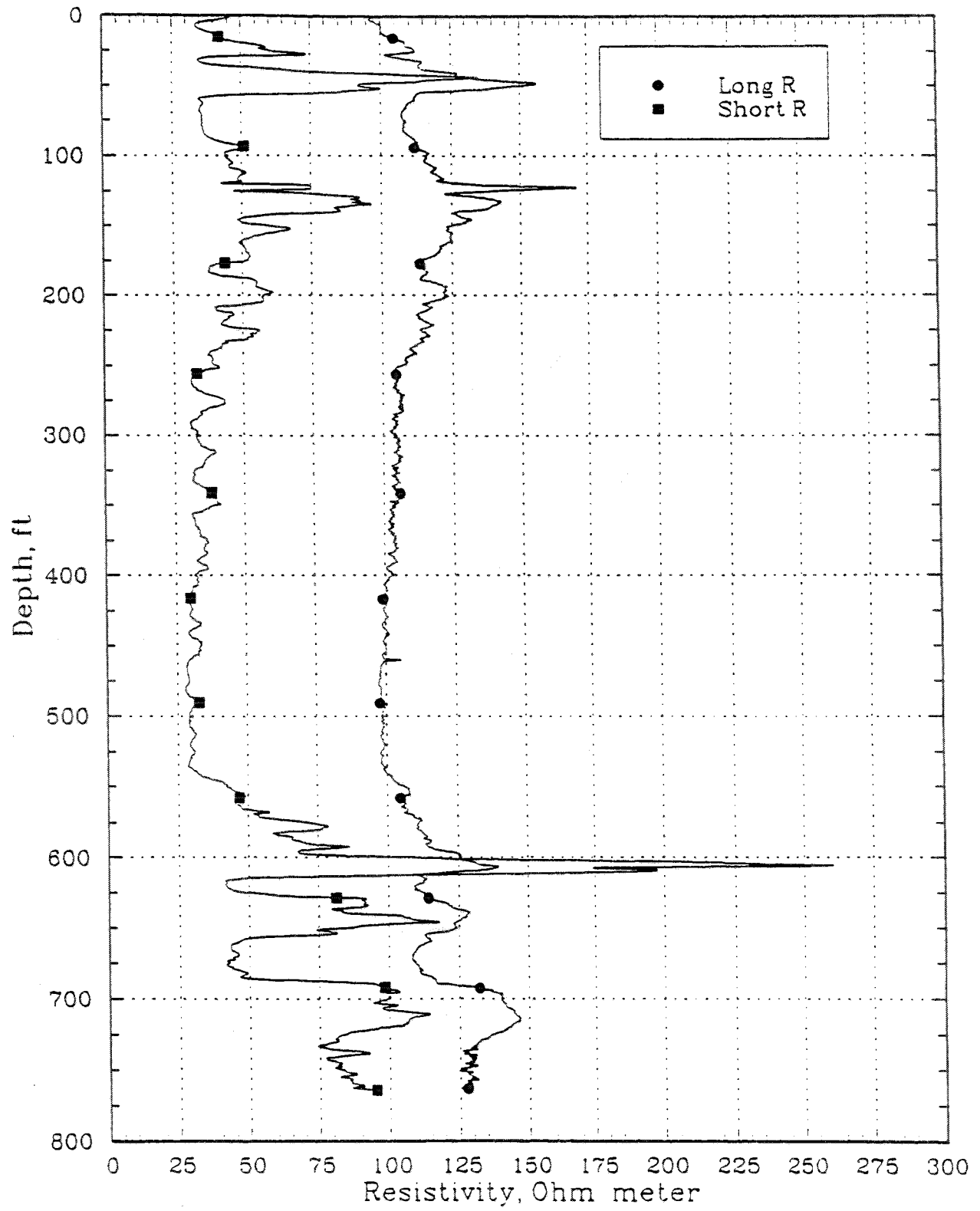


Figure 8.A.2-9  
Gilroy 2 resistivity data.

Data Collected Oct. 31-Nov. 1, 1991

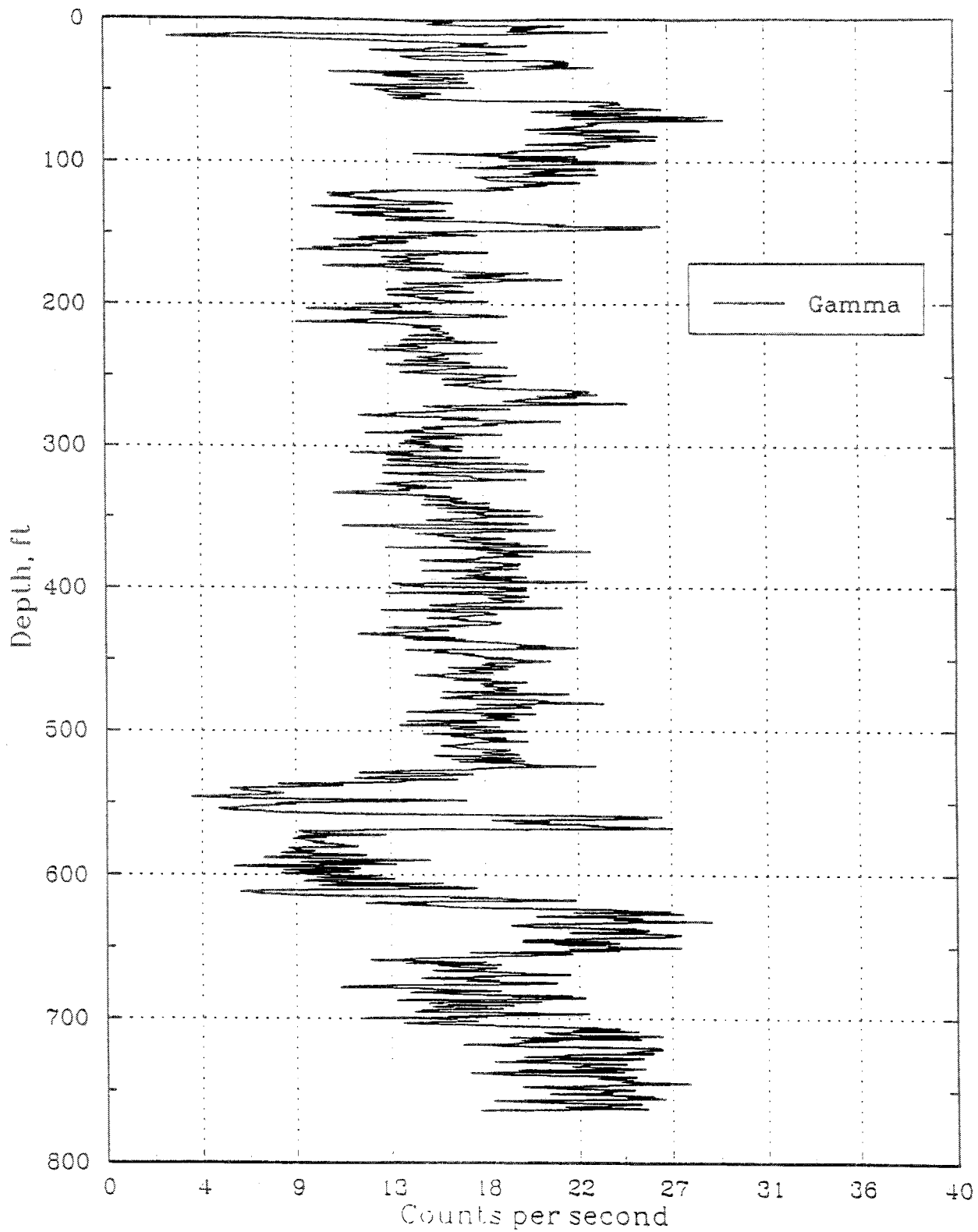


Figure 8.A.2-10  
Gilroy 2 natural Gamma data.

Data Collected Oct. 31-Nov. 1, 1991

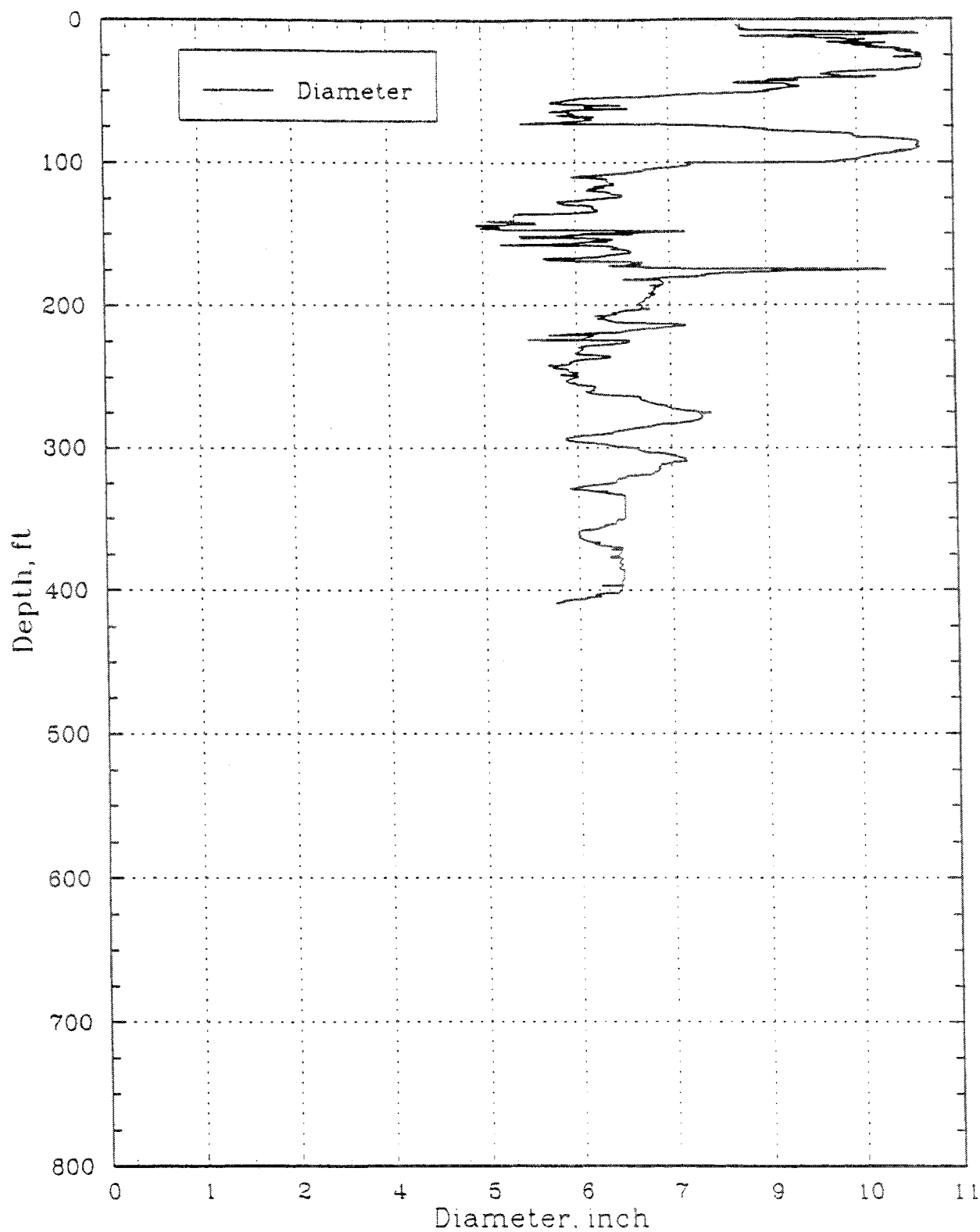
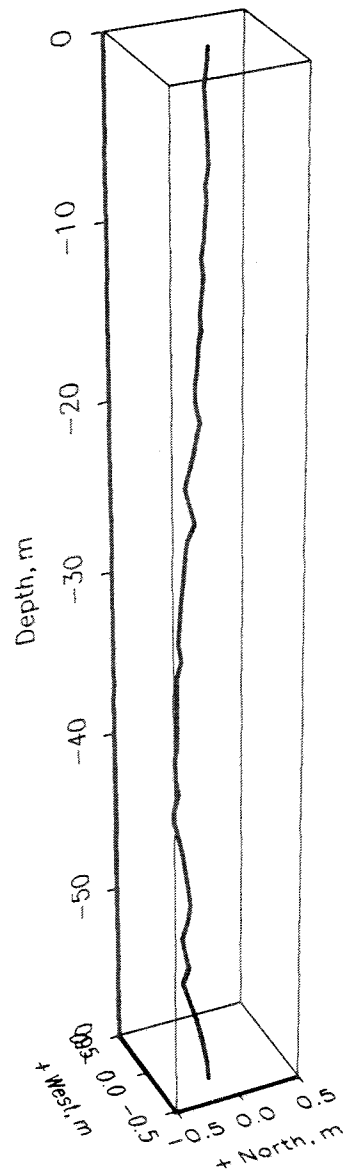


Figure 8.A.2-11  
Gilroy 2 caliper log data.



# MEASURED BOREHOLE DRIFT

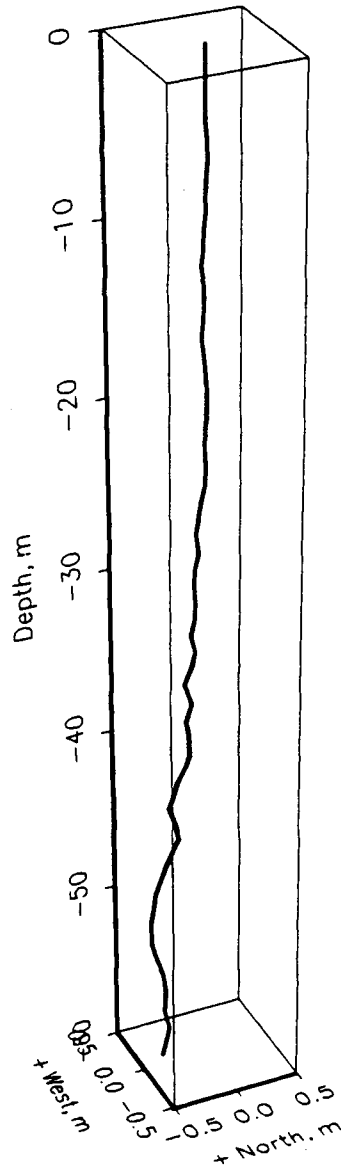
*Gilroy 2 Site, Borehole 1 (North-most)*



**Figure 8.A.2-12**  
Gilroy 2 drift data, Borehole 1.

# MEASURED BOREHOLE DRIFT

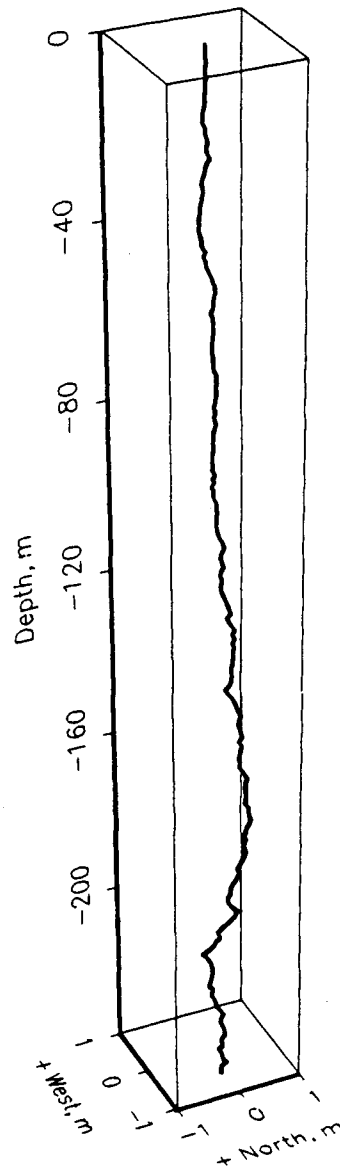
*Gilroy 2 Site, Borehole 2 (2nd from north)*



**Figure 8.A.2-13**  
Gilroy 2 drift data, Borehole 2.

# MEASURED BOREHOLE DRIFT

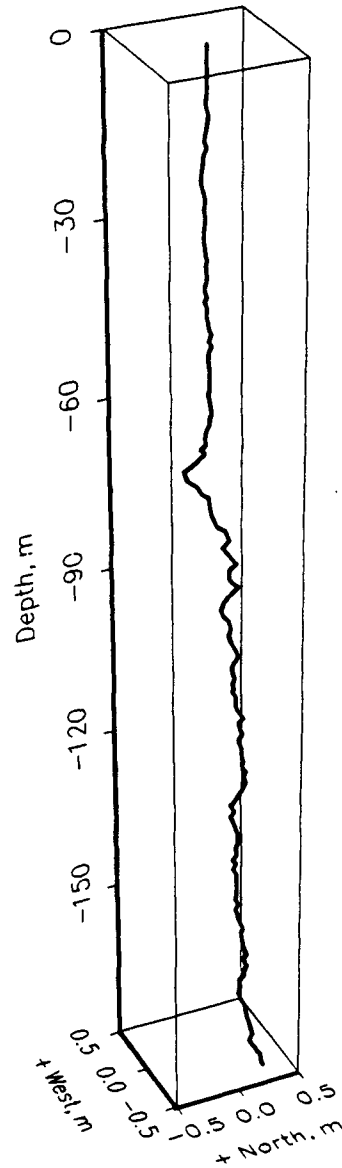
*Gilroy 2 Site, Borehole 3 (3rd from north)*



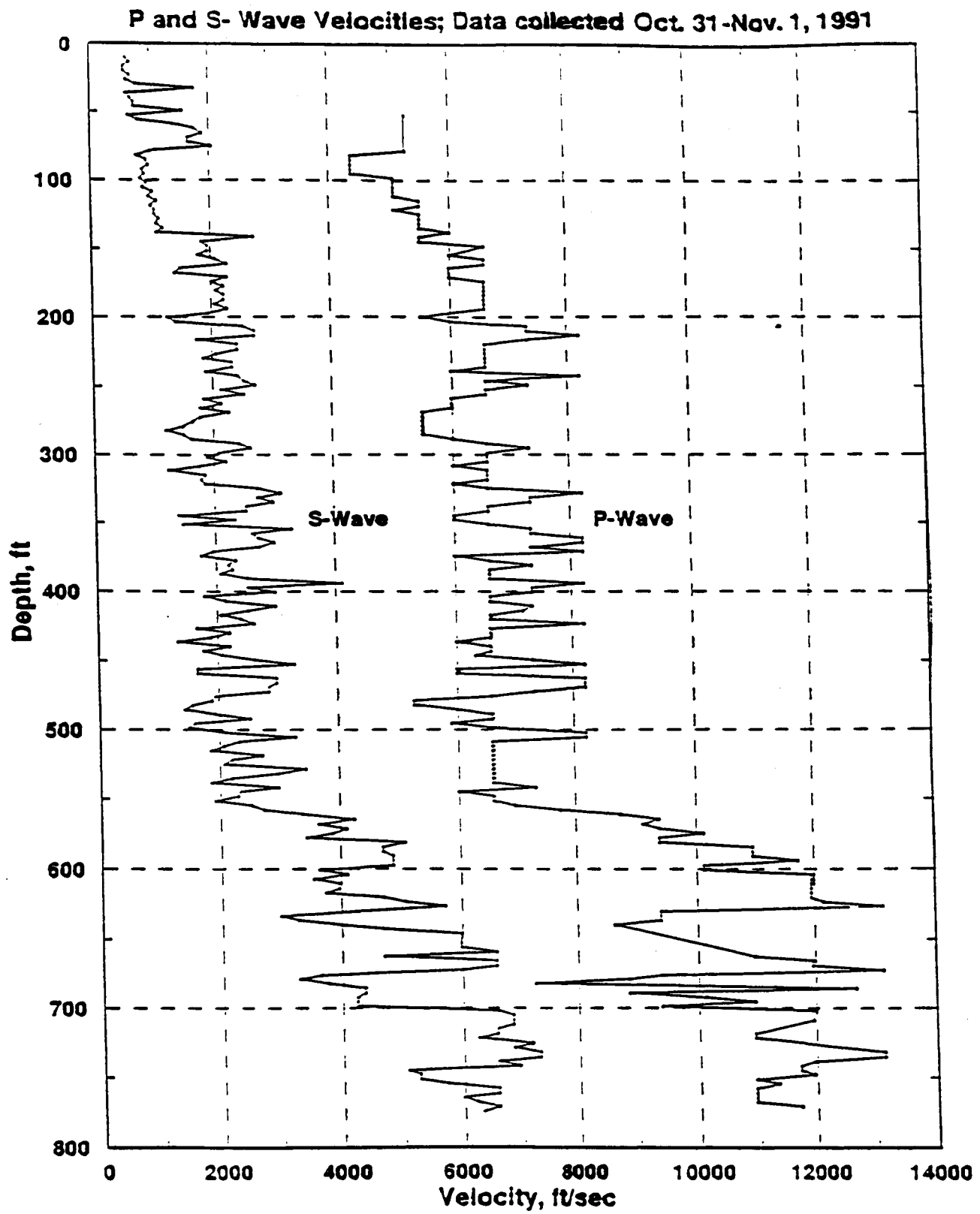
**Figure 8.A.2-14**  
Gilroy 2 drift data, Borehole 3.

# MEASURED BOREHOLE DRIFT

*Gilroy 2 Site, Borehole 4 (4th from north)*



**Figure 8.A.2-15**  
Gilroy 2 drift data, Borehole 4.



**Figure 8.A.2-16**  
Gilroy 2 suspension PS velocities.

#### **8.A.2.3.1.4 Cross-Hole Velocities**

The crosshole source was inserted in Borehole 3 and the two receivers in Boreholes 1 and 2 at the Gilroy 2 site. P- and S-wave velocities were then measured between the two receivers (differential) and between the source and each of the two receivers. The three measurements generally compared well, although there is additional uncertainty in the source-receiver measurements due to the mechanical and electrical delays in the source actuation. In general, the differential measurements are considered to be more precise.

Figures 8.A.2-17 and 8.A.2-18 plot the differential S-wave and P-wave velocities, respectively. These were measured to a depth of 200' (the bottom of boreholes 1 and 2).

We also attempted to measure crosshole velocities from source to receiver deeper than 200' using Boreholes 3 and 4. However, the measurement quality was unacceptable due to variability in the source actuation times.

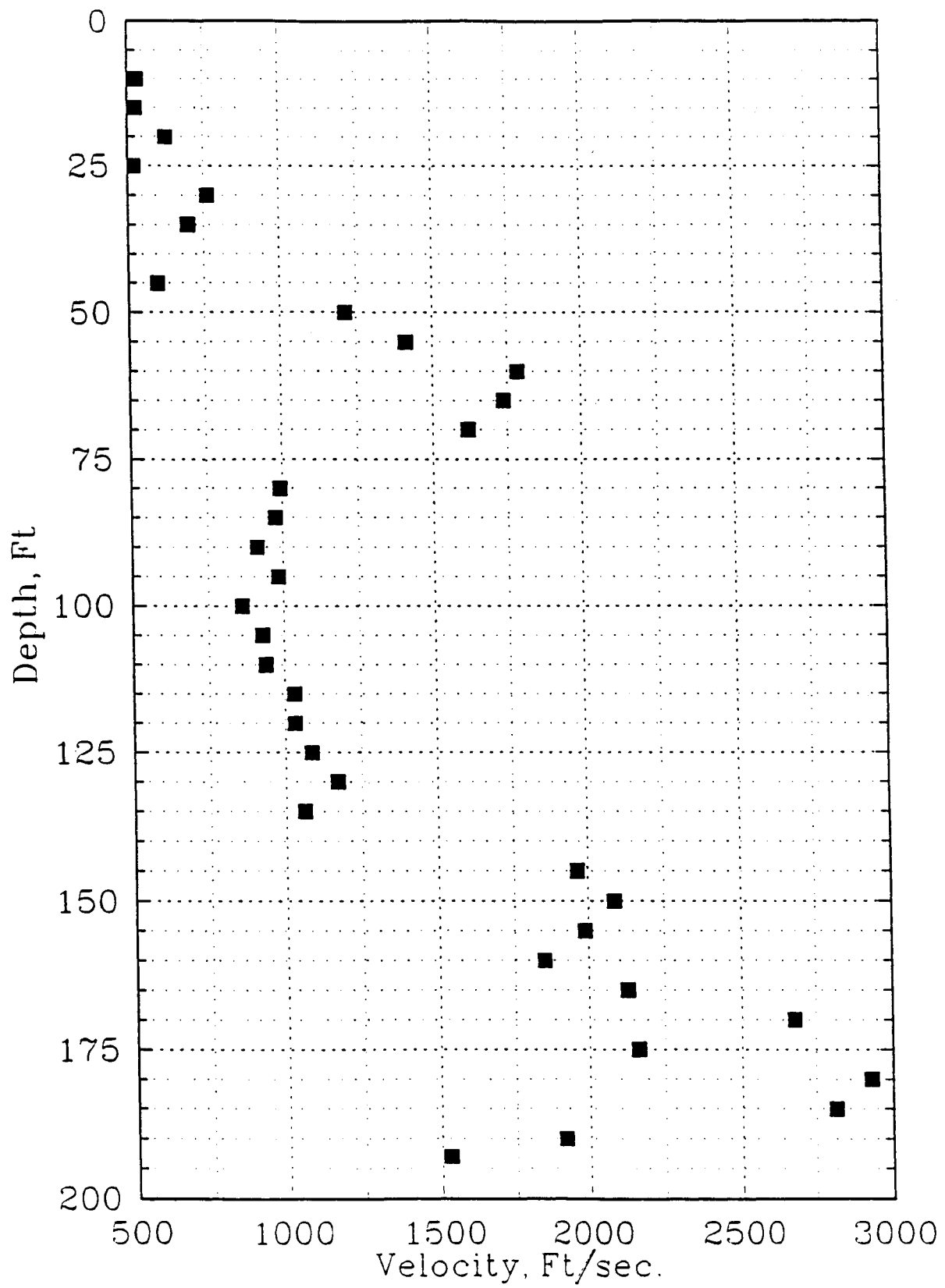
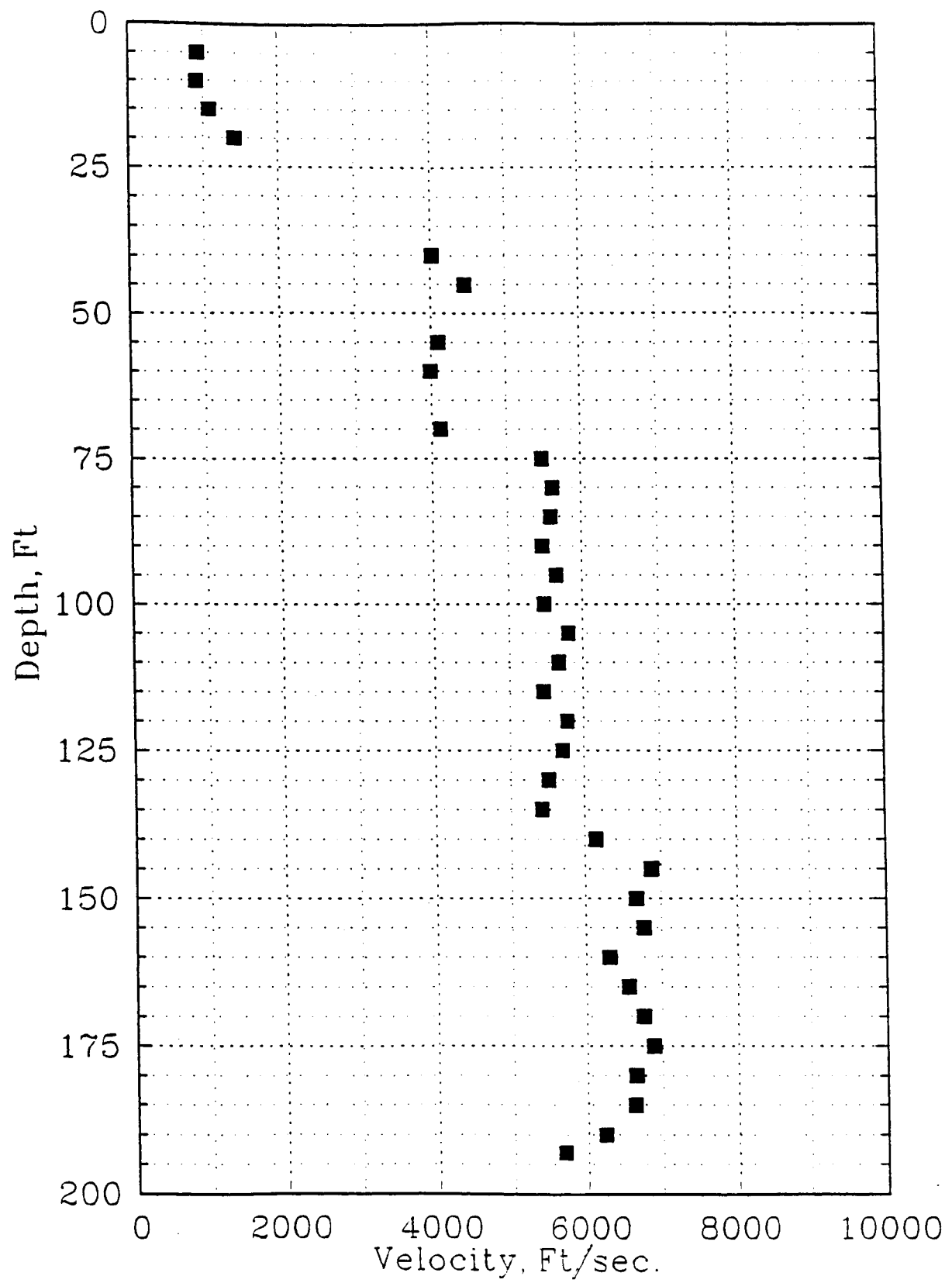


Figure 8.A.2-17  
Gilroy 2 crosshole velocities, S-wave.



**Figure 8.A.2-18**  
Gilroy 2 crosshole velocities, P-wave.



#### **8.A.2.3.1.5 Attenuation**

We successfully recorded attenuation data at Gilroy 2 using two of the holes for the two receivers. This was necessary because two receivers would not fit into the same 4" diameter casing. The reference receiver was inserted in Borehole 2 and locked at a depth of 50'. The moving receiver was then inserted in Borehole 3 and locked at depths of 50, 100, 150, 200, 300, and 450 feet. At each depth, the receivers were both oriented to the east, in line with the source directions.

Figure 8.A.2-19 shows the physical layout for the attenuation measurements. The rotary (large shaker), hammer plank, and Electroseis (small) shaker were installed between the two receiver boreholes as shown.

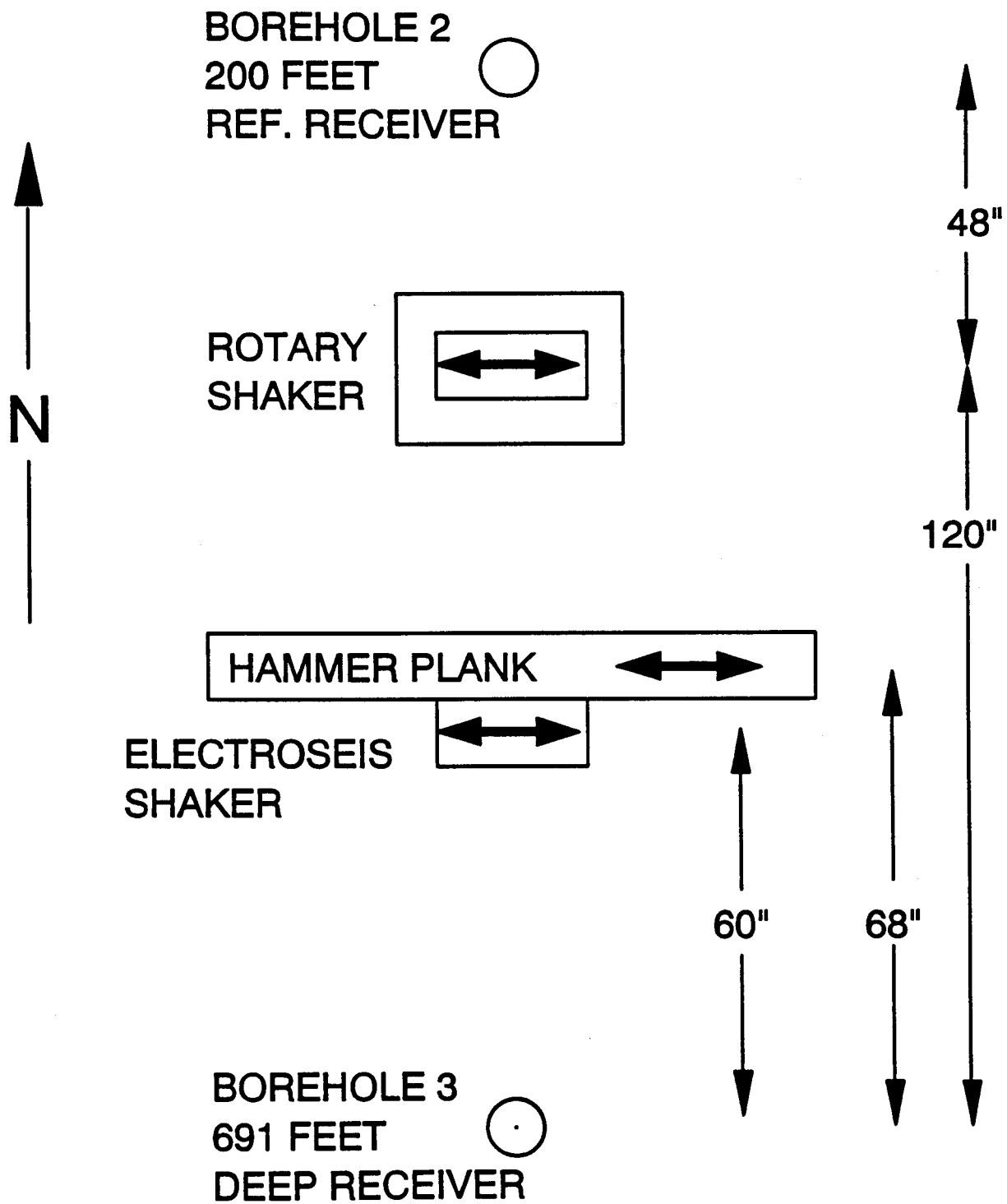
At each depth of the moving receiver, data were recorded for one or more hammer blows, sine dwells between 5 and 50 Hz for the large shaker, and sine dwells between 10 and 80 Hz for the small shaker.

Data taken with the moving receiver at 50' were used to normalize the other data sets during the spectral slope analysis.

The spectral slope method described in References (4) and (5) were then applied to the various excitation data sets. Attenuation (Q) and damping (D) were estimated from the spectral slopes for depth intervals to 300'. Data recorded at a receiver depth of 450' were too noisy to use in the calculations. Table 8.A.2-1 lists the estimated of Q and D for the corresponding depth intervals.

Measured attenuations using the hammer source are reasonable. However, measured attenuations for the sinusoidal sources are too small. It is likely that the spectral slope method does not work well for sinusoidal excitation because of wave scattering and trapping effects in the layered medium.

The digital time series data recorded during these attenuation measurements have been provided to the EPRI project manager for further analysis. Perhaps another analysis approach, for example a time domain wave propagation modelling approach, will lead to better results from this data set, especially from the sinusoidal source data.



**Figure 8.A.2-19**  
Gilroy 2 downhole damping measurement layout.

**Table 8.A.2-1**  
Gilroy 2 Attenuation Measurement Results

Depth Interval, ft	Source Type	Q	D, %
50 - 100	Hammer	33	1.5
50 - 200	Hammer	9	5.6
50 - 300	Hammer	22	2.3
200 - 300	Hammer	25	2.0
50 - 100	Small Shaker	3	17
50 - 100	Large Shaker	3	17
50 - 300	Large Shaker	13	3.8

#### **8.A.2.3.2 Treasure Island**

In February, 1992, borehole drift measurements were performed at the Treasure Island site. Crosshole velocity and attenuation studies were done in early March, 1992.

Results from each of the various measurements are presented below.

##### **8.A.2.3.2.1 Borehole Drift**

Figures 8.A.2-20 through 8.A.2-23 are 3-D plots of measured borehole drift for Boreholes B1-B4, respectively. Refer to Figure 8.A.2-2 for the borehole layout.

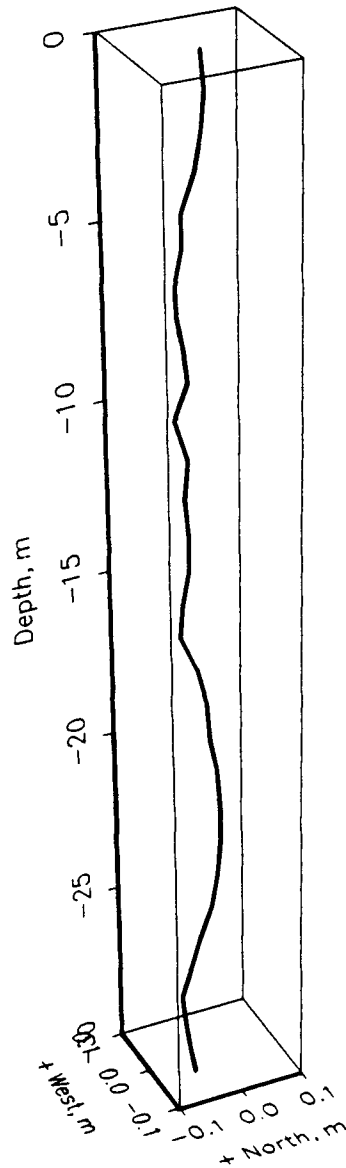
Digital drift data have previously been provided to the EPRI project manager and are included in the project database.

##### **8.A.2.3.2.2 Suspension Velocities**

Suspension velocity measurements were attempted in the deep borehole (Borehole B3) at Treasure Island in January, 1992. This borehole is cased with 5" PVC. These measurements were unsuccessful, as is sometimes the case when using the suspension logger in cased holes. The suspension logging technique is intended for use in uncased boreholes.

# MEASURED BOREHOLE DRIFT

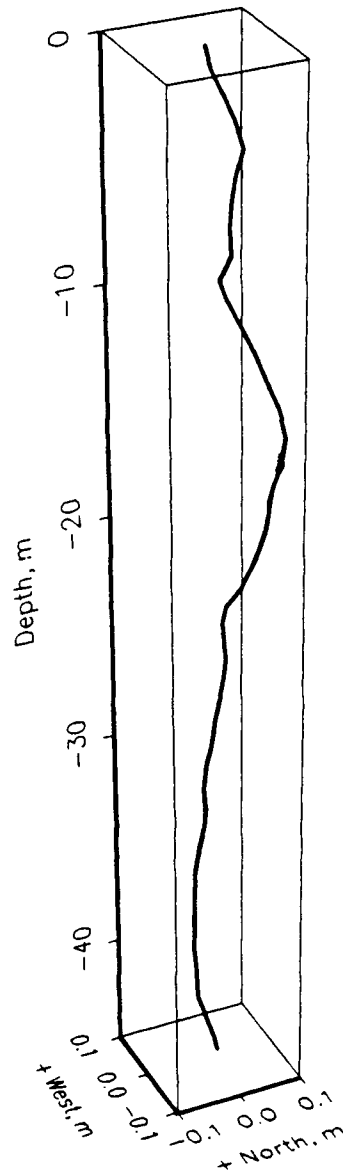
*Treasure Island Site, Borehole 1*



**Figure 8.A.2-20**  
Treasure Island drift data, Borehole B1.

# MEASURED BOREHOLE DRIFT

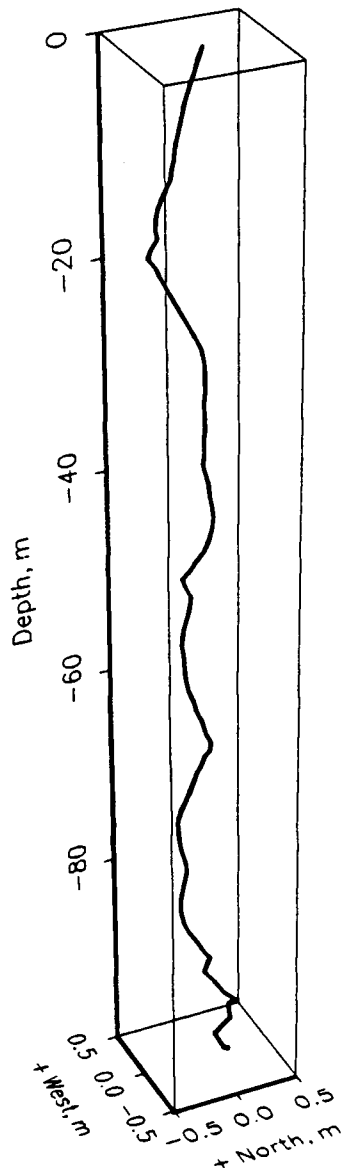
*Treasure Island Site, Borehole 2*



**Figure 8.A.2-21**  
Treasure Island drift data, Borehole B2.

# MEASURED BOREHOLE DRIFT

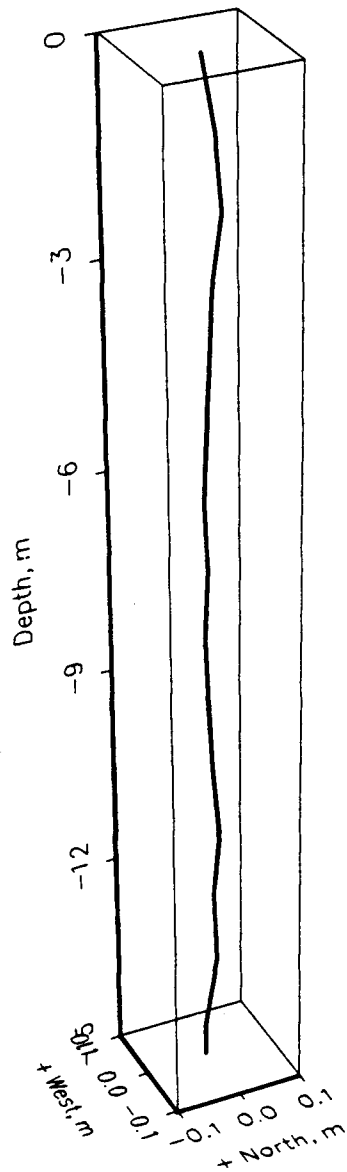
*Treasure Island Site, Borehole 3*



**Figure 8.A.2-22**  
Treasure Island drift data, Borehole B3.

# MEASURED BOREHOLE DRIFT

*Treasure Island Site, Borehole 4*



**Figure 8.A.2-23**  
Treasure Island drift data, Borehole B4.

#### **8.A.2.3.2.3 Cross-Hole Velocities**

The crosshole source was inserted in Borehole B3 and the two receivers in Boreholes B1 and B2 at the Treasure Island site. P- and S-wave velocities were then measured between the two receivers (differential) and between the source and each of the two receivers for data above 100' depth.

Our drift logging results were not available in time to use in these measurements. As a results, the Earth Technology borehole drift data was used to calculate the borehole spacings to be used in the velocity calculations. The three measurements generally compared well, although there is additional uncertainty in the source-receiver measurements due to the mechanical and electrical delays in the source actuation. In general, the differential measurements are considered to be more precise. From 100' to 140' depth, only the source to receiver velocities can be calculated, as Borehole B1 is only 100' deep.

Figures 8.A.2-24 and 8.A.2-25 plot the measured crosshole S-wave and P-wave velocities, respectively.



## Source to Receivers 1 and 2, Averaged

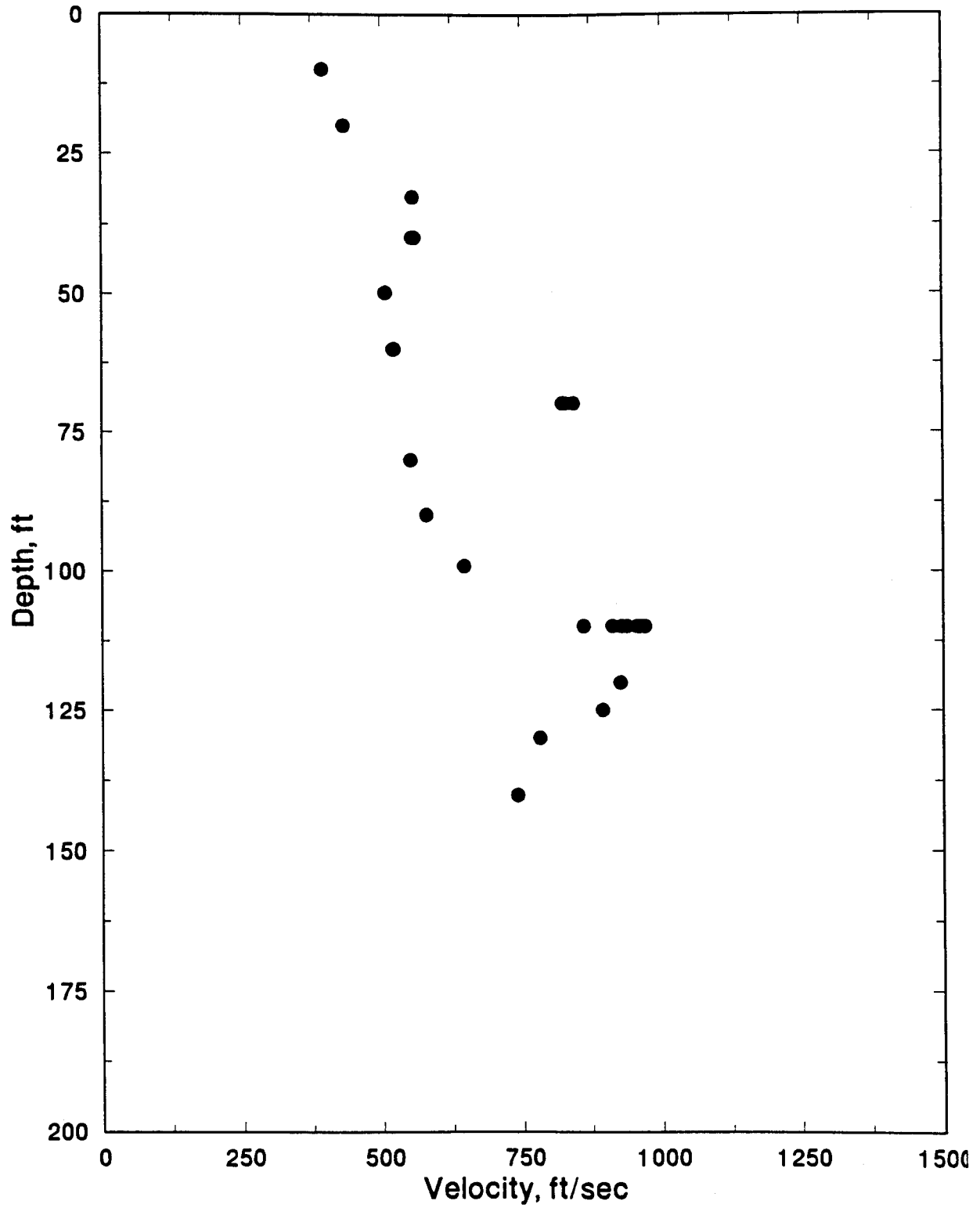


Figure 8.A.2-24  
Treasure Island crosshole velocities, S-wave.

## Source to Receivers 1 and 2, Averaged

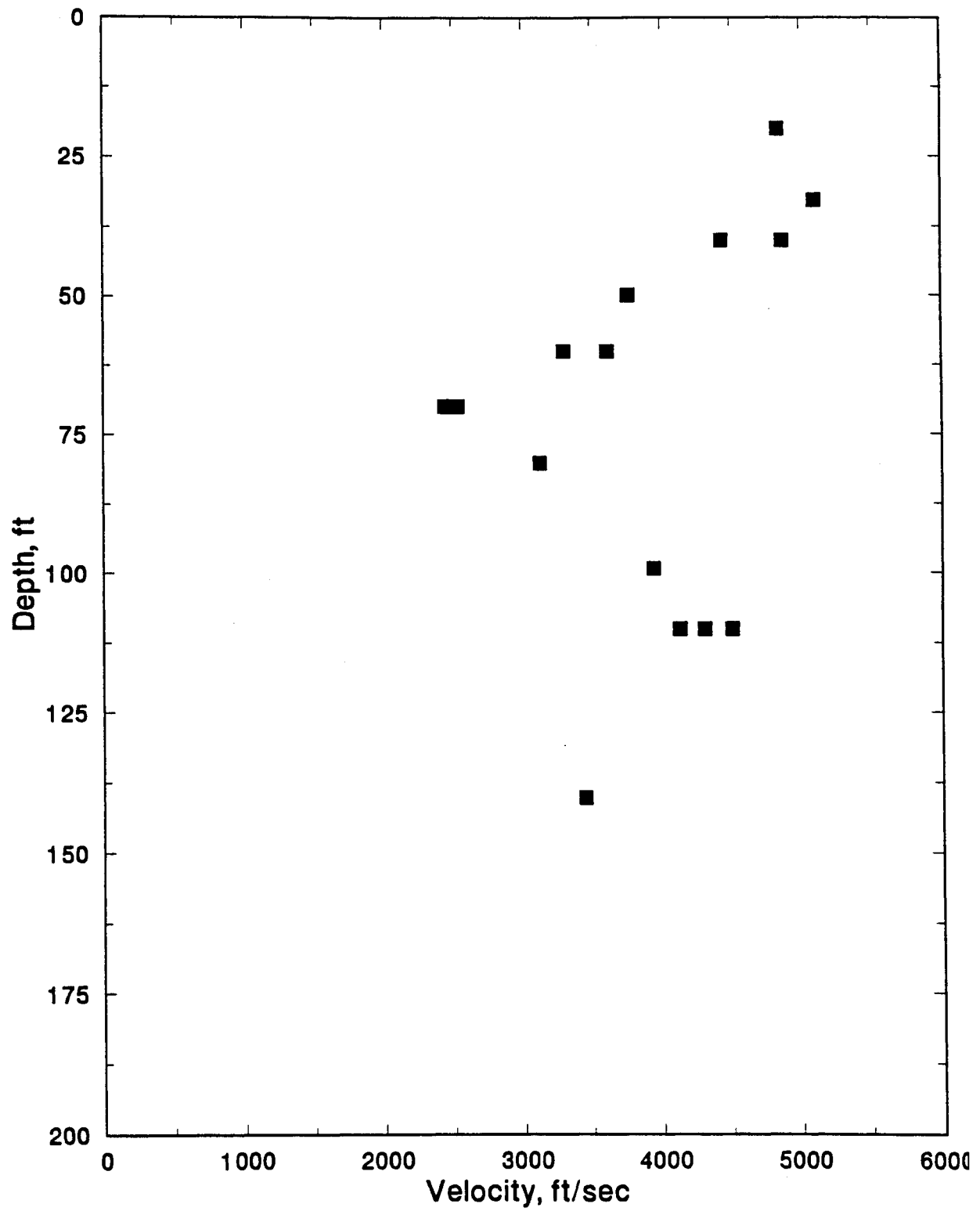


Figure 8.A.2-25  
Treasure Island crosshole velocities, P-wave.

#### **8.A.2.3.2.4 Attenuation**

We successfully recorded attenuation data at Treasure Island using a single borehole for both receivers. Borehole B3, cased with 5" PVC, was used. The moving receiver was inserted into the borehole first. The reference receiver was then inserted in Borehole 3 and locked at a depth of 50'. The moving receiver was locked at depths of 55, 100, 200, and 280 feet. At each depth, the receivers were both oriented in line with the source directions.

Figure 8.A.2-26 shows the physical layout for the attenuation measurements. The rotary (large shaker), hammer plank, and Electroseis (small) shaker were installed close to the borehole as shown.

At each depth of the moving receiver, data were recorded for one or more hammer blows, sine dwells between 5 and 50 Hz for the large shaker, and sine dwells between 10 and 80 Hz for the small shaker.

Data taken with the moving receiver at 55' were used to normalize the other data sets during the spectral slope analysis.

The spectral slope method described in References (4) and (5) were then applied to the various excitation data sets. Attenuation (Q) and damping (D) were estimated from the spectral slopes for depth intervals to 280'. Table 8.A.2-2 lists the estimated of Q and D for the corresponding depth intervals.

As for the Gilroy 2 data, measured attenuations using the hammer source are reasonable. However, measured attenuations for the sinusoidal sources are too small. It is likely that the spectral slope method does not work well for sinusoidal excitation because of wave scattering and trapping effects in the layered medium.

The digital time series data recorded during these attenuation measurements have been provided to the EPRI project manager for further analysis.

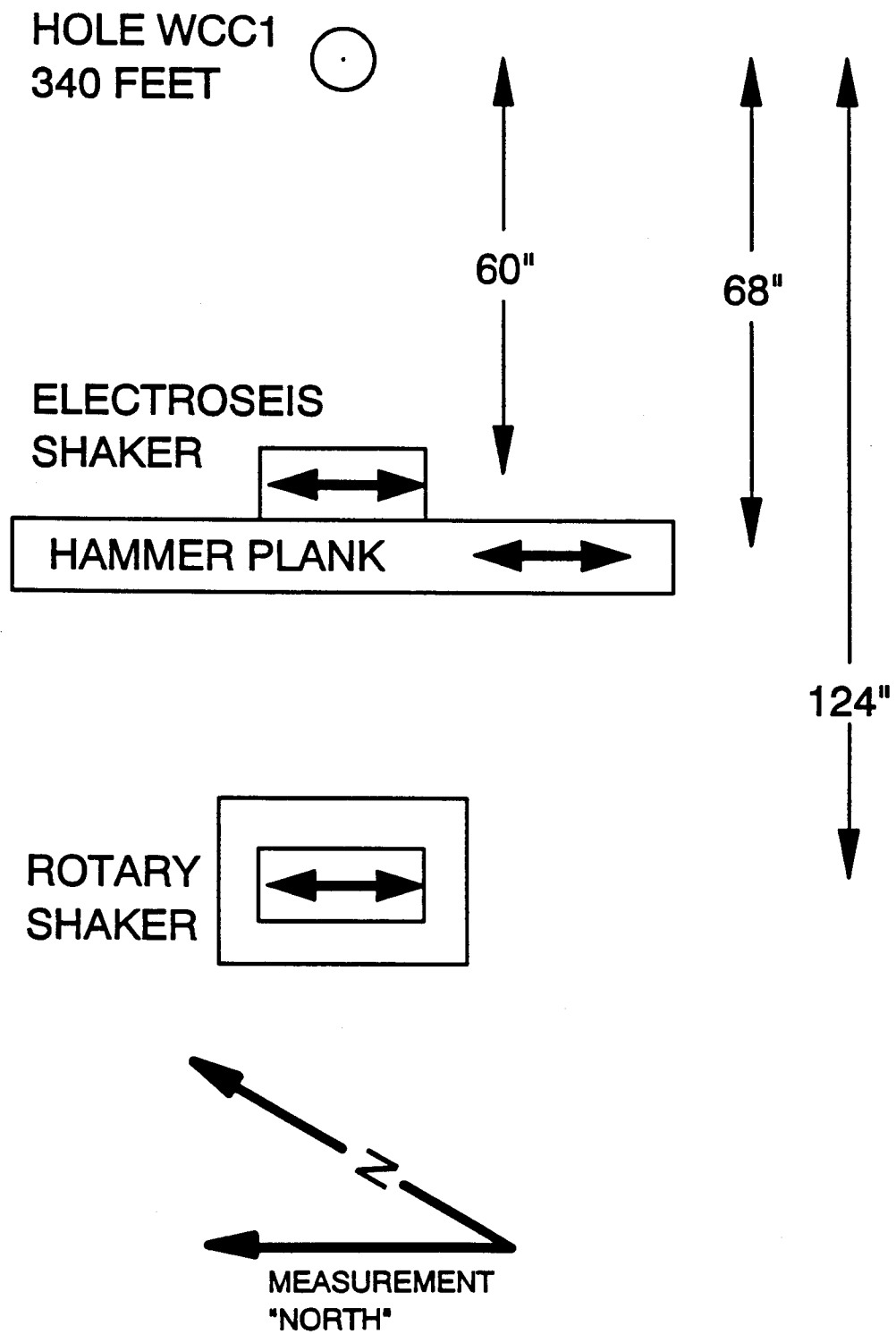


Figure 8.A.2-26  
Treasure Island downhole damping measurement layout.

**Table 8.A.2-2**

Treasure Island Attenuation Measurement Results

Depth Interval, ft	Source Type	Q	D, %
50 - 100	Hammer	9	5.6
50 - 280	Hammer	22	2.3
100 - 200	Hammer	33	1.5
200 - 280	Hammer	57	0.9
50 - 100	Small Shaker	12	4.2
50 - 280	Large Shaker	46	1.1

## 4—SUMMARY

The following geophysical measurements were successfully performed in the boreholes at the Gilroy 2 site:

- Resistivity Logging (Borehole 3 only)
- Natural Gamma Logging (Borehole 3 only)
- Caliper Logging (Borehole 3 only)
- Borehole Drift Logging (Boreholes 1–4)
- Suspension PS Velocity Logging (Borehole 3 only)
- Crosshole PS Velocity Measurement (to 200' depth)
- Downhole Attenuation Measurement

At the Treasure Island site, the following measurements were also successfully performed:

- Borehole Drift Logging (Boreholes 1–4)
- Crosshole PS Velocity Measurement (to 140' depth)
- Downhole Attenuation Measurement

Details of these measurements are presented in Section 8.A.2.2, and results in Section 8.A.2.3. In addition, results have been provided to the EPRI project manager throughout the project for use in the database and site response analysis.

These high quality data will enhance both this project and will provide data for future research.

## REFERENCES

1. M.G. Spangler and R.L. Handy. *Soil Engineering*. New York: Harper & Row, 1982, Sections 5.11 and 8.26.
2. *Procedures for Evaluation of Vibratory Ground Motions of Soil Deposits at Nuclear Power Plant Sites*. Los Angeles: Shannon & Wilson/Agbabian Associates, June 1975
3. *Soil Behavior Under Earthquake Loading Conditions*. Los Angeles: Shannon & Wilson/Agbabian Associates, January 1972.
4. *Development of Field Techniques to Measure Damping Values for Near-Surface Rocks and Soils*. San Francisco, Calif.: URS/John A. Blume & Associates, April 1982.
5. *In-situ Measurements of Shear-Wave Attenuation at a Strong-Motion Recording Site*. San Francisco, Calif.: URS/John A. Blume & Associates, May 1986.
6. P.S. Hauge. "Measurements of Attenuation From Vertical Seismic Profiles." In *Geophysics*, vol. 46, no. 11, 1981, pp. 1548–1558.
7. *Borehole Geophysical Measurements at Gilroy Strong Motion Array Station No. 2: Task 1*. Pasadena, Calif.: Agbabian Associates, November 27, 1991, Report 9139-6358

## **APPENDIX 8.A.3**

# **DETERMINATION OF IN SITU SEISMIC ATTENUATION**

---

### **SUMMARY**

Different aspects of seismic attenuation, including definitions and physical mechanisms responsible for attenuation are reviewed. Methods of in-situ measurements of seismic attenuation are discussed. A new method, based on waveform inversion, for determining the attenuation is developed. This method requires only two observations at different distances from the source and determines simultaneously the propagation velocity and the attenuation between the two receivers. Cross-hole data from the Gilroy 2 and Treasure Island sites, collected by the University of Texas, Austin (Fuhrimam and Stokoe, 1993), and VSP data at both sites, recorded by Agbabian Associates, are used for attenuation determination. The cross-hole measurements obtained at 5 and 10 ft depth intervals provide detailed damping profiles for this study. At the Treasure Island and Gilroy 2 sites there is a strong correlation between the damping and shear wave velocity. Damping increases with increasing velocity. Comparison of damping, velocity profiles, and geologic sections shows that high damping and high shear velocities are associated with sand and gravely strata.

In Appendix 8.A.3.B the sensitivity of attenuation measurements to geologic section velocity structures is investigated. Velocity variation with depth affects the geometric spreading, and the  $1/r$  value applicable for homogeneous media cannot be used. Layering and impedance contrasts affect amplitude due to reflection. We corrected for such effects by calculating the synthetic seismograms in order to obtain damping values at the Gilroy 2 and Treasure Island sites from VSP data.



# CONTENTS

---

Section	Page
<b>1—Introduction</b> .....	<b>8.A.3-7</b>
8.A.3.1.1 Definitions of the Attenuation Parameter .....	8.A.3-8
8.A.3.1.2 Determination of Site Attenuation .....	8.A.3-10
<b>2—In-Situ Measurement of Attenuation</b> .....	<b>8.A.3-12</b>
8.A.3.2.1 Field Measurements .....	8.A.3-12
8.A.3.2.1.1 <i>Suspension Logging</i> .....	8.A.3-12
8.A.3.2.1.2 <i>Vertical Seismic Profiling</i> .....	8.A.3-12
8.A.3.2.1.3 <i>Cross-Hole Measurements</i> .....	8.A.3-12
8.A.3.2.2 Attenuation Determination .....	8.A.3-13
8.A.3.2.2.1 <i>Determination of Attenuation From the Spectral Ratio</i> ....	8.A.3-13
8.A.3.2.2.2 <i>Determination of Attenuation From Amplitude Decay</i> <i>Versus Distance</i> .....	8.A.3-14
8.A.3.2.2.3 <i>Waveform Inversion Method to Determine Attenuation</i> ...	8.A.3-15
<b>3—Attenuation Results From Field Data</b> .....	<b>8.A.3-19</b>
8.A.3.3.1 Treasure Island Cross-Hole Data .....	8.A.3-19
8.A.3.3.2 Gilroy 2 Cross-Hole Data .....	8.A.3-34
8.A.3.3.3 Attenuation From Downhole (VSP) Data .....	8.A.3-34
8.A.3.3.3.1 <i>Treasure Island VSP Data</i> .....	8.A.3-55
8.A.3.3.3.2 <i>Gilroy 2 VSP Data</i> .....	8.A.3-55
<b>4—Conclusions</b> .....	<b>8.A.3-64</b>
<b>References</b> .....	<b>8.A.3-65</b>
<b>Appendix 8.A.3.A. Estimating Attenuation Through Waveform Inversion</b> .	<b>8.A.3-67</b>
<b>Appendix 8.A.3.B. Q Measurements: The Effect of Layering</b> .....	<b>8.A.3-73</b>

# LIST OF TABLES

---

Table		Page
8.A.3-1a	Cross well SV-wave velocities with depths at Treasure Island for the path BH2–BH1 (Profile #1). The two velocities (conventional arrival picking, and inversion values using the phase matching method discussed in the text) are tabulated with depths .....	8.A.3-22
8.A.3-1b	Cross well SV-wave velocities with depths for the path BH2–BH3 (Profile #1) .....	8.A.3-23
8.A.3-1c	Cross well SV-wave velocities with depths for the path BH4–BH5 (Profile #2) .....	8.A.3-23
8.A.3-2a	Estimated Qs and its error with depths at Treasure Island for the path BH2–BH1 (Profile #1) .....	8.A.3-24
8.A.3-2b	Estimated Qs and its error with depths for the path BH2–BH3 (Profile #1) .....	8.A.3-25
8.A.3-2c	Estimated Qs and its error with depths for the path BH4–BH5 (Profile #2) .....	8.A.3-25
8.A.3-3a	Cross well SV-wave velocities with depths at Gilroy 2 for the paths BH2–BH1 and BH3–BH4 (forward direction) .....	8.A.3-38
8.A.3-3b	Cross well SV-wave velocities with depths for the paths BH3–BH2 and BH2–BH1 (reverse direction) .....	8.A.3-40
8.A.3-4a	Estimated Qs and its error with depths at Gilroy 2 for the paths BH2–BH1 and BH3–BH4 (forward direction) .....	8.A.3-41
8.A.3-4b	Estimated Qs and its error with depths for the paths BH3–BH2 and BH2–BH1 (reverse direction) .....	8.A.3-42
8.A.3-5	Estimated Qs between different depth range from the Treasure Island and Gilroy 2 VSP data. The different geometric spreading corrections are applied. Gilroy data are very poor. Two different estimations for Gilroy 2 at different frequencies .....	8.A.3-58
8.A.3-6	Summary of damping values from different observations of cross-hole data at the Gilroy 2 site .....	8.A.3-61
8.A.3-7	The computed vertical interval velocities, Qs values, and damping from cross-hole data at the Gilroy 2 site .....	8.A.3-62
8.A.3-8	Comparison of cross-hole and VSP Q data from Tables 8.A.3-5 and 8.A.3-7 .....	8.A.3-63

# LIST OF FIGURES

---

Figure		Page
8.A.3-1	Waveform inversion procedure to obtain velocity and attenuation from cross-hole data. (a) The near receiver is migrated to the far receiver position using approximate velocity and $1/r$ geometric correction. (b) The two waveforms are filtered and windowed. (c) An inversion is carried out to match phase and amplitudes to obtain velocity and Q .....	8.A.3-17
8.A.3-2	Borehole arrangement and wave travel paths for cross-hole seismic testing at Treasure Island (after Fuhrimam and Stokoe, 1993) .....	8.A.3-20
8.A.3-3	Raw data (top) and inversion results (bottom) for Treasure Island cross-hole data at depth of 21 ft for Profile #2, Path #4. ....	8.A.3-21
8.A.3-4a	Measured shear (SV) Q values and estimated errors versus depth along Path BH2–BH1 at Treasure Island .....	8.A.3-26
8.A.3-4b	Measured shear (SV) Q values and estimated errors versus depth along Path BH2–BH3 .....	8.A.3-27
8.A.3-4c	Measured shear (SV) Q values and estimated errors versus depth along Path BH4–BH5 .....	8.A.3-28
8.A.3-5a	Damping values (shear) and estimated errors as a function of depth along Path BH2–BH1 at Treasure Island .....	8.A.3-29
8.A.3-5b	Damping values (shear) and estimated errors as a function of depth along Path BH2–BH3 .....	8.A.3-30
8.A.3-5c	Damping values (shear) and estimated errors as a function of depth along Path BH4–BH5 .....	8.A.3-31
8.A.3-6	Average shear damping versus depth based on cross-hole data at Treasure Island .....	8.A.3-32
8.A.3-7	Shear wave (SH) velocities for forward and reverse directions along Path 1 and the geologic log at Treasure Island (after Fuhrimam and Stokoe, 1993) .....	8.A.3-33
8.A.3-8	Schematic of borehole layout for in-situ damping measurements at Gilroy 2 (after Fuhrimam and Stokoe, 1993) ...	8.A.3-35
8.A.3-9	Raw data (top) and inversion results (bottom) for Gilroy 2 reverse cross-hole data at depth of 85 ft .....	8.A.3-36
8.A.3-10	Raw data (top) and inversion results (bottom) for Gilroy 2 forward cross-hole data at depth of 105 ft .....	8.A.3-37
8.A.3-11a	Measured shear (SV) Q values and estimated errors versus depth along Path BH2–BH1 of Gilroy 2 .....	8.A.3-43

<b>Figure</b>		<b>Page</b>
<b>8.A.3-11b</b>	Measured shear (SV) Q values and estimated errors versus depth along Path BH2–BH3 .....	<b>8.A.3-44</b>
<b>8.A.3-11c</b>	Measured shear (SV) Q values and estimated errors versus depth along Path BH3–BH2 .....	<b>8.A.3-45</b>
<b>8.A.3-11d</b>	Measured shear (SV) Q values and estimated errors versus depth along Path BH3–BH4 .....	<b>8.A.3-46</b>
<b>8.A.3-12a</b>	Damping values (shear) and estimated errors versus depth along Path BH2–BH1 of Gilroy 2 .....	<b>8.A.3-47</b>
<b>8.A.3-12b</b>	Damping values (shear) and estimated errors versus depth along Path BH2–BH3 .....	<b>8.A.3-48</b>
<b>8.A.3-12c</b>	Damping values (shear) and estimated errors versus depth along Path BH3–BH2 .....	<b>8.A.3-49</b>
<b>8.A.3-12d</b>	Damping values (shear) and estimated errors versus depth along Path BH3–BH4 .....	<b>8.A.3-50</b>
<b>8.A.3-13</b>	Average shear damping versus depth based on all cross-hole data at Gilroy 2 .....	<b>8.A.3-51</b>
<b>8.A.3-14</b>	Shear wave (SV) velocities versus depth for forward and reverse directions along Path 1 at Gilroy No. 2 (after Fuhriam and Stokoe, 1993) .....	<b>8.A.3-52</b>
<b>8.A.3-15</b>	Shear wave velocity versus frequency for Gilroy 2 cross-hole data .....	<b>8.A.3-53</b>
<b>8.A.3-16</b>	Shear Q versus frequency for Gilroy 2 cross-hole data .....	<b>8.A.3-54</b>
<b>8.A.3-17</b>	Preprocessed VSP data waveforms versus depth at Treasure Island. The reference waveform at a fixed geophone at 50 ft depth is shown at the top, in each case .....	<b>8.A.3-56</b>
<b>8.A.3-18</b>	Steps of waveform inversion for estimating Q and velocity for VSP data. The top box shows unfiltered waveforms at 50 and 100 ft depths with geometric correction ( $1/r^{1.5}$ ). The second box from the top shows the filtered signals. The third box shows the migration of the 50 ft waveform to 100 ft. The bottom box shows the match of waveforms after inversion for determining Q .....	<b>8.A.3-57</b>
<b>8.A.3-19</b>	Gilroy 2 VSP data versus depths. The reference geophone waveforms are shown at the top in each case .....	<b>8.A.3-59</b>
<b>8.A.3-20</b>	Steps of waveform inversion for estimating Q and velocity as described in Figure 8.A.3-18. The estimated $Q = 23$ and $V_s = 1144$ ft/s between 50 and 150 ft for geometric spreading correction of ( $1/r^{1.6}$ ) .....	<b>8.A.3-60</b>



## APPENDIX 8.A.3

### DETERMINATION OF IN SITU ATTENUATION

---

#### 1—INTRODUCTION

Seismic attenuation contributes significantly to the amplitudes and spectra of ground motion measured at the surface. Attenuation is greatest in soils (unconsolidated sediments), less, but significant, in consolidated sediments, and the least for crystalline rocks, especially below a depth of a few kilometers. Even at hard rock sites, attenuation takes place mostly in the upper few kilometers of the crust (Frankel *et al.*, 1990; Toksöz *et al.*, 1990). This is due primarily to physical mechanisms responsible for attenuation.

The three most important mechanisms for seismic attenuation are: (1) Relative motions and the resulting friction across grain boundaries, microfractures, and between zones with different mechanical properties; (2) motions of fluids, such as water, induced by seismic waves; and (3) scattering of waves by heterogeneity (i.e., mechanical properties contrasts) in materials. Friction is the single most important mechanism for seismic attenuation at shallow depths. Because of low confining pressure and large surface areas that are not bound strongly, seismic waves easily cause motions and loss of energy due to friction (Walsh, 1966; Mavko and Nur, 1979; Toksöz and Johnston, 1981). At greater depths the grains are bound more strongly due to overburden pressure, compaction, and lithification. Relative motions between grains induced by the waves decrease, with a resulting decrease in attenuation.

In rocks, frictional attenuation is independent of frequency but dependent on strain amplitude above a critical value—generally  $10^{-3}$  percent (Johnston *et al.*, 1979; Mavko and Nur, 1979; Toksöz *et al.*, 1979; Stewart *et al.*, 1983). Laboratory measurements in dry soils (see Stokoe in this report) show strong strain amplitude dependence at strains greater than about  $10^{-3}$  percent.

The presence of water contributes to attenuation in two ways. First, water between grains decreases the friction coefficient and increases relative motions induced by seismic waves. It also increases frictional attenuation. Even trace amounts of water, that could form mono layers at grain boundaries, cause an increase in attenuation (Tittmann, 1980). Water, even with low viscosity (0.01 poise), forms a double electrical layer at grain boundaries and creates an artificially high viscosity (Pride and Morgan, 1991). Another mechanism in which water contributes to attenuation is that seismic waves induce motions between the solid material (frame) and water in the pores (Biot, 1956a, b; O'Connell and Budiansky, 1977; Mavko and Nur, 1979; Spencer, 1981; White, 1992). The contribution of fluid flow to attenuation is strongly dependent on frequency. Frequency dependence is complex and depends on pore geometry, fluid properties such as viscosity, and wave type (P or S). Strain amplitude dependence can be significant, especially when porosity and pore geometries are affected by large deformations.

The third significant mechanism contributing to seismic wave attenuation is scattering. Multiple scattering from heterogeneities increases propagation paths, wave conversions (from P to S, S to P, body waves to surface waves and vice versa), and interference of scattered waves [see Wu and Aki (1988, 1989, 1990) for extensive references; also Toksöz *et al.* (1979); Frankel and Clayton (1986); Dainty *et al.* (1987)]. Attenuation due to scattering is generally dependent on frequency. Maximum attenuation occurs where the wavelength is comparable to the average dimension of heterogeneity. Attenuation is lower at frequencies that are higher and lower than the critical frequency. Since heterogeneities of many scales occur in the earth, it is difficult to establish a simple analytical expression for frequency dependence. Scattering attenuation should be independent of strain amplitude, except for the effects of decreasing modulus (hence the velocity and wavelength) at very high strains.

### 8.A.3.1.1 Definitions of the Attenuation Parameter

The attenuation properties in rocks and soils are specified by a wide range of measures in seismology and engineering. In order to avoid confusion, it is important to present a brief definition of terms that are used, and to show how they relate to each other. The most commonly used measures of attenuation are: Attenuation coefficient,  $\alpha$ ; quality factor,  $Q$ , and its inverse,  $Q^{-1}$ , commonly referred to as attenuation, logarithmic decrement,  $\delta$ , loss tangent,  $\tan \phi$ , and damping coefficient,  $D$ . Leaving out small second-order corrections proportional to  $\alpha^2$ , the above parameters are related by

$$\frac{1}{Q} = \frac{\alpha V}{\pi f} = \frac{\delta}{\pi} = \tan \phi = 2D \quad (1)$$

where  $V$  = wave velocity and  $f$  is frequency.

In order to illustrate how attenuation is measured, we start with a plane wave propagating in a homogenous medium (see Johnston and Toksöz, 1980). The amplitude is given by

$$A(x,t) = A_0 e^{i(kx - \omega t)} \quad (2)$$

where  $\omega$  is angular frequency and  $k$  is the wavenumber. To introduce the attenuation we can take  $k$  to be the complex

$$k = k_R + ik_I \quad (3)$$

Substituting in equation (2), we can factor out the attenuation

$$A(x,t) = A_0 e^{-k_I x} e^{i(k_R x - \omega t)} \quad (4)$$

where the attenuation coefficient is  $\alpha = k_I$ .

The attenuation coefficient,  $\alpha$ , can be obtained from equation (4) by determining the change of amplitude with the distance of a constant phase.

$$\alpha = -\frac{1}{A(x)} \frac{dA(x)}{dx} = -\frac{d}{dx} \ln A(x). \quad (5)$$

If we know amplitudes  $A_1$  and  $A_2$  at distances  $x_1$  and  $x_2$ , respectively, the attenuation coefficient,  $\alpha$ , can be written as

$$\alpha = \frac{1}{x_2 - x_1} \ln \left[ \frac{A(x_1)}{A(x_2)} \right]. \quad (6)$$

Units of  $\alpha$  are the inverse length.

The quality factor,  $Q$ , or its inverse can be defined in terms of energy loss per cycle. Let  $W$  be the elastic energy at maximum stress and  $\Delta W$  the energy loss per cycle. Then the attenuation

$$\frac{1}{Q} = \frac{\Delta W}{2\pi W}. \quad (7)$$

$\Delta W$  can be determined from the hysteresis loop in stress-strain measurements. In addition, there is a phase lag,  $\phi$ , between stress and strain in an attenuating medium.  $Q$  can be defined in terms of this phase lag as

$$\frac{1}{Q} = \tan \phi. \quad (8)$$

Since  $\phi$  is generally small,  $\frac{1}{Q} \cong \phi$ , where  $\phi$  is expressed in radians.

In resonant column-type measurements,  $Q$  can be determined in terms of the width of the resonance peak by

$$\frac{1}{Q} = \frac{\Delta f}{f_r} \quad (9)$$

where  $f_r$  is the resonance frequency and  $\Delta f$  is the frequency width between two half-power (3 dB in amplitude) points about the peak.

In a resonant system, the oscillations decay exponentially with time once the driving force is removed.  $Q$  can be determined from the decay rate of the oscillations. If  $A_1$  and  $A_2$  are the peak amplitudes of the two successive cycles, then

$$\frac{1}{Q} = \pi \ln \left[ \frac{A_1}{A_2} \right]. \quad (10)$$

In all of the above definitions, it was assumed that attenuation is small or moderate. If attenuation is very high ( $Q \leq 5$ ) it may be necessary to introduce a second-order correction factor between the attenuation coefficient defined in equation (5) and the  $Q$  value. The exact relationship is given by

$$\frac{1}{Q} = \frac{\alpha V}{\pi f - \frac{\alpha^2 V^2}{4\pi f}} = \frac{1}{\bar{Q} \left( 1 - \frac{1}{4Q^2} \right)} \quad (11)$$

where  $\bar{Q}$  is the nominal (i.e., approximate  $Q$ ) value used in the previous relationships. For  $\bar{Q} = 5$ , the above correction is about one percent, and can be ignored for all practical purposes.

In the laboratory, attenuation may be measured for P, S, and extensional waves, while in the field, P and S wave attenuations are measured. It is useful to express the relationships between extensional, shear, and compressional attenuations (Winkler and Nur, 1979).

Using the basic definition of attenuation in terms of a complex modulus,  $M = M_R + iM_I$ ,

$$Q_M^{-1} = \frac{M_I}{M_R}. \quad (12)$$

For shear waves,  $M = G$  is the shear modulus. For a one-dimensional extension,  $M$  is the Young's modulus,  $E$ . For hydrostatic stress,  $M$  is equal to the bulk modulus,  $K$ . For P waves,  $M = K + 4/3 G$ . Expressing velocities by the real part of the modulus,

$$V = \sqrt{\frac{M_R}{\rho}},$$



and taking the density to be real, we obtain three expressions relating attenuations:

$$\begin{aligned}\frac{3}{Q_E} &= \frac{1-2\nu}{Q_K} + \frac{2(\nu+1)}{Q_S} \\ \frac{1+\nu}{Q_K} &= \frac{3(1-\nu)}{Q_P} - \frac{2(1-2\nu)}{Q_S} \\ \frac{(1-\nu)(1-2\nu)}{Q_P} &= \frac{1+\nu}{Q_E} - \frac{2\nu(2-\nu)}{Q_S}\end{aligned}\quad (13)$$

In terms of velocities, the Poisson's ratio,  $\nu$ , is given by

$$\nu = \frac{V_P^2 - 2V_S^2}{2(V_P^2 - V_S^2)} = \frac{V_E^2 - 2V_S^2}{2V_S^2} \quad (14)$$

For sandy soils, a rough approximation for P and S velocity ratios are  $V_P/V_S \cong 2$  above the water table and  $V_P/V_S \cong 3$  below the water table. The corresponding Poisson's ratios are  $\nu \cong 1/3$  or dry and  $\nu \cong 7/16$  for saturated.

To determine the relationship between  $Q_P$  and  $Q_S$ , we need actual field or laboratory measurements. Unfortunately, there is a paucity of such data. However, for a vertically incident P wave in dry soil, it may be reasonable to assume that  $Q_P \cong Q_E$  at small strains. This assumption, when used in equation (13), gives  $Q_P \cong Q_S$ . Since shear velocities are much lower than P velocities in soils, and the amplitude decay is given by

$$e^{-\frac{\pi f}{QV} x},$$

the shear waves will attenuate much more than P waves at a given frequency, even when we assume  $Q_P \cong Q_S$ .

### 8.A.3.1.2 Determination of Site Attenuation

Three basic methods are used for estimating site attenuation. The first is the determination of a single parameter,  $\kappa$ , at a seismic station from records of many earthquakes (Anderson and Hough, 1984). Amplitude,  $A$ , at station,  $i$ , is expressed as

$$A_i(f) = e^{-\kappa_i f} \cdot \bar{u}_i(r, f)$$

where  $f$  is frequency, and  $\bar{u}_i(r)$  is the motion from an earthquake or explosion corrected for source and path effects. From equations (1) and (3),  $\kappa$  can be related to  $Q$  by

$$\kappa = \frac{\pi Z}{QV} \quad (15)$$

The above expression shows that  $\kappa$  represents the total attenuation over an unspecified depth,  $z$ , (generally a few kilometers), where the average  $Q$  values are quite low. It includes attenuation in the soil as well as the top of the bedrock, and assumes that the average  $Q$  is independent of frequency and has units of time (seconds). Although it is a convenient way for characterizing regional variations of near-surface attenuation,  $\kappa$  does not specifically address the attenuation properties of the soils.

The second and widely used approach for obtaining attenuation in soils is to make measurements in the laboratory using samples obtained from boreholes (see sections on laboratory measurements of this report). Laboratory measurements, while offering great flexibility, could be affected by the effects of sample disturbance during coring, transportation and handling, alterations due to fluid drainage, and sample size that represent only a very small fraction of the subsurface that may be quite heterogeneous.

The third approach is to make in-situ measurements of attenuation. This is described in detail in the next section.

## **2—IN-SITU MEASUREMENT OF ATTENUATION**

The three methods that are used for in-situ determination of seismic velocities and attenuations are borehole suspension logging, vertical seismic profiling, and cross-hole measurements.

### **8.A.3.2.1 Field Measurements**

#### **8.A.3.2.1.1 Suspension Logging**

Measurements of compressional and shear wave velocities, although used routinely in thousands of wells each year in the petroleum industry, have been used infrequently in geotechnical studies. The limited use of logging in geotechnical wells for velocity and attenuation determination may have been due to the absence of shear (i.e., dipole) logging tools until recently, requiring that the borehole contain water, and the difficulty in interpreting the acoustic logs. Obtaining compressional and shear wave attenuation involves extensive theoretical analysis. With the availability of low frequency monopole and dipole (shear) logging tools and a greater understanding of the theory, continuous measurement of shear velocity and attenuation can be accomplished (Cheng and Toksöz, 1981; Paillet *et al.*, 1989; Toksöz *et al.*, 1990, 1992). Suspension or wire-line logs will be used more extensively to obtain continuous shear velocity and attenuation data as a function of depth in geotechnical studies.

#### **8.A.3.2.1.2 Vertical Seismic Profiling**

Vertical seismic profiling (VSP) is a method used for obtaining seismic velocities and attenuations with the source at the surface and geophones at specified depth intervals in the borehole. The method has been used extensively by the petroleum industry since the 1930's, under the name of "check-shot surveys." More recently, advanced VSP concepts have been developed and used for subsurface imaging (Hardage, 1983; Balch and Lee, 1984; Toksöz and Stewart, 1984).

The VSP technique has been used for determining P-wave attenuation in the Pierre Shale in Colorado (McDonal *et al.*, 1958), the Gulf Coast sediments (Tullos and Reid, 1969), and Columbia Plateau basalts (Pujol and Smithson, 1991).

For geotechnical applications, Kudo and Shima (1970) demonstrated very clearly the use of VSP for obtaining shear wave velocities and attenuations in shallow (0–45 m) sediments in the greater Tokyo area. Kudo and Shima's work is similar to that of the Redpath-Agabian measurements in the Treasure Island and Gilroy sites described in detail in this report. Also, the USGS VSP measurements (Gibbs *et al.*, 1992) at Gilroy and other sites in California provide excellent data sets for the determination of shear velocity and attenuation.

#### **8.A.3.2.1.3 Cross-Hole Measurements**

Cross-hole measurements, with seismic sources and receivers in different boreholes, have been used primarily for tomographic imaging of the subsurface. Compressional wave traveltimes are used most frequently to obtain a velocity structure between boreholes (Saito, 1991). In some cases amplitude of first arrivals has been used to determine zones of higher and lower attenuation. Tomographic imaging is good for mapping lateral heterogeneities. Geotechnical applications require shear velocities and attenuations.

Seismic sources in boreholes have complicated radiation patterns for P and especially for S waves (Heelan, 1953; Balch and Lee, 1984; Meredith, 1990). Unless the amplitudes are corrected for the source radiation and the receiver coupling effects, seismic attenuation cannot be determined from two boreholes. This difficulty can be overcome by using three or more boreholes whose axes are aligned on a plane. With this arrangement, one borehole can be used for the source and the attenuations can be measured between two receivers aligned with the source in the other two boreholes. This geometry was used in studies carried out at the Treasure Island and Gilroy 2 sites in California (see Stokoe's section in this report).

### 8.A.3.2.2 Attenuation Determination

Attenuation is determined using waves recorded at two or more distances from a given source. Let us use the simplified far field expression for the displacement,  $u(r, f, \theta)$ , of a wave at distance,  $r$ , from the source:

$$u(r, f, \theta) = S(f, \theta) G(r) e^{-\frac{\pi f}{QV} r} e^{i(kr - \omega t)} \quad (16)$$

where  $f$  is the frequency,  $\theta$  is the azimuth from the source,  $V$  is velocity, and  $k$  is the wave number. The factor,  $S(f, \theta)$ , is the source function, which depends on frequency and azimuth ( $\theta$ ).  $G(r)$  is the geometric spreading factor,

$$e^{-\frac{\pi f}{QV} r}$$

is damping due to intrinsic attenuation, and  $e^{i(kr - \omega t)}$  is the phase (or propagation term). Assuming that the dependence of phase on attenuation is small, amplitude,  $A(r, f, \theta)$ , is given by

$$A(r, f, \theta) = S(f, \theta) G(r) e^{-\frac{\pi f}{QV} r} \quad (17)$$

If the wave is recorded at two or more distances along the same azimuth,  $\theta$ , from a given source, attenuation can be determined using amplitude ratios.

#### 8.A.3.2.2.1 Determination of Attenuation From the Spectral Ratio

At two distances,  $r_1$  and  $r_2$ , the ratio

$$\frac{A_2(r_2, f, \theta)}{A_1(r_1, f, \theta)} = \frac{G(r_2)}{G(r_1)} e^{-\frac{\pi f}{QV} (r_2 - r_1)}, \quad (18)$$

where the identical source terms,  $S(f, \theta)$ , cancel. Taking the natural log

$$\ln \left[ \frac{A_2(r_2, f)}{A_1(r_1, f)} \right] = \ln \left[ \frac{G(r_2)}{G(r_1)} \right] - \frac{\pi f}{QV} \Delta r \quad (19)$$

where  $\Delta r = r_2 - r_1$ . If geometric spreading factors,  $G(r_2)$  and  $G(r_1)$ , are independent of frequency, and if it is further assumed that  $Q$  is independent of frequency, the plot of

$$\ln \left[ \frac{A_2}{A_1} \right]$$

versus frequency would be linear with the slope equal to

$$-\frac{\pi \Delta r}{QV}$$

$\frac{\Delta r}{V}$  is the traveltime from  $r_1$  to  $r_2$ . The intercept is

$$\ln \left[ \frac{G(r_2)}{G(r_1)} \right]$$

Because of its simplicity, this method has been used extensively for  $Q$  determination (Toksöz *et al.*, 1979).

The accuracy of this method depends on the validity of the following assumptions: (1) the ground coupling and response of two sensors (geophones) are the same for all frequencies; (2) the geometric spreading factor  $G(r)$  is independent of frequency; and (3)  $Q$  is independent of frequency in the frequency band of interest. The frequency band is determined by the condition that amplitude spectra,  $A(r, f)$ , have both good frequency resolution and good signal-to-noise ratio. Then the error in estimating  $Q$  can be related to the errors in estimating  $\ln [A_2(r_2, f)/A_1(r_1, f)]$  (White, 1992). Using White's results gives

$$\text{var}\{\ln [A_2(f) / A_1(f)]\} = \frac{1}{2bT} \quad (20)$$

where  $T$  is the duration of the time signal (pulse) used to estimate the spectrum,  $A(f)$ , and  $b$  is the frequency bandwidth used to determine the spectral ratio slope.

Equation (20) defines the conditions under which  $Q$  can be determined accurately by the spectral ratio method. To maximize the bandwidth,  $b$ , we need wide-band signals (flat spectra) both for  $A_1(f)$  and  $A_2(f)$ . Because of the rapid attenuation of high frequencies, even if we have a broad-band source, because of the length of the path,  $A_2(f)$  would generally have a limited bandwidth, shifted toward the lower frequency end of the spectrum. Increasing the time window,  $T$ , in order to improve the spectral estimates of  $A_1(f)$  and  $A_2(f)$ , increases the signal-generated "noise," such as reflections and scattered arrivals, that are included in the time window. The interference of reflections and other signals produces peaks and troughs in the amplitude spectra. The "scallop" effect seen in spectral ratios is due primarily to interference effects.

#### **8.A.3.2.2 Determination of Attenuation From Amplitude Decay Versus Distance**

If there is an array of detectors (geophones, accelerometers) at several distances, attenuation can be determined from the decay of amplitude versus distance (Kudo and Shima, 1970; Pujol and Smithson, 1991; Gibbs *et al.*, 1992). Following equation (17), a natural log of amplitudes can be plotted versus distance at each frequency after correcting for geometric spreading. To compensate for any source variation, a reference geophone is generally placed near the source. Instead of the absolute amplitude the normalized amplitude (observed over reference) is used. The procedure is:

1. Determine the Fourier amplitude spectrum,  $A_i(f)$ , at all distances,  $r_1, r_2, r_3, \dots$
2. Make the geometric corrections by dividing each spectrum  $A_i(f)$  by  $G_i(r)$ .
3. Normalize the geometrically corrected spectra by dividing with the reference spectrum  $-A_1(f)/G_1(r_1)$ .

4. Plot  $\ln \left( \frac{\bar{A}_i}{A_1} \right)$  versus distance at each frequency  $f_1, f_2, \dots, f_n$ .

5. Ideally, at a given frequency,  $f$ ,

$$\ln \left[ \frac{A_i}{A_1} \right]$$

vs.  $r$  should be a straight line with slope

$$\frac{-\pi f}{QV}$$

Velocity,  $V$ , is determined from traveltimes and attenuation  $\left( \frac{1}{Q} \right)$  can be determined at frequency  $f$ .

The advantage of this method over the spectral ratio method, based on

$$\ln \left[ \frac{A_2}{A_1} \right]$$

versus frequency, is that the assumption that  $Q$  is independent of frequency is not used. Thus, frequency dependence of  $Q$  may be determined from the data. The disadvantage is that this method requires observations at a number of distances (minimum of about five).

The errors in this method come from three sources: (1) the errors that result from spectral estimates as given in equation (20); (2) errors due to amplitude variations between different receivers due to the detector amplification, frequency response, and coupling; and (3) since this method is primarily used in VSP mode with detectors downhole, the reflections and scattering that affect the amplitudes in layered or heterogeneous media. Although the method has the potential for determining frequency dependence of  $Q$ , the contribution of errors due to causes (2) and (3) could increase uncertainty as compared to the frequency independent analysis used in the first method.

The examples given by Kudo and Shima (1970) for SH wave attenuation are especially relevant. When good quality waveforms are obtained in the field, attenuation can be determined reliably. In the Adachi area of metropolitan Tokyo, Kudo and Shima obtained  $Q = 8$  in diluvial sands that had an SH velocity of 260 m/s. The  $Q$  was independent of a frequency in the range of 30 to 80 Hz.

The P-wave examples of Pujol and Smithson (1991) in the Columbia Plateau and in Idaho demonstrate the affects of scattering from thin, layered strata, and produce higher attenuation than those of the intrinsic attenuation of the rocks.

#### **8.A.3.2.2.3 Waveform Inversion Method to Determine Attenuation**

Given two waveforms recorded at different source-receiver distances along the wave path, to determine attenuation and velocity for the medium lying between the two receiver locations, a waveform inversion technique can be used (Tang *et al.*, 1988; Tang, 1992). This technique uses the phase and amplitude match between the two waveforms and nonlinear iterative inversion algorithm.

For a vertical point source in a borehole, the radiated far-field SV wave  $W(\omega, r)$  in the radial direction is given by (Meredith, 1990)

$$W(\omega, r) = \frac{S(\omega)}{r} \exp[i\omega/V(\omega)] \exp(-\omega r/2QV), \quad (21)$$

where  $S(\omega)$  is the source spectrum,  $r$  is radial distance,  $Q$  is the quality factor of the medium,  $V(\omega)$  is phase velocity, and  $\omega$  is angular frequency. Apart from the geometric spreading factor,  $1/r$ , the wave propagation and attenuation are controlled by  $Q$  and  $V$ . Assuming a constant- $Q$  model, the attenuation-dispersion pair ( $Q, V$ ) is given by the logarithmic dispersion law (Futterman, 1962; Aki and Richards, 1980). In a limited frequency band, velocity dispersion due to attenuation is insignificant and is not considered in this analysis.

The waveform inversion procedure consists of three major steps: (1) model-guided wave propagation; (2) phase minimization; and (3) amplitude inversion. In the first step the near-source waveform is propagated using equation (21) to the distance of the far-receiver waveform, assuming initial values of  $V$  and  $Q$ . This procedure reduces the phase and amplitude differences between the waveforms. To match waveforms of a particular event and in a particular frequency range, the waveforms are windowed and then filtered using an appropriate band-pass filter. Then, the phase difference between the waveforms is minimized with velocity as the adjustable model parameter. In the phase minimization procedure,  $Q$  is regarded as a constant (initial value) because dispersion due to  $Q$  is usually insignificant. The value of  $V$  required for the minimization is the velocity of the medium. After the phase minimization, the two

waveforms attain the optimum phase match, but their amplitudes may differ because the initial  $Q$  value used to propagate the wave from  $r_1$  to  $r_2$  may not be correct. The amplitude difference is minimized using the nonlinear, iterative algorithm described in Appendix 8.A.3.A, in which  $Q$  is the adjustable model parameter. Iterations are continued until the amplitude difference reaches the minimum. This minimizing value is taken as the  $Q$  of the medium.

The method is illustrated in Figure 8.A.3-1 using Gilroy 2 cross-hole data (Fuhrimam and Stokoe, 1993). The waveforms are recorded at the two receiver boreholes (forward direction at the depth of 15 ft). The waveform from the close receiver is corrected for geometric spreading and migrated to the far receiver distance (Figure 8.A.3-1a). The phase difference between two waveforms is minimized in this migration process and a value of velocity is determined. Both the waveforms are band-passed, filtered, and windowed (Figure 8.A.3-1b). At the final step, the  $Q$  value is adjusted iteratively to obtain the best match between the amplitudes of the two waveforms.

The error analysis for waveform matching can be carried out theoretically using White's (1992) approach. The error depends on the coherency of the two waveforms, as well as the errors in the spectra. The variance of the natural log of spectral ratios is

$$\text{var} \left\{ \ln \left[ |A_2(f)/A_1(f)| \right] \right\} = \frac{1-\gamma^2}{2bT} \quad (22)$$

where  $\gamma^2(f)$  is the spectral coherence between the two waveforms. In the worst case, where two waveforms are incoherent and  $\gamma = 0$ , equation (22) is reduced to (20), the variance of the spectral ratio method. If the two waveforms are perfectly coherent (i.e.,  $\gamma = 1.0$ ), the variance is zero. This assumes that the geometric spreading factor is known and instrument response and coupling are identical at both receivers.

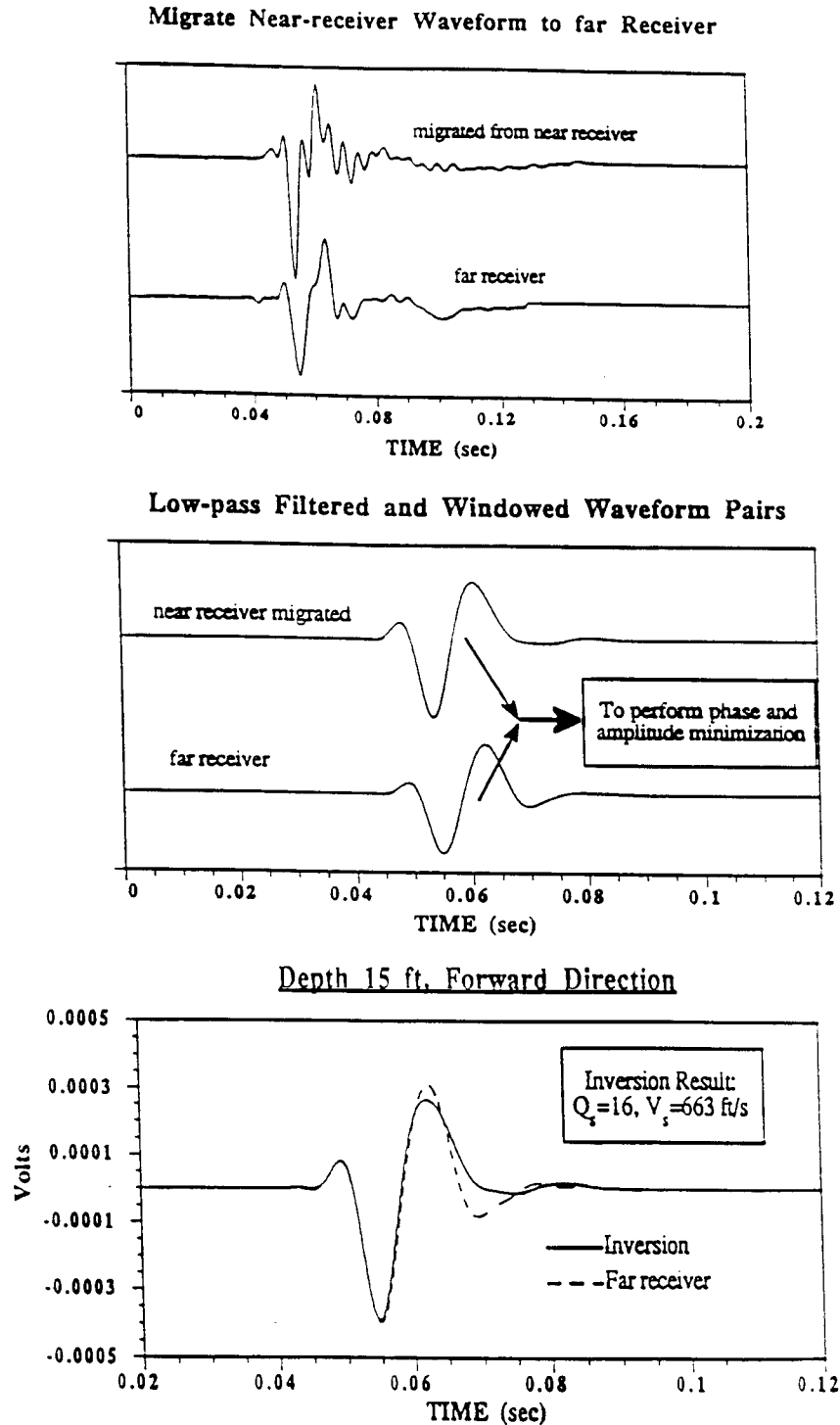
A realistic error estimate that includes all sources of errors in data is carried out for waveform inversions. Factors contributing to data errors include borehole-receiver coupling, far and near source receiver response difference, layering of the earth structure, scattering, and noise in the data. The following method is used to estimate the error in  $Q$  from the amplitude mismatch between the waveforms. This mismatch is the rms residual value from the amplitude inversion procedure.

Given amplitudes  $A_1$  and  $A_2$  of the near and far receivers, respectively, and using the wave propagation mode given in equation (21), the  $Q$  value can be calculated by

$$A_1 = (r_2/r_1) A_2 \exp \left( \frac{\pi f \Delta r}{QV} \right) \quad (23)$$

where  $r_1$  and  $r_2$  are near and far source receiver distances, respectively,  $\Delta r = r_1 - r_2$ , and  $f$  is the center frequency of the matched signals. Because of the amplitude mismatch,  $\Delta A$ , due to factors that are not included in the model, the actually inverted  $Q$  value is  $Q_c$  and equation (23) may be written as

$$A_1 = (r_2/r_1) A_2 \exp \left( \frac{\pi f \Delta r}{Q_0 V} \right) + \Delta A. \quad (24)$$



**Figure 8.A.3-1**

Waveform inversion procedure to obtain velocity and attenuation from cross-hole data. (a) The near receiver is migrated to the far receiver position using approximate velocity and  $1/r$  geometric correction. (b) The two waveforms are filtered and windowed. (c) An inversion is carried out to match phase and amplitudes to obtain velocity and  $Q$ .



A comparison of equations (23) and (24) gives

$$|\Delta Q| = \frac{Q_0^2 V}{\Delta r \pi f} \ln \left( 1 + |\Delta A / A_j| \right), \quad (25)$$

where we have used the approximation  $(1/Q_0 - 1/Q) \approx \Delta Q/Q_0^2$ .

In the analysis of the Treasure Island and Gilroy 2 field data, equation (25) was used to determine the error.

### 3—ATTENUATION RESULTS FROM FIELD DATA

The cross-hole and downhole data from the Treasure Island and Gilroy 2 sites were analyzed by the waveform inversion method to determine attenuations. We first present the results based on cross-hole data and then the downhole VSP data.

#### 8.A.3.3.1 Treasure Island Cross-Hole Data

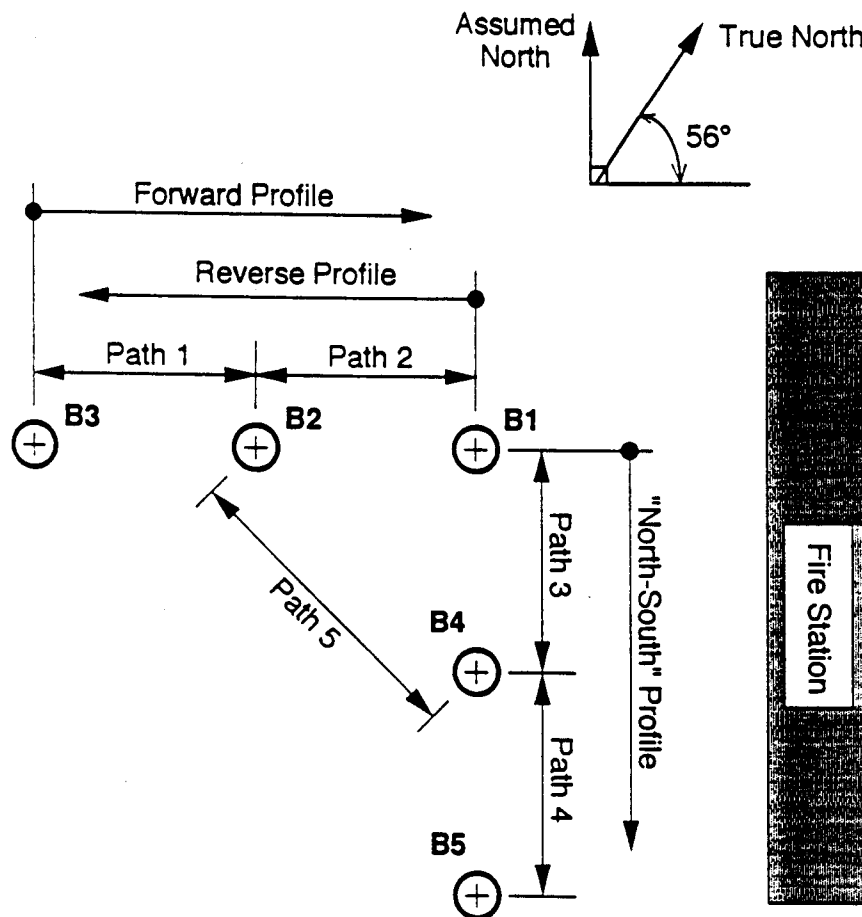
The waveform inversion method was used to analyze the cross-hole data recorded by the University of Texas (Austin). The geometry of the boreholes at Treasure Island is shown in Figure 8.A.3-2. The shear (SV) wave cross-hole data available for analysis were Profile 1-forward direction, with the source at borehole 3, and receivers at borehole 2 and borehole 1 for depths from 3 to 100 ft; Profile 1-reverse direction, with the source at borehole 1 and the receivers at borehole 2 and borehole 3 for depths from 6 to 35 ft; and Profile 2, with the source at borehole 1 and receivers at borehole 4 and borehole 5 for depths from 3 to 21 feet. The waveform inversion method was used to determine shear velocities and attenuations from the field data. Figure 8.A.3-3 (top) shows an example of the waveforms recorded along Profile 2 at a depth of 21 feet. The source is at borehole 1 and the receiver,  $R_1$ , is at borehole 4 and  $R_2$  at borehole 5. The shear waves (low frequency second arrivals in each record) are band-pass filtered, windowed, corrected for geometric spreading ( $1/R$ ), and  $R_1$  is migrated to  $R_2$ . The velocity is obtained by matching the phase. Then the amplitudes are matched to obtain  $Q_s$ . The final match of the waveforms is shown at the bottom in Figure 8.A.3-3. The shear velocity  $V_s = 474$  ft/sec and  $Q_s = 16$  are obtained in this process. The standard error for the  $Q_s$  value is determined using the difference between the amplitudes (the residual) and found to  $\pm 6$ .

Table 8.A.3-1 lists the cross-hole velocities obtained by waveform matching. These could differ from the first arrival velocities. The differences may be due to: (1) measurement errors; and (2) first arrivals provide the fastest path velocity (could be refraction), while wave matching gives the average velocity of energy propagation. Energy propagation velocity is used to calculate the  $Q$  values. Given relatively short distances, 5 to 10 percent variations in velocities are not unusual. Velocity variations between the paths include the effects to site heterogeneities as well as measurement errors.

Quality factor ( $Q$ ) values at the Treasure Island site are given in Table 8.A.3-2. There are variations of  $Q$  values between the paths. These may be due to a combination of measurement errors as well as site heterogeneities.

The plots of the  $Q$  values versus depth are shown in Figures 8.A.3-4a, b, and c. The corresponding damping values are given in Figures 8.A.3-5a, b, and c. Where there are three independent measurements of damping at shallow depths (3 to 35 ft), the values at a given depth vary by as much as a factor of 2. These variations are larger than the standard errors. The borehole 4–BH 5 segment along Profile 2 has lower damping than those of BH 2–BH 1 and BH 2–BH 3 along Profile 1. Percentage-wise, damping variations are greater than those of the velocities. It is difficult to determine how much of the difference is due to lateral heterogeneity of the site and how much is due to measurement errors. We averaged the three values to obtain a single damping versus depth curve for the site. The “averaged” curve is shown in Figure 8.A.3-6.

Figure 8.A.3-7, taken from Fuhrman and Stokoe (1993), shows the shear velocity profile and the geologic log for the Treasure Island site. Comparison of the velocity and damping profiles shows that higher velocities at depths of 30 ft and 70 ft are correlated with high damping values. The correlation at a depth of 70 ft is especially significant. Although the geologic log does not show a separate unit at this depth, most probably there is a sandy layer at 70 ft along Path 1 at the Treasure Island site.

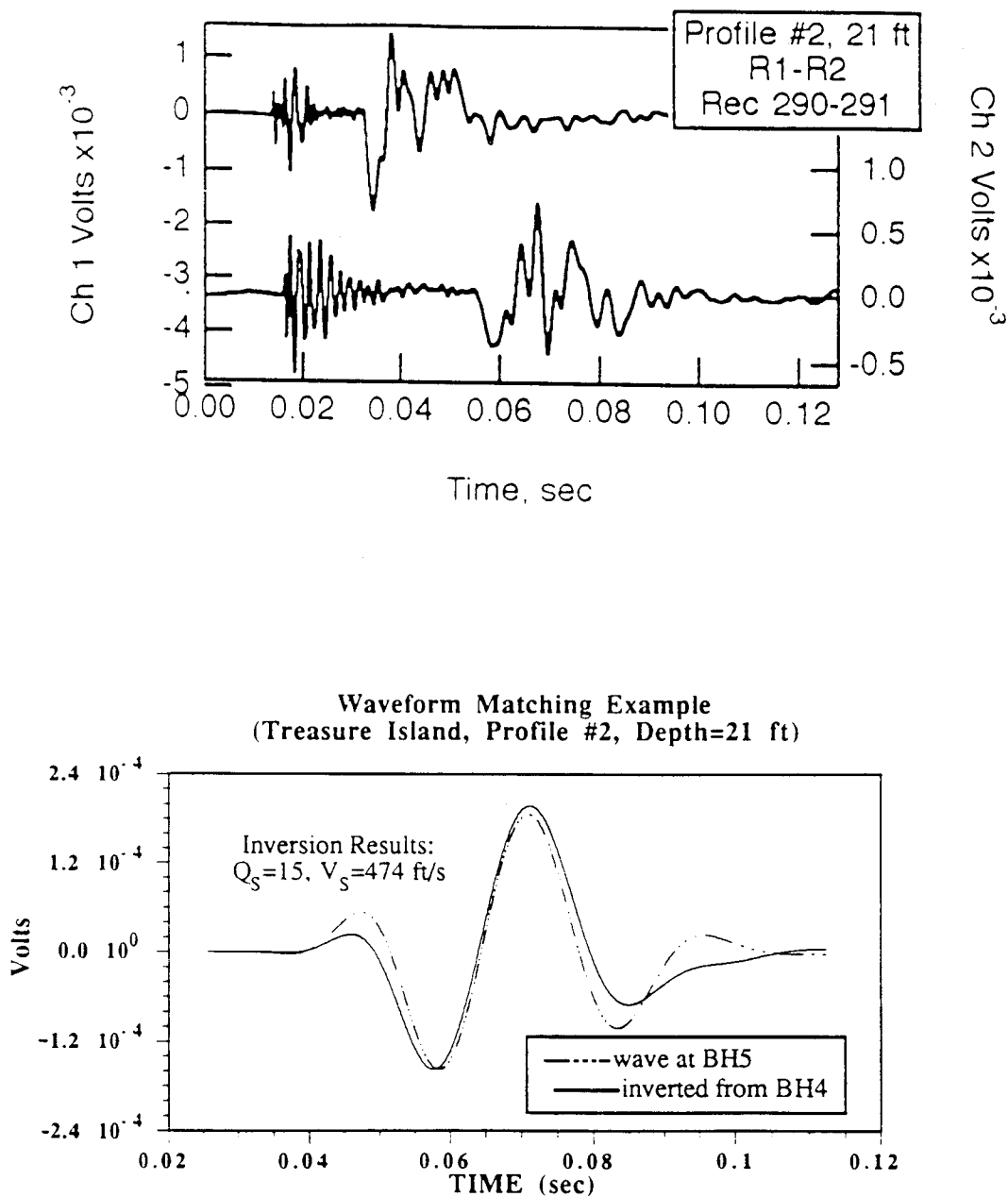


\*Notes: Drawing For Layout Only  
(Not to Scale)

Elevation Datum for Crosshole  
Tests is the Ground Surface  
at Borehole B3

**Figure 8.A.3-2**

Borehole arrangement and wave travel paths for cross-hole seismic testing at Treasure Island (after Fuhrimam and Stokoe, 1993).



**Figure 8.A.3-3**  
 Raw data (top) and inversion results (bottom) for Treasure Island cross-hole data at depth of 21 ft for Profile #2, Path #4.

**Table 8.A.3-1a**

Cross well SV-wave velocities with depths at Treasure Island for the path BH2-BH1 (Profile #1). The two velocities (conventional arrival picking, and inversion values using the phase matching method discussed in the text) are tabulated with depths.

**Forward Direction**

<b>Depth (ft)</b>	<b>Boreholes</b>	<b>Vs (ft/s) Arrival picking</b>	<b>Vs (ft/s) Phase Matching</b>
3	2-1	403	470
6	2-1	625	556
9	2-1	409	527
12	2-1	405	482
15	2-1	409	462
18	2-1	403	439
21	2-1	463	498
24	2-1	482	491
27	2-1	559	496
30	2-1	560	538
35	2-1	602	576
38	2-1	592	627
40	2-1	578	593
42	2-1	526	512
45	2-1	518	528
50	2-1	494	494
55	2-1	570	535
60	2-1	467	550
65	2-1	698	674
70	2-1	718	672
75	2-1	505	537
80	2-1	509	574
85	2-1	512	584
90	2-1	563	580
94	2-1	816	990
96	2-1	795	728
98	2-1	1204	1060
100	2-1	1180	1112

**Table 8.A.3-1b**

Cross well SV-wave velocities with depths for the path BH2–BH3 (Profile #1).

**Reverse Direction**

<b>Depth (ft)</b>	<b>Boreholes</b>	<b>Vs (ft/s) Arrival picking</b>	<b>Vs (ft/s) Phase matching</b>
6	2-3	593	491
12	2-3	413	429
18	2-3	449	459
24	2-3	533	549
30	2-3	596	620
35	2-3	672	629

**Table 8.A.3-1c**

Cross well SV-wave velocities with depths for the path BH4–BH5 (Profile #2).

**Forward Direction**

<b>Depth (ft)</b>	<b>Boreholes</b>	<b>Vs (ft/s) Arrival picking</b>	<b>Vs (ft/s) Phase matching</b>
3	4-5	509	454
6	4-5	374	482
9	4-5	459	422
12	4-5	456	424
15	4-5	423	415
18	4-5	412	414
21	4-5	463	474

**Table 8.A.3-2a**

Estimated Qs and its error with depths at Treasure Island for the path PH2-BH1 (Profile #1).

**Forward Direction (BH2-BH1)**

<b>Z (ft)</b>	<b>Qs</b>	<b>Error</b>
3	9	2
6	#no solution#	-
9	*7	2*
12	16	3
15	#no solution#	-
18	20	4
21	11	2
24	21	1
27	8	2
30	14	1
35	17	3
38	11	2
40	29	7
42	24	4
45	21	2
50	#no solution#	-
55	#no solution#	-
60	26	6
65	14	3
70	14	2
75	22	2
80	33	8
85	18	3
90	24	3
94	11	6
96	#no solution#	-
98	18	7
100	17	6

\*.....\* values estimated with  $1/\sqrt{r}$  spreading

**Table 8.A.3-2b**

Estimated Qs and its error with depths for the path BH2–BH3 (Profile #1).

**Reverse Direction (BH2–BH3)**

<b>Z (ft)</b>	<b>Qs</b>	<b>+ - Error</b>
6	19	4
12	21	3
18	11	1
24	14	2
30	12	3
35	12	1

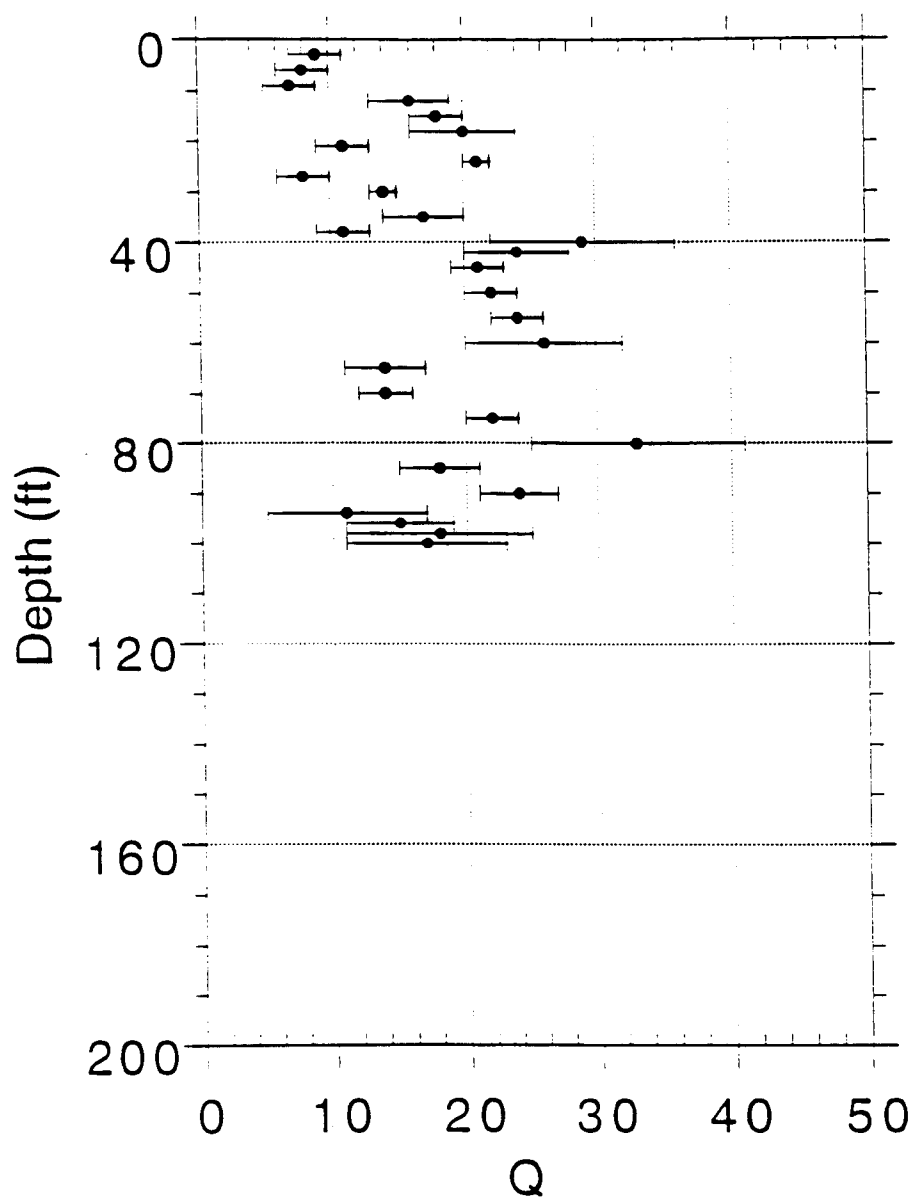
**Table 8.A.3-2c**

Estimated Qs and its error with depths for the path BH4–BH5 (Profile #2).

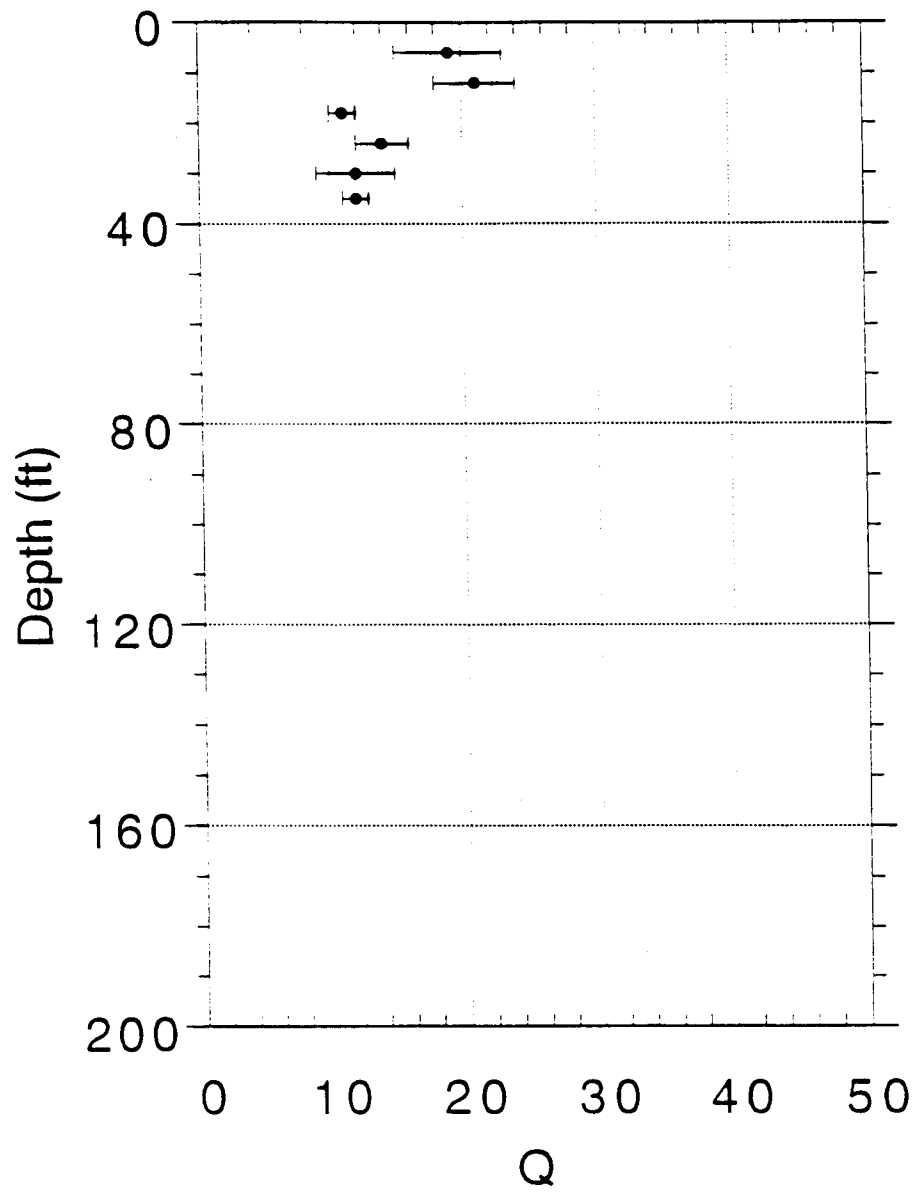
**BH4–BH5**

<b>Depth (ft)</b>	<b>Qs</b>	<b>Error</b>
3	16	3
6	16	4
9	15	1
15	25	5
18	31	13
21	15	6

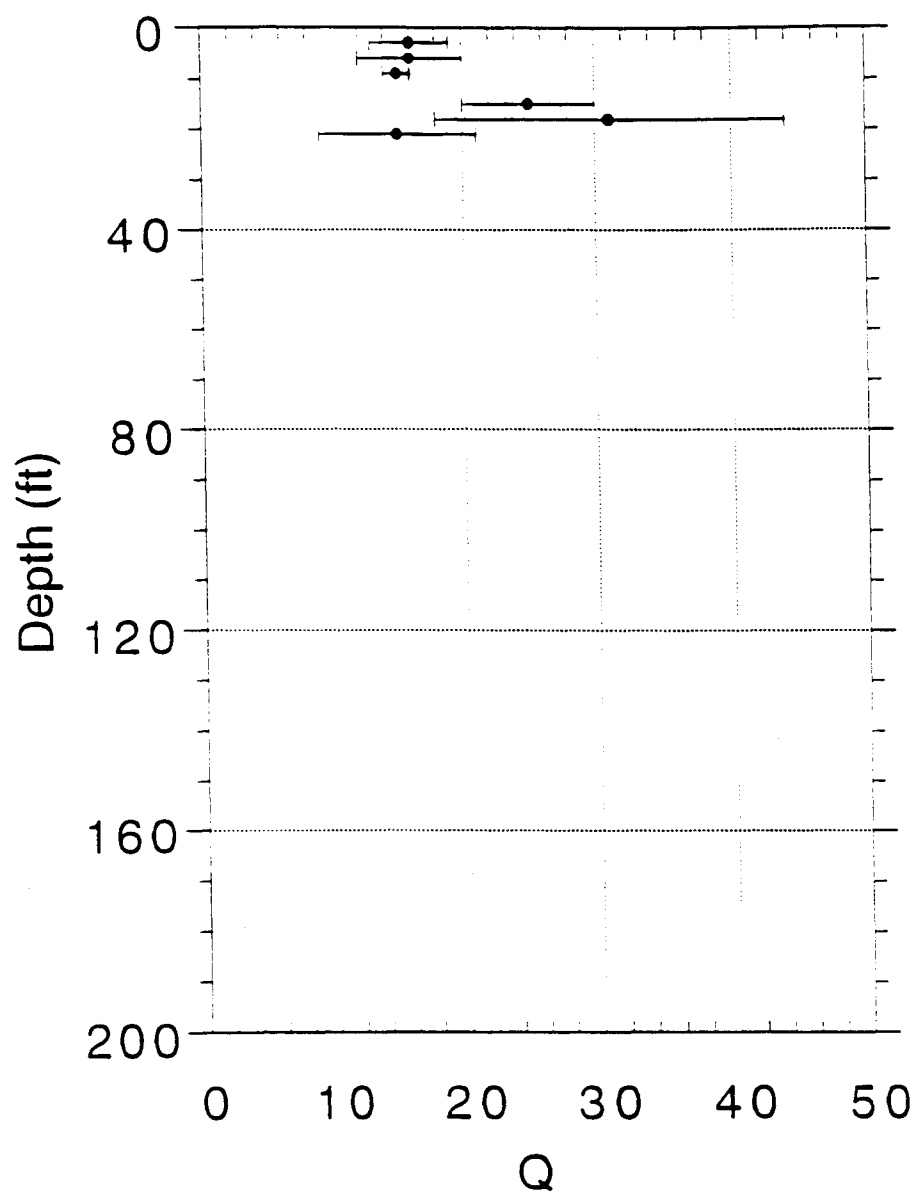




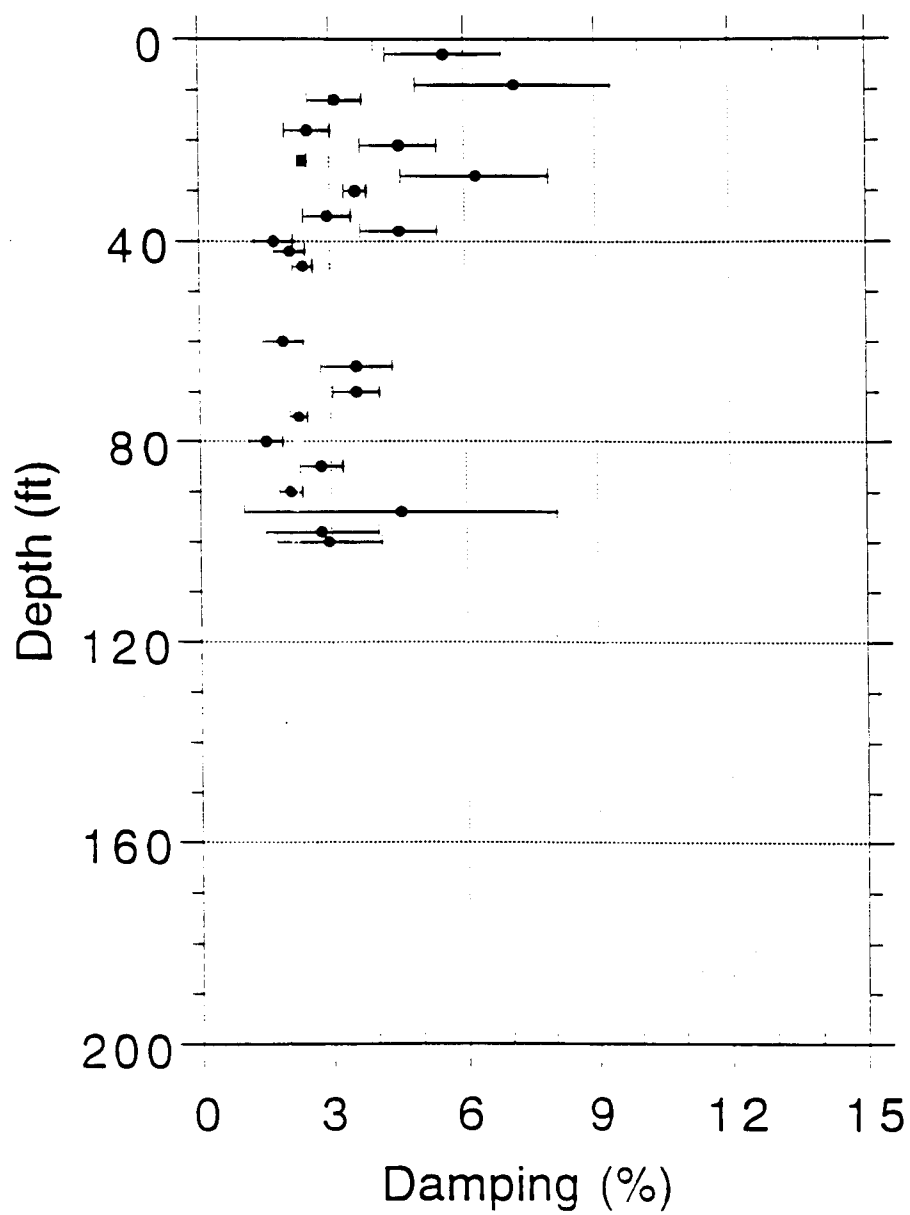
**Figure 8.A.3-4a**  
Measured shear (SV) Q values and estimated errors versus depth along Path BH2-BH1 at Treasure Island.



**Figure 8.A.3-4b**  
Measured shear (SV) Q values and estimated errors versus depth along Path BH2-BH3 at Treasure Island.

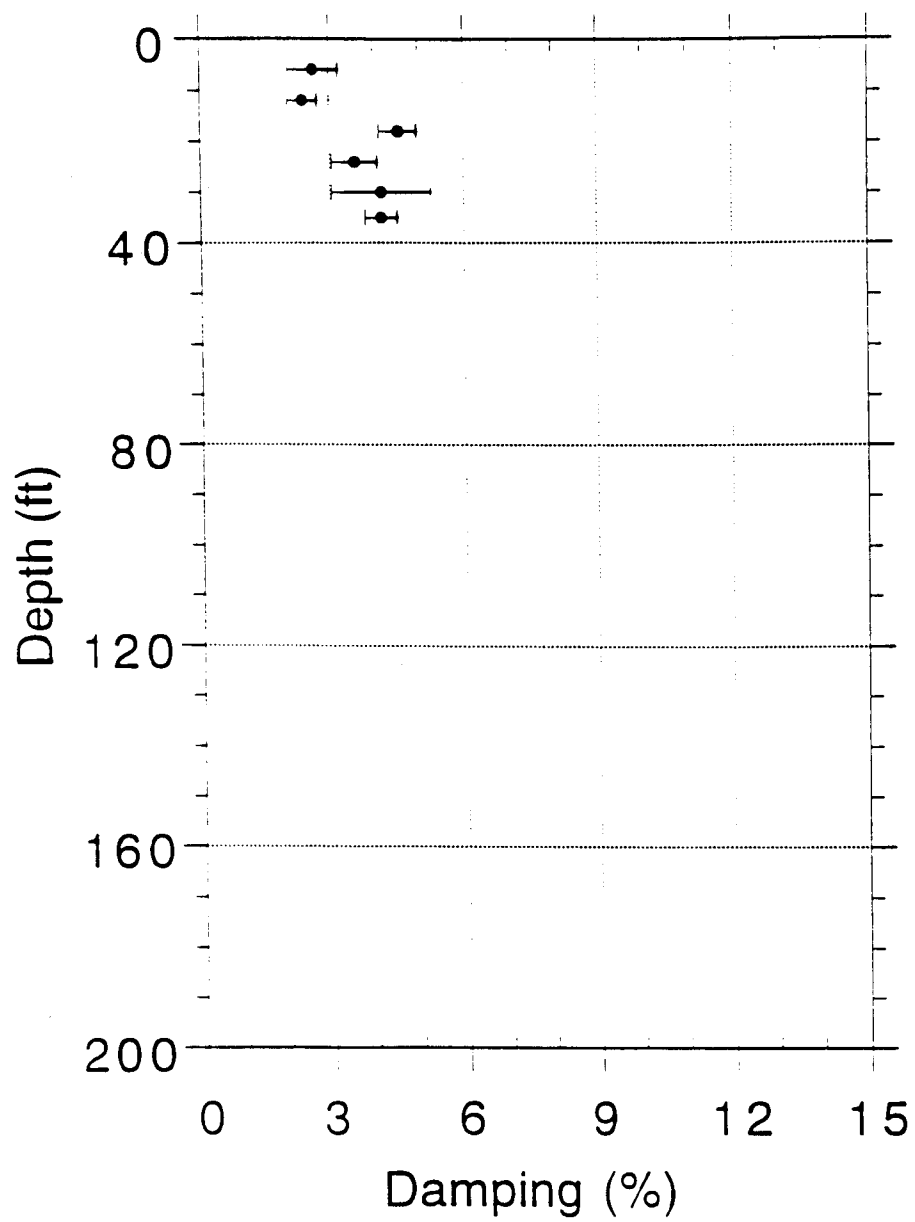


**Figure 8.A.3-4c**  
Measured shear (SV) Q values and estimated errors versus depth along Path BH4-BH5 at Treasure Island.

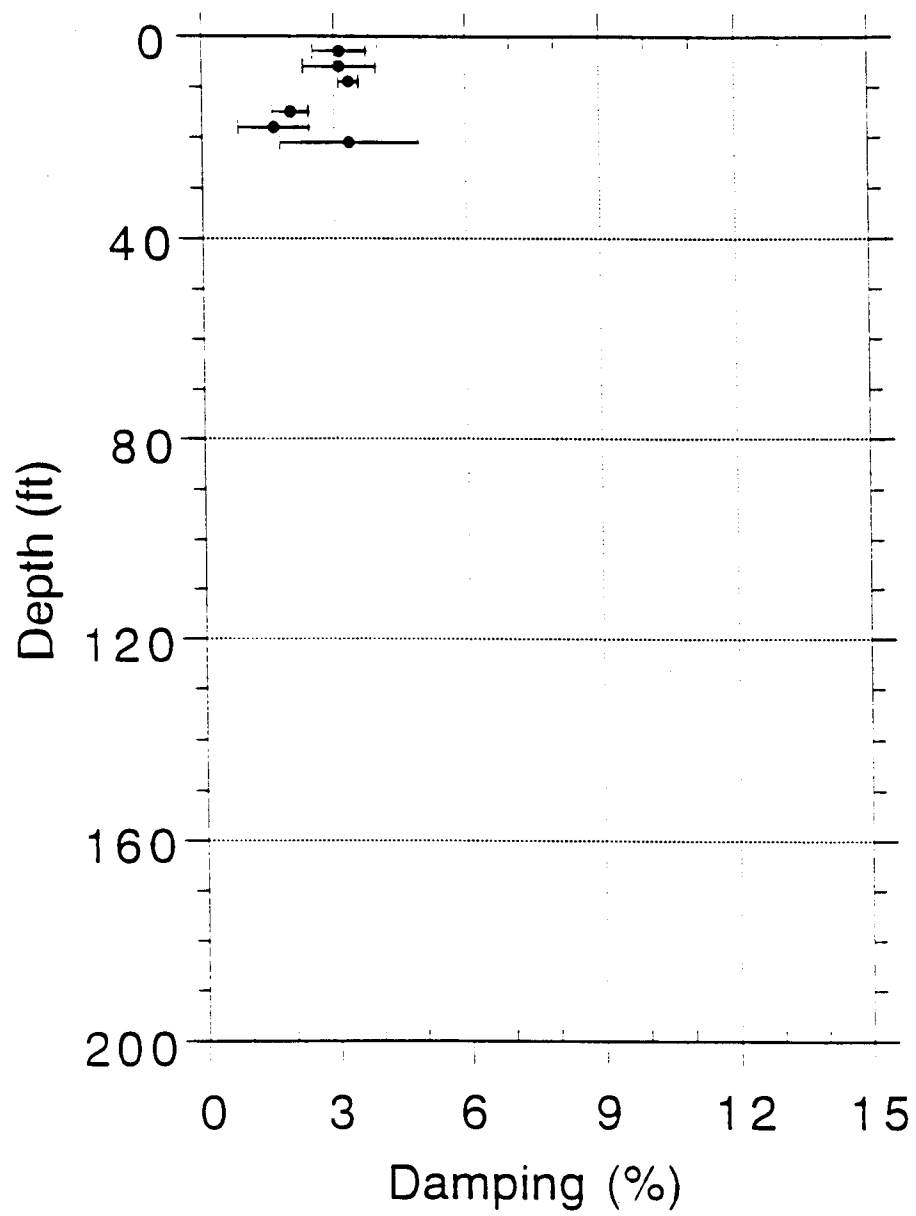


**Figure 8.A.3-5a**

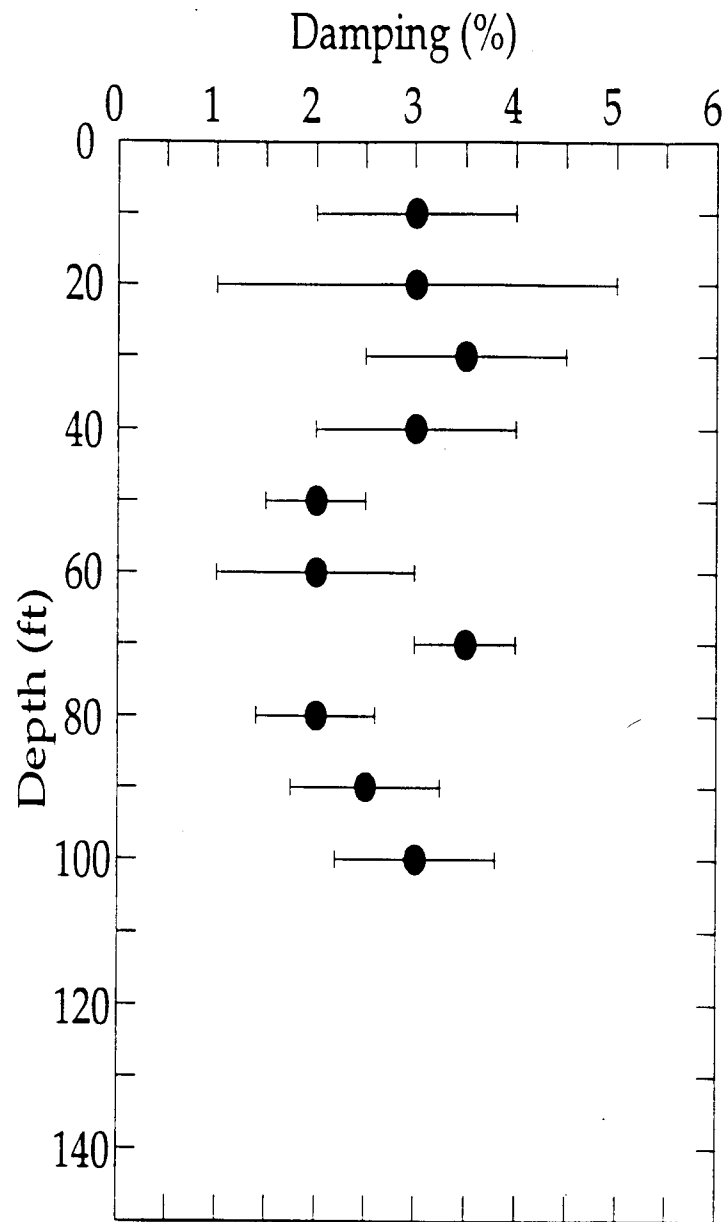
Damping values (shear) and estimated errors as a function of depth along Path BH2-BH1 at Treasure Island.



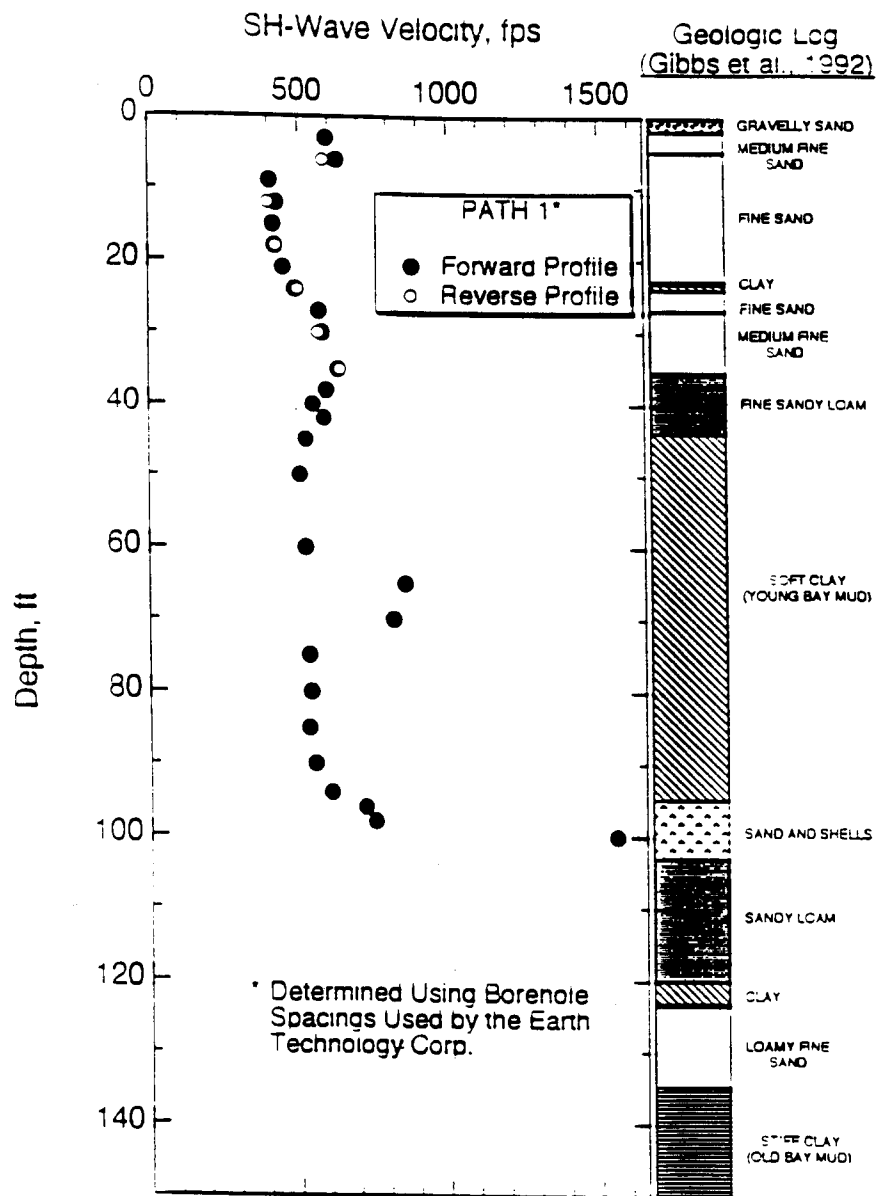
**Figure 8.A.3-5b**  
Damping values (shear) and estimated errors as a function of depth along Path BH2-BH3 at Treasure Island.



**Figure 8.A.3-5c**  
Damping values (shear) and estimated errors as a function of depth along Path BH4-BH5 at Treasure Island.



**Figure 8.A.3-6**  
Average shear damping versus depth based on cross-hole data at Treasure Island.



**Figure 8.A.3-7**

Shear wave (SH) velocities for forward and reverse directions along Path 1 and the geologic log at Treasure Island (after Fuhrimam and Stokoe, 1993).



### 8.A.3.3.2 Gilroy 2 Cross-Hole Data

Cross-hole data were acquired using various source-receiver combinations in the four collinear boreholes, shown in Figure 8.A.3-8, at the Gilroy 2 site. With the source at borehole 1, BH2–BH3 and BH3–BH4 receiver combinations were used to obtain data in the “forward” direction. Then the source was placed in borehole 4, and receiver combinations of BH3–BH2 and BH2–BH1 were used for the “reverse” direction. The depth range extended from 5 to 195 feet.

The cross-hole shear (SV) wave data were analyzed using the waveform inversion method. Figures 8.A.3-9 and 8.A.3-10 show two examples of the observed waveforms (depths at 85 and 105 ft) and how they matched with the best fitting velocity and Q values.

Cross-hole shear (SV) velocities at the Gilroy 2 site, between the depths of 5 and 195 ft, are tabulated in Table 8.A.3-3a and Table 8.A.3-3b in the “forward” and “reverse” directions, respectively. There are site-to-site variations in the velocities. These variations are generally less than about ten percent. Combinations of boreholes 2–3 in the forward direction and boreholes 3–2 in the reverse direction provide a common zone where one can determine the accuracy of velocities and attenuations. The mean difference between velocities measured in the forward and reverse directions is less than five percent. The greatest differences occur at depths where velocity gradients are high (e.g., depths of 35 ft, 75 ft, 145 ft). Small variations at depths of the source or receivers could result in different traveltimes because of refractions at such boundaries. The variation of velocities between different paths (e.g., BH2–BH3 and BH3–BH4) is somewhat larger than those of the common paths, indicating the presence of lateral heterogeneities of scale lengths of less than about 20 feet.

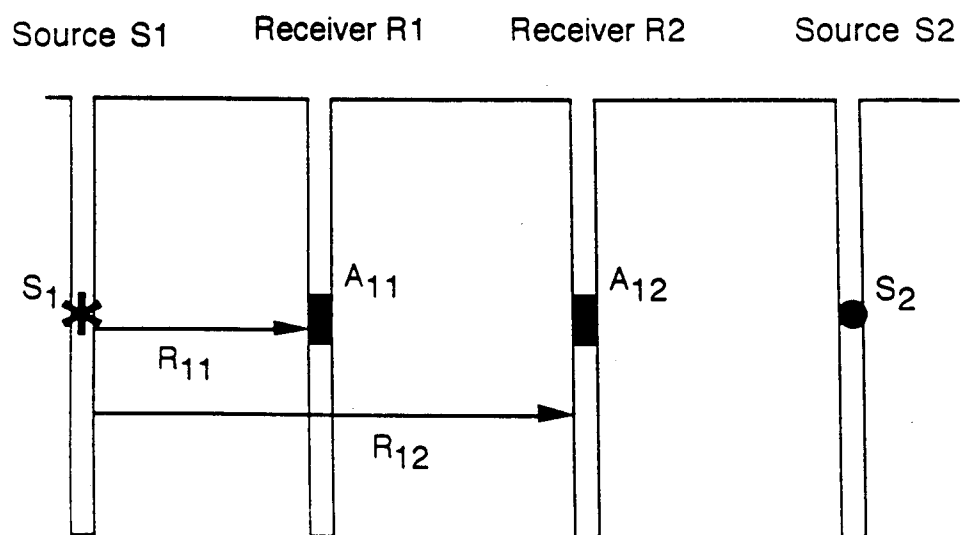
The shear wave Q values are tabulated in Table 8.A.3-4a and 8.A.3-4b for paths in the forward and reverse directions, respectively. The Q values are plotted in Figures 8.A.3-11a, b, c, d. The corresponding damping values are in Figures 8.A.3-12a, b, c, d. Damping over different paths varies significantly at some depths. In cross-hole measurements, wave shapes and amplitudes could be affected by layering, lateral heterogeneities, and geophone coupling. Large standard errors reflect these effects. The sensitivity of attenuation to layering is discussed in detail in Appendix 8.A.3.B.

The variation of damping as a function of depth is consistent between different profiles. To obtain a “mean” damping curve for Gilroy 2, values from four profiles are averaged and plotted in Figure 8.A.3-13. The shear velocity profiles of the University of Texas and the USGS Geologic Log (Gibbs *et al.*, 1992) are given in Figure 8.A.3-14. Comparison of Figures 8.A.3-13 and 8.A.3-14 give some surprising correlations. At this site, high damping is correlated with high shear velocities at depths of about 60 ft and 180 ft, corresponding to sandy, fine gravel and gravel units. In clay and sandy loam, and silty clay, both damping and shear velocities are lower.

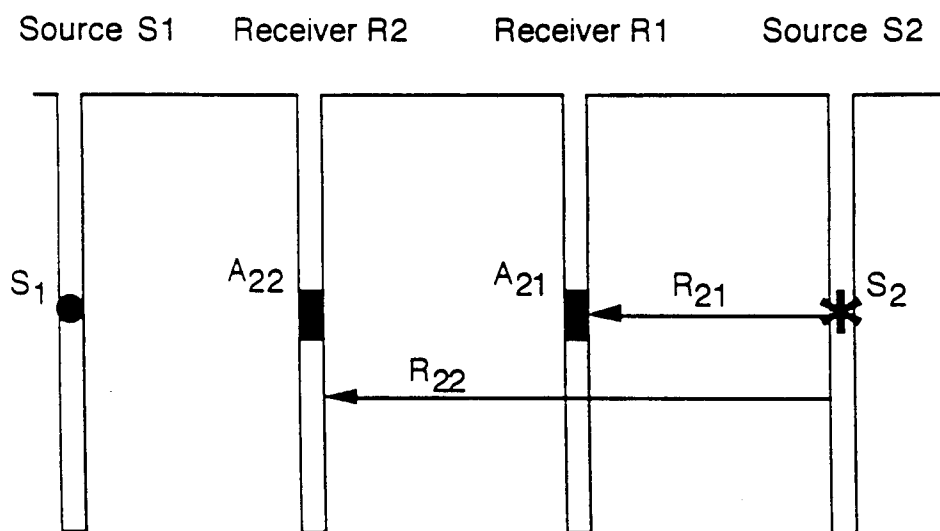
We also examined the frequency dependence of damping at the Gilroy 2 site. In the waveform inversion procedure the waveforms are band-pass filtered. By varying the pass-band of the filter, one can determine the frequency dependence of velocities and attenuation. Using BH2–BH3 waveforms velocity and Q values were obtained between 50–300 Hz, and are shown in Figures 8.A.3-15 and 8.A.3-16, respectively. There is small but noticeable shear velocity dispersion. Velocity at 300 Hz is about 5 percent higher than the velocity at 50 Hz. The sharp beginnings of the shear wave pulses observed in the field recordings are consistent with the early arrival of higher frequencies. The  $Q_s$  values decrease with increasing frequency in the range of 50–300 Hz. In the analysis of cross-hole data reported here, we used a pass-band of 100–150 Hz.

### 8.A.3.3.3 Attenuation From Downhole (VSP) Data

The waveform inversion method was also used to analyze the downhole (VSP) data recorded by Agbabian Associates. The data collection procedure is different at the two sites. The shear hammer source is placed at the surface with a 5 ft offset. Two geophones are used—one is fixed and the other is moved at different depths for the attenuation measurements. At the Gilroy 2 site, the two receivers are placed at



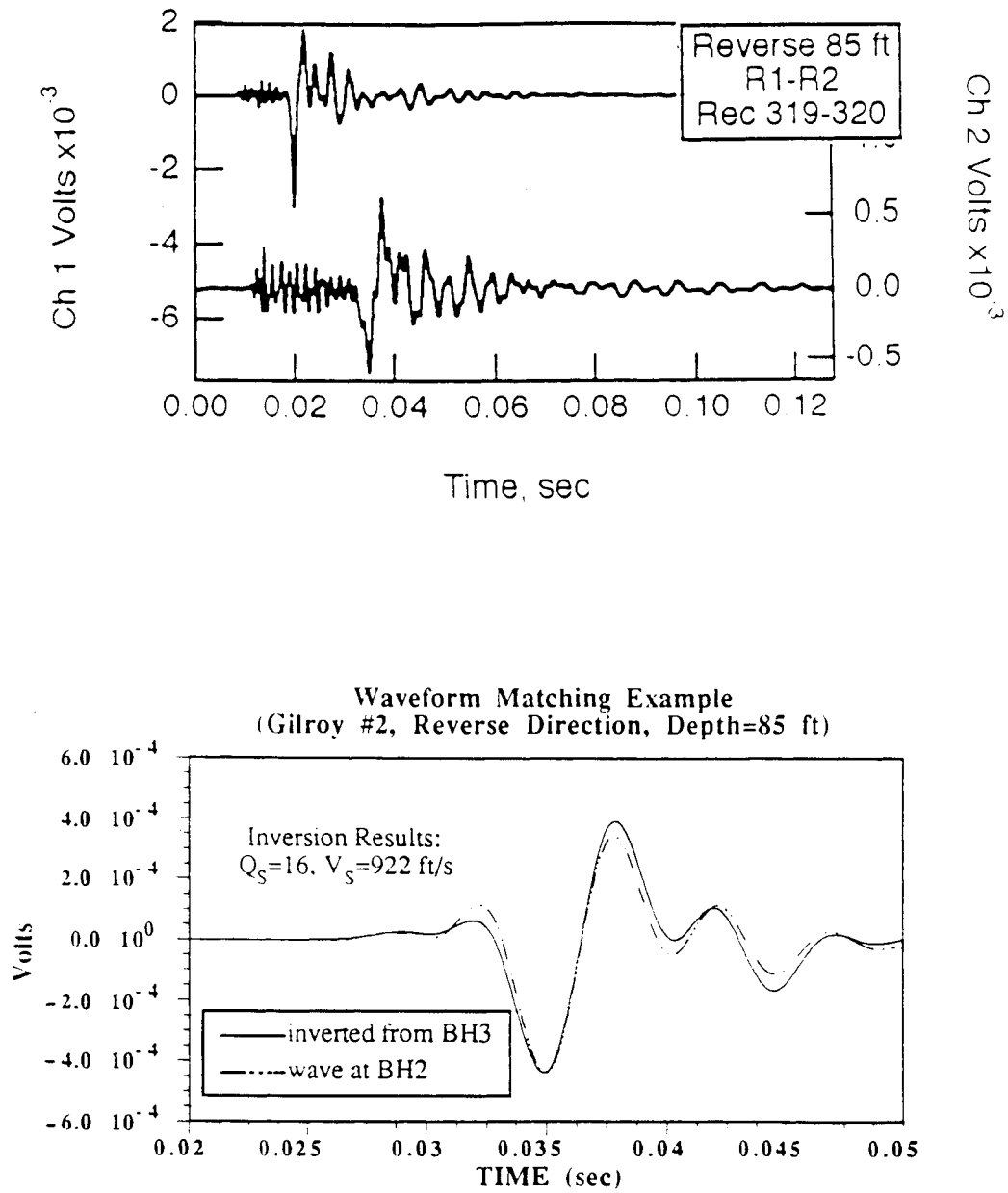
(a) Forward Direction



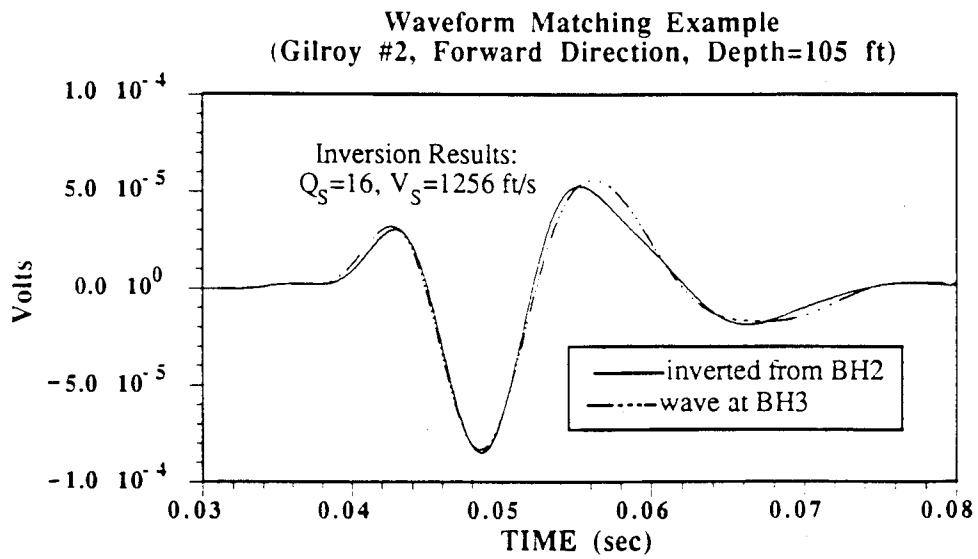
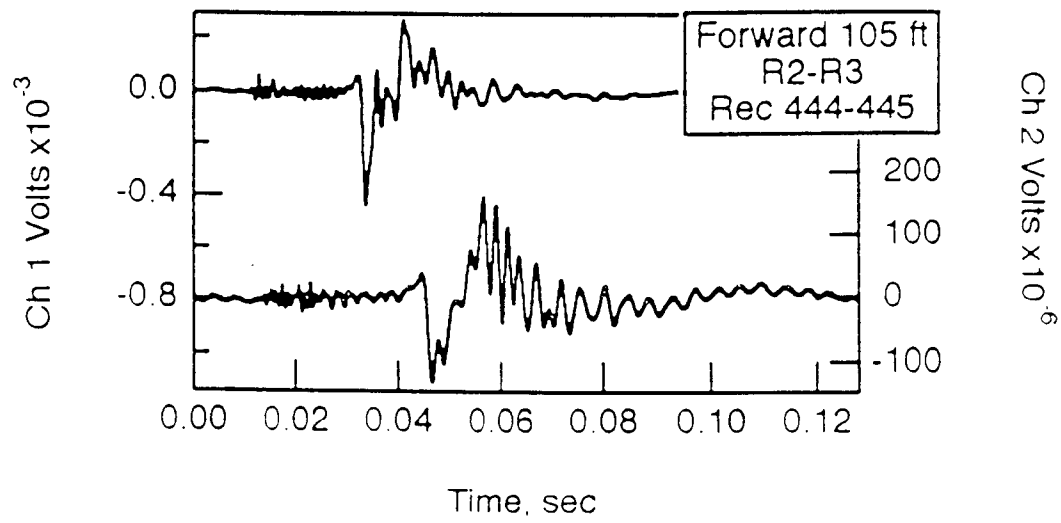
(b) Reverse Direction

**Figure 8.A.3-8**

Schematic of borehole layout for in-situ damping measurements at Gilroy 2 (after Fuhrimam and Stokoe, 1993).



**Figure 8.A.3-9**  
 Raw data (top) and inversion results (bottom) for Gilroy 2 reverse cross-hole data at depth of 85 ft.



**Figure 8.A.3-10**  
Raw data (top) and inversion results (bottom) for Gilroy 2 forward cross-hole data at depth of 105 ft.

**Table 8.A.3-3a**

Cross well SV-wave velocities with depths at Gilroy 2 for the paths BH2-BH1 and BH3-BH4 (forward direction).

**Forward Direction**

Depth (ft)	Boreholes	Vs (ft/s) Arrival picking	Vs (ft/s) Phase matching
5	2-3	646	520
	3-4	645	428
7.5	2-3	677	511
	3-4	671	680
10	2-3	693	698
	3-4	714	700
15	2-3	696	657
	3-4	652	702
20	2-3	681	658
	3-4	675	664
25	2-3	603	699
	3-4	713	723
30	2-3	726	826
	3-4	769	800
35	2-3	755	796
	3-4	not recorded	not recorded
40	2-3	963	1100
	3-4	1132	1179
45	2-3	1275	1367
	3-4	not recorded	not recorded
50	2-3	1446	1360
	3-4	1467	1489
55	2-3	1807	1684
	3-4	1803	1626
60	2-3	1932	2035
	3-4	1872	1839
65	2-3	1836	2033
	3-4	2090	1766
70	2-3	1770	1786
	3-4	1867	1836
75	2-3	1052	1311
	3-4	1194	1191
80	2-3	1021	1167
	3-4	1102	1184
85	2-3	984	1018
	3-4	1197	1156
90	2-3	913	1017
	3-4	1034	1063
95	2-3	973	1012
	3-4	1033	1105
100	2-3	909	1026
	3-4	947	1025

**Table 8.A.3-3a (continued)**

Cross well SV-wave velocities with depths at Gilroy 2 for the paths BH2–BH1 and BH3–BH4 (forward direction).

**Forward Direction**

Depth (ft)	Boreholes	Vs (ft/s) Arrival picking	Vs (ft/s) Phase matching
105	2-3	1070	1103
	3-4	1183	1143
110	2-3	1097	1125
	3-4	1152	1134
115	2-3	1087	1188
	3-4	1257	1174
120	2-3	1152	1152
	3-4	1267	1320
125	2-3	1163	1128
	3-4	1328	1357
130	2-3	1217	1393
	3-4	1391	1480
135	2-3	1278	1264
	3-4	1374	1373
140	2-3	2260	1960
	3-4	2335	2104
145	2-3	2174	2257
	3-4	2439	2333
150	2-3	2223	1938
	3-4	2460	2390
155	2-3	2090	2028
	3-4	2307	2531
160	2-3	1857	1957
	3-4	2343	2445
165	2-3	2055	2172
	3-4	2022	2100
170	2-3	2754	2592
	3-4	2872	2799
175	2-3	3123	2695
	3-4	2815	2779
180	2-3	2757	2773
	3-4	2908	3137
185	2-3	2684	2765
	3-4	3008	2909
190	2-3	2273	2370
	3-4	2520	2889

**Table 8.A.3-3b**

Cross well SV-wave velocities with depths for the paths BH3–BH2 and BH2–BH1 (reverse direction).

**Reverse Direction**

Depth (ft)	Boreholes	Vs (ft/s) Arrival picking	Vs (ft/s) Phase matching
5	3-2	525	576
	2-1	747	655
15	3-2	711	668
	2-1	687	688
25	3-2	712	722
	2-1	570	683
35	3-2	1082	846
	2-1	924	786
45	3-2	1374	1260
	2-1	1385	1300
55	3-2	1703	1825
	2-1	1870	1610
65	3-2	1862	1422
	2-1	1664	1502
75	3-2	1571	1798
	2-1	1659	1587
85	3-2	984	922
	2-1	976	924
95	3-2	920	928
	2-1	944	898
105	3-2	1019	1110
	2-1	1068	991
115	3-2	1085	1032
	2-1	1117	1087
125	3-2	1140	988
	2-1	1259	1188
135	3-2	1162	1314
	2-1	1186	1248
145	3-2	1809	1786
	2-1	2020	1735
155	3-2	1777	2006
	2-1	1826	1843
165	3-2	1787	1968
	2-1	1893	2079
175	3-2	2534	2652
	2-1	2412	2361
185	3-2	2405	2307
	2-1	2396	2265
195	3-2	1392	1671
	2-1	1017	1880

**Table 8.A.3-4a**

Estimated Qs and its error with depths at Gilroy 2 for the paths BH2-BH1 and BH3-BH4 (forward direction).

**Forward Direction**

Depth (ft)	BH2-BH3 Qs + - error		BH3-BH4 Qs + - error	
5	8	2	4	2
7.5	16	3	5	2
10	11	2	6	3
15	18	2	6	3
20	13	4	*29	7*
25	*25	8*	#no solution#	
30	20	5	6	1
35	22	3	7	3
40	13	4	7	2
50	23	6	9	4
55	22	7	23	15
60	10	2	6	4
65	7	1	10	2
70	12	3	6	2
75	7	1	6	3
80	*33	6*	6	1
85	*13	3*	21	4
90	*12	2*	*22	6*
95	*21	7*	*12	2*
100	#no solution#		*20	6*
105	*11	2*	16	3
110	11	2	37	11
115	10	3	25	4
120	10	5	12	2
125	*12	2*	18	3
130	*15	2*	15	3
135	8	1	11	3
140	10	3	12	10
145	10	5	11	3
150	8	4	10	3
155	8	3	6	1
160	16	10	9	1
165	8	3	6	2
170	8	2	5	2
175	8	2	6	1
180	7	3	8	4
185	7	2	10	3
190	8	1	8	2

\*...\* estimated with  $1/\sqrt{r}$  spreading



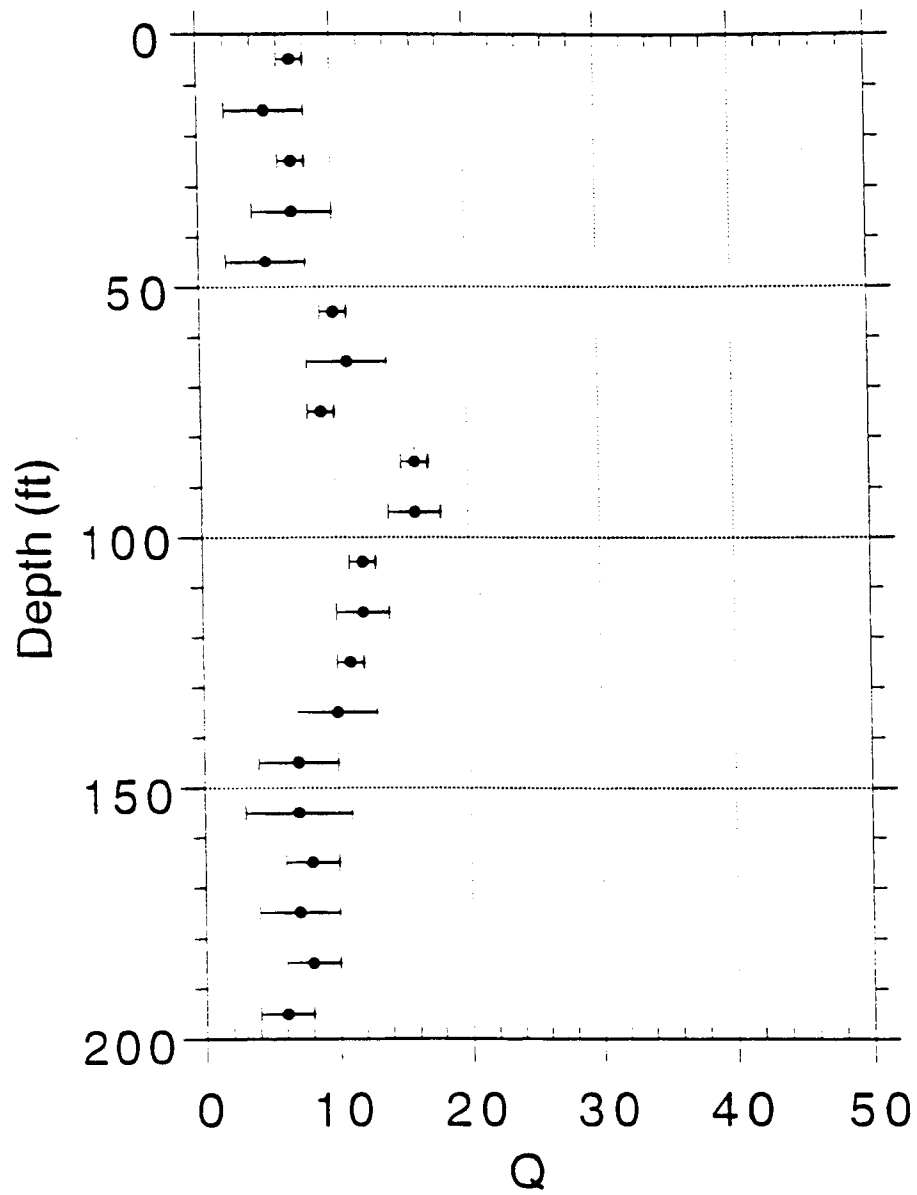
**Table 8.A.3-4b**

Estimated Qs and its error with depths for the paths BH3-BH2 and BH2-BH1 (reverse direction).

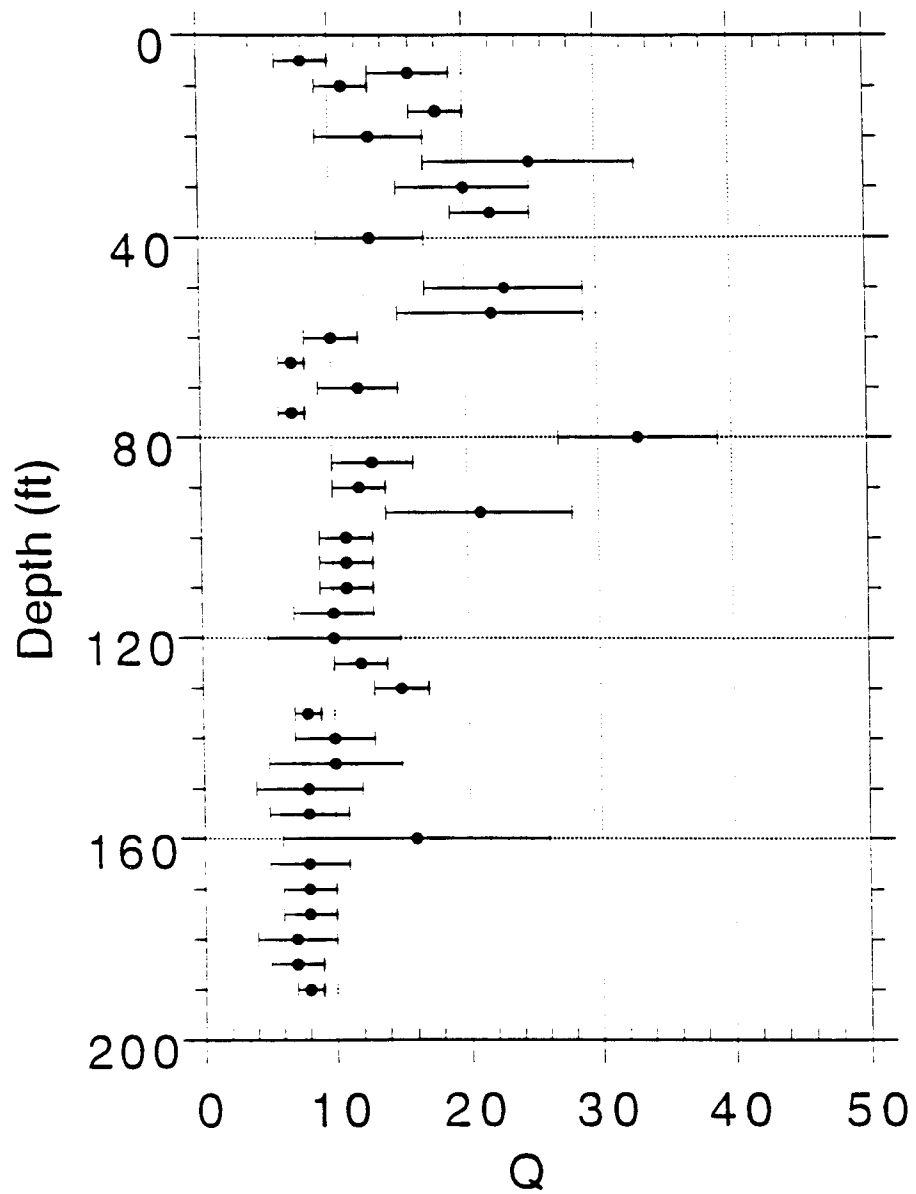
**Reverse Direction**

Depth (ft)	BH3-BH2 Qs + - error	BH2-BH1 Qs + - error
5	*11 2*	7 1
15	18 3	5 3
25	*13 2*	7 1
35	19 5	7 3
45	5 2	5 3
55	5 3	10 1
65	8 3	11 3
75	5 3	9 1
85	16 3	16 1
95	15 3	16 2
105	12 3	12 1
115	13 2	12 2
125	14 4	11 1
135	5 1	10 3
145	28 11	7 3
155	21 10	7 4
165	12 3	8 2
175	5 2	7 3
185	4 2	8 2
195	5 2	6 2

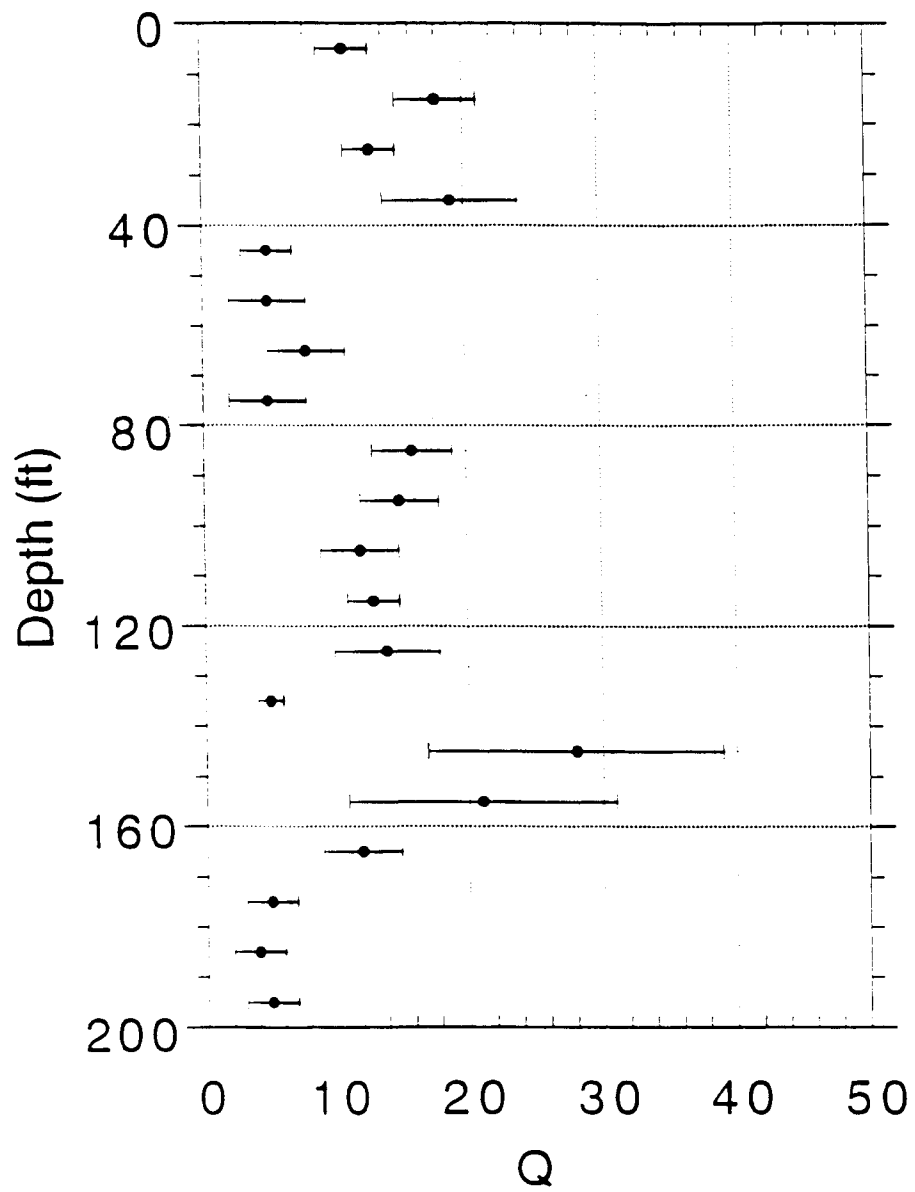
\*...\* estimated with  $1/\sqrt{r}$  spreading



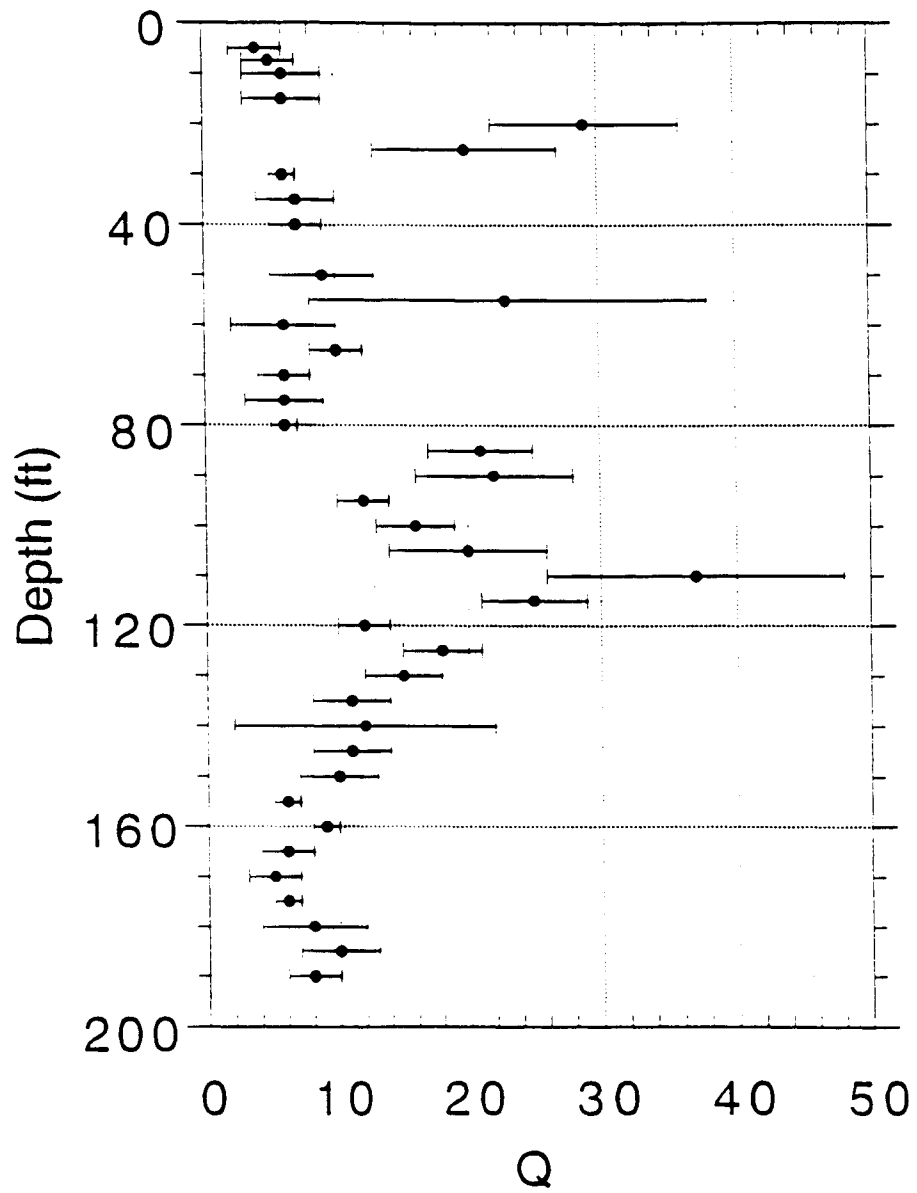
**Figure 8.A.3-11a**  
Measured shear (SV) Q values and estimated errors versus depth along Path BH2-BH1 at Gilroy 2.



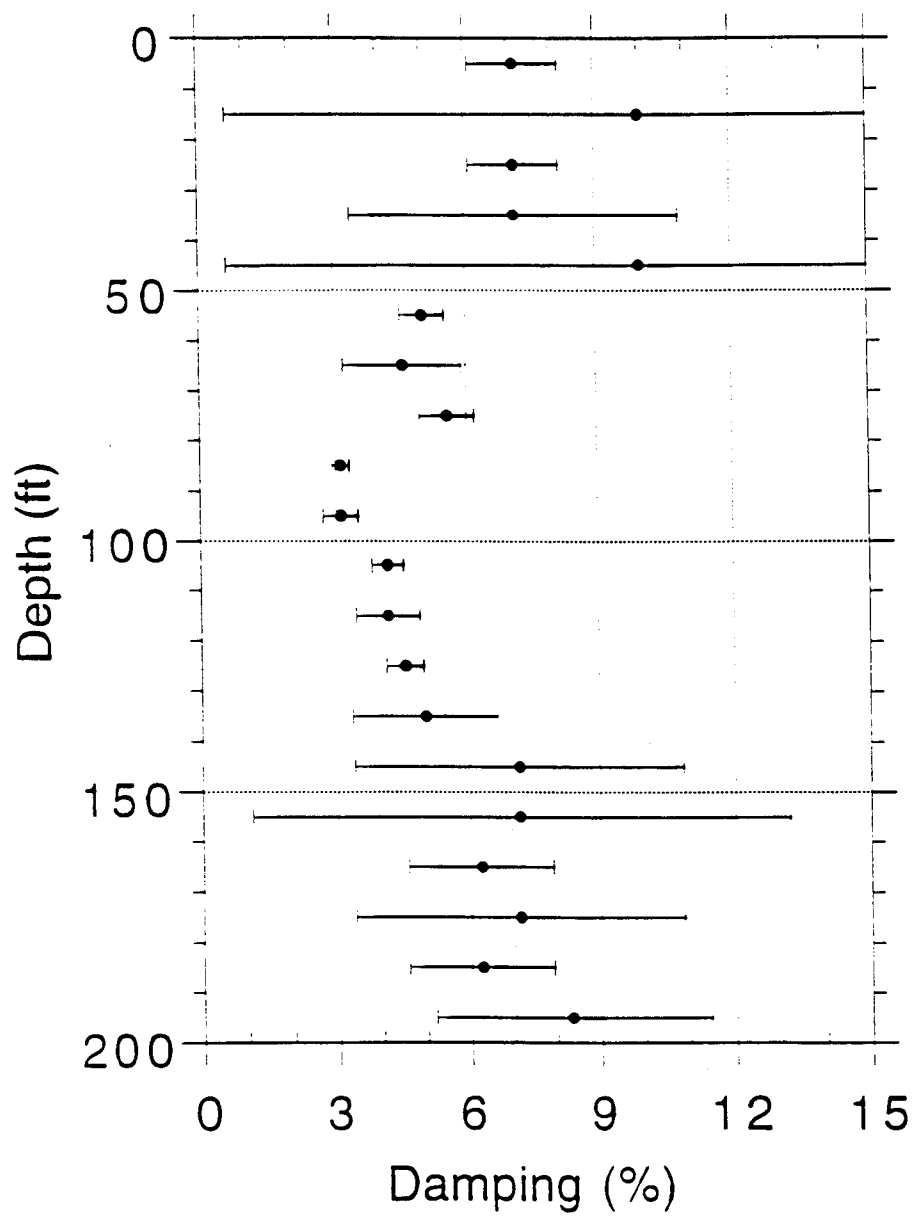
**Figure 8.A.3-11b**  
Measured shear (SV) Q values and estimated errors versus depth along Path BH2-BH3 at Gilroy 2.



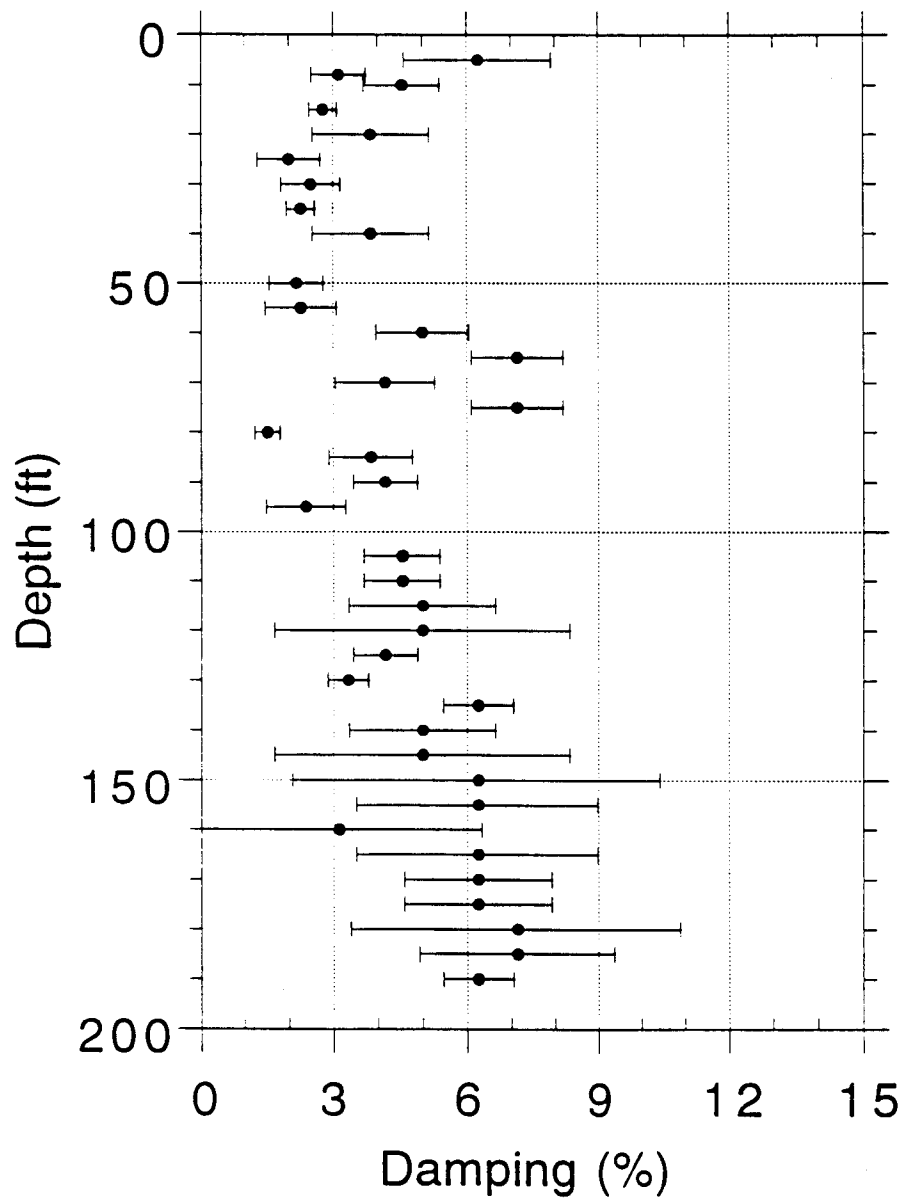
**Figure 8.A.3-11c**  
Measured shear (SV) Q values and estimated errors versus depth along Path BH3-BH2 at Gilroy 2.



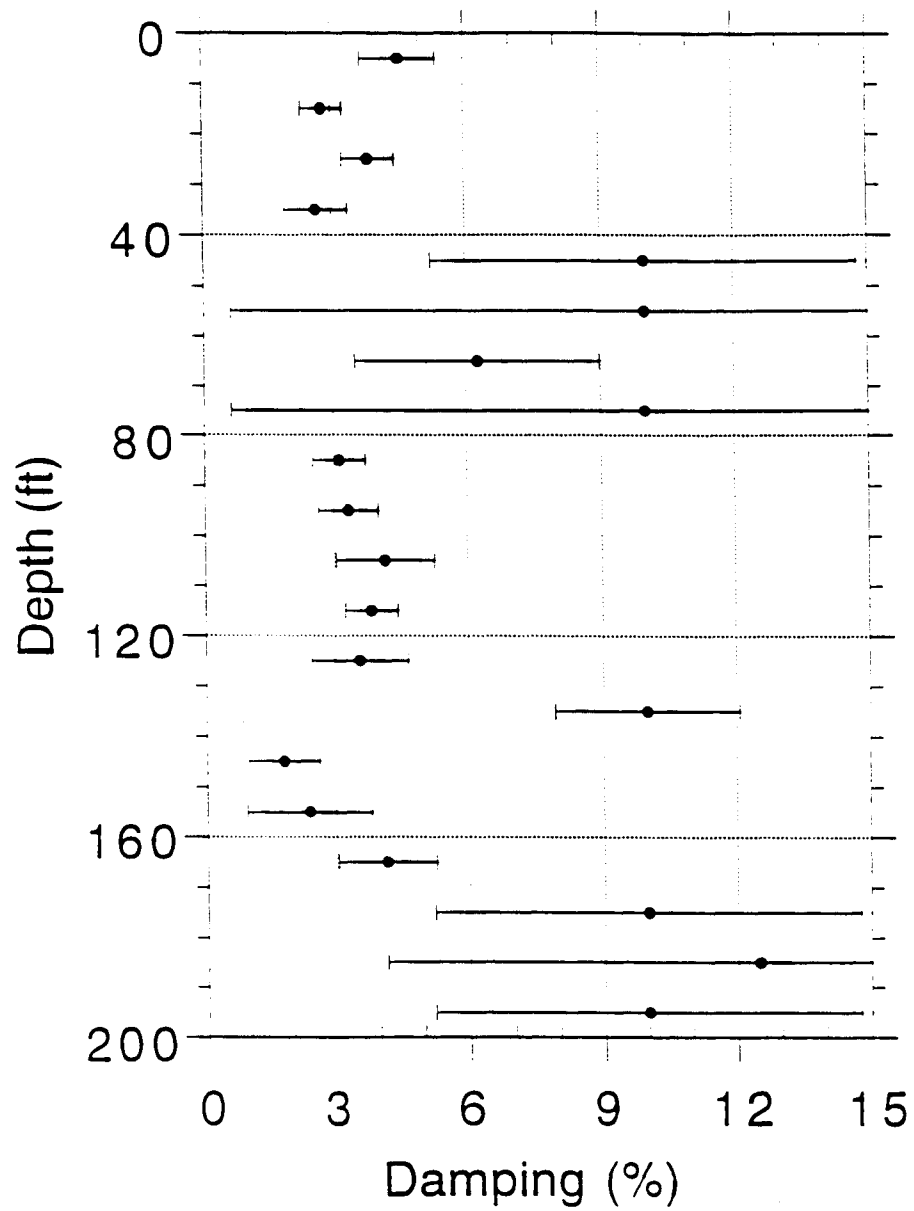
**Figure 8.A.3-11d**  
Measured shear (SV) Q values and estimated errors versus depth along Path BH3-BH4 at Gilroy 2.



**Figure 8.A.3-12a**  
Damping values (shear) and estimated errors versus depth along Path BH2-BH1 at Gilroy 2 .

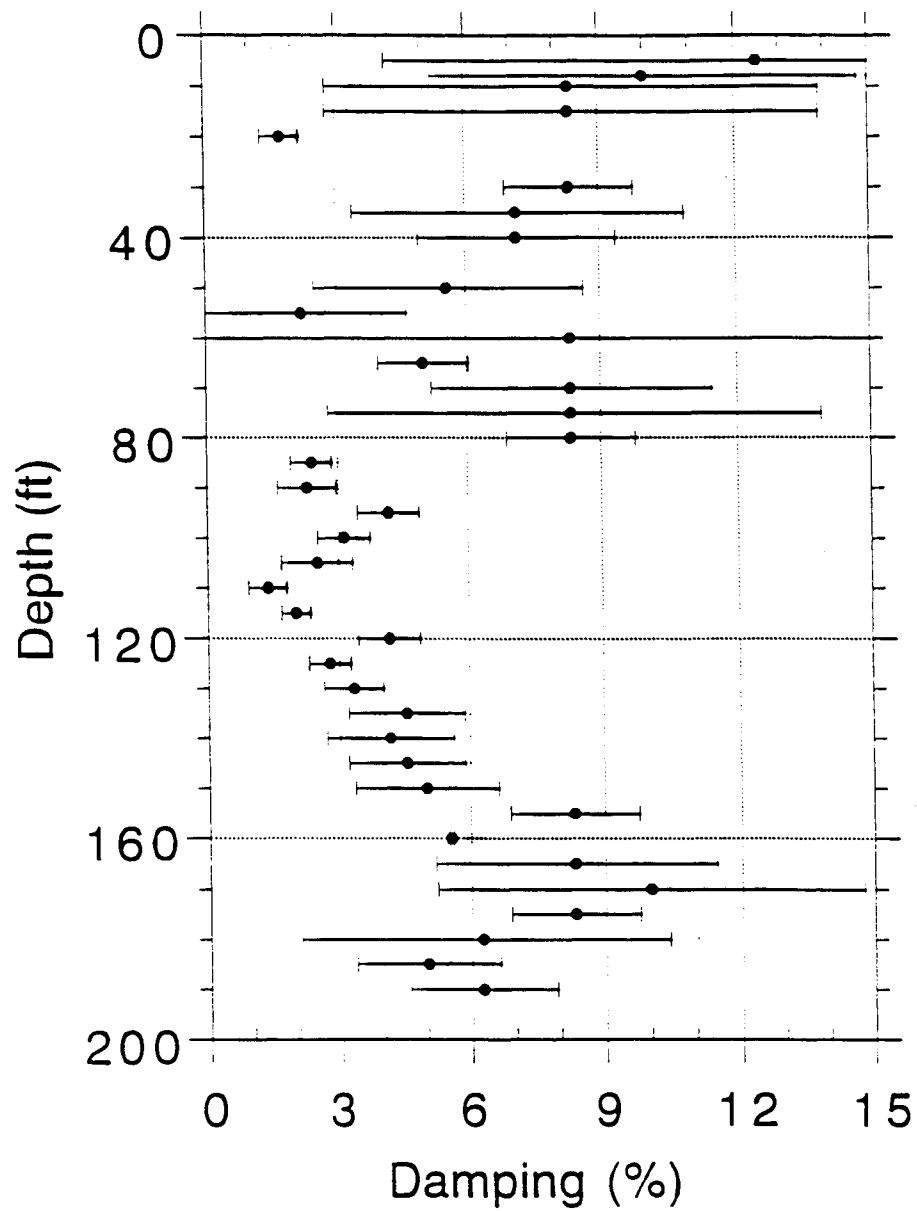


**Figure 8.A.3-12b**  
Damping values (shear) and estimated errors versus depth along Path BH2-BH3 at Gilroy 2.

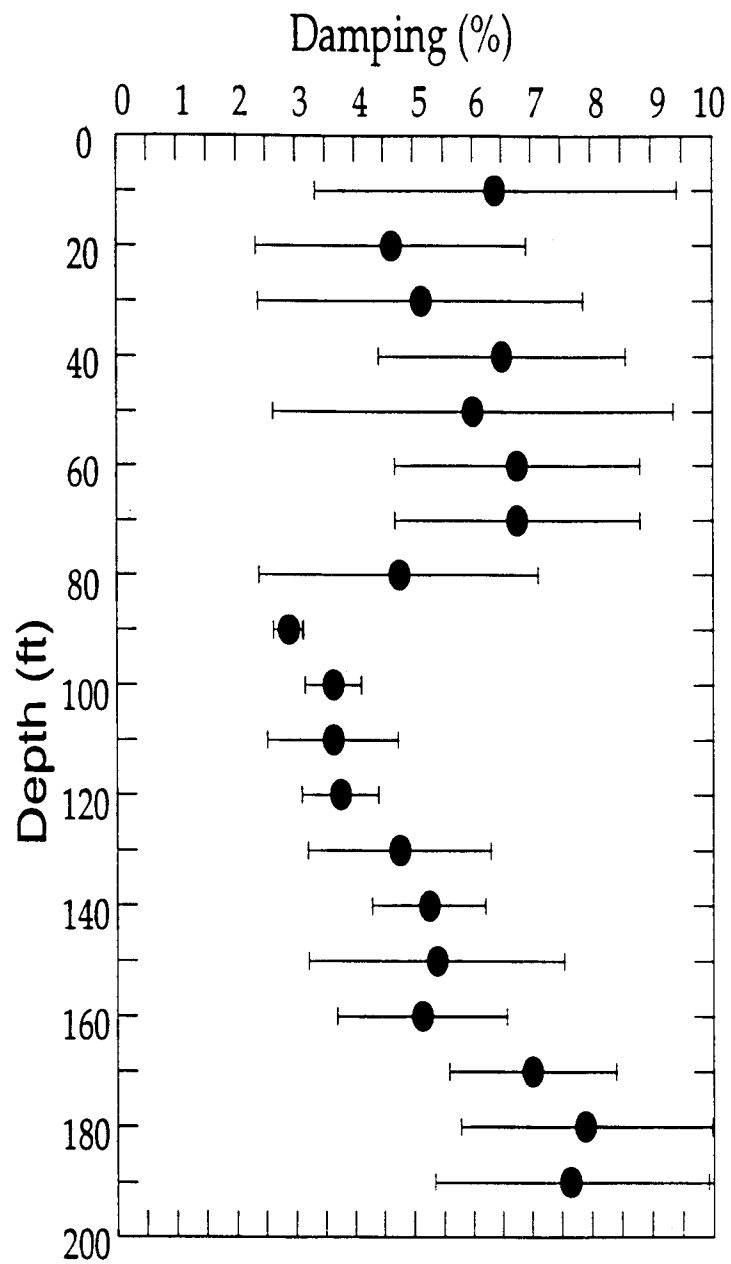


**Figure 8.A.3-12c**  
Damping values (shear) and estimated errors versus depth along Path BH3-BH2 at Gilroy 2.

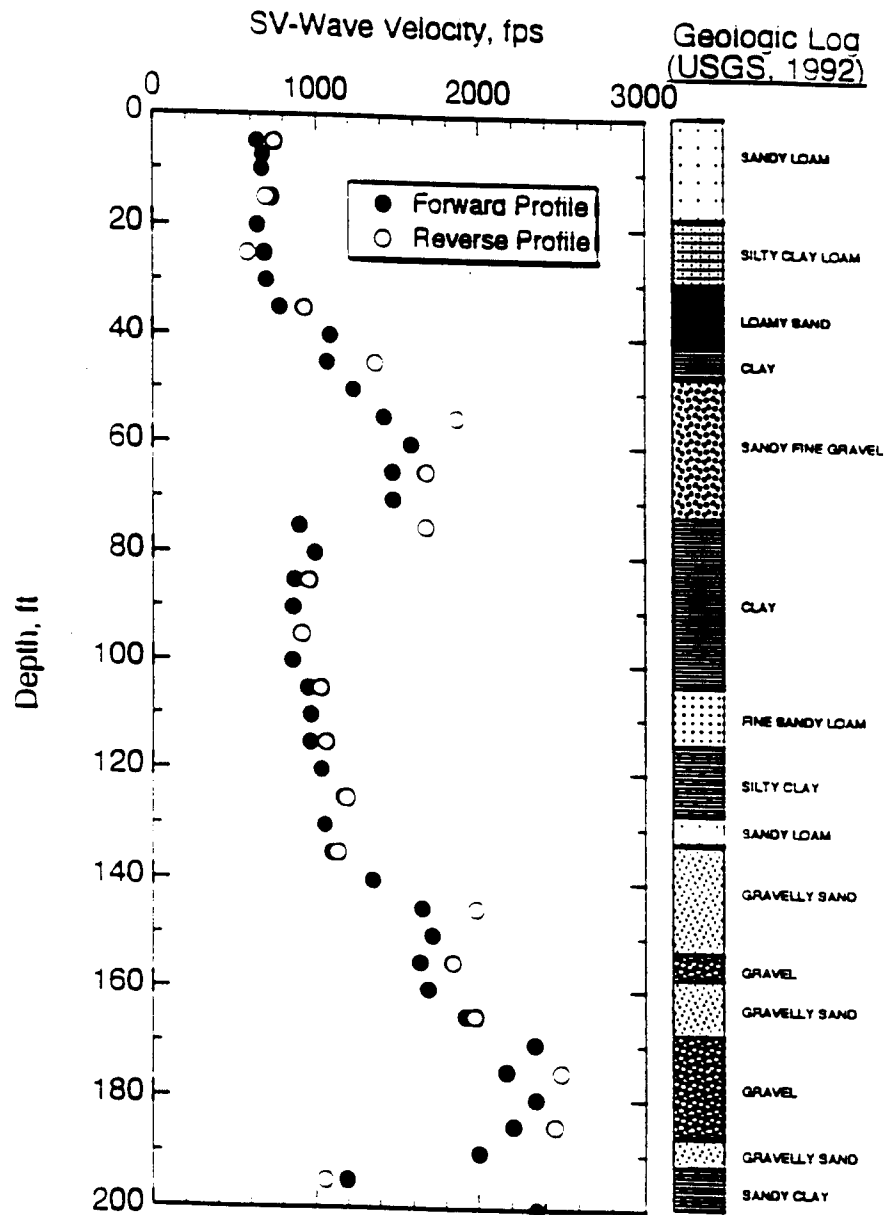




**Figure 8.A.3-12d**  
Damping values (shear) and estimated errors versus depth along Path BH3-BH4 at Gilroy 2.

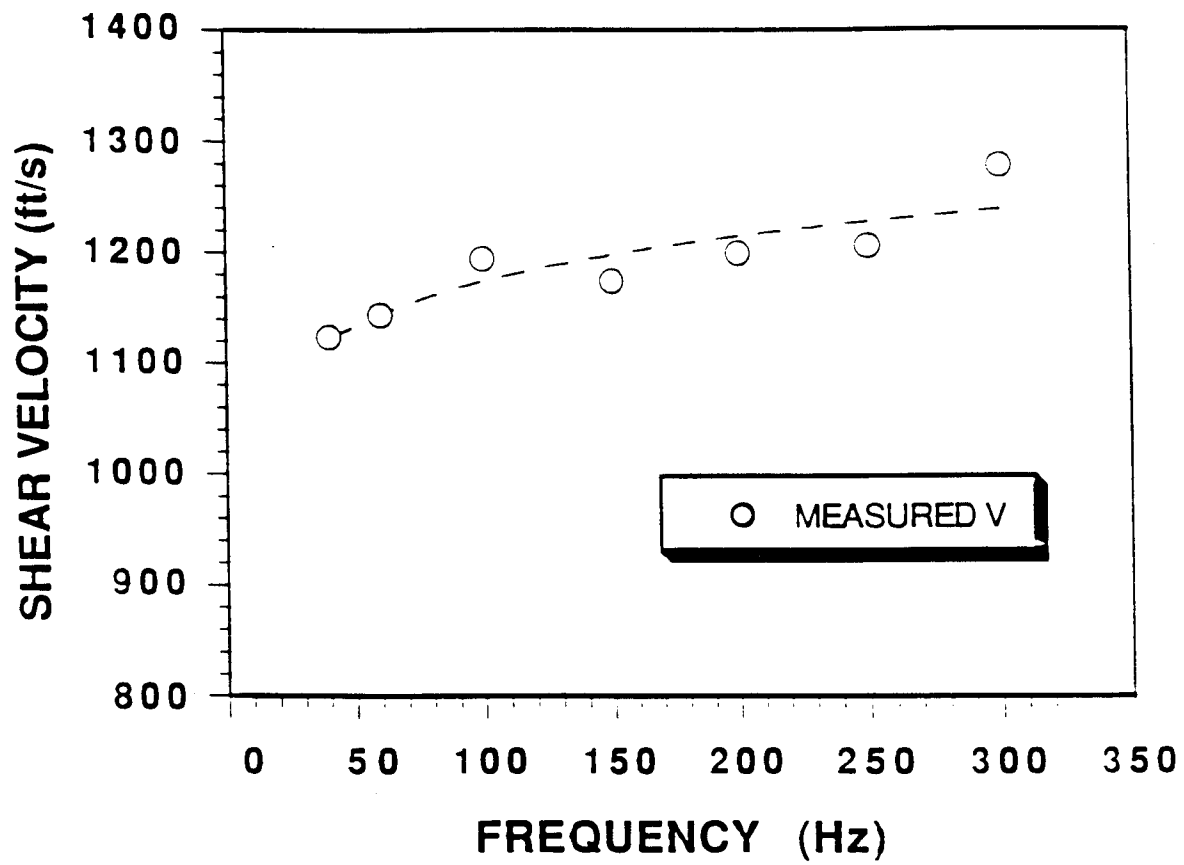


**Figure 8.A.3-13**  
Average shear damping versus depth based on all cross-hole data at Gilroy 2.

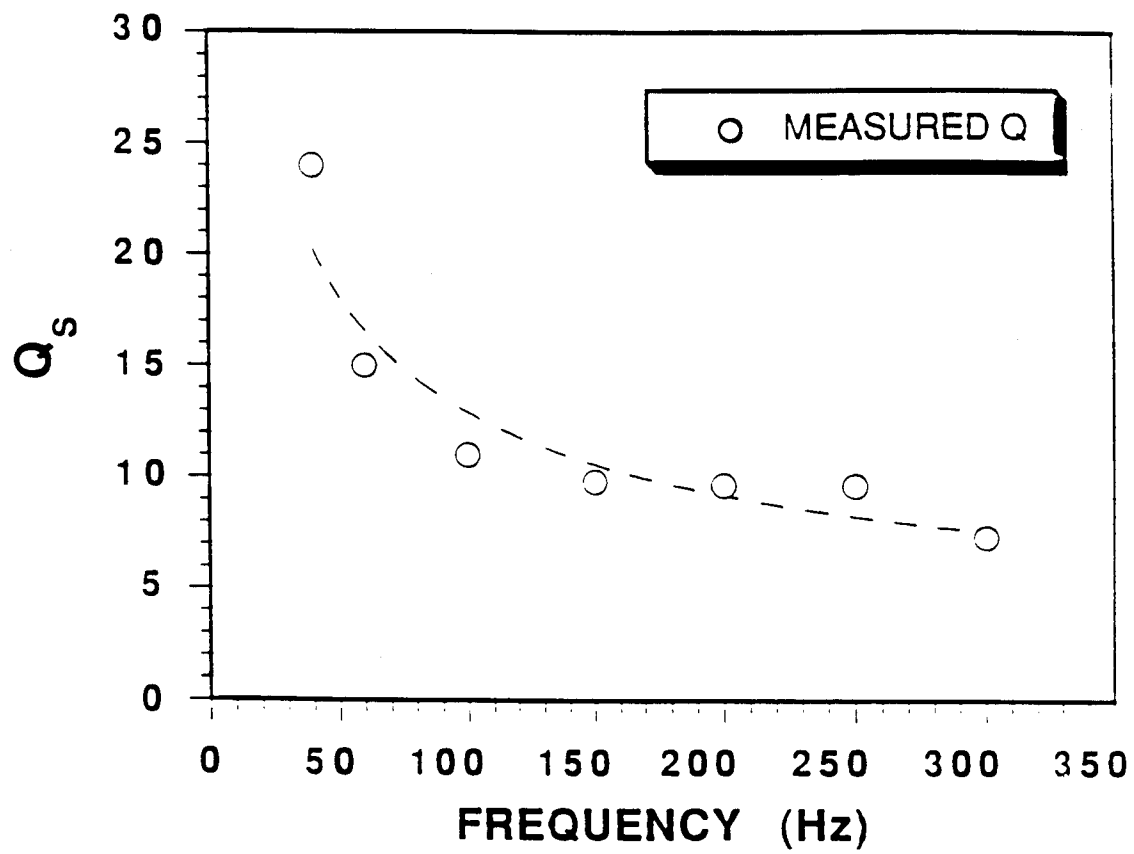


**Figure 8.A.3-14**

Shear wave (SV) velocities versus depth for forward and reverse directions along Path 1 at Gilroy 2 (after Fuhrimam and Stokoe, 1993).



**Figure 8.A.3-15**  
Shear wave velocity versus frequency for Gilroy 2 cross-hole data.



**Figure 8.A.3-16**  
Shear Q versus frequency for Gilroy 2 cross-hole data.

two different holes. The receiver near the source hole is clamped at 50 ft depth and the other moves from 50 to 100, 150, 200 and 300 ft depths. For each position of the second receiver, the seismograms at the two levels have been collected. For Treasure Island, both receivers are in the same hole. As in the Gilroy 2 site, the top receiver is fixed at 50 ft depth and the other receiver is placed at 55, 100, 200, and 280 ft depths. The seismograms observed at two depths from one source event are used to determine the attenuation between two depths. The theory of waveform inversion for determining the attenuation is given in Appendix 8.A.3.A. For VSP measurements, the layering could affect the actual attenuation measurements as discussed in Appendix 8.A.3.B. Considering these effects, we try to estimate true attenuation values for the Treasure Island and Gilroy 2 sites.

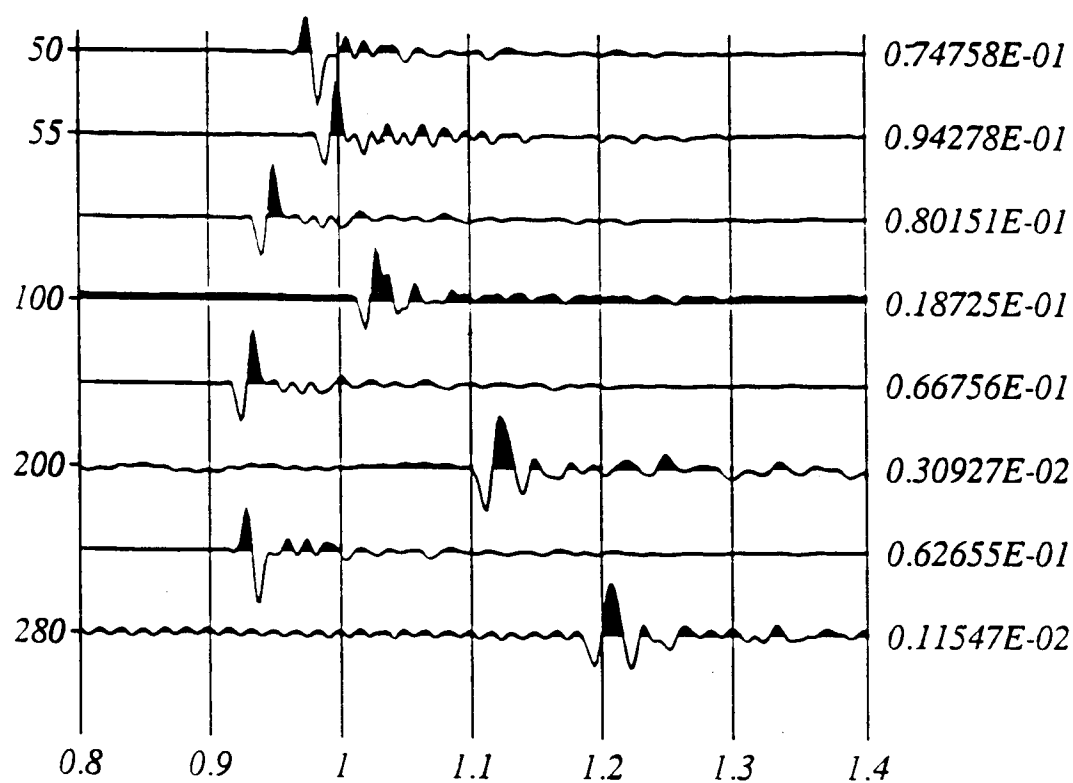
#### **8.A.3.3.3.1 Treasure Island VSP Data**

The unprocessed data observed at Treasure Island are shown in Figure 8.A.3-17. Each trace is self-normalized and the maximum amplitude is included with each seismogram. The data quality is poor and the analysis has been done for each pair of observations for a common source. From the velocity measurements (e.g., USGS, UT, Agbabian, Redpath), the structure between the two depths is complicated. The layering effect must be included for VSP attenuation measurements. The details of these analyses are given in Appendix 8.A.3.B. Figure 8.A.3-18 shows a typical procedure of our waveform inversion technique applied between 50 and 100 ft depth. The top box (out of four boxes) shows the raw data. The second box from the top represents the filtered data at a center frequency of 50 Hz. The third box from the top shows the migrated signal (dotted seismograms) observed at 50 ft to 100 ft depth with a phase velocity of 613 ft/sec. The bottom box shows the Q inversion results to match the observation at 100 ft depths. The summary of Q measurements is shown in Table 8.A.3-5. We determined three different Q values for different geometric spreadings. Most commonly, we used the spherical spreading effect as  $(1/r)$ , where  $r$  is the radial distance between the source and the receiver. Appendix 8.A.3.B shows that for a layer model the  $1/r$  spreading is no longer correct as a geometric correction of the propagation. This spreading correction depends on the layering and the velocity contrast of the layers. We calculated the spreading effects by producing complete wave synthesis using a known velocity structure of the medium. Theoretically (Appendix 8.A.3.B), we proved that the proper geometric correction is necessary to obtain correct attenuation between the two observations. The three attenuation values are shown for normal spherical spreading, including with reflection and without reflection (Table 8.A.3-5).

#### **8.A.3.3.3.2 Gilroy 2 VSP Data**

Figure 8.A.3-19 shows the unprocessed data observed at the Gilroy 2 site. The data are very poor due perhaps to bad clamping. The Q measurements are very difficult. We filtered two different centered frequencies (50 and 90 Hz). Figure 8.A.3-20 shows the typical procedure of the Q measurements between the 50 ft and 150 ft levels. The same procedure is used as in the Treasure Island case and it is also discussed in Appendix 8.A.3.B. In this case, we also correct for layering effect. A summary of these observations is given in Table 8.A.3-5. Question marks are shown in Table 8.A.3-5 for data where the matchings are not established properly. The damping measurements from the cross-hole Gilroy 2 data are summarized in Table 8.A.3-6 with a 10 ft interval. From these cross-hole damping data, we could transform the effective damping along the vertical direction, which is shown in Table 8.A.3-7. This table shows interval Q and damping, as well as the average vertical interval velocity at the Gilroy 2 site. The Q measurements from downhole observations and estimated Q values (averaged over depth) from cross-hole observations are summarized in Table 8.A.3-8 for the Gilroy 2 site. The observations are not consistent except for the measurement between 50–300 ft depth. The cross-hole observations of Q are lower than the VSP observations. No explanation of these observations could be made, because the Gilroy observations data quality is poor. The cross-hole measurements are more consistent because of the data quality and number of observations.

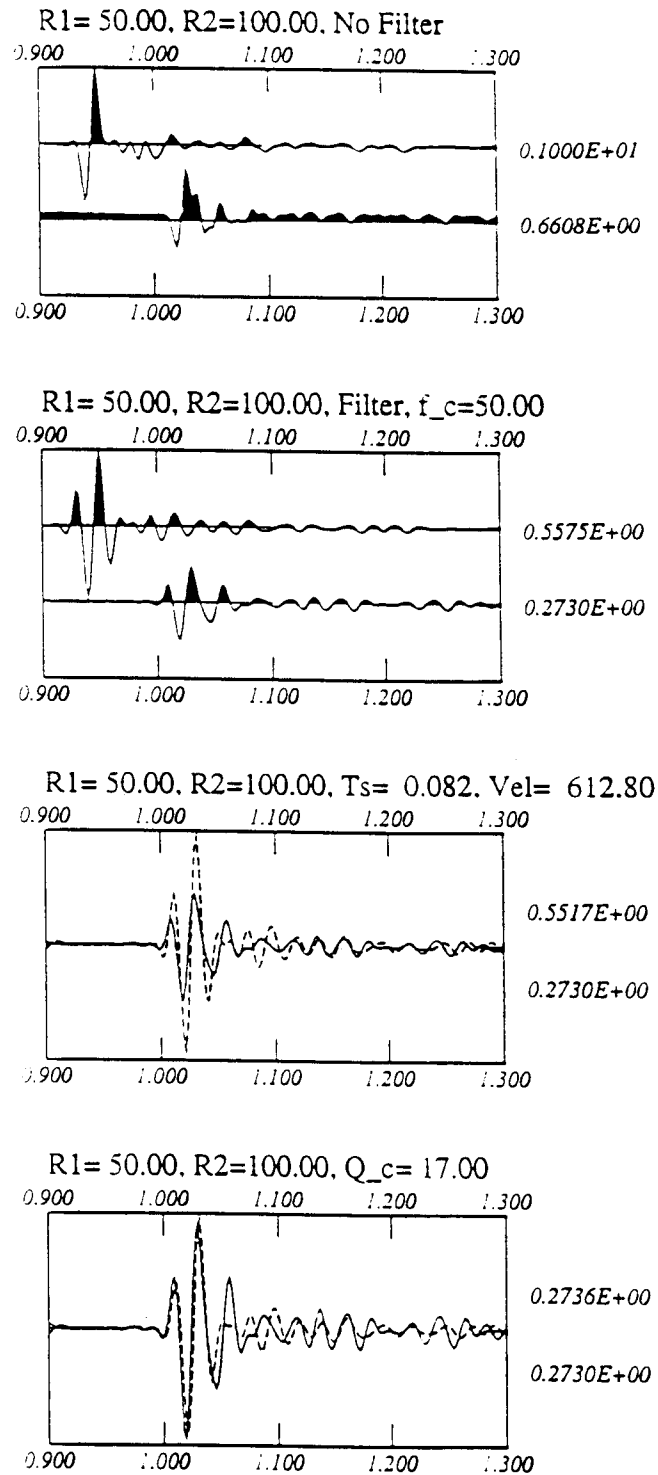
(feet)



*tisland*

**Figure 8.A.3-17**

Preprocessed VSP data waveforms versus depth at Treasure Island. The reference waveform at a fixed geophone at 50 ft depth is shown at the top, in each case.



**Figure 8.A.3-18**

Steps of waveform inversion for estimating Q and velocity for VSP data. The top box shows unfiltered waveforms at 50 and 100 ft depths with geometric correction ( $1/r^{1.5}$ ). The second box from the top shows the filtered signals. The third box shown the migration of the 50 ft waveform to 100 ft. The bottom box shows the match of waveforms after inversion for determining Q.

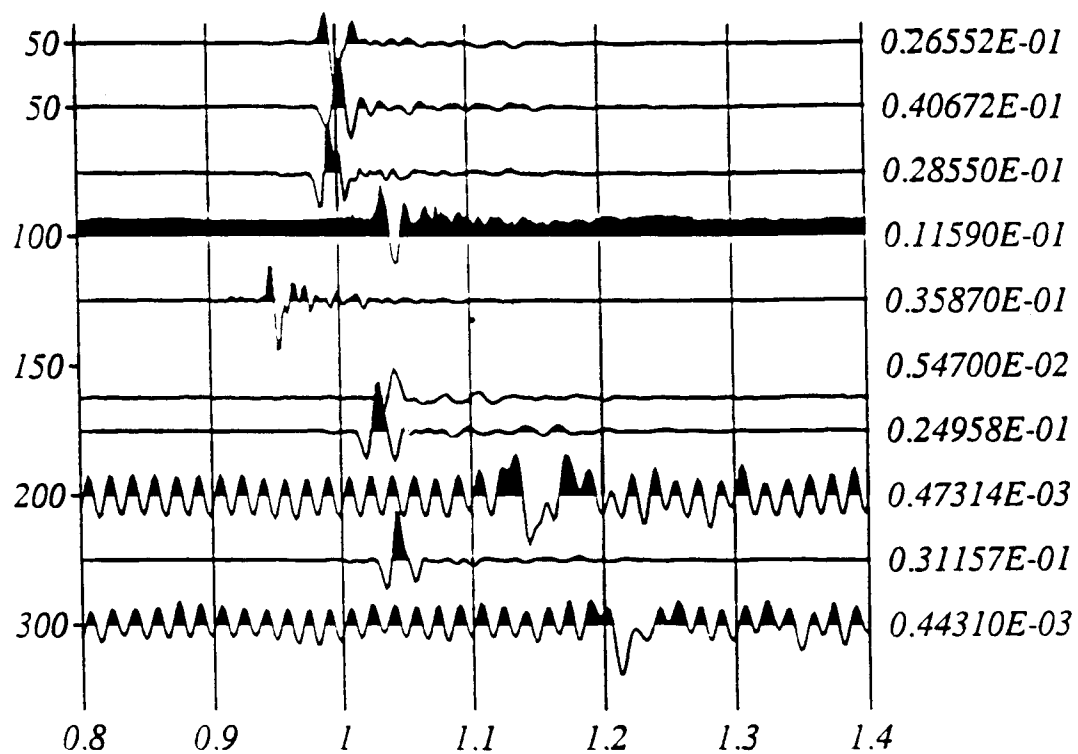


**Table 8.A.3-5**

Estimated Qs between different depth range from the Treasure Island and Gilroy 2 VSP data. The different geometric spreading corrections are applied. Gilroy data are very poor. Two different estimations for Gilroy 2 at different frequencies.

Depth Interval (ft)	Geometric Spreading Correction			Q	
	No reflection	Reflection	1/r	Including reflection	Intrinsic
<b>TREASURE ISLAND</b>					
50–100	1.15	1.80	11	14	24 (50 Hz)
50–150	1.33	1.70	15	17	35 (50 Hz)
50–280	1.35	1.75	15	18	35 (50 Hz)
<b>GILROY 2</b>					
50–100	1.40	1.28	40 ?	200 ?	120 (50Hz)
			20 ?	50 ?	35 (90Hz)
50–150	1.35	1.60	11	17	23 (50 Hz)
50–200	1.40	1.73	5 ?	6 ?	8 (50Hz)
			6 ?	8 ?	10 ?(90Hz)
50–300	1.46	1.70	8	12	16 (50 Hz)
			7 ?	12 ?	17 ?(90Hz)

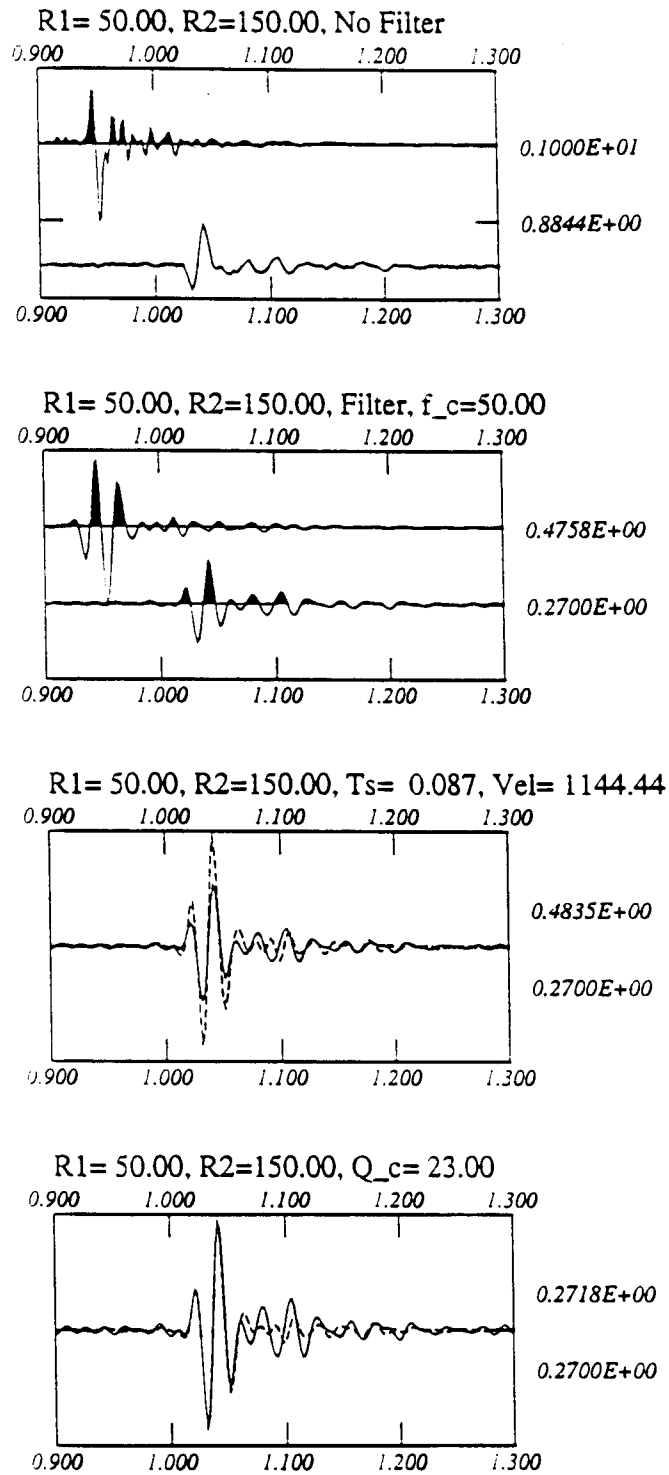
(feet)



*gilroy*

**Figure 8.A.3-19**

Gilroy 2 VSP data versus depths. The reference geophone waveforms are shown at the top in each case.



**Figure 8.A.3-20**

Steps of waveform inversion for estimating  $Q$  and velocity as described in Figure 8.A.3-18. The estimated  $Q = 23$  and  $V_s = 1144$  ft/s between 50 and 150 ft for geometric spreading correction of  $(1/r^{1.6})$ .

**Table 8.A.3-6**

Summary of damping values from different observations of cross-hole data at the Gilroy 2 site.

GILROY - 2 (Crosshole Data)					
Depth (ft)	DAMPING (%)				
	BH2-BH1	BH2-BH3	BH3-BH2	BH3-BH4	Average
10	9	4	3.5	9	6
20	8	4	3.5	3	5
30	7.5	2.5	3	2.5	5
40	9	4	6	7	6
50	7	2	10	5	6
60	5	5	9	8	7
70	5	5	7.5	8	7
80	3	3	5	8	5
90	3	3	3	2.5	3
100	3.5	4	4	3	4
110	4	4.5	4	2	4
120	4	4.5	3.5	3	4
130	4.5	4	7	3.5	5
140	6	5	6	4	5
150	7.5	6.5	2.5	5	6
160	7	5	3.5	5.5	5
170	6	6	7	9	7
180	6.5	7	11	7	8
190	6	7	11	6.5	8

**Table 8.A.3-7**

The computed vertical interval velocities, Qs values, and damping from cross-hole data at the Gilroy 2 site.

**GILROY - 2**  
Average over all crosshole observations

Depth Interval (ft)	Vertical Average Velocity (ft/sec)	Vertical Q   	Damping (%)
10 - 10	680	8	6
10 - 20	680	10	5
10 - 30	710	10	5
10 - 40	782	10	5
10 - 50	860	10	5
10 - 60	940	10	5
10 - 70	1004	9	5
10 - 80	1025	9	5
10 - 90	1020	10	5
10 - 100	1018	10	5
10 - 110	1024	10	5
10 - 120	1034	11	5
10 - 130	1048	11	5
10 - 140	1079	11	5
10 - 150	1113	11	5
10 - 160	1146	11	5
10 - 170	1184	10	5
10 - 180	1222	10	5
10 - 190	1253	10	5

**Table 8.A.3-8**

Comparison of cross-hole and VSP Q data from Tables 8.A.3-5 and 8.A.3-7

**GILROY - 2**  
(VSP and crosshole data )

Depth Interval (ft)	VSP	Crosshole (average over depth)
	Q	Q
50 - 100	35 (?)	10
50 - 150	23	11
50 - 200	8	10
50 - 300	16	

## 4—CONCLUSIONS

In-situ damping profiles for shear waves are obtained from cross-hole data at the Treasure Island and Gilroy 2 sites using a waveform inversion method. The limited amount of VSP data at the same sites are also analyzed at Treasure Island. Damping varies between about 2 and 4 percent in the depth range of 5 to 100 feet. Damping is correlated with shear velocity, high damping being associated with high velocity sand sections. At the Gilroy 2 site, damping ranges between about 2 and 7 percent. As in the Treasure Island case, the high damping is associated with high velocity sands and gravels.

The effects of layering on damping measurements are investigated using synthetic seismograms. The geometric spreading factor, normally assumed to be  $1/r$ , depends on velocity structure. In addition, wave reflection and scattering due to impedance contrasts affect damping measurements. When these are properly measured, in-situ damping can be determined accurately using cross-hole and/or VSP data.

## REFERENCES

- Aki, K., and P. G. Richards, 1980, *Quantitative Seismology: Theory and Methods*, W. H. Freeman and Co.
- Anderson, J. G. and S. E. Hough, 1984, A model for the shape of the Fourier amplitude spectrum at high frequencies, *Bull. Seism. Soc. Am.*, 74, 1969–1994.
- Balch, A. and M. Lee (eds.), 1984, *Vertical Seismic Profiling*, IHRDC, Boston, MA.
- Biot, M. A., 1956a, Theory of propagation of elastic waves in a fluid saturated solid, I. Low frequency, *J. Acous. Soc. Am.*, 28, 168–178.
- Biot, M. A., 1956b, Theory of propagation of elastic waves in a fluid saturated solid, I. High frequency, *J. Acous. Soc. Am.*, 28, 179–91.
- Cheng, C. H. and M. N. Toksöz, 1981, Elastic wave propagation in a fluid-filled borehole and synthetic acoustic logs, *Geophysics*, 46, 1042–1053.
- Dainty, A.M., R. M. Duckworth, and A. Tie, 1987, Attenuation and backscattering from local coda, *Bull. Seism. Soc. Am.*, 77, 1728–1747.
- Frankel, A. and R. Clayton, 1986, Finite difference simulations of seismic scattering: Implications for the propagation of short-period seismic waves in the crust and models of crustal heterogeneity, *J. Geophys. Res.*, 91, 6465–6489.
- Frankel, A., A. McGarr, J. Bucknell, J. Mori, L. Seeka, and E. Cranswide, 1990, Attenuation of high frequency shear waves in the crust: Measurements from New York, South Africa and southern California, *J. Geophys. Res.*, 95, 17441–17457.
- Fuhrimam, M. D. and K. D. Stokoe, 1993, Crosshole seismic tests at the Gilroy 2 and Treasure Island sites affected by the 1989 Loma Prieta earthquake, Geotech. Eng. Rept. GR93-1, Geotech. Eng. Center, Civil Eng. Dept., The Univ. of Texas at Austin, for Elec. Power Res. Inst., 259 pp.
- Futterman, W. I., 1962, Dispersive body waves, *J. Geophys. Res.*, 67, 5279–5291.
- Gibbs, J. F., T. E. Fumal, D. M. Boore, and W. B. Joyner, 1992, Seismic velocities and geologic logs from borehole measurements at seven strong-motion stations that recorded the Loma Prieta earthquake, *USGS Open File Report*, 92–287.
- Hardage, R., 1983, *Vertical Seismic Profiling: Principles*, Geophysical Press, London.
- Heelan, P., 1953, Radiation from a cylindrical source of finite length, *Geophysics*, 18, 685–696.
- Johnston, D. H. and M. N. Toksöz, 1980, Ultrasonic P and S wave attenuation in dry and saturated rocks under pressure, *J. Geophys. Res.*, 95, 925–936.
- Johnston, D. H., M. N. Toksöz, and A. Timur, 1979, Attenuation of seismic waves in dry and saturated rocks, II. Mechanisms, *Geophysics*, 44, 691–711.
- Kudo, K. and E. Shima, 1970, Attenuation of shear waves in soil, *Bull. Earthquake Res. Inst.*, 48, 145–158.
- Mavko, G. M. and A. Nur, 1979, Wave attenuation in partially saturated rocks, *Geophysics*, 44, 161–178.
- McDonal, F. J., F. A. Angona, R. L. Mills, R. L. Sengbush, R. G. Van Nostrand, and J. E. White, 1958, Attenuation of shear and compressional waves in Pierre shale, *Geophysics*, 23, 421–439.
- Meredith, J. A., 1990, Numerical and analytical modeling of downhole seismic source: The near and far field, Ph.D. thesis, Massachusetts Institute of Technology, Cambridge, MA.
- O'Connell, R. J. and B. Budiansky, 1977, Viscoelastic properties of fluid-saturated cracked solids, *J. Geophys. Res.*, 82, 5719–5737.
- Paillet, F. L., C. H. Cheng, and X. M. Tang, 1989, Theoretical models relating acoustic tube-wave attenuation to fracture permeability—Reconciling model results with field data, in *Full Waveform Acoustic Logging Consortium Annual Report*, Earth Resources Laboratory, Massachusetts Institute of Technology, 189–212.



- Pride, S. R. and F. D. Morgan, 1991, Electrokinetic dissipation induced by seismic waves, *Geophysics*, 56, 914–925.
- Pujol, J. and S. Smithson, 1991, Seismic wave attenuation from VSP experiments, *Geophysics*, 56, 1441–1455.
- Saito, H., 1991, Anisotropic travelttime tomography at the Buckhorn Facility in Illinois, in *Proc. Soc. Expl. Geophys., 1991 Meeting*, 123–126, SEG, Tulsa, OK, 1991, Expanded abstracts.
- Spencer, J. W., 1981, Stress relaxation at low frequencies in fluid saturated rocks: attenuation and modulus dispersion, *J. Geophys. Res.*, 86, 1803–1812.
- Stewart, R. R., M. N. Toksöz, and A. Timur, 1983, Strain dependent attenuation: observations and a proposed mechanism, *J. Geophys. Res.*, 88, 546–554.
- Tang, X. M., 1992, A waveform inversion technique for measuring elastic wave attenuation in cylindrical bar, *Geophysics*, 57, 854–859.
- Tang, X. M., M. N. Toksöz, P. Tarif, and R. H. Wilkens, 1988, A method of measuring acoustic wave attenuation in the laboratory, *J. Acous. Soc. Am.*, 83, 453–462.
- Tittmann, B. R., 1980, Internal friction measurements and their implication in seismic Q structure models of the crust, *The Earth's Crust*, AGU Monograph 20, 197–213.
- Toksöz, M. N. and D. H. Johnston (eds.), 1981, *Seismic Wave Attenuation*, Society of Exploration Geophysicists, 459 pp.
- Toksöz, M. N. and R. R. Stewart (eds.), 1984, *Vertical Seismic Profiling: Advanced Concepts*, vol. 14B, Handbook of geophysical Exploration, K. Helbig and S. Treitel (eds.), Geophysical Press, London, 419 pp.
- Toksöz, M. N., C. H. Cheng, and R. D. Cicerone, 1992, Fracture detection and characterization from hydrophone VSP data, in: Evans, B. (ed.), *Fault Mechanics and Transport Properties of Rock*, Academic Press, in press.
- Toksöz, M. N., D. H. Johnston, and A. Timur, 1979, Attenuation of seismic waves in dry and saturated rocks, I. Laboratory measurements, *Geophysics*, 44, 681–190.
- Toksöz, M. N., B. Mandal, and A. Dainty, 1990, Frequency-dependent attenuation in the crust, *Geophys. Res. Lett.*, 17, 973–976.
- Tullos, F. N. and A. C. Reid, 1969, Seismic attenuation of Gulf coast sediments, *Geophysics*, 34, 516–528.
- Walsh, J., 1966, Seismic wave attenuation in rock due to friction, *J. Geophys. Res.*, 71, 2591–2599.
- White, R. E., 1992, The accuracy of estimating Q from seismic data, *Geophysics*, 57, 1508–1511.
- Winkler, K. and A. Nur, 1979, Pore fluids and seismic attenuation in rocks, *Geophys. Res. Lett.*, 6, 1–4.
- Wu, R-S. and K. Aki (eds.), 1988, *Scattering and Attenuation of Seismic Waves*, Part I, Birkhauser Verlag, Boston/Basel.
- Wu, R-S. and K. Aki (eds.), 1989, *Scattering and Attenuation of Seismic Waves*, Part II, Birkhauser Verlag, Boston/Basel.
- Wu, R-S. and K. Aki (eds.), 1990, *Scattering and Attenuation of Seismic Waves*, Part III, Birkhauser Verlag, Boston/Basel.

## APPENDIX 8.A.3.A

### ESTIMATING ATTENUATION THROUGH WAVEFORM INVERSION

Seismic wave attenuation is an inherent property of material. In general, we introduce the attenuation mathematically by making the wavenumber of complex

$$\exp [i(kr - \omega t)] \rightarrow \exp [i(k_r - \omega t)] \quad (\text{A-1})$$

where

$$k_e \rightarrow k \left( 1 + \frac{i}{2Q} \right). \quad (\text{A-2})$$

Q is the quality factor of the medium. The attenuation is independent, and the wave dispersion is negligible.

The waveform inversion techniques for Q estimation involve comparing the waveforms observed at two different distances with a common path of propagation. In the frequency domain, the two observations are related by

$$\tilde{A}(\omega, r_2) = \tilde{A}(\omega, r_1) \exp [ik(1 + i/2Q)(r_2 - r_1)] \quad (\text{A-3})$$

and (in the time domain) by

$$A(t, r_2) = A(t, r_1) * D(t) * C(t) \quad (\text{A-4})$$

where

$$D(t) = F^{-1} \{ \exp [ik(r_2 - r_1)] \}$$

and

$$C(t) = F^{-1} \{ \exp [-k(r_2 - r_1) / 2Q] \}$$

are designated as the dispersion operator and attenuation operator, respectively. The symbol \* denotes convolution, and

$$F^{-1} \{ \dots \}$$

is the inverse Fourier transform operator. From equations (A-3) and (A-4), it is obvious that the difference between the waves,  $A(t, r_2)$  and  $A(t, r_1)$ , is due to two effects. The first is the waveform distribution due to the velocity dispersion,  $[D(t)]$ , along the  $r_2 - r_1$  section of the propagation path. The second is the amplitude decay due to intrinsic attenuation,  $[C(t)]$ . The first effect can be corrected using the cross-correlation method or the phase minimization method. The second effect is used to estimate Q of the propagation path between  $r_2 - r_1$ .

The waveform inversion procedure consists of two major steps. In the first, the measured waveform,  $A(t, r_2)$ , is theoretically propagated to distance,  $r_2$ , with no attenuation. Mathematically, this operation is expressed as

$$\hat{A}(t, r_2) = A(t, r_1) * D(t). \quad (\text{A-5})$$

If the velocity between the two distances is exact,  $\hat{A}(t, r_2)$ , will be aligned in phase with the measured waveform,  $A(t, r_2)$  (neglecting the dispersion due to attenuation). In practice, we perform this alignment (measuring the time-shift) by cross-correlation or by phase minimization.

In this procedure, we also estimate the velocity between  $r_2$  and  $r_1$ . This step may be called the dispersion correction. The second step is the inversion for  $Q$  by minimizing the difference between

$$\hat{A}(t, r_2) \text{ and } A(t, r_2).$$

To do so, we define the following misfit function

$$\begin{aligned} E(Q) &= \int_{T_0}^{T_0+\Delta T} [A(t, r_2) - \hat{A}(t, r_2) * C(t)]^2 dt \\ &= \int_{T_0}^{T_0+\Delta T} \left[ A(t, r_2) - F^{-1} \left\{ \bar{A}(\omega, r_2) \exp\left(\frac{-k(r_2 - r_1)}{2Q}\right) \right\} \right]^2 dt \end{aligned} \quad (A-6)$$

where  $T_0$  is the beginning time of  $A(t, r_2)$  and  $\Delta T$  is the duration of the time section in which

$$\hat{A}(t, r_2) \text{ and } A(t, r_2)$$

are matched. For a noise free signal,  $\Delta T$  can include any number of waveform cycles without altering the value of  $Q$ . In practice,  $\Delta T$  is equal to one or two cycles of the major phase of interest. The minimization of  $E(Q)$  is performed using the nonlinear least-squares procedure. At first, we assign an initial estimate of  $Q$ . Then we multiply the spectrum,

$$\bar{A}(\omega, r_2), \text{ with } \exp\left[-k \frac{r_2 - r_1}{2Q}\right]$$

and transform this product back to the time domain. This operation modifies mainly the amplitude of

$$\hat{A}(t, r_2)$$

without altering its phase. If the corrected  $Q$  waveform does not match  $A(t, r_2)$ , then  $Q$  is adjusted according to the method of nonlinear least-squares minimization (Moré, 1978) and the procedure is repeated. The iterations are continued until the misfit,  $E(Q)$ , reaches a minimum. The value of  $Q$  at this point is taken as the best estimation quality factor between the distances  $r_1$  and  $r_2$ .

To demonstrate this procedure, we first use synthetic examples. The waveforms are generated at four different depths (50, 100, 150, 200 ft) from a zero-offset transverse shear source in a medium with constant shear wave velocity of  $V_s = 480$  ft/sec. A  $Q_s = 40$  is used in the calculation of the synthetic seismograms. Figure 8.A.3.A-1 shows the synthetic waveforms at the four depths. The waveforms at 50 and 100 ft in Figure 8.A.3.A-2a indicate where we are going to estimate  $Q$ . The upper waveform is at a depth of 50 ft, and the lower is at 100 ft. In Figure 8.A.3.A-2b the waveform at 50 ft is propagated to 100 ft (dashed waveform) without the attenuation (i.e.,  $Q = \infty$ ). We use the cross-correlation method to calculate the time shift between the waveforms at 40 and 100 ft. The estimated velocity between 50 and 100 ft is 481.13 ft/sec. Figure 8.A.3.A-2b also shows that, after the propagation, the waveform,

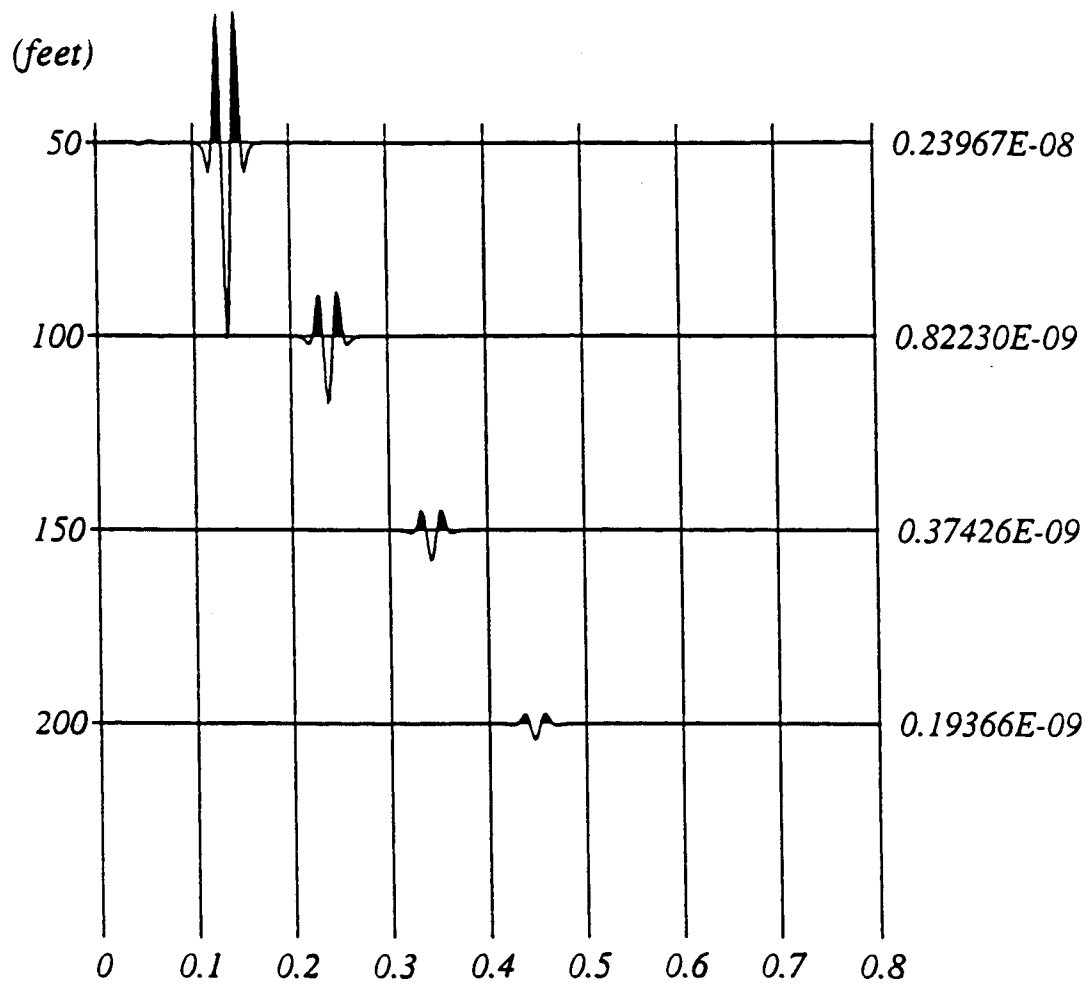
$$\hat{A}(t, r_2),$$

is aligned in phase with  $A(t, r_2)$ . However, the amplitudes of the two waveforms do not match because the attenuation effect is not included in the propagation. The next step is to minimize the amplitude difference between the two waveforms by using the inversion technique. After the inversion, the two waveforms coincide, as shown in Figure 8.A.3.A.1-2c. The  $Q$  value obtained from the inversion is 40, which is the same one used in the theoretical computation. In Figure 8.A.3.A.1-3, we demonstrate the same effect for the observation between 50 ft and 200 ft. In the case of synthetic data, the inverted  $Q$  is not sensitive to the time window used in the inversion because the waveforms do not contain errors or effects from extra arrivals, such as reflections.

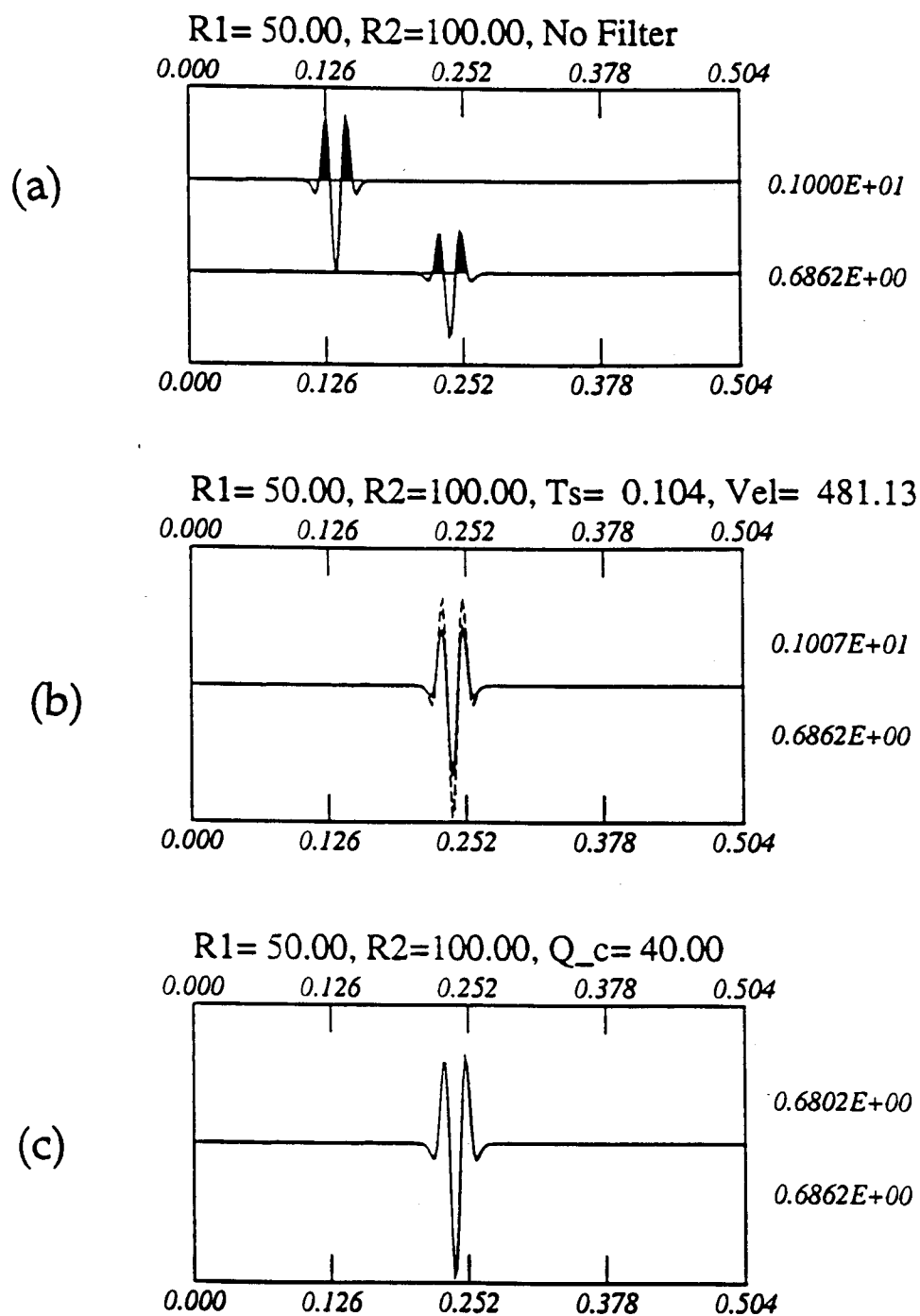
The procedure of matching the first part of  $\hat{A}(t, r_2)$  and  $A(t, r_2)$  using the inversion technique has two major advantages. The first is that only the first few cycles of the waveforms are needed for the  $Q$  estimation. This separates the effect of the intrinsic attenuation from the one due to later arrivals (i.e., multiple reflections). The second advantage is that the solution to the inversion problem is unique because only one parameter  $Q$  is estimated.

## Reference

Moré, J. J., 1978, The Levenberg-Marguard algorithm: Implementation and theory, in *Lecture Notes in Mathematics*, 53, G. A. Watson (ed.), 105–116.

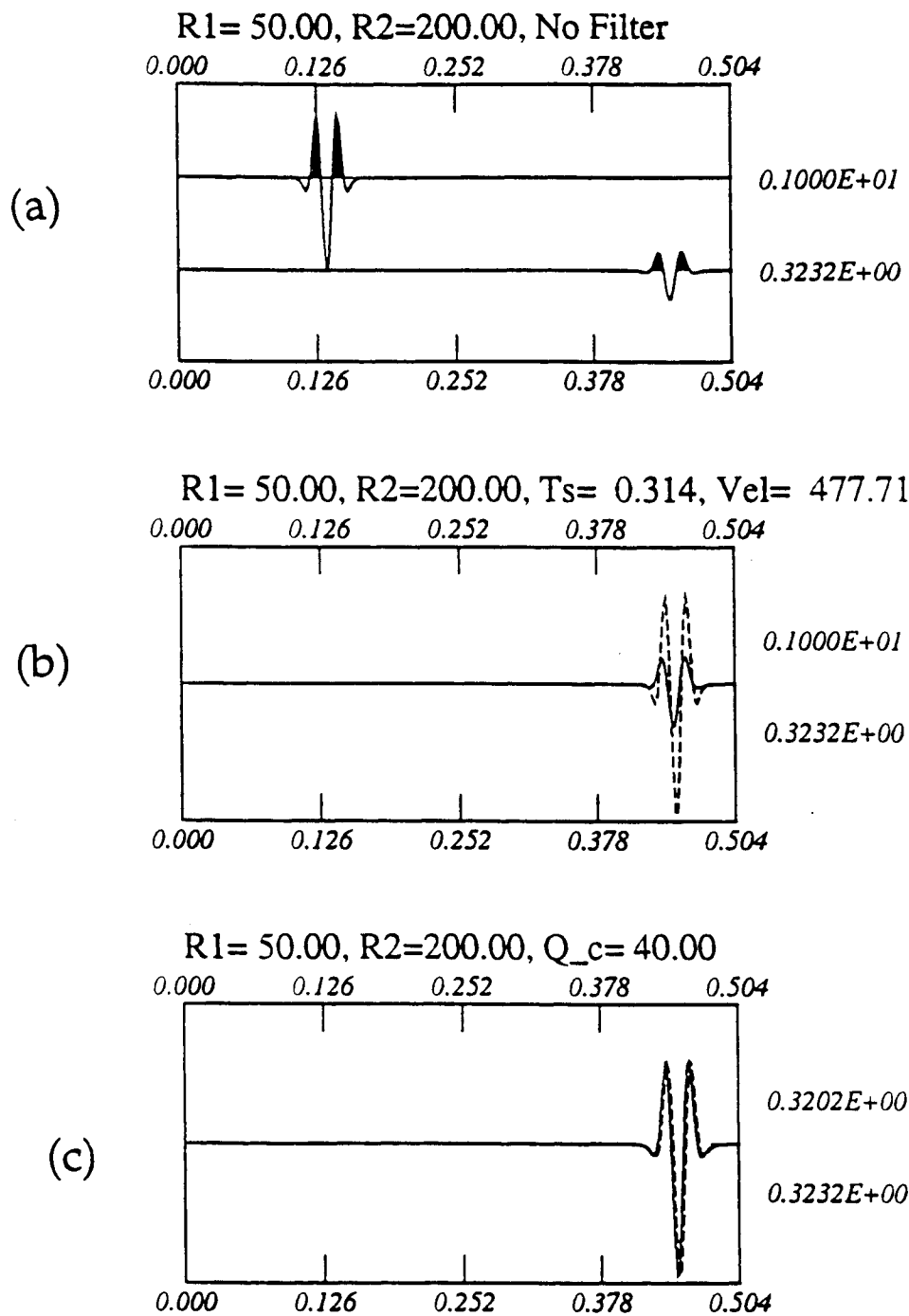


**Figure 8.A.3.A-1**  
Zero offset VSP synthetic seismograms for different depths.



**Figure 8.A.3.A-2**

Waveform inversion procedure: (a) Synthetic observation at 50 (top) and 100 (bottom) ft depth. (b) Results of dispersion correction: The waveforms are aligned in phase; the amplitude difference is due to attenuation and is to be minimized to find  $Q$ . (c) After inversion, the two waveforms are matched. The  $Q$  required for the match gives the estimated attenuation.



**Figure 8.A.3.A-3**

Same as shown in Figure 8.A.3.A-2 for depths between 50 and 200 feet.

## APPENDIX 8.A.3.B

### Q MEASUREMENTS: THE EFFECTS OF LAYERING

A major role of seismic interpretation is the inference of physical properties of propagation media. The inversion from seismic to physical properties is far from unique. This job requires a range of seismic measurements of seismic parameters, among which are seismic velocity, absorption, impedance, and Poisson's ratio. Seismic absorption may be difficult to measure. For example, seismic attenuation is more sensitive to clay content than seismic velocity (Klimentoes and McCann, 1990). There are many different mechanisms for seismic absorption. In this section we try to understand the role of layering in attenuation measurements, which may be a key to finding the actual intrinsic attenuation of the propagation media. We need to correct the geometrical spreading factor of the wave propagation before the actual measurements of intrinsic attenuation. In general, we correct the waveform using simple  $1/r$  as a spreading correction of the wave propagation from a point source where  $r$  is the distance between the source and receiver. For the layer medium, this correction needs to be modified. For example, if the velocity is increased, the ray will diverge. This will lead to an increase of the geometrical spreading and confine the propagating seismic energy within the ray tubes. Similarly, the geometrical spreading will decrease when propagation along the media takes place at decreasing velocities. These basic propagation properties need to be corrected before the evaluation of the intrinsic attenuation. In this section we will give a few simple examples of geometric spreading due to layering. We will demonstrate how the effect of layering generates complete waveforms in one-dimensional media.

#### 8.A.3.B.1 Numerical Simulation

To study the effect of layering on  $Q$  measurements, we calculate complete wave synthetic seismograms for a number of cases. The complete waveform synthetics have been computed by solving the integration numerically (discrete wavenumber) and getting the wavenumber response for each frequency by using the scattering or reflectivity matrix approach (Mandal, 1987). In this procedure all the waveforms are included in the computation, which can be compared directly to the observations. The intrinsic attenuation is incorporated in the calculation by using the propagation factor in elastic media by

$$\exp \left[ i \omega \left( \frac{r}{c_e} - t \right) \right].$$

The anelastic solution is reached by replacing the elastic velocity,  $c_e$ , with the rule (Aki and Richard, 1981)

$$\frac{1}{c_e} \rightarrow \frac{1}{c(\omega)} \left( 1 + \frac{i}{2Q(\omega)} \right).$$

This relation is used to incorporate the intrinsic attenuation in our computation. In general, we measure the attenuation by observing waveforms at two different distances along one direction so that they have a common path. In such a case we observe the gradual spatial decay of amplitude from the nearest point to the farthest. In such a measurement we must incorporate the geometric spreading effects at two distances. The study of geometric spreading is very important when the wave propagating takes place in heterogeneous media. Here we try to explain these effects with some simple examples.

#### 8.A.3.B.2 Layers

We studied two different source receiver arrangements: (a) vertical seismic profiling (VSP) and (b) cross-hole. Both arrangements were used to study the EPRI test sites—Treasure Island and Gilroy. The purpose of this theoretical study is to determine the actual condition of the test sites and to apply any correction required to improve the observation data. First, we study the effects on a simple layer model and then apply this understanding to real field data.



### 8.A.3.B.2.1 VSP

Four receivers are placed vertically in the borehole at 50 ft intervals. The source is only 5 ft offset from the hole. The arrangement and model are shown in Figure 8.A.3.B-1; the velocity model is shown in Figure 8.A.3.B-2. In this case we use full-space computation and incorporate all the waves. The 0–120 Hz frequency domain responses are convolved with a 50 Hz center frequency Hanning-windowed Ricker wavelet. The source is a shear source and the receiver is a transverse component response. Therefore, the synthetic seismograms represent the SH response of the medium. The complete synthetic seismograms are shown in Figure 8.A.3.B-3. In this example, the intrinsic attenuation is not considered. All the traces are plotted with reference to amplitudes and their maximum values are shown adjacent to each trace.

We use the same algorithm as described in Appendix 8.A.3.A (Tang, 1992) to estimate the velocity and attenuation for synthetic seismograms. Figure 8.A.3.B-4 describes the steps taken to estimate the velocity and attenuation. The upper box of the figure shows the two seismograms at depths of 50 and 100 ft; the  $(1/r)$  geometric spreading correction is incorporated at each depth. The upper trace is at a depth of 50 ft and the lower is at 100 ft. The bottom box is the time-migrated signal of the top trace (in this case the waveform at 50 ft) to the bottom trace. The dashed line shows the migrated waveform. This was done by a simple time shift after calculating the phase velocity by cross-correlation or with a phase matched filter. It was observed that the  $(1/r)$  spreading factor does not work correctly (note that no intrinsic attenuation is considered in this computation). In such a case if we do estimate  $Q$ , we would compute a finite attenuation value even if there is no intrinsic attenuation in the computation. The results, however, may be misleading, as shown in Figure 8.A.3.B-5 when  $Q_s = 33$ .

Figure 8.A.3.B-6 shows the proper geometric correction between 50 and 100 ft. In this case  $(1/r^{1.5})$  gives a perfect match between the 50 and 100 ft propagation. We show similar examples of the propagation paths at 50–150 ft (Figures 8.A.3.B-7–9) and 50–200 ft (Figures 8.A.3.B-10–12). None of these examples obey the  $(1/r)$  geometric spreading factor. Figures 8.A.3.B-7–9 and 8.A.3.B-10–12 show the identical procedure as those in Figures 8.A.3.A.B-6 but with different depth comparisons.

Figure 8.A.3.B-13 shows the complete synthetic seismograms with constant  $Q$ . All the layers have the same attenuations ( $Q_p = 80$  and  $Q_s = 40$ ). Figure 8.A.3.B-14 shows the results of  $(1/r)$  geometric spreading used with  $Q_s = 40$ . It is clear that we cannot migrate the waveform from one distance point to another with a conventional  $(1/r)$  geometric spreading factor for the layer medium. Figure 8.A.3.B-15 shows the misleading  $Q_s$  (=17 lower than the original) when  $(1/r)$  geometrical spreading has been considered. Figure 8.A.3.B-16 shows the appropriate results for the proper use of the  $(1/r^{1.5})$  geometrical spreading factor and  $Q_s = 40$ . This numerical test shows that correct geometrical spreading is necessary in order to estimate the actual spatial attenuation of the propagation path. Figures 8.A.3.B-17–19 show the same for the receiver pair at 50–200 feet.

Geometric spreading may also vary due to the impedance contrast of the layers. Higher impedance contrast leads to the escape of energy (reflection) from the direct propagation which in turn affects the geometric spreading correction. To understand this phenomenon, we computed the complete wave synthesis for the same model (Figure 8.A.3.B-2) where the shear wave impedance between the layers was almost negligible, by adjusting the density. Figure 8.A.3.B-20 shows the synthetic seismograms without intrinsic attenuation. We conducted the same type of experiment as before. Figures 8.A.3.B-21–23 and Figures 8.A.3.B-24–26 show the results for propagation depths at 50–100 and 50–200 ft, respectively. In this case the geometric spreading corrections were estimated lower than the one of the non-zero impedance model. We may conclude from this that the non-zero impedance needs a higher geometric spreading correction so as to compensate for the reflection energy.

Figure 8.A.3.B-27 shows the synthetic seismograms for the zero-impedance model with attenuation ( $Q_s = 40$  in each layer). Figures 8.A.3.B-28–33 show the geometric spreading correction and the  $Q$ -measurement for a zero-impedance model with attenuation.

**8.A.3.B.2.1 The Effect of a Low Velocity Layer.** The real earth is not velocity increasing with depth. To understand the geometric spreading correction for the inclusion of a low velocity layer, we alter the model (Figures 8.A.3.B-1-2) by lowering the velocity of the second layer, as shown in Figure 8.A.3.B-34. Figure 8.A.3.B-35 shows the synthetic seismograms for non-intrinsic attenuation. It estimates the  $(1/r)^8$  geometric spreading (Figure 8.A.3.B-36) which is lower than that of the increasing velocity model. In this case the  $Q$ -value is higher than the actual. For example, Figure 8.A.3.B-37 shows  $Q_s = 65$ , which is higher than the actual value  $Q_s = 40$ . Figure 8.A.3.B-38 represents the actual  $Q_s$  with the proper use of the geometric spreading factor. For the receivers between 50–150 ft, where the low velocity layer is between the two high speed layers, the geometric spreading factor is  $(1/r^{1.525})$  larger than  $(1/r)$ . This predicts a lower  $Q_s$  value, as shown in Figure 8.A.3.B-40. Figure 8.A.3.B-41 shows the correct usage of geometric spreading and estimation of  $Q_s$ .

### **Summary of VSP Synthetic Experiments**

- Objective: Examine the effect of layering on geometric spreading and  $Q$ -estimation.
- Procedure:
1. Generate complete waveforms with different models.
  2. Estimate the velocity and attenuation.
  3. Analyze the geometric spreading factor with a known model.
- Results:
1. The model with velocity increase at depth has a higher geometric spreading.
  2. Lack of proper geometric correction leads to:
    - (a) High attenuation or low  $Q$  for the increasing velocity model.
    - (b) Low attenuation or high  $Q$  for the decreasing velocity model.
  3. The zero-impedance model reduces the geometric spreading effect.

### **8.A.3.B.2.2 Cross-Hole**

In this numerical experiment we try to demonstrate the sensitivity to layering in cross-hole measurement. To do this, we conduct four basic tests:

1. A simple homogeneous model.
2. A 20 ft layer with two identical low-velocity half-spaces.
3. A model the same as (2) but with two identical high-velocity half-spaces.
4. Both models (2) and (3) at a thickness of 10 feet.

For these tests, the source is a vertical point force and the vertical component receivers are at two different horizontal distances of 14.02 and 27.63 ft, respectively. Figure 8.A.3.B-42 shows the schematic diagrams of these tests.

Figure 8.A.3.B-43 shows an example for a homogeneous half-space, where the inversion procedure estimates the exact velocity and  $Q$ -values used in theoretical modeling. In our second test the observation layer is at a higher velocity than two half-spaces. In this case the  $Q$ -value is somewhat underestimated and the signal is interfered with by the later arrival (Figure 8.A.3.B-44). Figure 8.A.3.B-45 shows more complicated waveforms when the observation layer is at low velocity. Here,  $Q_s$  is underestimated. Figures 8.A.3.B-46 and 8.A.3.B-47 show the last two experiments at a decreased intermediate layer thickness, which contributes complicated waveforms and causes some difficulty in estimating the proper  $Q$  values.

The cross-hole experiments show that the  $Q$  measurement is sensitive to the layering along with the impedance contrasts and the layer thicknesses.

### **8.A.3.B.3 Application of the Model to the Treasure Island and Gilroy VSP Data**

In the previous section we found that geometric spreading with impedance contrast plays an important role in the estimation of actual intrinsic attenuation. To determine the exact geometric spreading factor from the observation data is quite difficult. In general,  $(1/r)$  is used as a correction factor for geometric spreading, but it is misleading in the interpretation of  $Q$  measurements. We propose a technique to estimate the geometric spreading correction by using synthetic seismograms with some knowledge of the velocity structure of the medium. This will give a rough idea of how to estimate the error of the  $Q$  measurements from a conventional  $(1/r)$  geometric spreading correction. Using this approach, we estimate modified  $Q$  measurements for the downhole Treasure Island and Gilroy data.

#### **8.A.3.B.3.1 Modified $Q$ Estimations Steps**

1. Obtain the velocity structure of the sites from other observations.
2. Compute the complete synthetic seismograms without intrinsic  $Q$ .
3. Determine the effective geometric spreading between the propagation paths that are of interest.
4. Correct the geometric factor as obtained from synthetic waveforms in observed data.
5. Estimate the velocity and attenuation.

If we have good knowledge of the velocity structure of the sites of interest, we can use this procedure to estimate the average  $Q$  between the two observation points provided with a good S/N ratio signal.

#### **8.A.3.B.3.2 Treasure Island**

Figures 8.A.3.B-48–49 show the velocity structure for Treasure Island obtained from Redpath and USGS velocity data. Figure 8.A.3.B-50 represents the complete synthetic seismograms with no intrinsic attenuation from a 50 to 300 ft depth. The amplitude decay is due solely to the geometric spreading. Figures 8.A.3.B-51–52 demonstrate that the  $(1/r^{1.8})$  geometric spreading correction is required to explain the propagation between 50 and 100 feet. If there is no S-wave impedance in the medium, then the  $(1/r^{1.145})$  geometric spreading correction will be required (as shown in Figure 8.A.3.B-53). Figures 8.A.3.B-54–56 show the incorporation of intrinsic  $Q_s = 20$  in all the layers. It shows that the  $(1/r^{1.8})$  geometric spreading factor needs to be corrected to obtain actual intrinsic  $Q_s (=20)$ . If we use the conventional  $(1/r)$  geometric correction then the  $Q$  measurement will be underestimated, as shown in Figure 8.A.3.B-55. Using this knowledge, we apply it to real data for the receivers between 50 and 100 ft for three different geometric spreading factors, as shown in Figures 8.A.3.B-57–59.  $Q$  estimation may be between 12–25. Figures 8.A.3.B-60–62 show the estimated  $Q$  values for a 50–200 ft depth interval. In this case we observe a higher  $Q$  value when we corrected our predicted geometric spreading factor. Figures 8.A.3.B-64–66 show the results for a 50–280 ft depth interval.

#### **8.A.3.B.3.3 Gilroy**

Figures 8.A.3.B-67–68 show the velocity model for the Gilroy site used in synthetic modeling. Complete wave synthetic seismograms with no intrinsic attenuation are shown in Figure 8.A.3.B-69. Figure 8.A.3.B-70 shows that the  $(1/r)$  geometric spreading is not satisfied for the depth interval between 50–100 ft. The  $(1/r^{1.28})$  geometric spreading is required to explain the synthetic seismograms (Figure 8.A.3.B-71). The zero-impedance shear model increases the geometric spreading factor between a 50–100 feet interval, as shown in Figure 8.A.3.B-72. Figures 8.A.3.B-73–74 show the  $Q$ -estimation at this depth from Gilroy VSP data. Note that the S/N ratio of this observation is not good. Figures 8.A.3.B-75–77, Figures 8.A.3.B-78–79, and Figures 8.A.3.B-80–82 show the  $Q$ -estimation between 50–150 ft, 50–200 ft, and 50–300 ft, respectively.

### 8.A.3.B.4 Conclusions

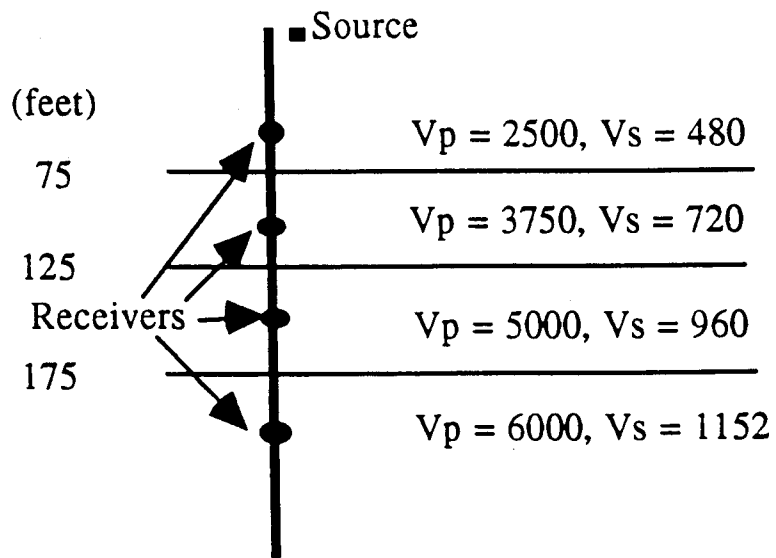
Theoretical experiments on  $Q$ -estimation with layering conclude that:

1. Layering changes the geometric spreading correction.
2. Proper use of geometric spreading correction is necessary in order to determine actual attenuation.
3. Conventional ( $1/r$ ) spreading correction may be misleading to the  $Q$ -estimation, hence also to the prediction of site response.
4. To estimate the geometrical spreading we need to know the approximate velocity structure with proper impedance contrast. Using a complete synthetic waveform synthesis, we can provide approximate geometric spreading correction which can be used to determine  $Q$  from the observation data. We can provide an error bound on the geometrical spreading from other geophysical observations at the sites. Using these we can also estimate an error bound for  $Q$  measurements.
5. Cross-hole measurements are also sensitive to layering. The direct wave may be contaminated by other arrivals that may cause wrong  $Q$ -estimation.
6. Using all these theoretical experiments on layering, we summarized the  $Q$ -estimations for Treasure Island and Gilroy 2 (as in Table 8.A.3-5 of the main text).

Depth Interval (ft)	Geometric Spreading Correction			Q	
	No reflection	Reflection	1/r	Including reflection	Intrinsic
<b>TREASURE ISLAND</b>					
50–100	1.15	1.80	11	14	24 (50 Hz)
50–150	1.33	1.70	15	17	35 (50 Hz)
50–280	1.35	1.75	15	18	35 (50 Hz)
<b>GILROY 2</b>					
50–100	1.40	1.28	40 ?	200 ?	120 (50Hz)
			20 ?	50 ?	35 (90Hz)
50–150	1.35	1.60	11	17	23 (50 Hz)
50–200	1.40	1.73	5 ?	6 ?	8 (50Hz)
			6 ?	8 ?	10 ? (90Hz)
50–300	1.46	1.70	8	12	16 (50 Hz)
			7 ?	12 ?	17 ? (90Hz)

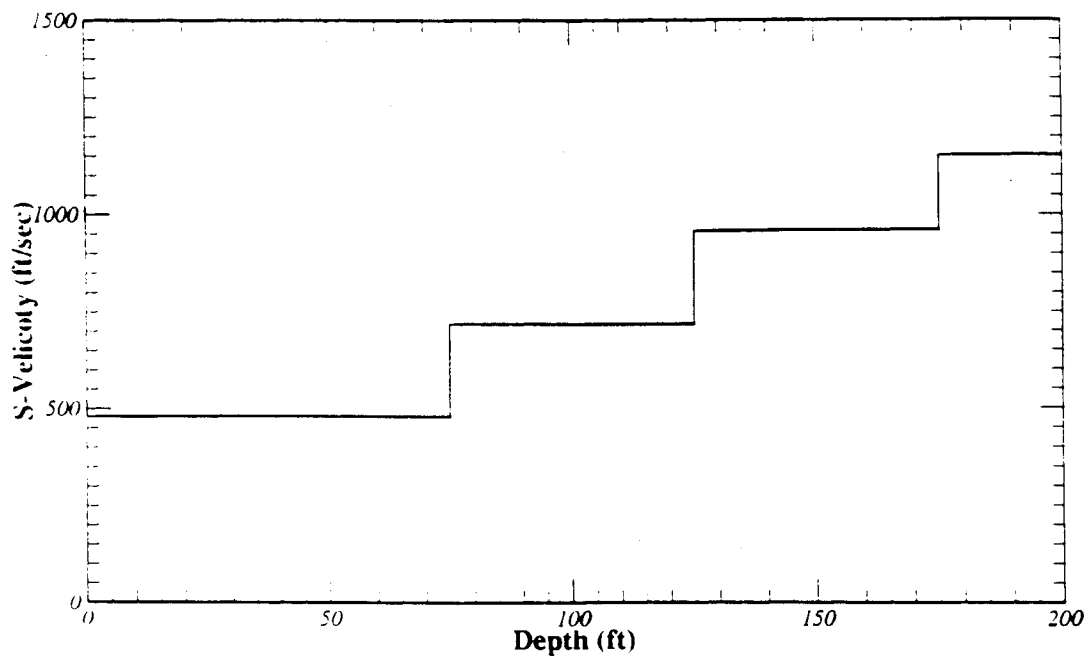
## References

- Klimentoes, T. and C. McCann, 1990, Relationships between compressional wave attenuation, porosity, clay content, and permeability of sandstones, *Geophysics*, 55, 998–1014.
- Mandal, B., 1987, Synthetic VSPs in vertical transversely isotropic media, Reservoir Delineation Consortium Annual Report, Earth Resources Laboratory, Massachusetts Institute of Technology, 3-1–3-24.
- Tang, X.-M., 1992, A waveform inversion technique for measuring elastic wave attenuation using cylindrical bars, *Geophysics*, 57, 854–859.

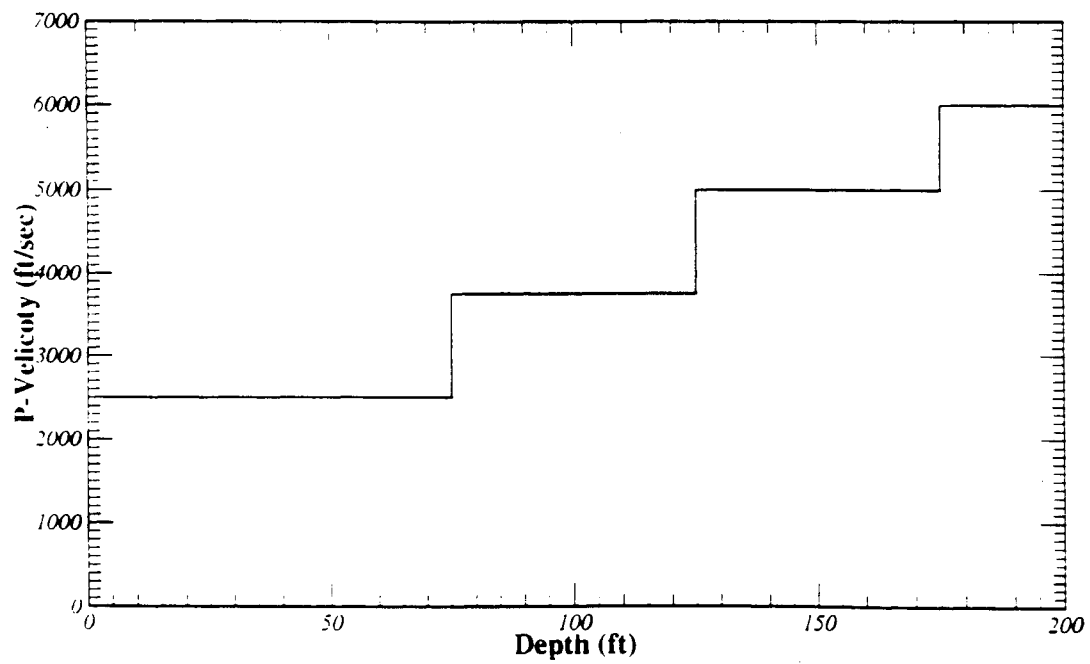


Same Q model used for all layers:  $Q_p = 80, Q_s = 40$

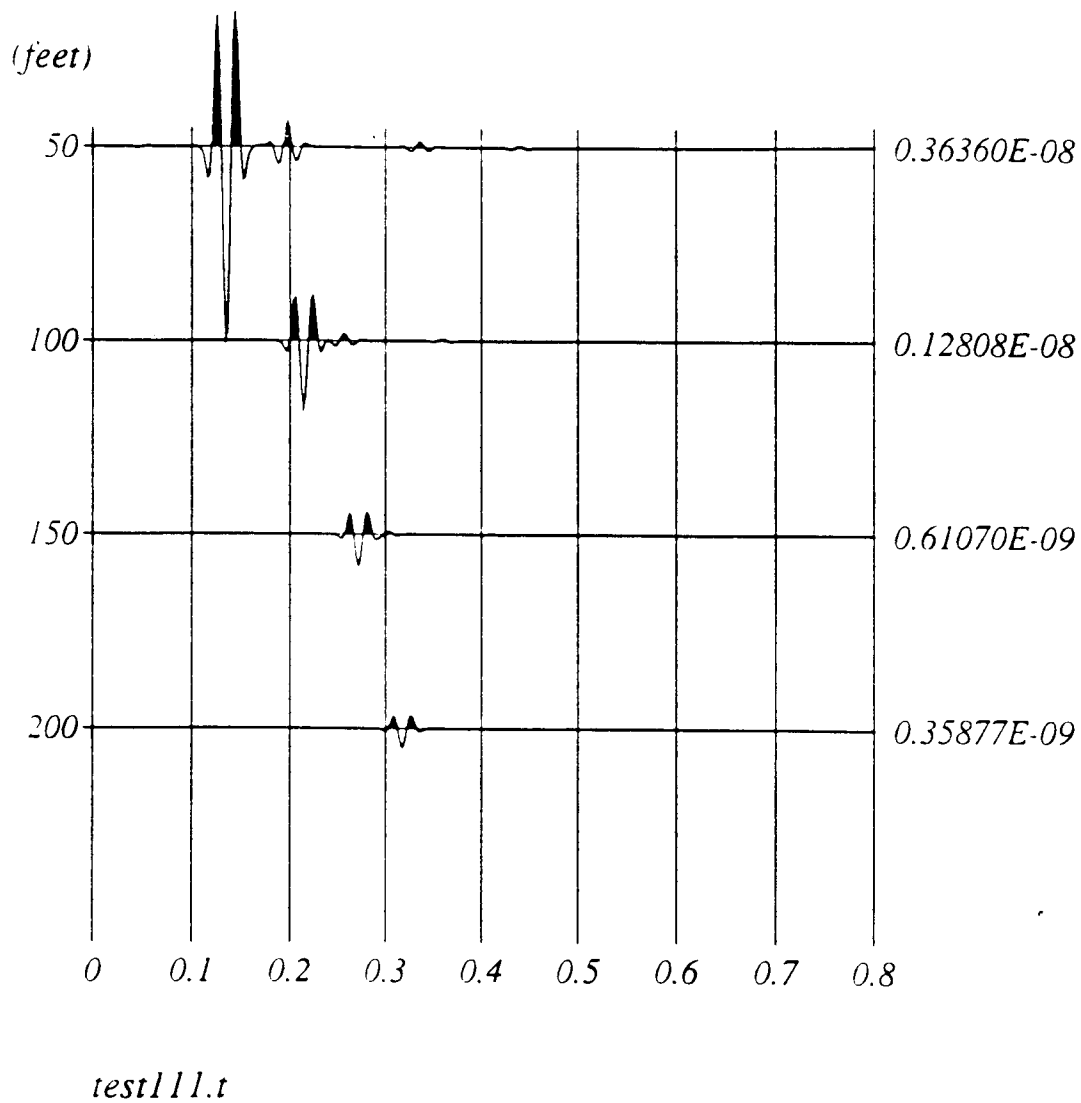
**Figure 8.A.3.B-1**  
Velocity model and source receiver arrangements.



mod-test11



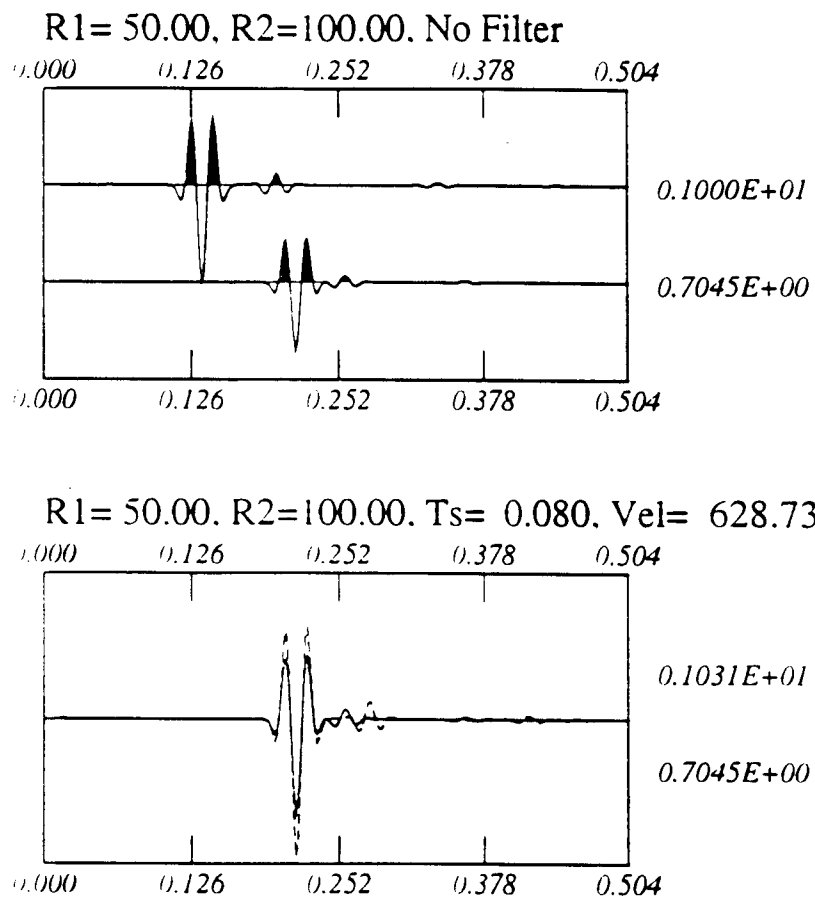
**Figure 8.A.3.B-2**  
Velocity model used for the simple test.



**Figure 8.A.3.B-3**

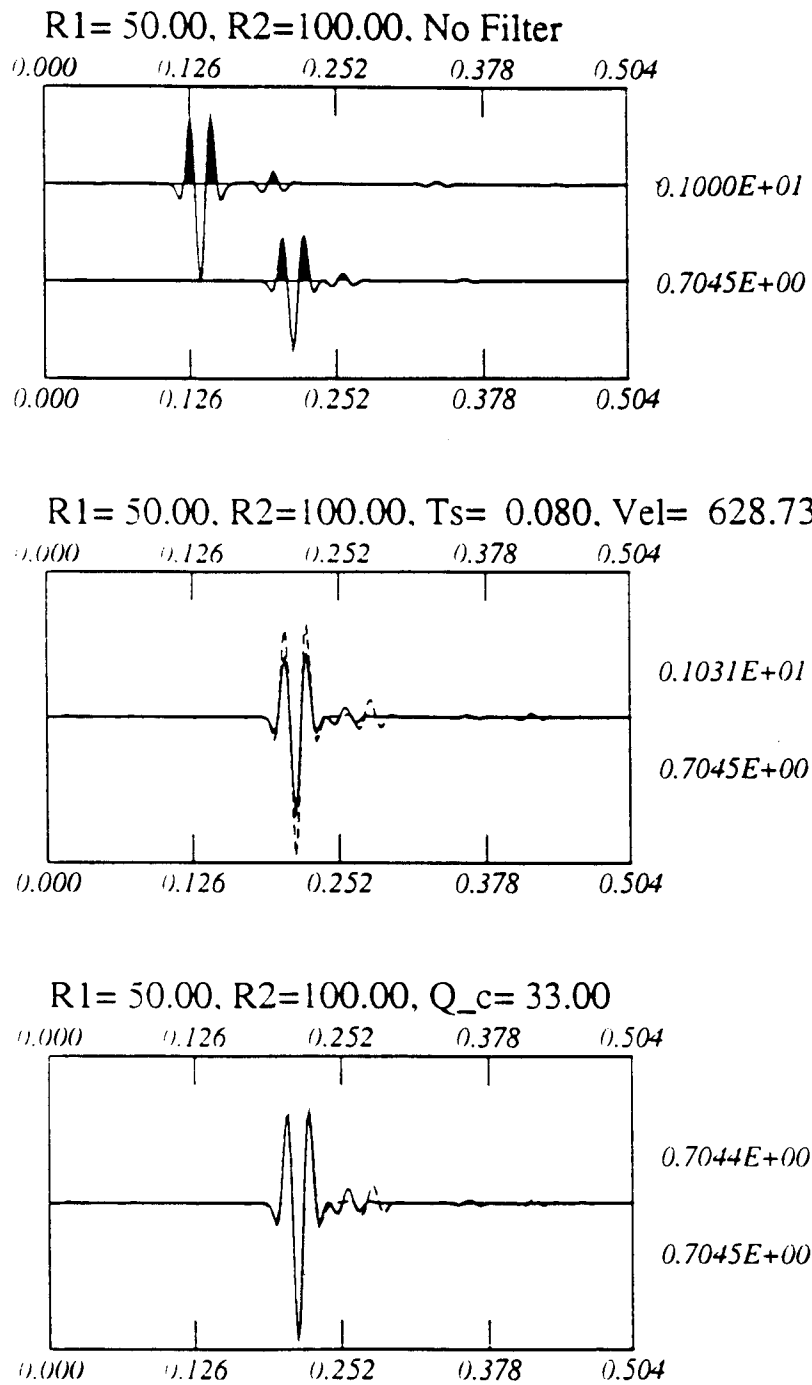
Transverse component complete synthetic seismograms at depths of 50 and 100–150 and 200 ft. The center frequency of the response is 50 Hz. All the traces are normalized. The source is a SH source at 0 ft with 5 ft offset from the vertical line. In this example no free surface is considered. There is no intrinsic attenuation in this computation.





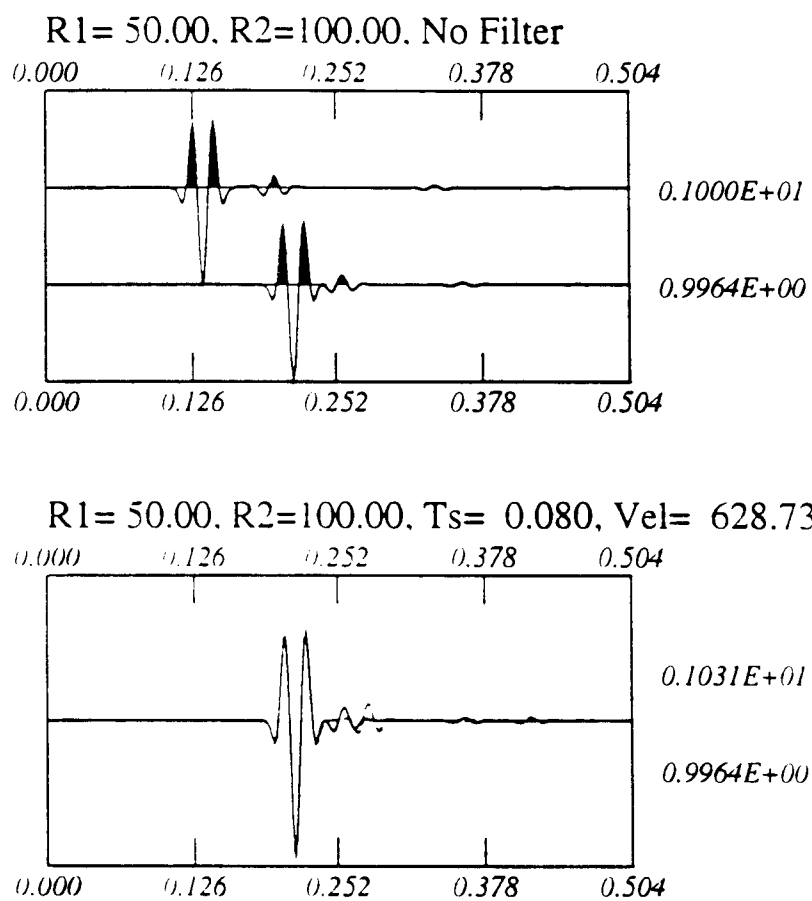
**Figure 8.A.3.B-4**

The top box displays the responses at a depth of 50 and 100 ft with the  $(1/r)$  geometric spreading correction. The bottom box is the time migrated signal of the top trace (50 ft). The dashed line is the migrated signal.



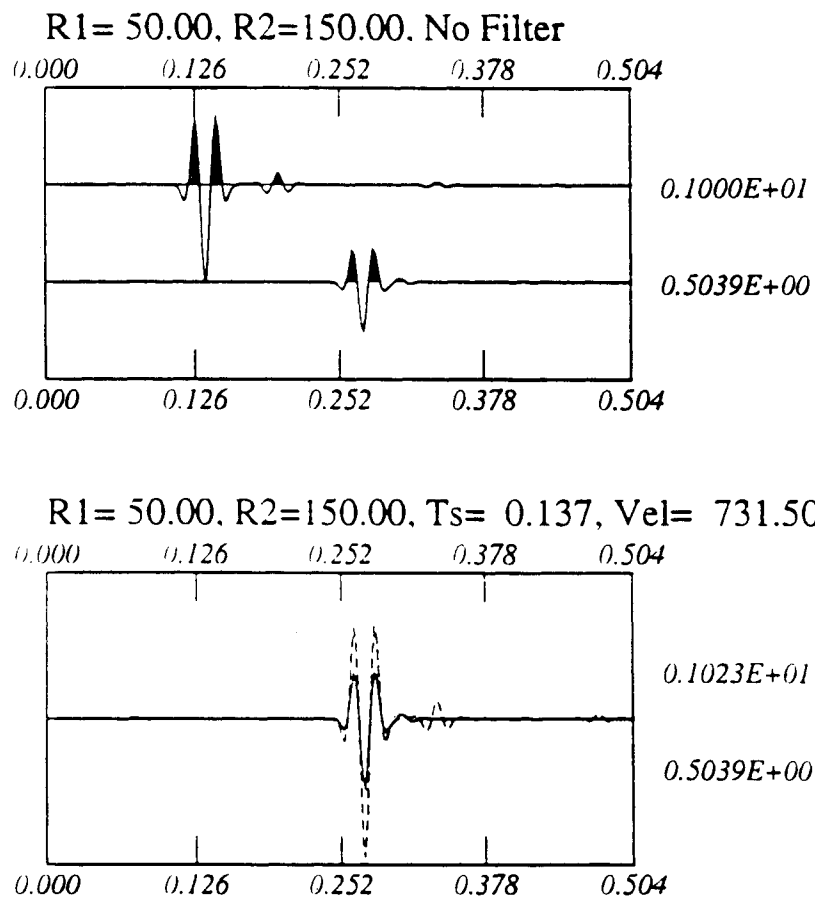
**Figure 8.A.3.B-5**

The top two boxes are the same as described in Figure 8.A.3.B-4. The bottom trace is the attenuation estimation. Note that in this example we have a  $Q$  value = 33 even though we did not use intrinsic attenuation in our computation.



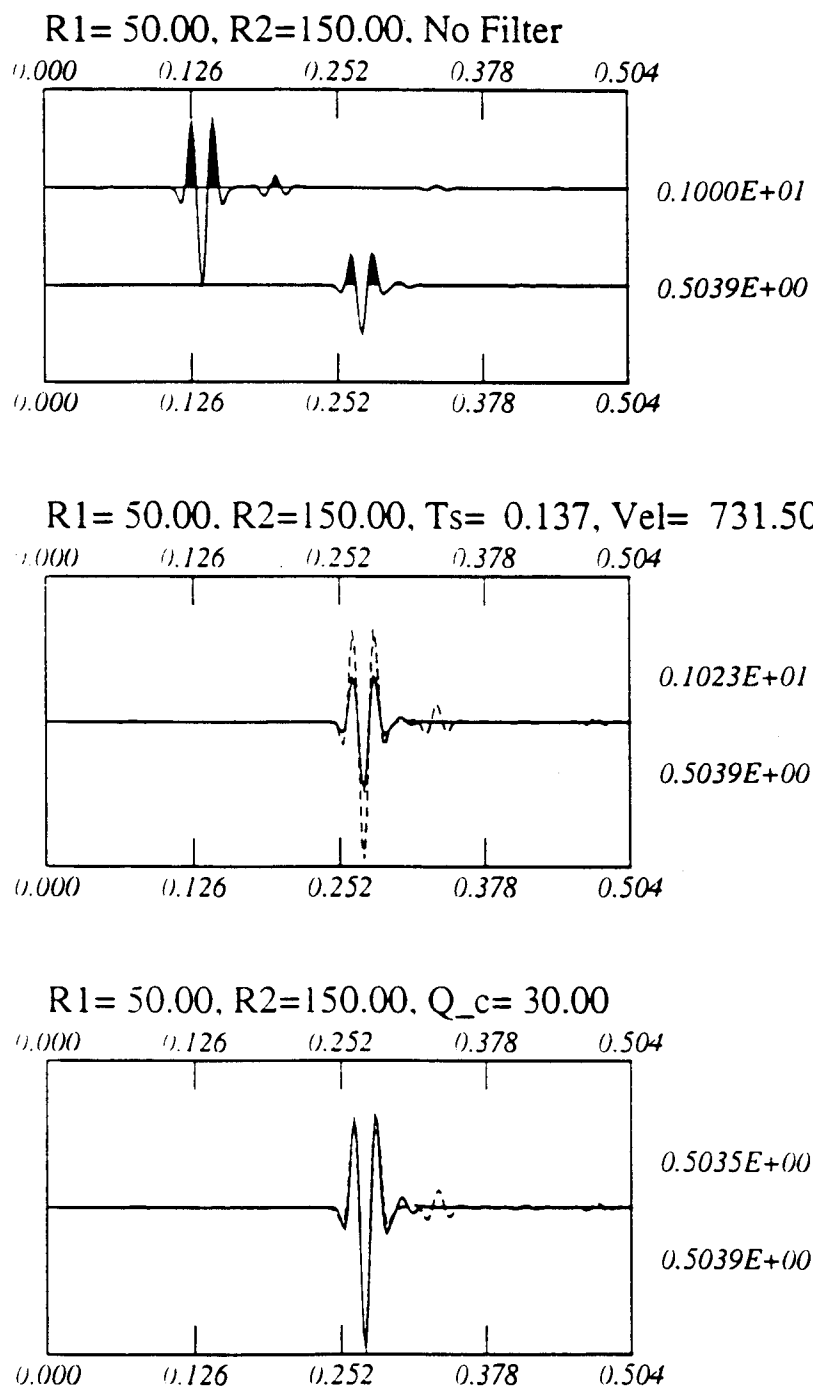
**Figure 8.A.3.A.2-6**

Same as Figure 8.A.3.A.2-4 but with  $(1/r^{1.5})$  geometric spreading correction.



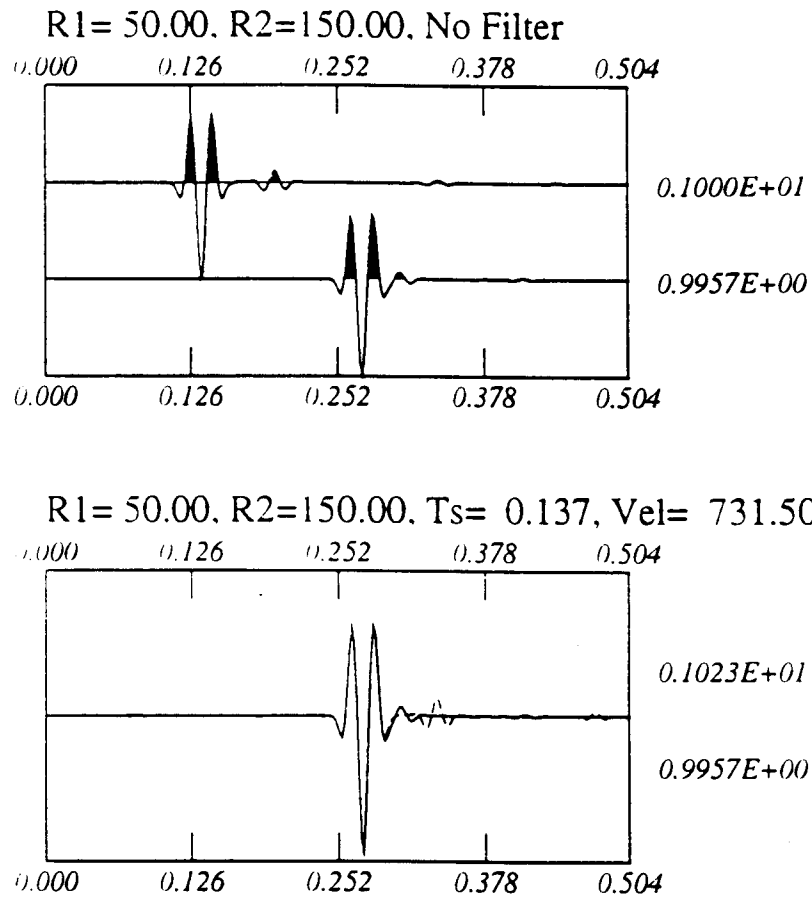
**Figure 8.A.3.A.2-7**

Same as Figure 8.A.3.B-4 but at two different depths between 50 and 150 feet.



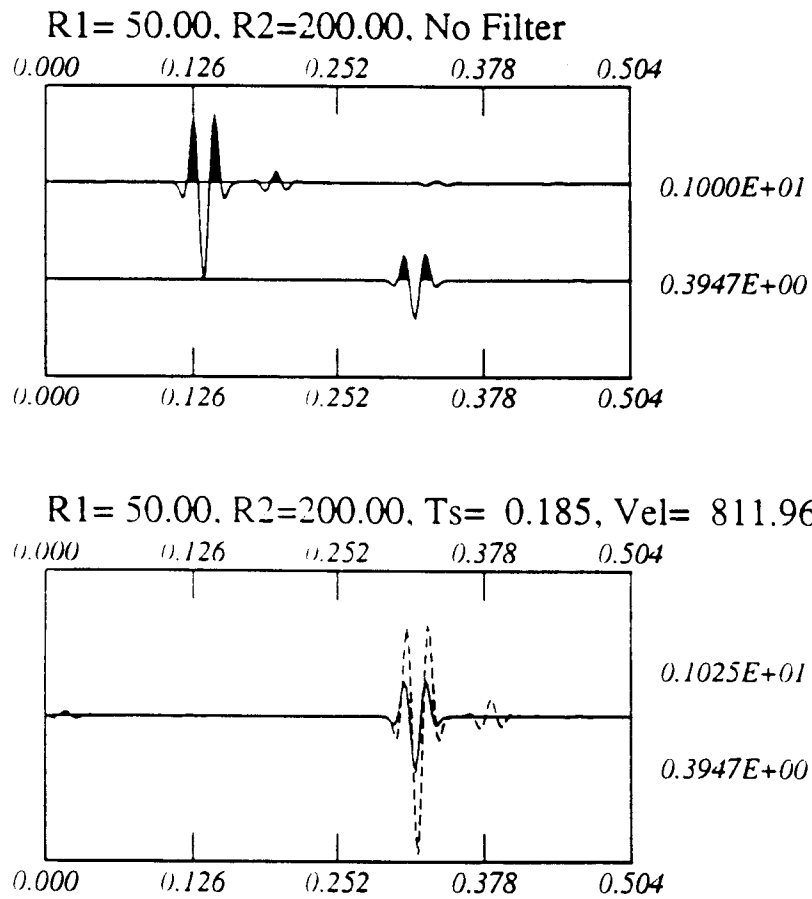
**Figure 8.A.3.B-8**

The  $Q$  estimate between 50 and 150 feet. The explanation of this figure is the same as Figure 8.A.3.B-5. Here we found  $Q = 30$  even though we did not use intrinsic attenuation.



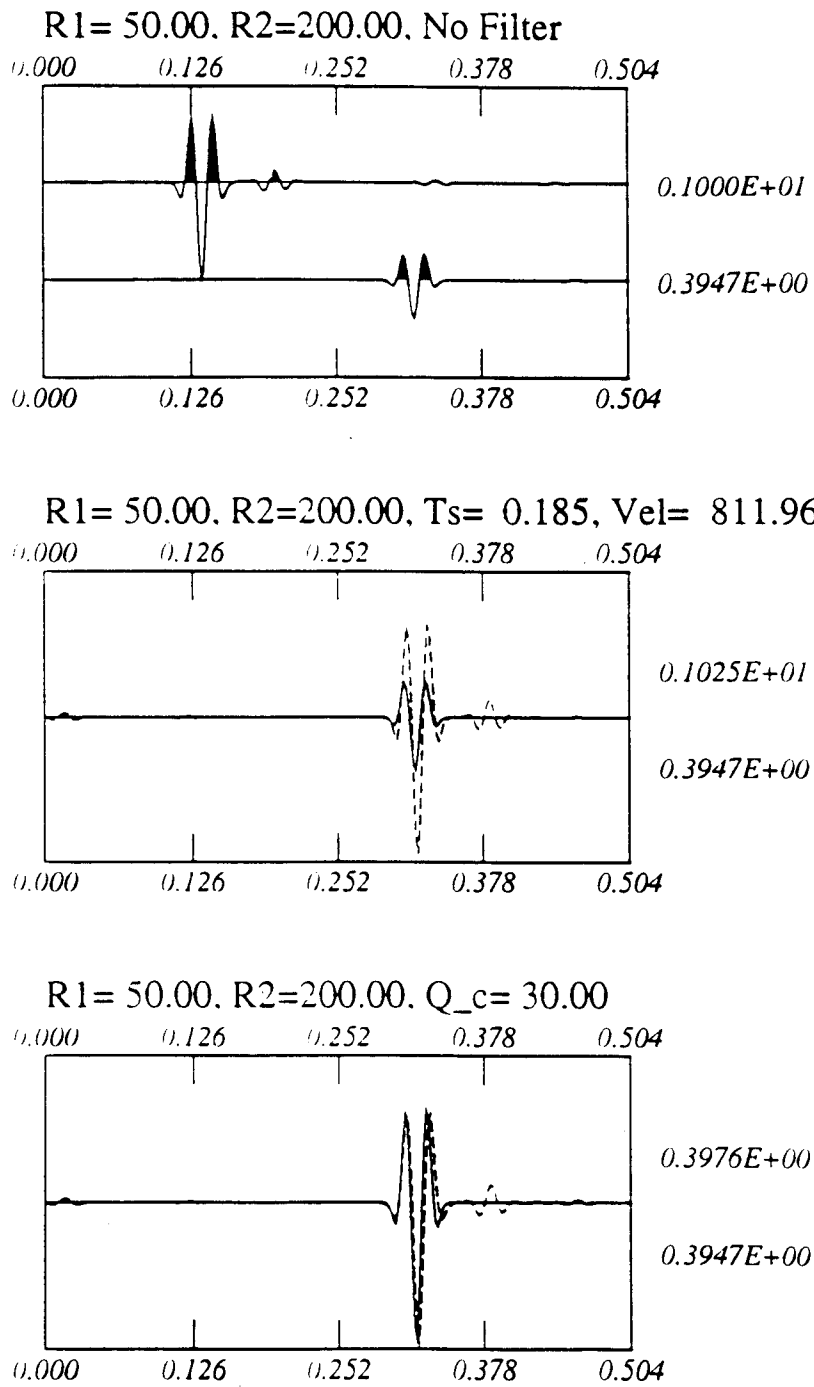
**Figure 8.A.3.B-9**

We find the  $(1/r^{1.62})$  geometric spreading correction between 50 and 150 ft depth.



**Figure 8.A.3.B-10**

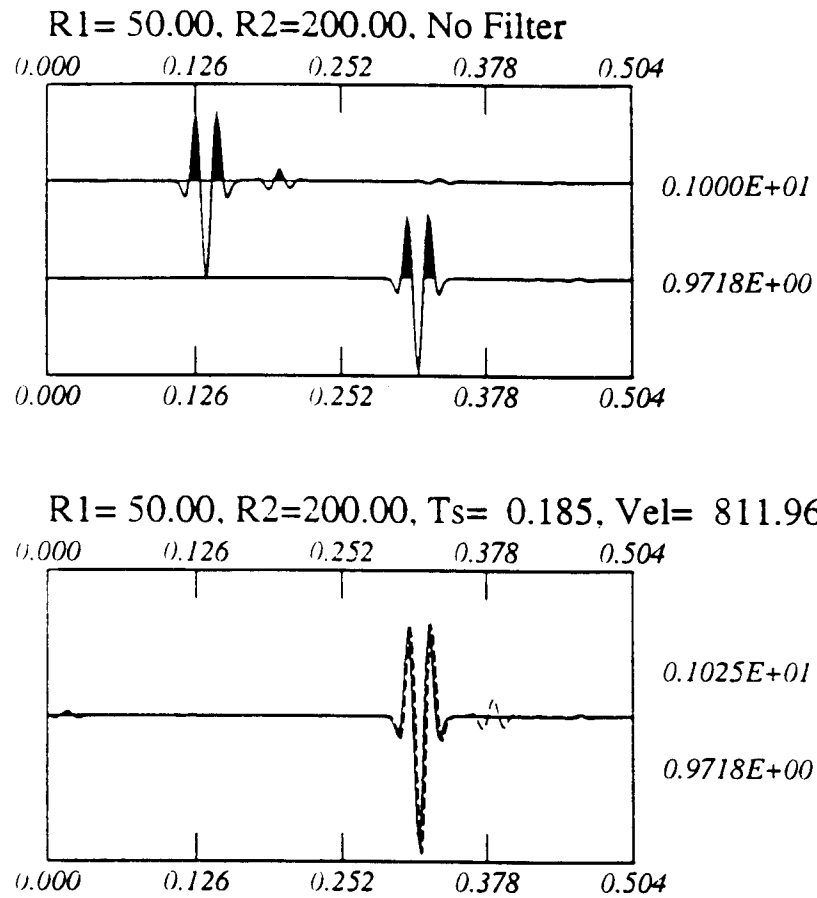
Same as Figure 8.A.3.B-4 but between the depths of 50 and 200 feet.



**Figure 8.A.3.B-11**

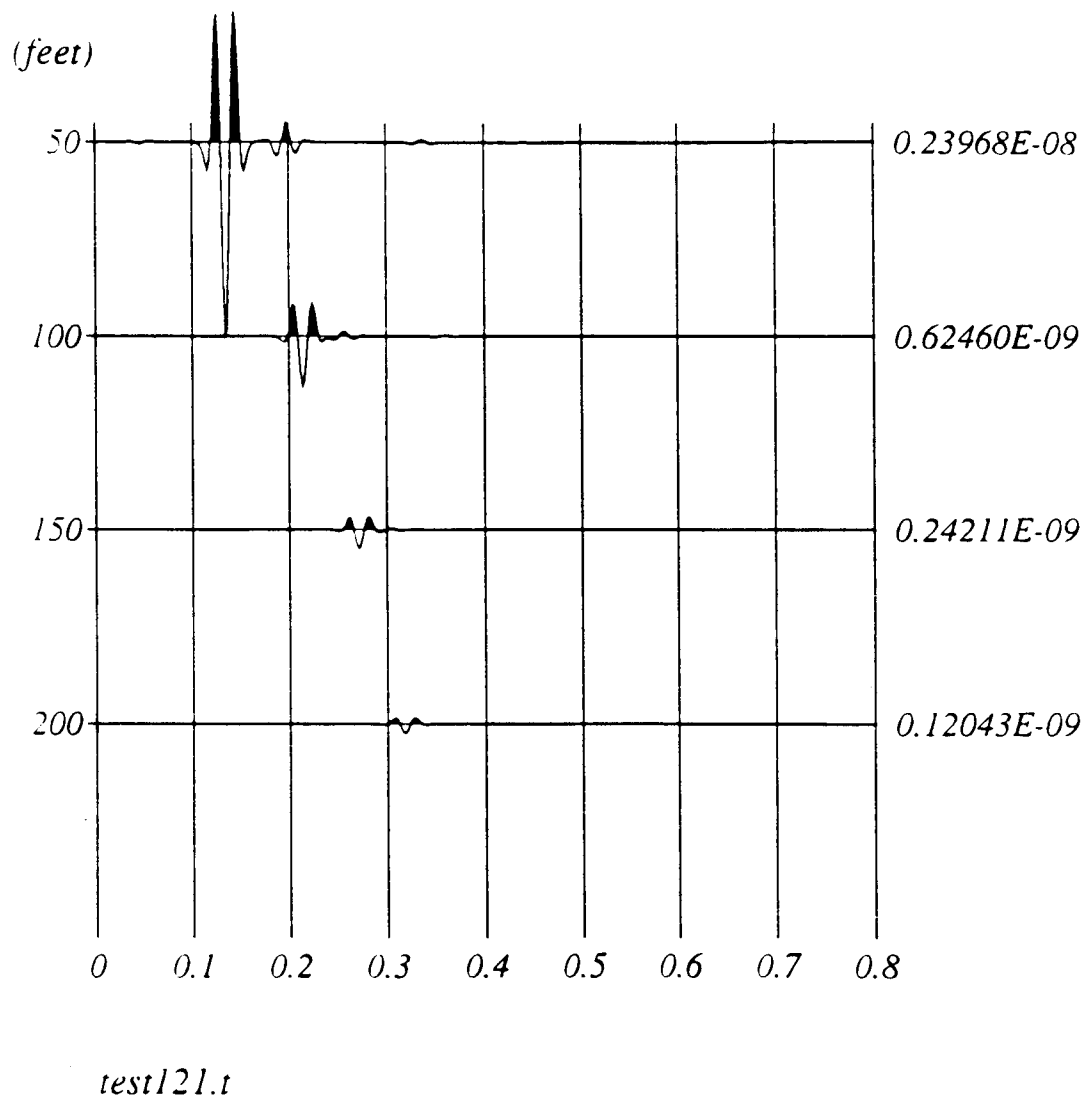
Same as Figure 8.A.3.B-5. The misleading  $Q$  value = 30 is found between the depths of 50 and 200 feet.





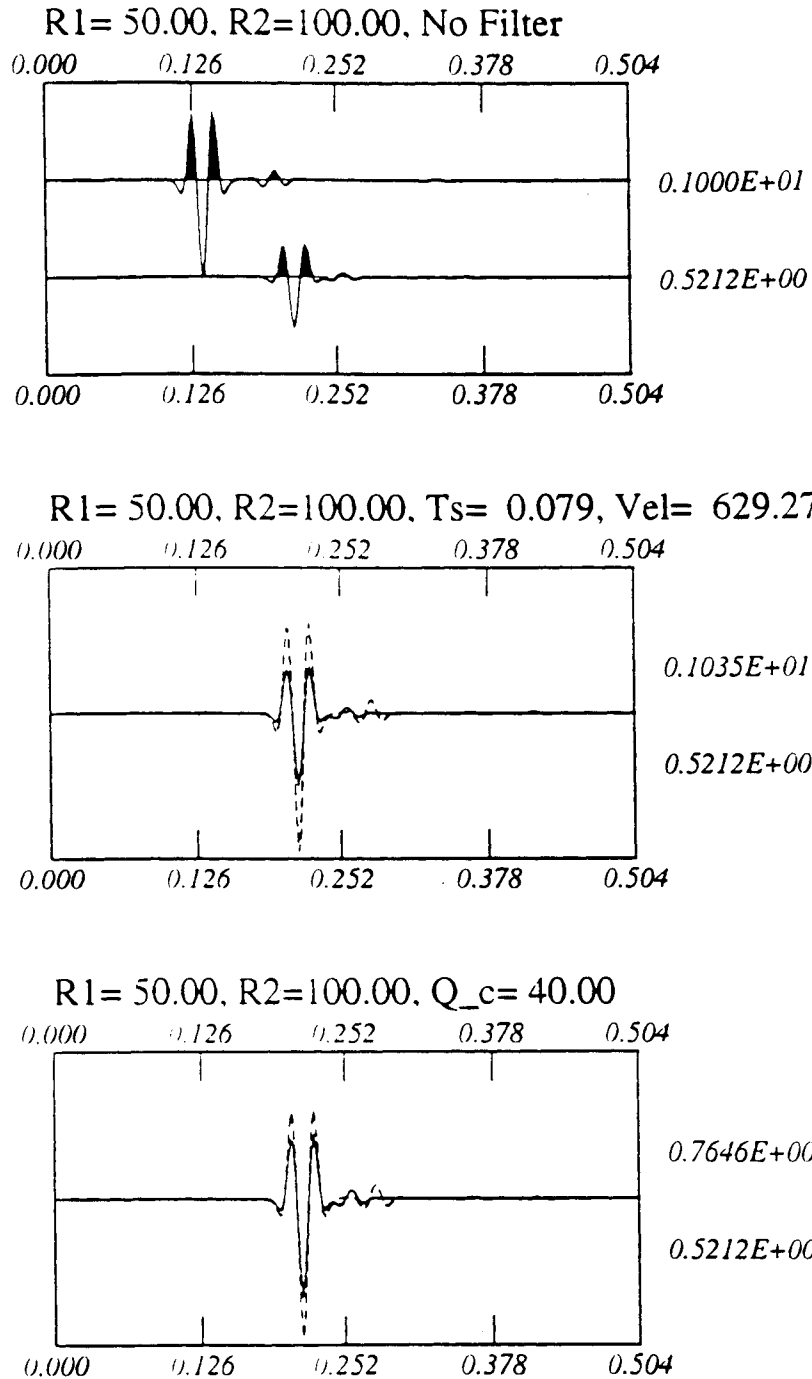
**Figure 8.A.3.B-12**

Same as Figure 8.A.3.B-6. The correct geometric spreading correction is  $(1/r^{1.65})$  between the depths of 50 and 200 feet.



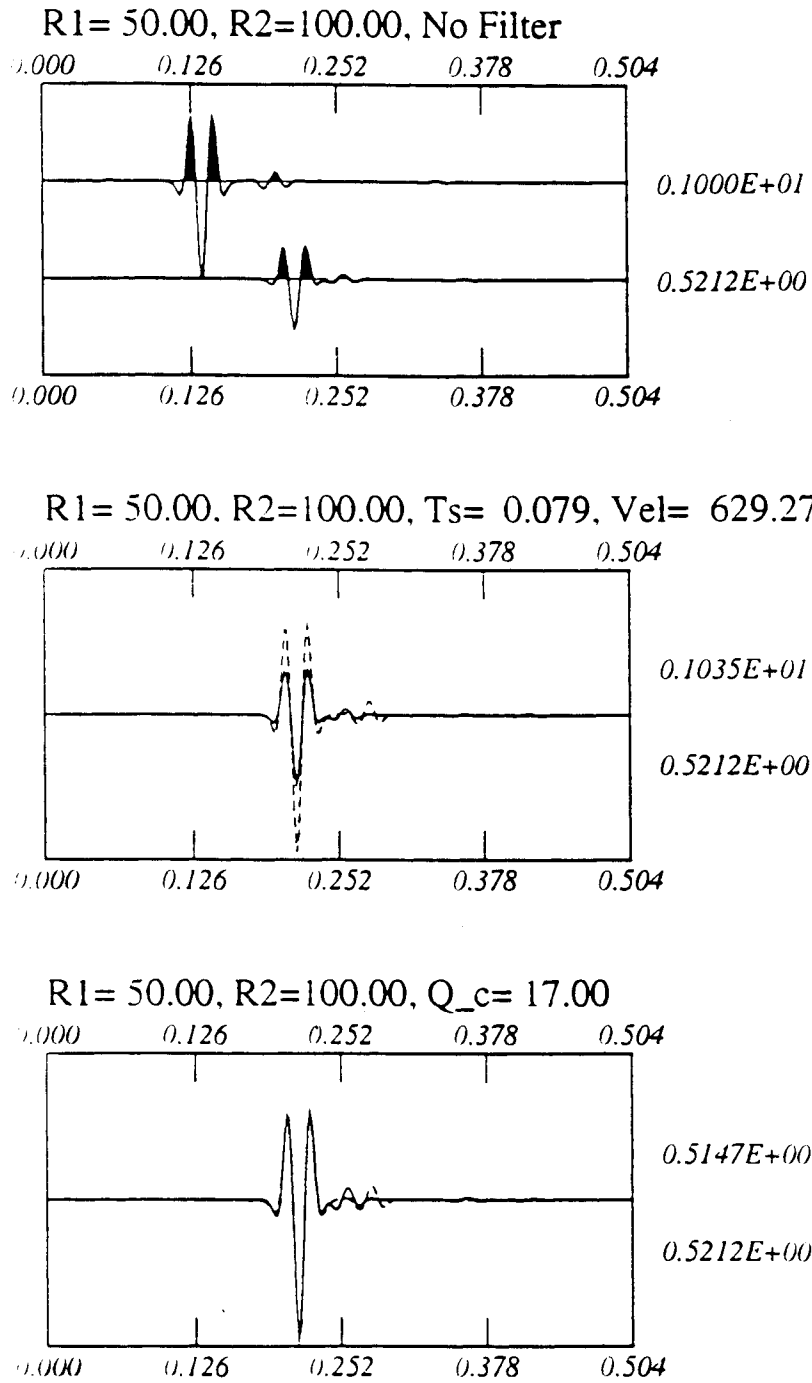
**Figure 8.A.3.B-13**

Complete synthetic seismograms as described in Figure 8.A.3.B-3 but in this case we have used the intrinsic  $Q$  ( $Q_p = 80$  and  $Q_s = 40$ ).



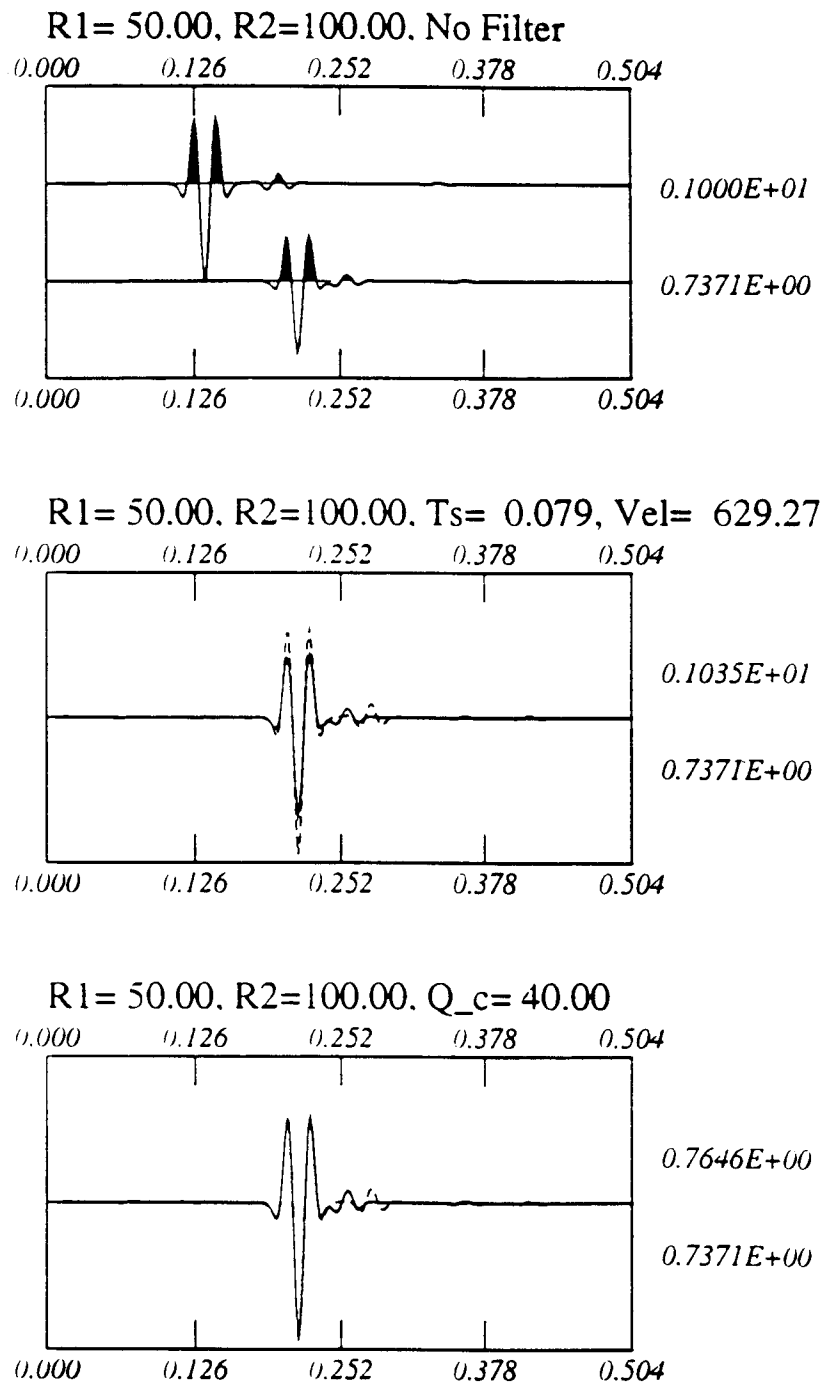
**Figure 8.A.3.B-14**

Velocity and Q estimation between the depths of 50 and 100 feet. The  $(1/r)$  geometric correction has been used. We show that the theoretical value of  $Q_s = 40$  is not satisfied.



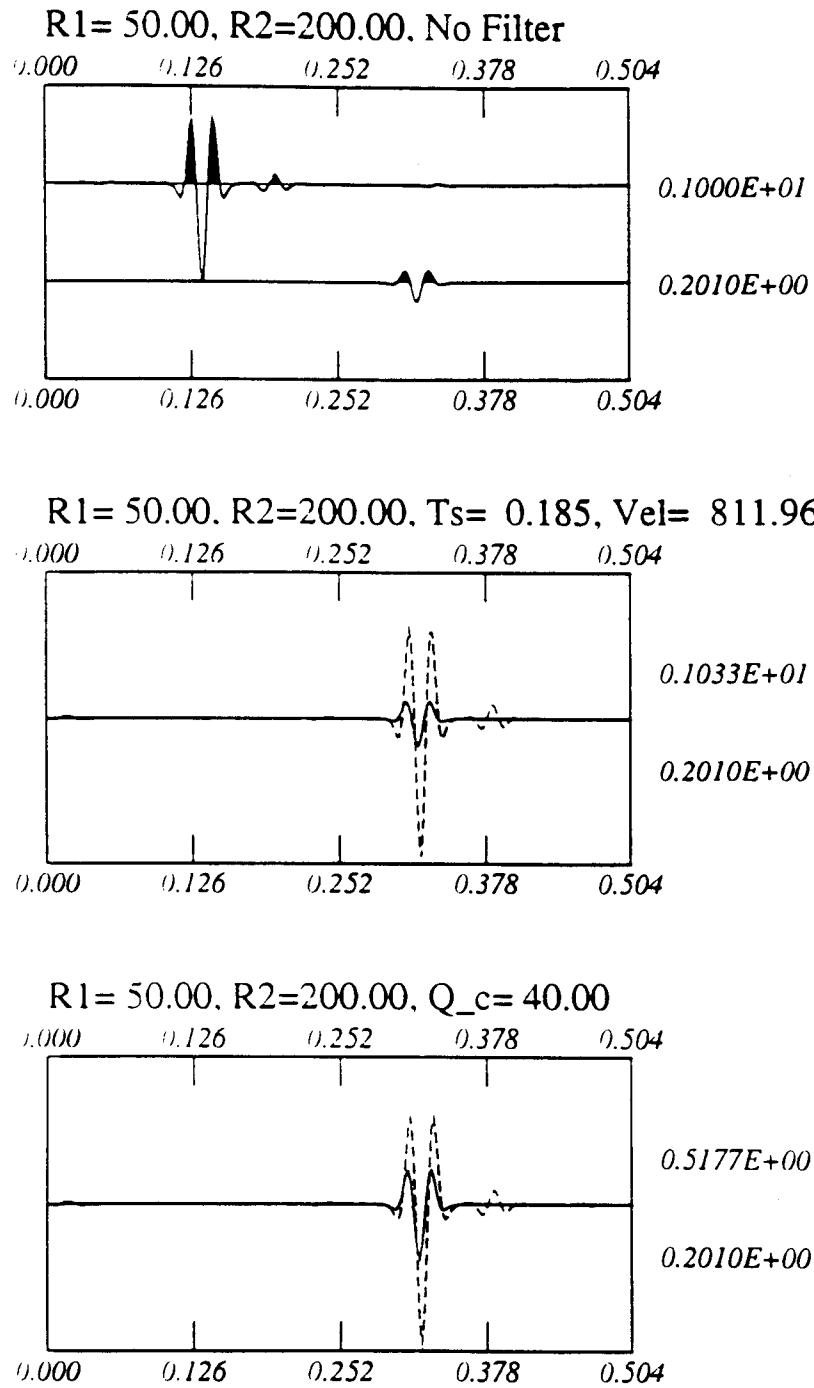
**Figure 8.A.3.B-15**

Same as Figure 8.A.3.B-14. In this case we estimated  $Q_s = 17$  instead of 40 to explain this observation.



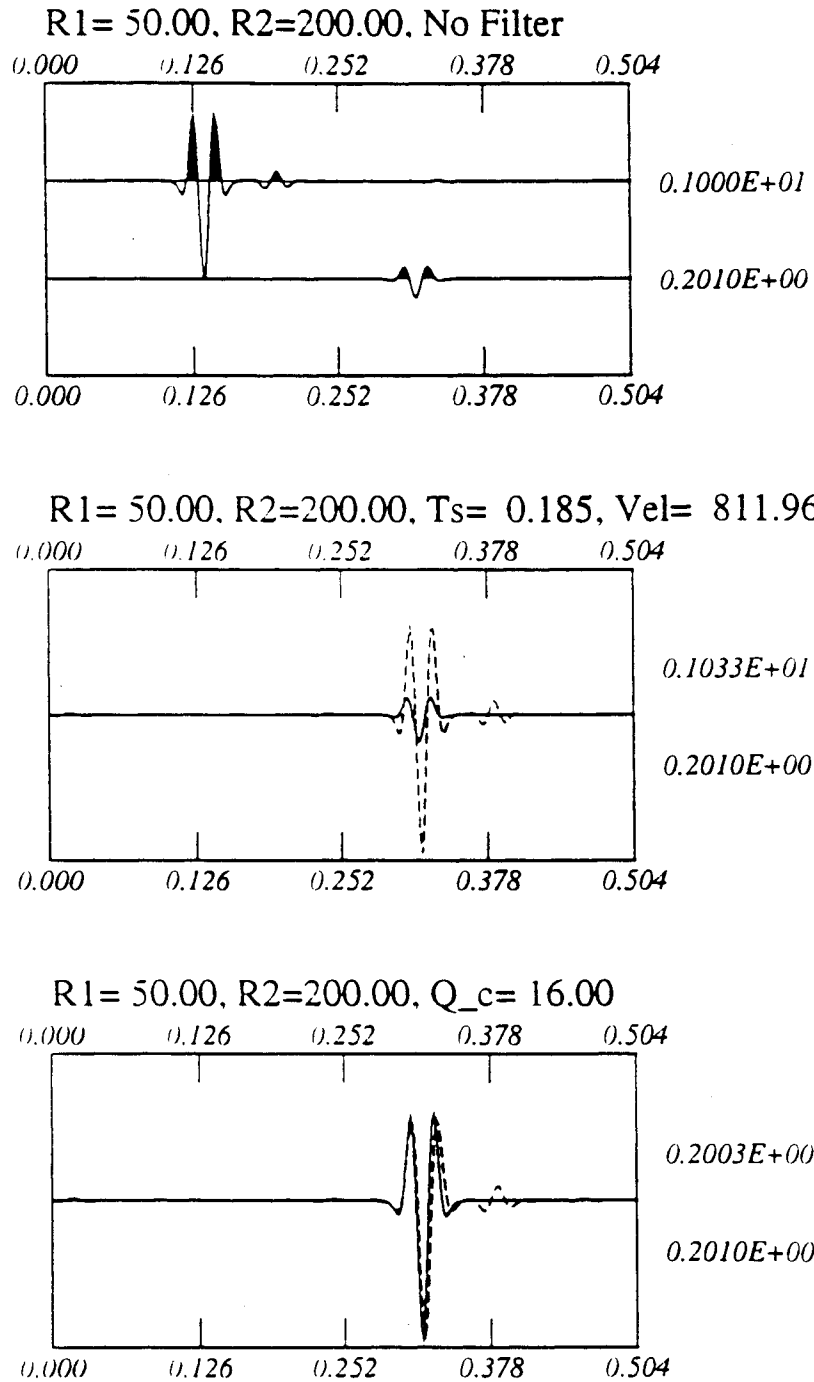
**Figure 8.A.3.B-16**

Shows that the correct geometric spreading ( $1/r^{1.5}$ ) (Figure 8.A.3.B-6) yields exactly the same Q (= 40) as was used in the computation.



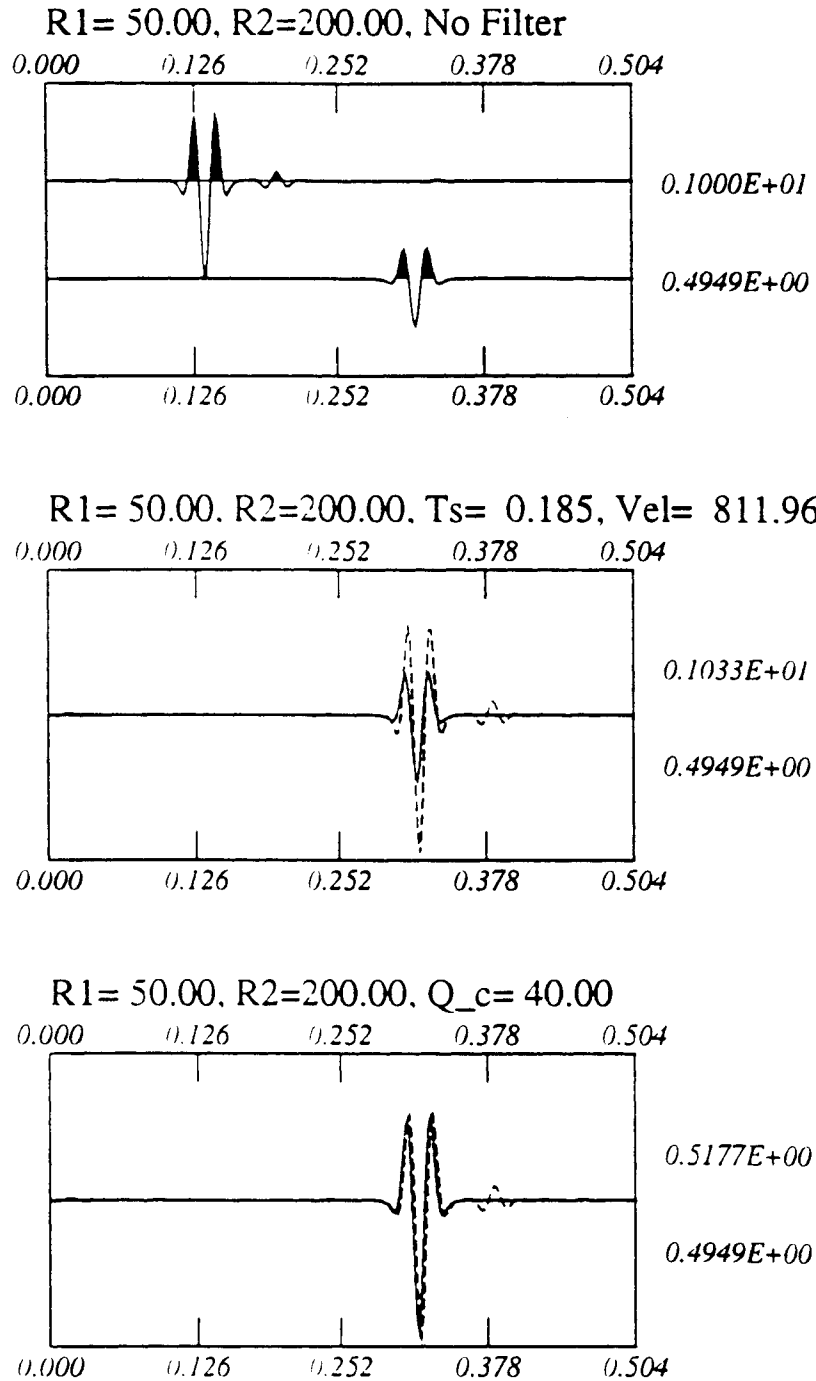
**Figure 8.A.3.B-17**

Same as Figure 8.A.3.B-14 but different depths between 50 and 150 feet.



**Figure 8.A.3.B-18**

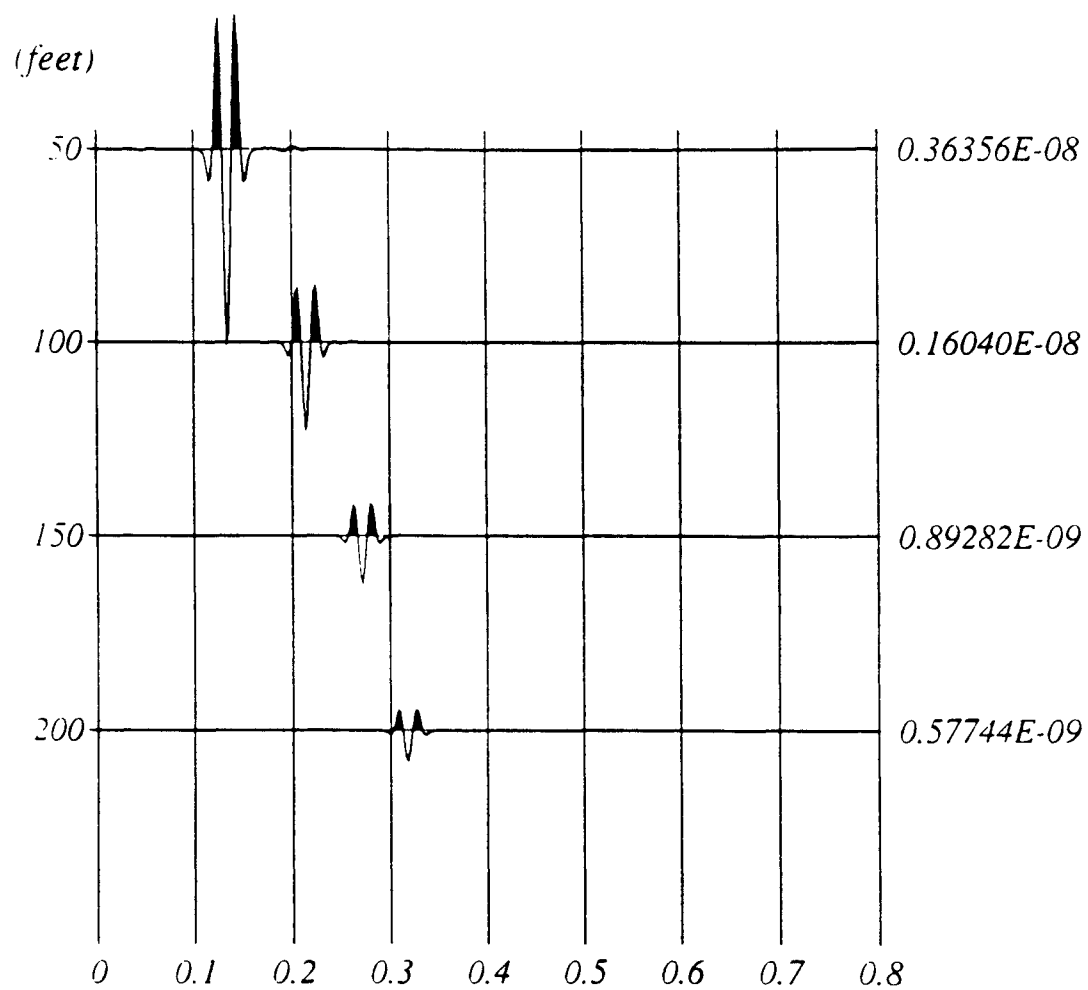
Same as Figure 8.A.3.B-15 with different depths between 50 and 150 feet. In this case we found that  $Q_s = 16$ .



**Figure 8.A.3.B-19**

Same as Figure 8.A.3.B-16 with different depths between 50 and 150 feet. The  $(1/r^{1.62})$  geometric correction needs to get exact results.

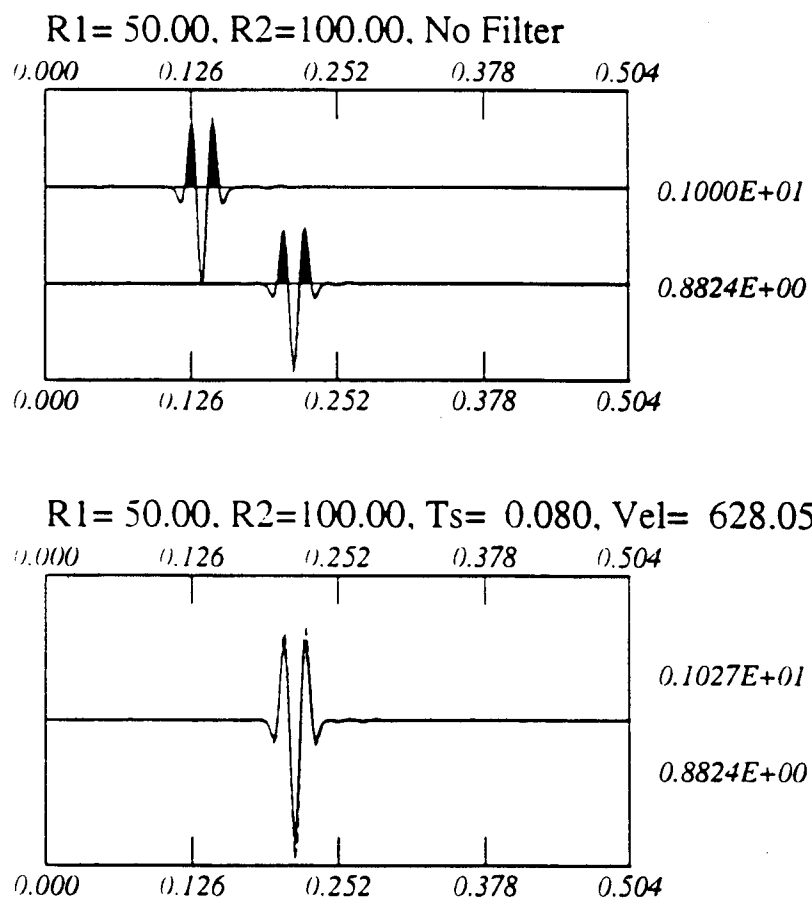




*test211.t*

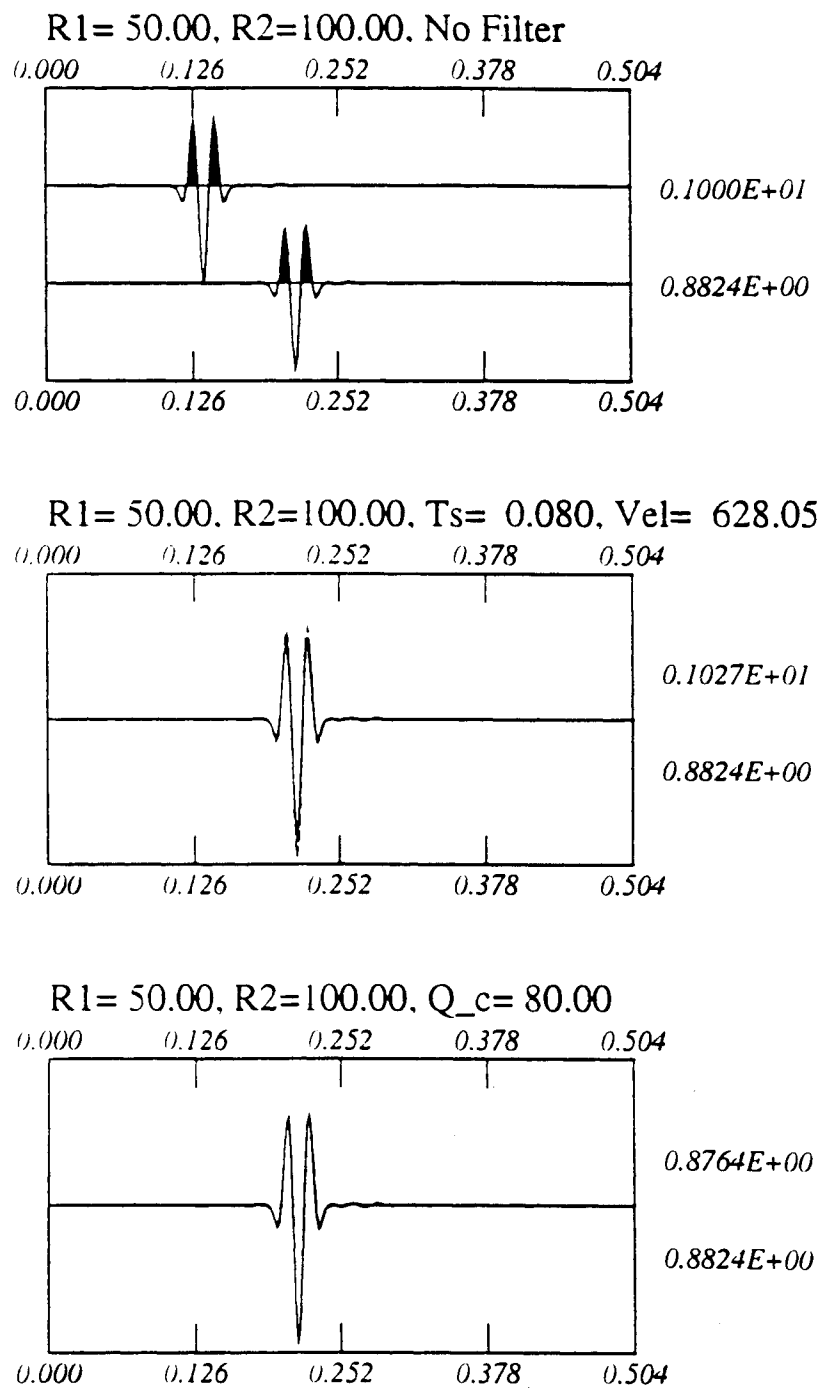
**Figure 8.A.3.B-20**

Synthetic seismograms are the same as in Figure 8.A.3.B-3, but the shear wave impedance contrasts between the layers are negligible.



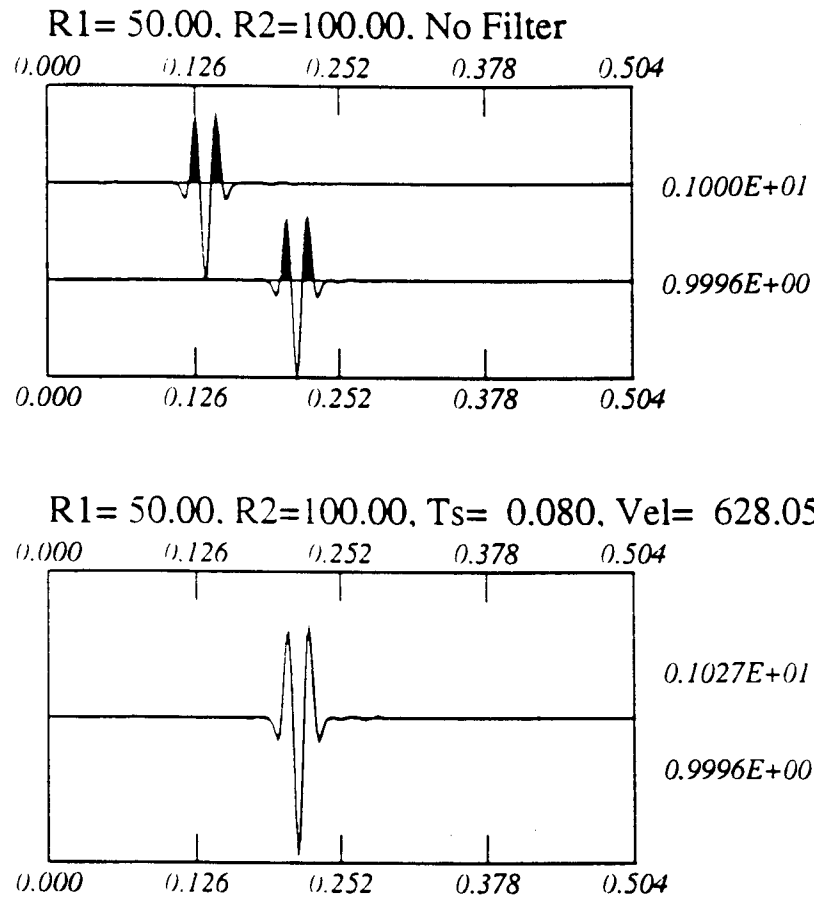
**Figure 8.A.3.B-21**

Same as Figure 8.A.3.B-4 for the zero-impedence model.



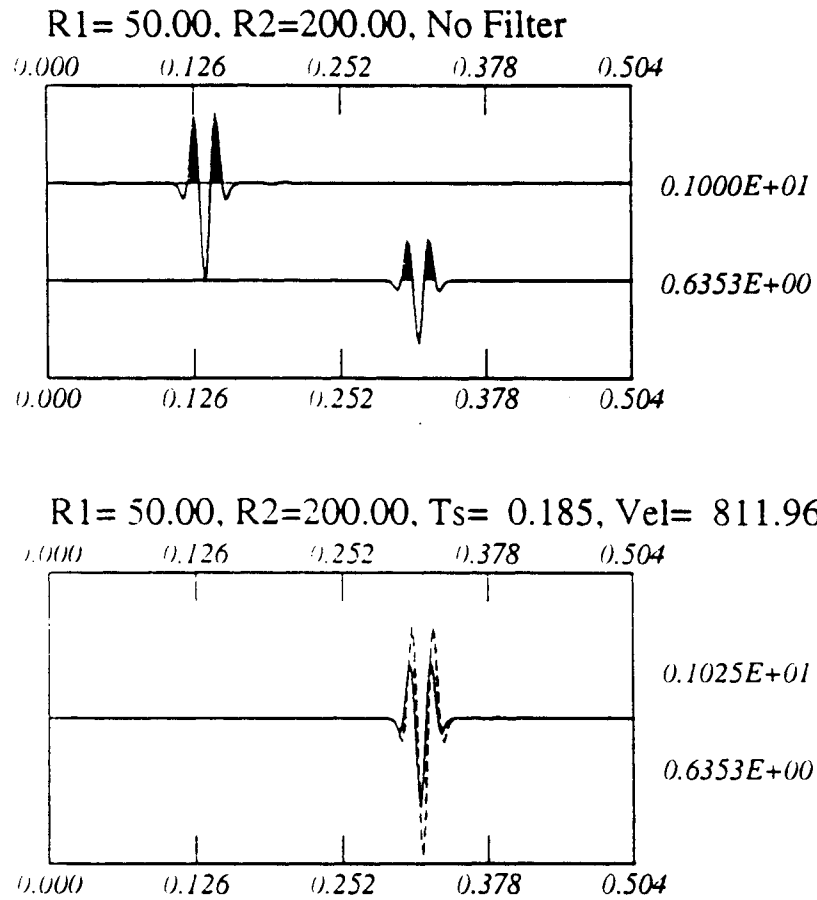
**Figure 8.A.3.B-22**

Same as Figure 8.A.3.B-5 for the zero-impedence model. Here we estimated  $Q_s = 80$  for the non-intrinsic Q model.

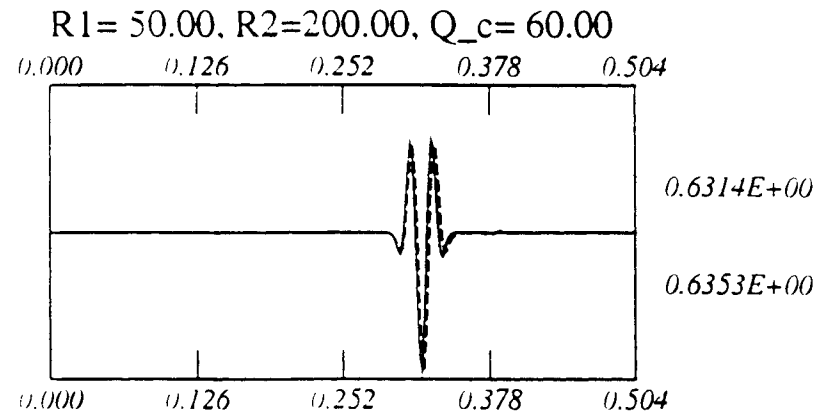
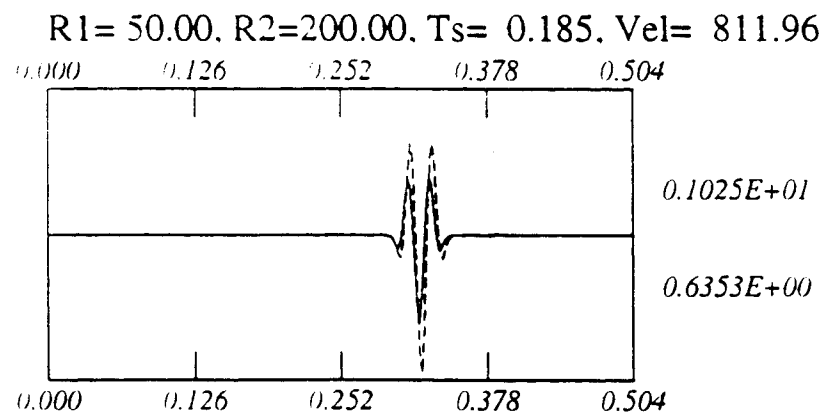
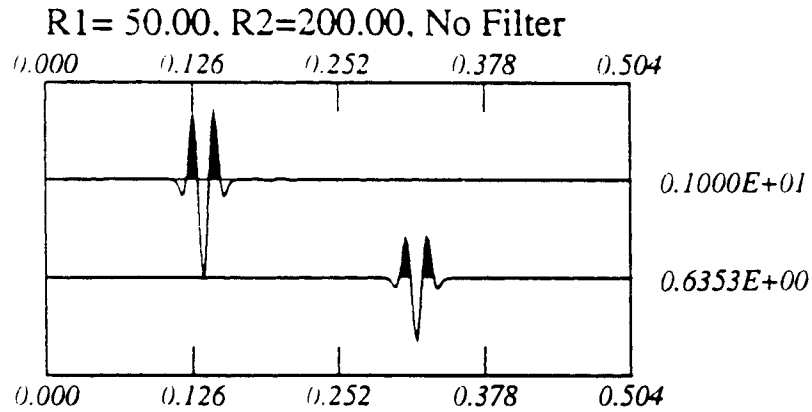


**Figure 8.A.3.B-23**

Same as Figure 8.A.3.B-6 for the zero-impedence model. The  $(1/r^{1.18})$  geometric correction is required to explain the propagation between 50 and 100 feet.

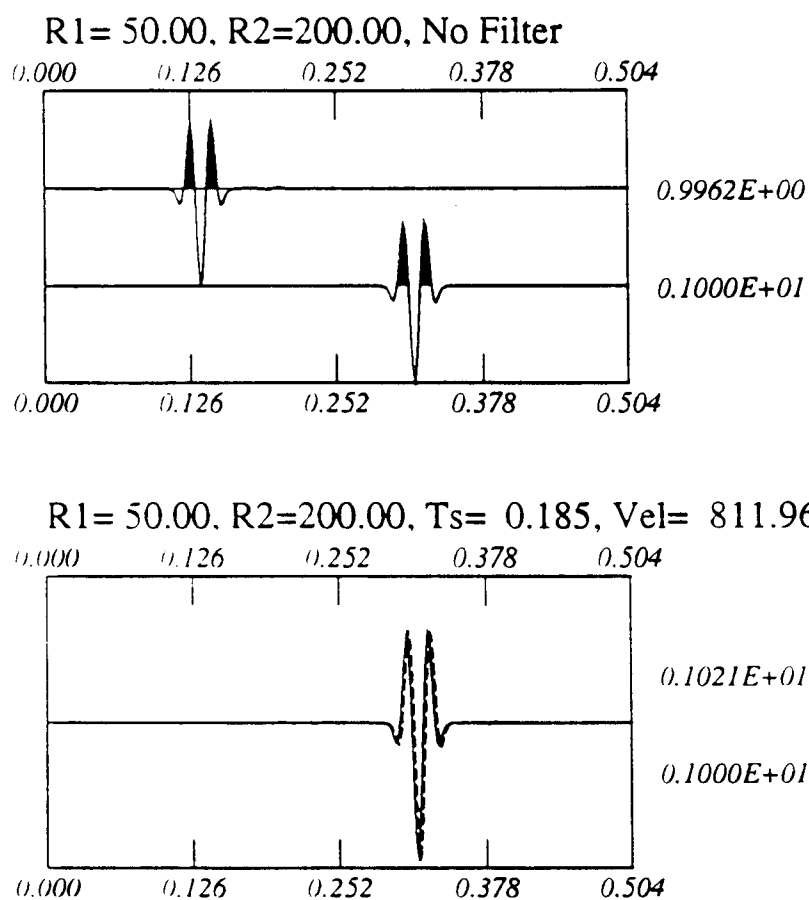


**Figure 8.A.3.B-24**  
Same as Figure 8.A.3.B-21 for depths between 50 and 200 feet.



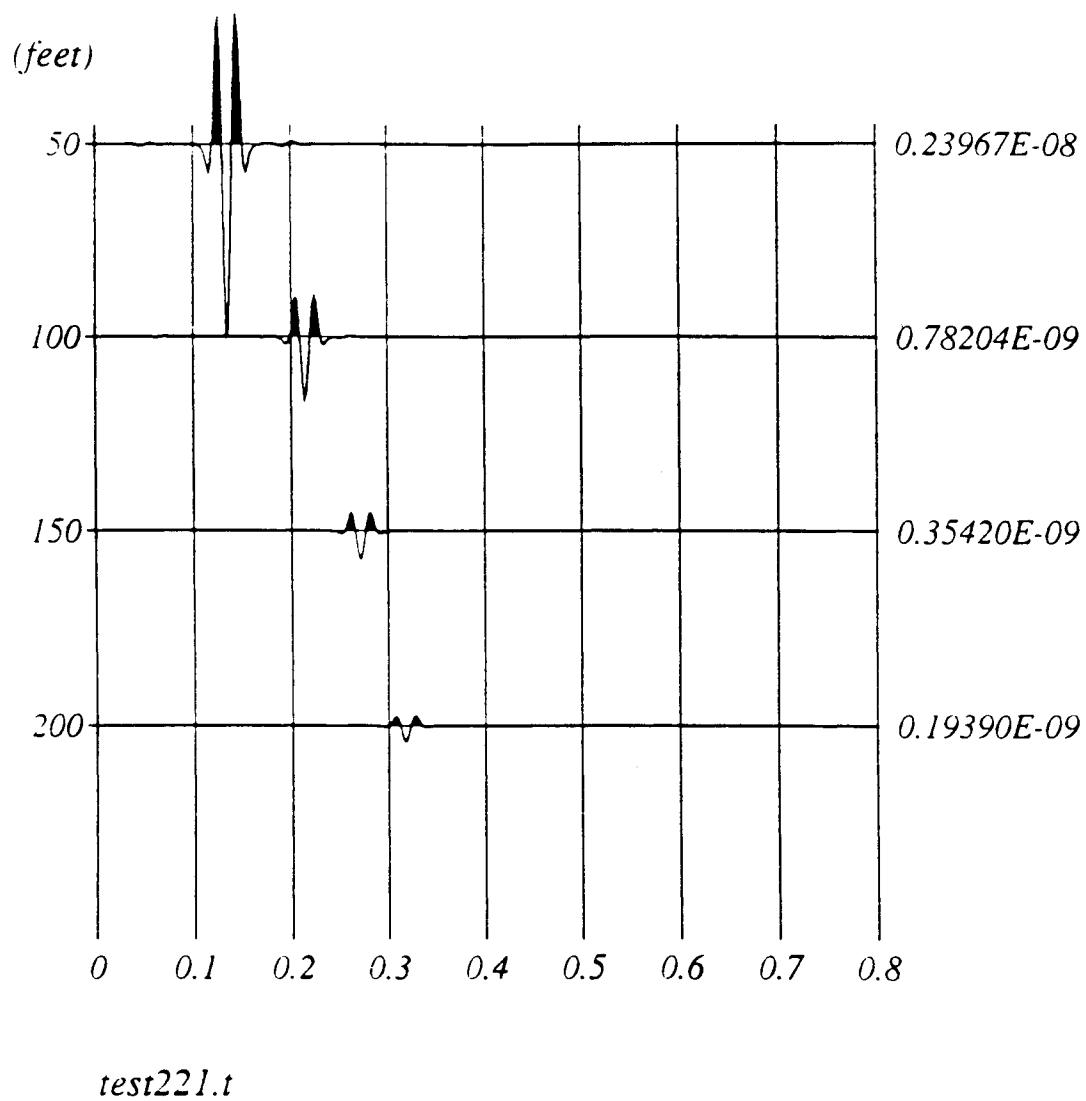
**Figure 8.A.3.B-25**

Same as Figure 8.A.3.B-22 for depths between 50 and 200 feet. Here we estimated  $Q_s = 60$  for the non-intrinsic model.



**Figure 8.A.3.B-26**

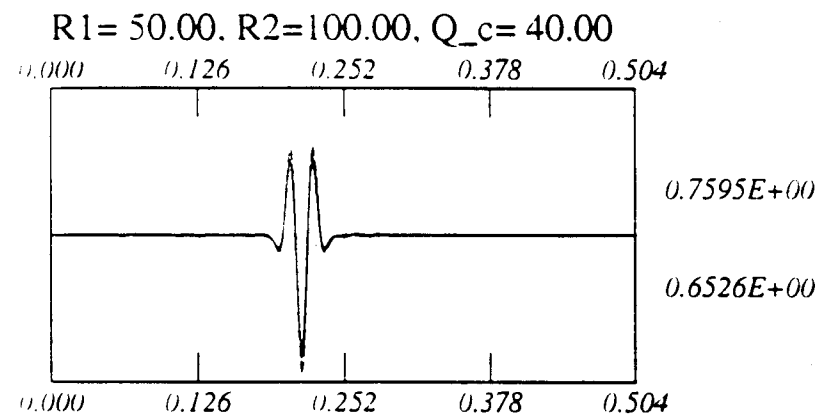
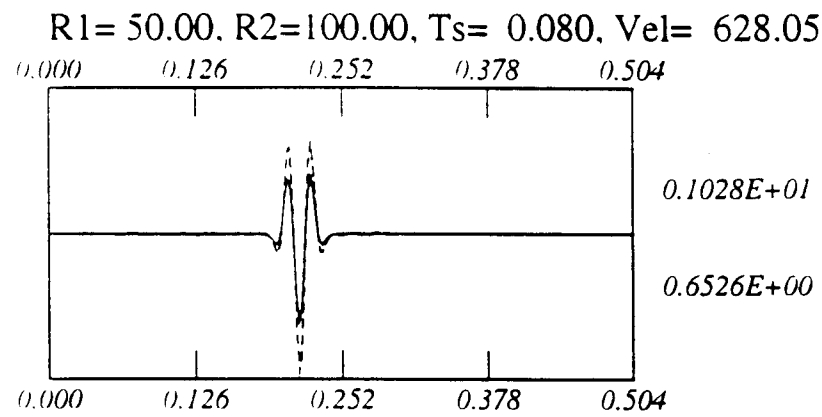
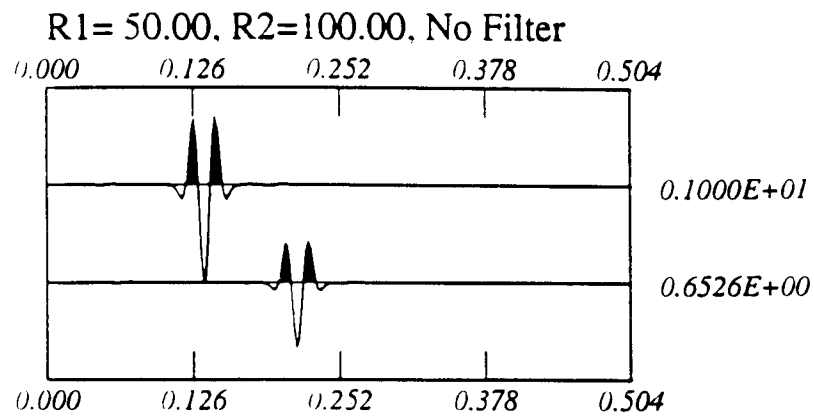
Same as Figure 8.A.3.B-23 for depths between 50 and 200 feet. Here we estimated the  $(1/r^{1.33})$  geometric spreading correction.



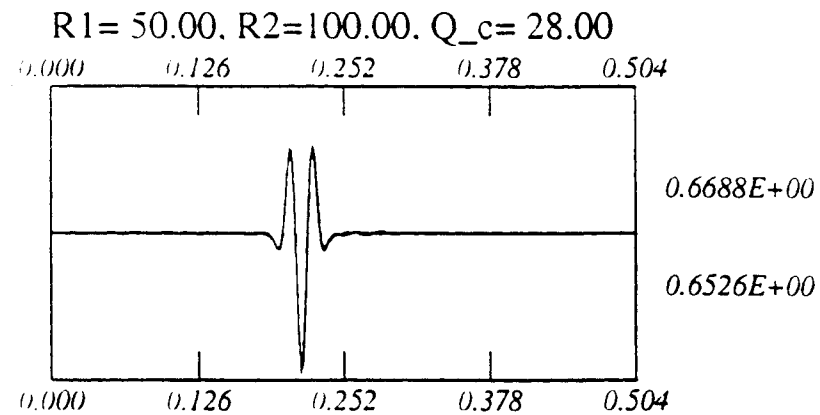
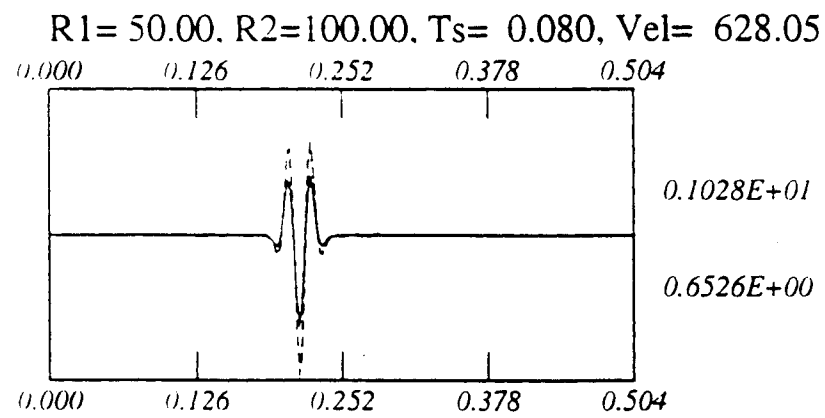
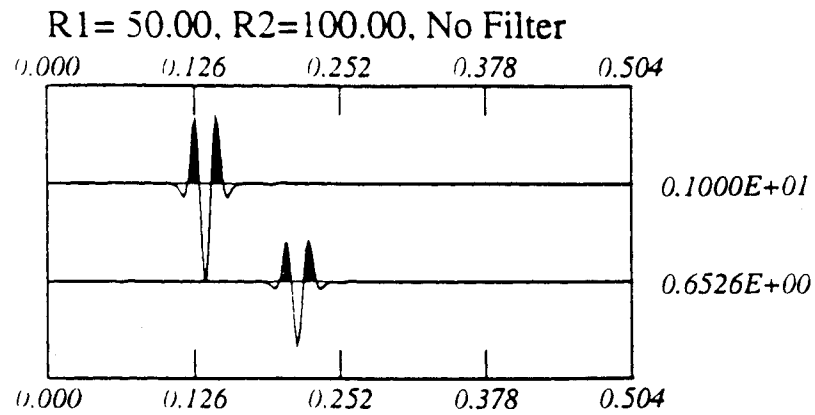
**Figure 8.A.3.B-27**

Synthetic seismograms (same as Figure 8.A.3.B-20) with  $Q$  ( $Q_p = 80$  and  $Q_s = 40$ ).



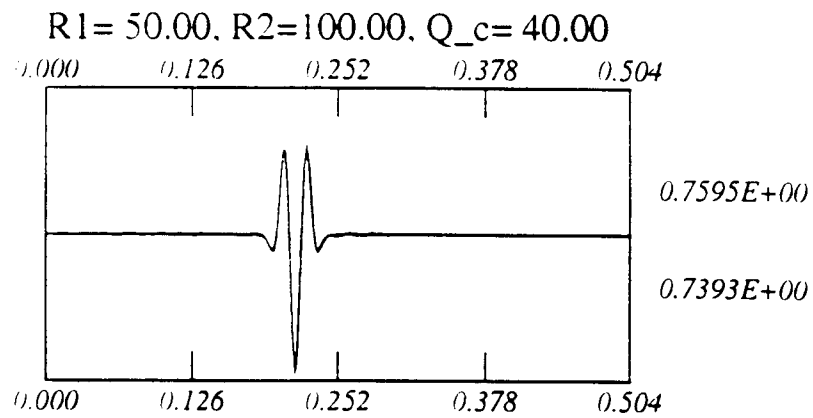
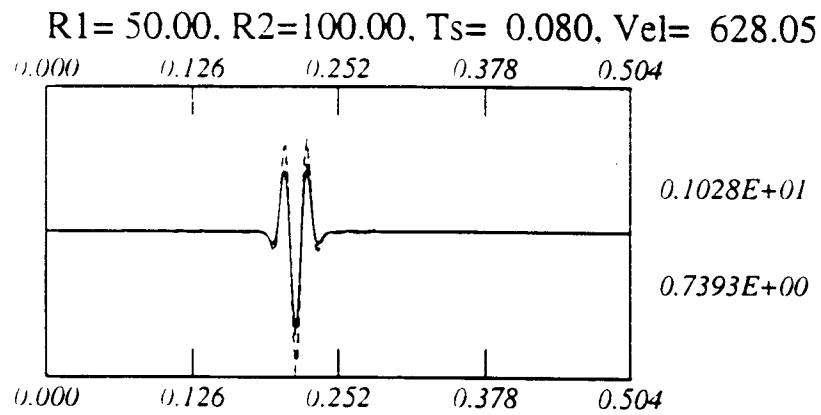
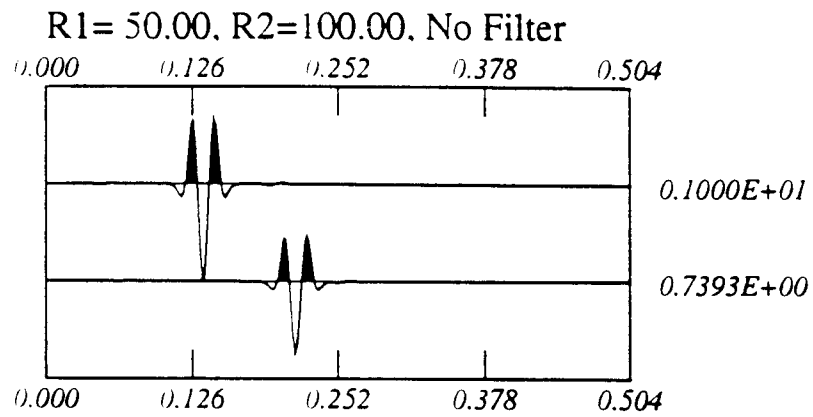


**Figure 8.A.3.B-28**  
Same as Figure 8.A.3.B-21 but for the attenuation model.



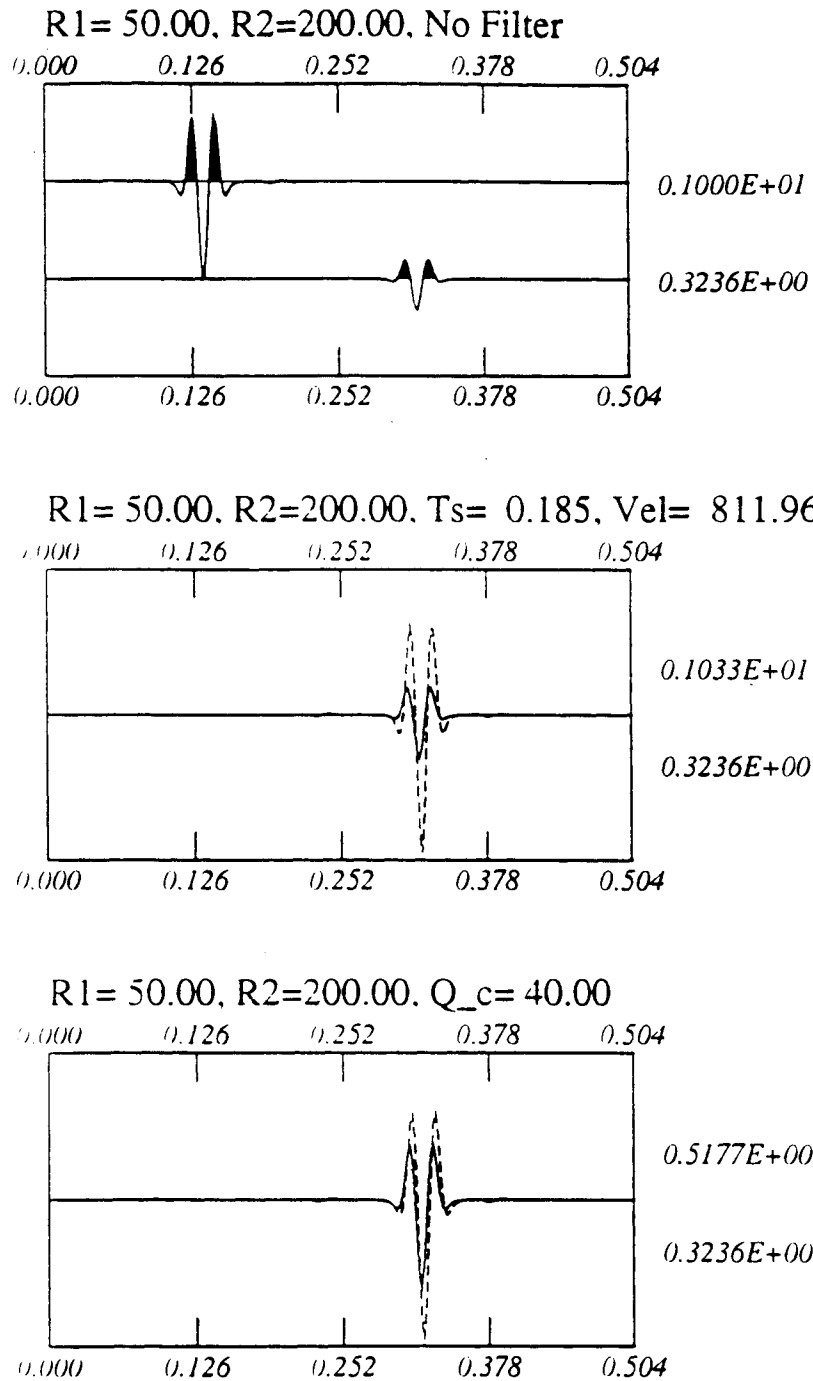
**Figure 8.A.3.B-29**

Same as Figure 8.A.3.B-22 but for the attenuation model. Here we estimated  $Q_s = 28$  instead of 40.

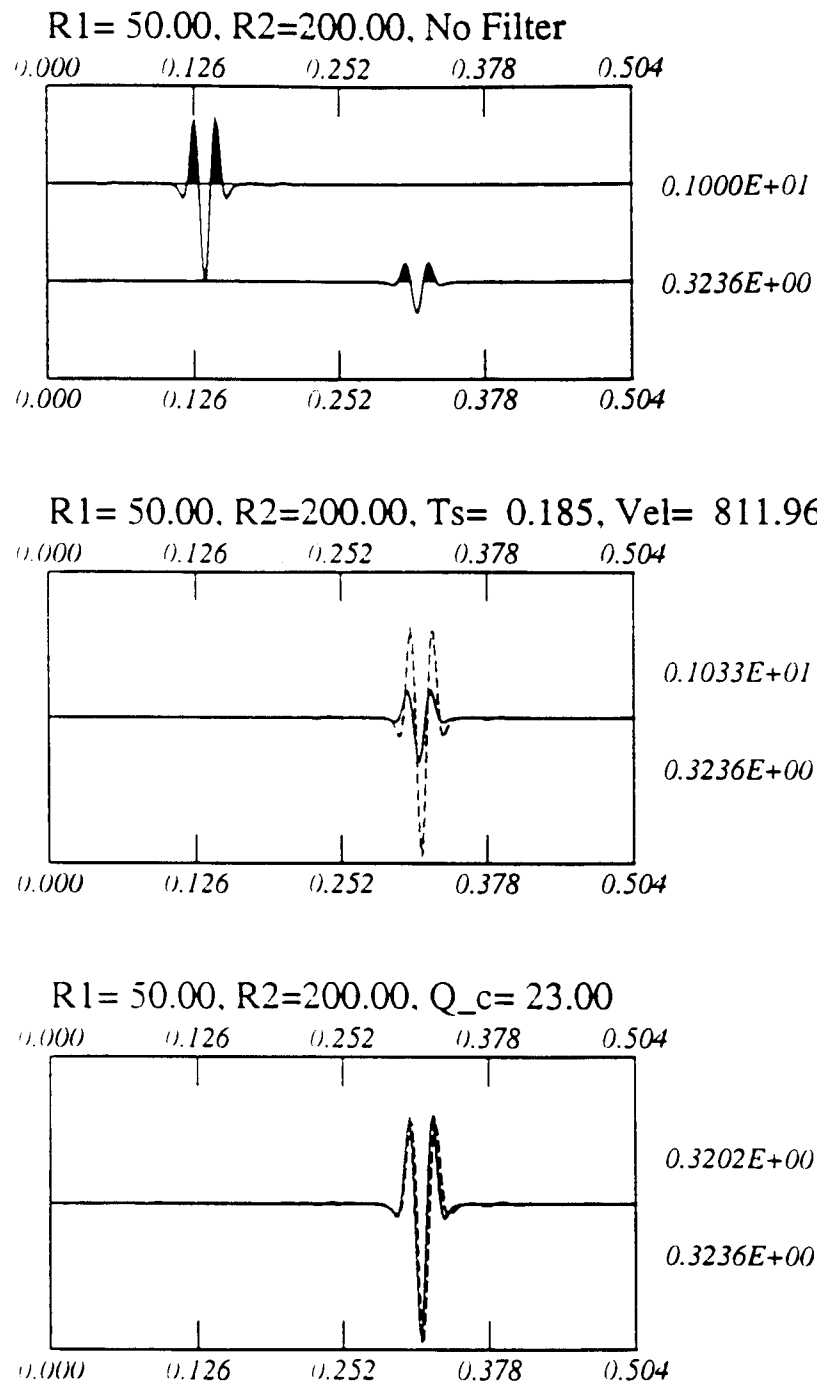


**Figure 8.A.3.B-30**

Same as Figure 8.A.3.B-23 but for the attenuation model. The  $(1/r^{1.18})$  geometrical spreading needs to estimate the correct Q values.

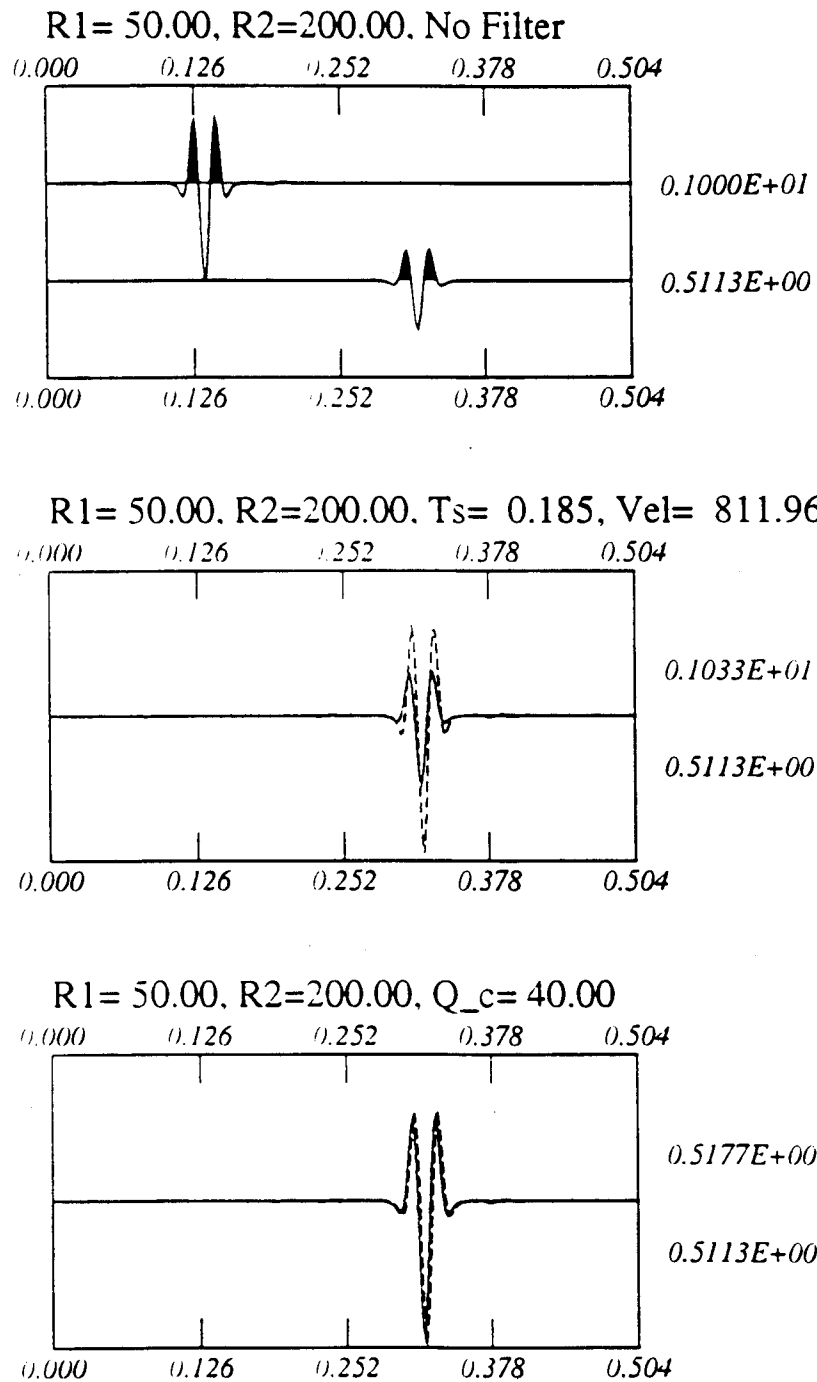


**Figure 8.A.3.B-31**  
Same as Figure 8.A.3.B-24 but for the attenuation model.



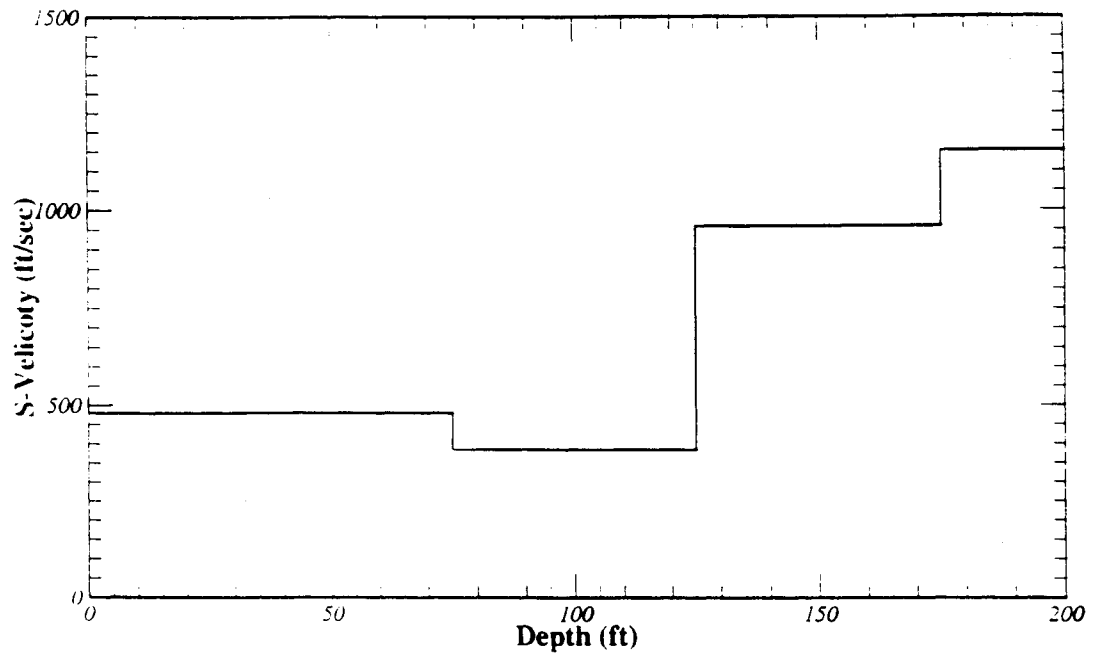
**Figure 8.A.3.B-32**

Same as Figure 8.A.3.B-25 but for the attenuation model. Here we estimated  $Q_s = 23$  instead of 40.

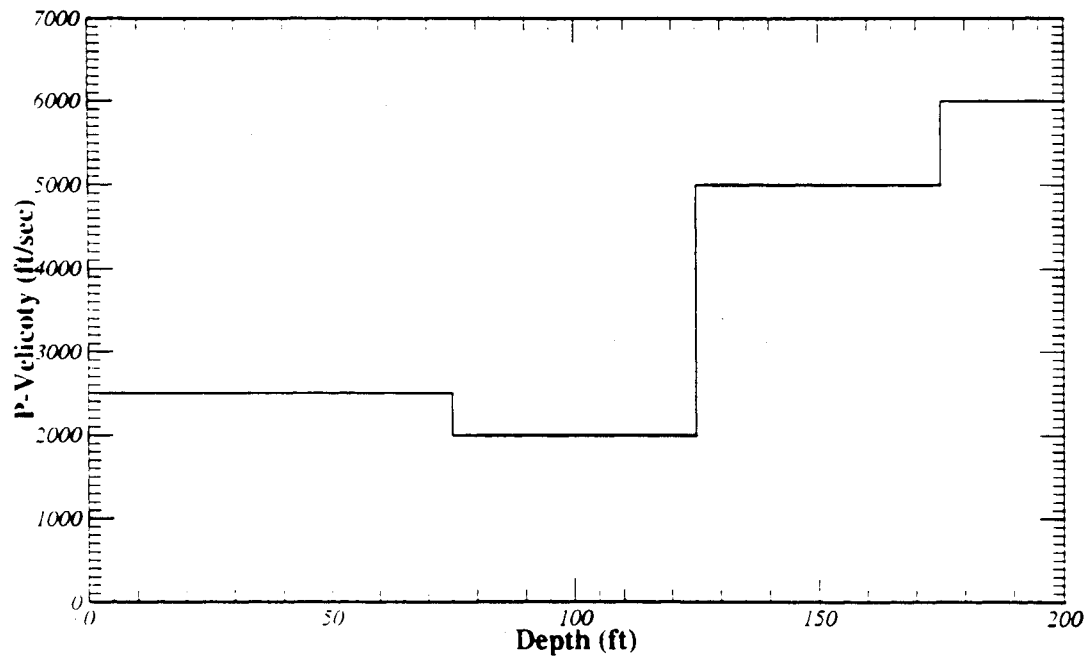


**Figure 8.A.3.B-33**

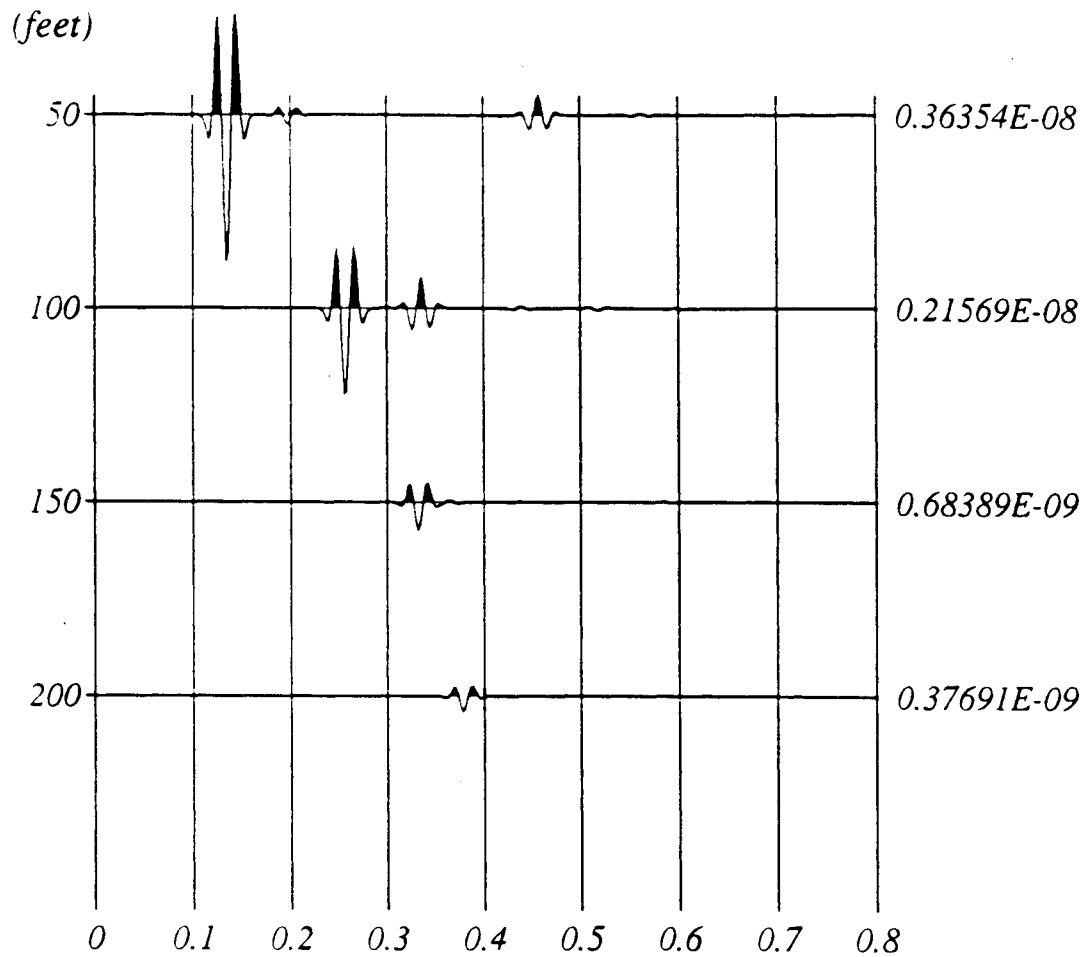
Same as Figure 8.A.3.B-26 but for the attenuation model. The  $(1/r^{1.33})$  geometrical spreading needs to estimate the correct Q values.



mod-test31



**Figure 8.A.3.B-34**  
Velocity model for a low-velocity layer example.

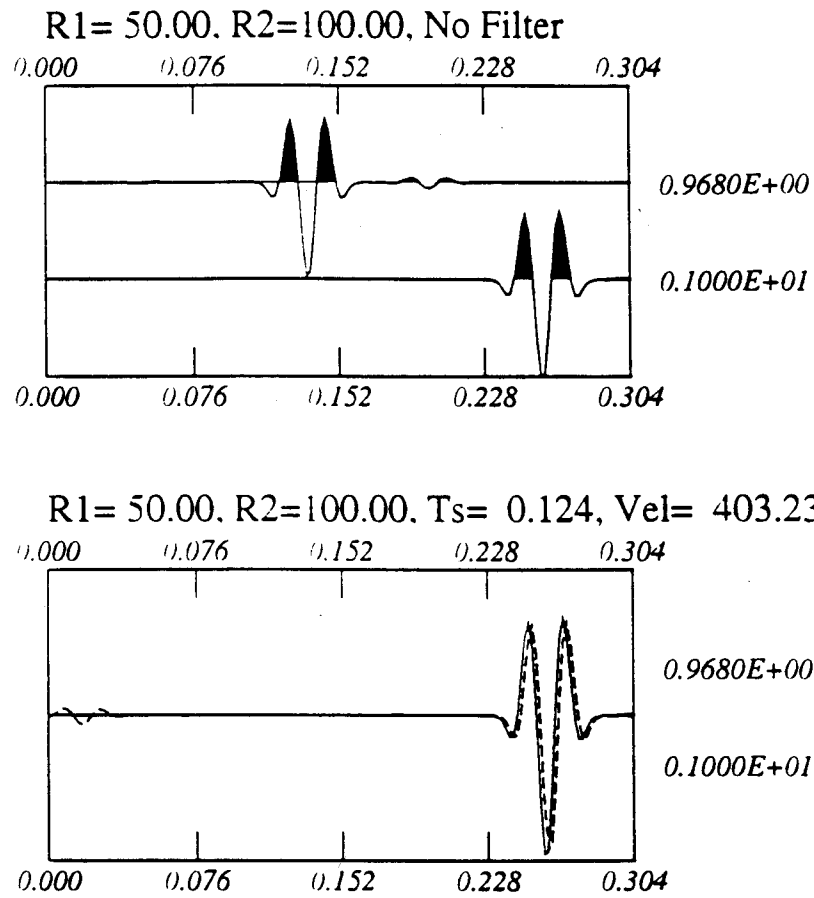


*test311.t*

**Figure 8.A.3.B-35**

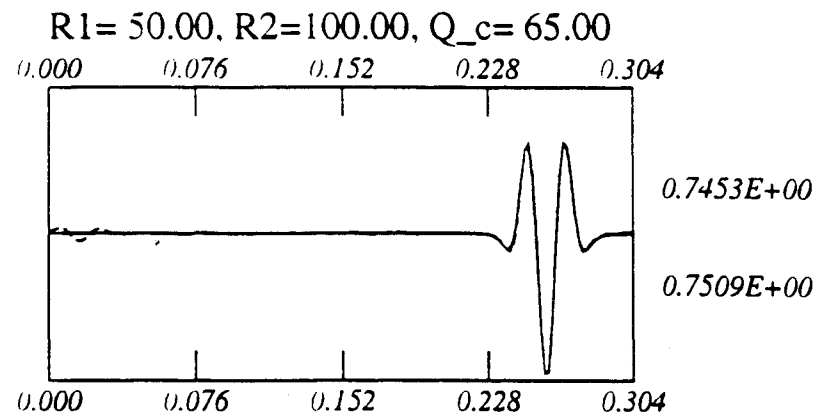
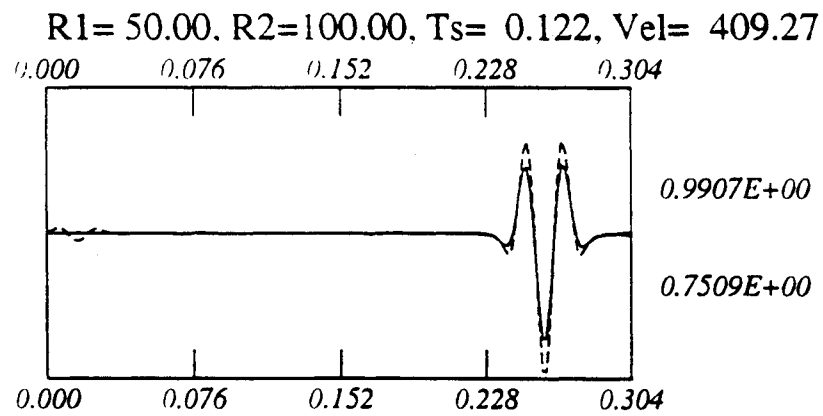
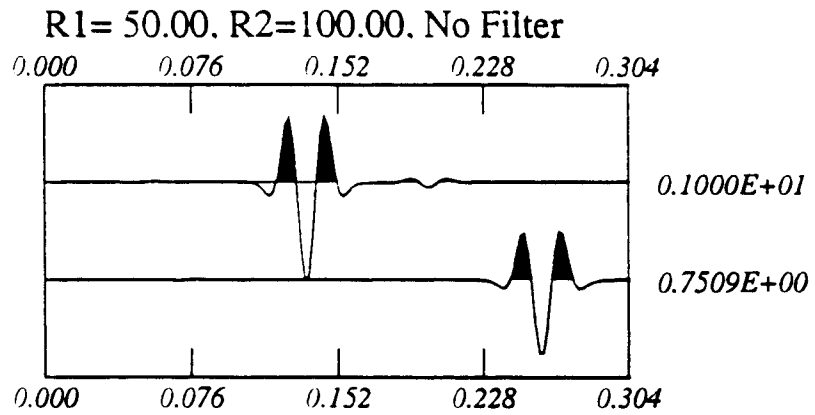
Synthetic seismograms for the model for the low-velocity layer test model as shown in Figure 8.A.3.B-34. There is no intrinsic attenuation in this computation.





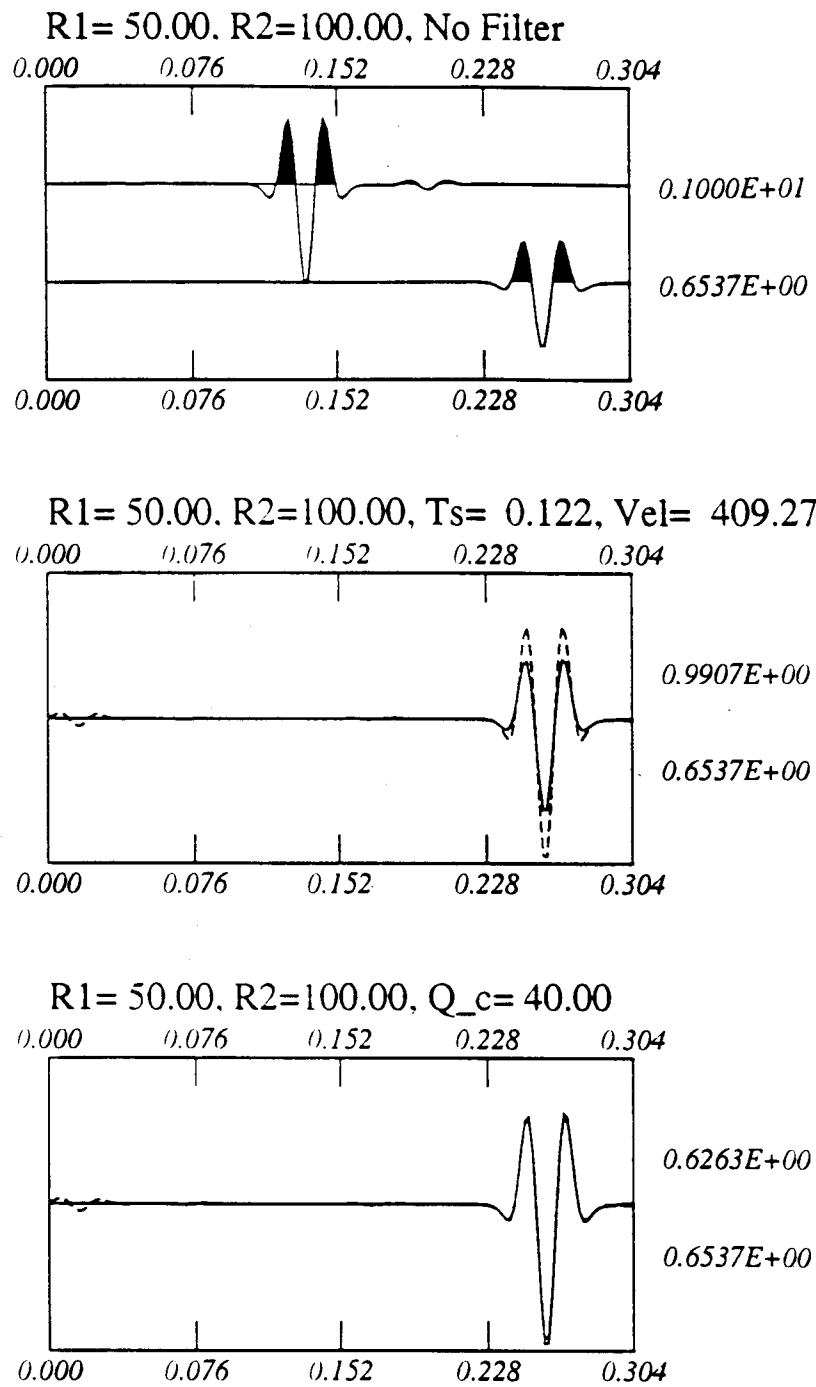
**Figure 8.A.3.B-36**

The  $(1/r^{0.8})$  geometric correction needed to explain the propagation between the depths of 50 and 100 ft for the low-velocity layer model.



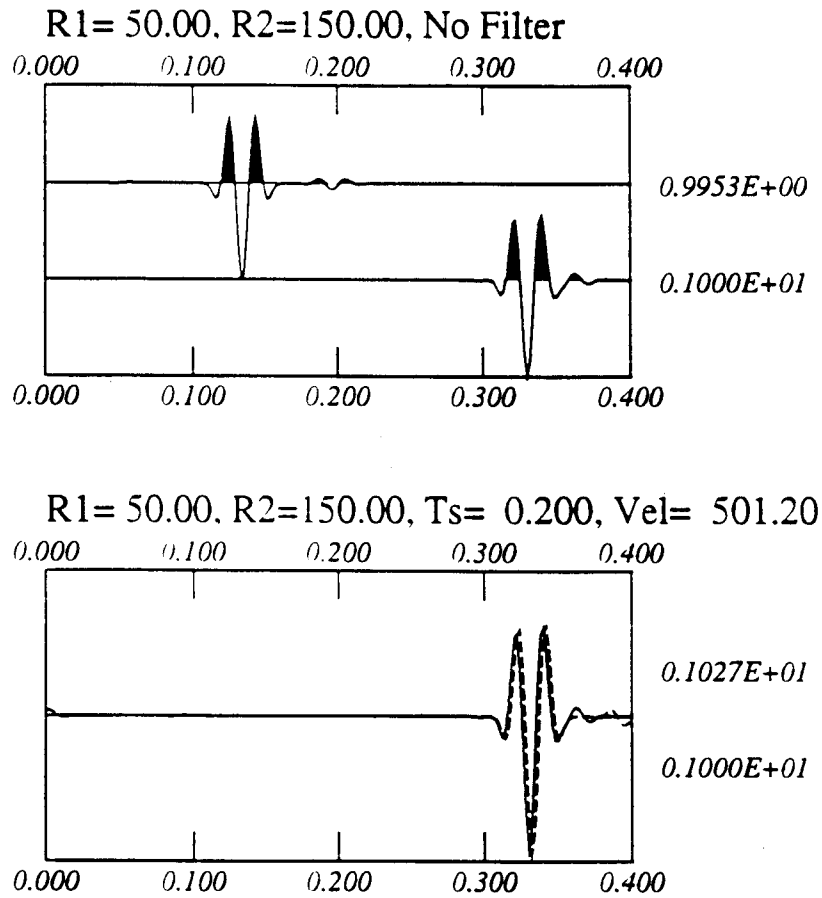
**Figure 8.A.3.B-37**

Estimates  $Q = 65$  instead of  $Q = 40$  for the  $(1/r)$  geometric spreading correction. In this case the attenuation model is used in computation.



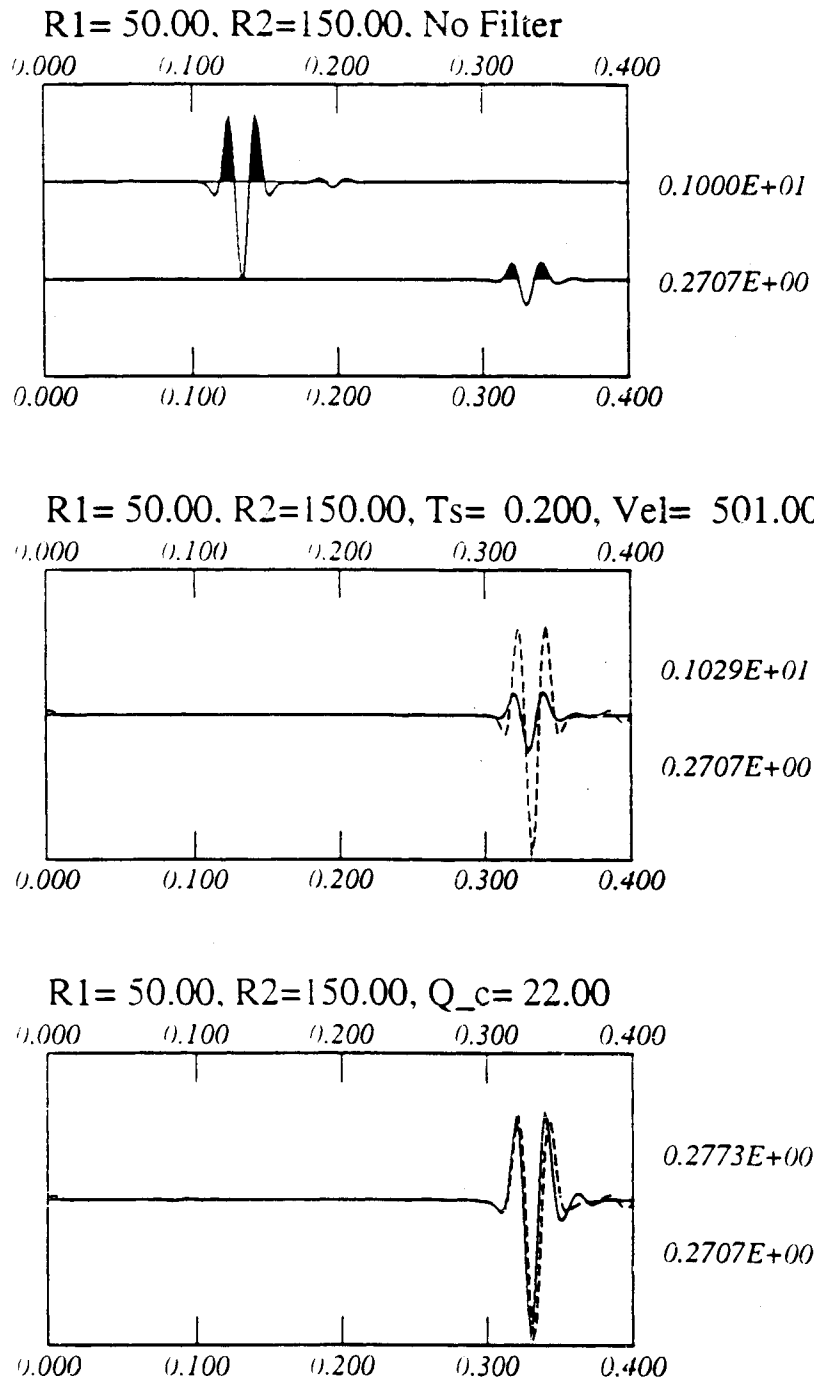
**Figure 8.A.3.B-38**

Shows the proper use of the geometric spreading and of the Q model to explain the propagation between depths of 50 and 100 feet.



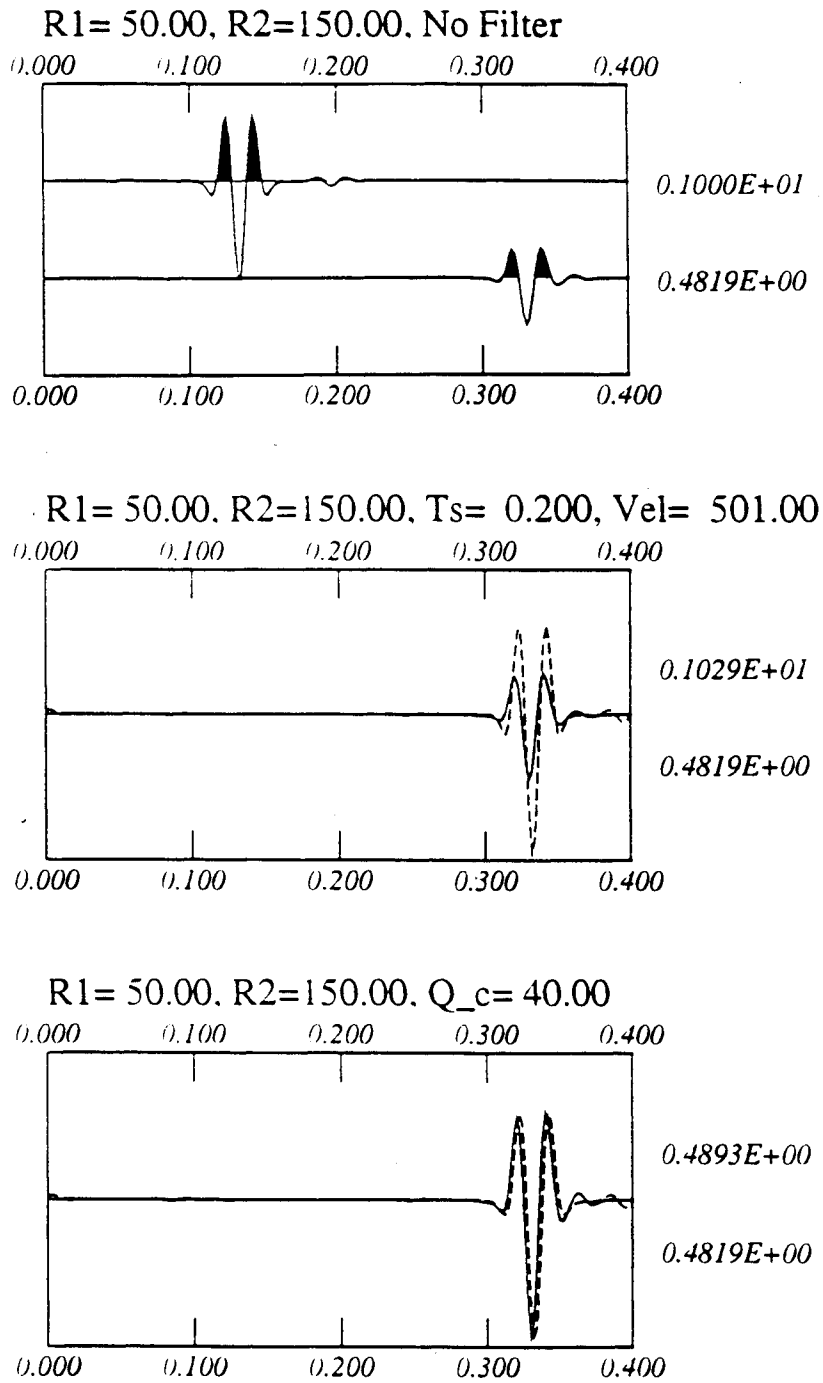
**Figure 8.A.3.B-39**

Same as Figure 8.A.3.B-36 for the propagation between depths of 50 and 150 feet. Note that the 50 and 150 feet depth receivers are in a higher-velocity layer than the in between low-velocity layer (Figure 8.A.3.B-34). In this case the  $(1/r^{1.525})$  geometric spreading is needed to explain the propagation.



**Figure 8.A.3.B-40**

Same as Figure 8.A.3.B-37. Here the  $(1/r)$  spreading gives  $Q_s = 22$  instead of 40.

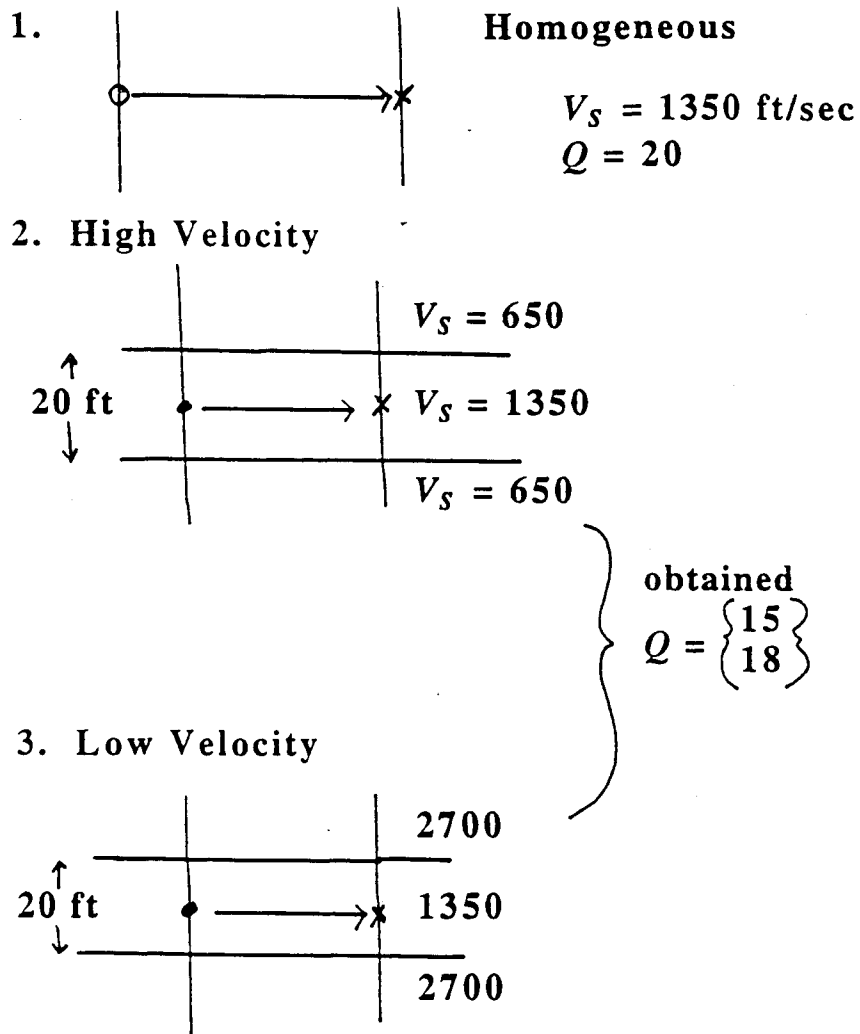


**Figure 8.A.3.B-41**

Same as Figure 8.A.3.B-38 but for propagation between the depths of 50 and 150 feet.

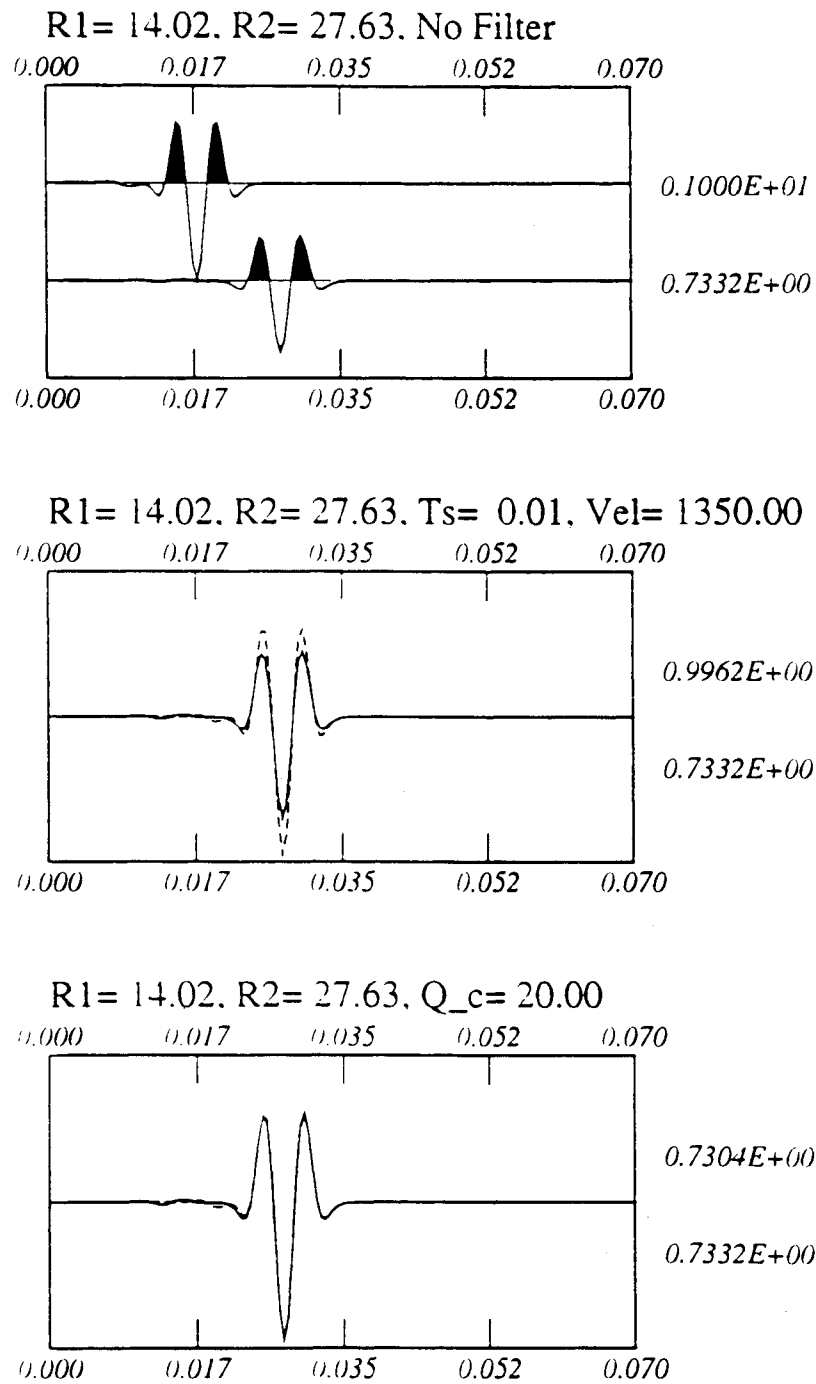
# SENSITIVITY TO LAYERING

## A. Cross-Hole



**Figure 8.A.3.B-42**

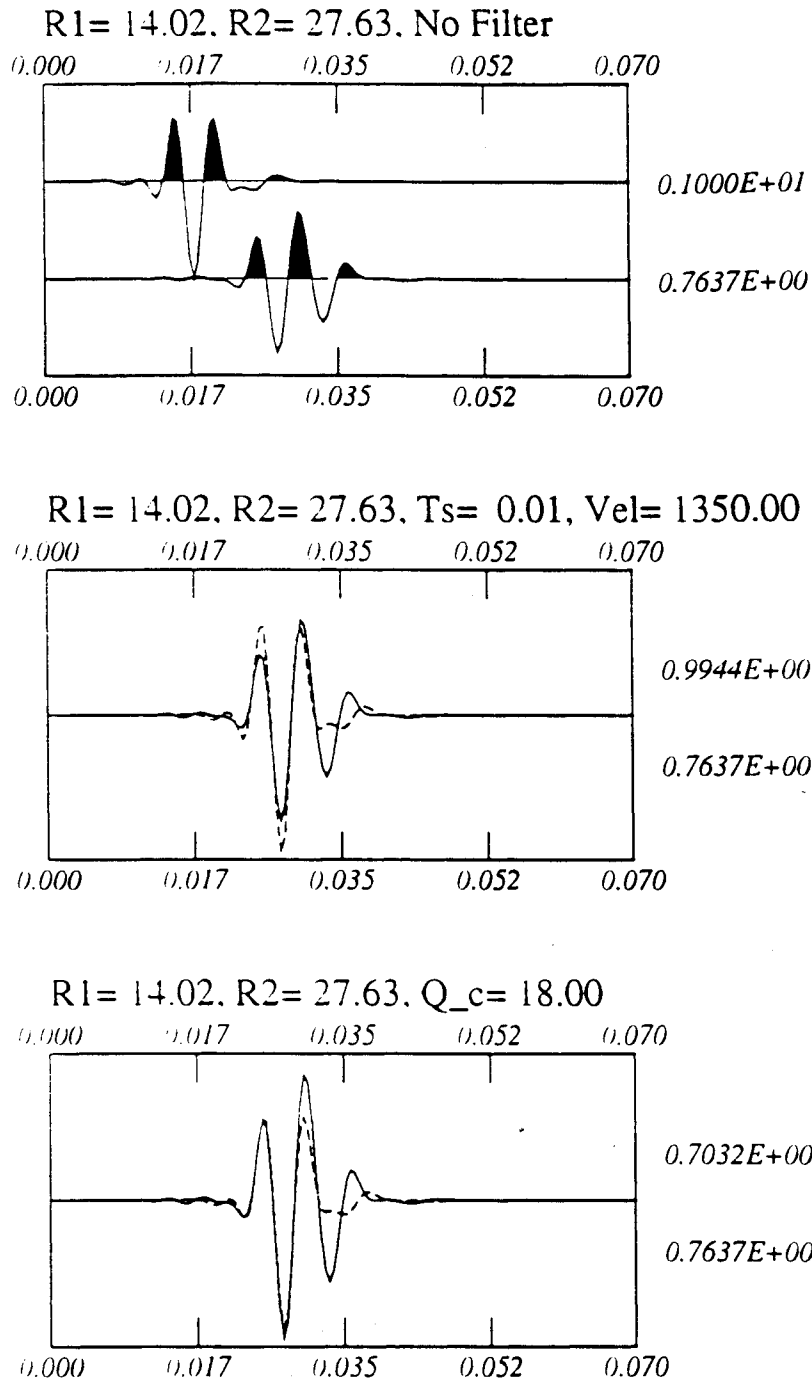
Schematic diagrams for crosshole synthetic tests. (1) Simple homogenous medium; (2) a 20 ft layer sandwiched between two low-velocity half-spaces; (3) same as (2) but two high-velocity half-spaces; and (4) a 10 ft thickness for models (2) and (3). The intrinsic attenuation used is  $Q_p = 40$  and  $Q_s = 20$ .



**Figure 8.A.3.B-43**

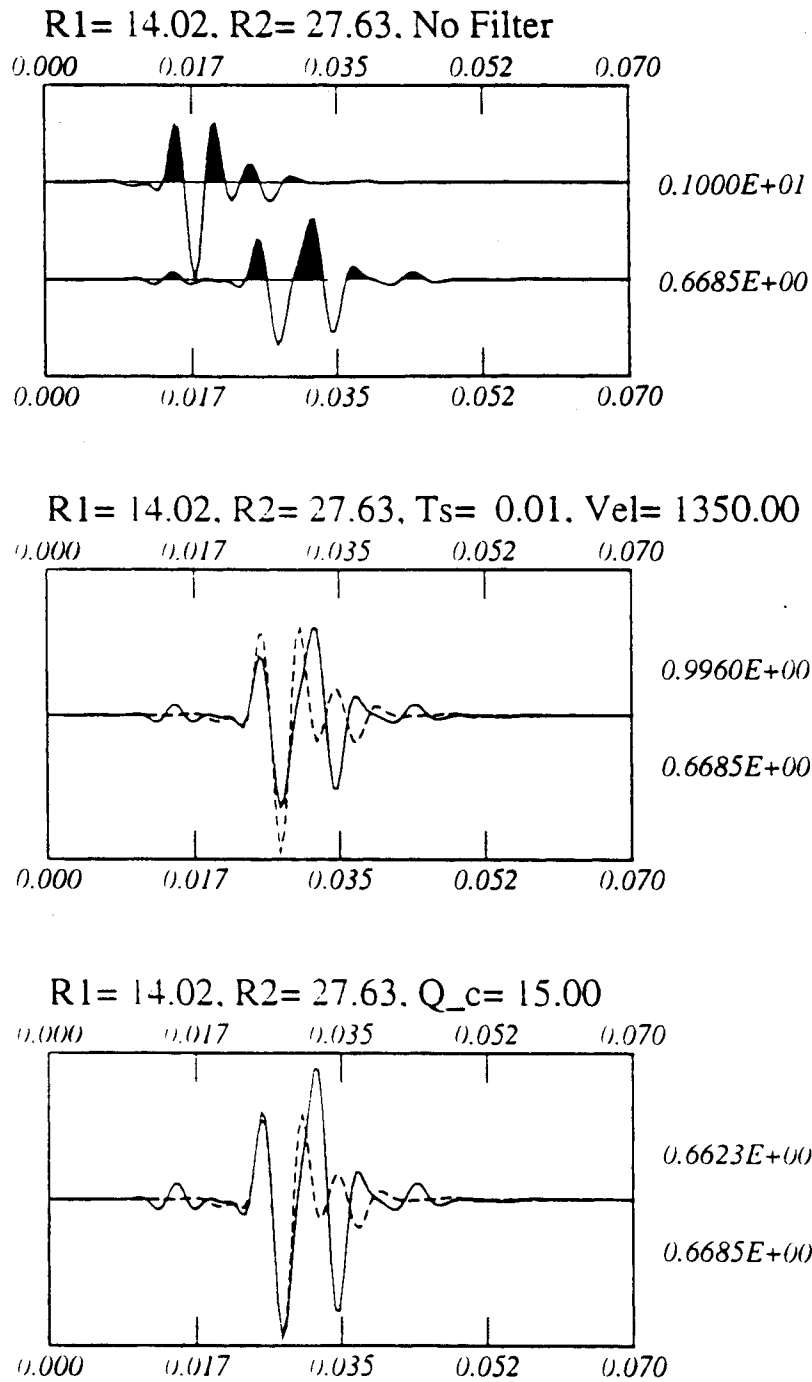
Estimates  $Q_s = 20$  exactly for the homogenous model between the horizontal propagation distances 14.02 and 27.63 feet.





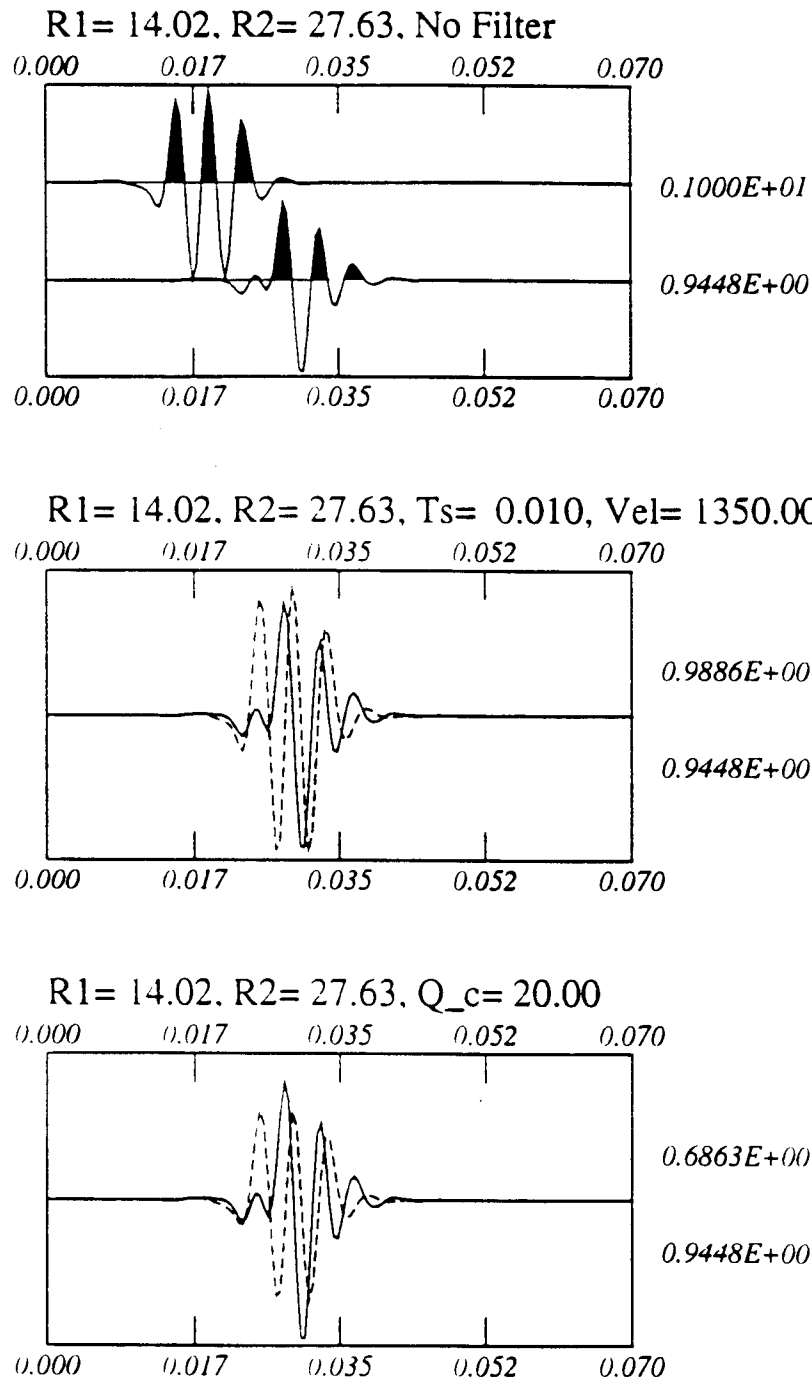
**Figure 8.A.3.B-44**

Estimates  $Q_s = 18$  instead of 20 for model (2) (low-high-low). Note that the signal is interfered with by a later arrival.



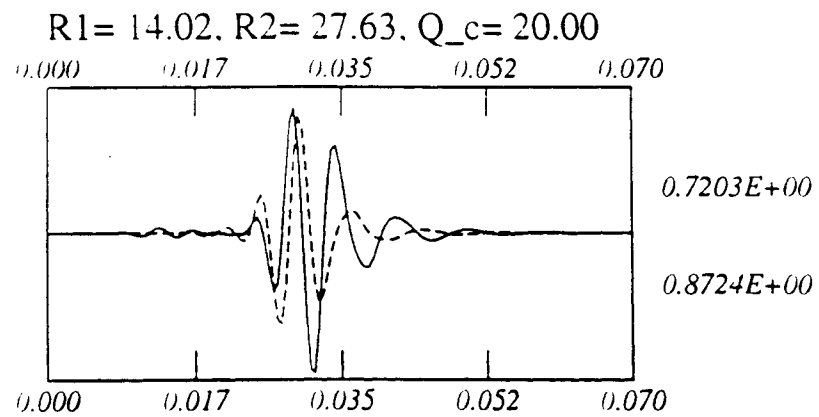
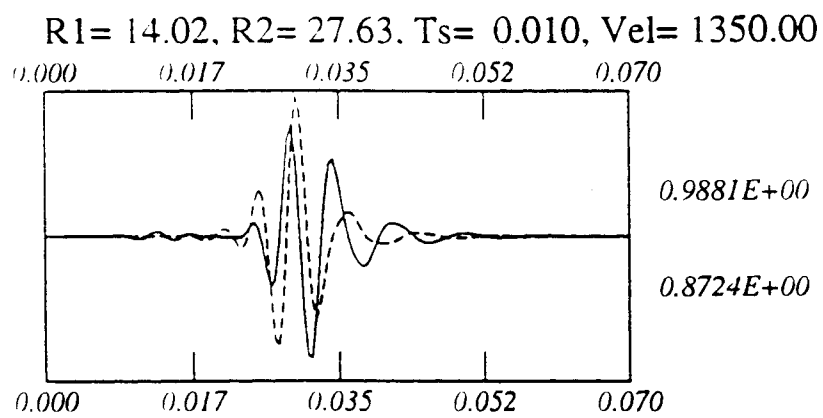
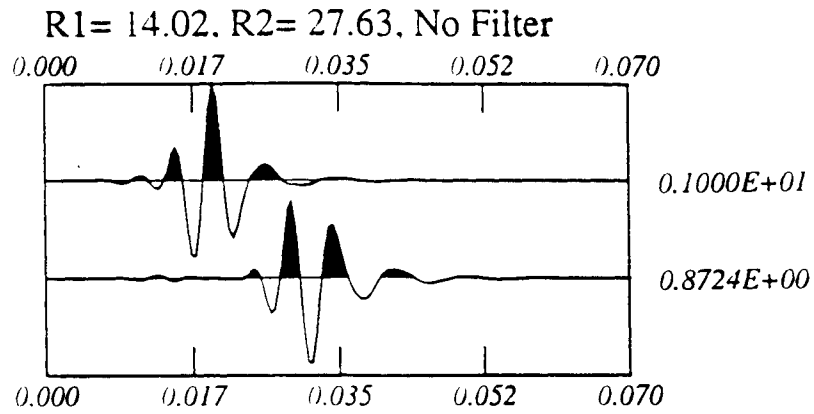
**Figure 8.A.3.B-45**

Estimates  $Q_s = 15$  for model (3) (high-low-high). The interference is more complicated than in Figure 8.A.3.B-44.



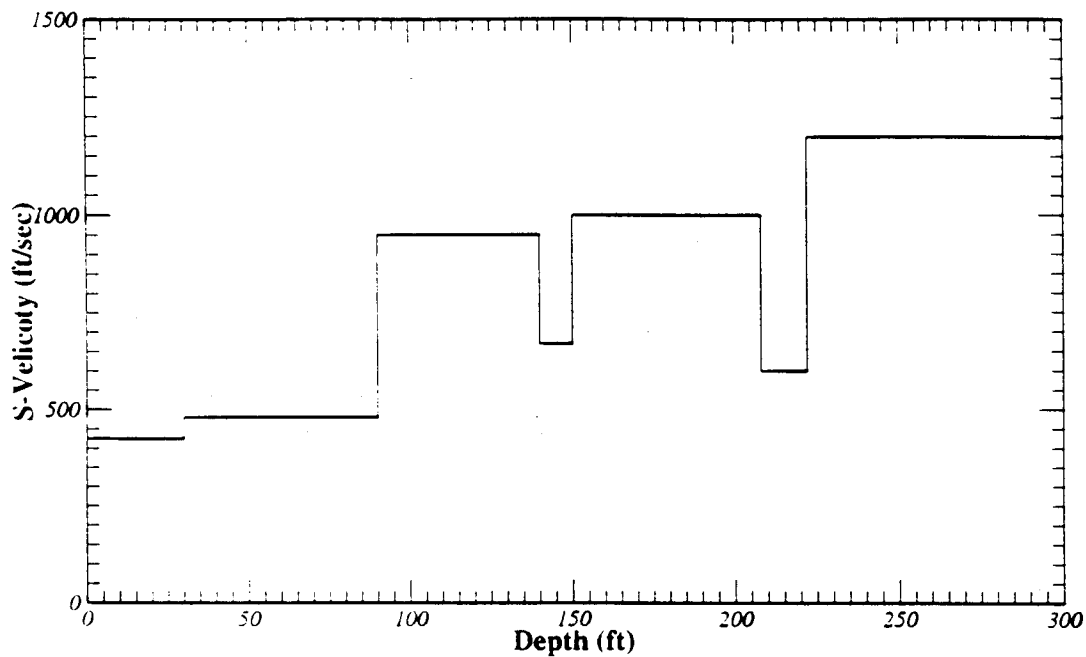
**Figure 8.A.3.B-46**

Could not be estimated due to a strong interference signal for model (4a) (low-10 feet high-low).

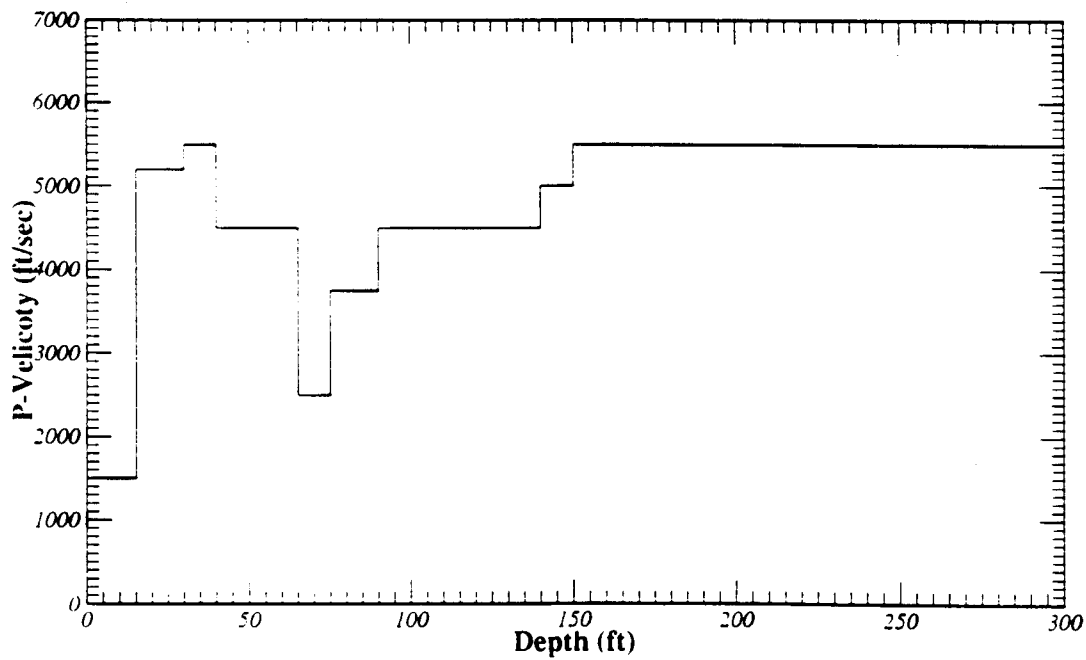


**Figure 8.A.3.B-47**

Could not be estimated due to a strong interference signal model (4b) (high-10 feet low-high).

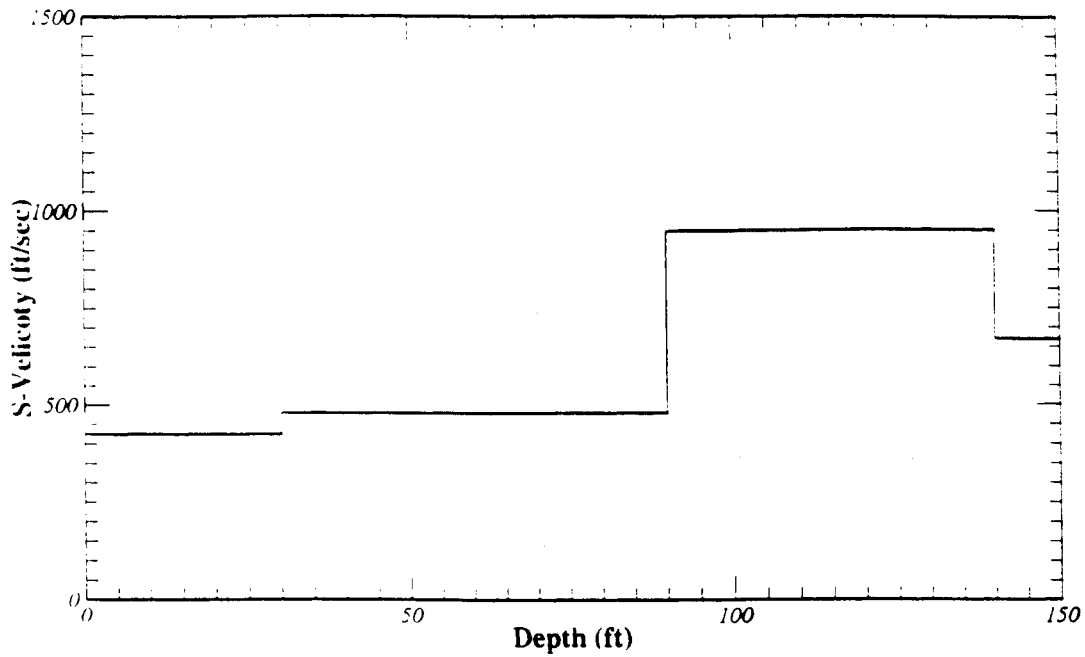


mod-treasure

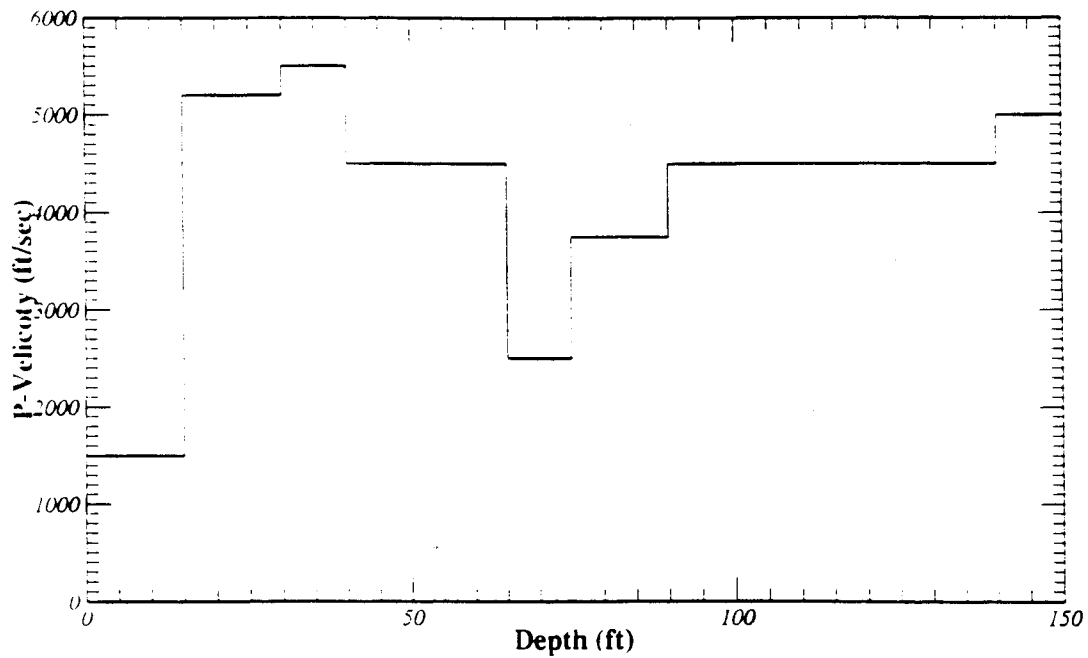


**Figure 8.A.3.B-48**

Velocity model for the Treasure Island site compiled from Redpath and USGS velocity data.

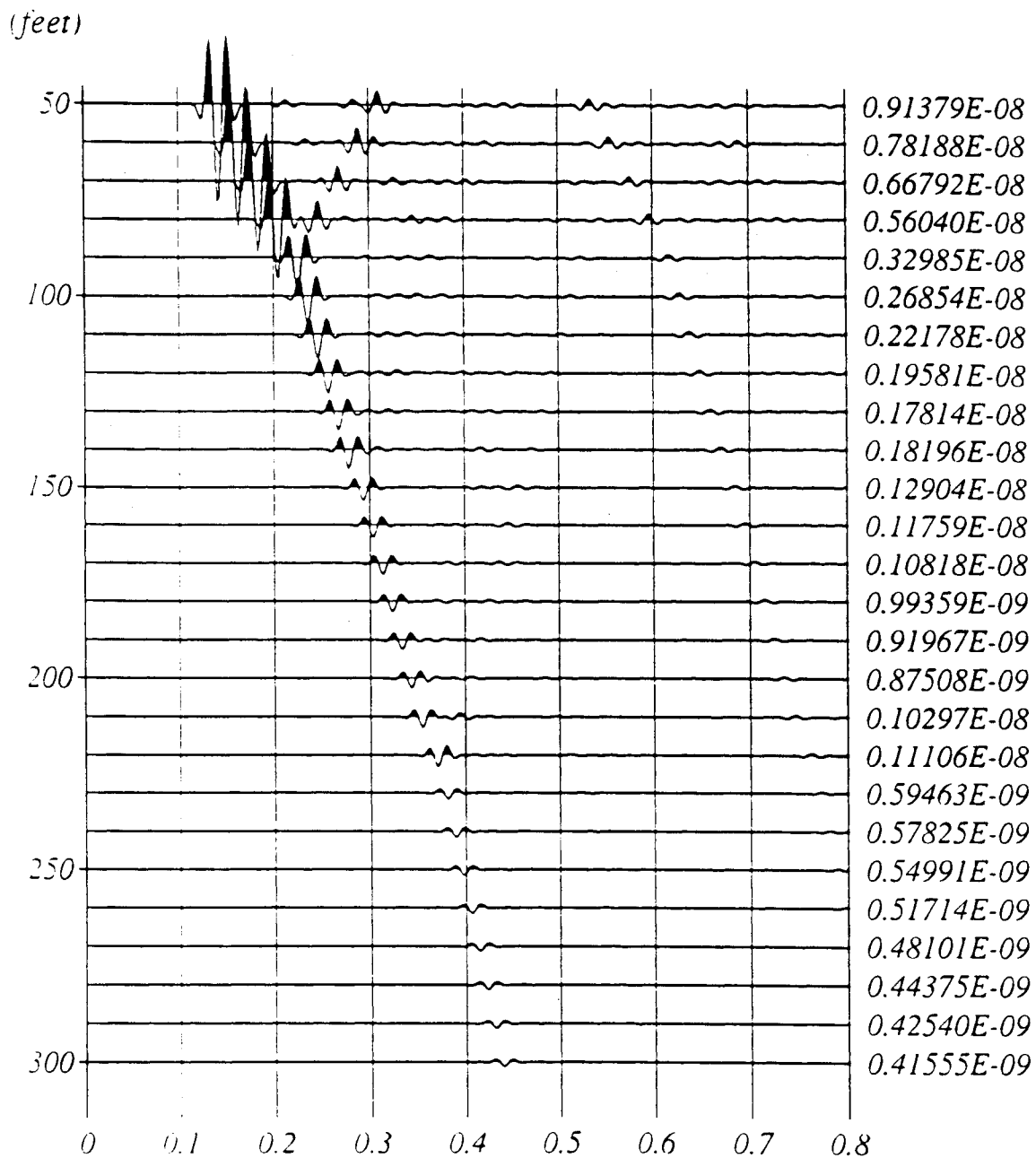


mod-treasure



**Figure 8.A.3.B-49**

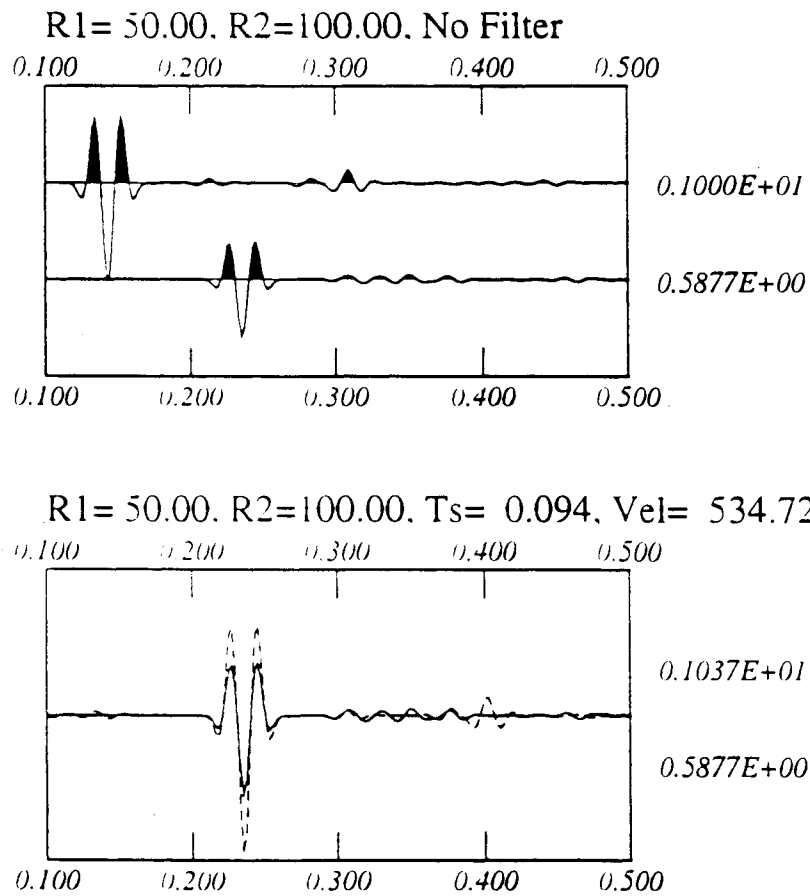
Same as Figure 8.A.3.B-48. The velocity model is shown in enhanced form between a depth of 0–150 feet.



*treasure03nql.t*,  $f_c = 50$  Hz

**Figure 8.A.3.B-50**

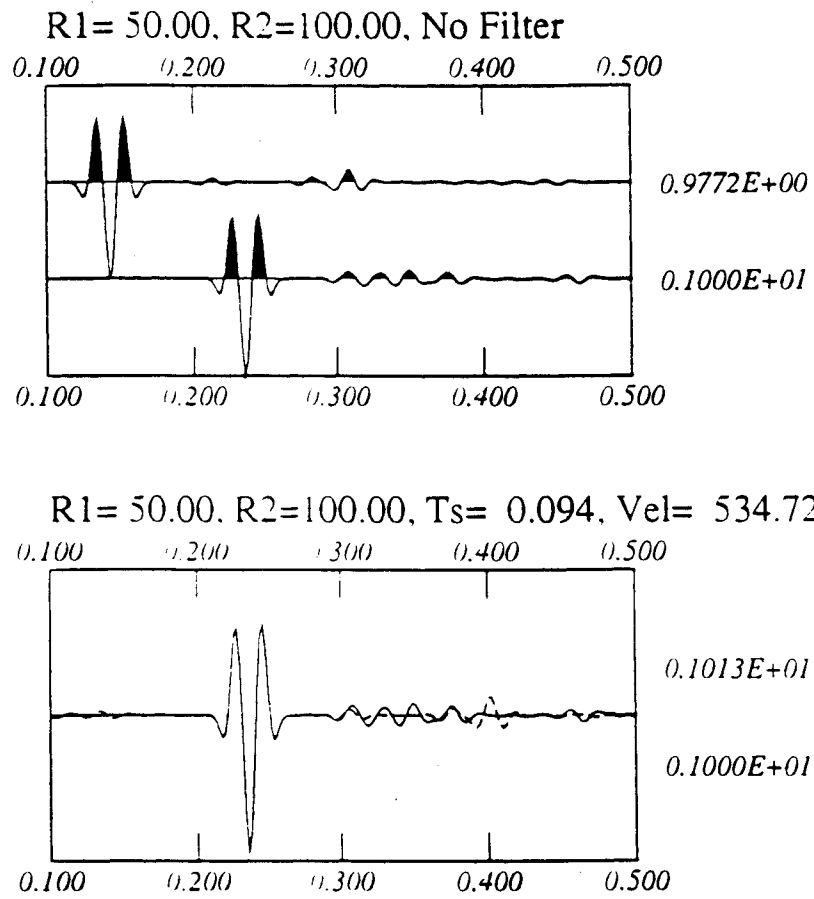
The synthetic seismograms (VSPs) from depths of 50 to 300 ft with a 10 ft interval. The center frequency is 50 Hz. No intrinsic attenuation is considered.



**Figure 8.A.3.B-51**

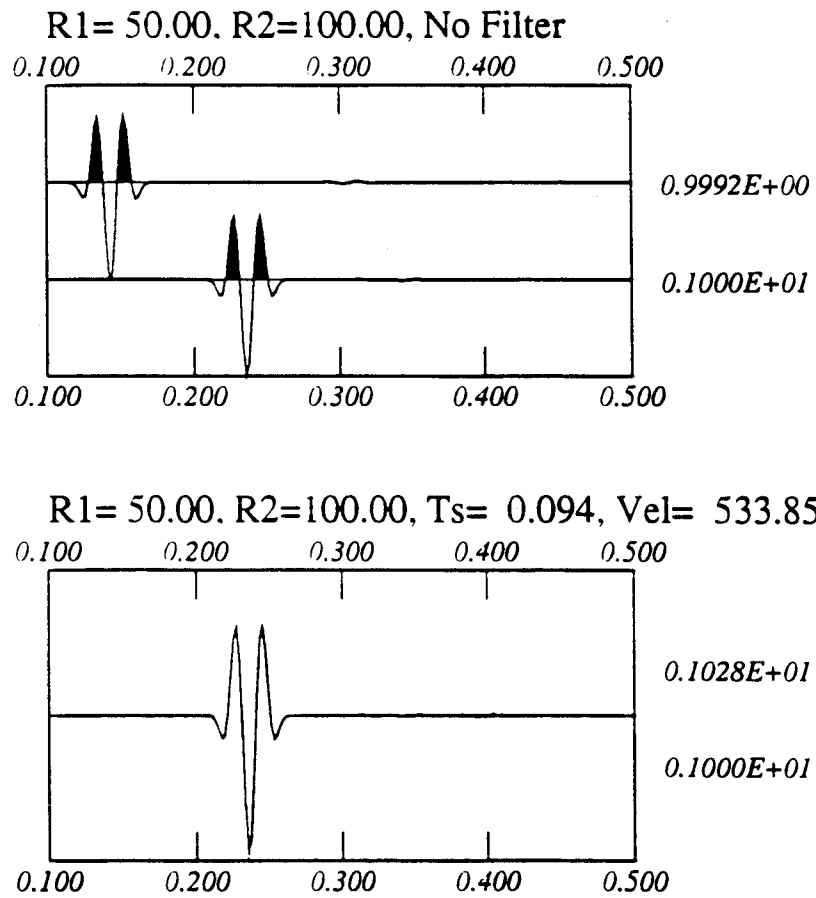
Demonstrates the  $(1/r)$  geometric spreading correction which does not satisfy the propagation between 50 and 100 feet.





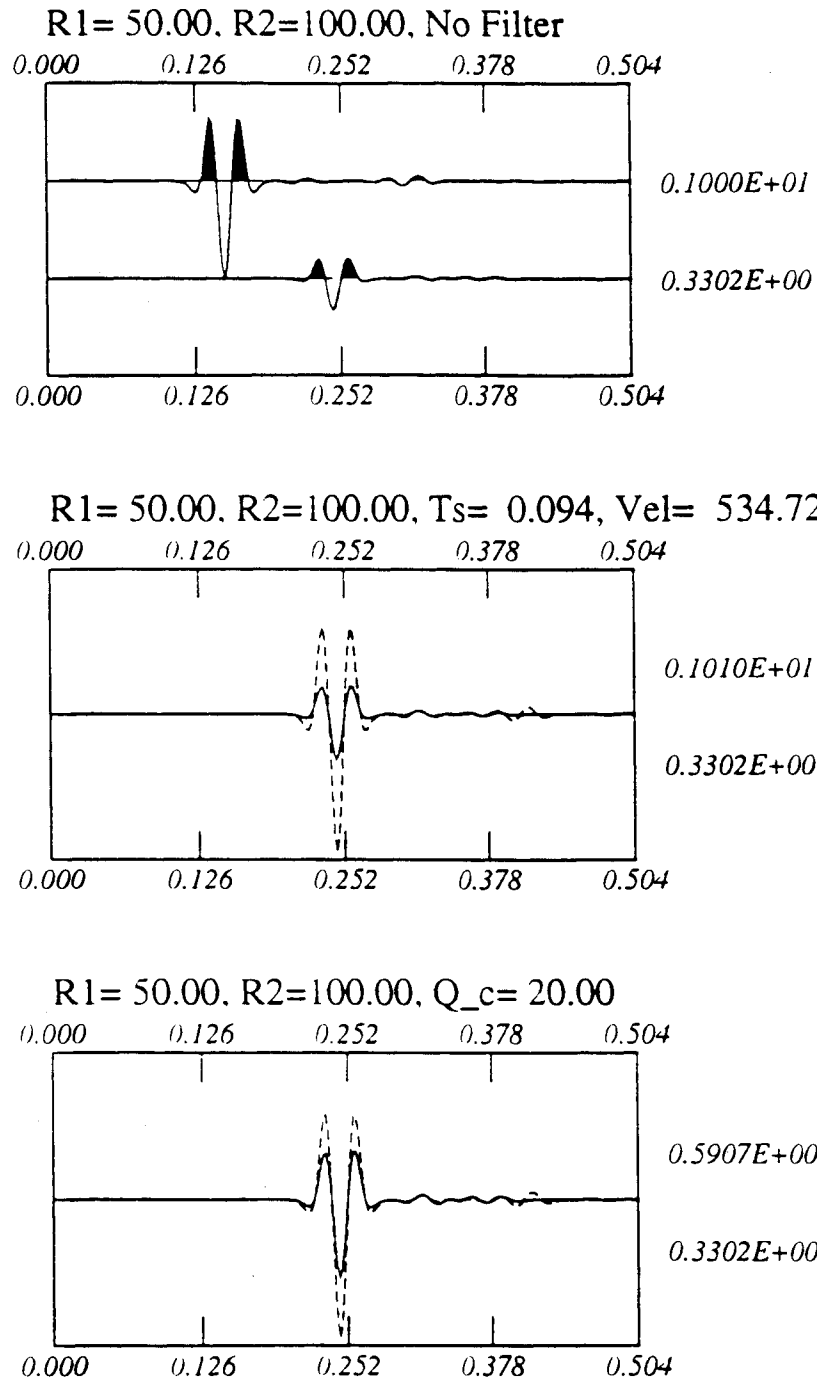
**Figure 8.A.3.B-52**

The  $(1/r^{1.8})$  geometric spreading correction needed for Figure 8.A.3.B-51.



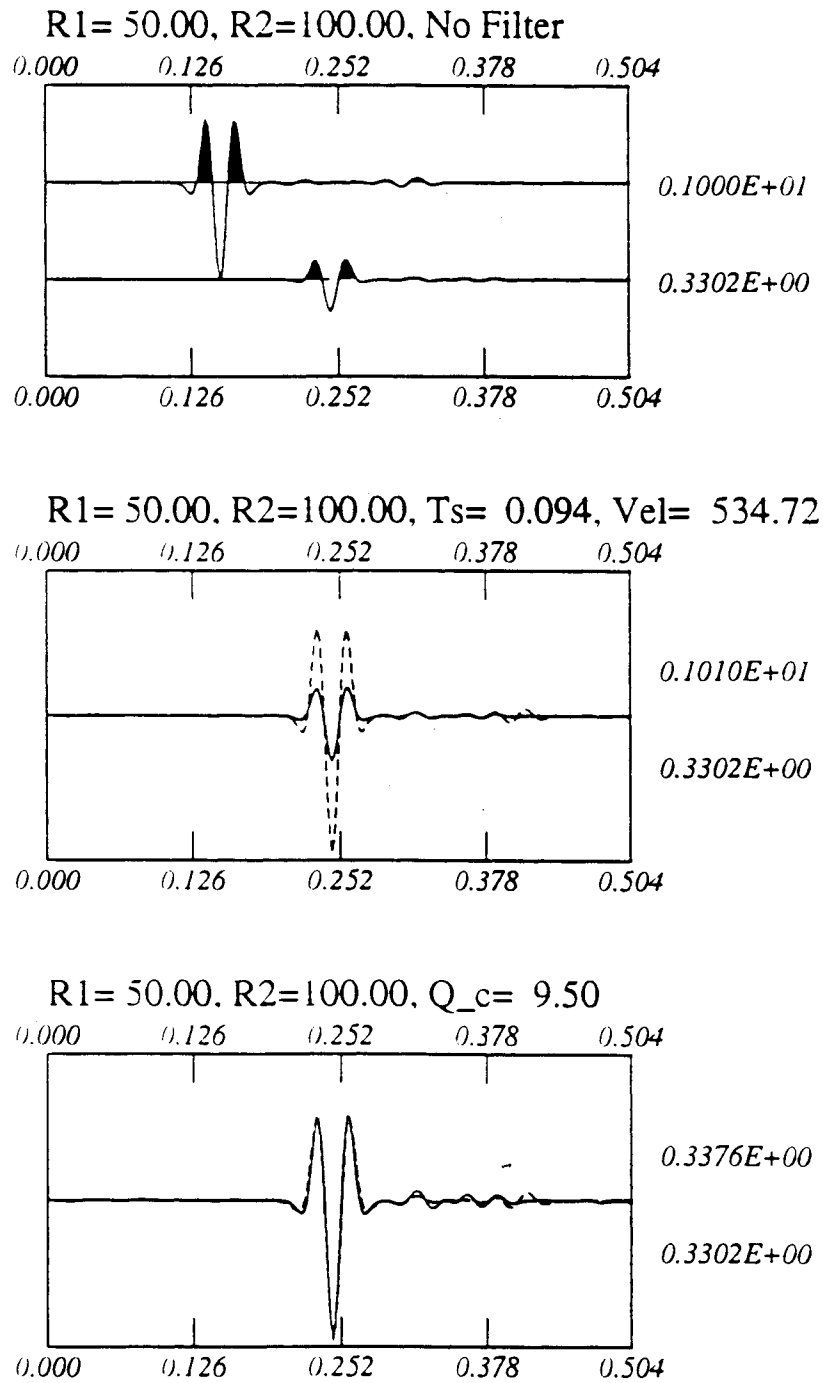
**Figure 8.A.3.B-53**

Same as Figure 8.A.3.B-52 but for the zero-impedance shear wave model. The  $(1/r^{1.145})$  geometric correction is needed to explain the propagation.



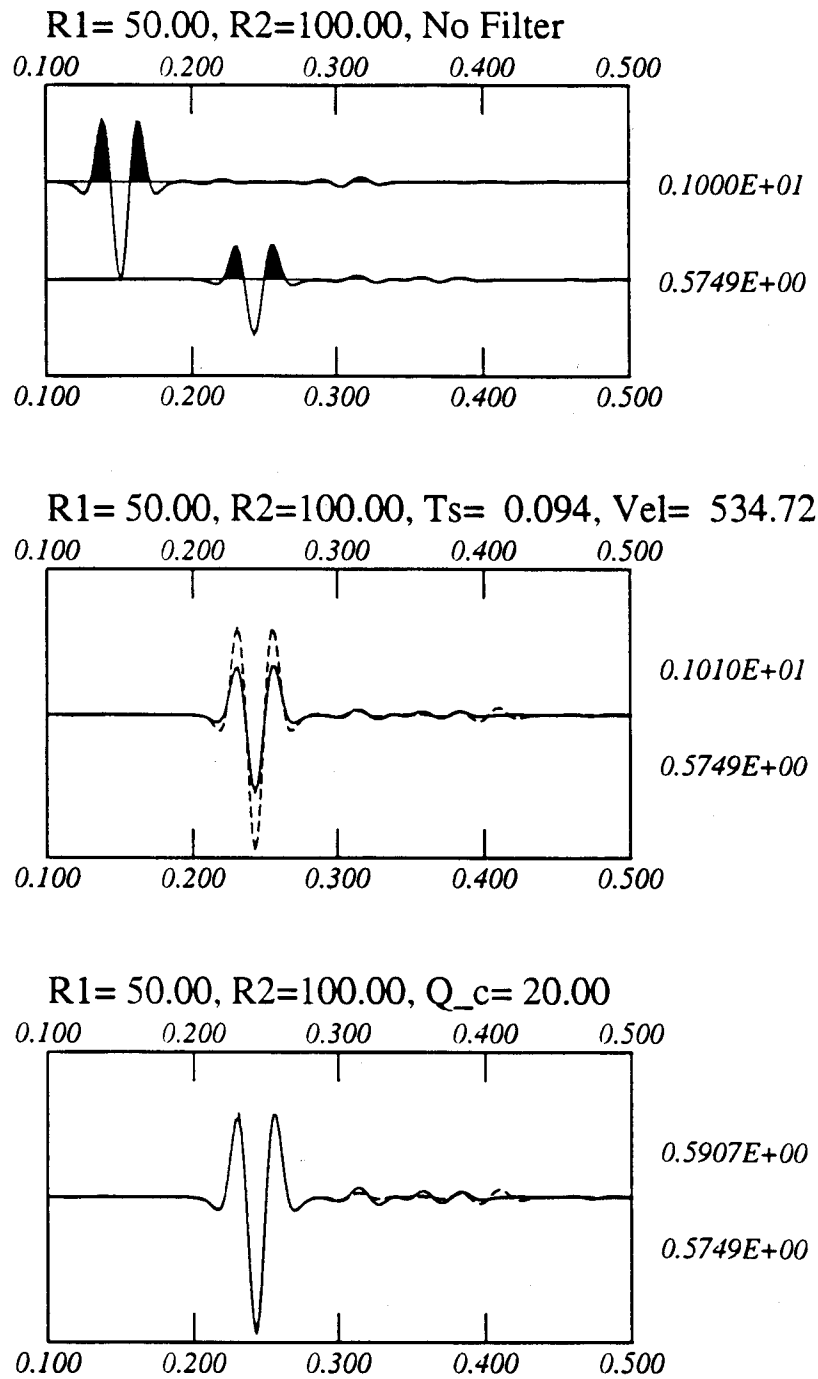
**Figure 8.A.3.B-54**

Demonstrates the use of the  $(1/r)$  geometric spreading correction. For the synthetic computation we use  $Q_s = 20$  throughout.



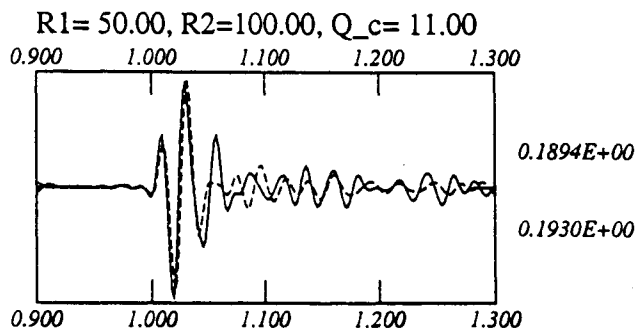
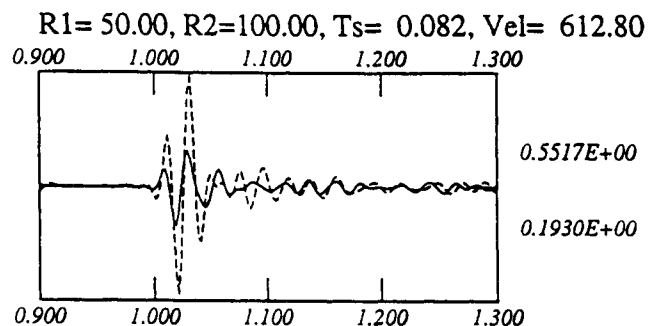
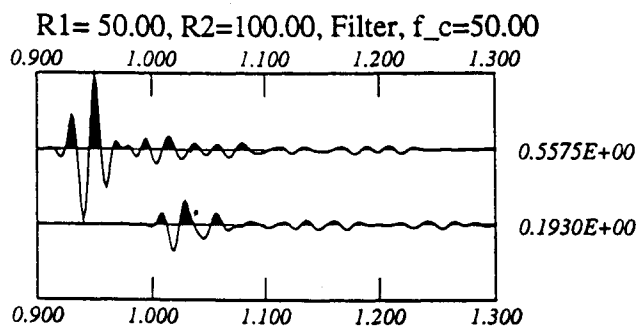
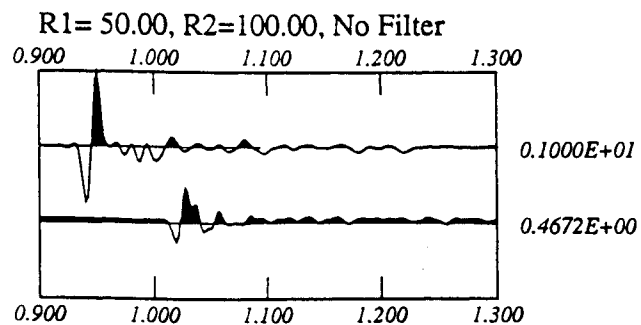
**Figure 8.A.3.B-55**

Estimates  $Q_s = 9.5$  instead of 20 using the  $(1/r)$  geometric spreading correction.



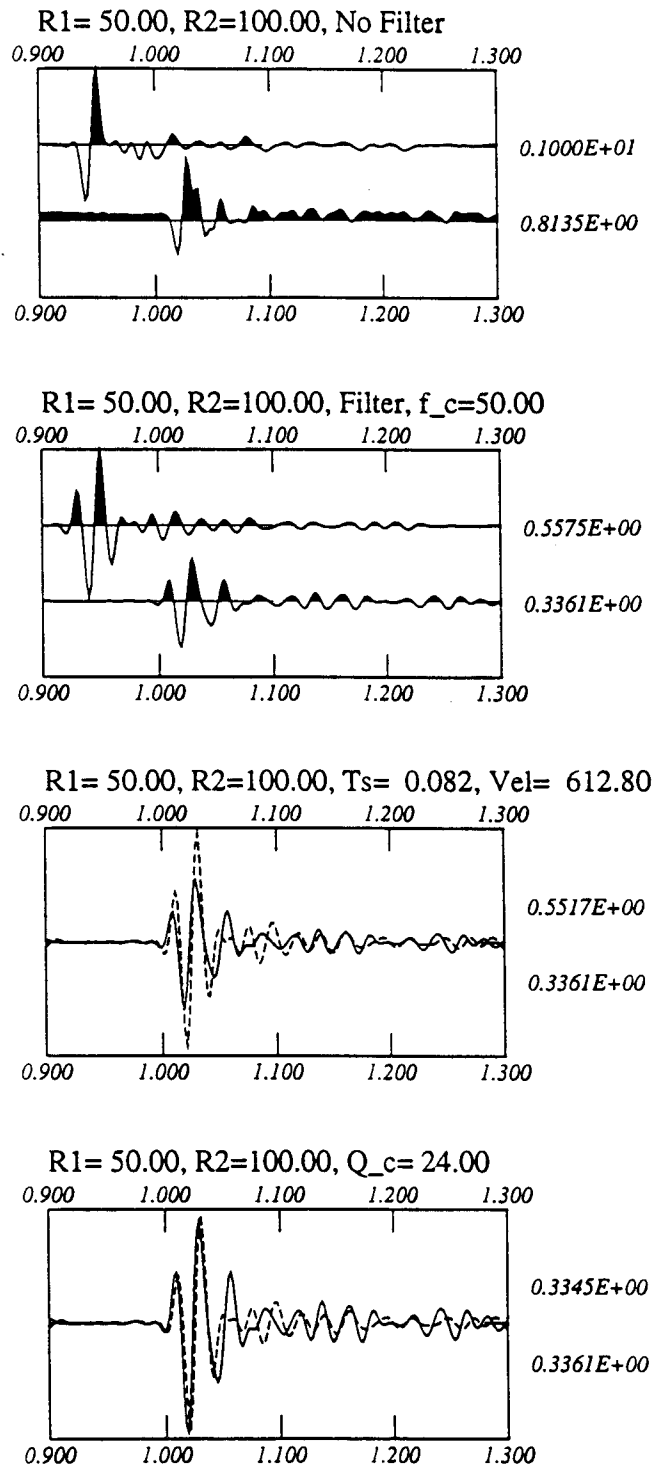
**Figure 8.A.3.B-56**

The correct geometric spreading ( $1/r^{1.8}$ ) estimating the correct  $Q_s = 20$ , as used in the computation.



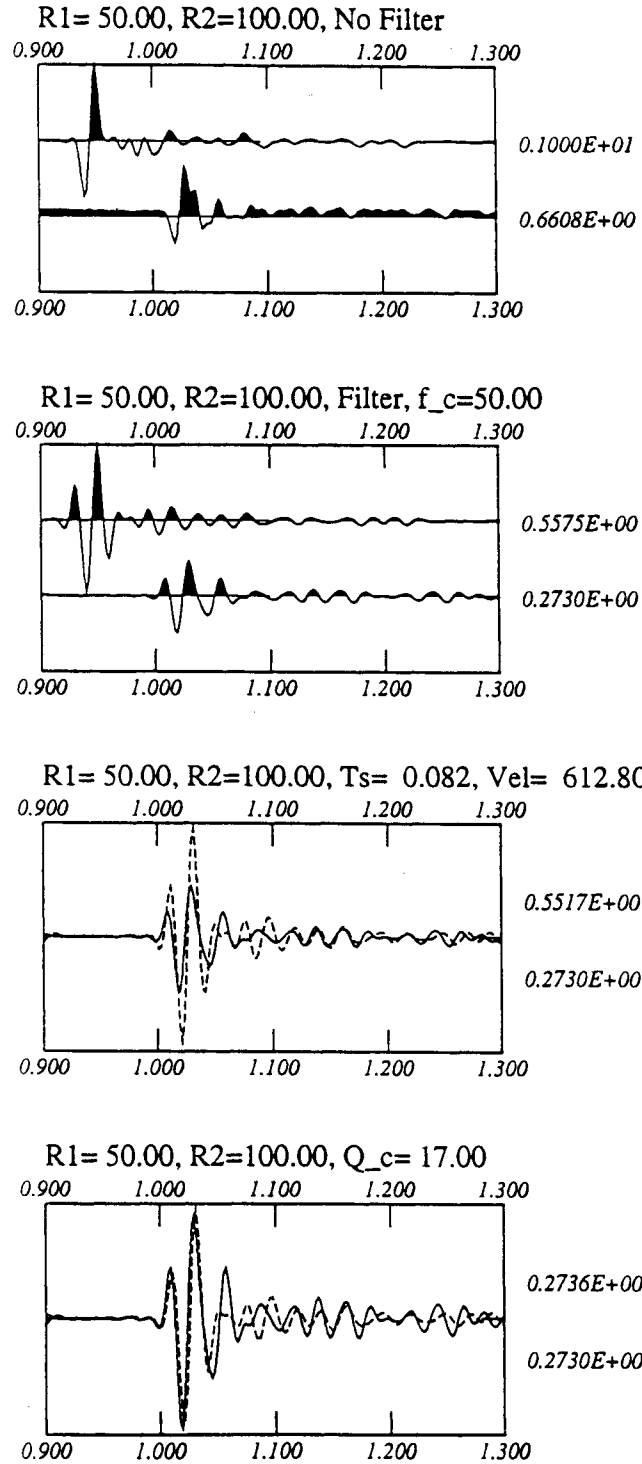
**Figure 8.A.3.B-57**

Estimates  $Q_s$  between the depths of 50 and 100 ft from real VSP Treasure Island data when the  $(1/r)$  geometric correction is applied. The observed seismograms are filtered with 50 Hz center frequency wavelets, as shown in the second box from the top. Estimated  $Q_s = 11$ .



**Figure 8.A.3.B-58**

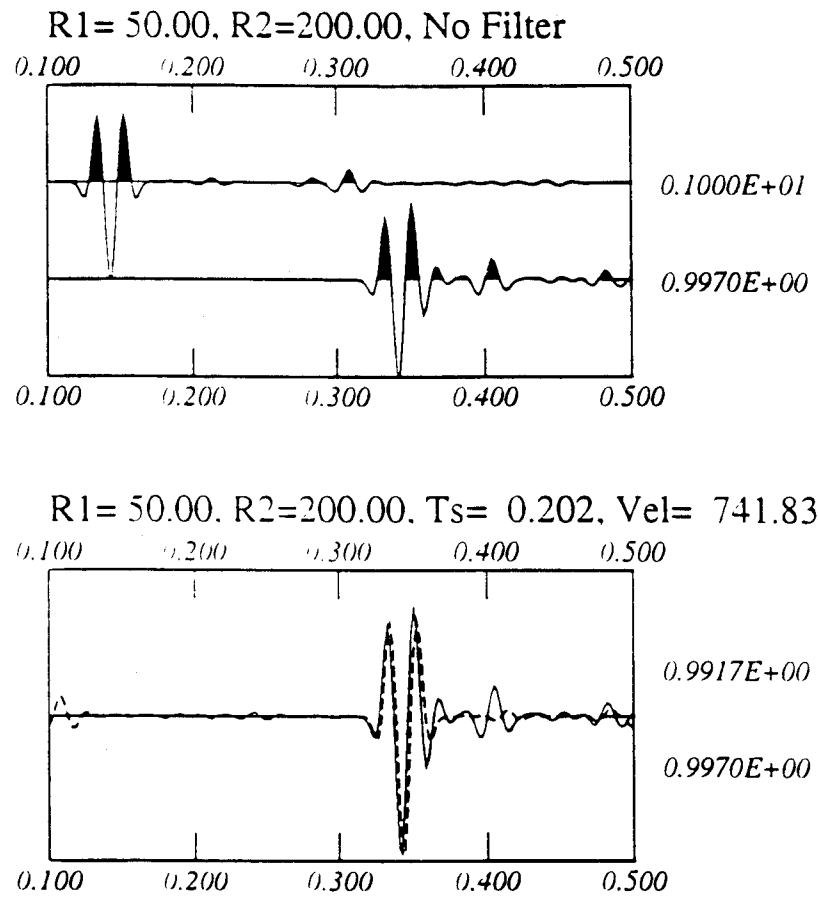
Estimates  $Q_s$  between the depths of 50 and 100 ft from real VSP Treasure Island data when the  $(1/r^{1.8})$  geometric correction is applied. Estimated  $Q_s = 24$ .



**Figure 8.A.3.B-59**

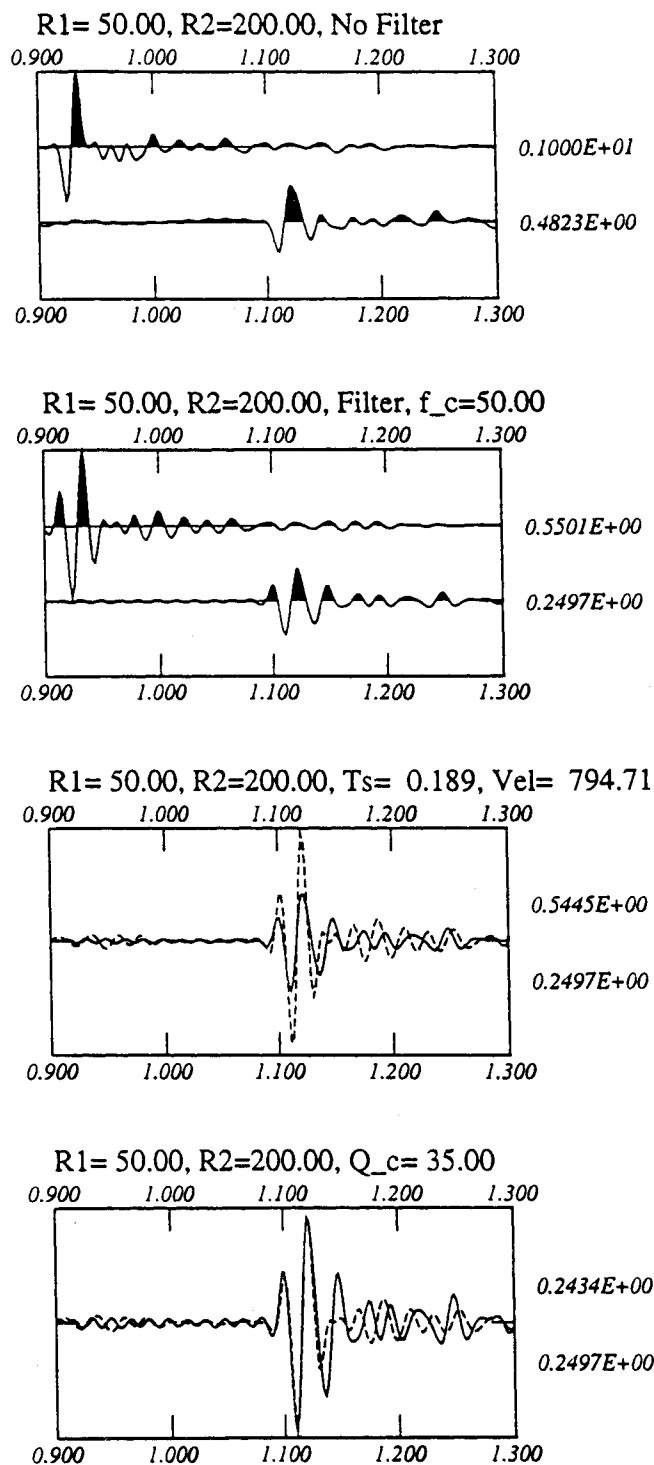
Estimates  $Q_s$  between the depths of 50 and 100 ft from real VSP Treasure Island data when the  $(1/r^{1.5})$  geometric correction is applied. Estimated  $Q_s = 17$ .





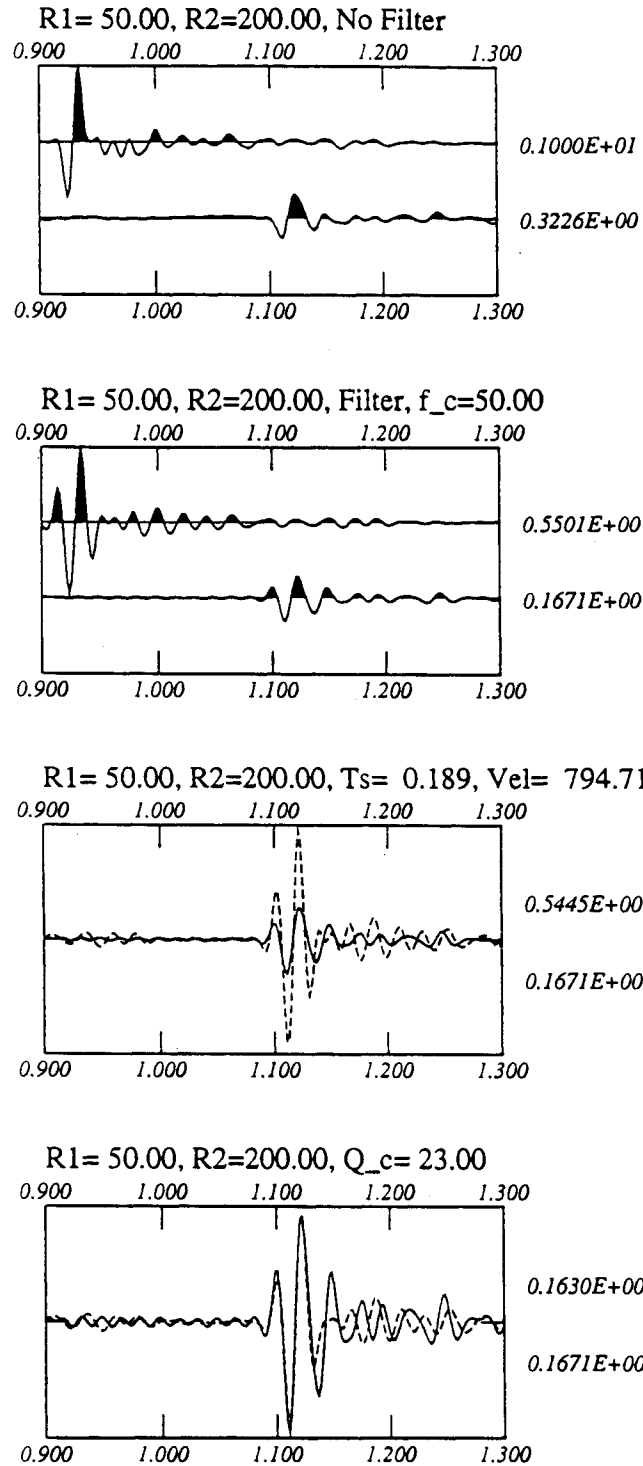
**Figure 8.A.3.B-60**

The  $(1/r^{1.69})$  geometric correction is required between 50 and 200 ft with a non-intrinsic attenuation synthetic model.



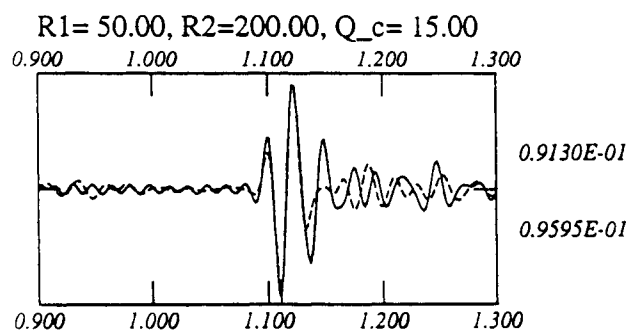
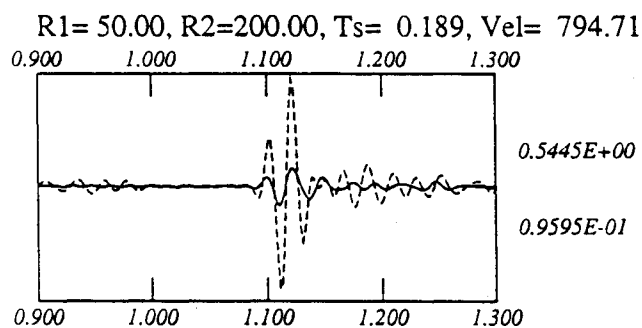
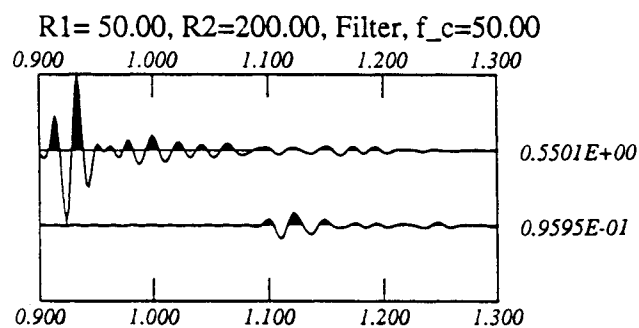
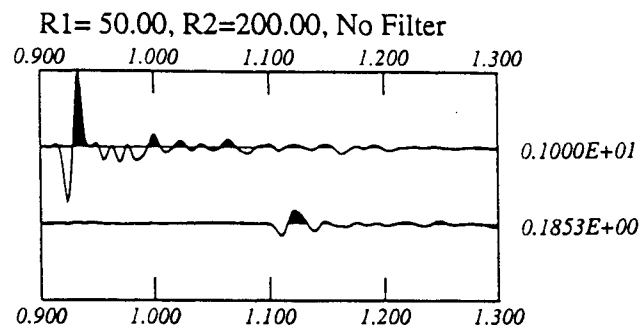
**Figure 8.A.3.B-61**

Same as Figure 8.A.3.B-58 but for the propagation between 50 and 200 ft of the Treasure Island data. The  $(1/r^{1.69})$  geometric correction is applied. Estimated  $Q_s = 35$ .



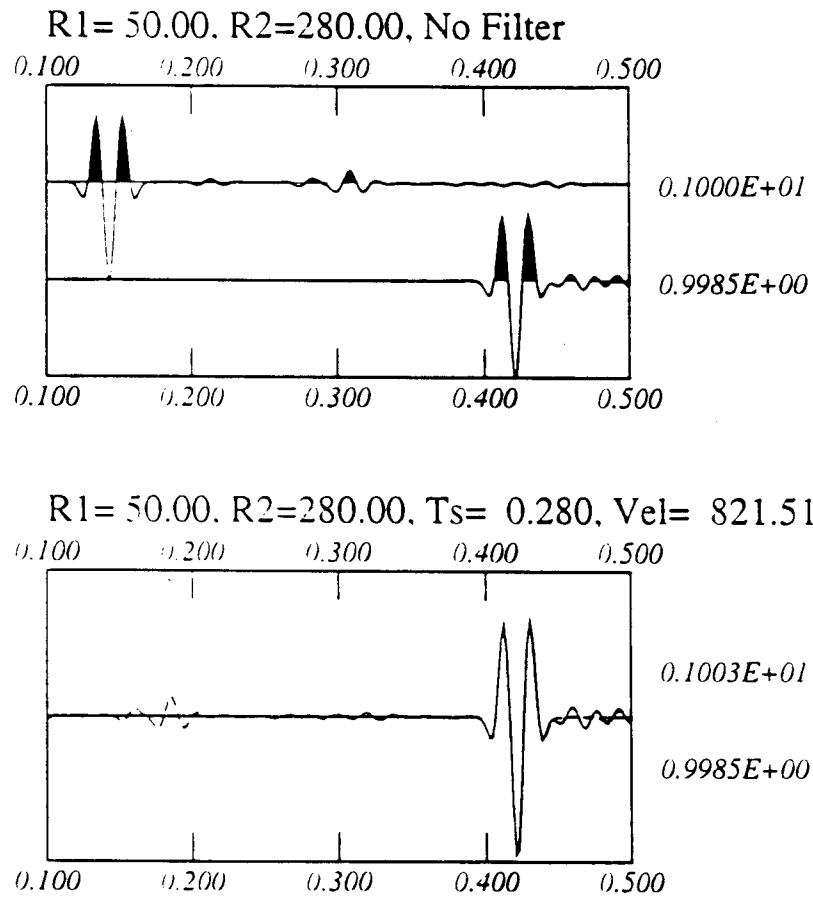
**Figure 8.A.3.B-62**

Same as Figure 8.A.3.B-61 but the  $(1/r^{1.4})$  geometric correction is applied. Estimated  $Q_s = 23$ .



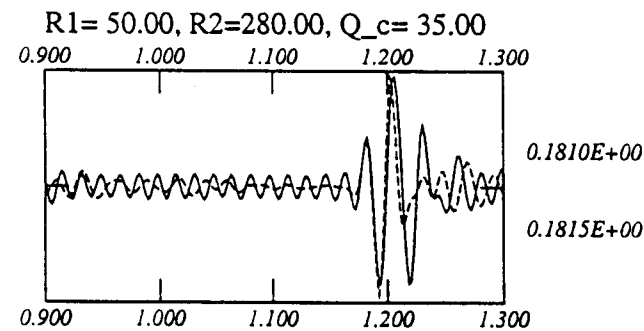
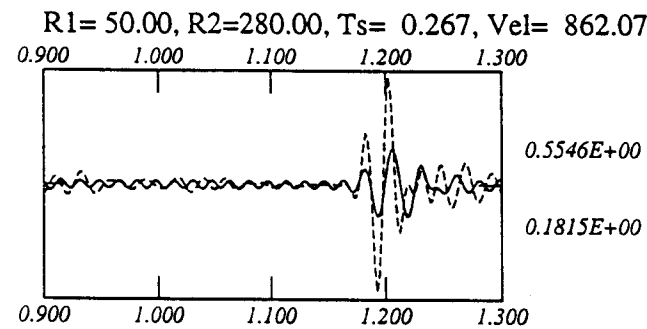
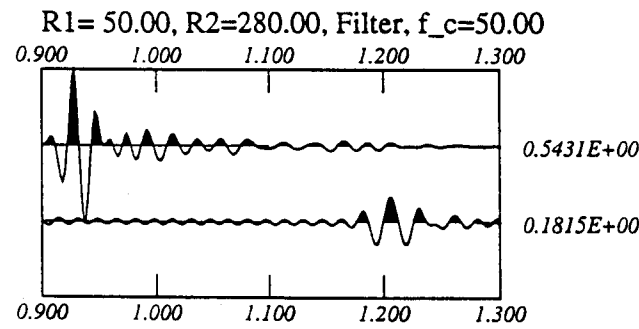
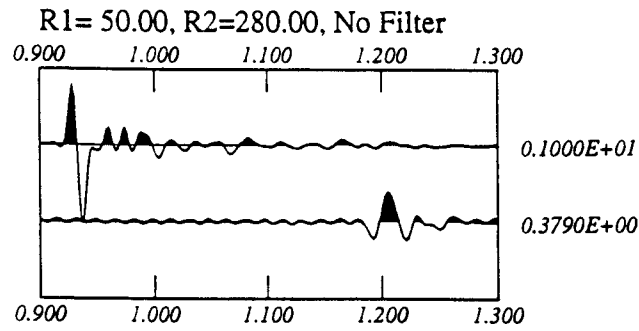
**Figure 8.A.3.B-63**

Same as Figure 8.A.3.B-61 but the  $(1/r)$  geometric correction is applied. Estimated  $Q_s = 15$ .



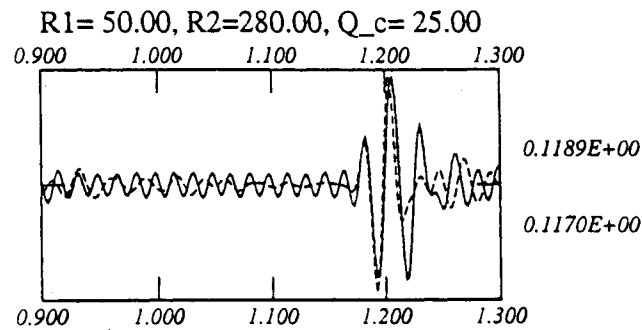
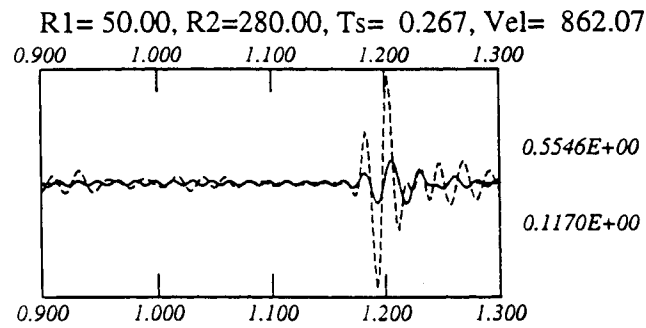
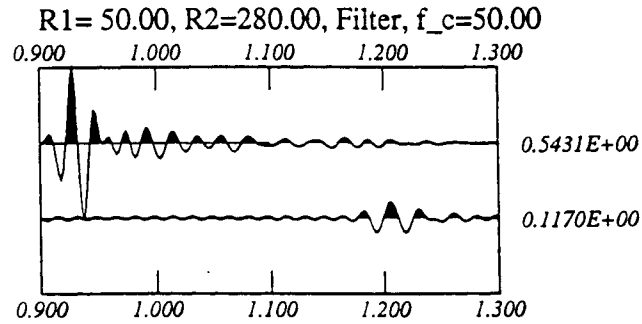
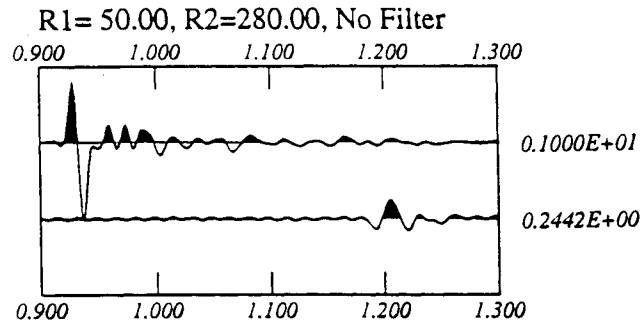
**Figure 8.A.3.B-64**

The  $(1/r^{1.755})$  geometric correction is required between 50 and 280 ft with the non-intrinsic attenuation synthetic model.

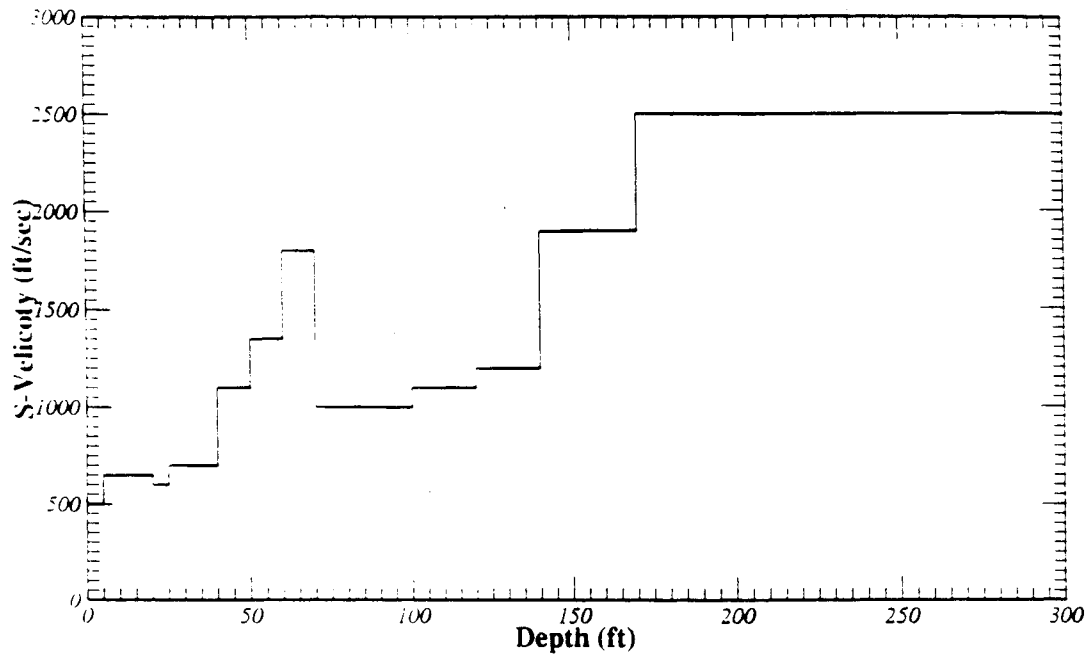


**Figure 8.A.3.B-65**

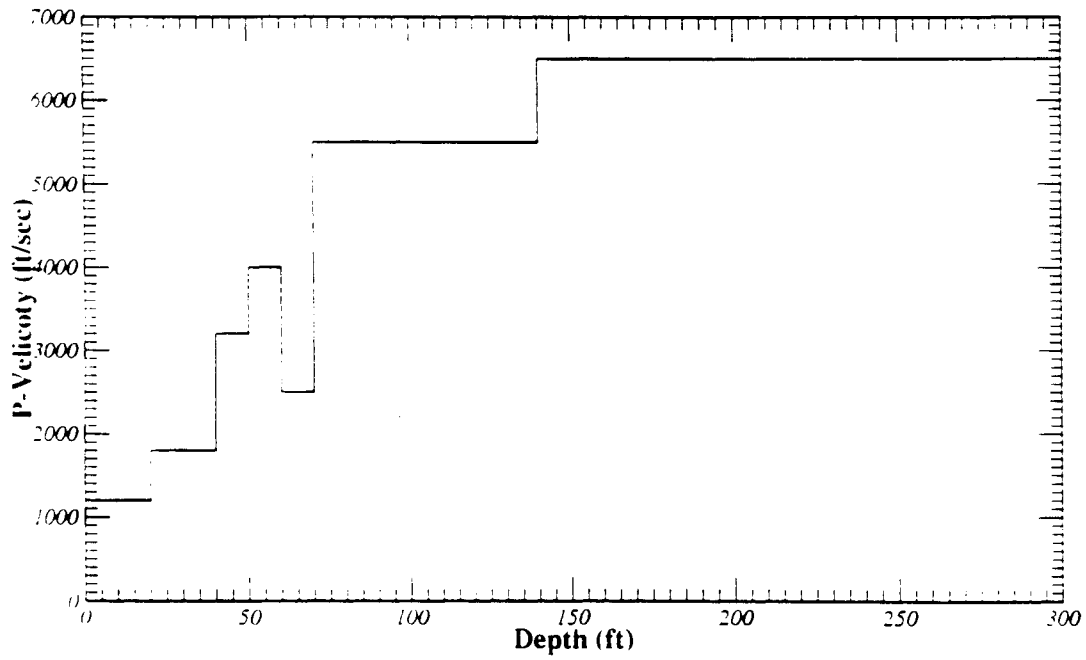
Same as Figure 8.A.3.B-58 but for the propagation between 50 and 200 ft of the Treasure Island data. The  $(1/r^{1.755})$  geometric correction is applied. Estimated  $Q_s = 35$ .



**Figure 8.A.3.B-66**  
Same as Figure 8.A.3.B-65 but the  $(1/r^{1.5})$  geometric correction is applied. Estimated  $Q_s = 25$ .

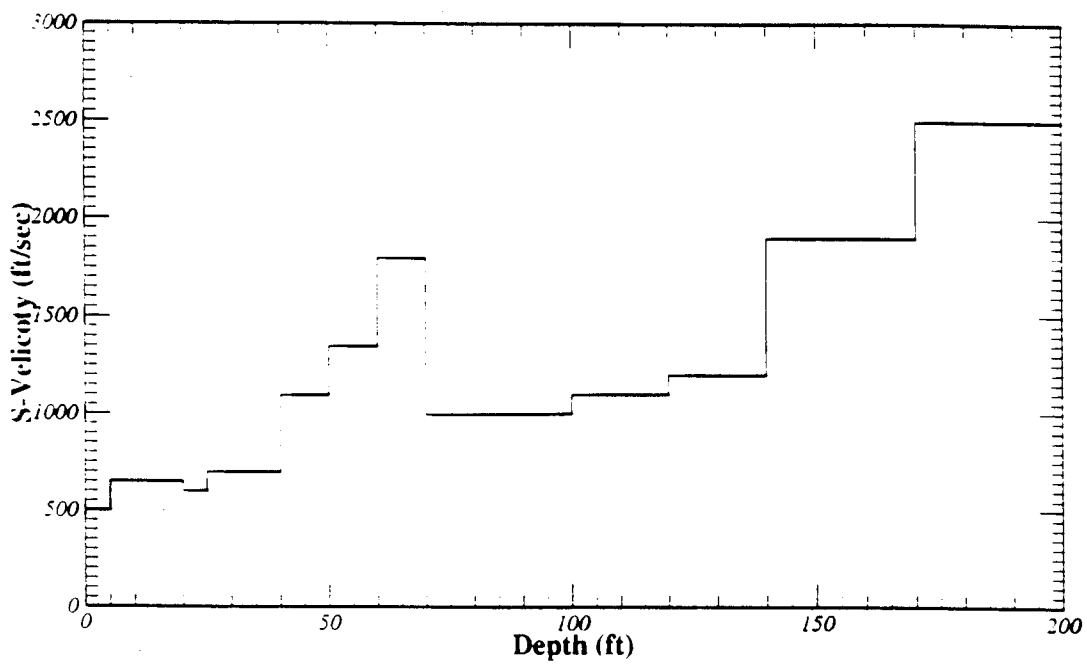


mod-gilroy

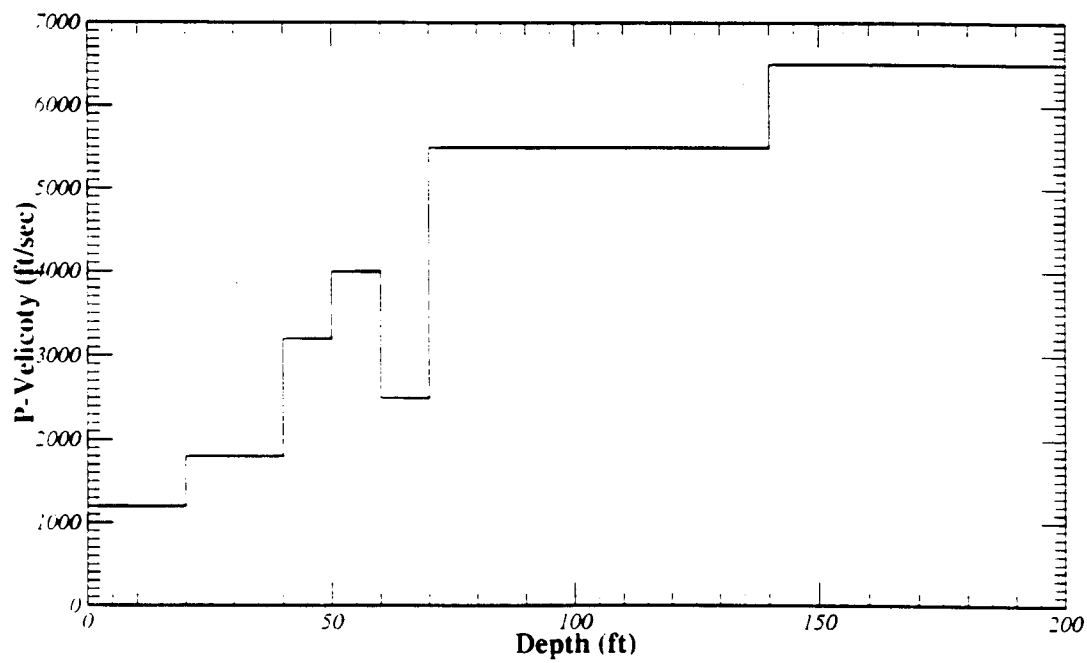


**Figure 8.A.3.B-67**  
Velocity model used for Gilroy synthetic waveform simulation.



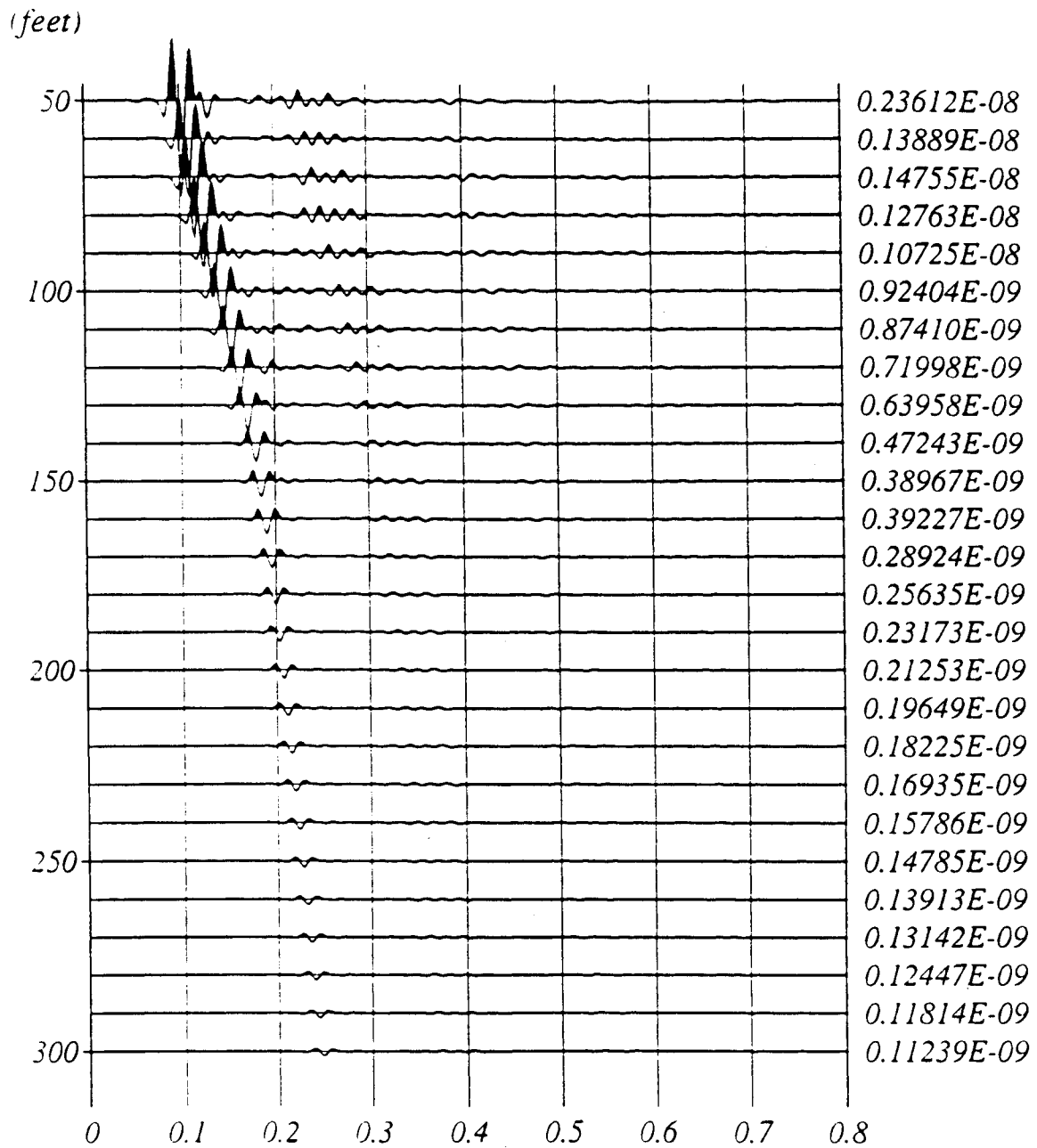


mod-gilroy



**Figure 8.A.3.B-68**

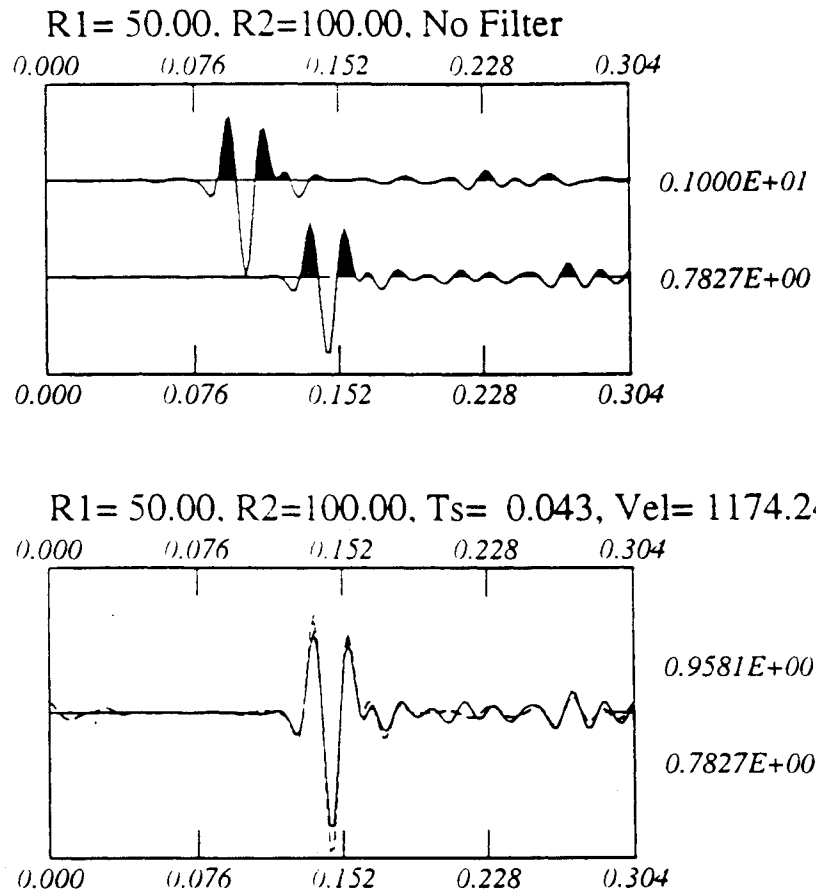
Same as Figure 8.A.3.B-67 but shows 0-200 ft velocity model.



*gilroynql.t*,  $f_c = 50$  Hz

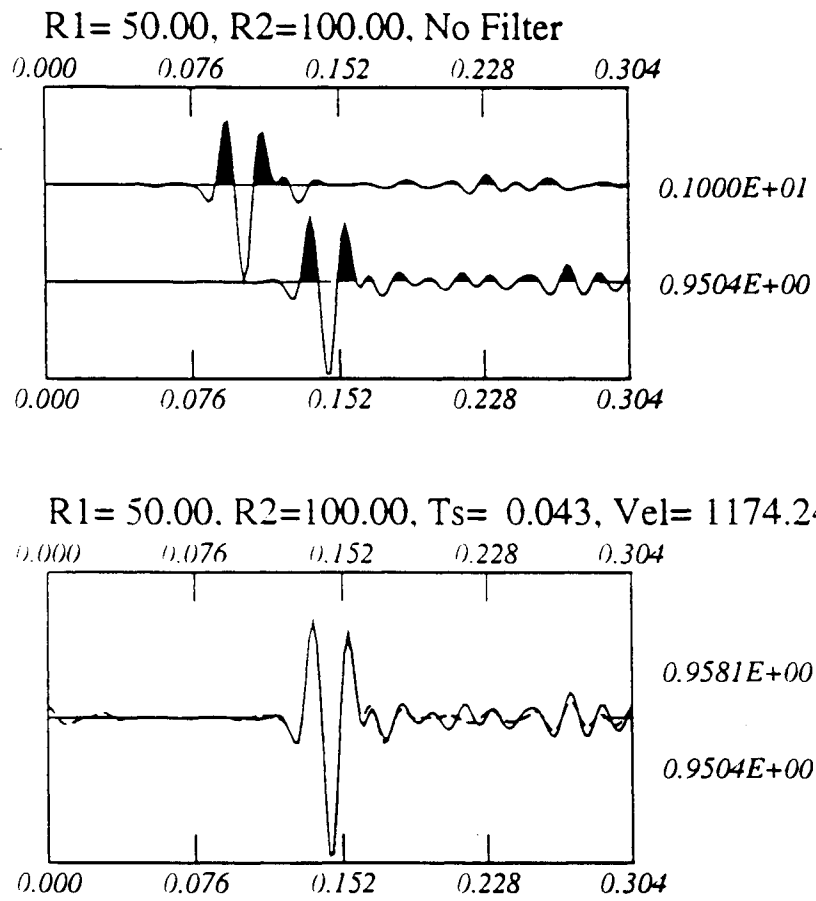
**Figure 8.A.3.B-69**

The vertical synthetic seismograms from 50 to 300 ft depth with a 10 ft interval. No intrinsic attenuation is assumed in this computation.

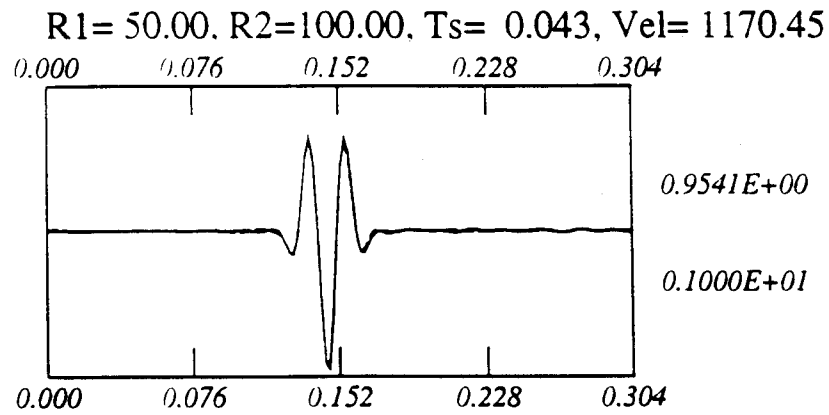
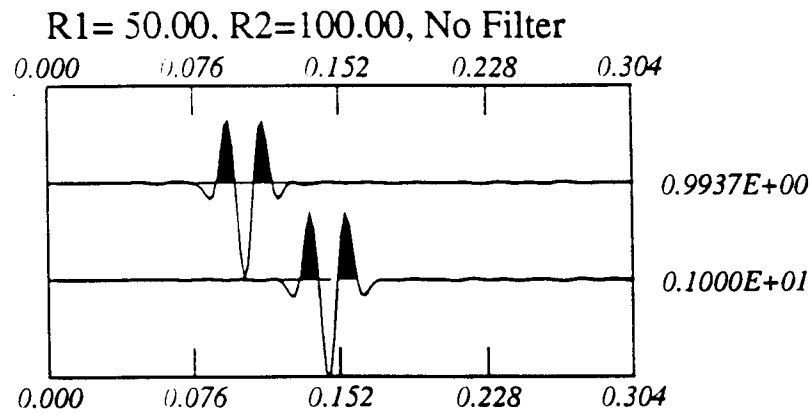


**Figure 8.A.3.B-70**

The  $(1/r)$  geometric spreading correction is not satisfied for the propagation between 50 and 100 feet.

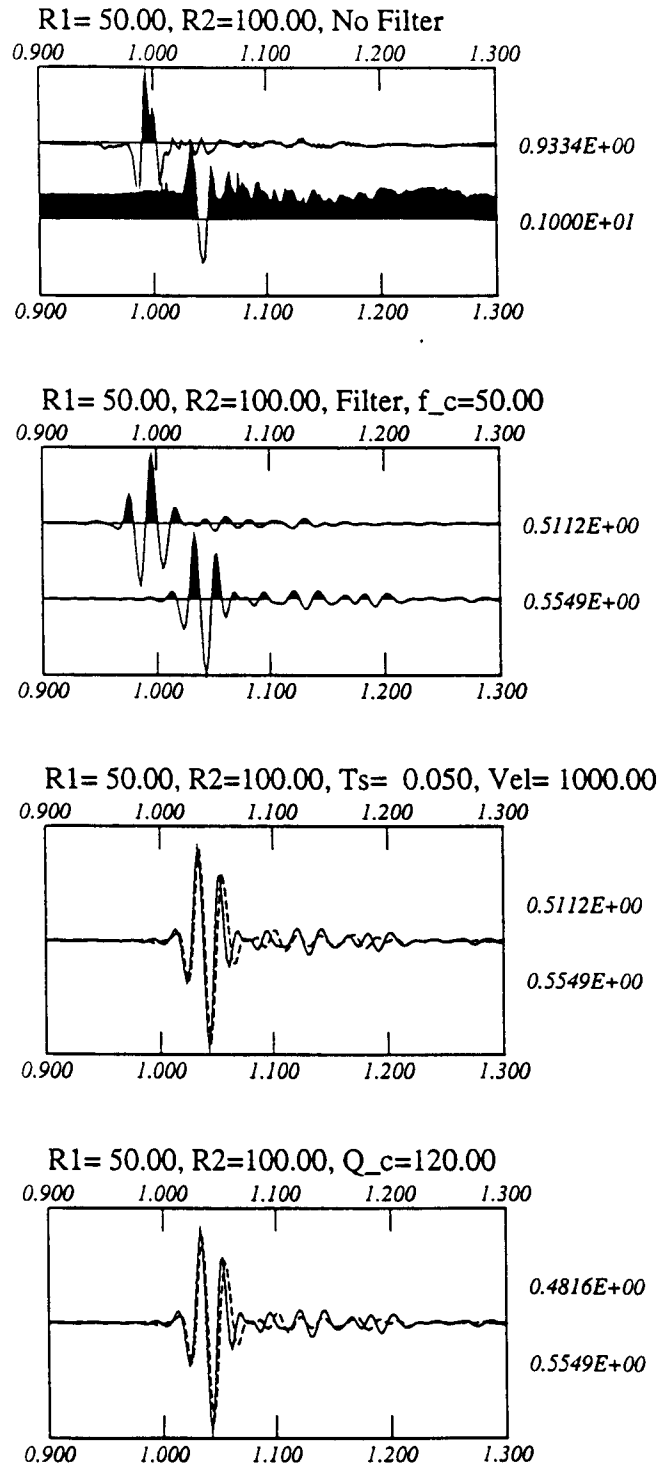


**Figure 8.A.3.B-71**  
Needs the  $(1/r^{1.28})$  geometric correction to explain the propagation described in Figure 8.A.3.B-70.



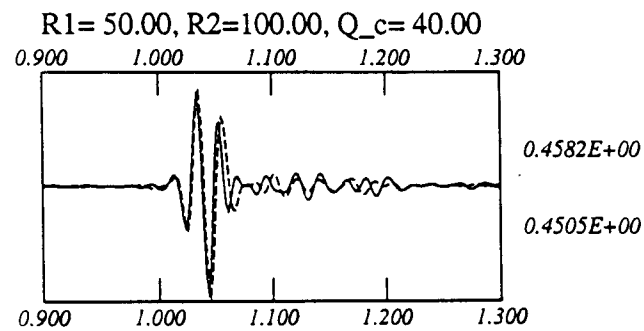
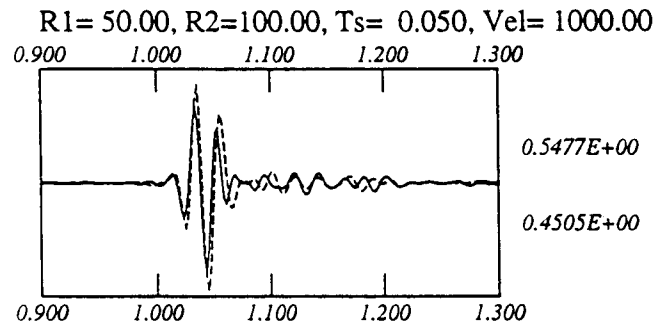
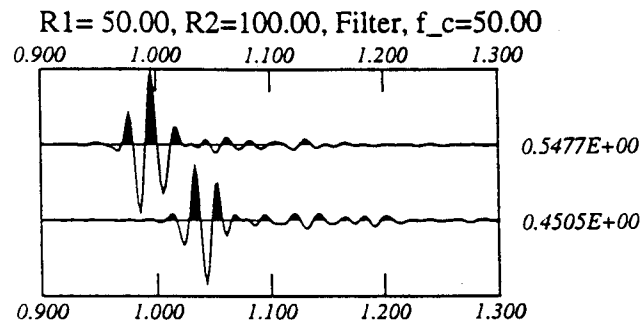
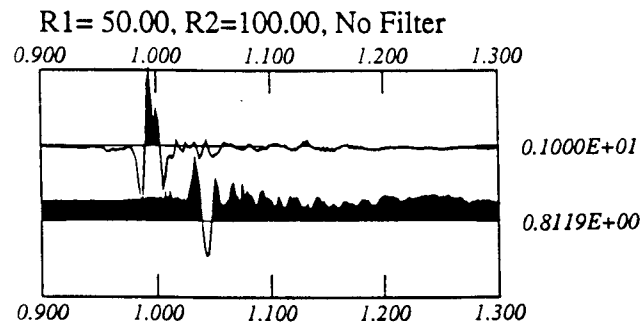
**Figure 8.A.3.B-72**

Needs the  $(1/r^{1.39})$  geometric correction to explain propagation between the depths of 50 and 100 ft for the zero-impedence shear wave model.



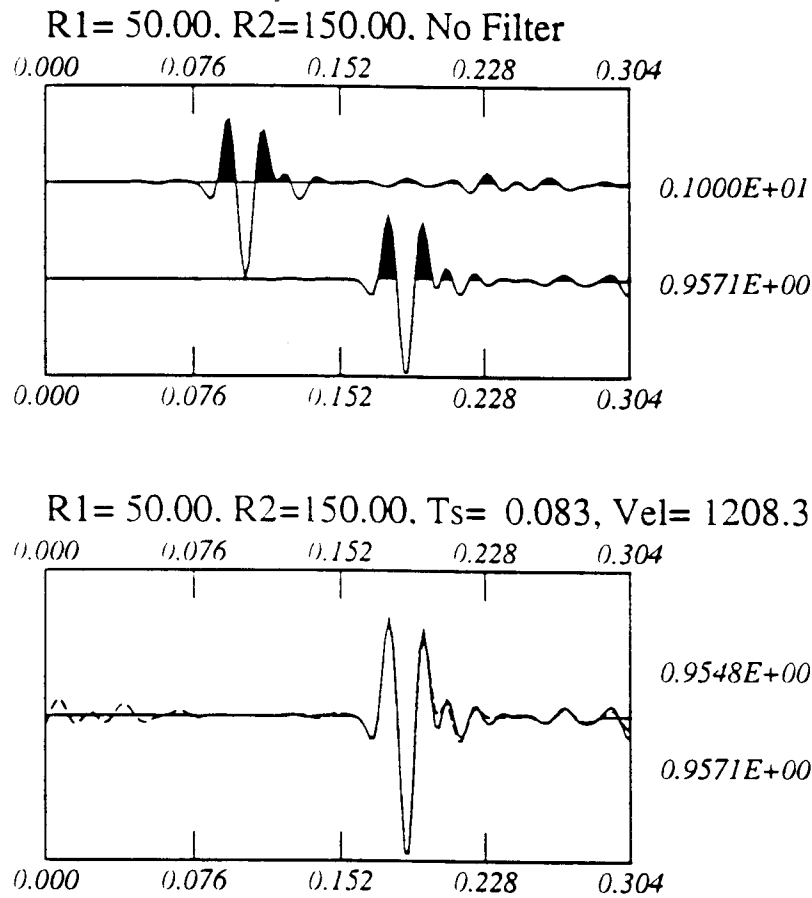
**Figure 8.A.3.B-73**

Estimation of  $Q_s$  using the  $(1/r^{1.4})$  geometric spreading correction for the propagation depth of 50 and 100 ft of real Gilroy data. The observation is filtered with a 50 Hz centered frequency wavelet. Estimated  $Q_s = 120$ .



**Figure 8.A.3.B-74**

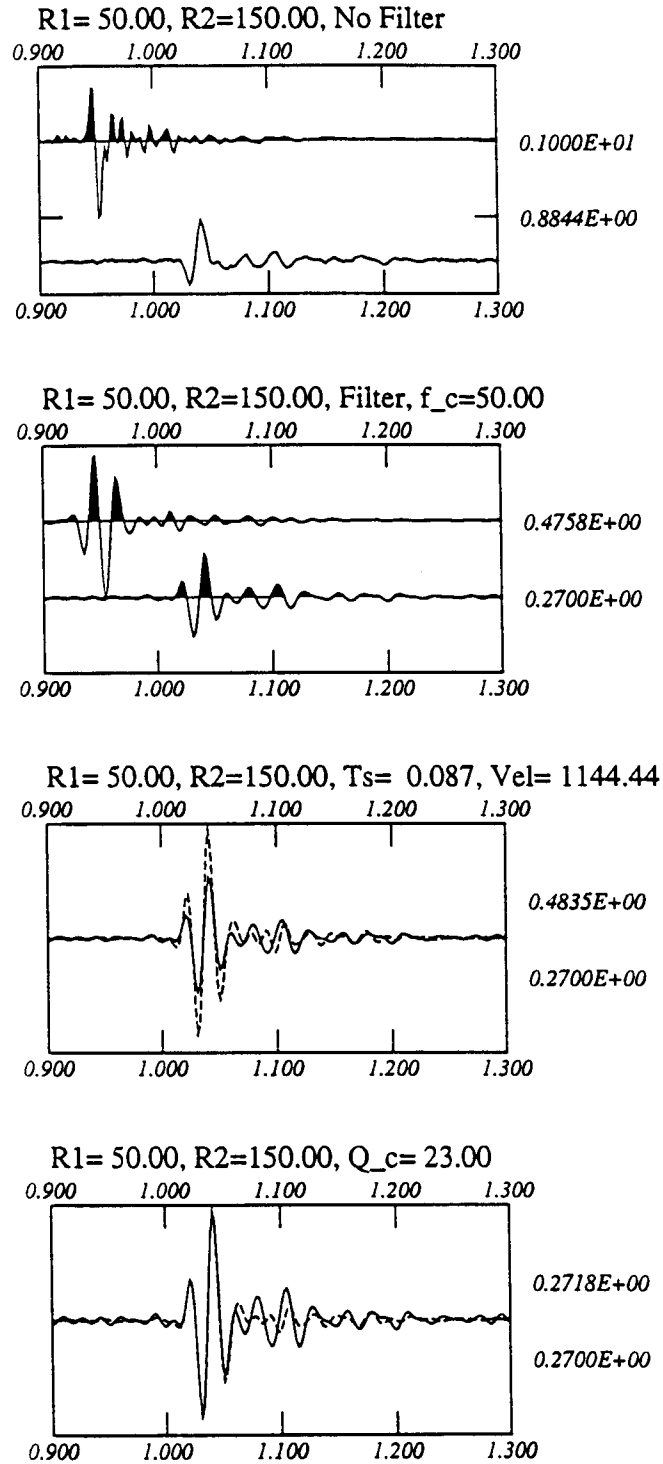
Same as Figure 8.A.3.B-73 for the  $(1/r)$  geometric spreading correction. Estimated  $Q_s = 40$ .



**Figure 8.A.3.B-75**

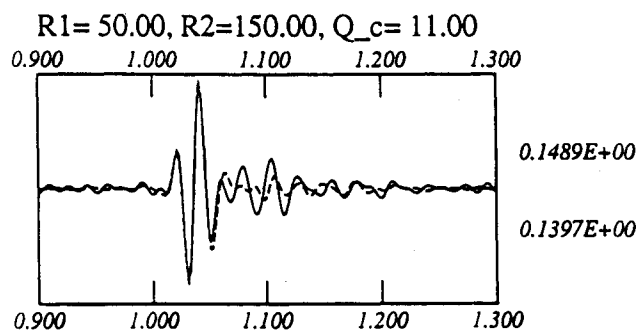
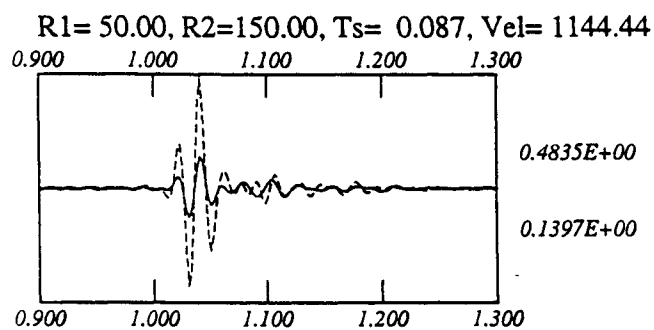
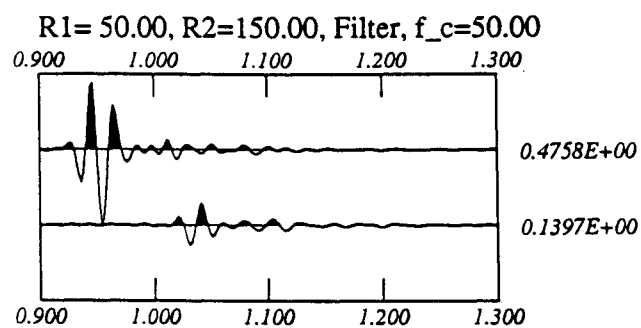
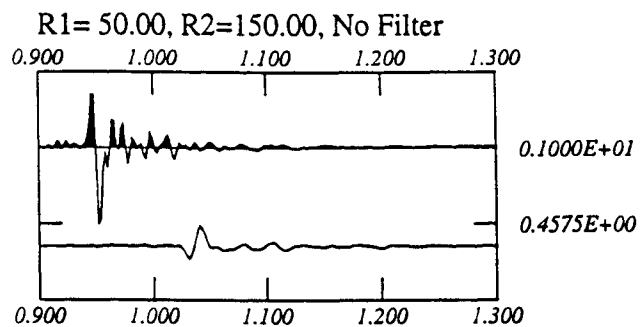
The synthetic propagation between 50 and 150 ft estimating the  $(1/r^{1.6})$  geometric spreading correction for no attenuation model.





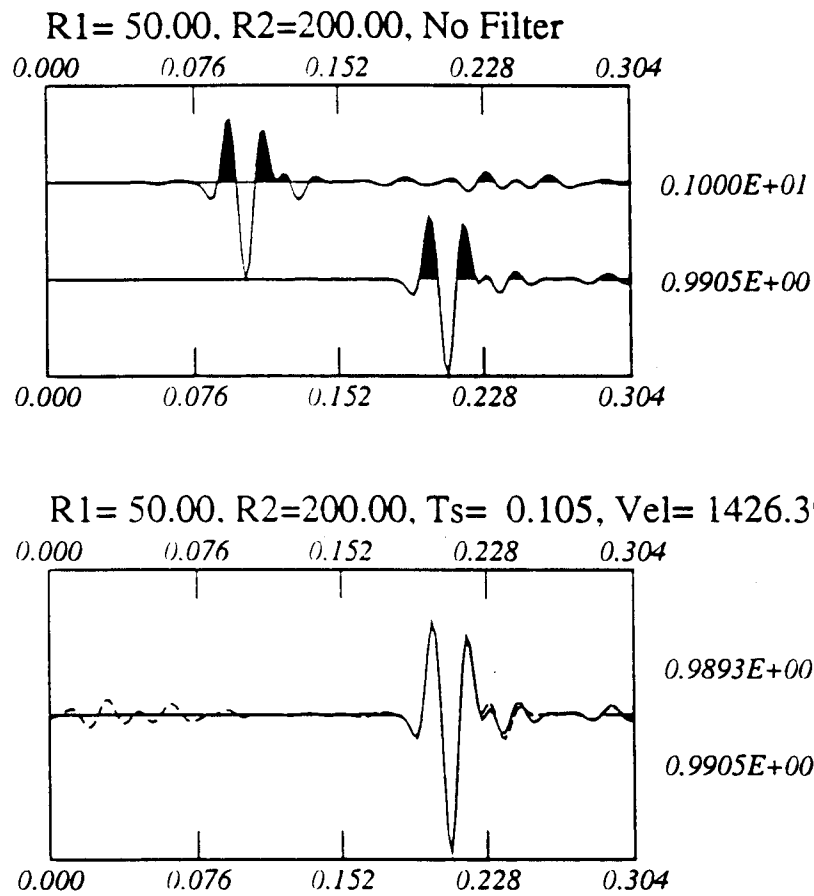
**Figure 8.A.3.B-76**

Estimation of  $Q_s$  using the  $(1/r^{1.6})$  geometric spreading correction for the propagation depth of 50 and 150 ft of real Gilroy data. Estimated  $Q_s = 23$ .



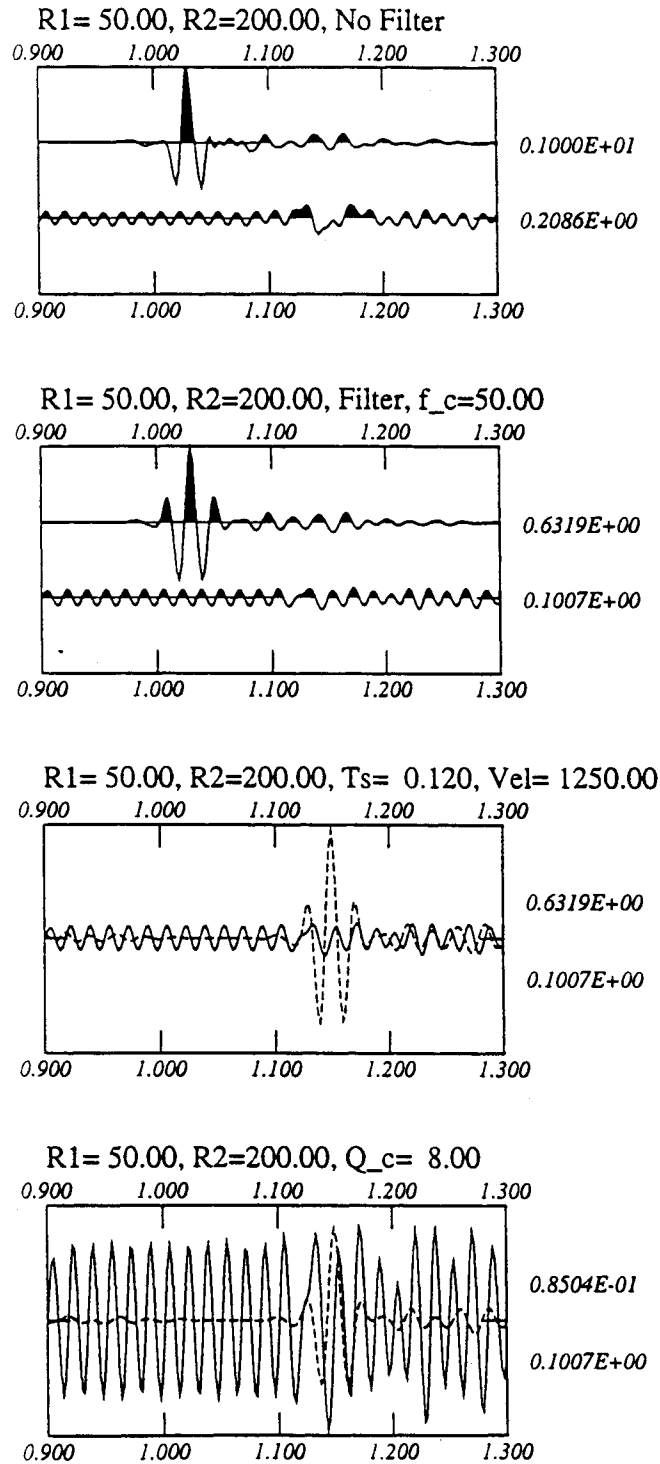
**Figure 8.A.3.B-77**

Same as Figure 8.A.3.B-76 for the  $(1/r)$  geometric spreading correction. Estimated  $Q_s = 11$ .



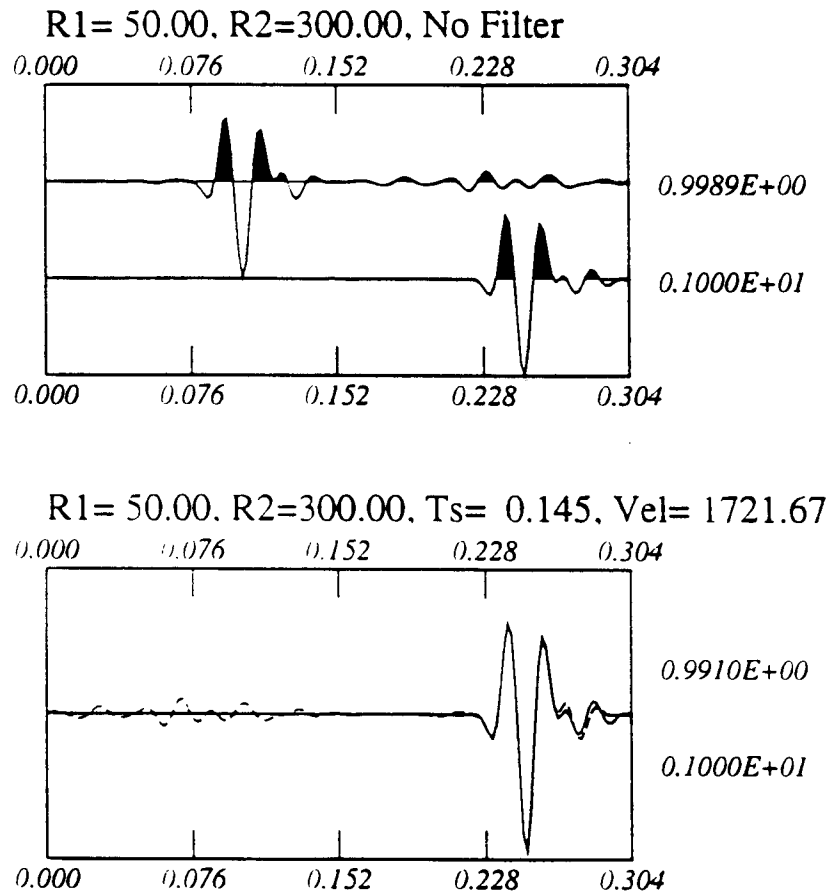
**Figure 8.A.3.B-78**

The synthetic propagation between 50 and 200 feet estimating the  $(1/r^{1.73})$  geometric spreading correction for no attenuation model.



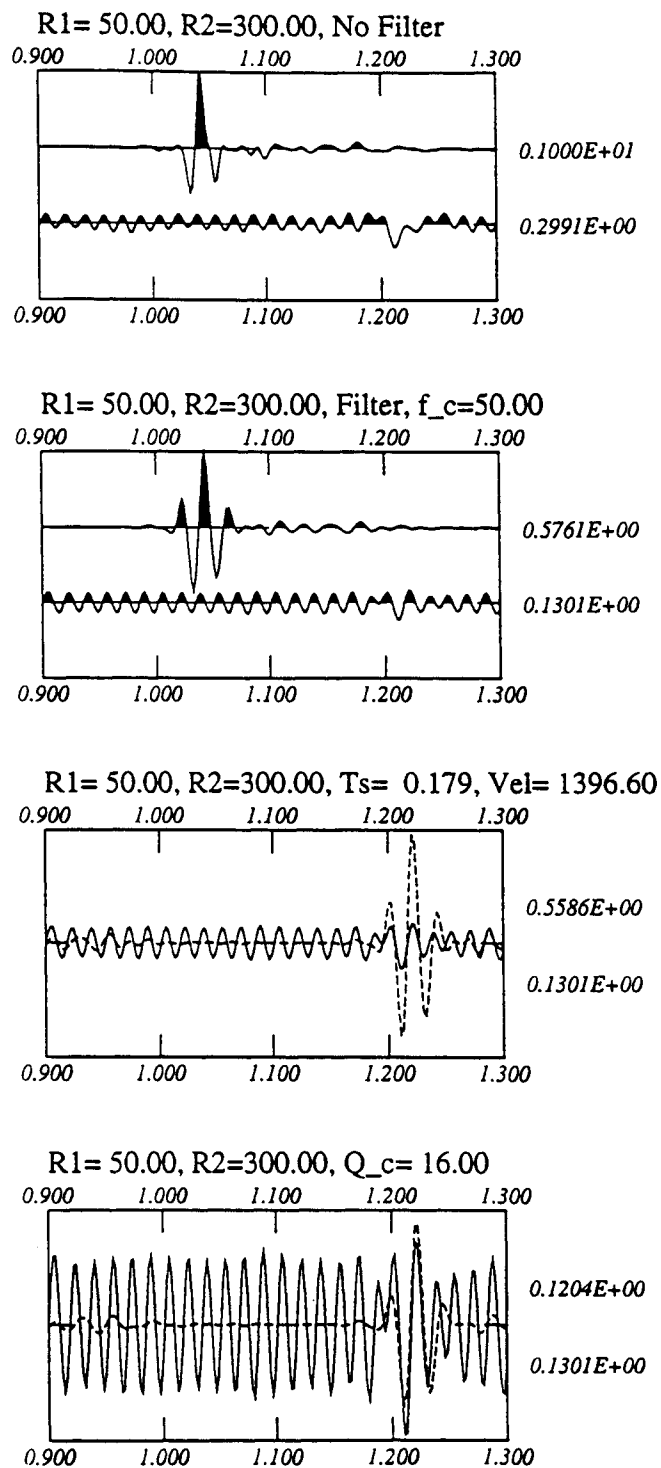
**Figure 8.A.3.B-79**

Estimation of  $Q_s$  using the  $(1/r)^{1.73}$  geometric spreading correction for the propagation depth of 50 and 200 ft of real Gilroy data. Estimated  $Q_s = 23$ .

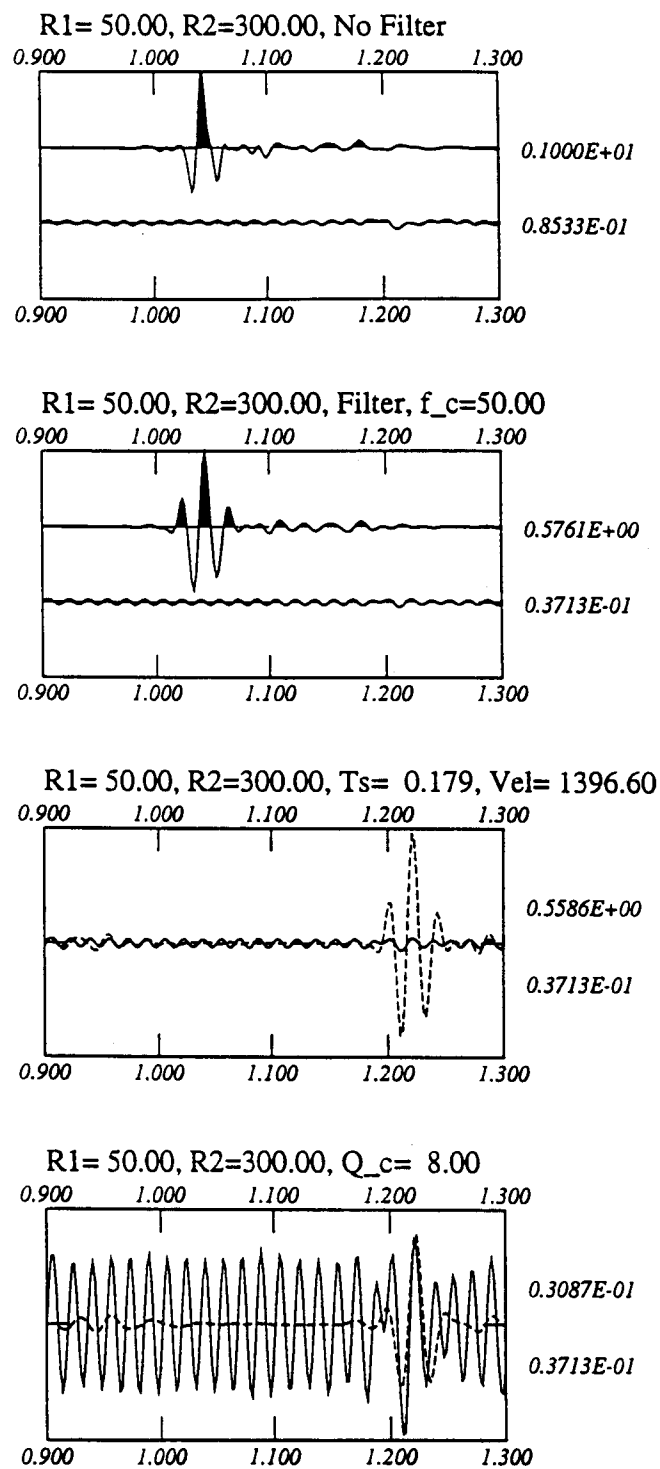


**Figure 8.A.3.B-80**

The synthetic propagation between 50 and 300 ft estimating the  $(1/r^{1.7})$  geometric spreading correction for no attenuation model.



**Figure 8.A.3.B-81**  
 Estimation of  $Q_s$  using the  $(1/r^{1.7})$  geometric spreading correction for the propagation depth of 50 and 300 ft of real Gilroy data. Estimated  $Q_s = 16$ .



**Figure 8.A.3.B-82**

Same as Figure 8.A.3.B-81 for the  $(1/r)$  geometric spreading correction. Estimated  $Q_s = 8$ .

# APPENDIX 8.A.4

## DOWNHOLE SEISMIC TESTS AT GILROY 2 AND TREASURE ISLAND

---

### 8.A.4.1 Introduction

This report presents the results of borehole velocity surveys that were performed in holes drilled into bedrock at Gilroy 2 and Treasure Island. The purpose of these measurements was to acquire shear- and compressional-wave velocities as a function of depth which, in turn, were to be used to compute the ground response to earthquake motion at each site.

### 8.A.4.2 Instrumentation and Procedures

#### 8.A.4.2.1 Downhole Velocity Surveys

A downhole triaxial geophone manufactured by Slope Indicator Co. was used as the sensor in the boreholes. Although the transducer is designed to track along the internal grooves in standard inclinometer casing, it can also be used in conventional PVC casing. the geophone assembly is mechanically locked to the casing at any desired depth by inflating a rubber bladder with nitrogen; the pressure is adjusted with a regulator to compensate for the hydrostatic head of water in the casing. The transducer cable has depth markers molded on to it at one-foot intervals.

Signals from the transducer were recorded on a Geometrics 2401 24-channel seismograph operated in a 12-channel mode. This instrument is of the 'instantaneous floating point' design with a dynamic range of 114 dB, and it is not necessary to set gain levels prior to recording. Trace amplitudes are adjusted after data acquisition and before printing on the built-in printer. Raw data are recorded on a 3.5-in 1,44 Mbyte disk drive for late retrieval and, if desired, digital filtering. The data on any channel(s) can be 'frozen,' leaving the remaining channels free to acquire new data. Four channels, consisting of the 'positive' and 'negative' shear-wave pulses detected on each of the two horizontal axes, were recorded at each depth point; the shear-wave signals from 3 depths can therefore be recorded on a 12-channel record.

The shear-wave energy source was a 7-ft-long 6 × 6 wood plank with steel end caps that was held in contact with the ground by the front wheels of an automobile. Horizontal blows with a 16-lb. hammer to each of the plank generate shear-wave pulses with opposite polarities. Because the azimuthal orientation of the horizontal geophones in the borehole is not know, it is necessary to record the signals detected by both of them. The signals from the downhole geophones can be routed to any desired channel on the seismograph by means of a simple switchbox.

At any given depth the 'positive' pulse from the energy source is detected by both horizontal geophones [H1 and H2], and these signals are routed to, say, channels 1 and 3 of the seismograph. The 'negative' blow to the other end of the plank is then recorded on channels 2 and 4. The positive and negative shear waves are subsequently superimposed graphically, i.e., channel 1 and 2 and channel 3 and 4, to more clearly show the shear wave. As a survey progresses deeper it is generally necessary to 'stack' repeated blows at each end of the plank to improve the signal-to-noise ratio.



## **8.A.4.3 Results**

### **8.A.4.3.1 Downhole Surveys**

The downhole shear-wave surveys started 15 December, 1990, at Gilroy 2 and, on the following day, in the hole behind the fire station on Treasure Island. Although an inspection of individual records in the field suggested that there might be problems with the quality of the data, it was not until the records could be subsequently examined as a complete set for each of these two holes that the problem of 'tube waves' became apparent.

A tube wave is a pressure pulse in the fluid [water] inside the casing that propagates down the hole nearly unattenuated and manifests itself by a radial displacement of the borehole wall. Tube waves with a relatively high amplitude can be generated near the top of the hole by the shear wave impinging on the hole. Their velocity is determined primarily by the bulk modulus of the fluid, the elastic modulus of the casing and the shear modulus of the surrounding material.

At shallow depths, less than about 150 ft., the amplitude of the shear wave exceeded that of the tube wave and the shear signals could be identified. As the surveys progressed deeper and the amplitude of the shear wave decreased due to geometric spreading and material damping, the higher-velocity, unattenuated tube wave began to obscure or mask the shear waves. The polarity of the tube wave appears to reverse, just as that of the shear wave itself does, when opposite ends of the source are struck. Consequently, an inspection of the seismograph records in the field during these initial attempts did not conclusively reveal that a tube wave was over-riding the desired shear signals at the deeper depths; the appearance and spectral content of the tube wave were close to those of the shear wave. Only when the records from the top of the borehole to the bottom could be assembled into a complete set was the problem readily apparent. Although tube waves are frequently observed in downhole surveys, they were especially pronounced in these 5-in. holes.

The solution to the problem, suggested by Walt Silva, was to pump the water out of the upper portion of the hole. We used a 1/2-hp submersible pump to do this prior to all subsequent downhole surveys, lowering the water level by approximately 100 ft before starting our measurements.

An example of tube waves observed in Gilroy 2 is shown in Fig. 8.A.4-1. The set of records at the top of Fig. 8.A.4-4 are from our initial attempt on 15 December when the hole was full of water, and the records shown at the bottom of the figure are from a repeat survey on 28 December, obtained after the water had been pumped down to a depth of 125 ft. It is evident that the tube wave [ $\sim 3150$  ft/sec] has completely obscured the shear wave at these depths. Figure 8.A.4-2 shows a similar example of tube waves observed in the hole at Treasure Island.

A persistent problem with downhole shear-wave surveys is that of tracking a consistent part or characteristic of the recorded waveforms with increasing depth. The transducer assembly can rotate as it is lowered down the hole, and the individual horizontal geophones can turn into and out of alignment with the source on the ground surface. Consequently, the strongest or 'best' signal can shift randomly from one geophone to the other and back again. The resulting changes in the shape of the waveforms, coupled with the existence of anisotropy, can complicate the task of following a particular phase of the shear signal down the hole.

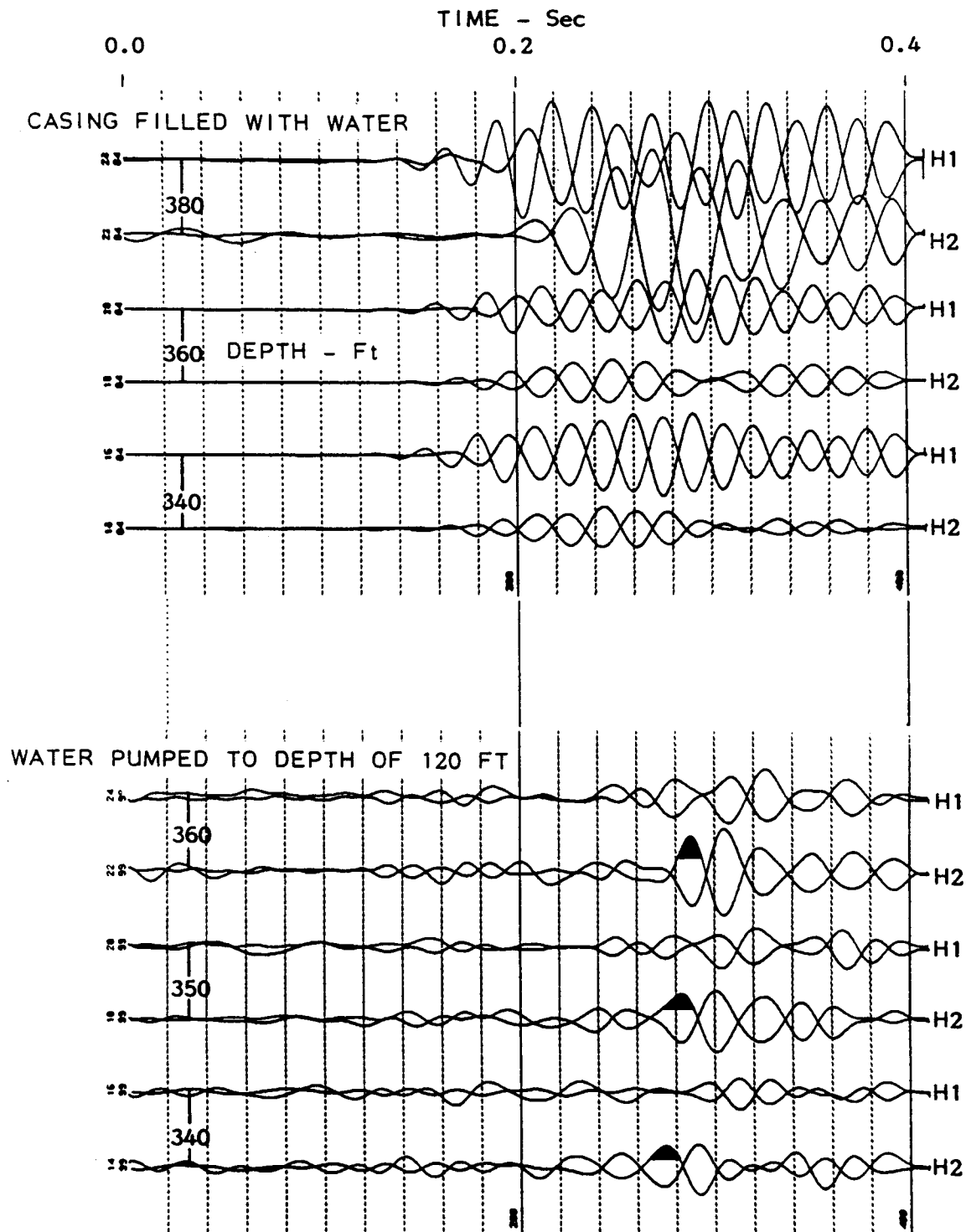
The assignment of arrival times to specific layers was done by working with large-scale plots of the data points. In many instances slightly different arrival times were observed on the two horizontal geophones. When judged appropriate, both arrival times were included in the least-squared fits to the data points.

A supplemental downhole survey was carried out on 23 April, 1991, at Gilroy 2 to acquire more closely spaced data points in the top of the hole; arrival times were measured by 5-ft depth increments to a depth of 150 ft. These data are indicated by the designated symbols in Fig. 8.A.4-3a, and were used to determine the final velocity profile over the upper portion of the hole.

The final results of the downhole velocity surveys are presented in two formats: (a) downhole travel times plotted against their corresponding depths together with least-squares fits to the data points, and (b) a graph of shear-velocity vs. depth. Figures 8.A.4-3 and 8.A.4-4 show the results for the boreholes at Gilroy and Treasure Island. Table 8.A.4-1 is a summary of the shear-wave velocities.

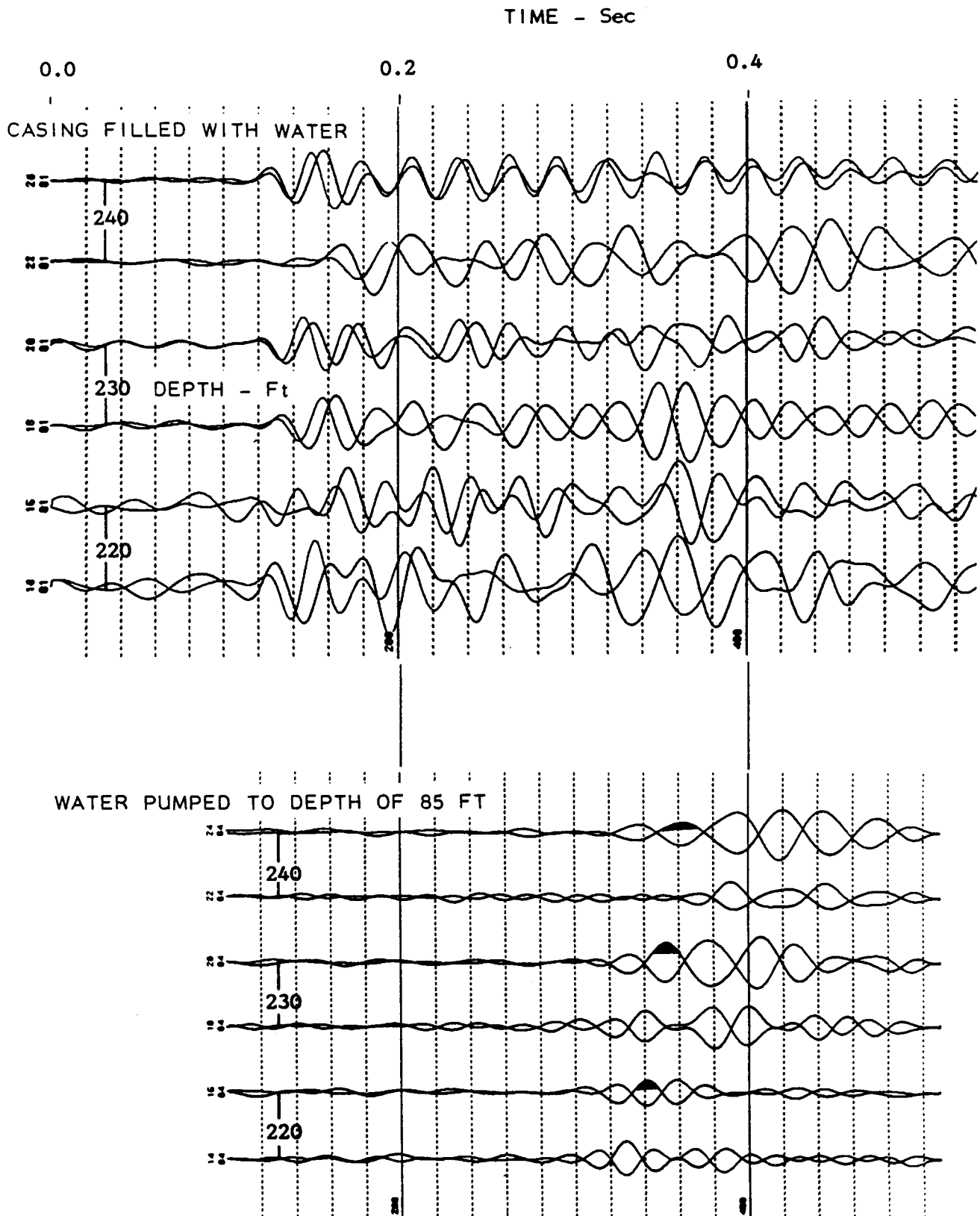
Shear-wave velocities were not obtained in the rock at the bottom of any of the deep holes. Shear wave amplitudes in rock were too weak to detect, despite stacking signals from up to 9 blows at each end of the plank. An example of the absence of recognizable signals in rock can be seen in the records for Treasure Island [Fig. 8.A.4.A-2 in Appendix 8.A.4.A] where identifiable shear waves abruptly disappear below a depth of 280 ft; according to the drill log, rock was encountered at a depth of 290 ft.

The appendix to this report contains copies of the downhole shear wave records collected in this program of measurements.



**Figure 8.A.4-1**

Comparison of downhole shear-wave records near depths of 350 ft at Gilroy 2 obtained with casing full of water (top) and with water pumped down to a depth of 120 ft (bottom). The 'tube waves' in the top record have completely obscured the shear waves that can be seen in the bottom record.



**Figure 8.A.4-2**

Comparison of downhole shear-wave records at depths of 220, 230, and 240 ft at Treasure Island obtained with casing full of water (top) and with water removed to a depth of 85 ft (bottom). Note that the 'tube waves' on the top records almost completely mask the shear waves that are visible on the bottom records.

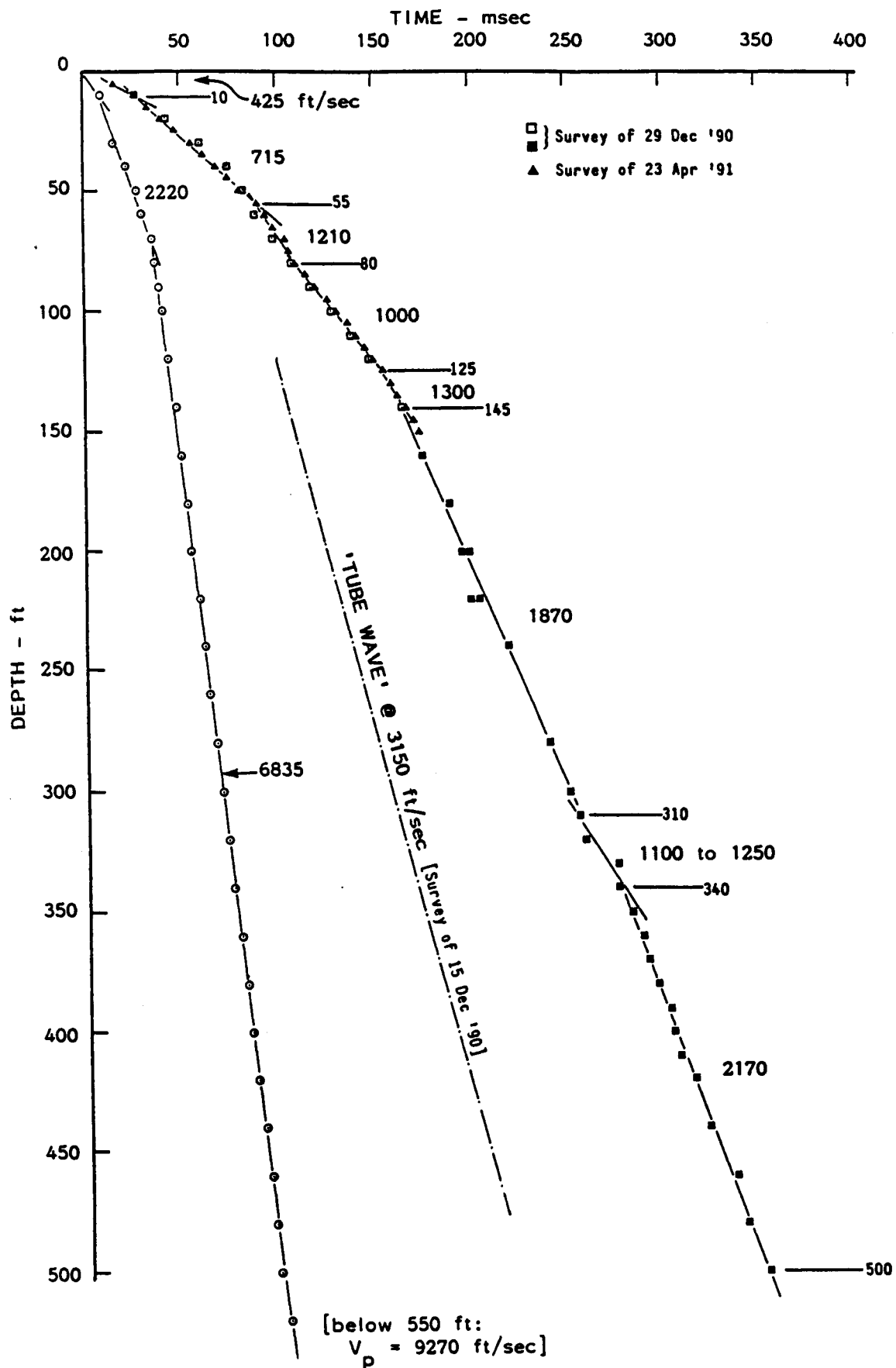


Figure 8.A.4-3a  
 Downhole travel times and corresponding least-squares velocities; Gilroy 2.

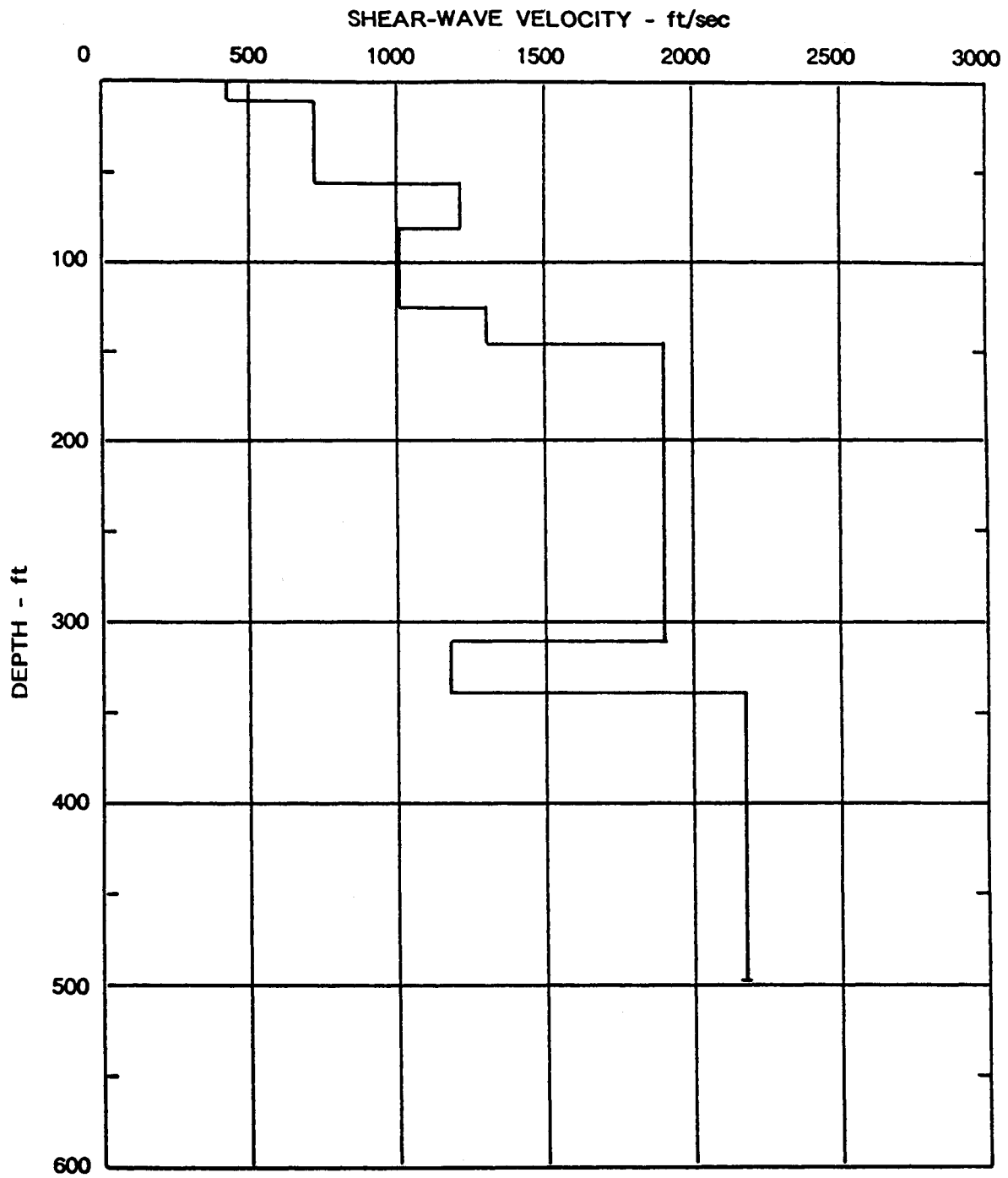


Figure 8.A.4-3b  
Shear-wave velocity profile; Gilroy 2.

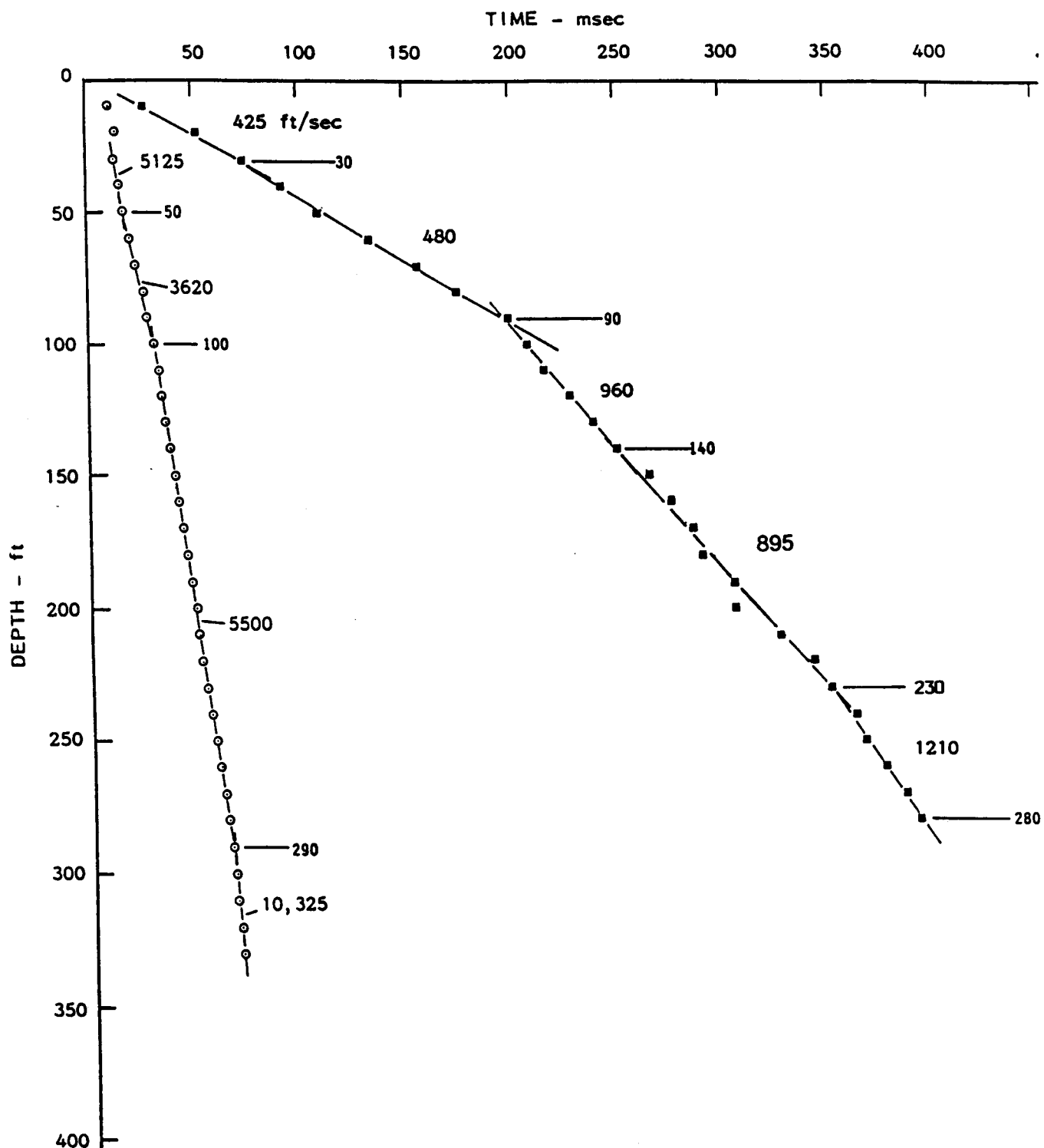


Figure 8.A.4-4a  
Downhole travel times and corresponding least-squares velocities; Treasure Island.

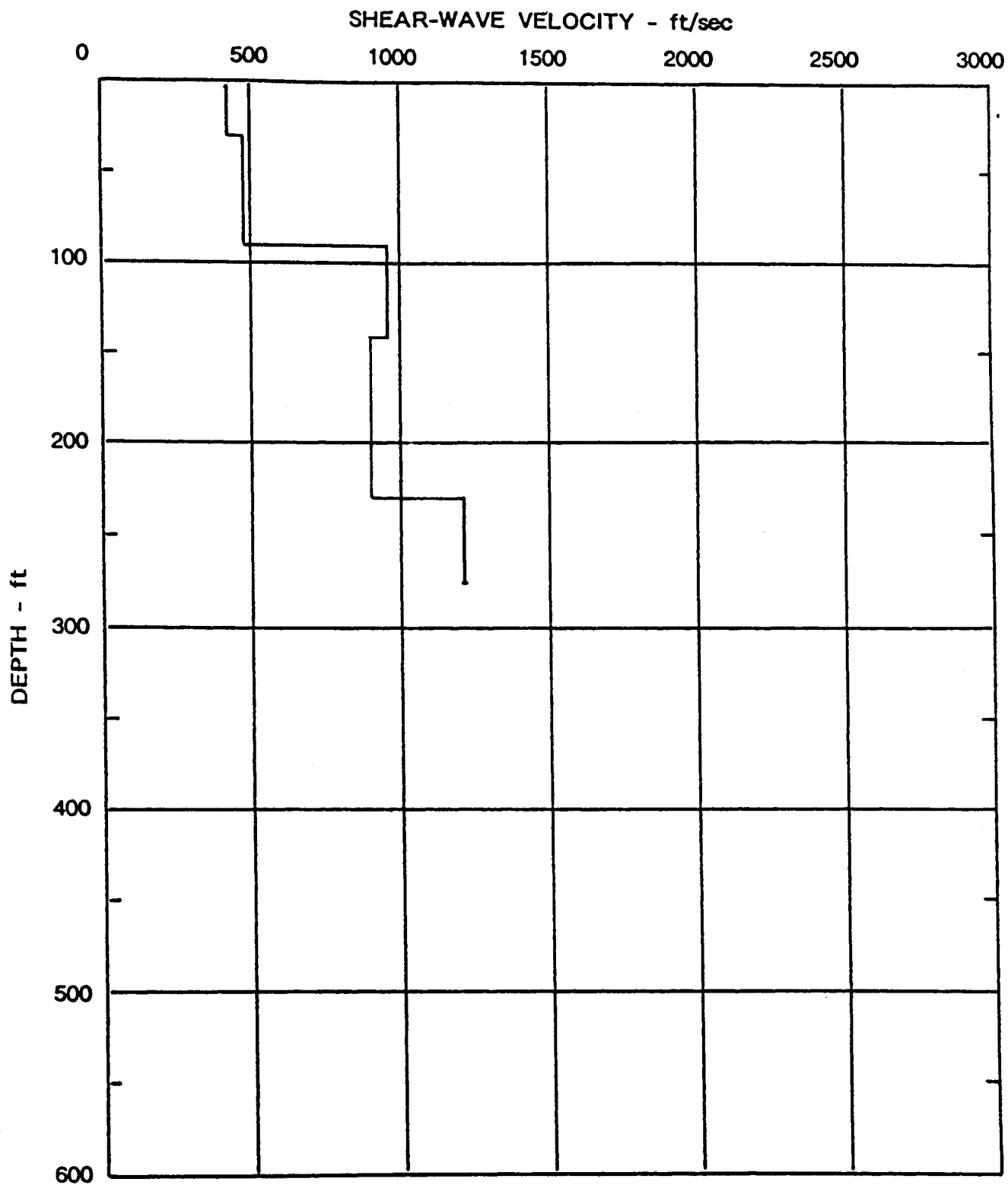


Figure 8.A.4-4b  
Shear-wave velocity profile; Treasure Island.

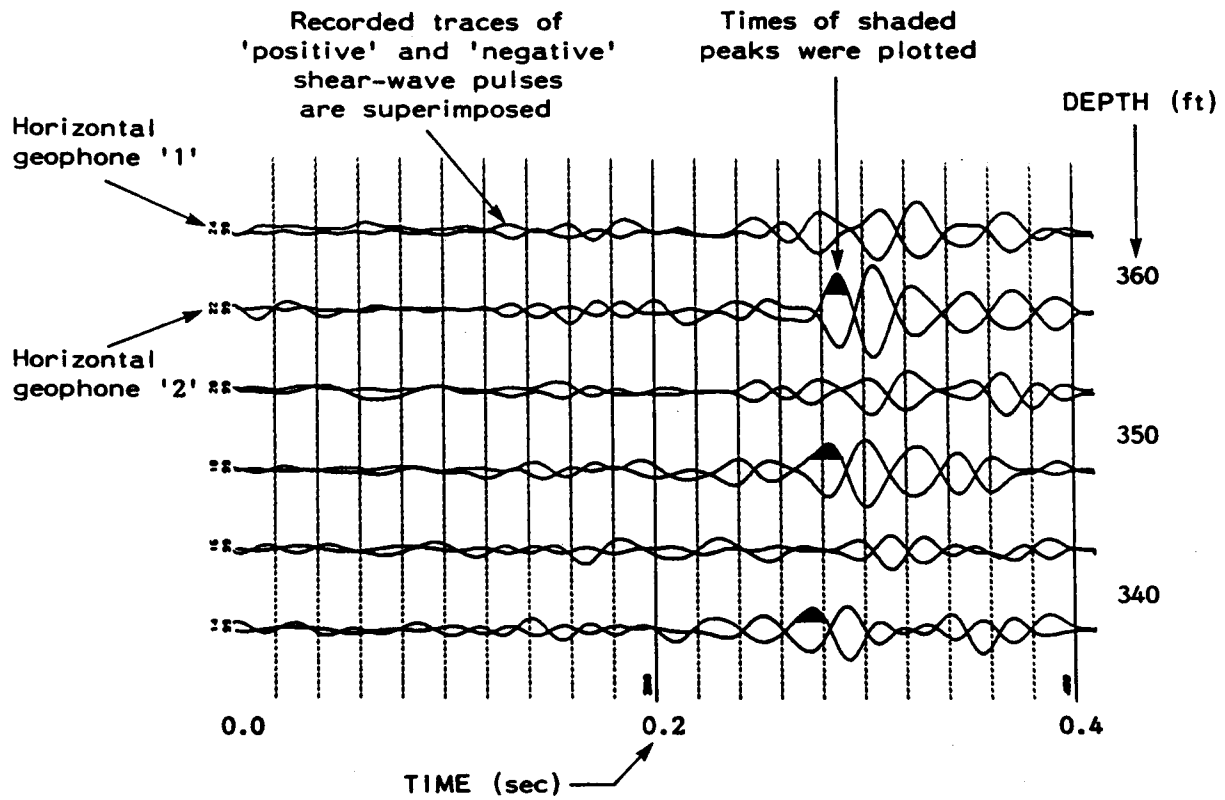


**Table 8.A.4-1**  
Shear-Wave Velocities

<b>Borehole</b>	<b>Depth Internal</b>	<b>Velocity</b>
<b>Gilroy 2</b>	0-10 ft	425 ft/sec
	10-55	715
	55-80	1210
	80-125	1000
	125-145	1300
	145-310	1870
	310-340	1175
	340-500	2170
<b>Treasure Island</b>	0-30 ft	425 ft/sec
	30-90	480
	90-140	960
	140-230	895
	230-280	1210

## APPENDIX 8.A.4.A

Reproductions of the downhole shear-wave records are contained in this section. The format of the records is shown below.



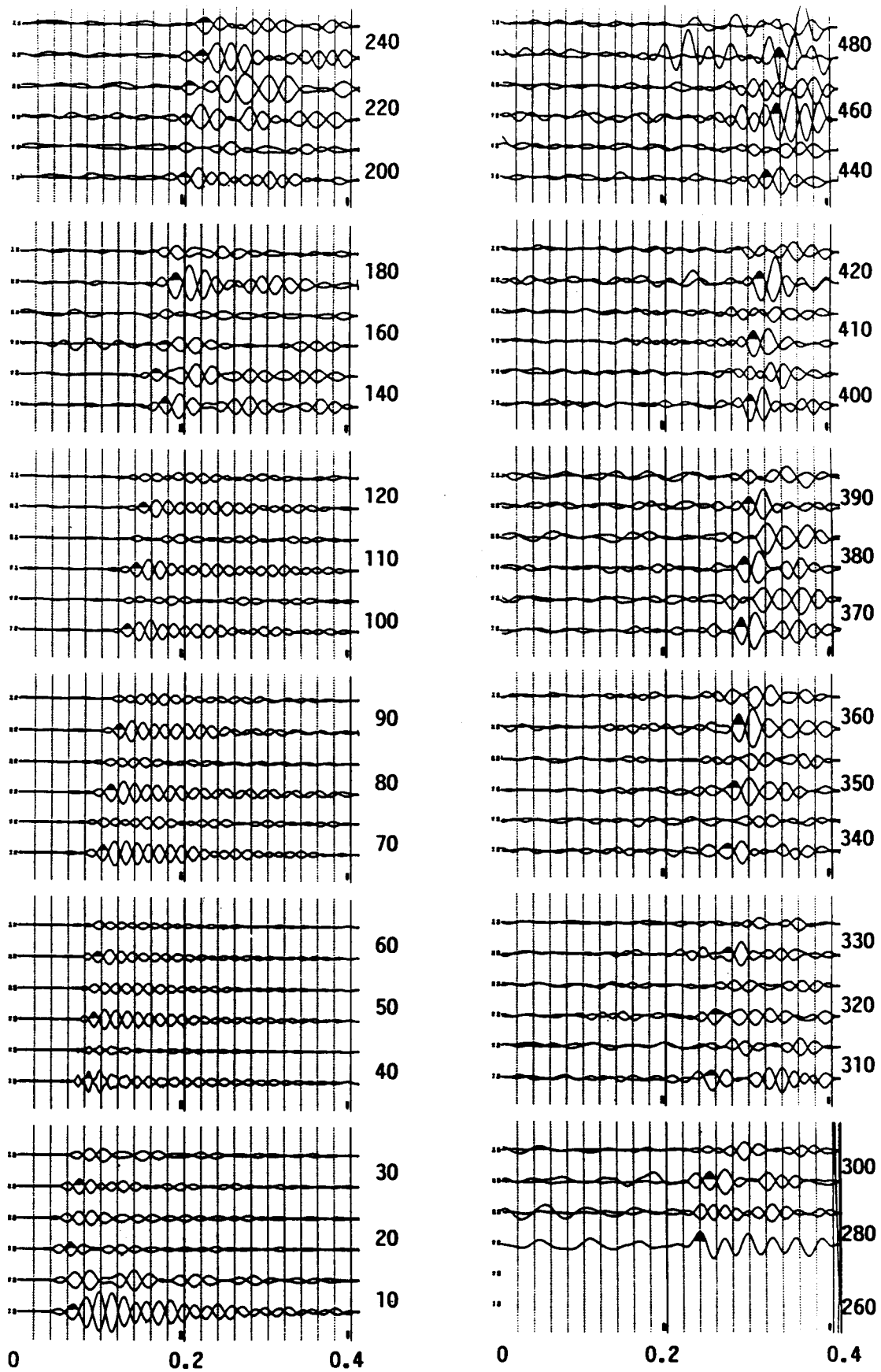
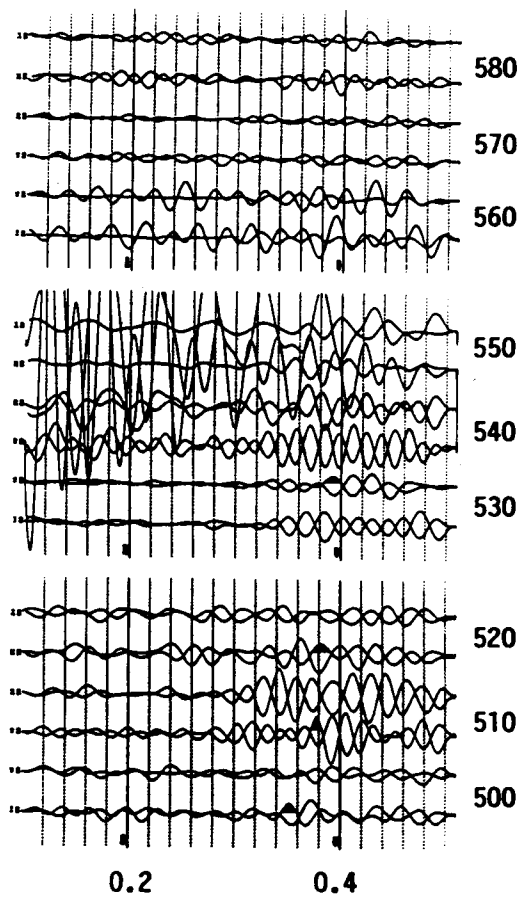


Figure 8.A.4.A-1a  
Downhole shear-wave records; Gilroy 2.



**Figure 8.A.4.A-1b**  
Downhole shear-wave records; Gilroy 2.

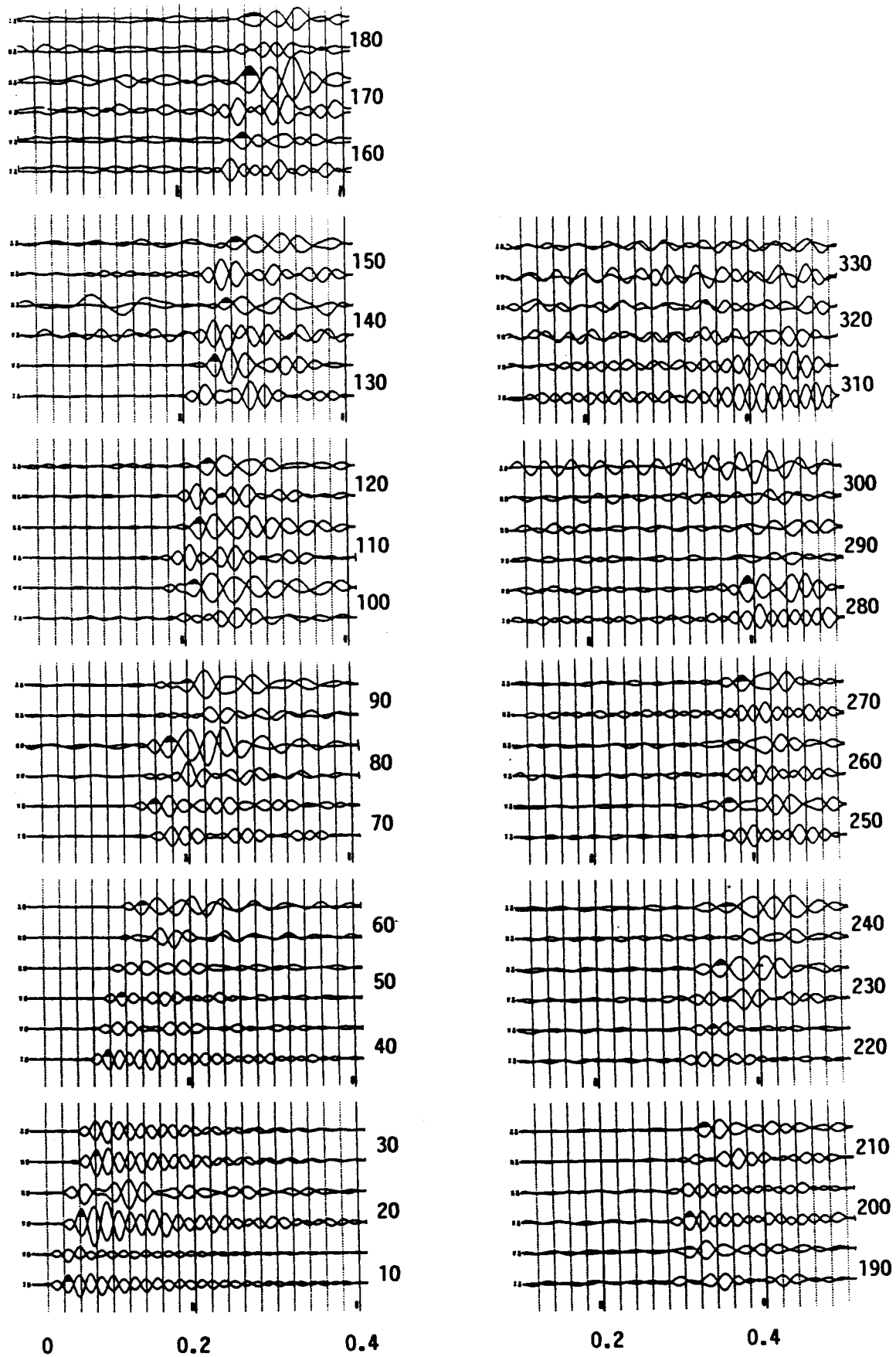


Figure 8.A.4.A-2  
Downhole shear-wave records; Treasure Island.

# **APPENDIX 8.A.5 GEOTECHNICAL BORING AND SAMPLING AT TREASURE ISLAND AND GILROY 2 STRONG MOTION ACCELEROGRAPH SITES**

---

## **1—INTRODUCTION**

As part of the Electric Power Research Institute's (EPRI) research program to develop guidelines for estimation of earthquake ground motions for application to seismic design of future power plants, a geotechnical site-exploration program was undertaken to study the subsurface conditions at two strong ground-motion sites where ground motions were recorded during the October 17, 1989, Loma Prieta earthquake. The two sites under investigation were Naval Station Treasure Island, located in the middle of San Francisco Bay, and Gilroy array 2 located in southern Santa Clara County, California. Both stations are owned and operated by the California Division of Mines and Geology (CDMG) Strong Ground Motion Instrumentation Program (SMIP). Woodward-Clyde Consultants (WCC) was retained by EPRI to coordinate the subsurface investigation program under EPRI Contract No. RP-3302-15. The California Division of Mines and Geology (CDMG) and the U.S. Geological Survey (USGS) participated in the field investigation program.

Permits and arrangements for drilling were coordinated by Dr. Joseph I. Sun and Ms. Susan Chang of WCC. All borings were drilled by Pitcher Drilling Company of Palo Alto, California. Mr. Thomas Fumal (USGS) logged the borings at these two sites. A number of parties participated in the geophysical investigations at these two sites; they include: University of Texas, Austin (Dr. Ken Stokoe), Agbabian Associates (Mr. Robert Steller), Redpath Geophysics (Mr. Bruce Redpath), USGS (Mr. James Gibbs), University of New Hampshire (Dr. Pedro de Alba), and University of Michigan (Dr. Roman Hryciw). Investigations performed by the University of Texas, Agbabian Associates, and Redpath Geophysics are under EPRI's contract and investigations performed by the University of New Hampshire and the University of Michigan were sponsored by the National Science Foundation (NSF).

Section 2 of this report includes a description of the field investigation procedures. Sections 3 and Section 4 describe the details of the permitting, subsurface conditions encountered, site contacts, site plans, and geologic maps for these two sites. Borings logs for these two sites are presented in USGS Open File Report 92-287 (1992) and are included in Appendix 8.A.5.A for reference.

## **2—GEOTECHNICAL FIELD INVESTIGATION PROCEDURES**

### **8.A.5.2.1 Soil Sites**

#### ***8.A.5.2.1.1 Drilling and Sampling***

A truck-mounted Failing 1500 rotary wash drill rig was used to advance the borings drilled for this study. Bentonite drilling mud was used when necessary to stabilize the hole. The borings were initially drilled to their full depth using a 5-inch nominal-diameter tri-cone bit (pilot hole). Soil samples in sandy materials were taken with a Standard Penetration Test (SPT) split-spoon sampler (1-3/8-inch I.D.) using a 140-lb safety hammer dropping 30 inches. Hydraulically pushed Shelby tubes (3-inch O.D.) were used to take "undisturbed" samples in soft to medium stiff cohesive materials. A Pitcher barrel sampler (3-inch-O.D. Shelby tubes) was used to take "undisturbed" samples in materials too stiff to push Shelby tubes. Modified California drive samples (2-1/2-inch I.D.) were taken with 325-lb downhole hammer (jars) below 100 feet deep at the Gilroy site. All samples were taken from the pilot holes. "Undisturbed" soil samples were stored in water-tight tubes, sealed, and labelled immediately upon retrieval from the borehole. All 3-inch-O.D. samples were allowed to drain of free water and were sealed with wax plugs and endcaps. Disturbed samples taken with the SPT split spoon were labeled and put in sealed plastic bags after retrieval for soil index property testing.

SPT samples taken in sandy strata from the sites were sent to Dr. I.M. Idriss of the University of California at Davis for index testing. All "undisturbed" samples, including Pitcher barrel samples, push Shelby samples, and 2-1/2-inch O.D. modified California samples taken from these two sites were shipped to Dr. Kenneth Stokoe at the University of Texas, Austin for dynamic and static strength tests.

#### ***8.A.5.2.1.2 Reaming and PVC Casing***

After drilling and sampling in the 5-inch pilot hole, the boreholes in soil were reamed to a nominal diameter of 10 inches or 8 inches to permit installation of 5-inch and 4-inch PVC casings, respectively. The purpose of the casing is to allow seismic wave velocity measurements to be made in the boreholes. The boreholes drilled at Treasure Island (WCC-1 in Figure 8.A.5-1) and at Gilroy (EPRI-1 in Figure 8.A.5-4) was cased with 5-inch (nominal), solvent-weld-bell-end class 200 PVC pipe with ASTM F480 crush strength rating. The bottom 7 feet of the 5-inch PVC casing contains a downhole accelerometer orientation package (Bishop's hat). This package will be used by CDMG at a later date to install a downhole accelerometer. Both the 5-inch PVC pipe and the Bishop's hat were supplied by the CDMG Strong Motion Instrumentation Program (SMIP). The second, third, and fourth boreholes drilled at Gilroy 2 (EPRI-2,3, & 4 in Figure 8.A.5-4) were cased with a nominal 4-inch schedule 40 PVC without the Bishop's hat. The schedule 40 PVC is slightly thicker than the class 200 PVC and has a higher crush strength rating.

#### ***8.A.5.2.1.3 Grouting and Protective Covering***

The annular space around the PVC pipe was tremie grouted with a cement-bentonite grout to establish good contact between the pipe and the wall of the borehole. The thickness of the grout seal was approximately 2-1/2 inches for the 5-inch casing and about 3 inches for the 4-inch casing. The grout used was a mixture of water, cement, and bentonite proportioned using four 94-lb bags of cement and 17 lb (one-third 50-lb bag) of bentonite for one 55-gallon drum of grout. The grout was applied in stages, depending on the depth of the boring, to prevent the grout pressure from collapsing the pipe. The maximum height for each grout stage was about 150 feet.

After grouting of the PVC casing, the hole collars were fitted with an 8-inch-diameter 3-foot length of steel casing and a Christy box set in grout. A locking mechanism either on the steel casing or the PVC pipe itself was provided for each hole. The top of the inner PVC pipe was capped with a vented PVC cover and was within 2 inches of the top of the steel pipe.

Boreholes drilled by University of New Hampshire (UNH-1 through UNH-5 in Figure 8.A.5-2), which were used in conjunction with WCC-1 in the crosshole velocity measurements, were drilled, cased, and grouted with the same procedure as those specified for WCC-1.

#### ***8.A.5.2.1.4 Disposal of Waste Material from Drilling***

Waste material (drill cuttings) generated from the drilling operations consisted of soil, drilling mud, and water. The volume of the waste generated is typically three to five times the volume of the excavated borehole. The cuttings were temporarily stored in 20-cubic-yard capacity bins (provided by Erickson Inc.) or in 55-gallon drums before final disposal. At Treasure Island, a representative from the Naval Station's civil engineering department (Mr. Donald Brown) was able to help us locate a suitable site for disposal of the waste material on site. At Gilroy 2, the waste materials were transported off site and disposed of at a commercial landfill facility by Able Septic Service in accordance with local environmental jurisdiction.



### **3—NAVAL STATION TREASURE ISLAND**

#### **8.A.5.3.1 Authorization and Permitting**

The strong motion instrument (no. 58117) is located in Building 157, at the corner of D and 10th streets on Treasure Island, as shown in Figure 8.A.5-1. Currently, the Treasure Island Fire Department is occupying this building and the strong motion instrument is located at the northwest corner of the fire truck bay, as shown in Figure 8.A.5-2. On November 2, 1990, WCC wrote to Mr. Tom Cuckler, Civil Engineer at Naval Station Treasure Island, regarding the proposed drilling program. The drilling program was approved by A.E. Spencer (Lt. CEC, U.S. Navy, Naval Station Treasure Island) on November 8, 1990, and WCC also received a License Contract (No. 6247491RP00P47) from Ms. Beverly Freitas (U.S. Navy Real Estate Division) on April 5, 1990, permitting WCC to install the downhole accelerometer. The borehole is located in the lawn area in the back of the building, approximately 60 feet west of the instrument, as shown in Figure 8.A.5-2. The drilling program and the disposal of drill cuttings were arranged with Mr. Donald C. Brown of the Naval Station Treasure Island. The drilling started on November 19, 1990, and ended on November 30, 1990. The top of the 5-inch PVC was enclosed in a Christy box flush with the adjacent ground.

#### **8.A.5.3.2 Subsurface Site Conditions**

Treasure Island was created by placing artificial fill in relatively shallow waters over bay mud and a former natural sand spit known as Yerba Buena Shoals, on the northern side of Yerba Buena Island. The fill consists of sand, shells, and mud dredged from the bay, and placed within a sea wall by pumping. Constructed in 1936 to 1938 as the site for the Golden Gate International Exposition of 1939, it has been a U.S. Naval reservation since World War II.

Woodward-Clyde-Sherard and Associates performed a soil investigation for the U.S. Naval School Command Barracks on Treasure Island in 1966. One of the borings drilled for that study extended to baserock; the location of that boring is also shown in Figure 8.A.5-1. The subsurface soil encountered in that boring consisted of 40 feet of loose to medium dense sand overlying 60 feet of soft Bay mud and, in turn, underlain by 15 feet of medium dense sand and followed by 175 feet of medium stiff clay. Sandstone was encountered at a depth of 290 feet below existing ground surface.

The borehole drilled behind the fire station for this study was logged by Mr. Thomas Fumal (USGS) and showed similar subsurface conditions. At this location, the site is underlain by 44 feet of loose to very loose uniformly graded medium to fine sand, followed by 50 feet of soft, very dark greenish gray Bay mud. Beneath the Young Bay mud, we encountered 40 feet of greenish gray sand and sandy loam with occasional pieces of gravel overlying 155 feet of dark greenish gray stiff clay that extends to 290 feet. We encountered deeply weathered shale, pale olive in color, at about 290 feet. This is underlain by 20 feet of hard greenish gray to dark brownish gray shale and 20 feet of fine-grained sandstone to the bottom of the boring at 340 feet. The water table was measured at a depth of 4 feet at the time of drilling. A copy of this boring log is included in Appendix 8.A.5.A for reference.

In August 1991, Professor Pedro de Alba of the University of New Hampshire was funded by the National Science Foundation to install five more boreholes close to the one drilled for this study. These five were drilled to a maximum depth of 145 feet. The PVC casing and grout specification followed the same procedure used in this study. The locations of these six borings are shown in Figure 8.A.5-2. A geologic map of the site is shown in Figure 8.A.5-3.

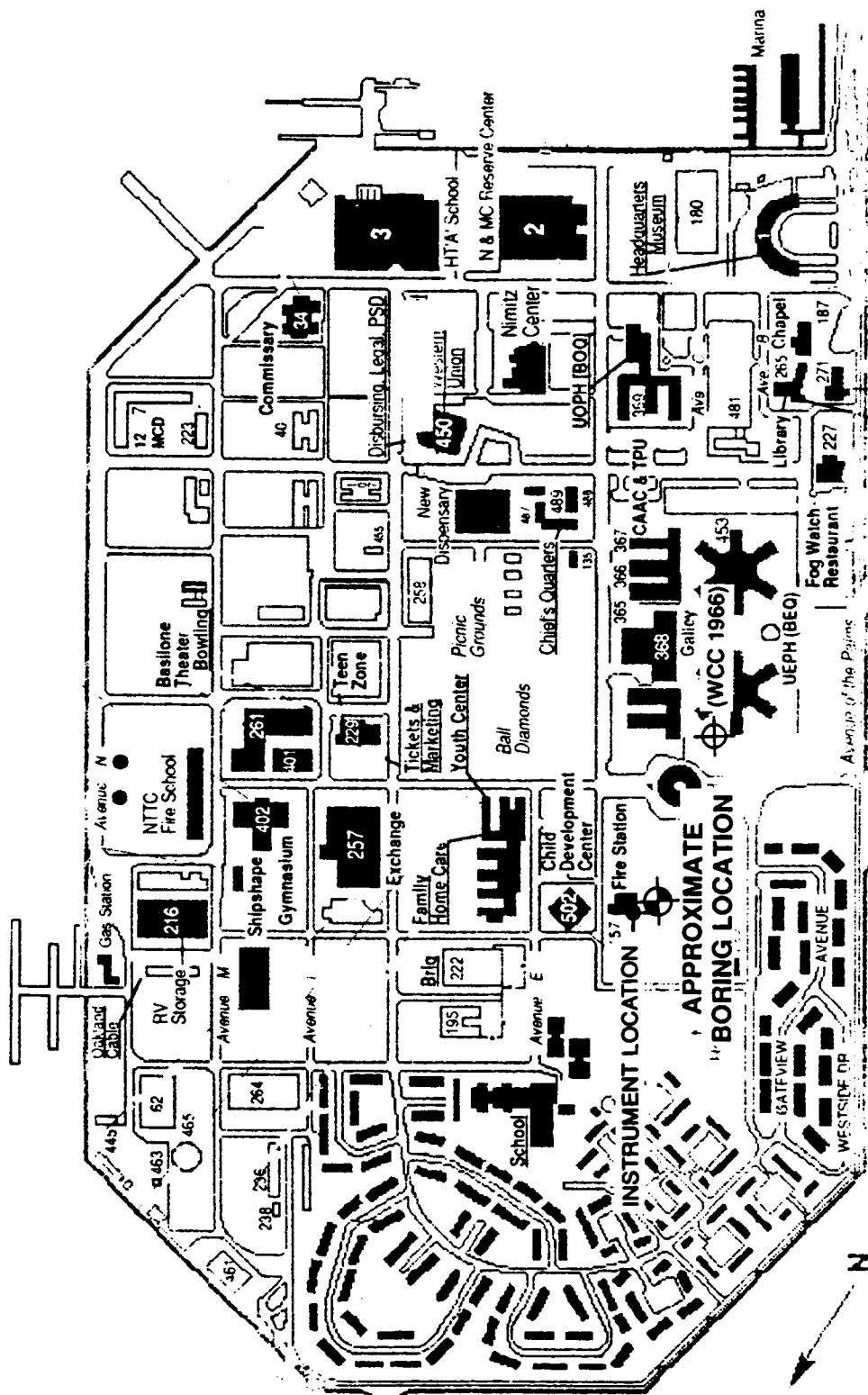


Figure 8.A.5-1  
Site plan, Treasure Island fire station.

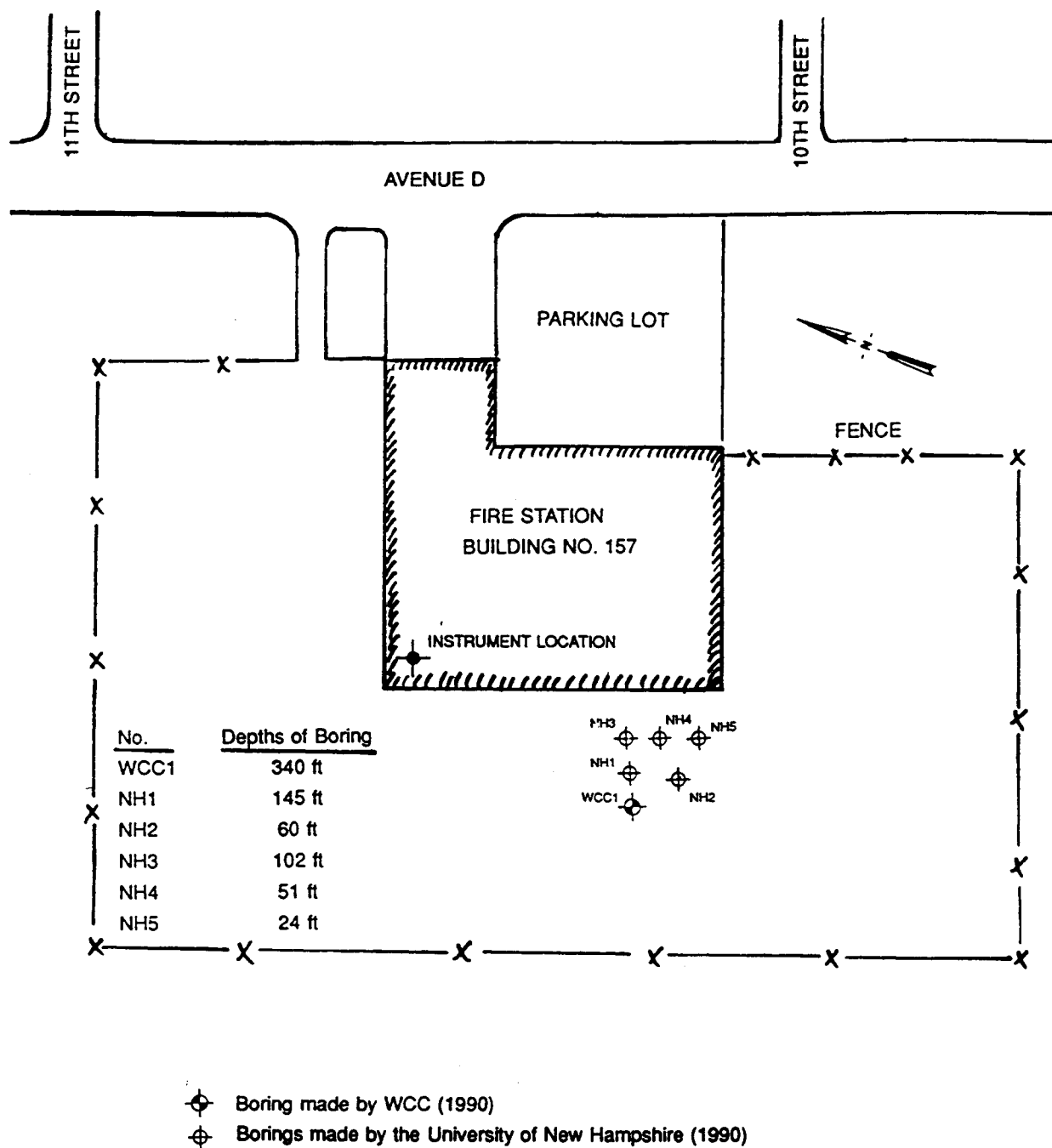
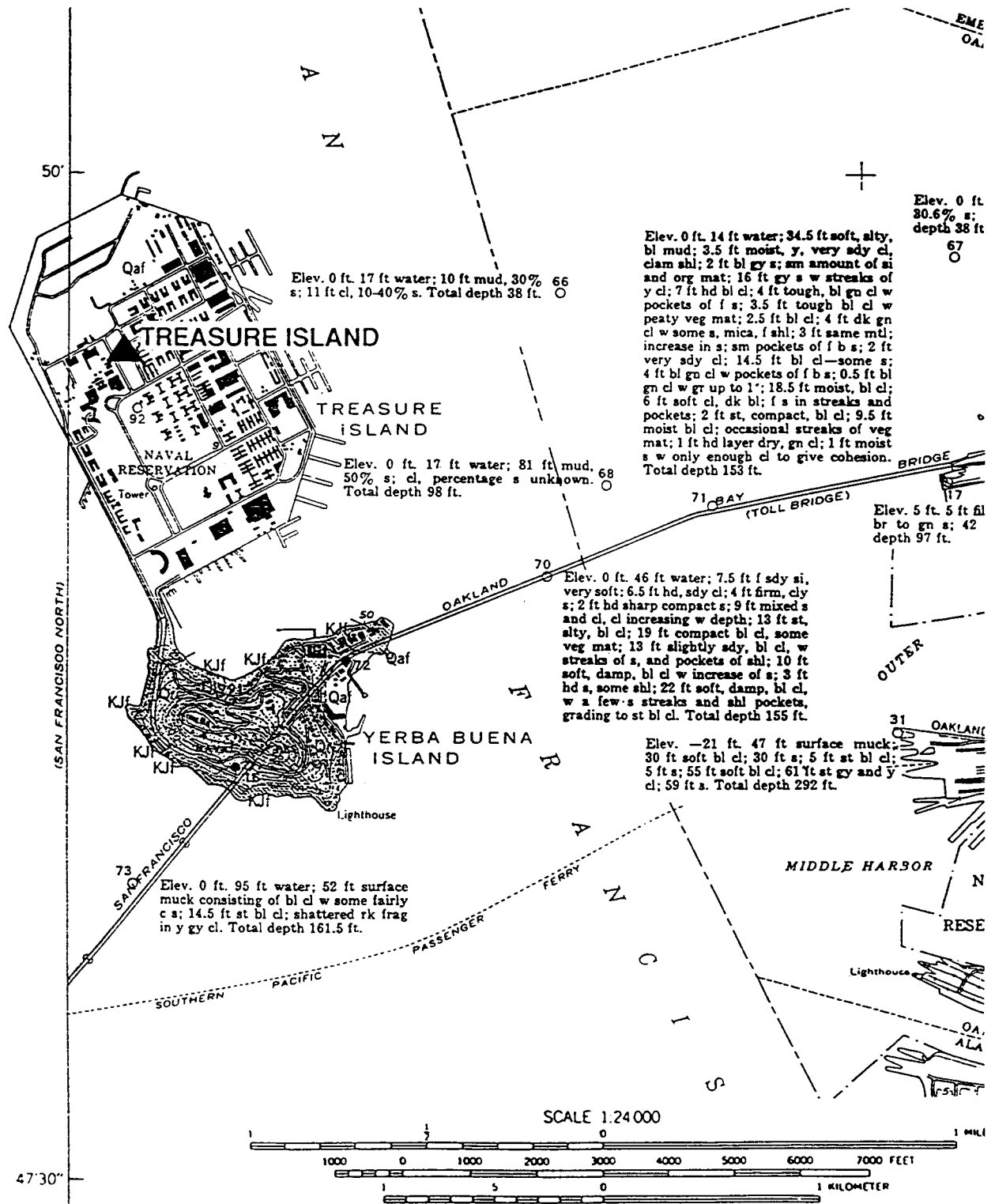


Figure 8.A.5-2  
Boring location plan, Treasure Island fire station.



**Figure 8.A.5-3**

Areal and engineering geology of the Oakland west quadrangle, California, USGS miscellaneous geologic investigations map I-239 (Radbruch, 1957).

#### **8.A.5.3.3 Loma Prieta Earthquake**

The site is located about 80 km north of the epicenter of the 1989 Loma Prieta earthquake. The ground motion instrument on Treasure Island recorded horizontal accelerations of 0.16 and 0.11 g's during the event. The strong ground shaking of the Loma Prieta earthquake liquefied the hydraulic fill above the Bay mud on Treasure Island. This was evident by the numerous sand boils present on the island after the earthquake. However, we understand that there were no sand boils within the fire station property where the instrument and the boreholes are located.

#### **8.A.5.3.4 Site Contacts**

Mr. Tom Cuckler  
Code 82  
Naval Station Treasure Island  
San Francisco, CA 94130  
(415) 395-5446

Mr. Donald C. Brown  
Naval Station Treasure Island  
San Francisco, CA 94130  
(415) 395-5446

Ms. Beverly Freitas  
Head, Central Section  
Realty Operations Branch  
Real Estate Division  
P.O. Box 727  
San Bruno, CA 94066-0720  
(415) 244-3805

## **4—GILROY ARRAY 2 (NATIONAL 9 INN)**

### **8.A.5.4.1 Authorization and Permitting**

Gilroy Array 2 is located at the National 9 Inn in Gilroy, California, as shown in Figure 8.A.5-4. The strong motion instrument (no. 47380) is located in the filter room near the swimming pool. The existing USGS boreholes and the boreholes made for this study are both located towards the back of the motel. On August 30, 1990, WCC wrote to Mr. John Belleau, the property owner, addressing the purpose of this field study and requesting permission to drill on the property. Mr. Belleau gave WCC verbal authorization to drill in early September. WCC applied for a drilling permit from the Santa Clara Valley Water District, and it was approved on September 5, 1990 (Permit No. 90W1846). WCC coordinated the drilling schedule with Marie and Roger Elissondo (the motel managers).

### **8.A.5.4.2 Subsurface Site Conditions**

The first boring (EPRI-1 in Figure 8.A.5-4) was drilled between September 21 and October 12, 1990 to a depth of 600 feet. The top of the 5-inch PVC was made flush with the ground. According to the boring log by Mr. Thomas Fumal (USGS), the subsurface soil consists of 70 feet of brown sandy loam with gravels and pebbles overlying 60 feet of dark to very dark, greenish grey silty clays with sand lenses and, in turn, underlain by about 190 feet of yellowish brown sand and gravels with occasional olive brown clay lenses. Between depths of 320 feet and 550 feet, the soil consists of yellowish brown clayey sands. Bedrock was encountered at 550 feet, and drilling was continued in the rock for another 50 feet. The bedrock encountered in the 50 feet of drilling consisted of 27 feet of brown siltstone overlying serpentine. The bottom of the borehole is 600 feet below ground surface.

Three additional borings were drilled between October and November of 1991 at Gilroy 2 site. The four borings were aligned and the distance between each boring is 14-feet on-center as shown in Figure 8.A.5-5 to facilitate crosshole shear wave velocity measurements. Boring EPRI-2 was drilled next to EPRI-1 to a depth of 780 ft, and the remaining two borings (EPRI-3 and EPRI-4) both were drilled to 200 feet deep. The boring logs for EPRI-1 and EPRI-2 are presented in Appendix 8.A.5.A for reference.

Available geological data show that the Gilroy site is located in the southern Santa Clara Valley on “young alluvial fan deposits” of Holocene age. This material has been described as consisting of unconsolidated, moderately sorted permeable sand and silt with coarse sand and gravel. Rogers and Williams (1974) summarized well logs in Santa Clara County and plotted the estimated depth to bedrock contour map, as shown in Figure 8.A.5-6. The number adjacent to the closed symbol indicates the depth to bedrock below the ground surface encountered at each well, in feet. Open symbols indicate that the wells did not penetrate into bedrock. It is apparent that the Gilroy site is close to the eastern edge of the Santa Clara Valley, underlain by the steeply dipping Carlyle Hills on the west. It can also be seen from Figure 8.A.5-5 that, approximately 1 mile east of the site, near the middle of the valley, depth to bedrock may be in excess of 2,000 feet, as indicated by one well drilled to 1,890 feet that did not hit bedrock.

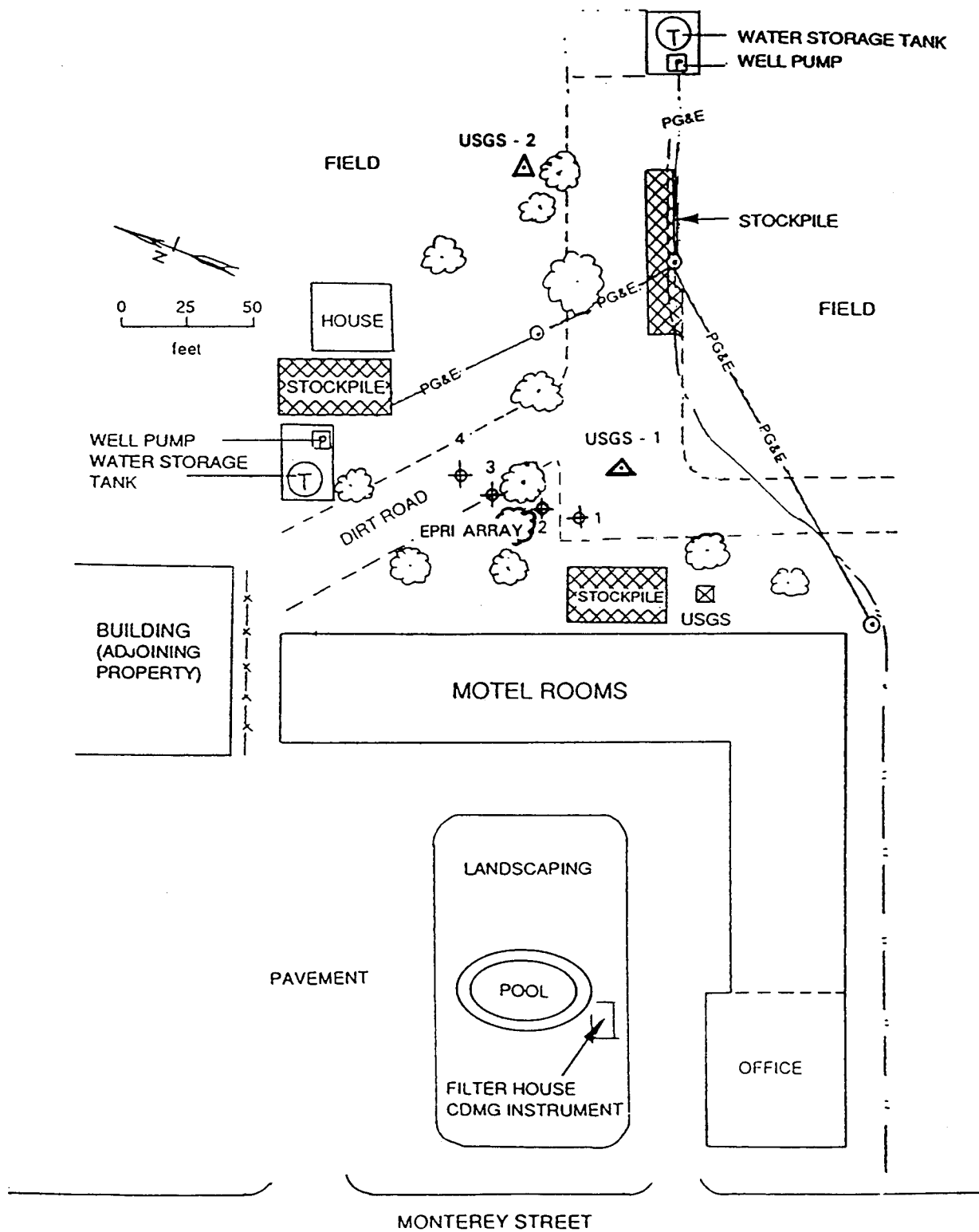
In addition to the four boreholes mentioned above, USGS drilled two boreholes at the same site in 1979. The first of these two (USGS-1 on Figure 8.A.5-5) was drilled to a maximum depth of about 130 feet. The boring log and wave velocity measurements of this borehole are presented in USGS Open-File Report 82-407 (1982) and are included in Appendix 8.A.5.B for reference. We were unable to locate this borehole during this study and believe that this borehole is buried and lost.

The second USGS boring (USGS-2 on Figure 8.A.5-5) was also drilled in September of 1979 to a maximum depth of 600 feet. This borehole is located about 100 feet east of EPRI-1. USGS was able to recover this borehole in 1991. The borehole is accessible and in-situ wave velocity measurements performed. The boring log and wave velocity measurements are presented in Appendix 8.A.5.B for reference.

GEOLOGIC UNIT	LITHOLOGY	DISTRIBUTION AND THICKNESS	TOPOGRAPHIC FORM	ORIGIN OF DEPOSIT
Artificial fill Qaf	Consists of miscellaneous refuse, bay mud, or sand dredged from bay; composition varies from place to place; may be difficult to distinguish from natural bay mud or Merritt sand. In most places overlies bay mud.	Along shore of bay and on Treasure Island. Maximum known thickness 25 feet.	Flat, level areas a few feet above sea level.	Manmade.
Reworked colluvium Qrc	Sand, fine-grained. Moderate yellowish-brown. Predominantly quartz and feldspar, mostly highly altered; some magnetite and biotite, minor amounts of other minerals; contains fragments of sandstone up to three-eighths inch in diameter; slightly cemented with silt and clay. Grains subangular to subrounded, frosted. Well-sorted. Varies from loose windblown sand to slightly coherent clayey, silty sand, which can be crumbled between the fingers. Lies on sandstone of the Franciscan group.	Fills ravines, mantles slopes and hilltops on Yerba Buena Island. Maximum known thickness 90 feet.	Ravine filling, follows contours of hills; forms flat benches in places.	Residual, derived from underlying sandstone of the Franciscan group; reworked by gravity, water, and wind.
Bay mud Qbm	Silt, clayey, sandy, with small lenses of sand; contains shells and organic material, which in some places is abundant enough to form thin layers of peat. Olive-gray. Massive, structureless. Soft and fluid at top, increasingly consolidated with depth. Plastic. Swells when wetted, shrinks and cracks upon drying. Overlies Temescal formation, Merritt sand, or Alameda formation.	Underlies water of bay and most artificial fill; ranges in thickness from a few inches to 85 feet; exposed on north side Alameda.	Slopes gently from landward edge toward the center of the bay; cut by meandering tidal channels.	Fine material held in suspension in bay water, deposited in quiet reaches of San Francisco Bay.
Merritt sand Qm	Sand, fine-grained, silty, clayey, with lenses of sandy clay and clay. Yellowish-brown to dark yellowish-orange. Grains consist of quartz and feldspar, some magnetite, flakes of white chert from the Claremont, minor amounts of sandstone, shale, hornblende, pyroxene, biotite. Grains angular to subrounded, frosted. Well-sorted. Contains small fragments of roots, twigs, grass. No bedding observed. Slightly coherent, in most places consolidation increases at depth; number of clay lenses increases to north; upper 1 to 2 feet loose, contains humus. Overlies Alameda formation; grades laterally into Temescal formation.	Covers Alameda and southern part of Oakland, underlies bay mud in bay south and west of Alameda and west of Oakland. Thickness varies from a few inches to known maximum of 65 feet.	Where exposed at surface forms low, rounded hills.	Wind- and water-deposited beach and near-shore deposits.
Temescal formation Qtc	Gravel, clayey, clay, sandy, silty; and sand-clay-silt mixtures. Pale yellowish-orange to dark yellowish-orange. Pebbles in gravel consist largely of quartz, sandstone (most very soft), chert from the Franciscan, shale, white banded chert from the Claremont, and miscellaneous igneous rocks. In some places beds of differing composition (as gravel and clay) grade into each other laterally and vertically; in other places the contact between beds is sharply defined. Some crossbedding. Most is coherent; may be crumbled between the fingers. Grades laterally into Merritt sand; overlies the Alameda formation.	Covers most of surface between Berkeley Hills and shore of bay; from 5 to 60 feet in thickness.	Gently sloping coastal plain, in some places dissected by streams.	Alluvial fan material brought down from Berkeley Hills.
Alameda formation Qa	Upper exposed part is clay, sandy, silty, with few pebbles. Formation includes several hundred feet of sediments underlying the bay and coastal plain, comprising continental and marine gravels, sands, silts, and clays, with some shells and organic material in places. Olive-gray to moderate yellowish-brown. Consolidation increases with depth, except that upper portion has been preconsolidated, possibly by desiccation (Trask and Rolston, 1951, p. 1082). Borings indicate soil zones within the Alameda; in places an old soil is exposed at the top of the formation. Overlain by Temescal formation, Merritt sand, or bay mud.	Underlies the bay and the coastal plain alluvium. Maximum known thickness 1,050 feet (south of quadrangle).	No surface expression; exposed only in stream cuts and wave-cut banks.	Continental and marine sediments deposited in valley of San Francisco Bay.
Knoxville formation Jk	Predominantly shale, sandy, silty, with beds of fine- to medium-grained graywacke. Sandstone light olive-gray to dark yellowish-orange; thin-bedded to massive. Shale medium light-gray and light olive-gray to moderate yellowish-brown; breaks easily into small pieces, so that slopes underlain by shale are covered with a layer of loose fragments. Light-brown iron staining and clay minerals in joints, fractures, and bedding planes. Contorted in some places; some fracture surfaces are slickensided.	In extreme northeast corner of quadrangle. Thickness estimated to be approximately 1,000 feet.	Steep slope along front of Berkeley Hills.	Deposited in shallow marine waters.
Franciscan group KJf	Sandstone, arkosic to graywacke; fine to very coarse grained, with some shale beds. Sand grains consist largely of quartz, feldspar, and shale, with some chert and biotite and minor amounts of epidote, chlorite, clay, and carbonaceous material. Fresh rock is medium gray; weathered or altered rock is light brown or very pale orange. Fresh rock dense, hard; altered rock may be scratched with fingernail. Sandstone varies from massive to thin bedded, is cut by veins of quartz or calcite. Rock jointed, fractured; contorted in some places; many fracture surfaces coated with iron, manganese, and clay minerals.	In northeastern corner and east-central part of quadrangle; on Yerba Buena Island; probably underlies alluvium throughout quadrangle. Total thickness unknown.	Forms rather steep, rounded hills.	Marine deposit in geosyncline; source of sediments thought to be land mass west of present coastline.

Figure 8.A.5-4

Legend for areal and engineering geology of the Oakland west quadrangle, California, USGS miscellaneous geologic investigations map I-239 (Radbruch, 1957).



**Figure 8.A.5-5**  
Site plan, Gilroy 2.



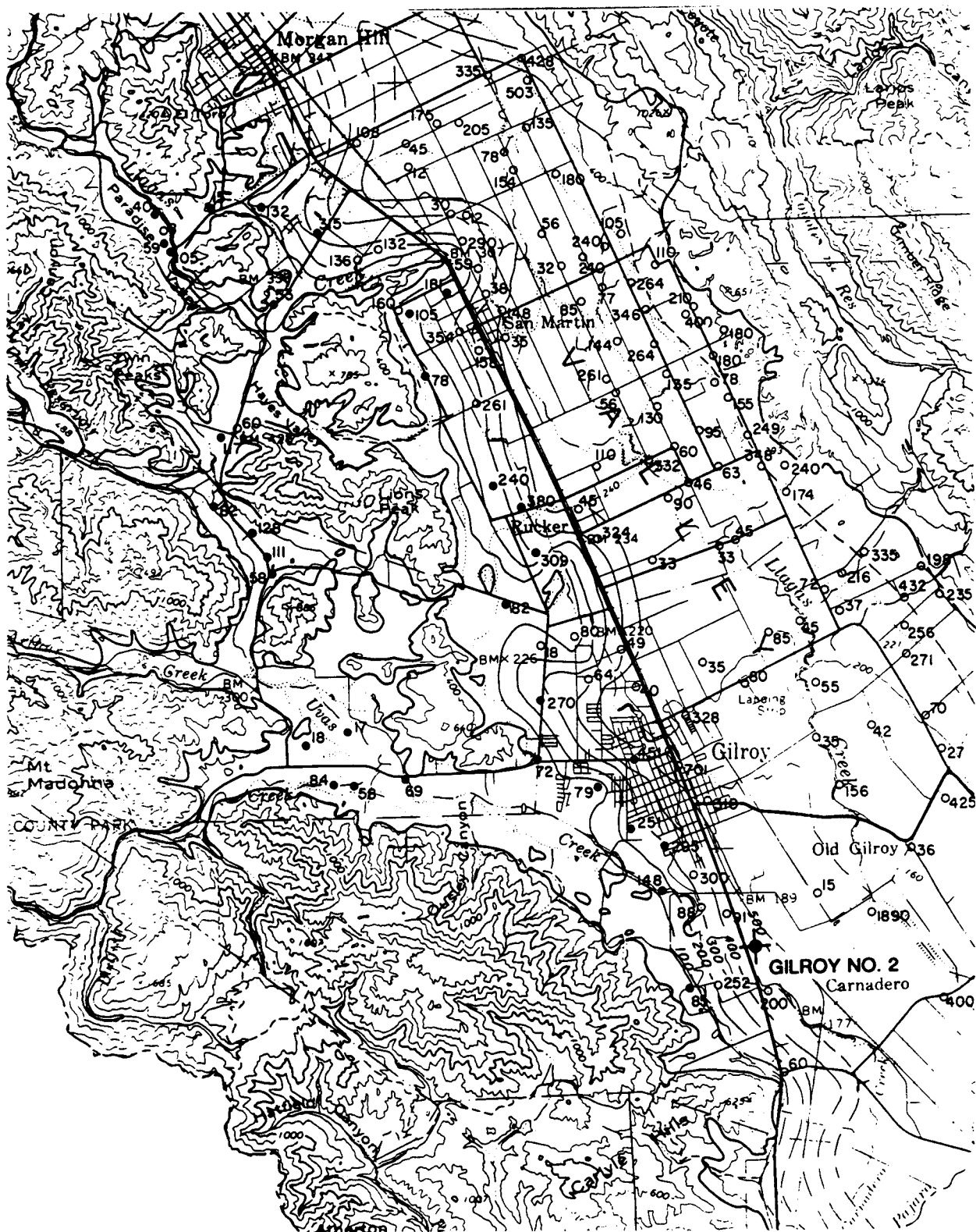


Figure 8.A.5-6  
Depth to bedrock contour map, Santa Clara County, CDMG Special Report 107.

#### **8.A.5.4.3 Loma Prieta Earthquake**

Gilroy array station 2 is located 16 km from the epicenter of the 1989 Loma Prieta earthquake. The instrument recorded peak horizontal accelerations of 0.50 and 0.43 g. The subsurface soils appeared to be stable during the event and, according to the Motel owner, the site did not show sign of liquefaction.

#### **8.A.5.4.4 Site Contacts**

Mr. John Belleau—Property Owner  
635 Healdsburg Avenue  
Santa Rosa, CA 95401  
(707) 544-4141

Marie and Roger Elissondo—Motel Managers  
5520 Monterey  
Gilroy, CA 95020  
(408) 842-6464

## **5—LIMITATIONS**

Woodward-Clyde's role in this project was limited to establishing site contacts, obtaining permits and authorization and coordinating drilling and geophysical work at each of the sites. Subsurface soil information presented in this report is the based on the work of other collaborators on this project.

## **APPENDIX 8.A.5.A—BORING LOGS FOR TREASURE ISLAND AND GILROY 2**

**Definitions of terms used for descriptions of sedimentary deposits and bedrock materials**

**Rock hardness:** response to hand and geologic hammer: (Ellen et al., 1972)

**hard** - hammer bounces off with solid sound

**firm** - hammer dents with thud, pick point dents or penetrates slightly

**soft** - pick points penetrates

**friable** material can be crumbled into individual grains by hand.

**Fracture spacing:** (Ellen et al., 1972)

cm	in	fracture spacing
0-1	0-1/2	v. close
1-5	1/2-2	close
5-30	2-12	moderate
30-100	12-36	wide
>100	>36	v. wide

**Weathering:**

**Fresh:** no visible signs of weathering

**Slight:** no visible decomposition of minerals, slight discoloration

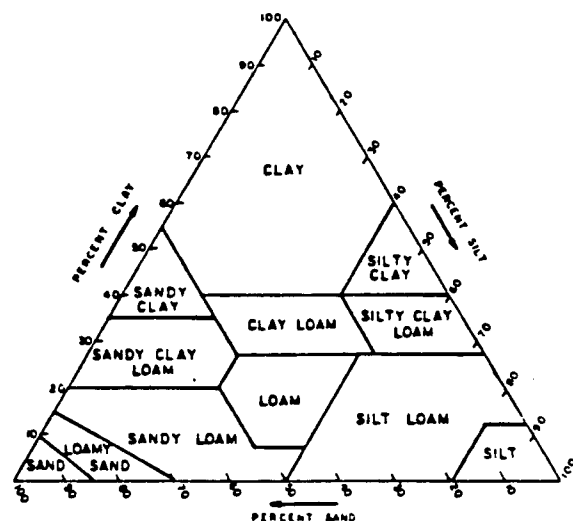
**Moderate:** slight decomposition of minerals and disintegration of rock, deep and thorough discoloration

**Deep:** extensive decomposition of minerals and complete disintegration of rock but original structure is preserved.

**Relative density of sand and consistency of clay is correlated with penetration resistance:** (Terzaghi and Peck, 1948)

blows/ft.	relative density	blows/ft.	consistency
0-4	v. loose	<2	v. soft
4-10	loose	2-4	soft
10-30	medium	4-8	medium
30-50	dense	8-15	stiff
>50	v. dense	15-30	v. stiff
		>30	hard

**Texture:** the relative proportions of clay, silt, and sand below 2mm. Proportions of larger particles are indicated by modifiers of textural class names. Determination is made in the field mainly by feeling the moist soil (Soil Survey, Staff, 1951).



**Color:** Standard Munsell color names are given for the dominant color of the moist soil and for prominent mottles.

**Types of samples**

SP - Standard Penetration (1 + 3/8 in ID sampler)

S - Thin-wall push sampler

O - Osterberg fixed-piston sampler

P - Pitcher Barrel sampler

CH - California Penetration (2 in ID sampler)

DC - Diamond Core

Figure 8.A.5-7

Explanation of geologic log.

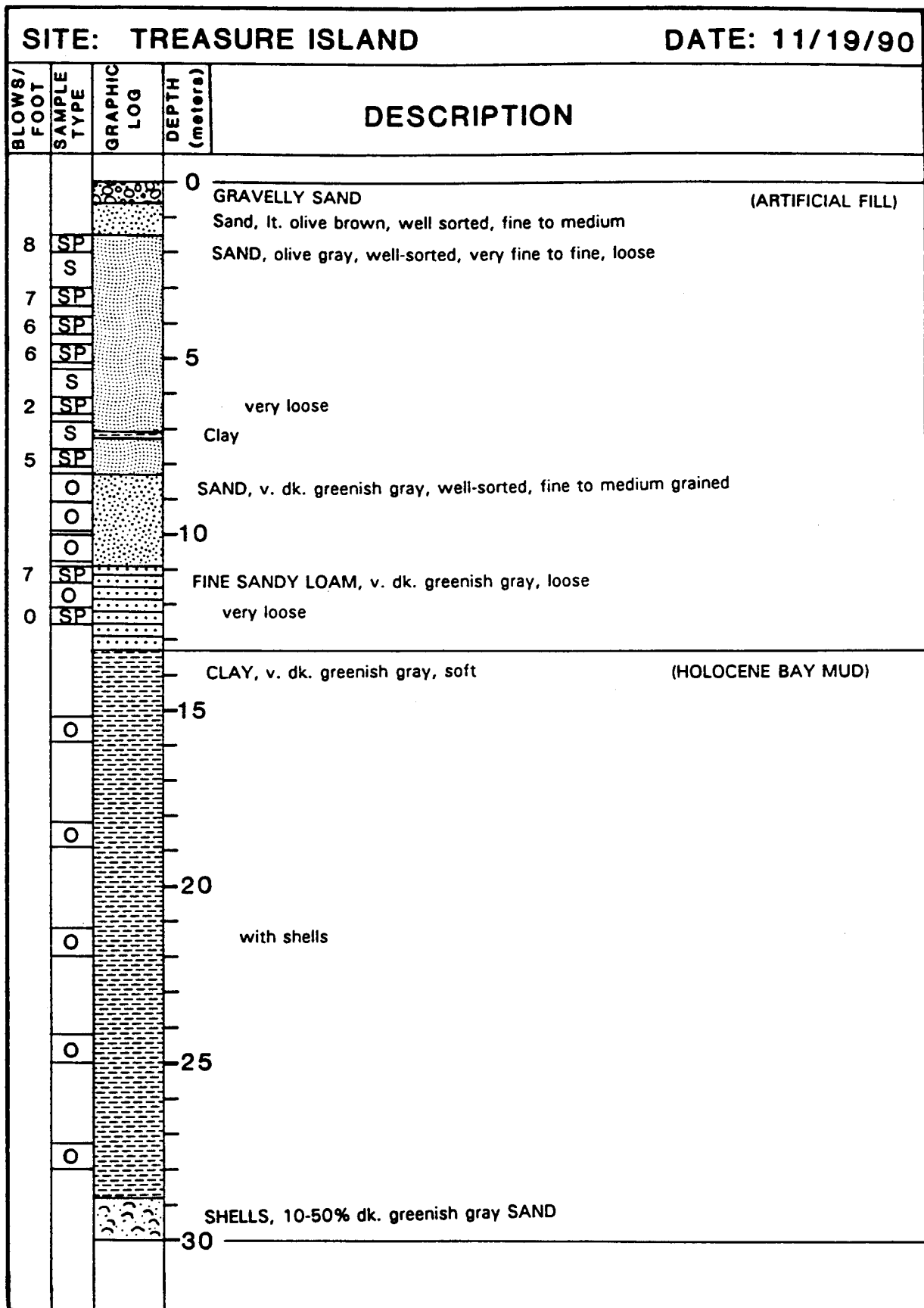


Figure 8.A.5-8  
Geologic log for Treasure Island.

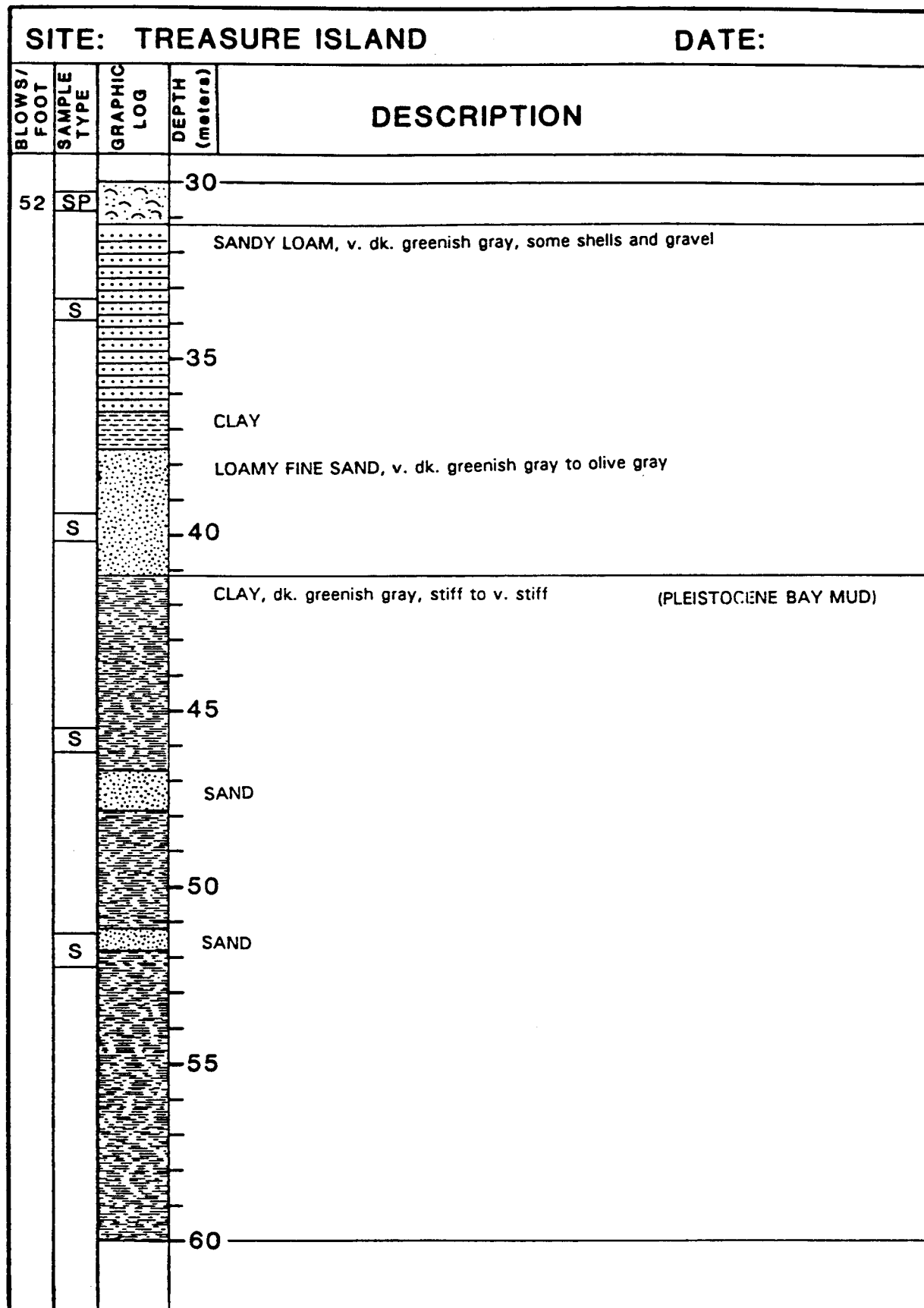


Figure 8.A.5-8 (continued)  
Geologic log for Treasure Island.

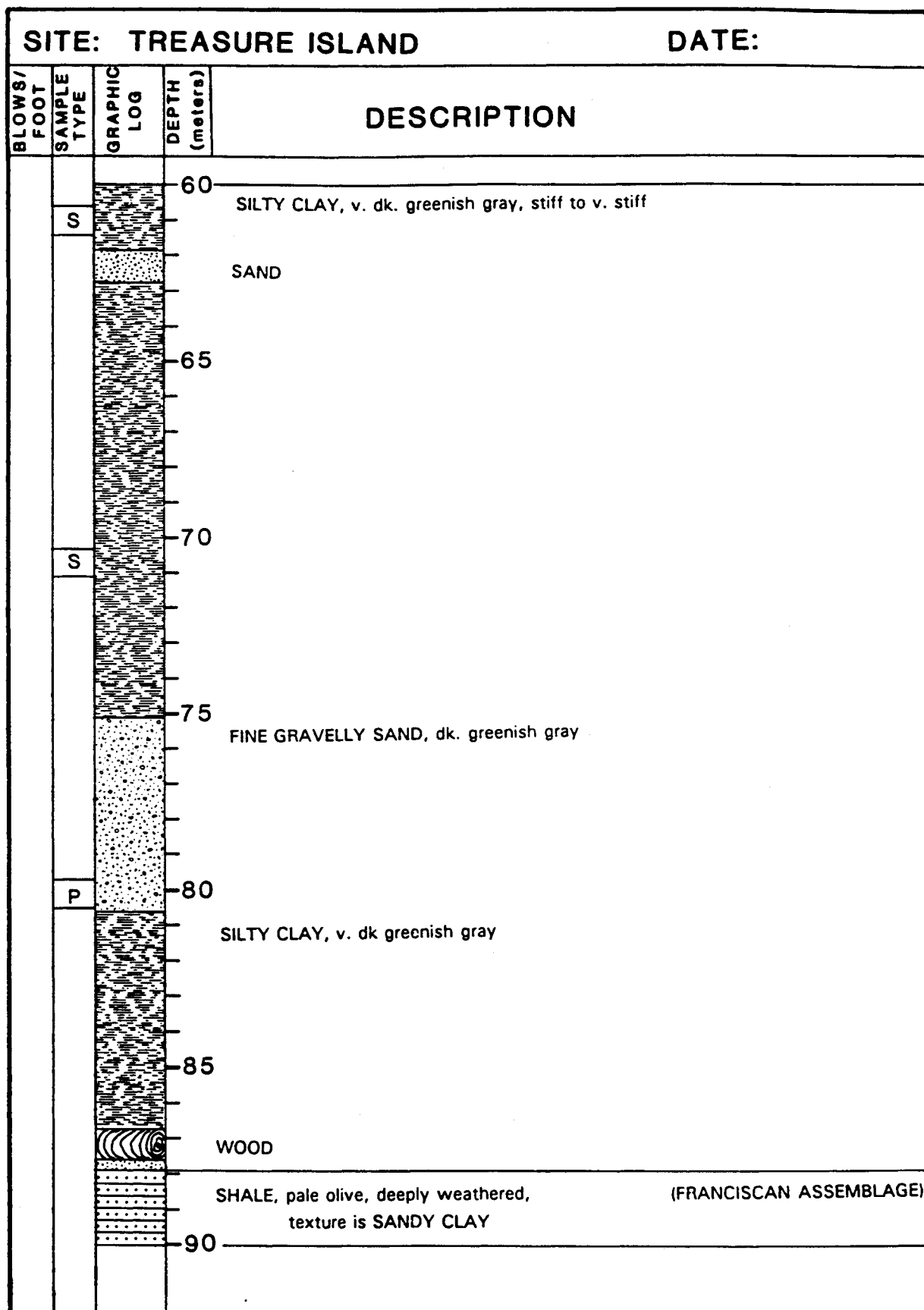


Figure 8.A.5-8 (continued)  
Geologic log for Treasure Island.



SITE: TREASURE ISLAND				DATE:
BLOWS/ FOOT	SAMPLE TYPE	GRAPHIC LOG	DEPTH (meters)	DESCRIPTION
			90	
	P			SHALE, lt. greenish gray to dk. brownish gray, firm black, hard, v. closely fractured, fresh
			95	SANDSTONE, dk. gray, fine-grained SHALE
			100	SANDSTONE, dk. gray, fine-grained
			105	
			110	
			115	
			120	

Figure 8.A.5-8 (continued)  
Geologic log for Treasure Island.

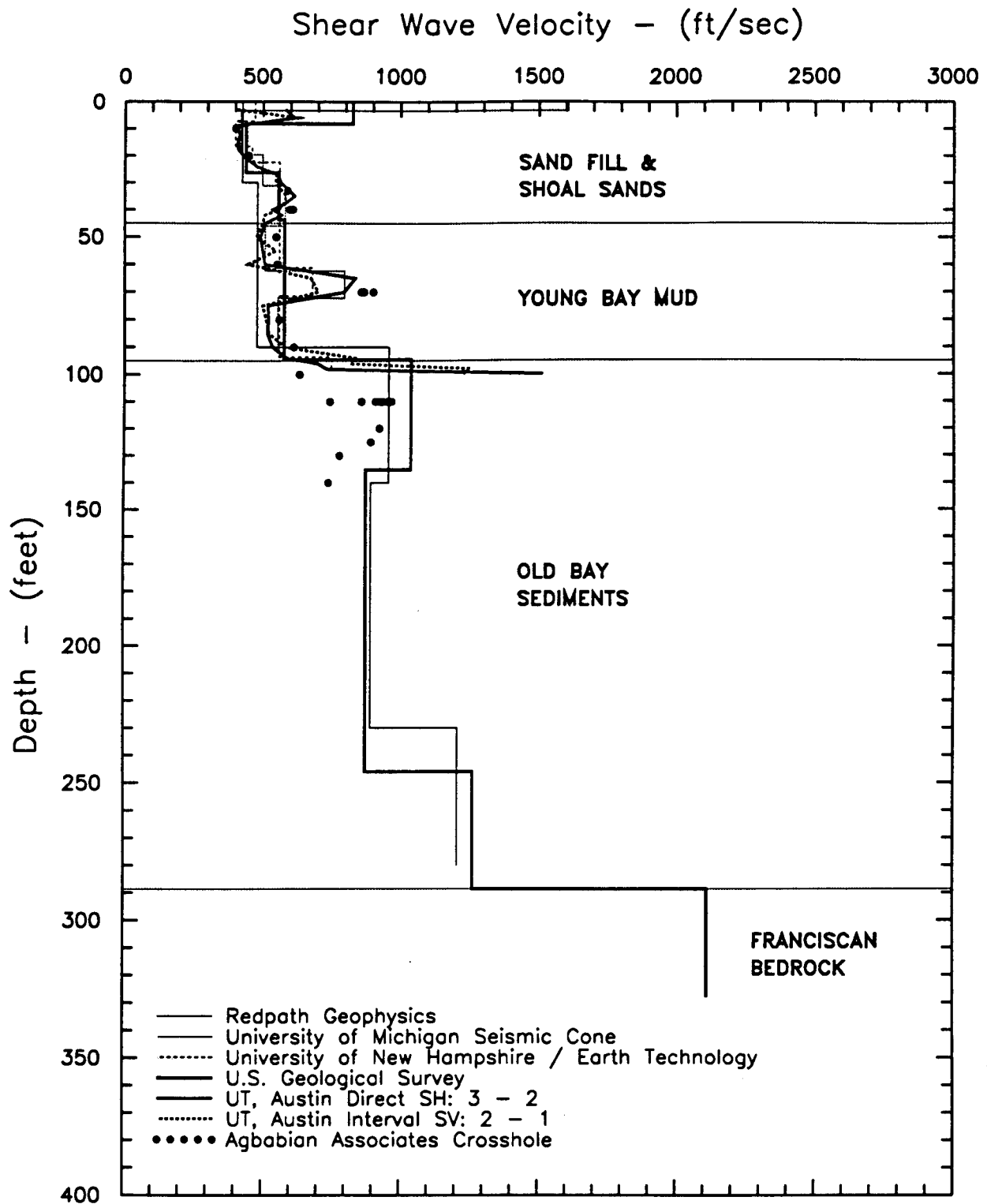
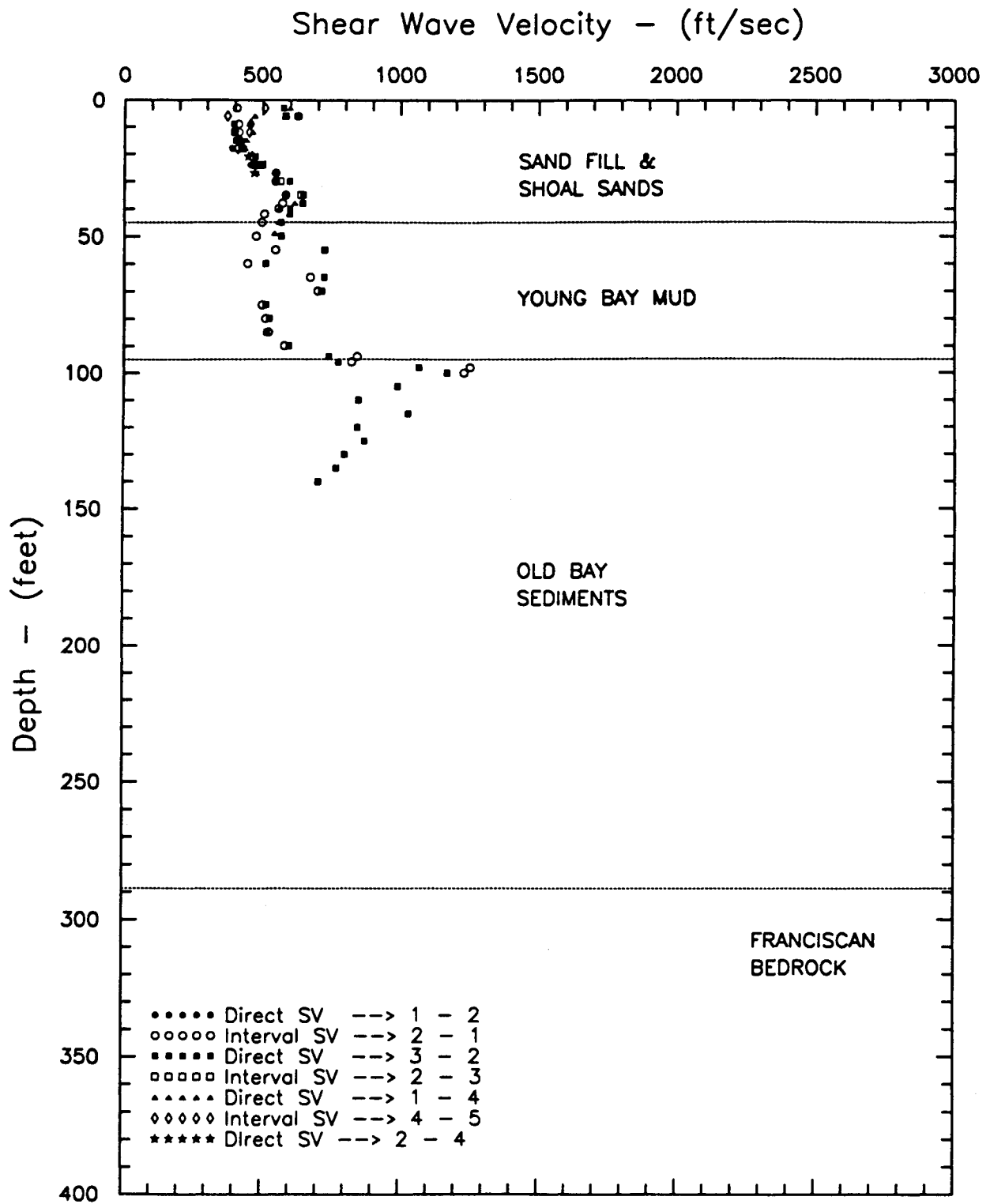
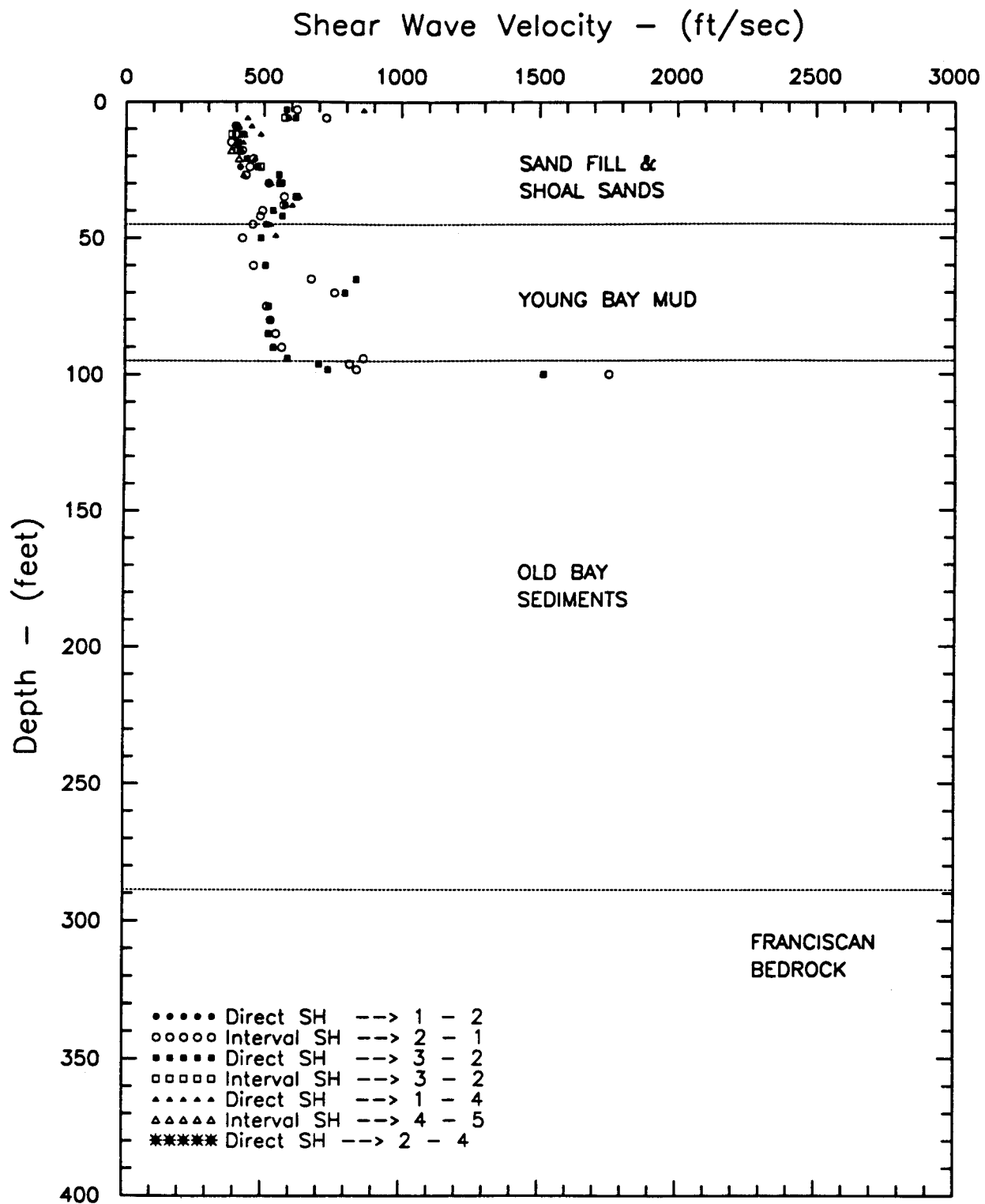


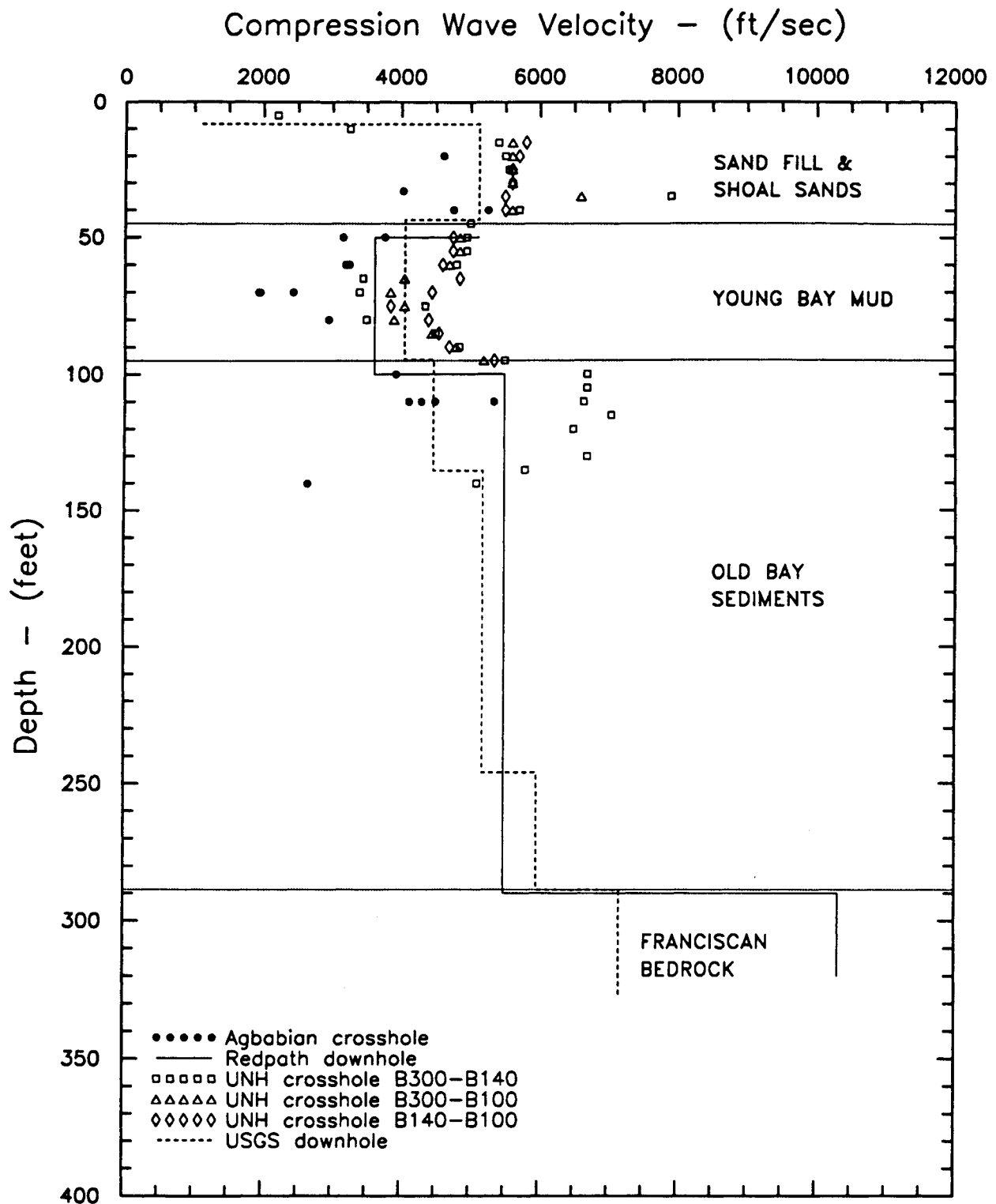
Figure 8.A.5-9  
Shear wave velocity measurements, Treasure Island site.



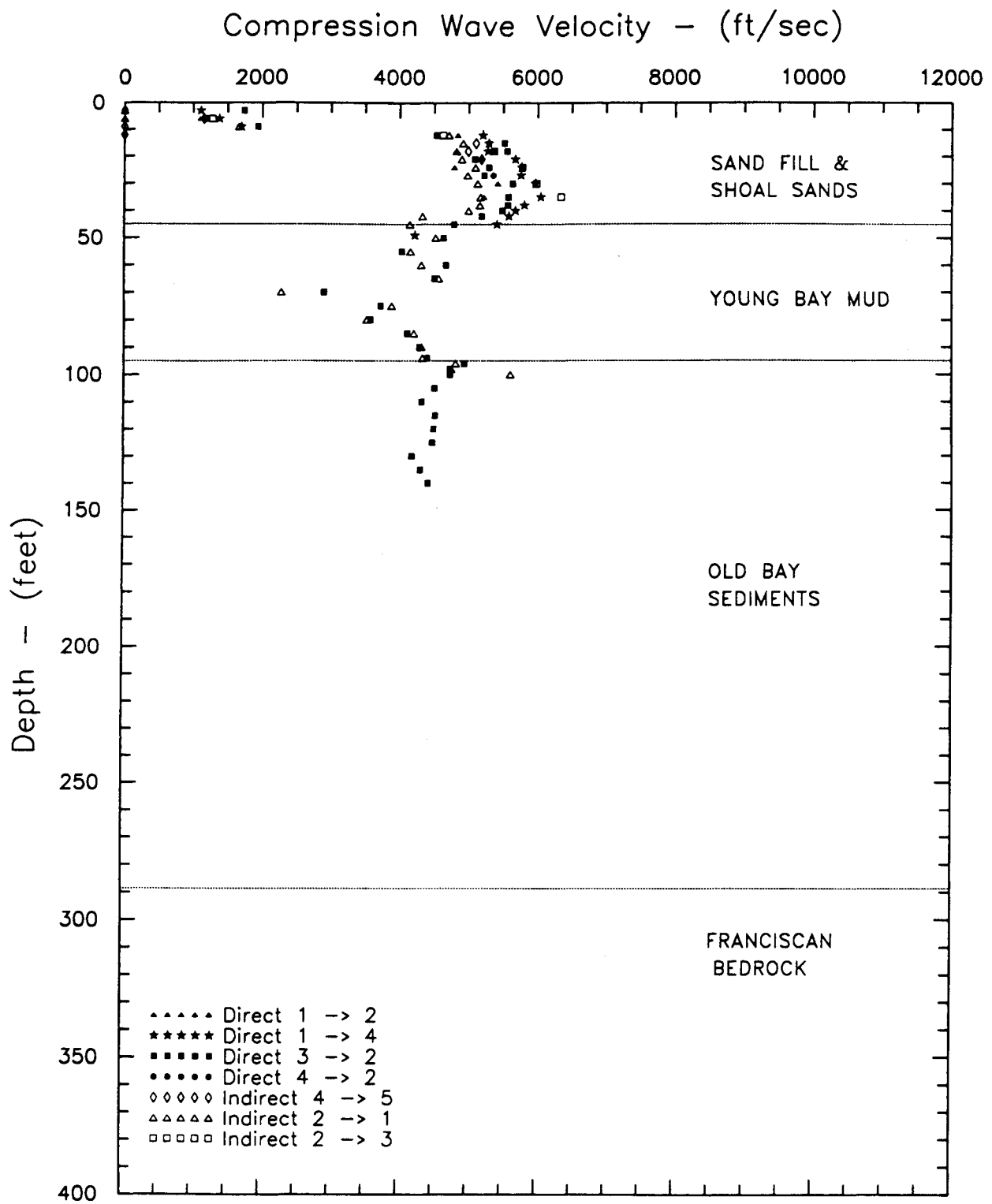
**Figure 8.A.5-10**  
Shear wave velocity measurements (SV), Treasure Island site by U. of Texas.



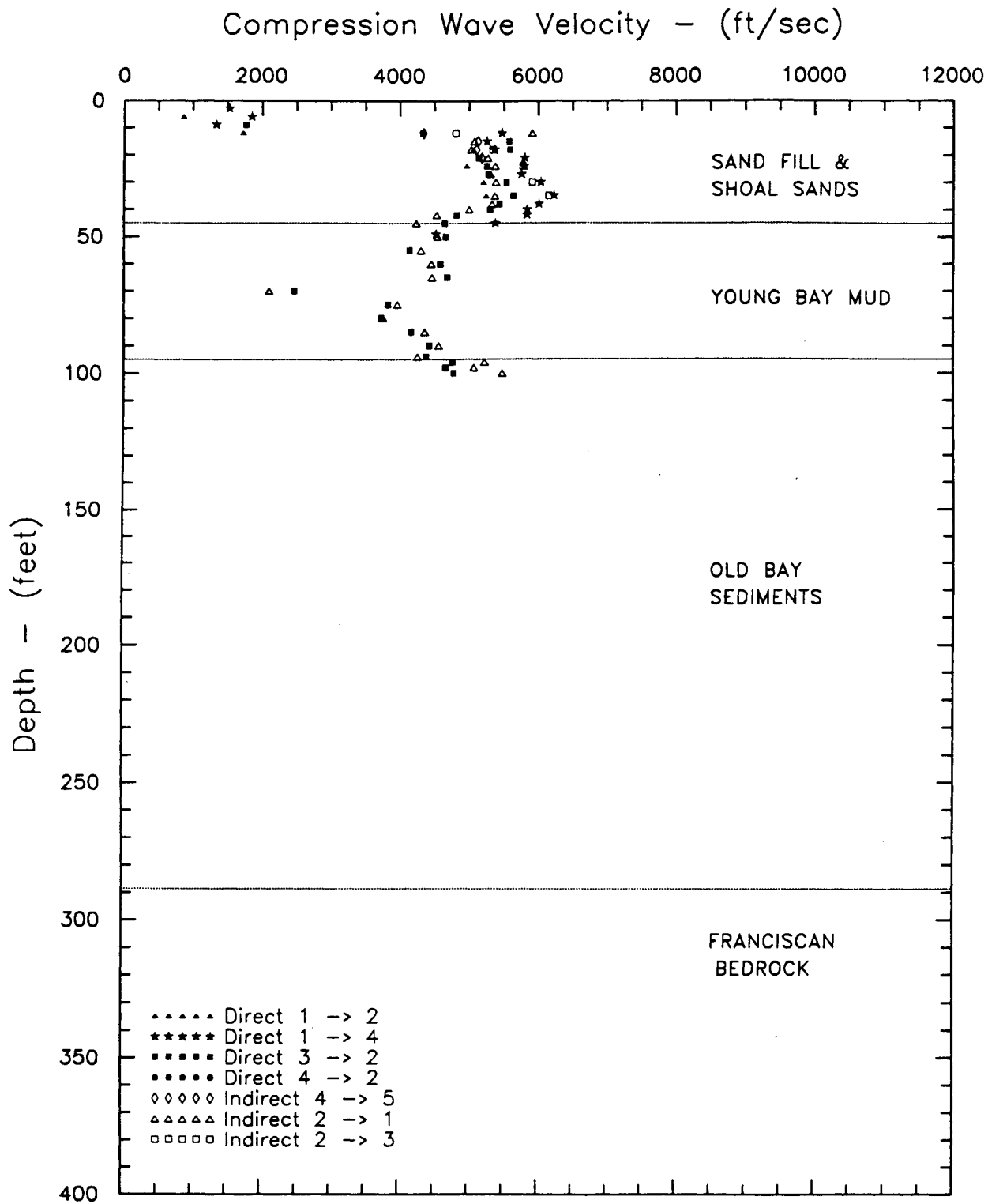
**Figure 8.A.5-11**  
Shear wave velocity measurements (SH), Treasure Island site by U. of Texas.



**Figure 8.A.5-12**  
P-wave velocity measurements, Treasure Island fire station.



**Figure 8.A.5-13**  
P-wave velocity measurements, U.T. Austin (drop hammer source), Treasure Island fire station.



**Figure 8.A.5-14**

P-wave velocity measurements, U.T. Austin (solenoid source), Treasure Island fire station.

**Definitions of terms used for descriptions of sedimentary deposits and bedrock materials**

**Rock hardness:** response to hand and geologic hammer: (Ellen et al., 1972)

**hard** - hammer bounces off with solid sound  
**firm** - hammer dents with thud, pick point dents or penetrates slightly  
**soft** - pick points penetrates  
**friable** material can be crumbled into individual grains by hand.

**Fracture spacing:** (Ellen et al., 1972)

cm	in	fracture spacing
0-1	0-1/2	v. close
1-5	1/2-2	close
5-30	2-12	moderate
30-100	12-36	wide
> 100	> 36	v. wide

**Weathering:**

**Fresh:** no visible signs of weathering

**Slight:** no visible decomposition of minerals, slight discoloration

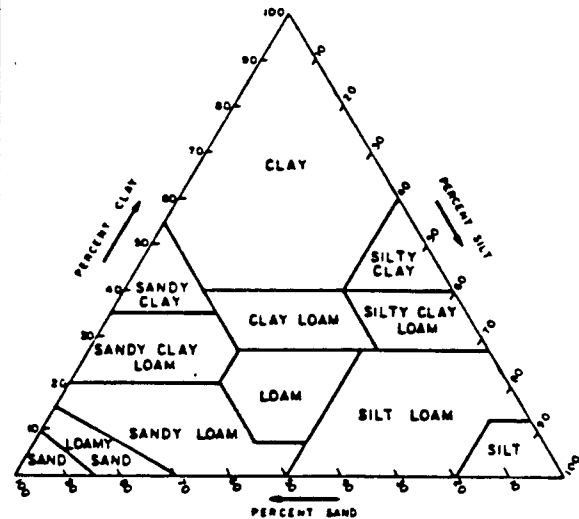
**Moderate:** slight decomposition of minerals and disintegration of rock, deep and thorough discoloration

**Deep:** extensive decomposition of minerals and complete disintegration of rock but original structure is preserved.

**Relative density of sand and consistency of clay is correlated with penetration resistance:** (Terzaghi and Peck, 1948)

blows/ft.	relative density	blows/ft.	consistency
0-4	v. loose	< 2	v. soft
4-10	loose	2-4	soft
10-30	medium	4-8	medium
30-50	dense	8-15	stiff
> 50	v. dense	15-30	v. stiff
		> 30	hard

**Texture:** the relative proportions of clay, silt, and sand below 2mm. Proportions of larger particles are indicated by modifiers of textural class names. Determination is made in the field mainly by feeling the moist soil (Soil Survey, Staff, 1951).



**Color:** Standard Munsell color names are given for the dominant color of the moist soil and for prominent mottles.

**Types of samples**

SP - Standard Penetration 1 + 3/8 in in ID sampler)  
 S - Thin-wall push sampler  
 O - Osterberg fixed-piston sampler  
 P - Pitcher Barrel sampler  
 CH - California Penetration (2 in ID sampler)  
 DC - Diamond Core

Figure 8.A.5-15  
 Explanation of geologic log for Gilroy 2 (EPRI 1).



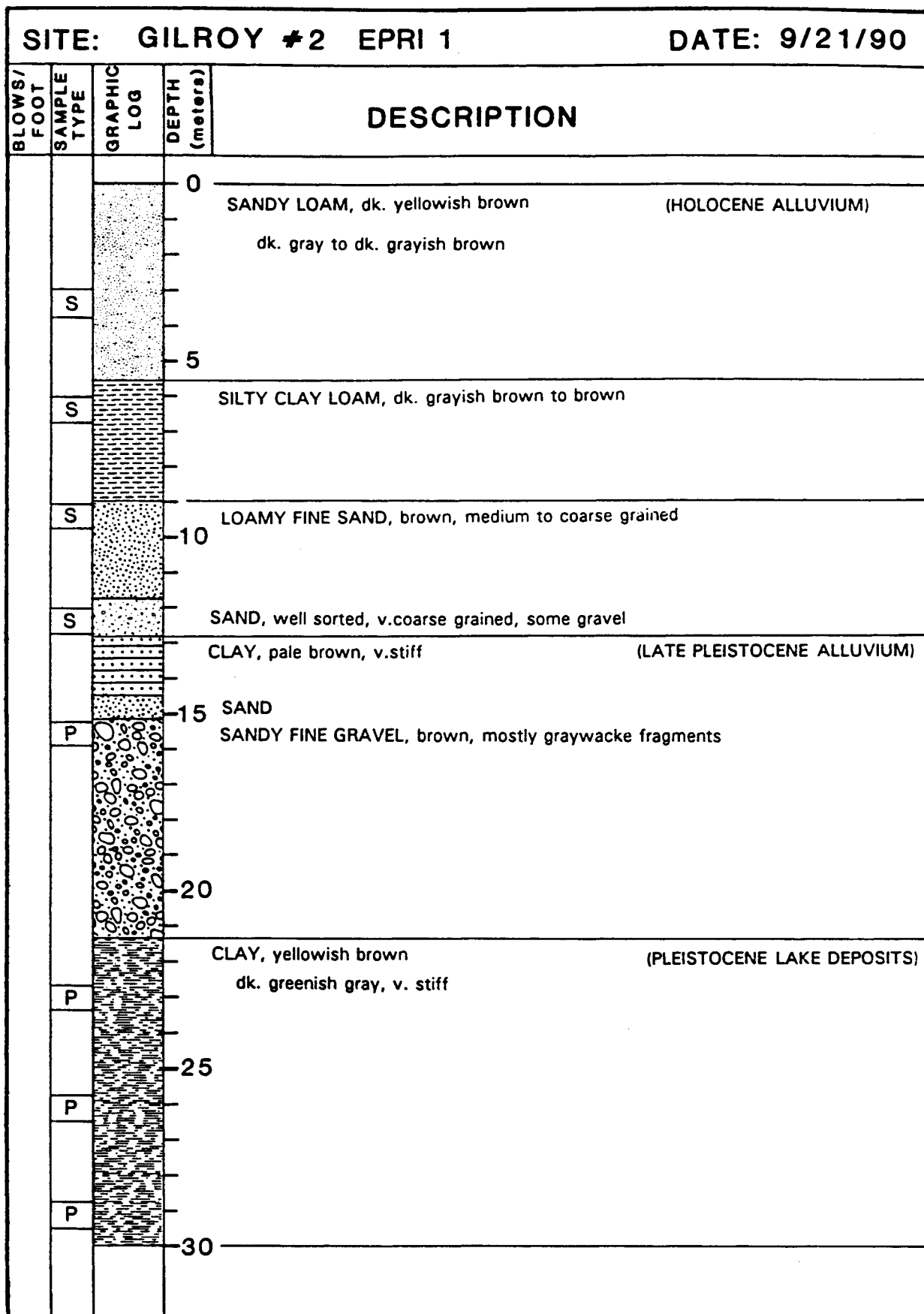


Figure 8.A.5-16  
Geologic log for Gilroy 2 (EPRI 1).

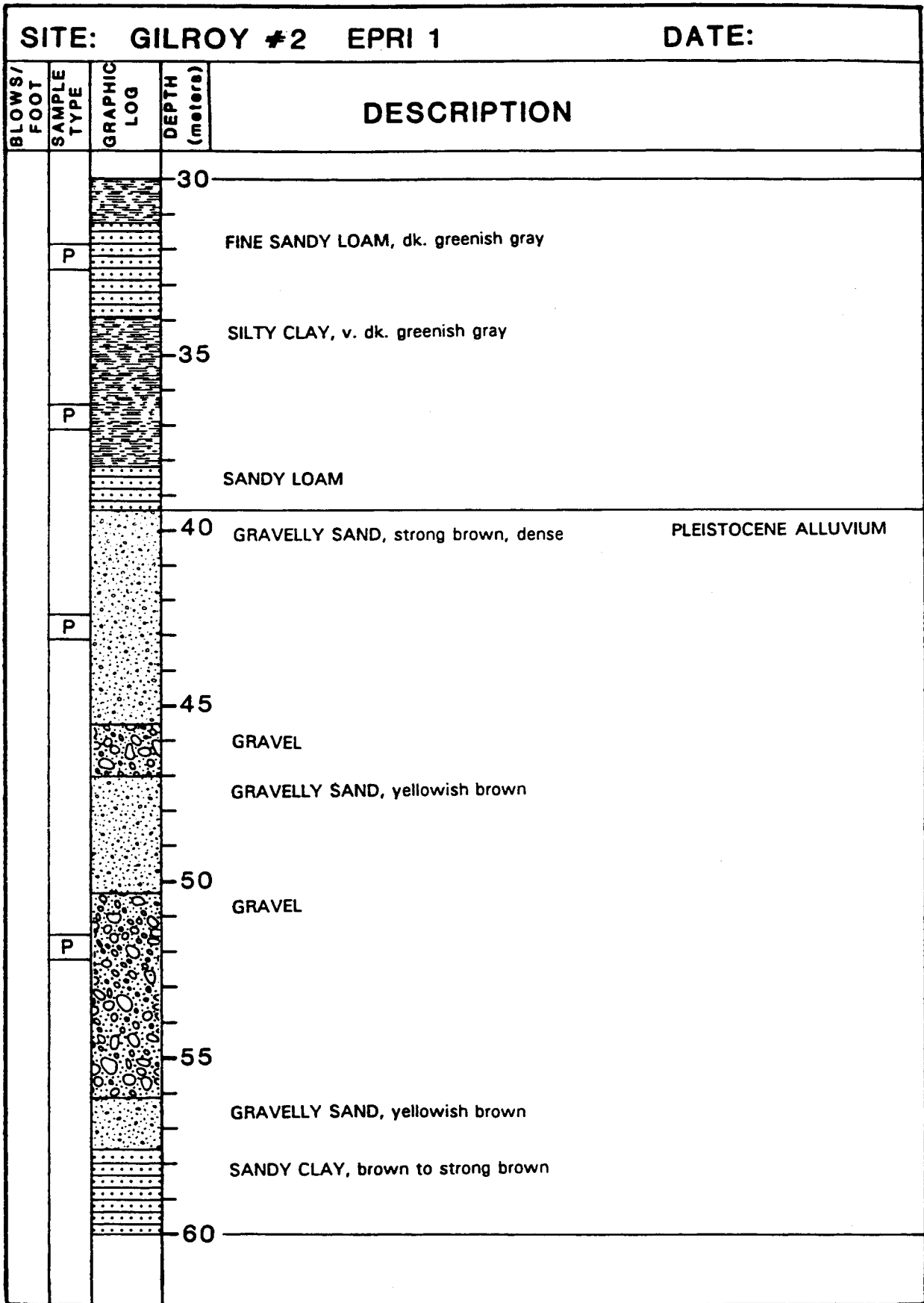


Figure 8.A.5-16 (continued)  
Geologic log for Gilroy 2 (EPRI 1).

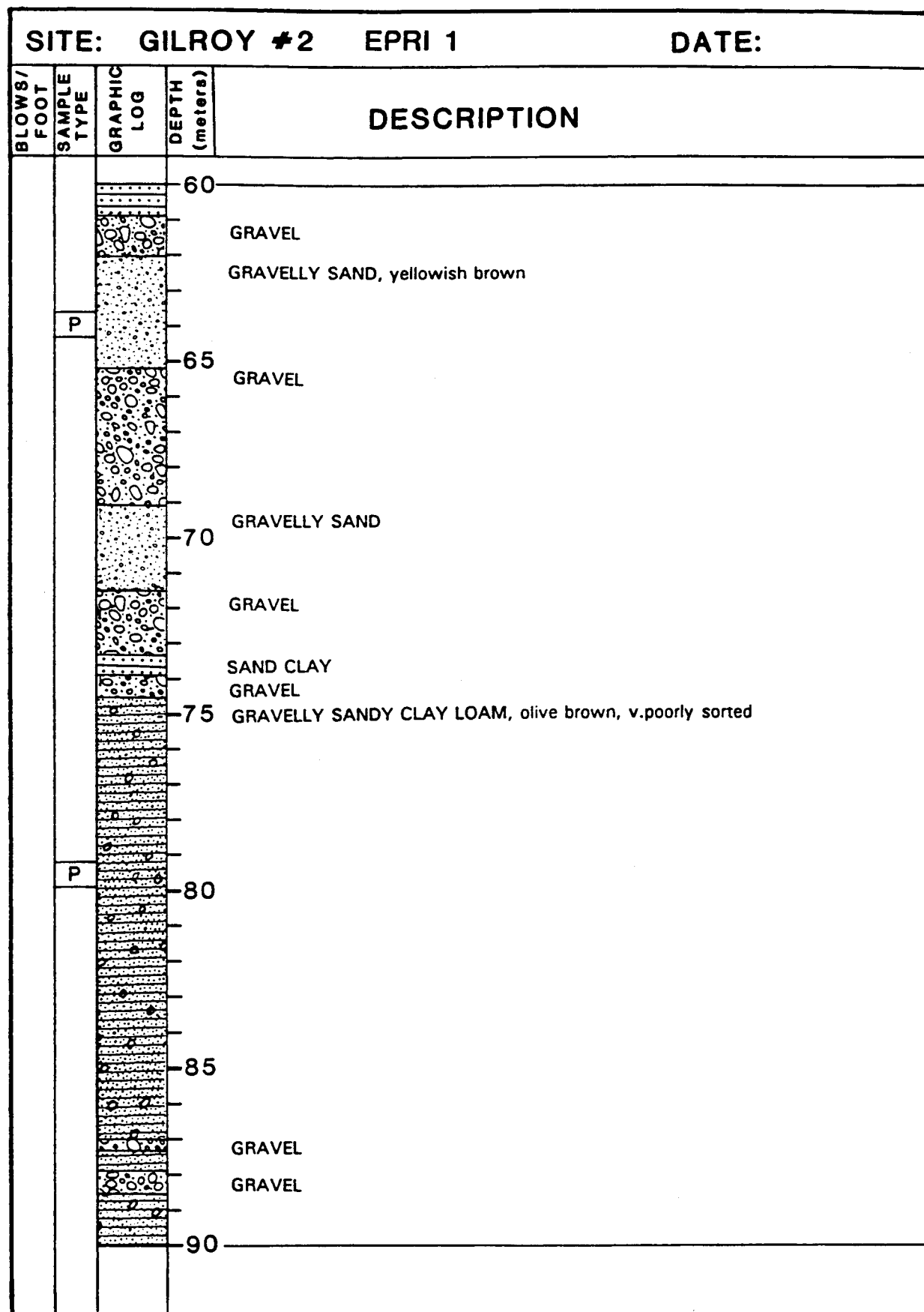


Figure 8.A.5-16 (continued)  
Geologic log for Gilroy 2 (EPRI 1).

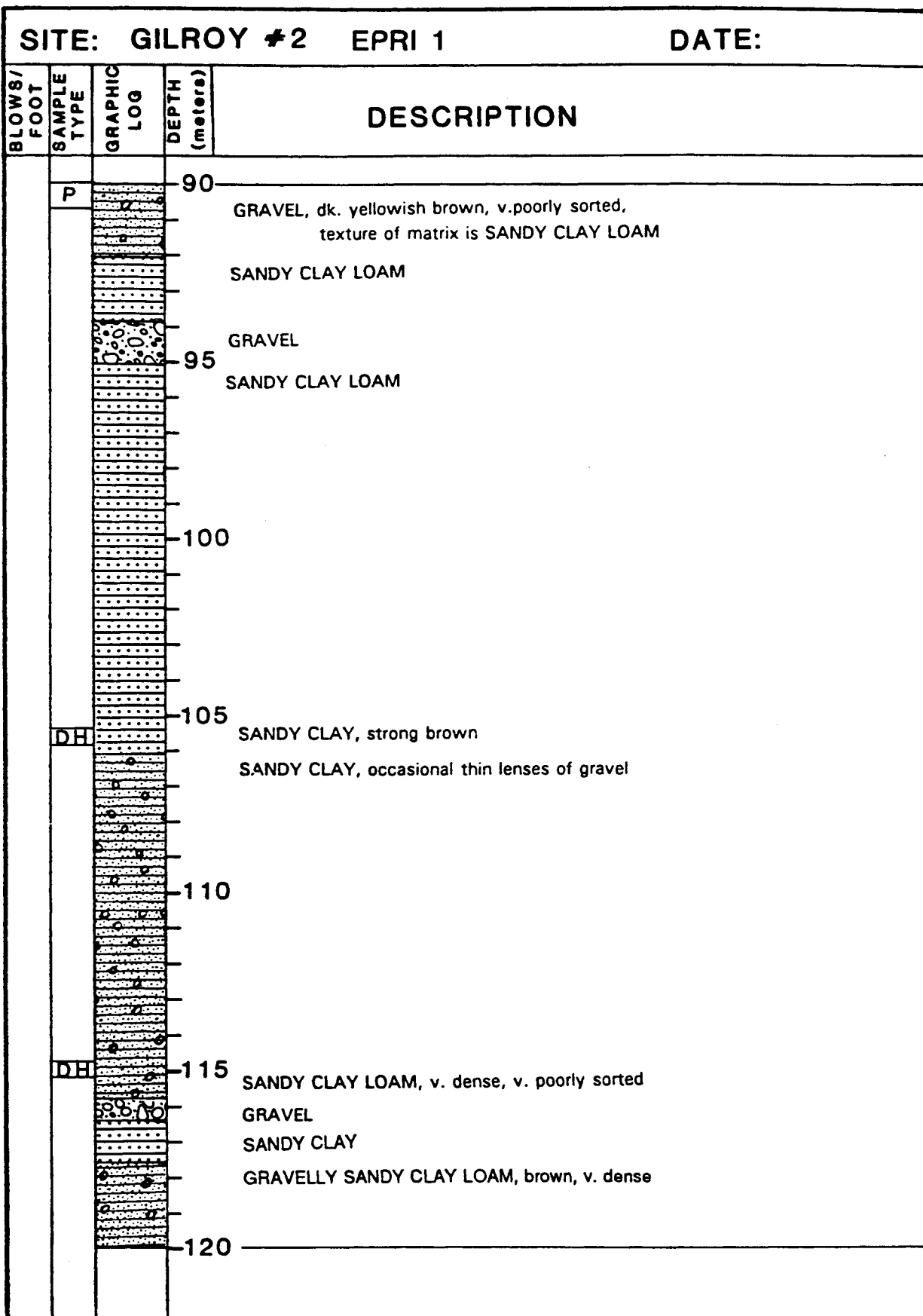


Figure 8.A.5-16 (continued)  
Geologic log for Gilroy 2 (EPRI 1).

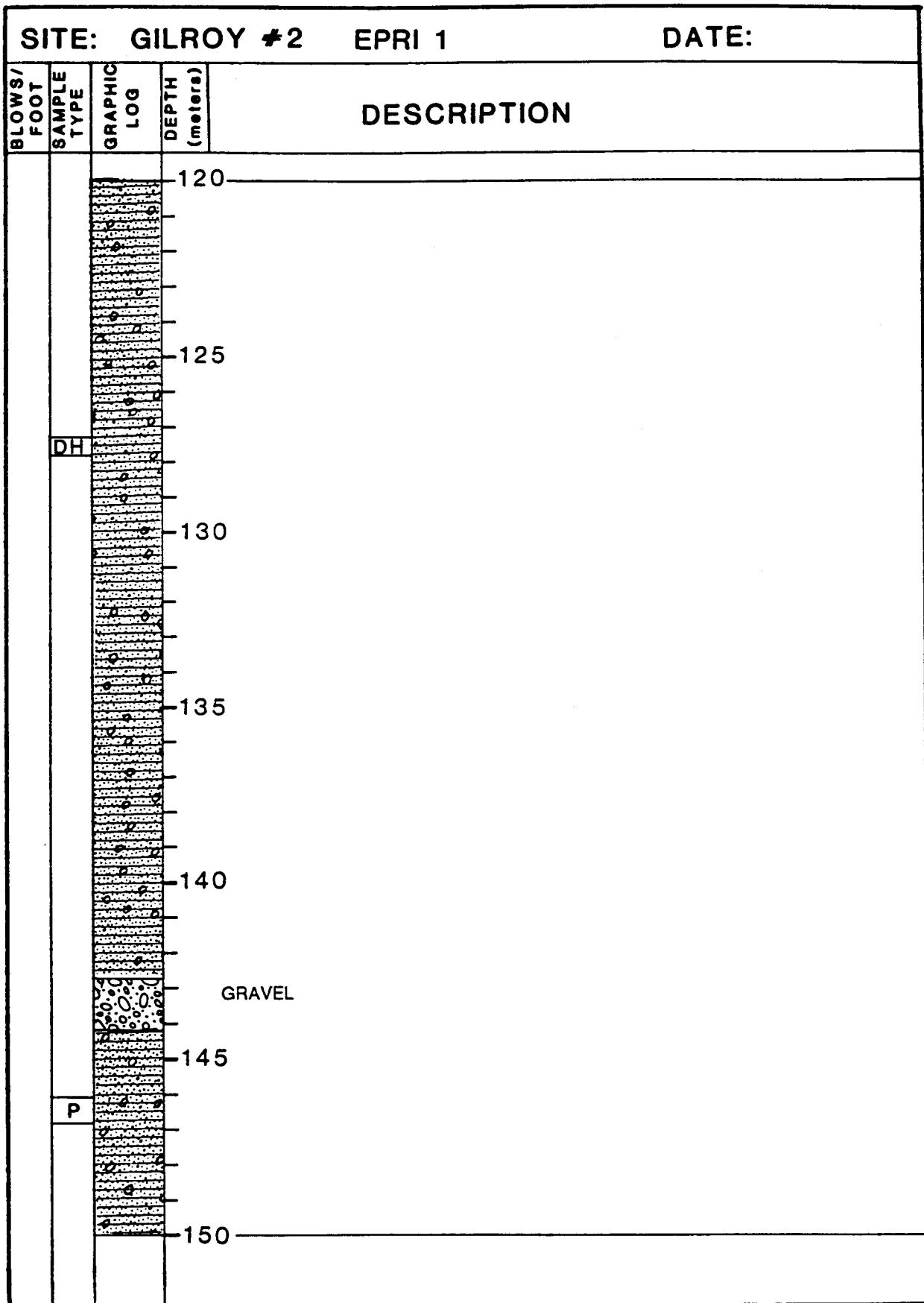


Figure 8.A.5-16 (continued)  
Geologic log for Gilroy 2 (EPRI 1).

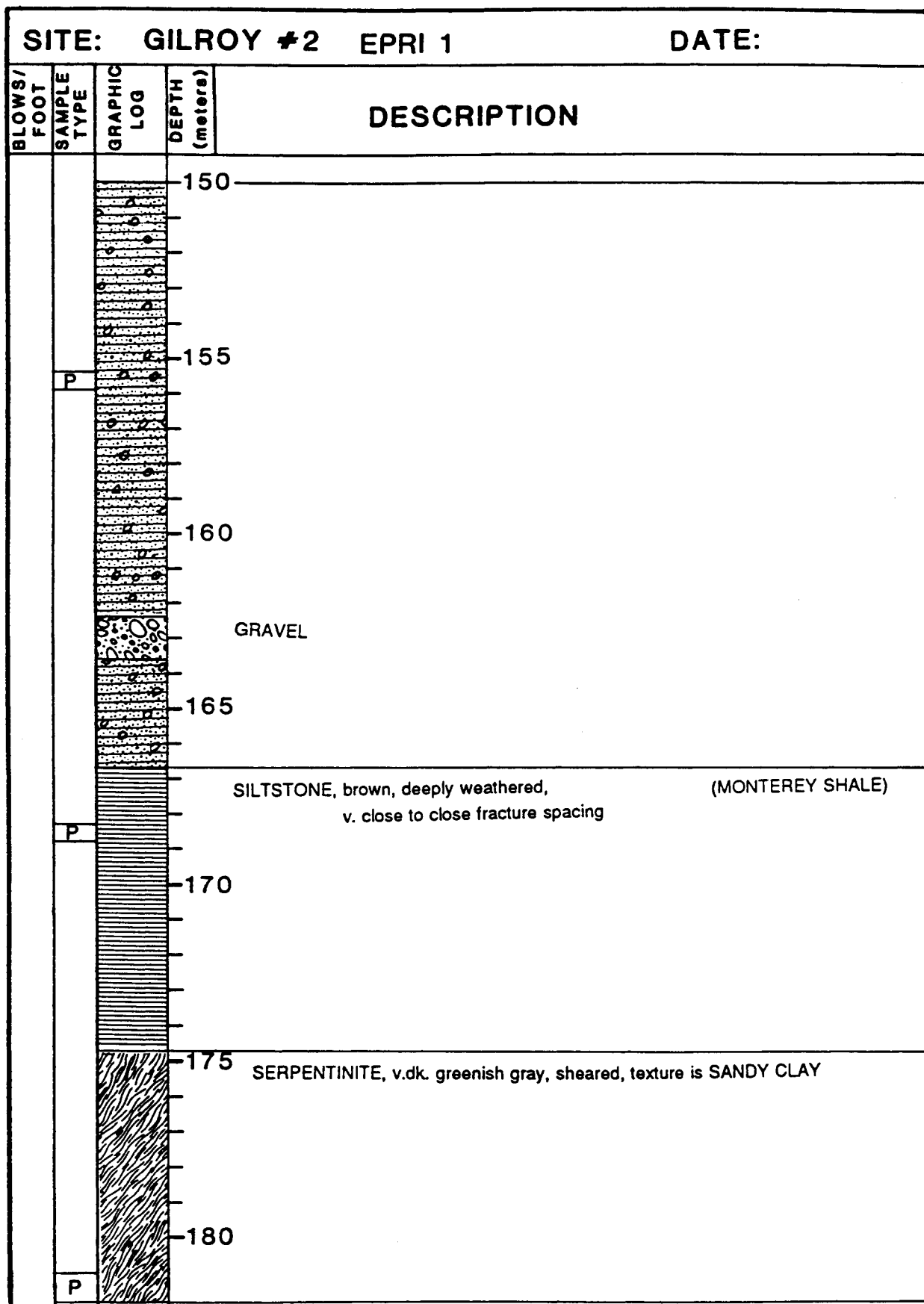


Figure 8.A.5-16 (continued)  
Geologic log for Gilroy 2 (EPRI 1).

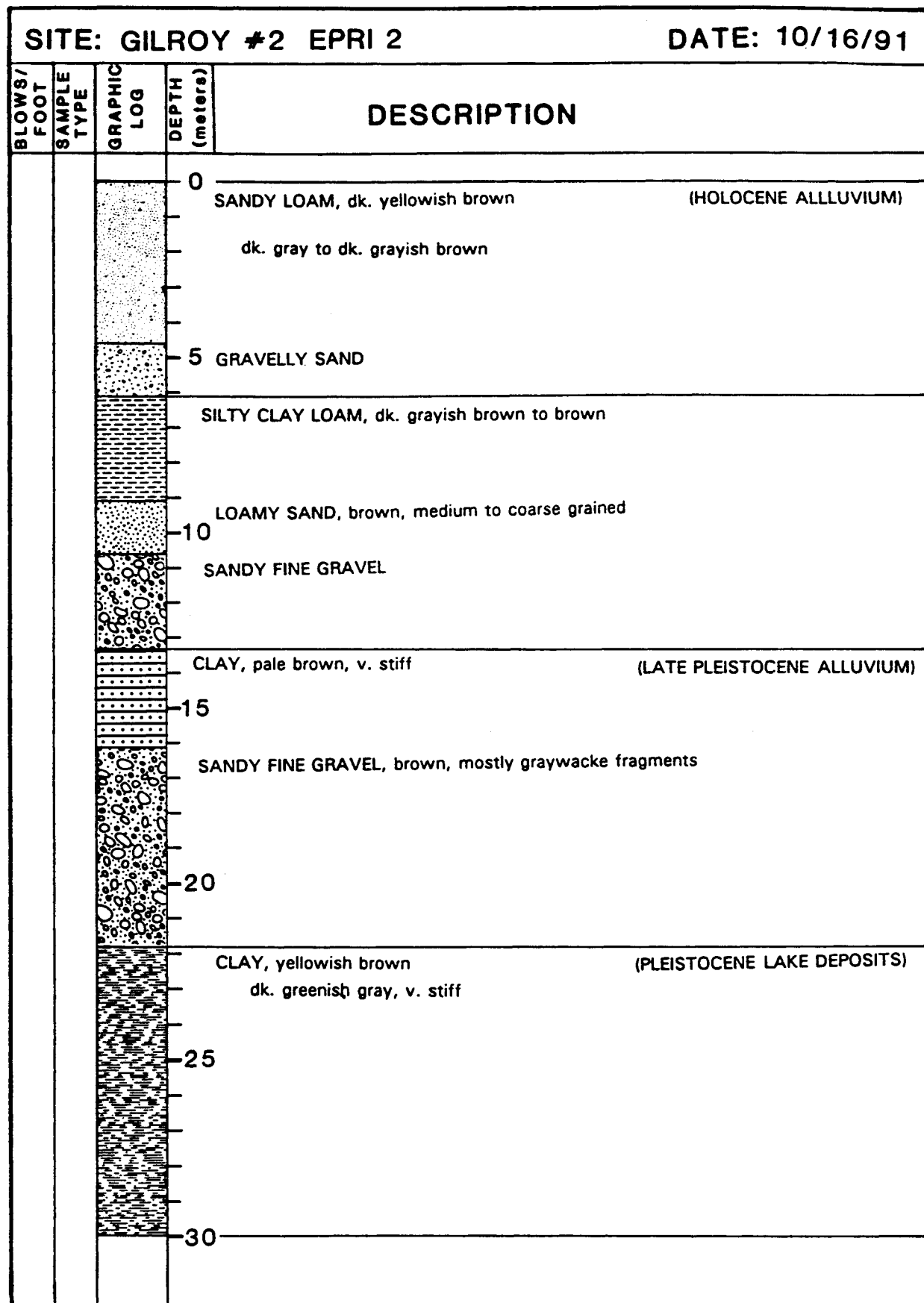


Figure 8.A.5-17  
Geologic log for Gilroy 2 (EPRI 2).




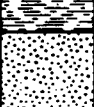
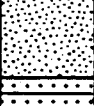
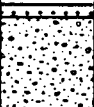

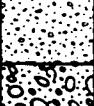
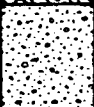




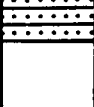
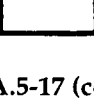
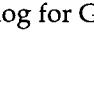
SITE: GILROY #2 EPRI 2				DATE:
BLOWS/ FOOT	SAMPLE TYPE	GRAPHIC LOG	DEPTH (meters)	DESCRIPTION
			30	
				FINE SANDY LOAM, dk. greenish gray
			35	SILTY CLAY, v. dk. greenish gray
				SANDY LOAM
			40	
				SANDY CLAY
				GRAVELLY SAND, strong brown, dense
				GRAVEL
			45	
				GRAVELLY SAND, yellowish brown
				GRAVEL
				GRAVELLY SAND, yellowish brown
			50	
				GRAVEL
			55	
				SANDY CLAY, brown to strong brown
			60	

Figure 8.A.5-17 (continued)  
Geologic log for Gilroy 2 (EPRI 2).



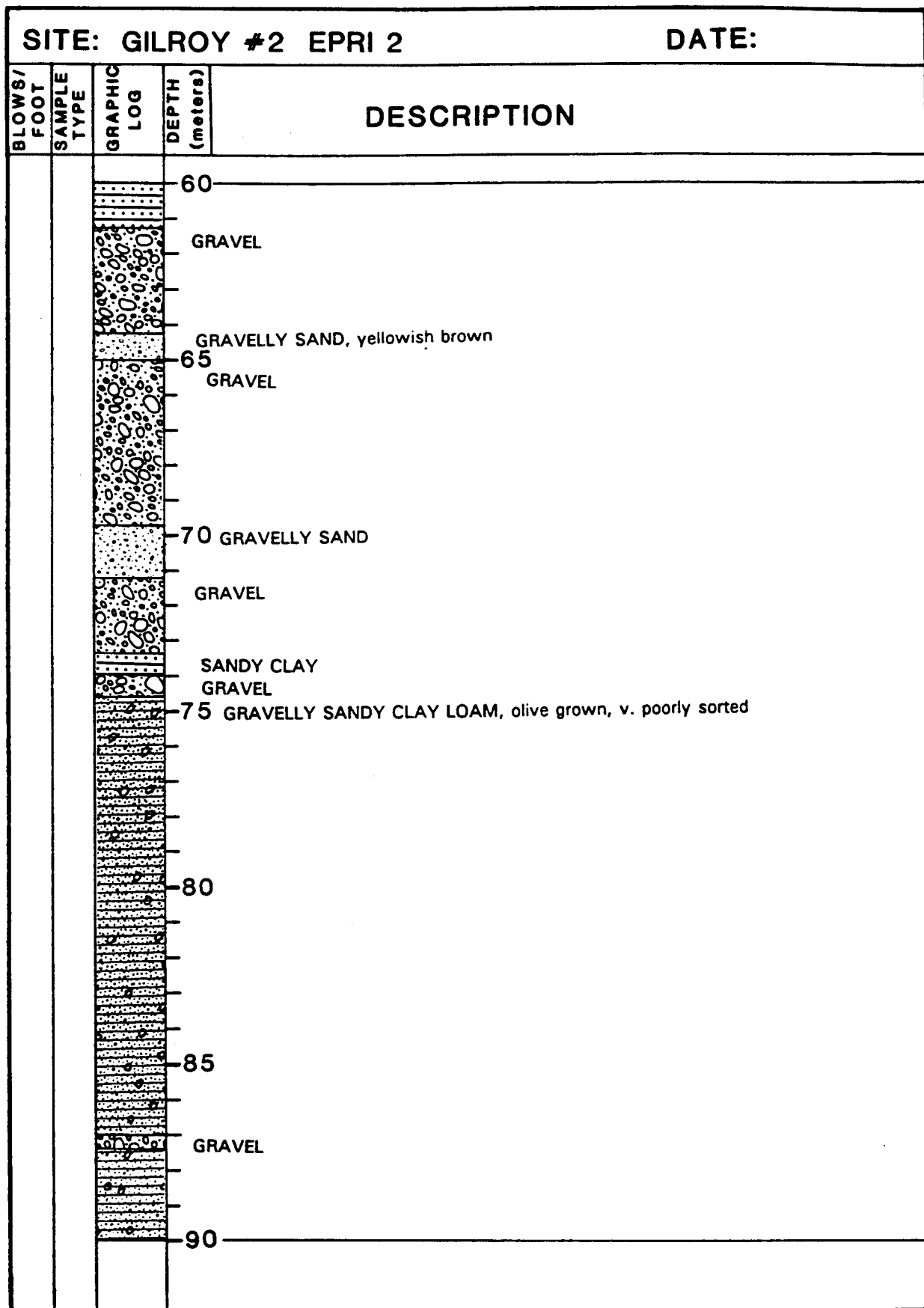


Figure 8.A.5-17 (continued)  
Geologic log for Gilroy 2 (EPRI 2).

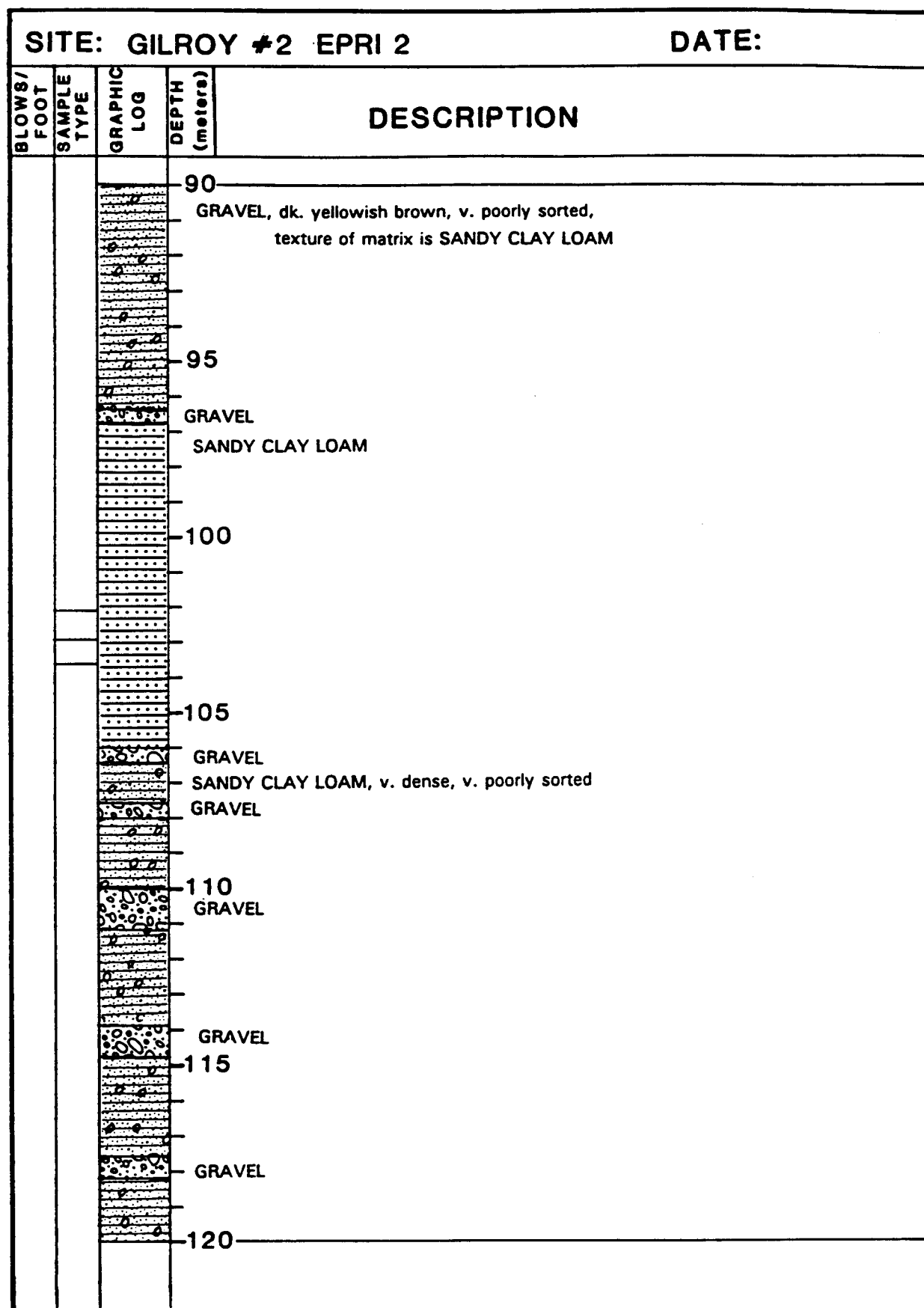


Figure 8.A.5-17 (continued)  
Geologic log for Gilroy 2 (EPRI 2).

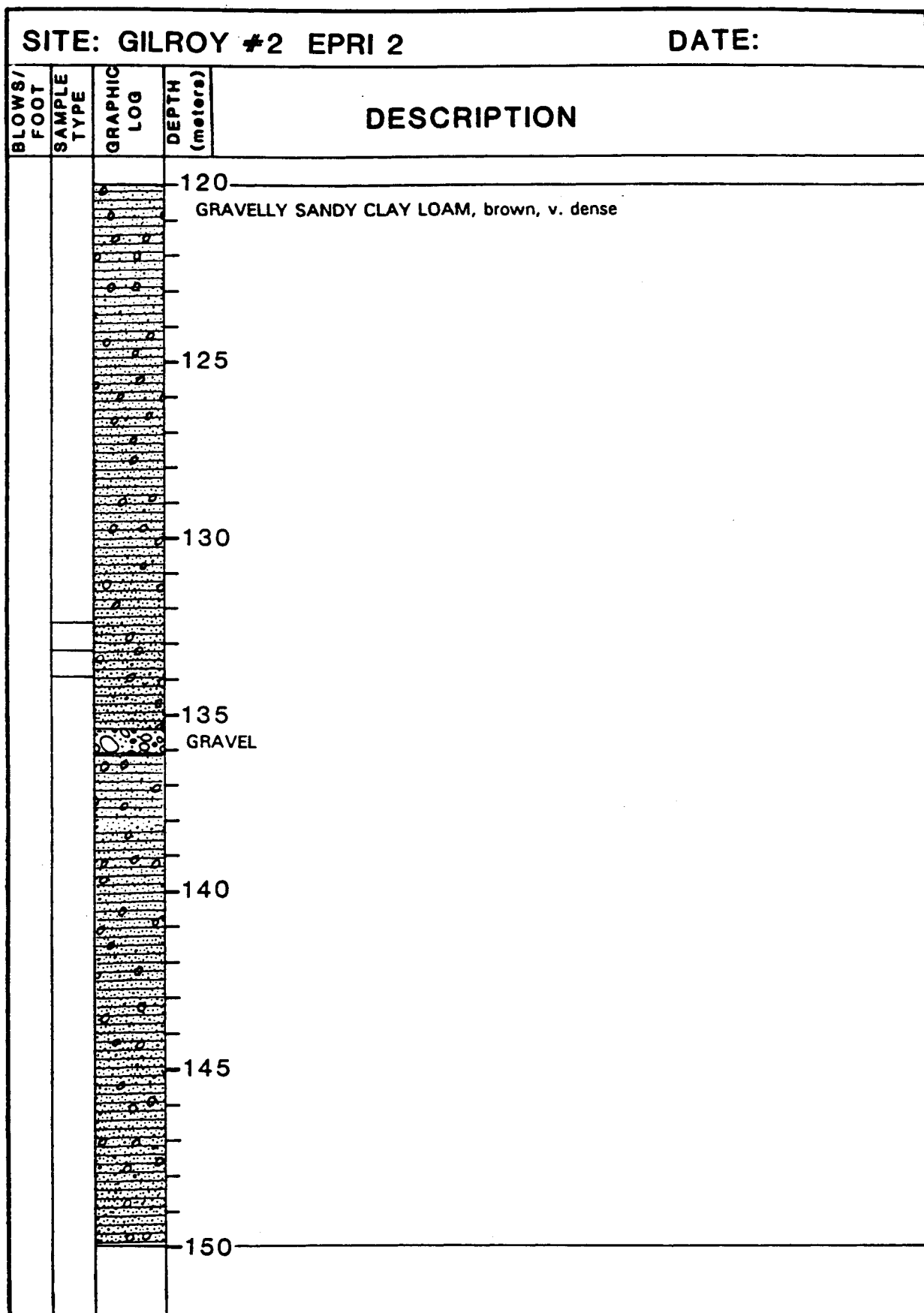


Figure 8.A.5-17 (continued)  
Geologic log for Gilroy 2 (EPRI 2).

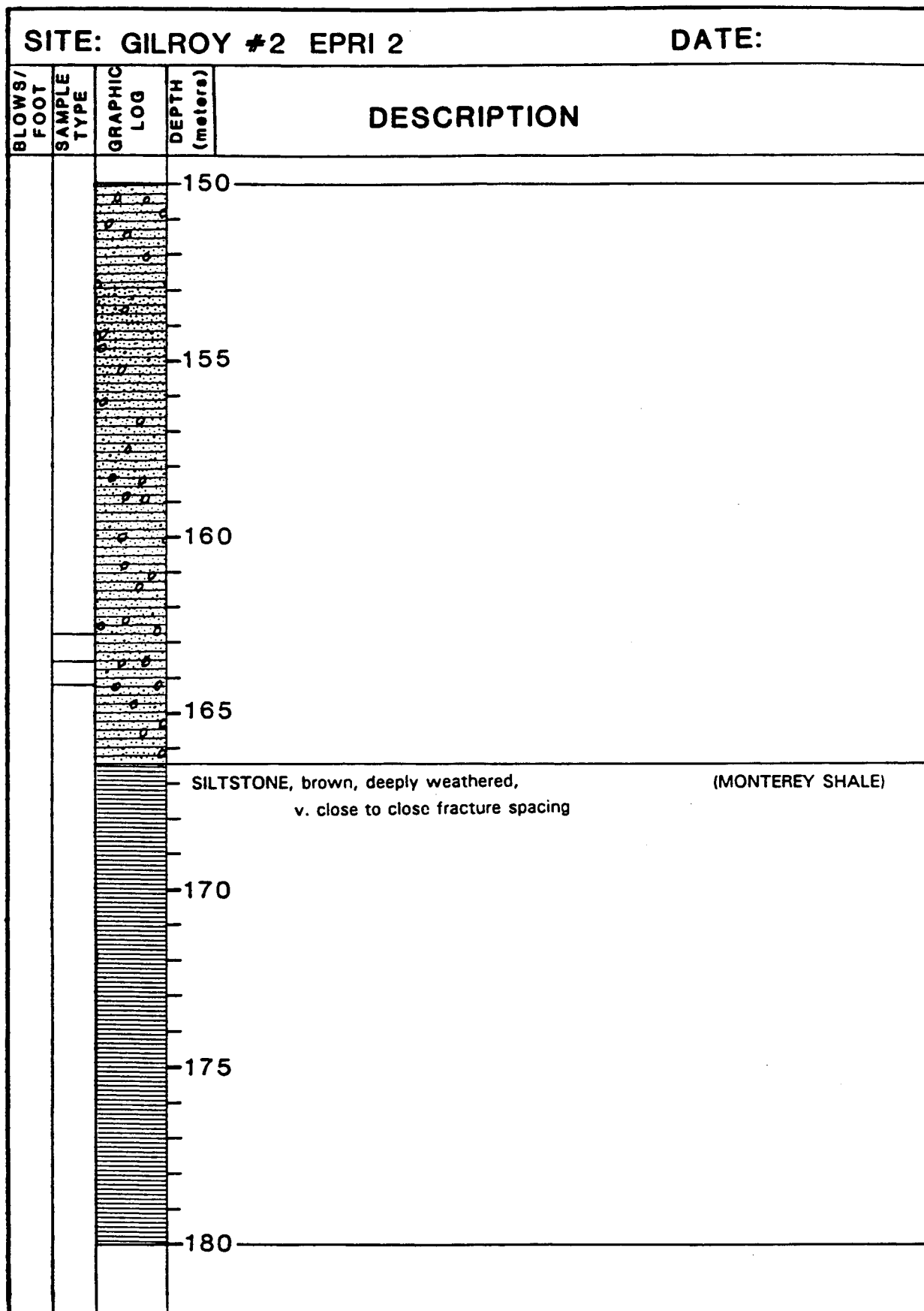


Figure 8.A.5-17 (continued)  
Geologic log for Gilroy 2 (EPRI 2).

SITE: GILROY #2 EPRI 2				DATE:
BLOWS/ FOOT	SAMPLE TYPE	GRAPHIC LOG	DEPTH (meters)	DESCRIPTION
			180	
				SERPENTINITE, v. dk. greenish gray, sheared, texture is SANDY CLAY Some hard, closely fractured blocks
			185	
			190	
				SHALE, gray, sheared to v. closely fractured
			195	
			200	
			205	
			210	

Figure 8.A.5-17 (continued)  
Geologic log for Gilroy 2 (EPRI 2).

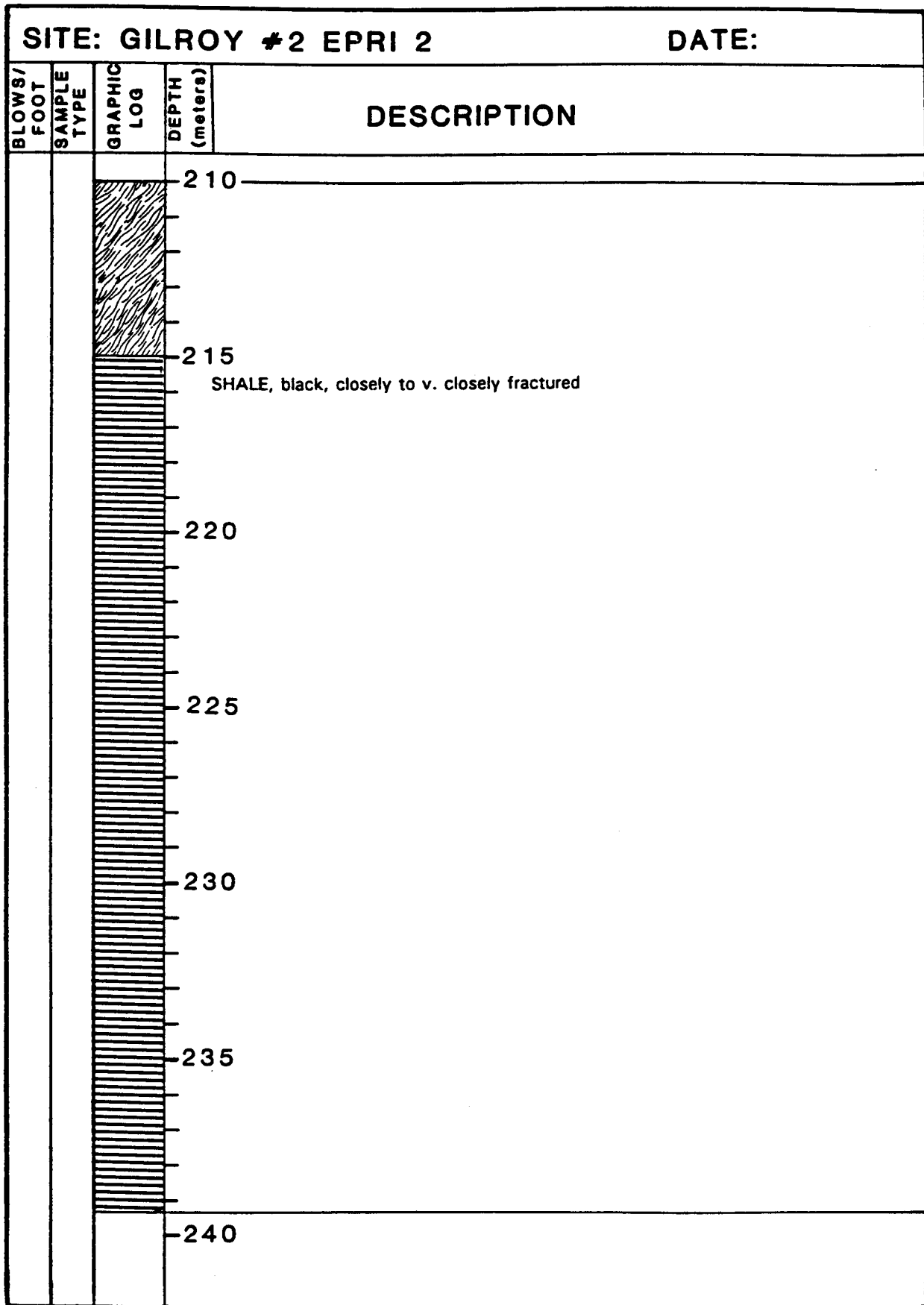
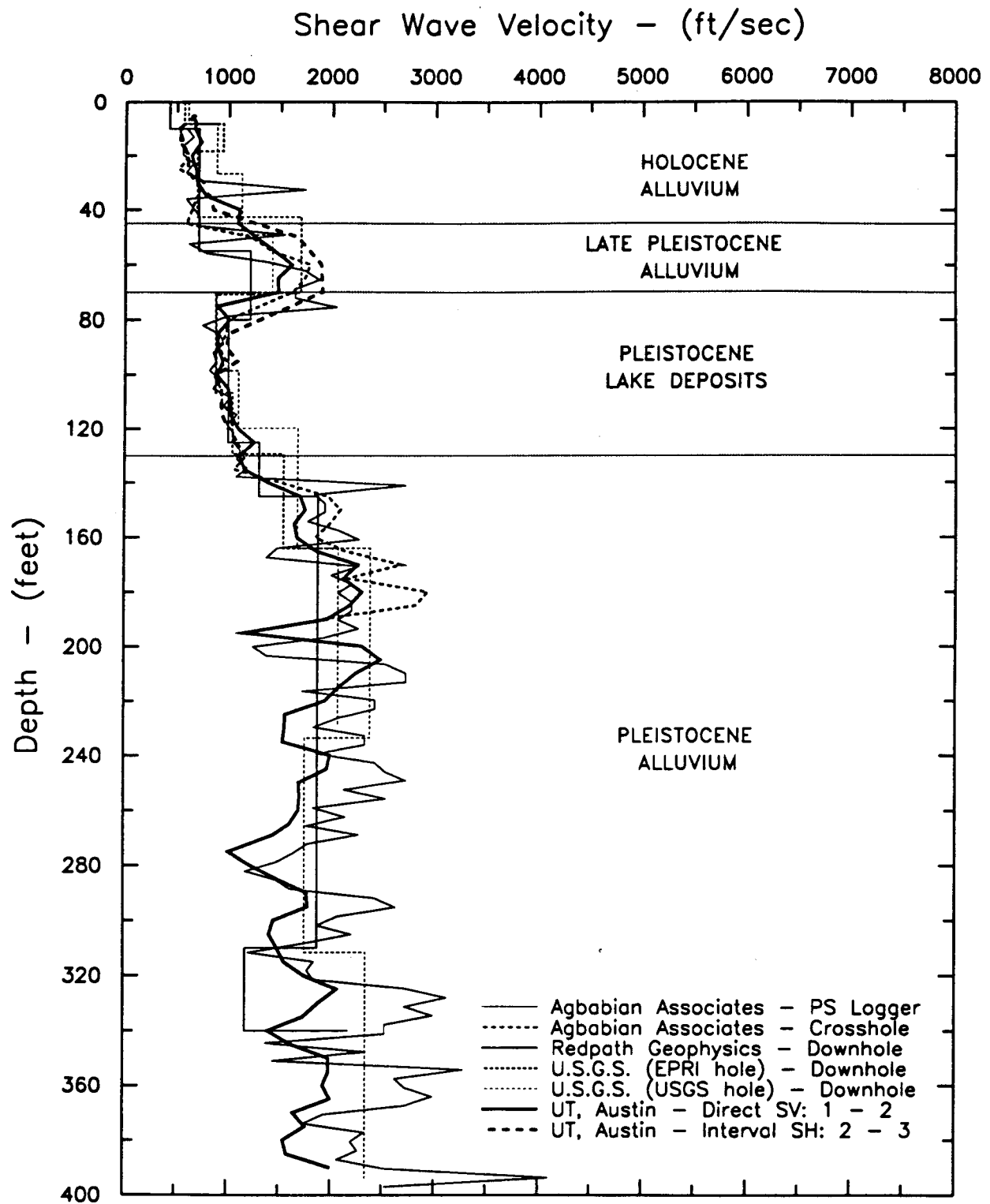
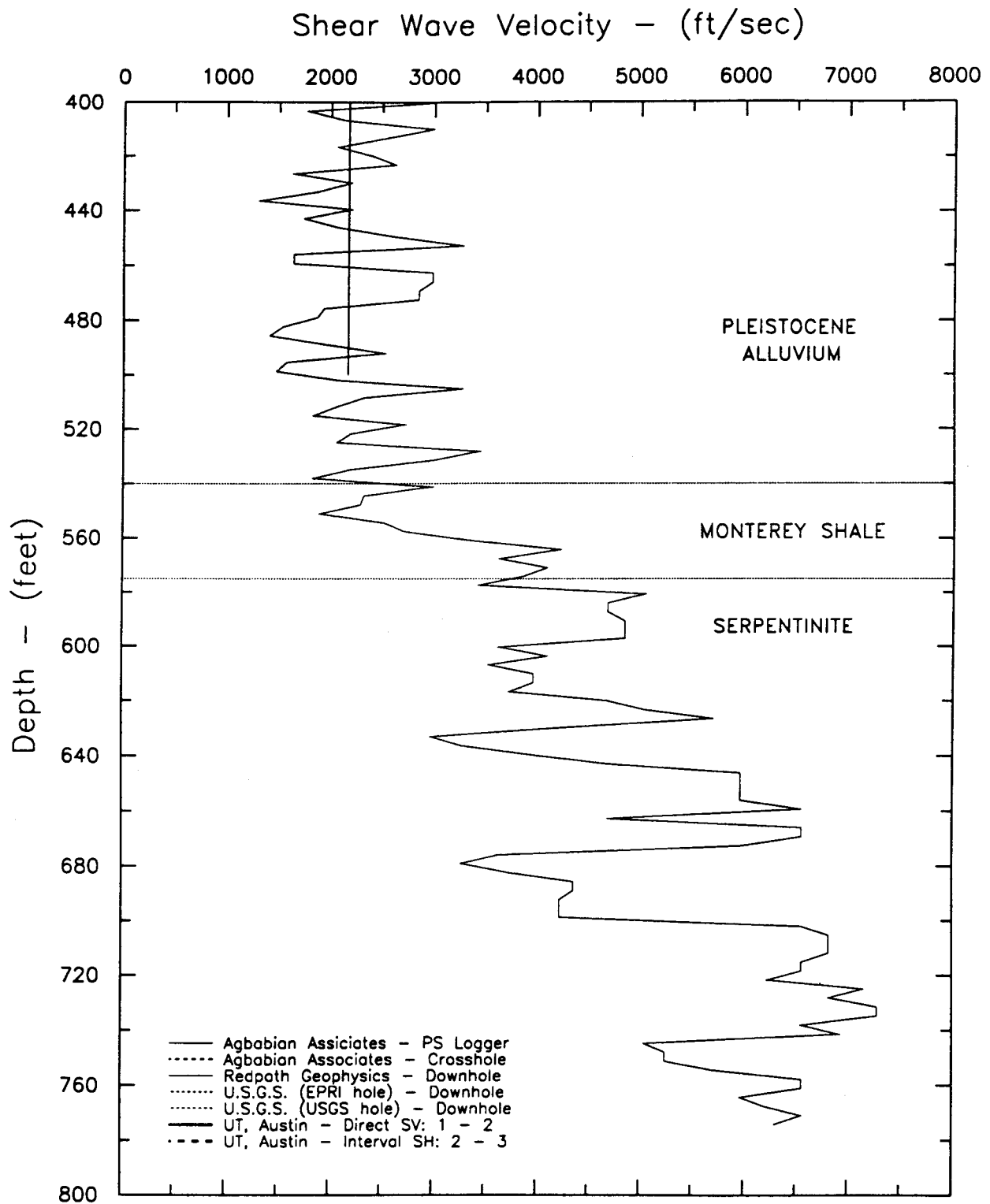


Figure 8.A.5-17 (continued)  
Geologic log for Gilroy 2 (EPRI 2).

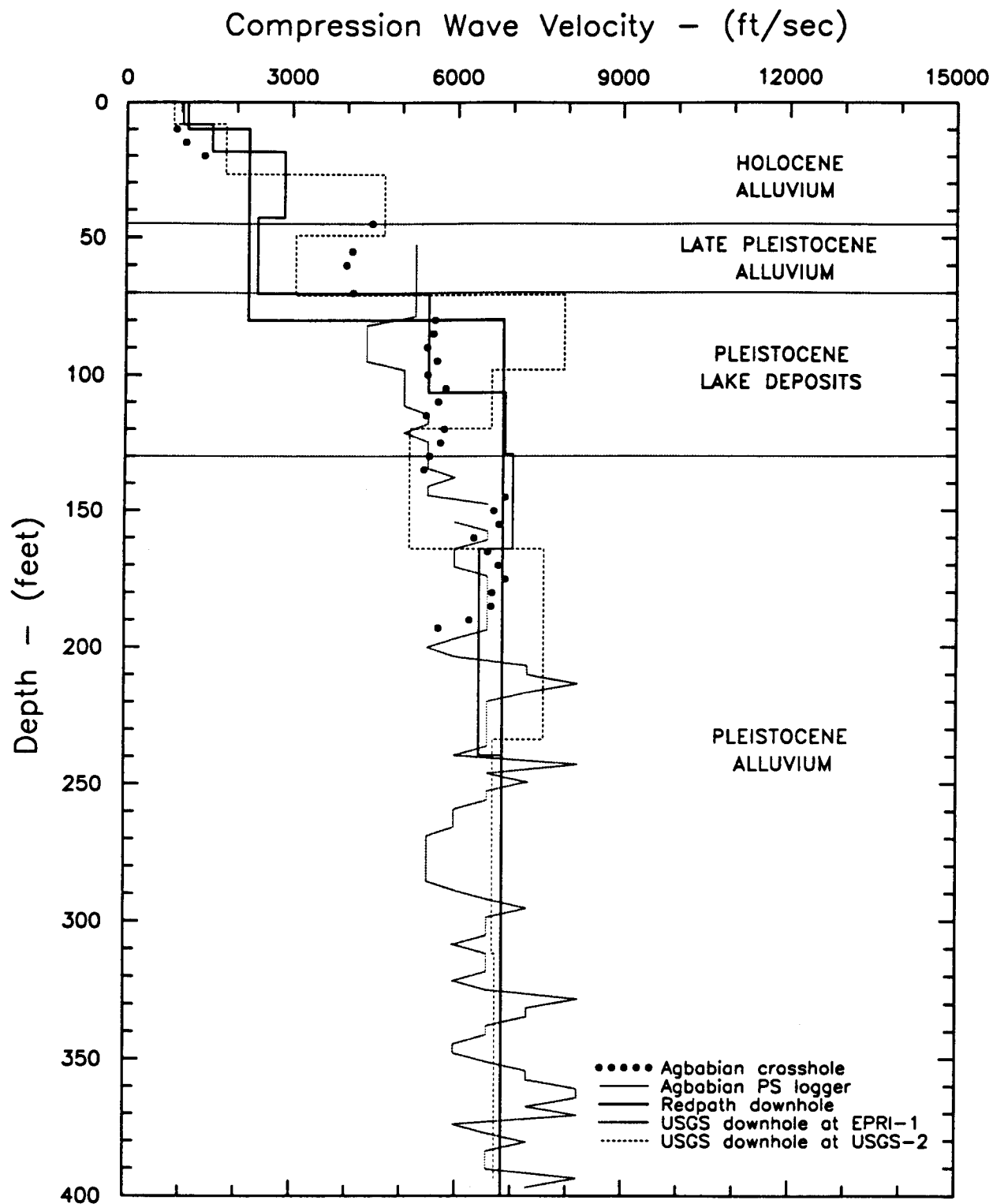


**Figure 8.A.5-18**  
Shear wave velocity measurements, Gilroy array 2.



**Figure 8.A.5-18 (continued)**  
 Shear wave velocity measurements, Gilroy array 2.





**Figure 8.A.5-19**  
P-wave velocity measurements, Gilroy array station 2.

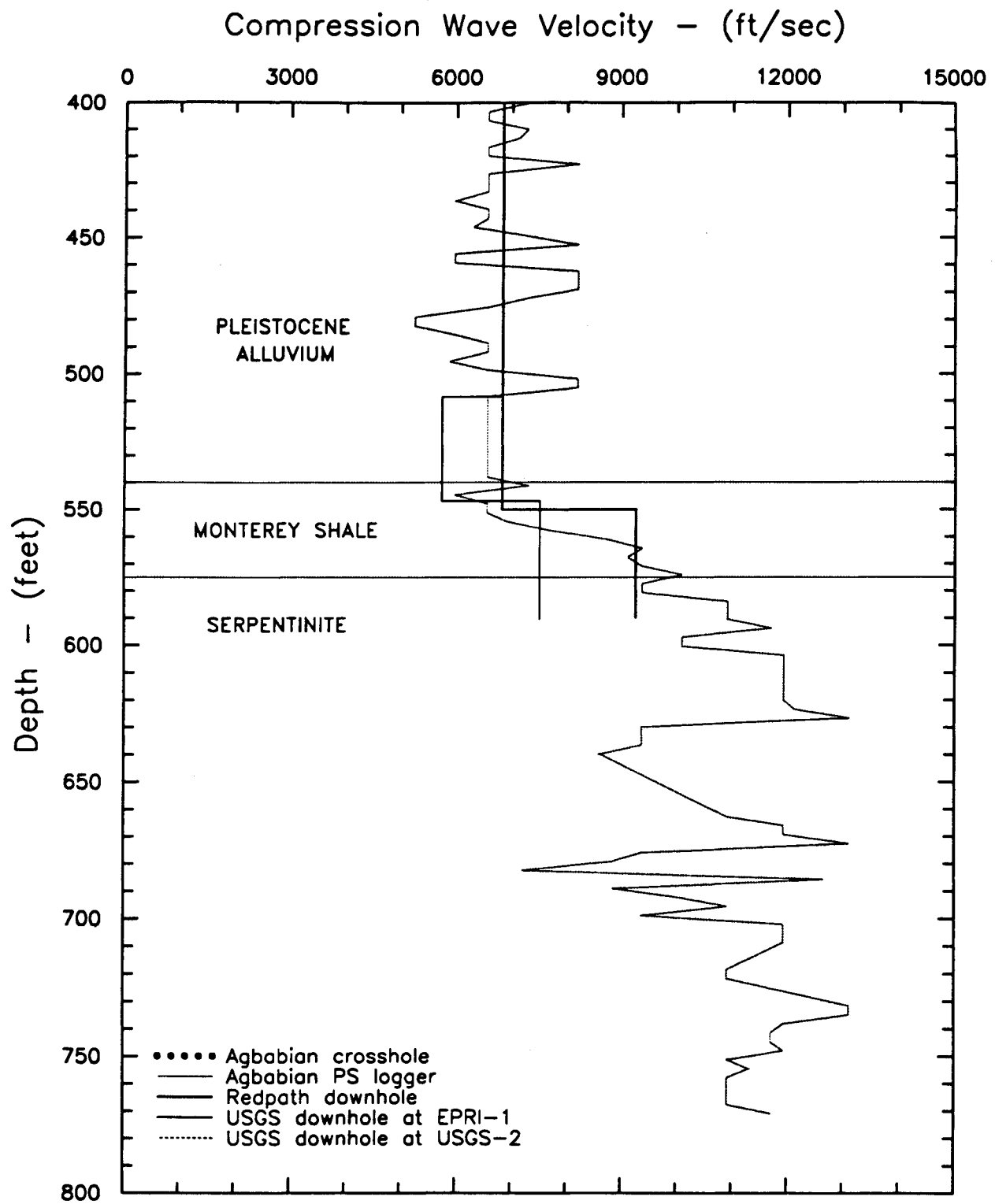
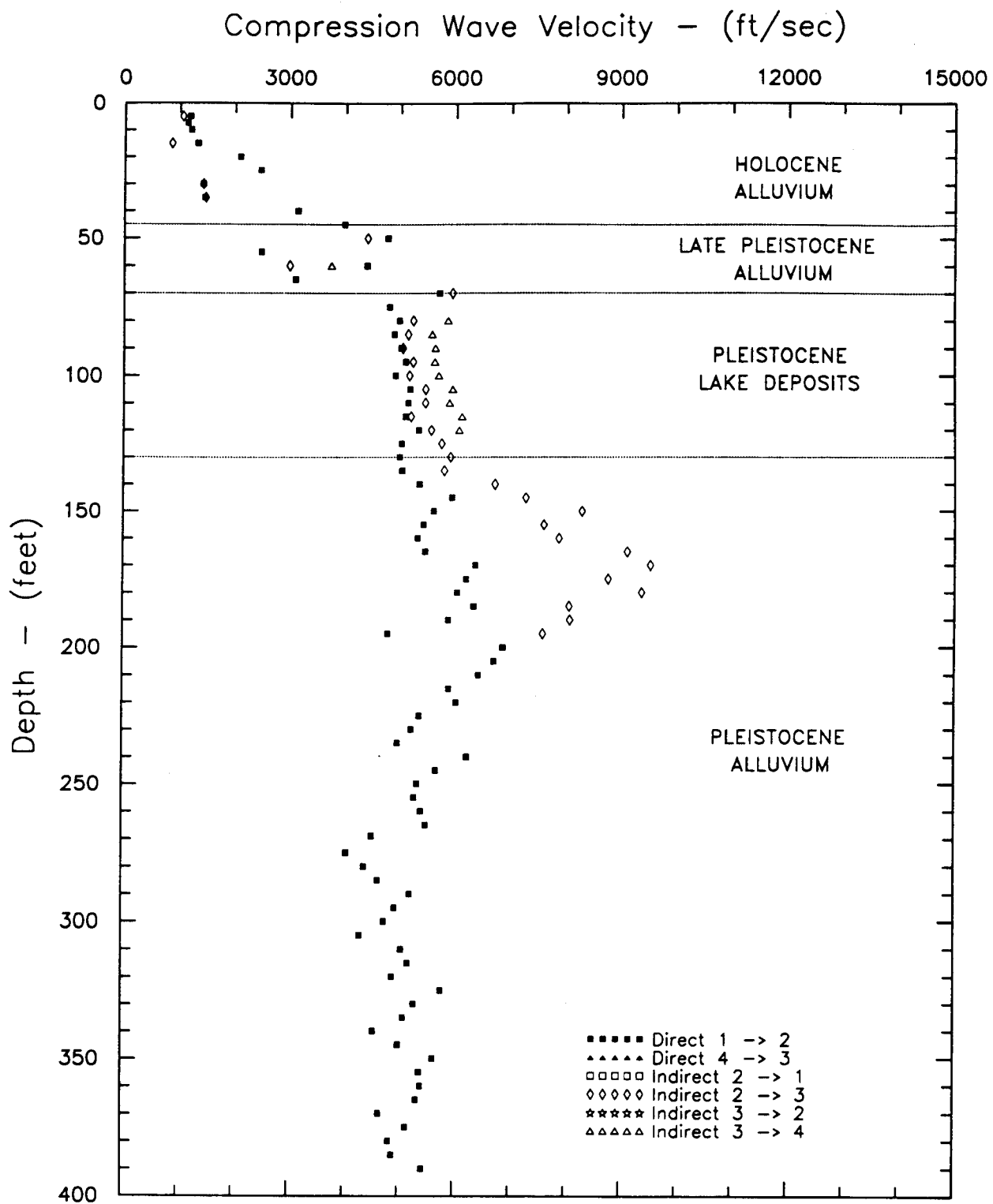
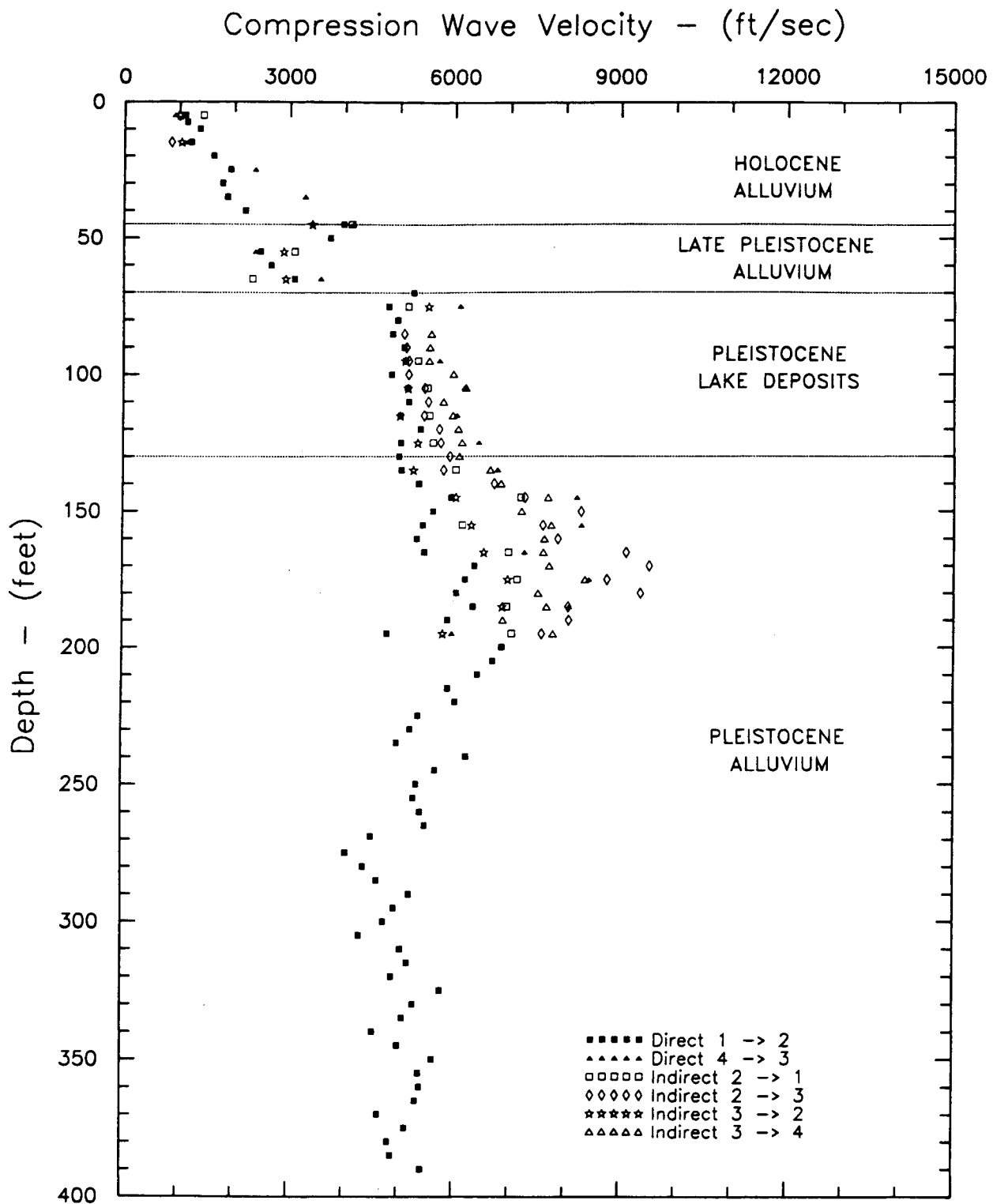


Figure 8.A.5-19 (continued)  
P-wave velocity measurements, Gilroy array station 2.



**Figure 8.A.5-20**

P-wave velocity measurements, U.T. Austin (solenoid source), Gilroy array station 2.



**Figure 8.A.5-21**

P-wave velocity measurements, U.T. Austin (drop hammer source), Gilroy array station 2.

**APPENDIX 8.A.5.B—ADDITIONAL BORING LOGS AT GILROY 2 BY  
USGS**

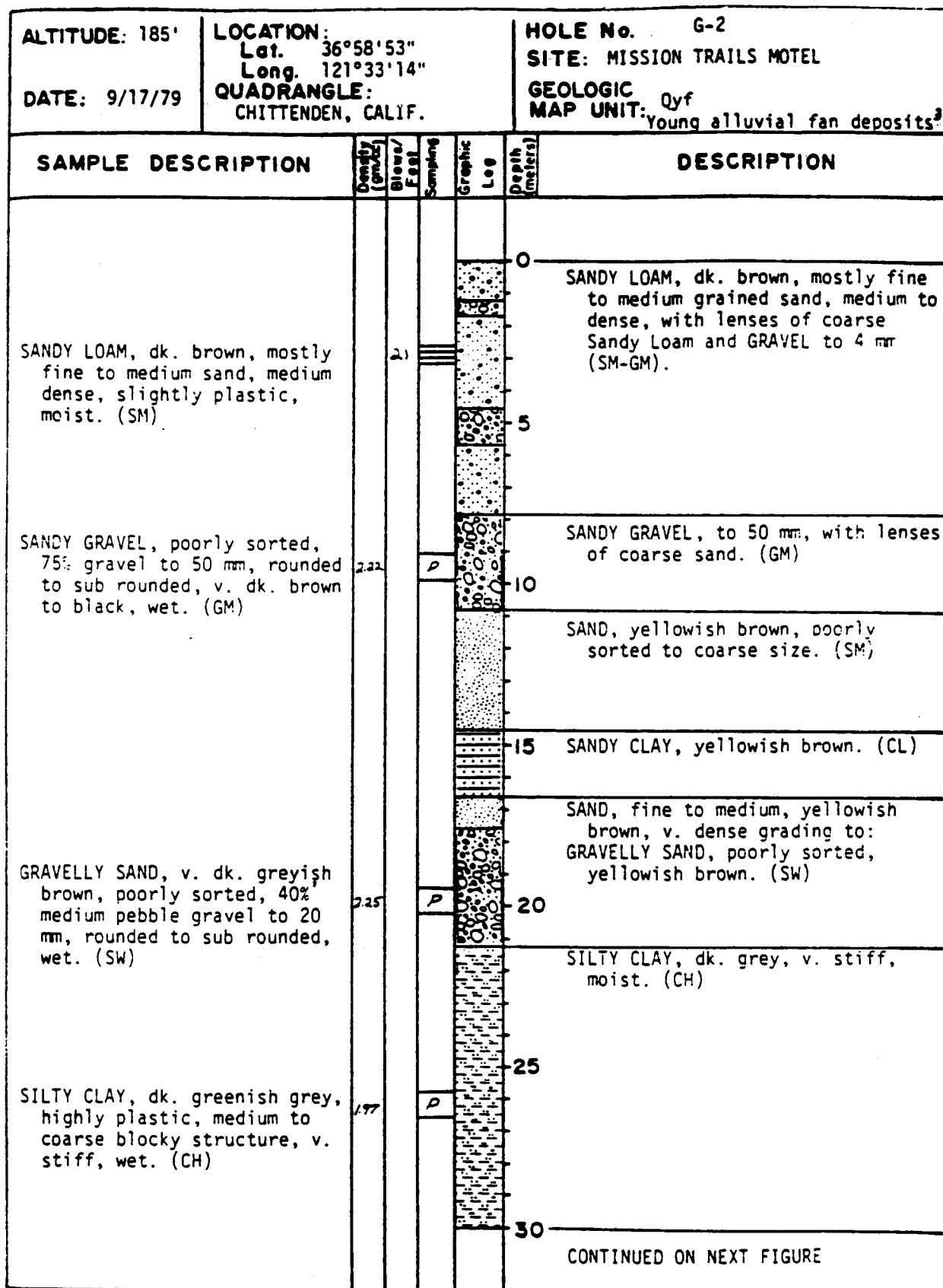


Figure 8.A.5-22  
Borehole USGS-1.

ALTITUDE:	LOCATION: Lat. Long.	HOLE No. GILROY #2	
DATE:	QUADRANGLE:	SITE: MISSION TRAILS MOTEL	
		GEOLOGIC MAP UNIT:	

SAMPLE DESCRIPTION	Sandy (m/s)	Blow/ Foot	Sampling	Graphic Log	Depth (meters)	DESCRIPTION
					30	
					35	with lenses of v. fine SANDY LOAM. (ML)
					40	GRAVEL, well-sorted, little or no fines (GP)
					45	
					50	

Figure 8.A.5-22 (continued)  
Borehole USGS-1.

MISSION TRAILS MOTEL SITE G-2

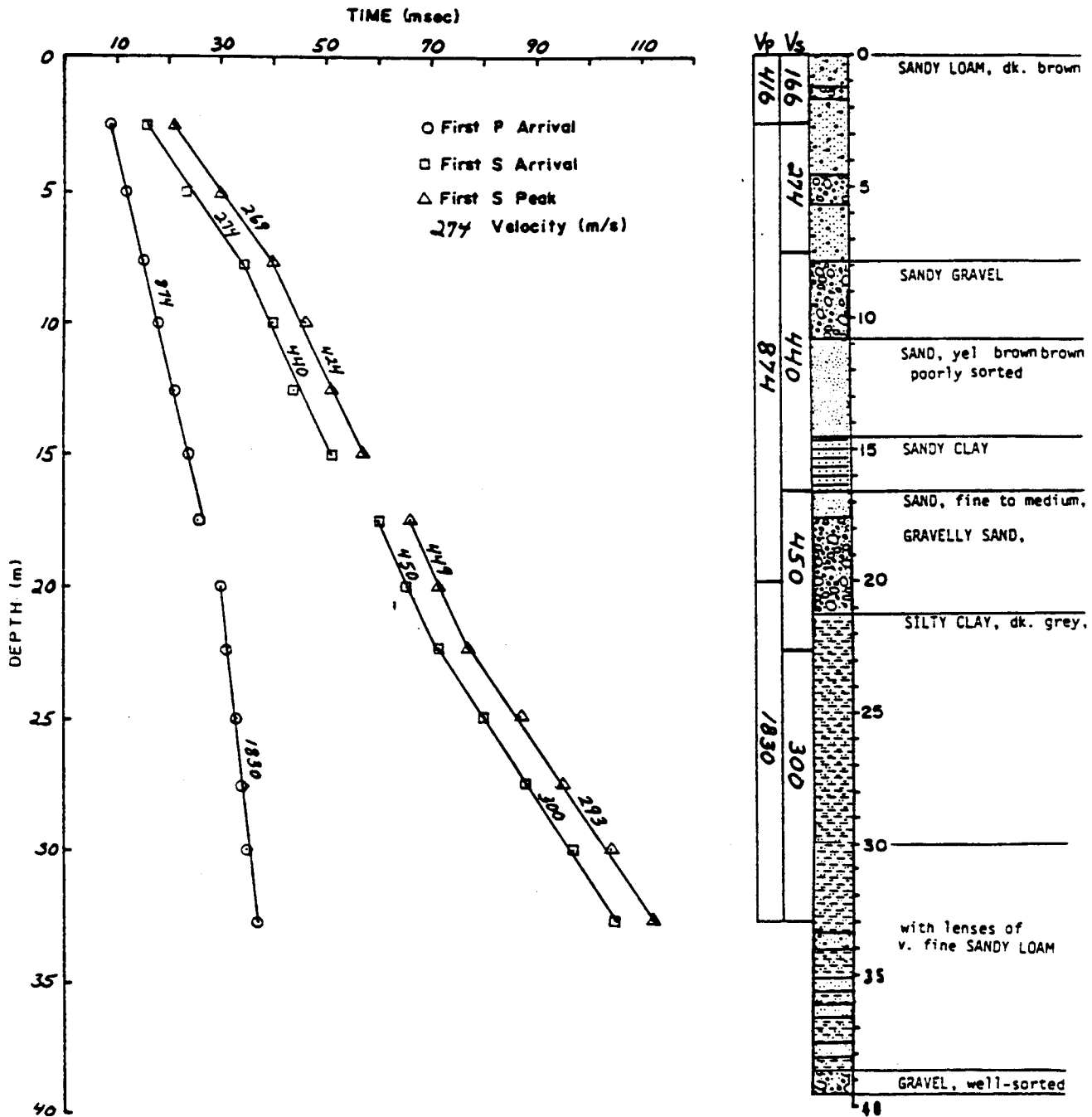
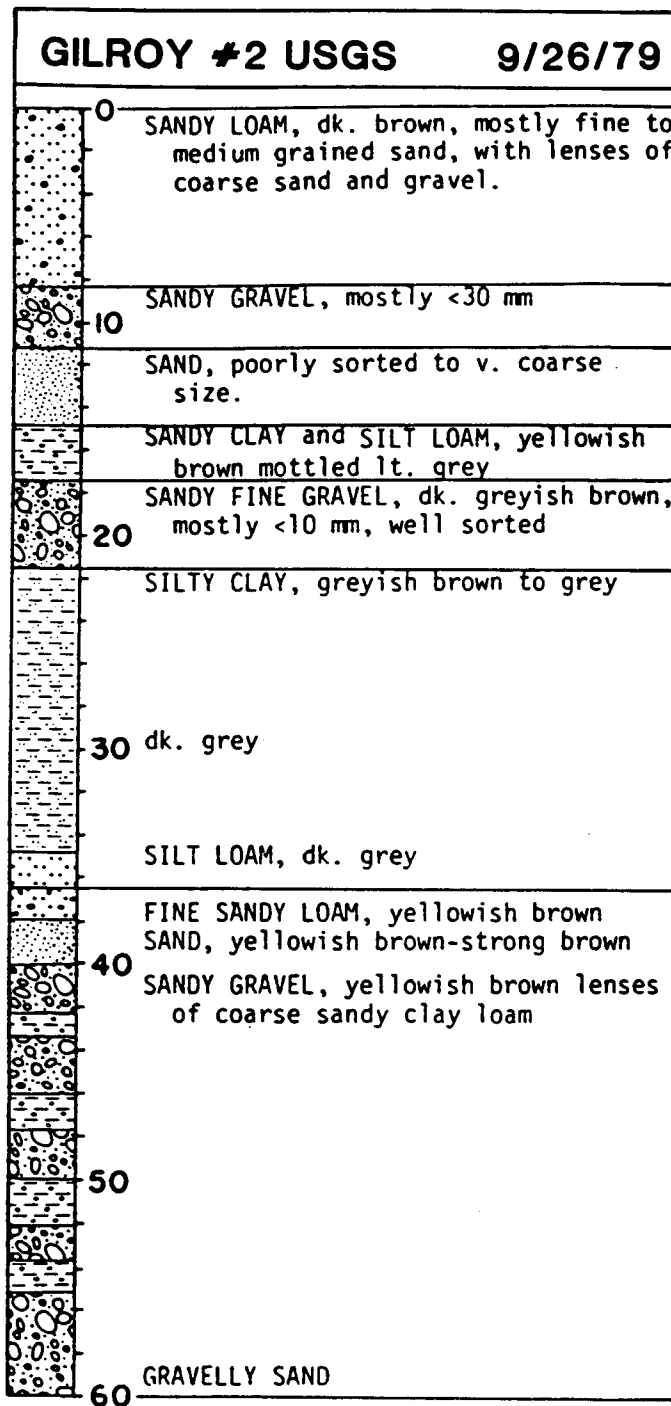


Figure 8.A.5-22 (continued)  
Borehole USGS-1.





**Figure 8.A.5-23**  
Borehole USGS-2, Geologic log of Gilroy 2 (USGS) borehole.

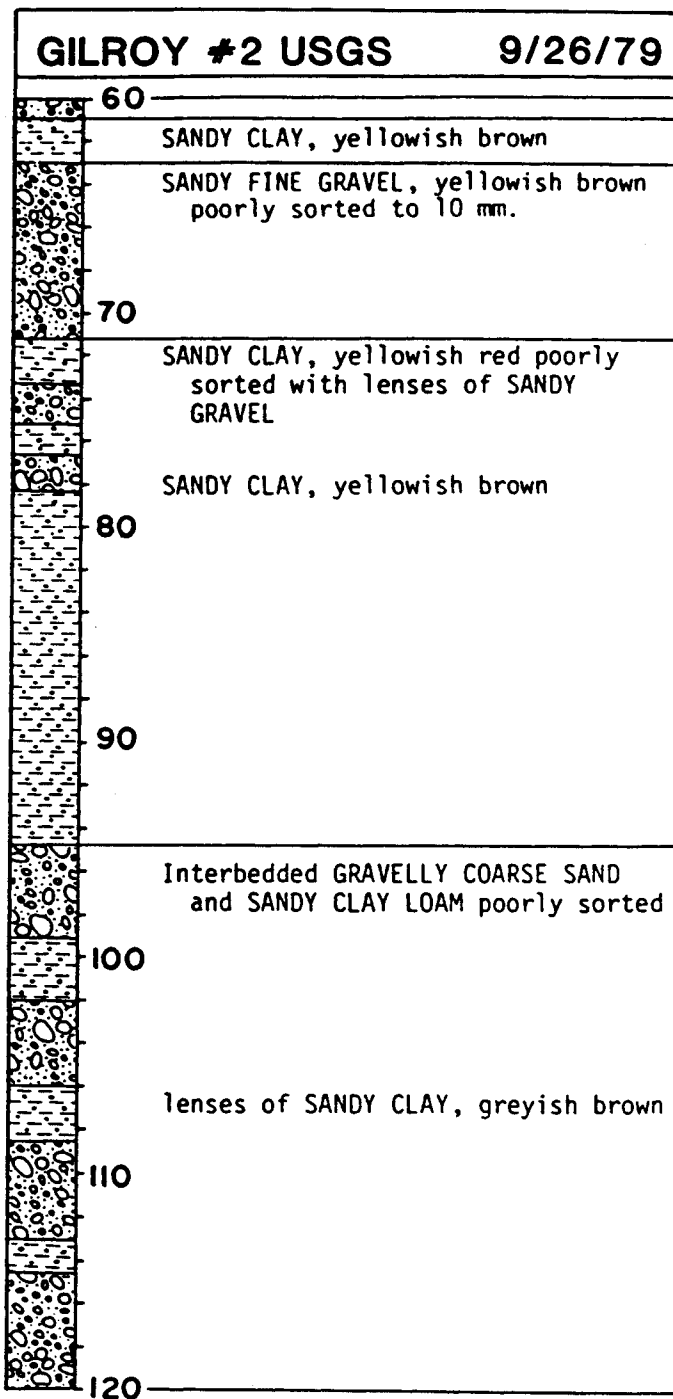


Figure 8.A.5-23 (continued)  
Borehole USGS-2, Geologic log of Gilroy 2 (USGS) borehole.

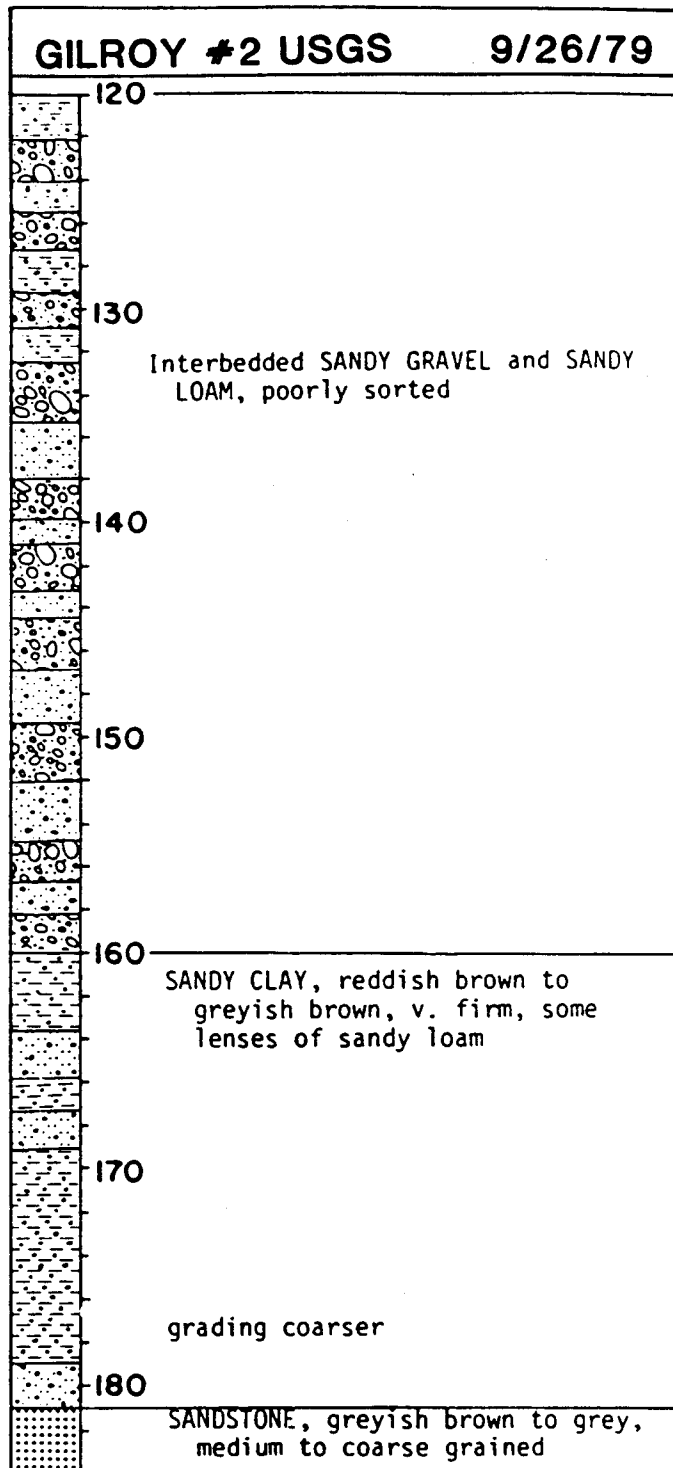
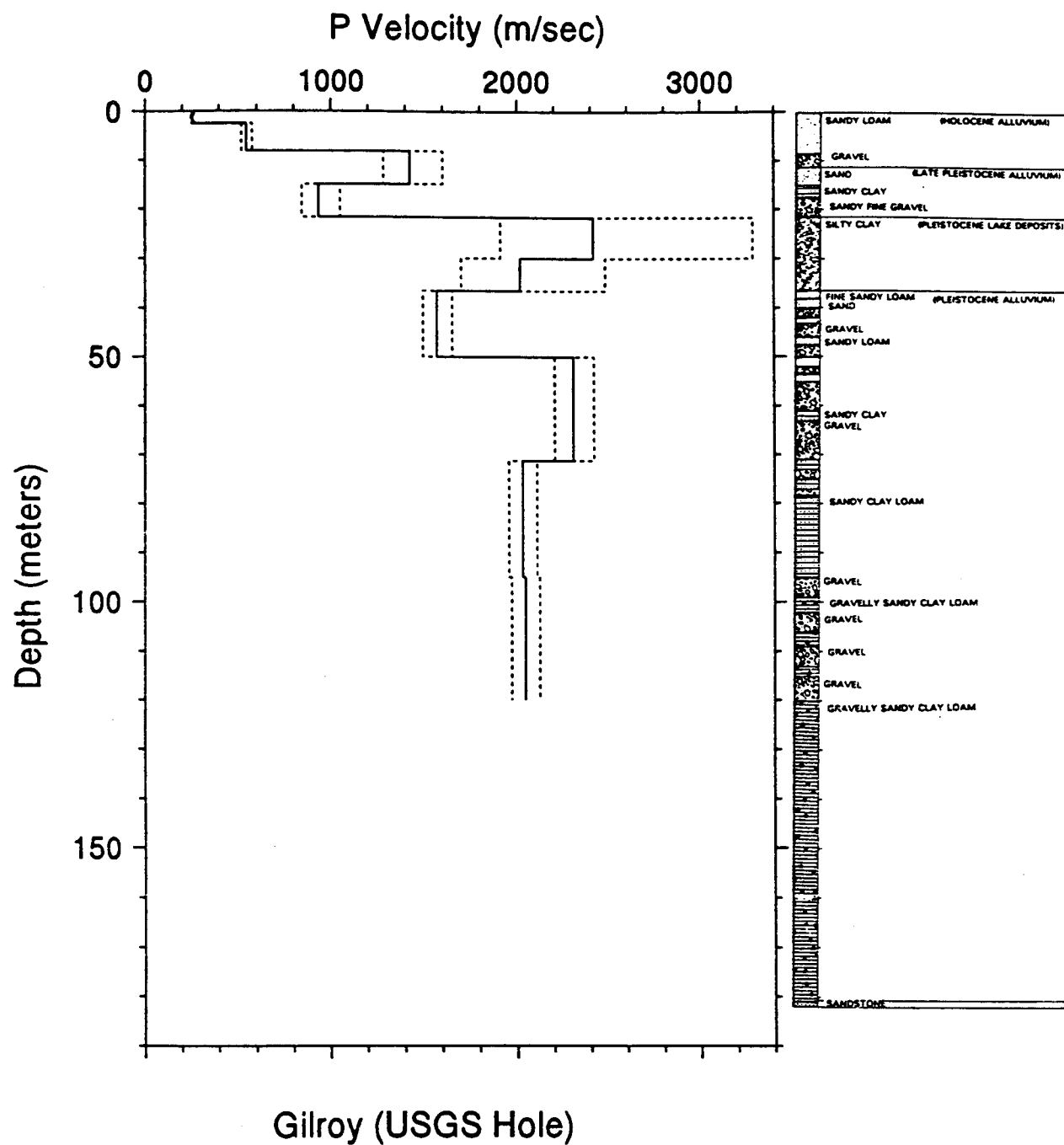
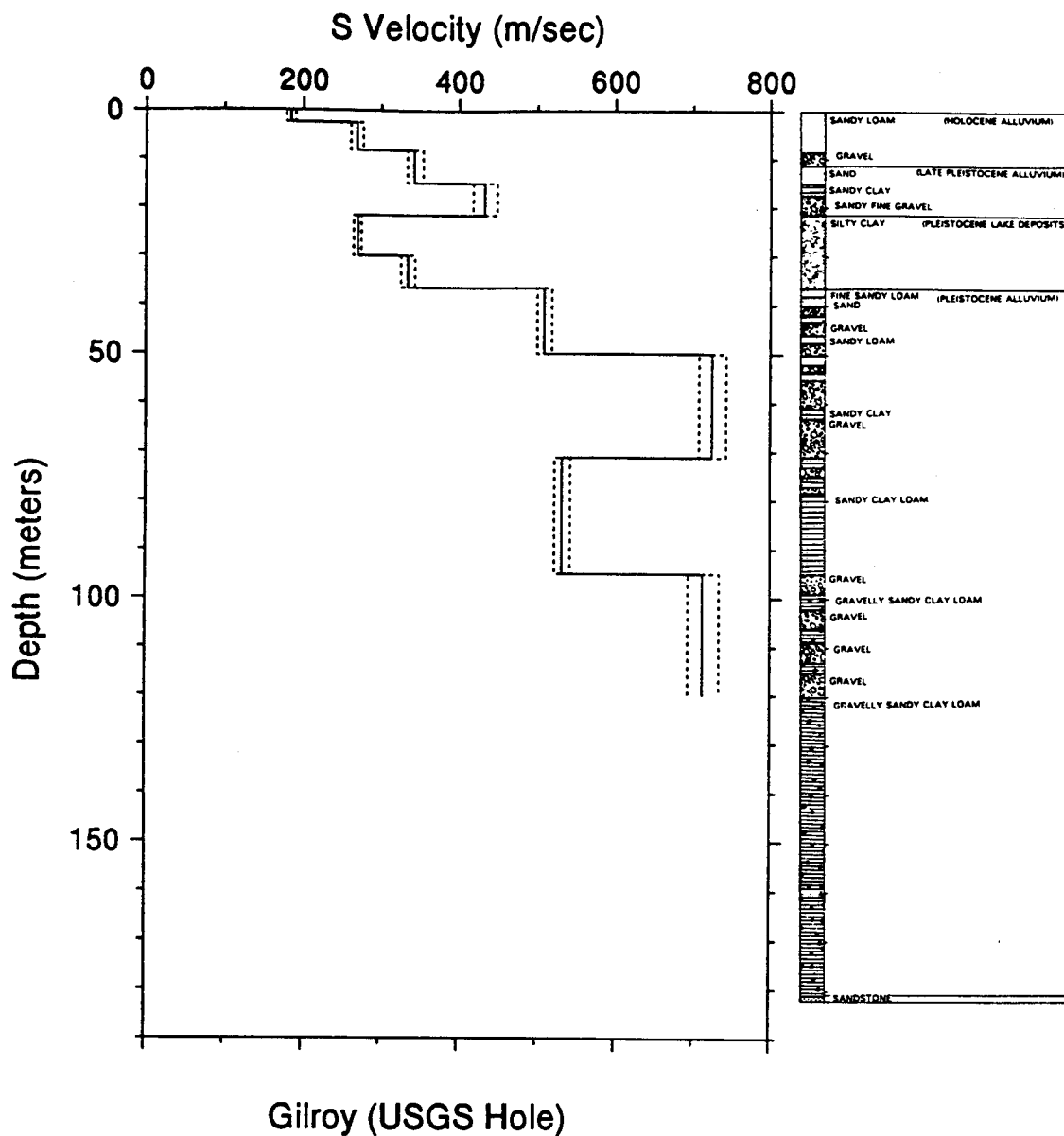


Figure 8.A.5-23 (continued)  
Borehole USGS-2, Geologic log of Gilroy 2 (USGS) borehole.



**Figure 8.A.5-24**

Borehole USGS-2, S-wave velocity profiles with dashed lines representing plus and minus one standard deviation. The statistics are done on the slope (reciprocal velocity) so that some of the limits will not appear symmetrical. Simplified geologic log is shown for correlation with velocities.



**Figure 8.A.5-25**

Borehole USGS-2, P-wave velocity profiles with dashed lines representing plus and minus one standard deviation. The statistics are done on the slope (reciprocal velocity) so that some of the limits will not appear symmetrical. Simplified geologic log is shown for correlation with velocities.

## **APPENDIX 8.A.6**

# **GEOTECHNICAL BORING AND SAMPLING OF THE LOTUNG, TAIWAN SITE**

---

### **SUMMARY**

This report summarizes geotechnical work that was carried out by Moh and Associated, Inc. (MAA) at a Taiwan Power Company (Taipower) substation in Lotung, Taiwan, R.O.C. The major tasks involved in the project were geotechnical drilling and sampling of two boreholes, the installation of PVC casing in the boreholes, selected laboratory testing and data report preparation.

The work described in this report was carried out by MAA under the authorization of a contract awarded by CH2M HILL International, Ltd. Taiwan Branch on December 31, 1991. CH2M HILL contracted the work as part of a research study for the Electric Power Research Institute (EPRI), Palo Alto, California. The EPRI research program involves evaluation of procedures currently being used to predict soil and soil/structure response during seismic loading. Field work for the MAA work commenced on February 10, 1992 and was completed on March 6, 1992. All soil samples were then returned to the MAA laboratory. Laboratory tests were completed by March 26, 1992. The laboratory tests included water content and density determinations, grain-size analyses, Atterberg limits tests, and consolidation tests.

Results of field exploration and laboratory testing programs indicate that the subsurface materials consist primarily of fill in the top 1.5 m, underlain by cohesionless soils to a depth of about 18 m to 22 m. The cohesionless soils are then underlain by cohesive soils, including clayey silt and silty clay, to the maximum explored depth of 45 m. A sand-gravel mixture was encountered between 31 m and 33 m below the existing ground. Artesian conditions were identified from depths of about 13 m to 33 m.

A PVC casing was installed in each hole after drilling. A mixture of bentonite, cement and water was used to grout the space between casing and borehole.

# CONTENTS

---

Section	Page
<b>1—Introduction .....</b>	<b>8.A.6-5</b>
<b>2—Scope of Work .....</b>	<b>8.A.6-6</b>
<b>3—Site Investigation .....</b>	<b>8.A.6-7</b>
8.A.6.3.1 Background .....	8.A.6-7
8.A.6.3.2 Drilling and Sampling .....	8.A.6-7
8.A.6.3.3 SPT's .....	8.A.6-8
8.A.6.3.4 PVC Casing Installation .....	8.A.6-8
8.A.6.3.5 Laboratory Testing .....	8.A.6-8
8.A.6.3.6 Subsoil Conditions .....	8.A.6-8
8.A.6.3.7 Groundwater Condition .....	8.A.6-9
<b>References .....</b>	<b>8.A.6-10</b>
<b>Appendix 8.A.6.A—Subsurface Exploration Logs .....</b>	<b>8.A.6-19</b>
<b>Appendix 8.A.6.B—Laboratory Testing .....</b>	<b>8.A.6-28</b>

# LIST OF TABLES

---

<b>Table</b>		<b>Page</b>
8.A.6-1	Summary of Sampling and Field Testing Program .....	<b>8.A.6-11</b>
8.A.6-2	Summary of Laboratory Testing Program .....	<b>8.A.6-11</b>
8.A.6-3	Results of Hammer Performance Analyzer Tests .....	<b>8.A.6-12</b>



# LIST OF FIGURES

---

<b>Figure</b>		<b>Page</b>
8.A.6-1	Location of Project Site .....	<b>8.A.6-13</b>
8.A.6-2	Borehole Location .....	<b>8.A.6-14</b>
8.A.6-3	Layout of Hammer Performance Analyzer Test .....	<b>8.A.6-15</b>
8.A.6-4	Summary of Boring Logs, SPT-N Values, and Soil Properties .....	<b>8.A.6-16</b>
8.A.6-5	SPT-N Values Distributed with Depth for Boring CH-1 .....	<b>8.A.6-17</b>
8.A.6-6	SPT-N Values Distributed with Depth for Boring CH-2 .....	<b>8.A.6-18</b>

# **APPENDIX 8.A.6 GEOTECHNICAL BORING AND SAMPLING OF THE LOTUNG, TAIWAN SITE**

---

## **1—INTRODUCTION**

The work described in this report was carried out by MAA under the authorization of a contract awarded by CH2M HILL International, Ltd. Taiwan Branch in December 31, 1991. CH2M HILL contracted the work as part of a research study for the Electric Power Research Institute (EPRI), Palo Alto, California. The EPRI research program involves evaluation of procedures currently being used to predict soil and soil/structure response during seismic loading.

The project site is located at a Taiwan Power Company (Taipower) substation in Lotung, Taiwan, ROC. The major tasks involved in the project were geotechnical drilling and sampling of two boreholes, the installation of PVC casing in the boreholes, selected laboratory testing and data report preparation.

Field work for the MAA work commenced on February 10, 1992 and was completed on March 6, 1992. A PVC casing was installed in each hole after drilling. All soil samples were then returned to the MAA Laboratory. Laboratory tests were completed by March 26, 1992. This report summarizes the results of field exploration and laboratory testing.

## **2—SCOPE OF WORK**

The scope of the MAA program involved the following tasks:

1. Obtained a working permit from Taipower Company;
2. Subcontracting a drilling contractor to drill and sample two 45-m deep boreholes;
3. Overseeing the drilling and sampling program, including preparation of field borehole logs;
4. Performing selected measurements of SPT energy by the use of a Hammer Performance Analyzer (HPA);
5. Installing 45 m of 100 mm I.D. PVC casing and a 1 m long protective steel casing in each borehole;
6. Packing ten undisturbed Shelby tubes of soil and shipping via air to Professor Ken Stokoe at the University of Texas in Austin for special confining pressure and rate of loading studies;
7. Conducting laboratory tests assigned by CH2M HILL which included water content and dry density determinations, grain-size analyses, Atterberg limits tests, and one-dimensional consolidation testing;
8. Preparing a data report describing drilling methods, boring logs and laboratory testing results;

### **3—SITE INVESTIGATION**

#### **8.A.6.3.1 Background**

The project site as shown in Figure 8.A.6-1 is at a Taipower substation in Lotung, Taiwan. Taipower and EPRI have jointly funded construction of two model structures at the site, scaled to one-quarter and one-twelfth the size of a typical reinforced concrete containment building. Various instrumentation, including accelerometers and settlement devices, have been installed at this site in order to study the soil-structure interaction during earthquakes. Additional details about the project are provided by Tang (1987). Information about soil conditions at the Lotung site is summarized by Anderson and Tang (1989).

MAA installed settlement monitoring instrumentation at the Lotung site in June 1988. The results of this work are summarized in MAA report No. 418-1 Taipower, dated October 1988.

It is our understanding that Taipower is planning to construct a new transmission tower near the boreholes. The approximate location of this tower is shown in Figure 8.A.6-2. All the elevations used in this report refer to a reference benchmark (see Figure 8.A.6-2) assumed as EL.+ 10.00 m.

#### **8.A.6.3.2 Drilling and Sampling**

The two borehole locations are shown in Figure 8.A.6-2. These boreholes are located near five existing accelerometer hole, presently being used by the Institute of Earth Science (IES) for free-field ground response studies.

Drilling and sampling was performed by Shin Yang Company, Limited under contract to MAA. Boreholes were advanced by the use of a power auger in soil stratum above the groundwater table and by use of a wash-boring method in soil stratum below the groundwater table. Depending upon the local soil conditions at the site, the upper 27 m of the holes were cased during drilling with 15.58 cm (6 in), 14.22 cm (5.6 in), 11.58 cm (5 in), or 10.67 cm (4.2 in) diameter steel casings. Drilling mud was used to prevent the collapse of boreholes below 27 m. Shelby tube samples were taken at 10 to 12 depths in each borehole using a fixed-piston sample. The diameter of the Shelby tube samples are identified on the subsurface exploration logs in Appendix 8.A.6.A.

After sampling, all Shelby tubes with cohesionless soil were kept vertical. A free-drainage condition was maintained for one to two days in order to drain pore water from the cohesionless soils. The ends of the Shelby tubes were then sealed with wax. The cohesive samples were sealed with wax immediately after sampling.

A total of 22 Shelby tube samples were placed in a sample storage box and surrounded by sponge and foam rubber cushioning materials. The samples were then placed within a vehicle with cushioning and transported to the MAA soil laboratory in Taipei for temporary storage. Split-spoon samples were also sent to the MAA laboratory and were used for physical property tests.

Ten Shelby tube samples were subsequently packed and shipped via air on March 16, 1992 to Professor Ken Stokoe at the University of Texas in Austin for special confining pressure and rate of loading studies. CH2M HILL and Professor Stokoe identified which samples to ship. The remaining Shelby tubes are being stored at MAA until CH2M HILL and EPRI have reviewed the effects of transporting the 10 Shelby tube samples.

A summary of the sampling and field testing program is also presented in Table 8.A.6-1. The boring logs are included in Appendix 8.A.6.A.

#### **8.A.6.3.3 SPT's**

In addition to drilling and Shelby tube sampling, the field work included Standard Penetration Tests (SPT's) and selected SPT energy measurement by using a Hammer Performance Analyzer (HPA). The SPT sampler with 8 brass rings inside was used for sampling. Each ring is about 7 cm high with an I.D. of 3.5 cm. Standard Penetration Tests (SPT's) were carried out at 1.5 m intervals or immediately after a Shelby tube sample was taken.

Standard Penetration Tests were carried out in accordance with the ASTM D1586-84 test method (ASTM, 1987). During the SPT, a 140-lb. hammer was lifted to a height of 76.2 cm (30 in), then dropped to create an impact with the anvil, thus driving the sampler into the soil. Two types of hammers were used during the SPT's: 1) donut or center-hole hammer with 2-1/2 wraps around the cathead and 2) an automatic trip hammer. The automatic trip hammer was used during a series of hammer energy calibration tests.

Hammer energy calibration tests were conducted in both boreholes to quantify levels of energy developed during the SPT's. If the SPT hammer had been in a free-fall condition, the theoretical impact energy would have been 4200 in.-lb. However, factors such as the friction produced by the rope and guiderod, the number of rope turns, operator technique, and hammer type made the actual impact energy on the anvil less than 4200 in.-lb. The delivered energy was measured between 20 m to 30 m for Boring No. CH-1 and in the upper 30 m of soil stratum for Boring No. CH-2 with an automatic trip hammer, and by using a HPA energy calibrator, manufactured by pile Dynamic, Inc., U.S.A. A sketch of the HPA test's layout is shown in Figure 8.A.6-3. The HPA results are summarized in Table 8.A.6-3.

#### **8.A.6.3.4 PVC Casing Installation**

At the completion of drilling, the 100 mm I.D. PVC casing was installed. The bottom of the PVC casing was sealed with an end cap. A small grout pipe was attached on bottom of the casing and along the PVC casing. The casing was then filled with water and carefully lowered into the hole.

The annulus between the PVC casing and the soil was grouted from the bottom up with a cement-bentonite-water mixture. The ratio of cement to bentonite to water was about 1 to 1.2 to 10. This grout mixture gives an undrained shear strength of 0.31 kg/sq. m after 28 days according to the MAA Report No. 418-1, (MAA, 1988). A jar filled with grout was also obtained and sent to the MAA office for study at a later date.

Once the boreholes were grouted but before the grout set up, the steel casing used during drilling and sampling was removed. A protective steel casing with total length of 1 m was then installed at the surface of each borehole. The site was cleared following completion of field work.

#### **8.A.6.3.5 Laboratory Testing**

A laboratory test program was conducted on selected soil samples, per the instruction of CH2M HILL. The tests included water content and dry density determinations, grain-size analyses, Atterberg limits, and one-dimensional consolidation tests. A bag sample of surface fill obtained near the one-quarter scale structure was also tested for grain-size.

Detailed results of the laboratory tests are presented in Appendix 8.A.6.B. These results indicate that cohesionless materials had dry densities ranging from 1.29 to 2.0 gram per cubic centimeter (g/cc), and moisture content from 11.2 to 38 percent. Dry densities for cohesive materials ranged from about 1.1 to 1.5 g/cc, and moisture contents from 25.7 to 43.8 percent.

#### **8.A.6.3.6 Subsoil Conditions**

Based on the results from the drilling and laboratory testing programs, the subsurface materials can be divided into four strata to the maximum explored depth of 45 m. Figure 8.A.6-4 presents the boring logs, SPT-N value and soil properties. Figures 8.A.6-5 and 8.A.6-6 present the distribution of SPT-N value with depth for each boring.

The top fill stratum consists of sandy to clayey silt with gravel. The fill was encountered to depths of about 1.0 to 1.5 m below the ground surface. The second stratum consist primarily of fine sand with interbedded silt soils to a depth of 18.0 to 21.6 m. The SPT-N value in this stratum ranged from 1.5 to 28 and generally became greater with depth. The third and fourth strata consist mainly of silt and clay materials with average SPT-N value of 16 and 20, respectively. A thin layer consisting of sand and gravel mixture with blow counts higher than 40 was also encountered between 31.0 to 33.0 m below the ground surface.

#### **8.A.6.3.7 Groundwater Condition**

No observation wells and piezometers were installed at this time. However, the groundwater level was recorded each day during drilling. These observation indicate that the groundwater table ranged from 0.4 to 0.5 m below the ground surface. Artesian conditions were also encountered in two borings at the depths from 13.0 to 33.0 meters.

## REFERENCES

- Anderson, D.G and Tang, Y.K. "Summary of Soil Characterization Program for the Lotung Large-Scale Seismic Experiment," *Proceedings: EPRI/NRC/TPC Workshop on Seismic Soil-Structure Interaction Analysis Techniques Using Data from Lotung, Taiwan*, EPRI NP6154, Volume 1, March 1989.
- ASTM, *Annual Book of ASTM Standards Vol. 04.08, Soil and Rock; Building Stones; Geotextiles*, American Society for Testing and Materials, 1987.
- Moh and Associates, Inc., "Report on The Installation of Settlement Monitoring Instruments for Lotung Seismic Experiment Station", Report No. 418-1, dated October 1988.
- Tang, H.T. *Large-Scale Soil-Structure Interaction*, Electric Power Research Institute, EPRI NP-5513-SR, November, 1989.

**Table 8.A.6-1**

Summary of Sampling and Field Testing Program

Hole No.	Elevation m	Depth m	Standard Penetration Test No.	Split-Spoon Sample Set	Shelby Tube Sample No.
CH-1	+ 10.080	45.00	27	27	10
CH-2	+ 10.105	45.00	27	27	12

Note: The elevation at the reference benchmark is assumed as EL. +10.0 m.

**Table 8.A.6-2**

Summary of Laboratory Testing Program

Hole No.	Dry Density & Water Content	Atterberg Limits	Grain size	Consolidation Test
CH-1	19	4	11	2
CH-2	16	4	7	0
BA-1			1	

Remarks: 1. All laboratory tests were assigned by CH2M HILL.

2. Ten undisturbed shelly tubes have been transferred to Professor Ken Stokoe at the University of Texas, Austin for special testing.



**Table 8.A.6-3**  
Results of Hammer Performance Analyzer Tests

Boring No.	Depth (m)	SPT-N	Energy Ratio (%)
CH-1	21.05 - 21.5	7	75.87
	23.09 - 23.54	9	75.32
	25.25 - 25.60	9	75.93
	28.05 - 28.50	14	72.03
	Average = 74.04%		
CH-2	3.65 - 4.10	1.5	78
	5.60 - 6.05	3	64.92
	7.70 - 8.15	8	68.08
	9.05 - 9.50	3	67.12
	15.05 - 15.5	9	68.24
	19.70 - 20.15	14	69.65
	22.55 - 23.0	9	68.91
	24.05 - 24.5	16	70.84
	25.55 - 26.0	10	71.30
	Average = 69.67%		

Remarks: 1. HPA was performed in the upper 30m. only.  
2. Automatic trip hammer was applied during HPA tests.

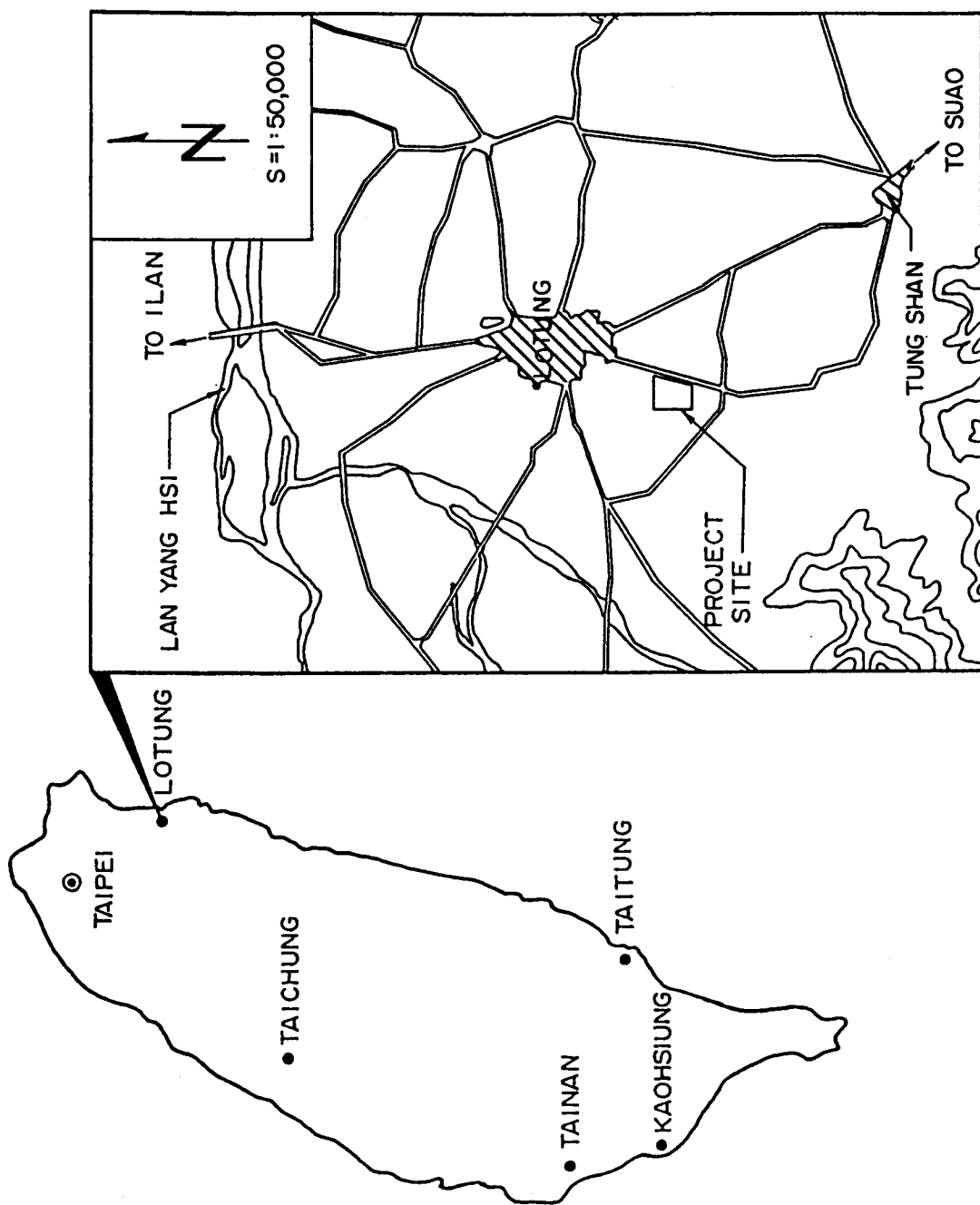
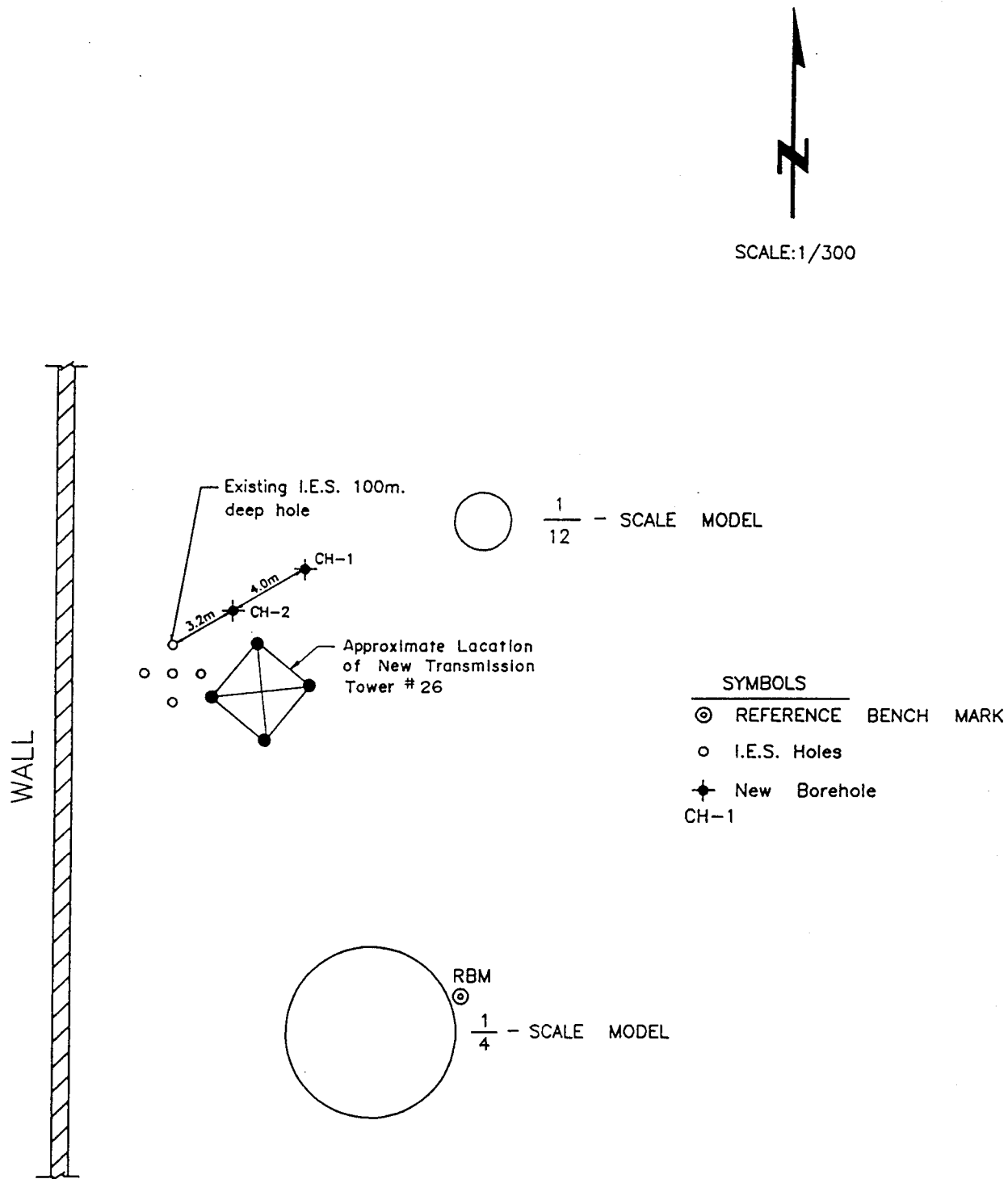
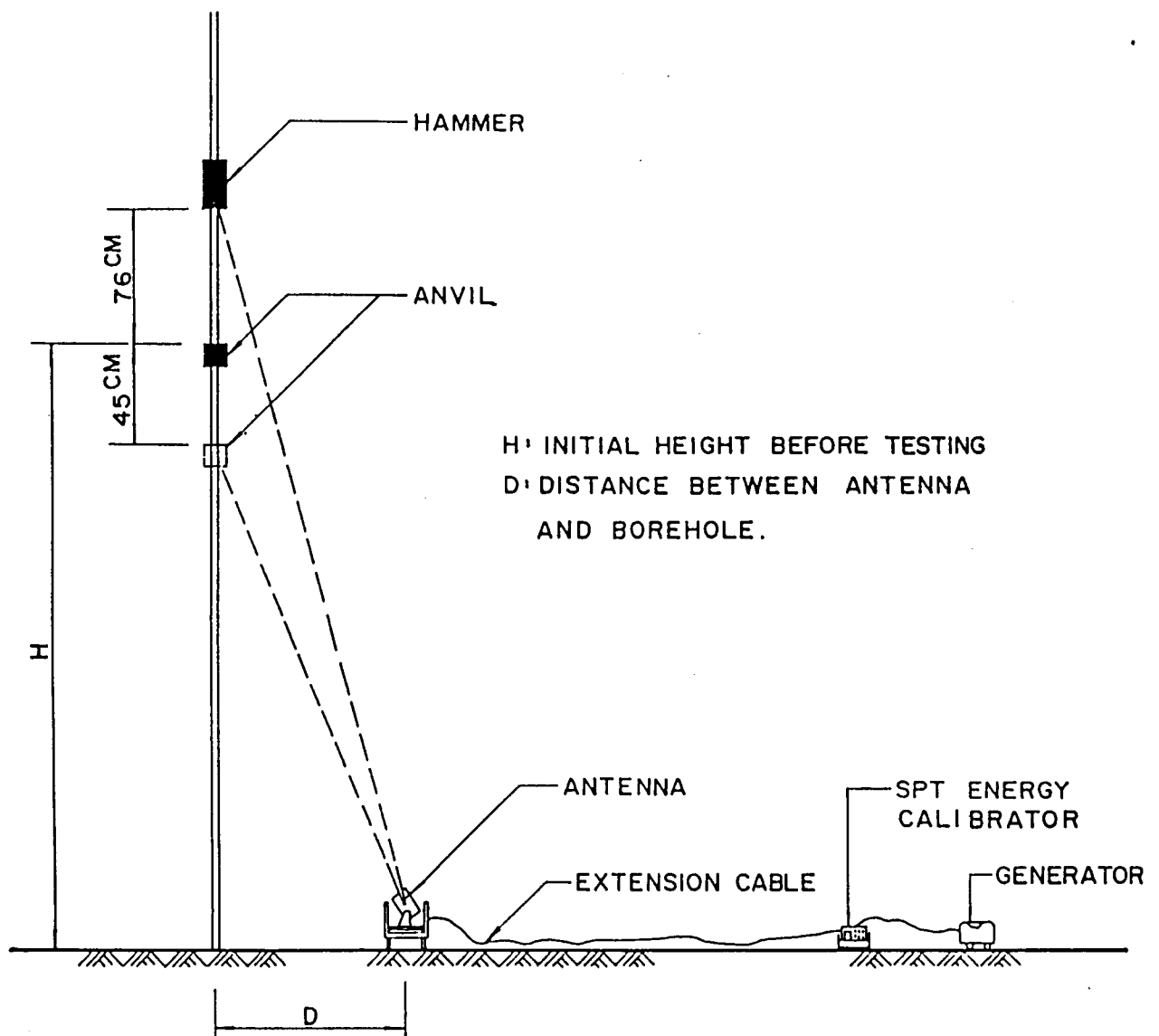


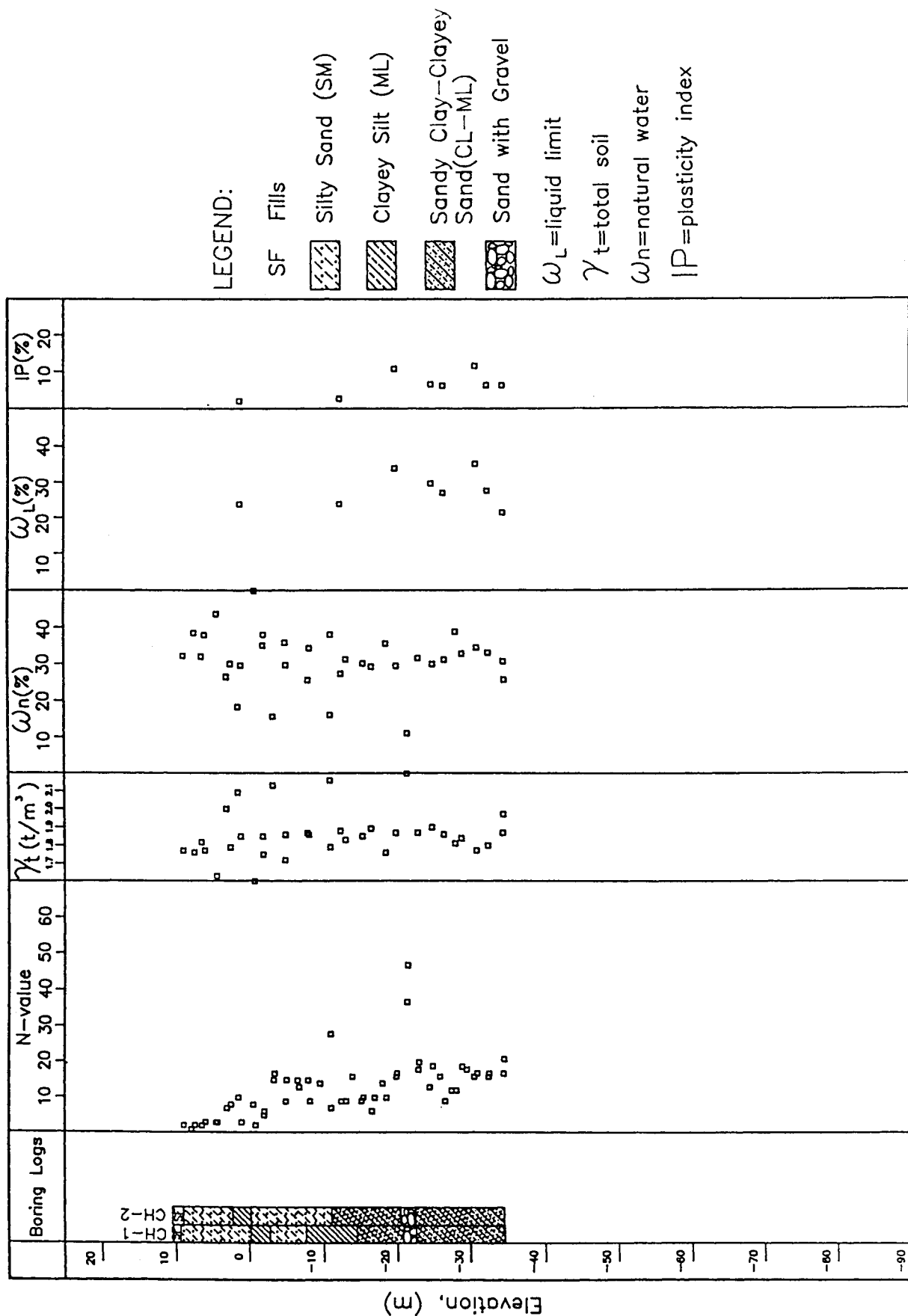
Figure 8.A.6-1  
Location of project site.



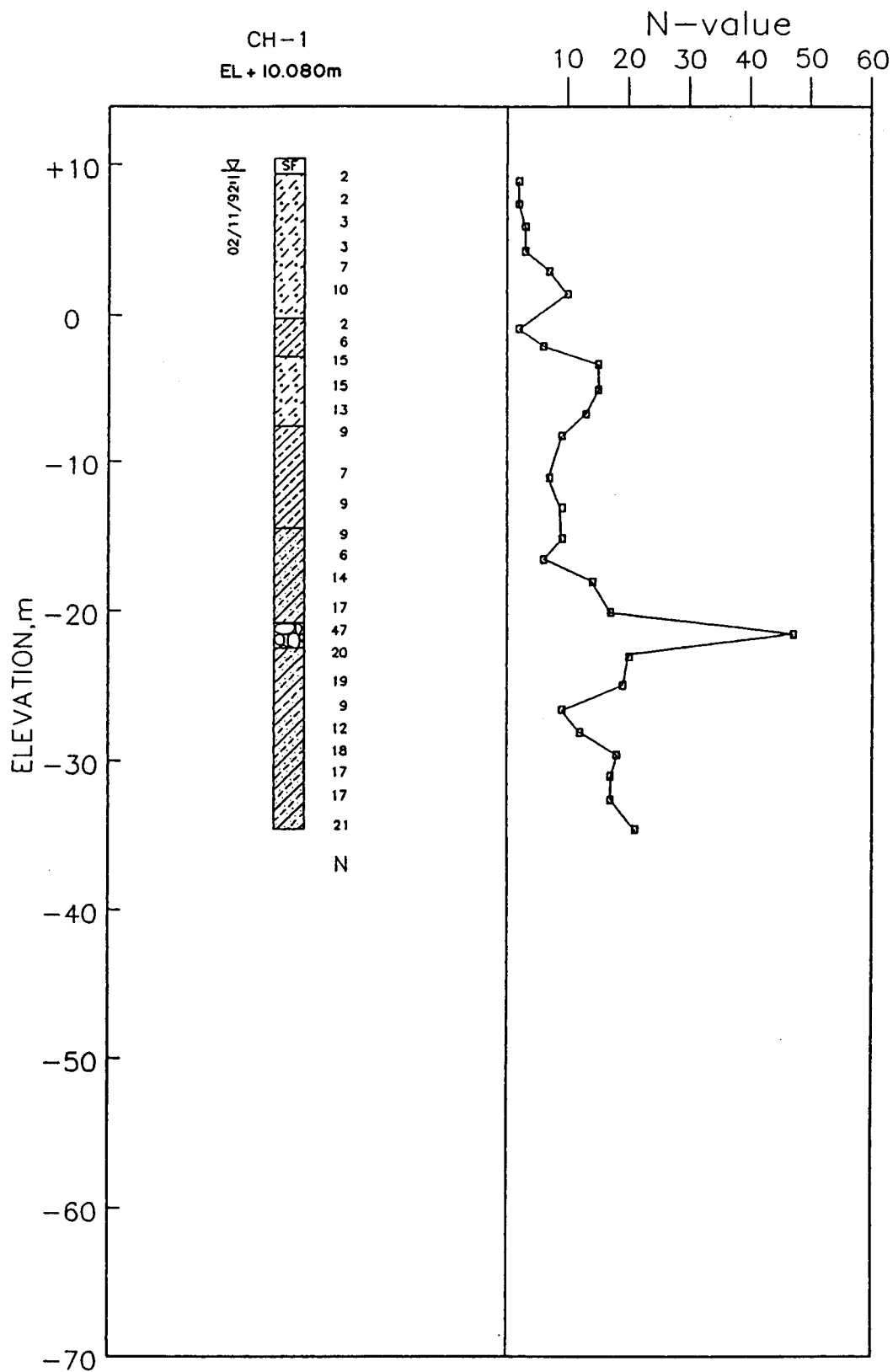
**Figure 8.A.6-2**  
Borehole location.



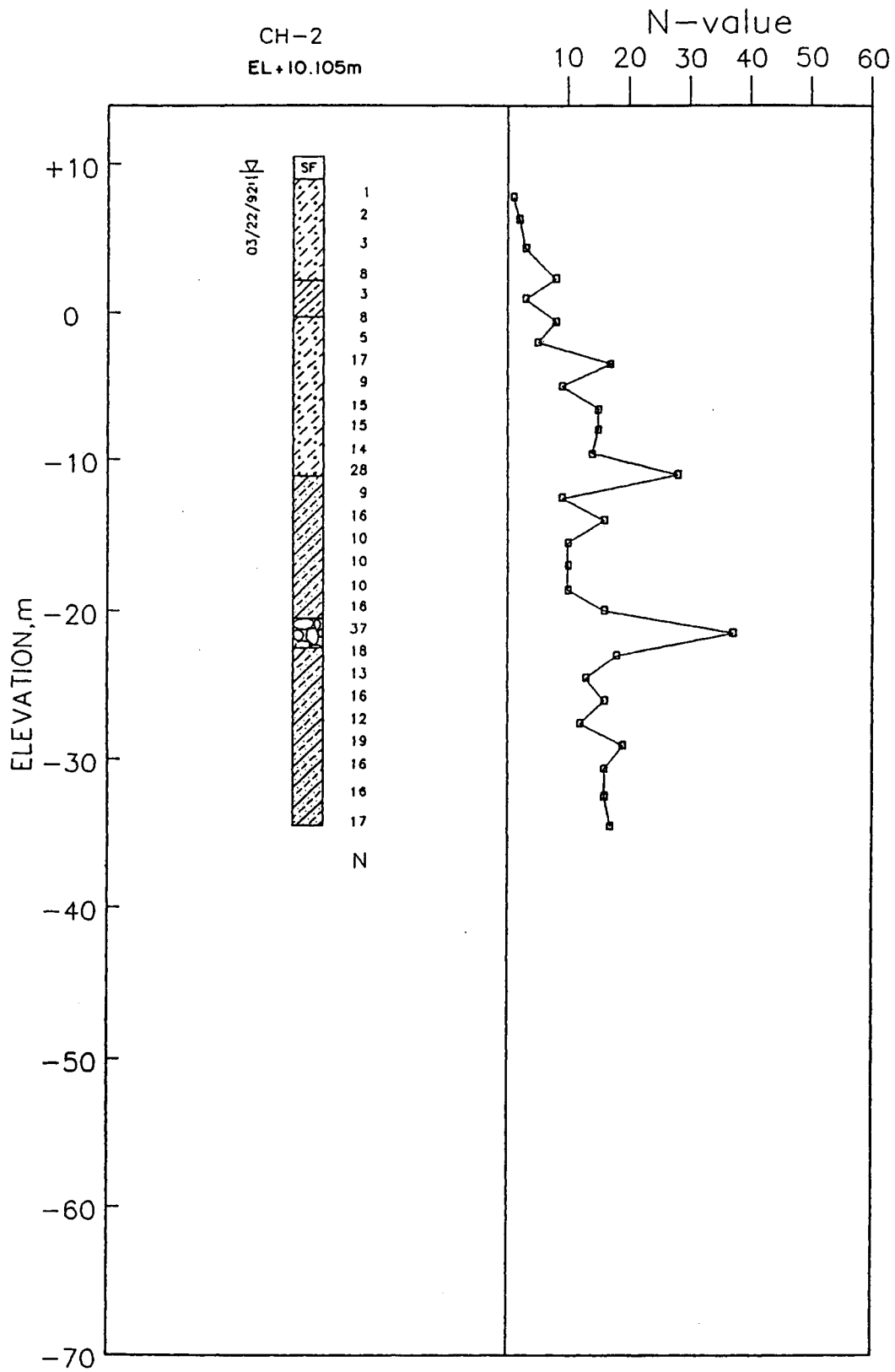
**Figure 8.A.6-3**  
Layout of hammer performance analyzer test.



**Figure 8.A.6-4**  
Summary of boring logs, SPT-N values, and soil properties.



**Figure 8.A.6-5**  
SPT-N values distributed with depth on boring CH-1.



**Figure 8.A.6-6**  
SPT-N values distributed with depth on boring CH-2.

## APPENDIX 8.A.6.A—SUBSURFACE EXPLORATION LOGS

### Description Guide for Consistency and Density of Soils

Cohesionless Soil		Cohesive Soil	
N-value of SPT	Description	N-value of SPT	Description
0 - 4	Very Loose	0 - 2	Very Soft (extruded between fingers when squeezed)
4 - 10	Loose	2 - 4	Soft (molded by light finger pressure)
10 - 30	Medium Dense	4 - 8	Medium (molded by strong finger pressure)
30 - 50	Dense	8 - 15	Stiff (readily indented by thumb but penetrated with great effort)
>50	Very Dense	15 - 30	Very Stiff (readily indented by thumbnail)
		>30	Hard (indented with difficulty by thumbnail)



## Soil Description Terms

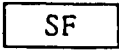


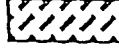
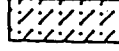

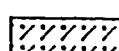
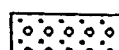
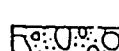

### (1) Soil Thickness

Term	Soil Thickness
Parting	< 1.6 mm
Seam	1.6 - 12.7 mm
Layer	12.7 - 300 mm
Stratum	> 300 mm





### (2) Quantitative of Materials

Term	Percentage Requirement
Trace	1 - 10 %
Little	10 - 20 %
Some	20 - 35 %
Intermixed	35 - 50 %

Legend :

	Pavement , Fill or Topsoil
	Silty Clay or Sandy Clay (CL)
	Silty Clay or Clayey Silt with High Plasticity (CH or MH)
	Silty Clay or Clayey Silt (CL-ML)
	Clayey Silt or Sandy Silt (ML)
	Clayey sand or Sand-clay Mixture (SC)
	Silty sand or Sand-silt Mixture (SM)
	Sand or Gravelly Sand with Little or No Fines (SW or SP)
	Silty Gravel (GM)
	Gravel or Sand-gravel Mixture with Little or No Fine (GW or GP)

N      Blow count of SPT , blows / 30cm

	T-1	Shelby tube Sample
	S-0	No Recovery
	S-1	Split Spoon Sample by Using Donut Hammer
	S-1*	Split Spoon Sample by Using Automatic Trip Hammer

Legend for Results of Subsurface Exploration

RESULTS OF SUBSURFACE EXPLORATION																			
PROJECT: LOTUNG EXPLORATION PROGRAM				Ground EL.: +10.080m		Date: 02/11/92 - 02/18/92		MOH AND ASSOCIATES Consulting Engineers		亞新工程顧問公司									
Hole No.: CH-1		Location: LOTUNG				G.W.L.: +9.680m		Sheet No.: 2 of 3											
Depth m	Sample No.	S. P. T.			Core Rec.	RQD %	F.I.	LOG	Description	Grain Size %			USCS Classi- fication	$\gamma_t$ t/m <sup>3</sup>	$\omega_n$ %	$G_s$	$\omega_L$ %	$I_p$ %	
		15 cm	15 cm	15 cm						Gravel	Silt	Clay							
-10	S-10	5	7	8					Silty Fine to Coarse Sand; gray, medium dense. some gravel with max. size less than 1.5 cm; (SM).	0	73	23	4	SM	1.86	29.7	2.70	-	NP
-17	T-3 S-11	3	4	9					- 13.2-14.8m: artesian encountered. - 14.8-17.1m: interbedded with sandy silt, decayed wood.										
-19	T-4 S-12	2	3	6					18.0 m						1.86	34.4			
-21	S-13	1	2	5					Sandy Silt to Clayey Silt; gray, stiff, low plastic. trace fine sand;(ML).	0	22	48	30	-	1.79	38.2	2.70	-	-
-23	T-6 S-14	2	4	5					- 19.4-20.5m: Silty Fine to Coarse Sand with Gravel; medium dense, artesian encountered. - 20.5-23.8m: occasionally wit silty clay seams.						1.83	31.4			
-25	T-7 S-15	3	3	6					24.9 m										
-27	S-16	2	2	4					Silty Clay to Clayey Silt gray, medium stiff, low plastic . trace fine sand; (CL-ML).	0	9	72	19	-	1.89	29.4	2.70	-	-
-29	S-17	3	5	9					- 28.0-31.2m: stiff.										

RESULTS OF SUBSURFACE EXPLORATION																			
PROJECT: LOTUNG EXPLORATION PROGRAM				Ground EL.: +0.080m				Date: 02/11/92 - 02/18/92		MOH AND ASSOCIATES Consulting Engineers 亞新工程顧問公司									
Hole No.: CH-1		Location: LOTUNG						G.W.L.: +9.680m		Sheet No.: 3 of 3									
Depth Sample m	No.	S. P. T.			Core Rec. %	RQD %	F.I. LOG	Description	Grain Size %			USCS Classi- fication	r <sub>f</sub> t/m <sup>2</sup>	ω <sub>n</sub> %	G <sub>s</sub> %	ω <sub>L</sub> %	I <sub>p</sub> %		
		15 cm	15 cm	15 cm					Gravel	Sand	Silt							Clay	
-	S-18	4	7	10				31.2 m											
-32	S-19	25	23	24				Sandy Gravel; gray, dense, some fine to coarse sand. artesian encountered; (GP).											
-	S-20	5	9	11				32.9 m											
-34	T-8							Silty Clay to Clayey Silt; gray, stiff, low-plastic; (CL-ML). - 32.9-37.5m: with sandy silt, very stiff - 39.5-44.3m: very stiff, organic matter.											
-	S-21	5	7	12					ML	1.90	30.0	-	29.8	6.6					
-36	S-22	2	3	6					CL-ML	1.86	31.2	-	27.1	6.2					
-38	S-23	4	5	7						1.81	38.9								
-40	S-24	5	8	10															
-	T-9																		
-	S-25	6	7	10															
-42	S-26	4	7	10															
-44	T-10							45.0 m											
-	S-27	6	10	11					CL-ML	1.97	25.8	2.70	21.5	6.3					

RESULTS OF SUBSURFACE EXPLORATION																
PROJECT : LOTUNG EXPLORATION PROGRAM				Ground EL. : + 10.105m		Date: 03/02/92 - 03/05/92		MOH AND ASSOCIATES Consulting Engineers 亞新工程顧問公司								
Hole No.: CH-2		Location: LOTUNG		G.W.L. : + 9.605m		Sheet No.: 1 of 3										
Depth Sample m	No.	S. P. T.			Core Rec. %	F.I. LOG	Description	Grain Size %			USCS Classi- fication	$\gamma_t$ t/m <sup>3</sup>	$\omega_n$ %	$G_s$	$\omega_L$ %	$I_p$ %
		15 cm	15 cm	15 cm				Gravel	Sand	Silt						
-						SF	Fill: Clayey Silt with Gravel; grayish brown; (SF).									
- 2	T-1 S-0	0.3	0.3	0.3			Silty Fine Sand; gray. very loose; (SM). - 2.8-4.0m: interbedded with clayey silt, decayed wood. - 4.0-8.3m: loose.									
- 4	T-2 S-1	0.5	0.5	1				0	40	43	17		1.82	32.1	2.70	-
- 6	T-3 S-2	2	1	2												
- 8	T-4 S-3	1	2	6				0	68	29	3		1.79	30.2	2.70	NP
- 10	S-4 T-5 S-5	1	1	2			Clayey Silt to Sandy Silt; gray, soft, low plastic; (ML).	0	48	44	8		1.85	29.8	2.70	24.1
- 12	S-6	2	2	3			Silty Fine Sand; gray, loose. interbedded with silty clay and sandy silt; (SM). - 13.0-14.6m: with gravel. medium dense, artesian encountered.	0	62	34	4		1.85	35.2	2.70	-
- 14	S-7	8	8	9												NP

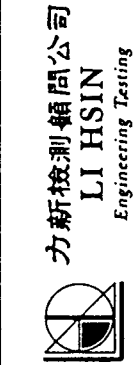
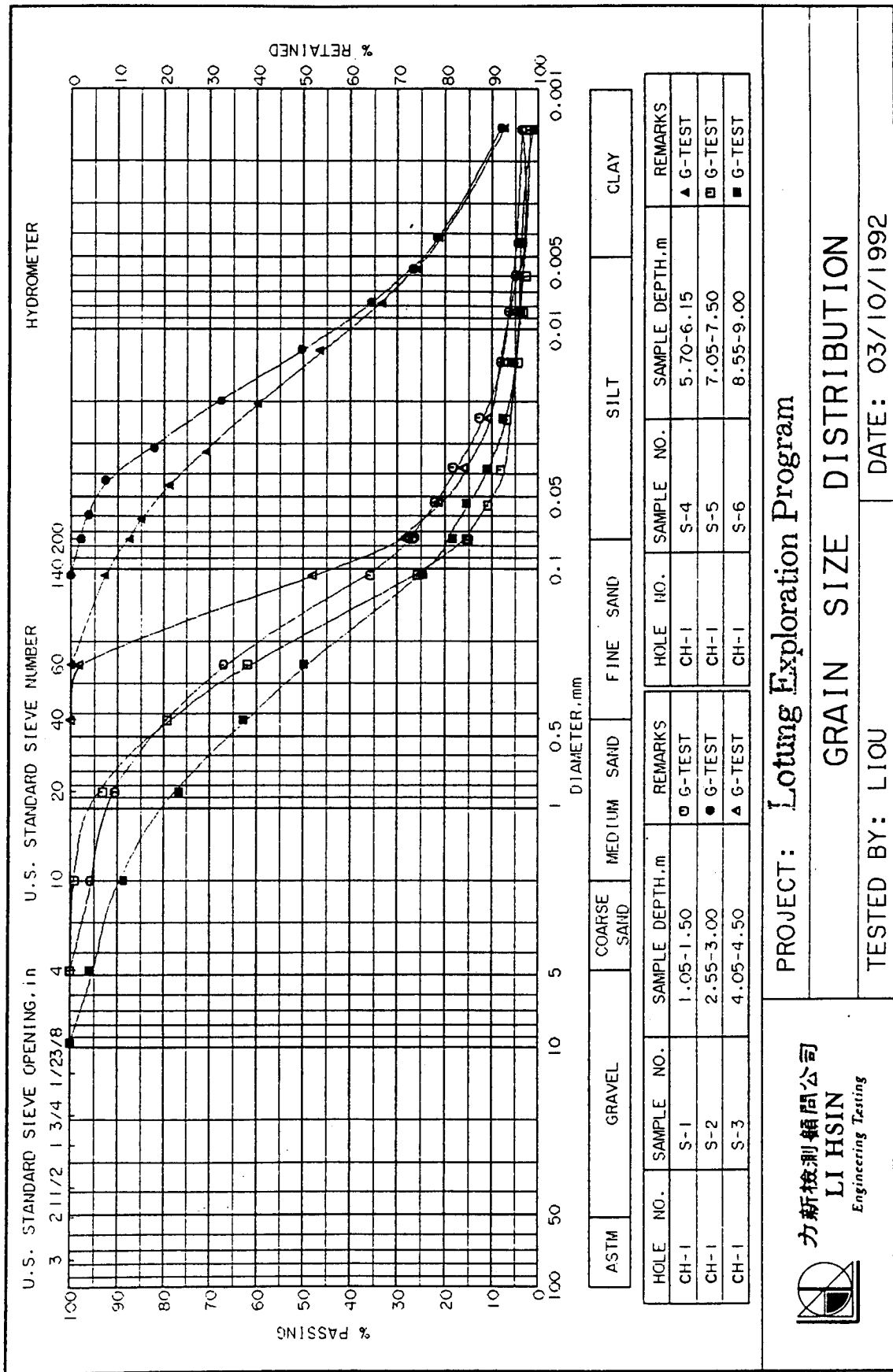
RESULTS OF SUBSURFACE EXPLORATION																			
PROJECT : LOTUNG EXPLORATION PROGRAM				Ground EL.: +10.105m		Date: 03/02/92 - 03/05/92		MOH AND ASSOCIATES Consulting Engineers 亞新工程顧問公司											
Hole No.: CH-2		Location: LOTUNG		G.W.L.: +9.605m		Sheet No.: 2 of 3													
Depth m	Sample No.	S. P. T.				Core Rec. %	RQD %	F.I.	LOG	Description	Grain Size %			USCS Classi- fication	r <sub>f</sub> 1/m <sup>2</sup>	ω <sub>n</sub> %	G <sub>s</sub> %	ω <sub>L</sub> %	I <sub>p</sub> %
		15 cm	15 cm	15 cm	15 cm						Gravel	Sand	Silt						
-	S-8*	3	4	5						- 14.6-18.5m: organic matter and decayed wood. - 17.1-18.5m: interbedded with clayey silt. - 20.9-21.6m: artesian encountered.	0	17	75	8	-	1.72	36.0	2.70	-
-	T-6																		
- 17	S-9	3	7	8															
-	S-10	4	5	10							0	48	43	9	-	1.87	25.7	2.70	-
- 19	T-7*									21.6 m Silty Clay to Clayey Silt; gray, stiff, low plastic; (CL-ML). - 23.9-24.8m: Silty Fine to Medium Sand with Gravel; medium dense, artesian encountered. - 24.8-28.4m: occasionally with medium to coarse sand partings and gravel, decayed wood. - 28.4-31.0m: interbedded with sandy silt.									
-	S-11	7	7	7															
- 21	S-12	11	15	13											2.16	16.3			
-	S-13*	3	4	5															
- 23	S-14	5	7	9							0	6	66	28	1.88	27.5	2.70	24.0	2.7
-	T-8*																		
- 25	S-15*	3	4	6											1.85	30.3			
-	S-16	4	4	6															
- 27	T-9																		
-	S-17	2	4	6											1.76	35.7			
- 29																			

RESULTS OF SUBSURFACE EXPLORATION																			
PROJECT: LOTUNG EXPLORATION PROGRAM				Ground EL.: +10.105m				Date: 03/02/92 - 03/05/92				MOH AND ASSOCIATES Consulting Engineers 亞新工程顧問公司							
Hole No.: CH-2				Location: LOTUNG				G.W.L.: +9.605m				Sheet No.: 3 of 3							
Depth m	Sample No.	S. P. T.			Core Rec. %	ROD F.I. LOG	Description	Grain Size %			USCS Classi- fication	$\gamma_t$ t/m <sup>3</sup>	$\omega_n$ %	$G_s$ %	$\omega_L$ %	$I_p$ %			
		15 cm	15 cm	15 cm				Gravel	Sand	Silt							Clay		
-	S-18	5	7	9			31.0 m	-	-	-	CL	1.87	29.6	-	34.1	10.8			
-32	S-19	12	19	18			Sandy Gravel (max. size less than 2 cm); gray, dense, artesian encountered; (GP).					2.23	11.2						
-	S-20	4	8	10			33.0 m					1.87	31.8						
-34	T-10						Silty Clay to Clayey Silt; gray, very stiff, low plastic; (CL-ML). - 39.1-40.6m: organic matter and decayed wood. - 44.3-45.0m: interbedded with silty sand.												
-	S-21	3	5	8															
-36	S-22	4	6	10															
-	S-23	3	5	7									1.84	32.9					
-38	S-24	5	7	12															
-40	T-11																		
-	S-25	5	7	9															
-42	S-26	5	7	9				-	-	-	CL-ML	1.80	33.2	-	27.8	6.4			
-	S-27	4	7	10			45.0 m					1.87	30.8						
-44	T-12																		

RESULTS OF SUBSURFACE EXPLORATION																		
PROJECT : LOTUNG EXPLORATION PROGRAM				Ground EL.: +10.080m		Date: 02/11/92 - 02/18/92		MOH AND ASSOCIATES Consulting Engineers 亞新工程顧問公司										
Hole No.: CH-1		Location: LOTUNG		G.W.L.: +9.680m		Sheet No.: 1 of 3												
Depth m	Sample No.	S. P. T.				Core Rec. %	ROD F.I. %	LOG	Description	Grain Size %			USCS Classi- fication	$\gamma_t$ t/m <sup>3</sup>	$\omega_n$ %	$G_s$ %	$\omega_L$ %	$I_p$ %
		15 cm	15 cm	15 cm	15 cm					Gravel	Sand	Silt						
-	S-1	0.5	0.5	1			SF	Fill: Sandy Silt to Clayey Silt with Gravel; grayish brown, low-plastic:(SF), 1.0m	0	73	22	5	SM	1.77	32.3	2.70	-	NP
- 2	S-2	1	1	1					0	2	73	25	-	1.76	38.6	2.70	-	-
- 4	S-3	1.5	1.5	1					0	71	26	3	SM	1.77	38.0	2.70	-	NP
-	T-1																	
- 6	S-4	1	1	2					0	13	63	24	-	1.63	43.8	2.70	-	-
-	S-5	2	2	5					0	84	13	3	SM	2.00	26.6	2.70	-	NP
- 8	S-6	5	5	5					5	76	15	4	SM	2.09	18.4	2.70	-	NP
- 10	T-2																	
-	S-7	2	1	1										1.44	83.4			
- 12	S-8	2	2	4					0	21	74	5	-	1.75	38.2	2.70	-	-
-	S-9	5	7	8										2.13	15.7			
- 14																		



## **APPENDIX 8.A.6.B–LABORATORY TESTING**



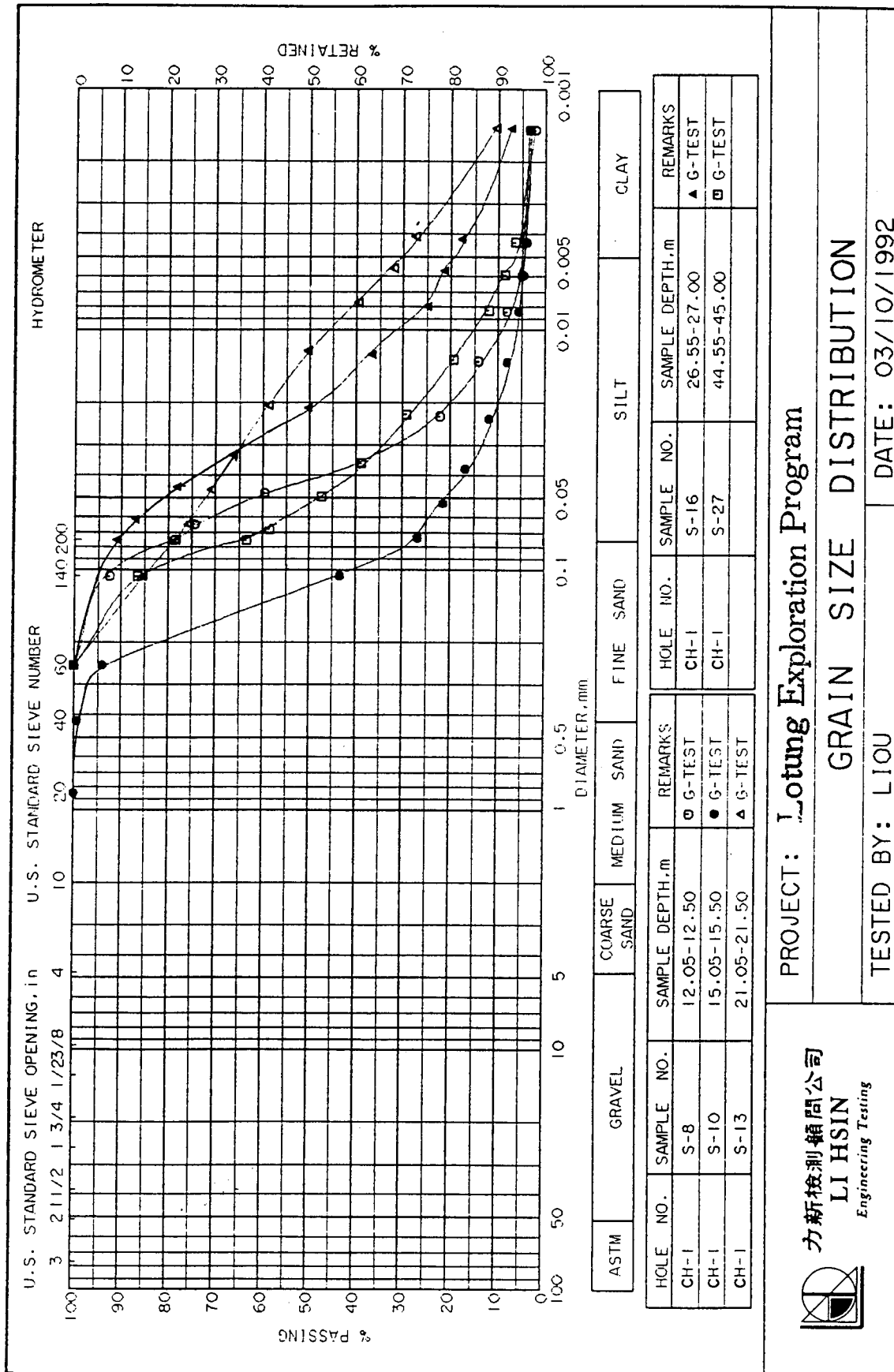
力新檢測顧問公司  
LI HSIN  
Engineering Testing

PROJECT: Lotung Exploration Program

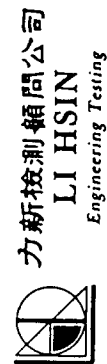
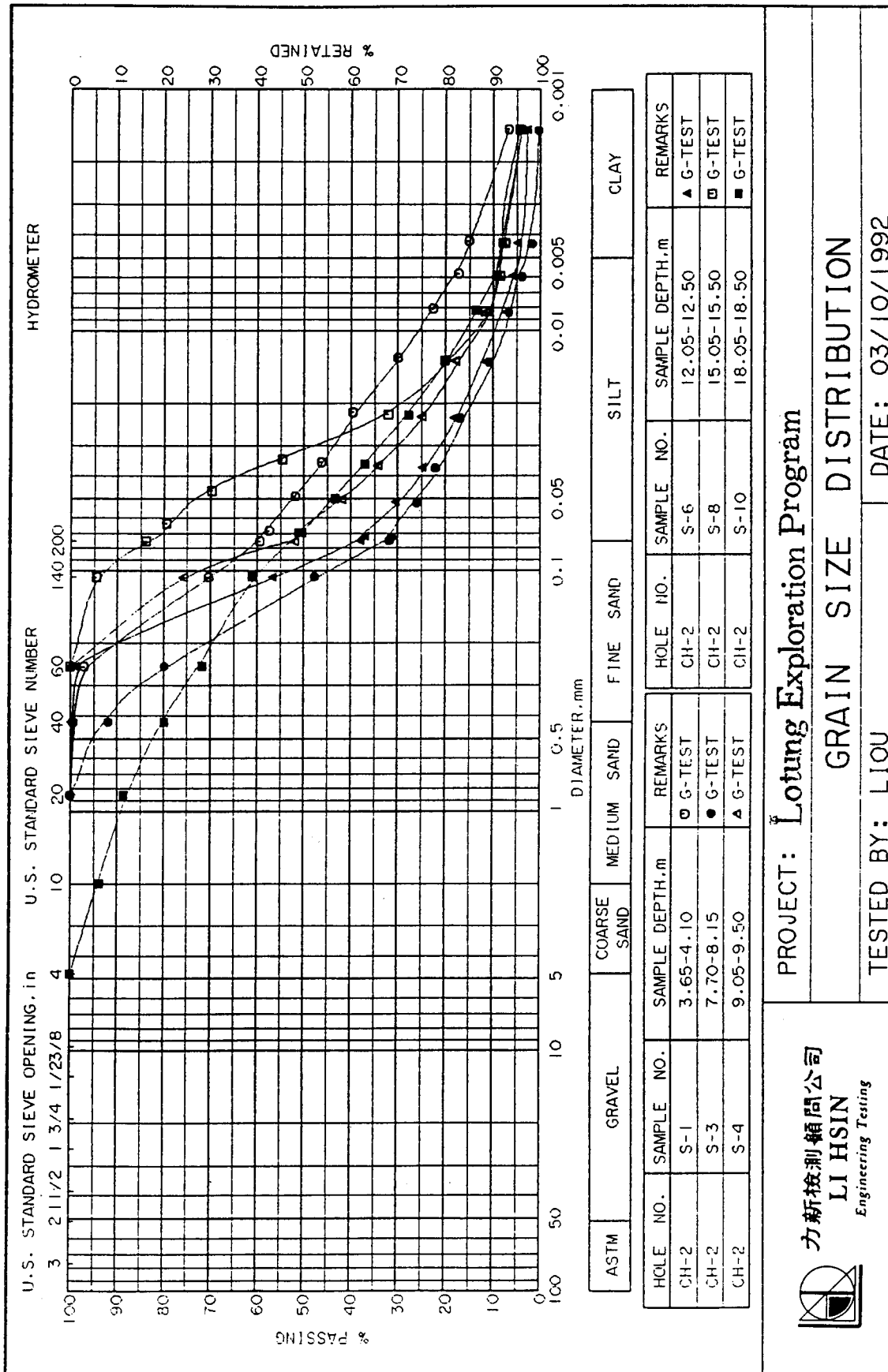
### GRAIN SIZE DISTRIBUTION

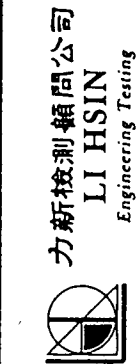
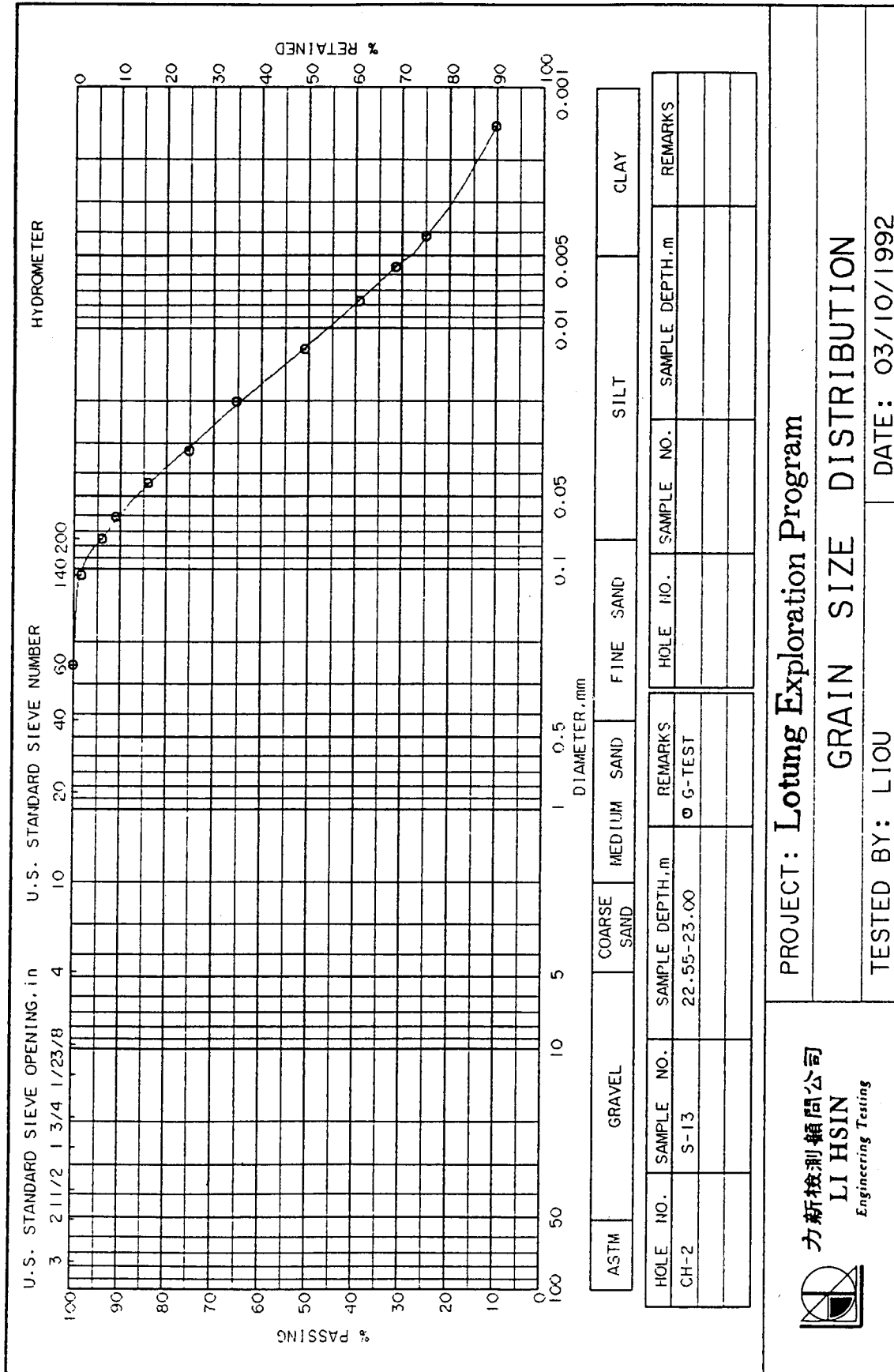
TESTED BY: LIOU

DATE: 03/10/1992







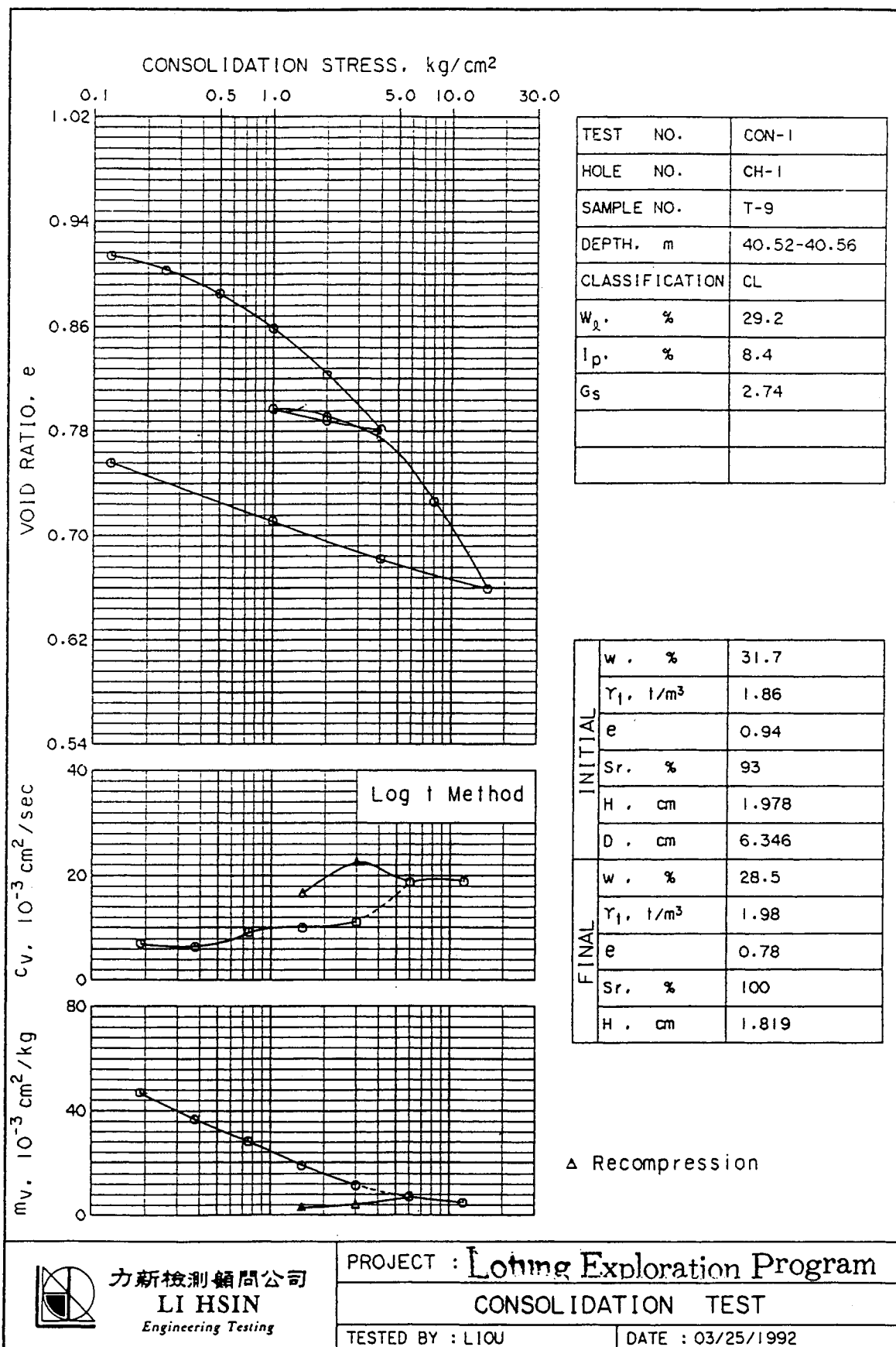


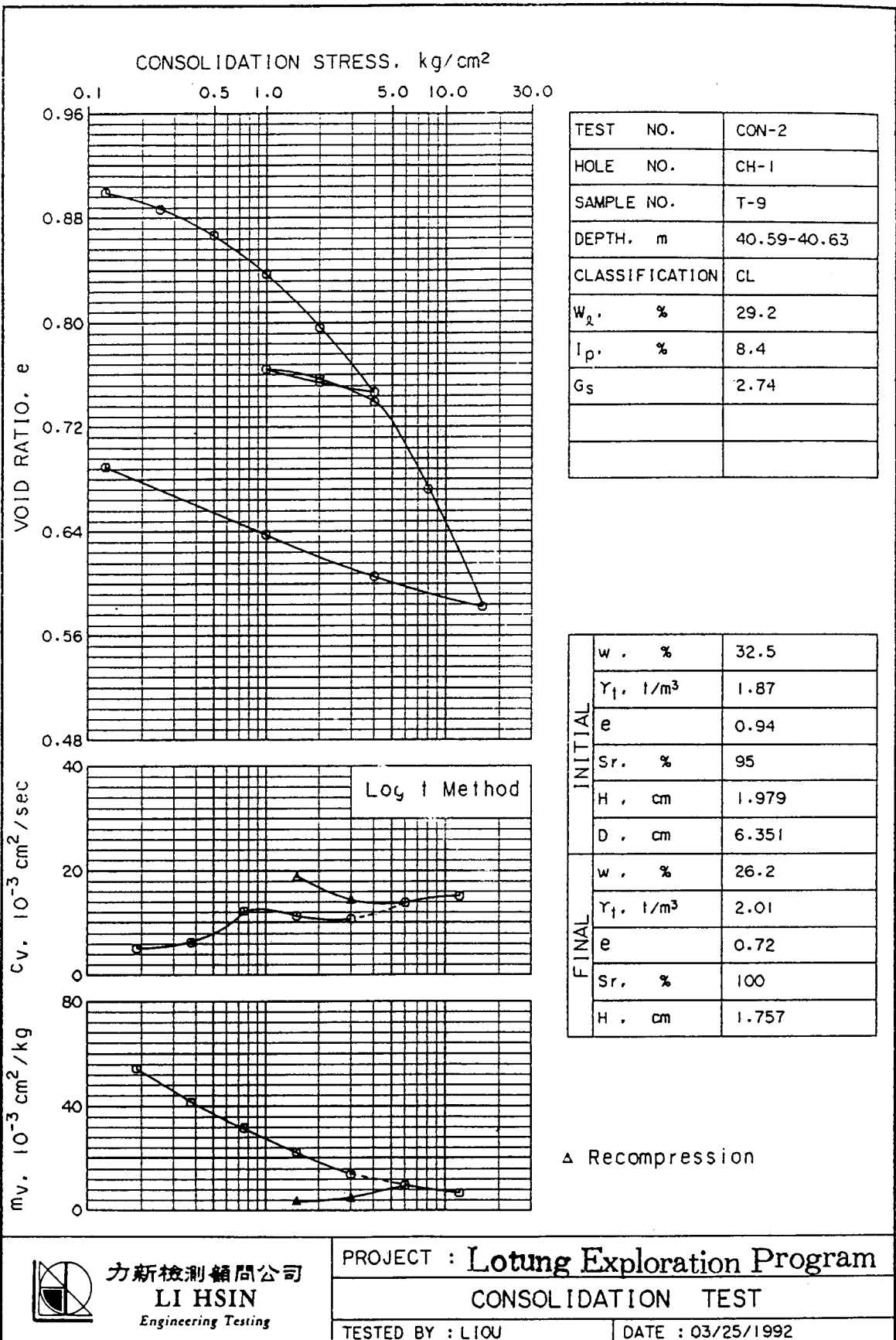
PROJECT: Lotung Exploration Program

# GRAIN SIZE DISTRIBUTION

TESTED BY: LIOU

DATE: 03/10/1992







### Test Results of Bag Sample

Water Content (%) : 7.5

Specific Gravity : 2.73

Grain-Size : Gravel - 78%

Sand - 16%

Silt - 5%

Clay - 1%

Soil Classification : Sandy Gravel (GP-GM);  
brownish, little fine  
to coarse sand.







**WARNING:** This Document contains information classified under U.S. Export Control regulations as restricted from export outside the United States. You are under an obligation to ensure that you have a legal right to obtain access to this information and to ensure that you obtain an export license prior to any re-export of this information. Special restrictions apply to access by anyone that is not a United States citizen or a Permanent United States resident. For further information regarding your obligations, please see the information contained below in the section titled "Export Control Restrictions."

### Export Control Restrictions

Access to and use of EPRI Intellectual Property is granted with the specific understanding and requirement that responsibility for ensuring full compliance with all applicable U.S. and foreign export laws and regulations is being undertaken by you and your company. This includes an obligation to ensure that any individual receiving access hereunder who is not a U.S. citizen or permanent U.S. resident is permitted access under applicable U.S. and foreign export laws and regulations. In the event you are uncertain whether you or your company may lawfully obtain access to this EPRI Intellectual Property, you acknowledge that it is your obligation to consult with your company's legal counsel to determine whether this access is lawful. Although EPRI may make available on a case by case basis an informal assessment of the applicable U.S. export classification for specific EPRI Intellectual Property, you and your company acknowledge that this assessment is solely for informational purposes and not for reliance purposes. You and your company acknowledge that it is still the obligation of you and your company to make your own assessment of the applicable U.S. export classification and ensure compliance accordingly. You and your company understand and acknowledge your obligations to make a prompt report to EPRI and the appropriate authorities regarding any access to or use of EPRI Intellectual Property hereunder that may be in violation of applicable U.S. or foreign export laws or regulations.

### About EPRI

EPRI creates science and technology solutions for the global energy and energy services industry. U.S. electric utilities established the Electric Power Research Institute in 1973 as a nonprofit research consortium for the benefit of utility members, their customers, and society. Now known simply as EPRI, the company provides a wide range of innovative products and services to more than 1000 energy-related organizations in 40 countries. EPRI's multidisciplinary team of scientists and engineers draws on a worldwide network of technical and business expertise to help solve today's toughest energy and environmental problems.

EPRI. Electrify the World

---

TR-102293-V3

---

© 1993 Electric Power Research Institute (EPRI), Inc. All rights reserved. Electric Power Research Institute and EPRI are registered service marks of the Electric Power Research Institute, Inc. EPRI. ELECTRIFY THE WORLD is a service mark of the Electric Power Research Institute, Inc.

Printed on recycled paper in the United States of America